ISTANBUL TECHNICAL UNIVERSITY ★ INSTITUTE OF SCIENCE AND TECHNOLOGY

175814

MODELING LONG RANGE TRANSPORT OF EUROPEAN AIR POLLUTANTS TO THE EAST MEDITERRANEAN REGION: AN EPISODIC ANALYSIS FOR ANTALYA

Ph.D. Thesis by

Muwaffaq FREIWAN, M.Sc. Eng.

(511022008)

Date of submission : 25 August 2005

Date of defence examination : 11 October 2005

Supervisor (Chairman) : Prof. Dr. Selahattin İNCECİK

Members of the Examining Committee : Prof. Dr. Gürdal TUNCEL (METU)

Assoc. Prof. Dr. Yurdanur S. ÜNAL (ITU)

Prof. Dr. Orhan YENİGÜN (BU)

Assoc. Prof. Dr. Kadir ALP (ITU)

OCTOBER 2005

İSTANBUL TEKNİK ÜNİVERSİTESİ ★ FEN BİLİMLERİ ENSTİTÜSÜ

AVRUPA HAVA KİRLETİCİLERİNİN DOĞU AKDENİZ BÖLGESİNE UZUN MENZİL TAŞIMININ MODELLENMESİ: ANTALYA İÇİN BİR EPİSODİK ANALİZ

DOKTORA TEZİ
Y. Müh. Muwaffaq FREIWAN
(511022008)

Tezin Enstitüye Verildiği Tarih: 25 Ağustos 2005
Tezin Savunulduğu Tarih: 11 Ekim 2005

Tez Danışmanı :	**Prof. Dr. Selahattin İNCECİK**
Diğer Jüri Üyeleri	**Prof. Dr. Gürdal TUNCEL (ODTÜ)**
	Doç. Dr. Yurdanur S. ÜNAL (İTÜ)
	Prof. Dr. Orhan YENİGÜN (BÜ)
	Doç. Dr. Kadir Alp (ITÜ)

EKİM 2005

ACKNOWLEDGMENT

Firstly, I thank God because he has awarded me the willpower, patience, health and sedulity to bring this endeavor to completion.

Secondly, I wish to express my eternal appreciations to my life-partner, my darling, Hana for her great support and encouragement since the first day of my graduate study. I too much appreciate her altruism, patience and great efforts; she accomplished to sail alone in a huge boat through a stormy ocean with our four lovely children - Laith, Marah, Saif and Mohammad. I apologize to all of them for any inconvenience that I probably caused while I am abroad away from home, wishing to have more motivating and illuminating future together.

I am pleased to express my deep gratitude and great appreciation to my supervisor Prof. Dr. Selahattin İncecik for his valuable help, support, patience and successful guidance during all the stages of the study and for his beneficial scientific discussions and constructive suggestions during the preparation of this thesis.

I am grateful to the supervision committee members Prof. Gürdal Tuncel and Assoc. Prof. Yurdanur S. Ünal for their beneficial discussions and valuable suggestions. I also acknowledge the examining committee Prof. Gürdal Tuncel, Assoc. Prof. Yurdanur S. Ünal, Prof. Orhan Yenigün and Assoc. Prof. Kadir Alp for their meaningful discussions, patience and cooperation. Special thanks to Prof. Gürdal Tuncel for his appreciated contributions since the beginning of the study.

I would like to thank Dr. Ümit Anteplioğlu, Dr. Tayfun Kindap, Dr. Marina Astitha, Dr. Talat Odman, Dr. Chris Emery, Dr. Sebnem Andreani-Aksoyoglu, Suha Syouf and Ufuk Utku Turuncuoğlu for their assistance. I also thank Deniz Demirhan, Dr. Sevinç Sırdaş, Dr. Ahmet Duran Sahin, Ahmet Oztopal, Ceyhan Kahya and all the staff members of the Department of Meteorological Engineering and the Faculty of Aeronautics and Astronautics in Istanbul Technical University for their kindness and hospitality.

Finally I am grateful for all assistance, material and moral support given by my brothers and sisters and any relative or friend of mine.

October 2005 Muwaffaq FREIWAN

CONTENTS

ACKNOWLEDGMENT iii
CONTENTS iv
ABBREVIATIONS vii
LIST OF TABLES ix
LIST OF FIGURES x
LIST OF SEMBOLS xvi
ÖZET xix
SUMMARY xxi

1. INTRODUCTION 1
1.1 Objectives 11
1.2 Methodology 12

2. CLIMATOLOGY OF THE MEDITERRANEAN AND SOUTHEASTERN EUROPE 14
2.1 Topography 14
2.2 Cyclogenesis 15
2.2.1 Spatial and temporal variability of cyclogenesis 16
2.3 Anticyclogenesis 18
2.4 Analysis of Sulfate Measurements in Antalya and Episode Selection 21
2.5 Climatological Characteristics of the Study Period, 24 – 31 August 1998 23
2.5.1 Climatology during the two days before the episode, 24 and 25 August 1998 23
2.5.2 Climatology of the episodic period, 26 – 29 August 1998 25
2.5.3 Climatology during the two days after the episode, 30 and 31 August 1998 26

3. ATMOSPHERIC CHEMISTRY AND PHYSICS OF AEROSOLS 27
3.1 Physical and Chemical Processes in the Atmosphere 28
3.1.1 Physical processes 29
3.1.1.1 Nucleation 29
3.1.1.2 Particle growth 31
3.1.1.3 Coagulation 33
3.1.1.4 Deposition 34
3.1.2. Chemical processes 34
3.1.2.1 Gas phase reactions 34
3.1.2.2 Vapor-particle equilibrium 35
3.2 Chemical Composition 36
3.2.1 Acid aerosols (sulfates-nitrates) 36
3.2.2 Carbon-containing aerosols 37
3.2.2.1 Elemental carbon- primary organic carbon 37

3.2.2.2. Secondary organic matter formation (secondary organic carbon) 37
3.2.2.3. Metal and other trace elements 38
3.3. Biological Aerosols 39
3.4. Status of Modeling Aerosol Processes 39
3.4.1. Mesoscale models 40
3.4.2. Long range transport models 40
3.5. Effects of Aerosols on Ecosystems, Climate and Materials 41
3.5.1. Acidification-Eutrophication 41
3.5.2 Visibility reduction 41
3.5.3 Radiative forcing 41
3.5.4 Soiling and damage to materials 42

4. THE MESOSCALE METEOROLOGICAL MODEL, MM5 43
4.1 Brief Description 43
4.2 Some Features of MM5 Modeling System – Version 3.61, the Latest Release 44
4.3 The MM5 Model Horizontal and Vertical Grid 45
4.4 Nesting 48
4.5 Lateral Boundary Conditions 48
4.6 Nonhydrostatic Dynamics versus Hydrostatic Dynamics 49
4.6.1 Reference state in the nonhydrostatic model 51
4.7 Four-Dimensional Data Assimilation 52
4.8 Land-Use Categories 52
4.9 Map Projections and Map-Scale Factors 52
4.10 The Auxiliary Programs of the Mesoscale Modeling System, MM5 53
4.11 The Basic Equations of MM5 56
4.12 Derivation of the Basic Equations of MM5 57

5. THE AIR QUALITY MODELING SYSTEM 63
5.1 The Comprehensive Air Quality Model with Extension (CAMx) 63
5.1.1 Description of the model 63
5.1.1.1 CAMx grid configuration 66
5.1.2 Transport fundamentals 67
5.1.3 Chemistry 70
5.1.3.1 Gas phase chemistry 70
5.1.3.2 Aerosol chemistry 72
5.1.4 Pollutant removal 73
5.1.4.1 Pollutant removal by precipitation (wet deposition) 73
5.1.4.1.1 Wet scavenging of ambient gasses 75
5.1.4.1.2 Wet scavenging of gasses dissolved in cloud water 77
5.1.4.1.3 Wet scavenging of in-cloud aerosols 78
5.1.4.1.4 Wet scavenging of dry particles 78
5.1.4.2 Dry deposition 79
5.1.4.2.1 Dry deposition of gasses 80
5.1.4.2.2 Dry deposition of aerosols 72
5.2 European Anthropogenic Sulfur Emissions 84

6. RESULTS AND DISCUSSION 89
6.1 The Mesoscale Meteorological Model, MM5 89

6.1.1 Air mass trajectories to the southeastern Mediterranean region 95
6.1.1.1 Definition 95
6.1.1.2 Trajectory calculation and plot for the southeastern Mediterranean Region 95
6.1.2 Performance verification of the Mesoscale Meteorological Model, MM5 98
6.2 The Air Quality Chemical Model, CAMx 102
6.2.1 CAMx Inputs 102
6.2.2 Results of CAMx Model 106
6.2.3 Performance verification of the CAMx Model 108

7. CONCLUSION **112**

REFERENCES **115**

APPENDICES **128**

CURRICULUM VITAE **315**

ABBREVIATIONS

ALD2 : CB4 higher **ALD**ehyde
AMS : American **M**eteorological **S**ociety
CAMx : **C**omprehensive **A**ir Quality **M**odel with e**x**tension
CBM : **C**arbon **B**ond **M**echanism
CCRS : Primary PM-**C**oarse **CRuS**tal
CGs : **C**ondensible **O**rganic **G**ases
CISK : **C**onditional **I**nstability of the **S**econd **K**ind
CIT : **C**alifornia **I**nstitute of **T**echnology
CLRTAP : **C**onvention on **L**ong-**R**ange **T**ransboundary **A**ir **P**ollution
CMU : **C**arnegie **M**ellon **U**niversity
CORINAIR : **COR**e **IN**ventory of **AIR** Emissions
CPRM : **C**oarse **PRiM**ary PM
DAQM : **D**enver **A**ir **Q**uality **M**odel
EC : **E**lemental **C**arbon
ECMWF : The **E**uropean **C**entre for **M**edium-Range **W**eather **F**orecasts
EEA : **E**uropean **E**nvironment **A**gency
EMEP : **C**ooperative Programme for **M**onitoring and **E**valuation of the Long Range Transmission of **A**ir **P**ollutants in **E**urope
EPA : **E**nvironmental **P**rotection **A**gency
ETH : **ETH**ene
EU : The **E**uropean **U**nion
FAC : **F**ractional **A**erosol **C**oefficient
FDDA : **F**our-**D**imensional **D**ata **A**ssimilation
FPRM : **F**ine **PRiM**ary PM
FCRS : Primary PM-**F**ine **CRuS**tal
FORM : **FORM**adehyde
GATOR : **G**as, **A**erosol, **T**ransport and **R**adiation Model
GRIB : **GRI**dded **B**inary Format
hPa : **h**ecta**Pa**scal
HMSO : **H**er **M**ajesty's **S**tationary **O**ffice
HYPACT : **HY**brid **PA**rticle and **C**oncentration **T**ransport Package
HYSPLIT : **HY**brid **S**ingle **P**article **L**agrangian **I**ntegrated **T**rajectory
IPCC : **I**ntergovernmental **P**anel on **C**limate **C**hange
ISOP : **ISOP**rene
METU : **M**iddle **E**ast **T**echnical **U**niversity
MINOS : **M**editerranean **IN**tensive **O**xidant **S**tudy
MM5 : **M**esoscale **M**eteorological **M**odel, the 5th Generation
MRPO : **M**idwest **R**egional **P**lanning **O**rganization
MSL : **M**ean **S**ea **L**evel
NCAR : **N**ational **C**enter of **A**tmospheric **R**esearch
NCEP : **N**ational **C**enters for **E**nvironmental **P**rediction
OECD : **O**rganization for **E**conomic **C**o-operation and **D**evelopment
OLE : CB4 **OLE**fins (anthropogenic)

OTAG : **O**zone **T**ransport **A**ssessment **G**roup
PAR : CB4 **PAR**affin
PAVE : **P**ackage for **A**nalysis and **V**isualization of **E**nvironmental data
PEC : **P**rimary **E**lemental **C**arbon
PBAP : **P**rimary **B**iological **A**erosol **P**articles
PM : **P**articulate **M**atter
POA : **P**rimary PM-fine **O**rganic **A**erosol
PSU : **P**ennsylvania **S**tate **U**niversity
RADM : **R**egional **A**cid **D**eposition **M**odel
RADM-AQ : **R**egional **A**cid **D**eposition **M**odel with **AQ**ueous chemistry
RAMS : **R**egional **A**tmospheric **M**odeling **S**ystem
RAOB : The Universal **RA**winsonde **OB**servation program
REMSAD : **RE**gulatory **M**odeling **S**ystem for **A**erosols and **D**eposition
RIP : **R**ead **I**nterpolate and **P**lot Software
RPM : **R**egional **P**articulate **M**odel
SAIMM : **S**ystem **A**pplications **I**nternational **M**esoscale **M**odel
SAPRC : **S**tatewide **A**ir **P**ollution **R**esearch **C**enter
SAQM-AERO: SARMAP **A**ir **Q**uality **M**odel with **AERO**sols
SEQUILIB : **S**ectional **EQILIB**rium Model
SOA : **S**econdary **O**rganic **A**erosol
TOL : CB4 **TOL**uene
TUV : **T**ropospheric **U**ltraviolet & **V**isible Radiation Model
UAM : **U**rban **A**irshed **M**odel
UAMAERO : **U**rban **A**irshed **M**odel for **AERO**sols
UAM-LC : **U**rban **A**irshed **M**odel Version IV with **l**inearized **C**hemistry
UNDP : **U**nited **N**ations **D**evelopment **P**rogramme
UNECE : **U**nited **N**ations **E**conomic **C**ommission for **E**urope
USGS : **U**nited **S**tates **G**eological **S**urvey
USSR : **U**nion of **S**ocialist **S**oviet **R**epublics
VISHWA : **VIS**ibility and **H**aze in the **W**estern **A**tmosphere Model
VOCs : **V**olatile **O**rganic **C**ompounds
WHO : **W**orld **H**ealth **O**rganization
WMO : **W**orld **M**eteorological **O**rganization
XYL : CB4 **XYL**ene

LIST OF TABLES

	Page No.
Table 5.1: Total national emissions of sulfur.	86
Table 5.2: Percentage of sulfur reduction (1990 – 1999) of 1990 level.	87
Table 6.1: Vertical layer structure of CAMx.	102
Table 6.2: Daily average predicted versus observed concentrations of PSO_4 and SO_2 in Antalya and Cubuk EMEP station during the period between 26 and 29 August 1998.	110
Table A.1: The largest 100 sulfur emitters in Europe.	130
Table A.2: USGS 30 second landuse categories.	133
Table A.3: CAMx landuse categories and default surface roughness Values (m) assigned to each category within CAMx.	134

LIST OF FIGURES

		Page No.
Figure 2.1	: The Mediterranean region.	14
Figure 2.2	: The average synoptic pattern represented by MSL pressure during winter months, November – March.	19
Figure 2.3	: The average synoptic pattern represented by MSL pressure during summer months, June – October.	19
Figure 2.4	: The location and topography of the Antalya station.	21
Figure 2.5	: The highest 20% discrete measurements of sulfate in Antalya.	22
Figure 4.1	: A schematic representation of the MM5 modeling system.	44
Figure 4.2	: The vertical structure of MM5 model.	46
Figure 4.3	: Schematic representation showing the horizontal Arakawa B-grid staggering of the dot and cross (x) grid points.	47
Figure 4.4	: Horizontal interpolation of regular latitude longitude onto mesoscale domain.	53
Figure 5.1	: A horizontal representation of the Arakawa C variable configuration used in CAMx.	66
Figure 5.2	: The study domain and the included countries.	85
Figure 5.3	: Total national anthropogenic sulfur emissions.	85
Figure 5.4	: Distribution of the largest 100 Sulfur emitters in Europe. ...	88
Figure 6.1	: The background maps of the coarse and nest domain.	91
Figure 6.2	: The terrain elevation in the coarse and fine domain.	92
Figure 6.3	: The USGS 24 category land-use and vegetation distribution in the coarse domain and the fine domain.	93
Figure 6.4	: Hourly temperatures (°C) observed in meteorological stations of Istanbul (Goztepe), Izmir and Antalya versus predicted by MM5 modeling system for the period from 00 Z 25 – 08 – 1998 to 00 Z 30 – 8 – 1998,.	99
Figure 6.5	: Hourly wind speed (m/s) observed at 10m height in Istanbul (Goztepe), Izmir and Antalya meteorological stations versus predicted by MM5 modeling system for the period from 00 Z 25 – 08 – 1998 to 00 Z 30 – 8 – 1998.	100
Figure 6.6	: Scattered diagram of the model predicted versus observed hourly temperature and 10m wind speed in Istanbul (Goztepe), Izmir and Antalya meteorological stations for the period from 00 Z 25 – 08 – 1998 to 00 Z 30 – 8 – 1998.	101
Figure 6.7	: The predicted hourly concentration time series of PSO4 (a) and SO_2 (b) in Antalya and Cubuk/Ankara during the period between 00 UTC 26 Aug. and 23 UTC 29 Aug. 1998.	109
Figure 6.8	: Sulfate concentration time series predicted by CAMx model using different emission inventory inputs of SO_2	111
Figure B.1	: Synoptic and climatologic situation on 24 August 1998, two days before the episode.	136

Figure B.2 : Daily mean U and V wind components (m/s) on 24 August 1998, two days before the episode. 137
Figure B.3 : The wind vector (m/s) and relative vorticity (s^{-1}) on 24 August 1998, two days before the episode. 138
Figure B.4 : Synoptic and climatologic situation on 25 August 1998, one day before the episode. 139
Figure B.5: Daily mean U and V wind components (m/s) on 25 August 1998, one day before the episode. 140
Figure B.6: The wind vector (m/s) and relative vorticity (s^{-1}) on 25 August 1998, one day before the episode. 141
Figure B.7: Synoptic and climatologic situation on 26 August 1998, the first day of the episode. 142
Figure B.8: The wind vector (m/s) and relative vorticity (s^{-1}) on 26 August 1998, the first day of the episode. 143
Figure B.9: Daily mean U and V wind components (m/s) on 26 August 1998, the first day of the episode. 144
Figure B.10: Synoptic and climatologic situation on 27 August 1998, the second day of the episode. 145
Figure B.11: Daily mean U and V wind components (m/s) on 27 August 1998, the second day of the episode. 146
Figure B.12: The wind vector (m/s) and relative vorticity (s^{-1}) on 27 August 1998, the second day of the episode. 147
Figure B.13: Synoptic and climatologic situation on 28 August 1998, the third day of the episode. 148
Figure B.14: Daily mean U and V wind components (m/s) on 28 August 1998, the third day of the episode. 149
Figure B.15: The wind vector (m/s) and relative vorticity (s^{-1}) on 28 August 1998, the third day of the episode. 190
Figure B.16: Synoptic and climatologic situation on 29 August 1998, the fourth and the last day of the episode. 151
Figure B.17: Daily mean U and V wind components (m/s) on 29 August 1998, the fourth and last day of the episode. 152
Figure B.18: The wind vector (m/s) and relative vorticity (s^{-1}) on 29 August 1998, the fourth and last day of the episode. 153
Figure B.19: Synoptic and climatologic situation on 30 August 1998, one day after the episode. 154
Figure B.20: Daily mean U and V wind components (m/s) on 30 August 1998, one day after the episode. 155
Figure B.21: The wind vector (m/s) and relative vorticity (s^{-1}) on 30 August 1998, one day after the episode. 156
Figure B.22: Synoptic and climatologic situation on 31 August 1998, two days after the episode. 157
Figure B.23: Daily mean U and V wind components (m/s) on 31 August 1998, two days after the episode. 158
Figure B.24: The wind vector (m/s) and relative vorticity (s^{-1}) on 31 August 1998, two days after the episode. 159
Figure C.1 : Predicted Sea level pressure, temperature and horizontal wind velocity. 00 hours forecast on 25 – 08 – 1998, 0000 UTC. ... 161

Figure C.2 : Predicted 850 hpa geopotential heights, temperature and horizontal wind velocity. 00 hours forecast on 25 – 08 – 1998, 0000 UTC. 162
Figure C.3 : Predicted 700 hpa geopotential heights, temperature and horizontal wind velocity. 00 hours forecast on 25 – 08 – 1998, 0000 UTC. 163
Figure C.4 : A NW – SE vertical cross section of the potential vorticity, potential temperatures and the wind circulation. 00 hours forecast on 25 – 08 – 1998, 0000 UTC. 164
Figure C.5 : An estimated Skew – T Plot diagram for Antalya (36.70 °N, 30.73 °E). 00 hours forecast on 25 – 08 – 1998, 0000 UTC. ... 165
Figure C.6 : The same as Figure C.1, but 12 hours forecast for 25 – 08 – 1998, 1200 UTC. 166
Figure C.7 : The same as Figure C.2, but 12 hours forecast for 25 – 08 – 1998, 1200 UTC. 167
Figure C.8 : The same as Figure C.3, but 12 hours forecast for 25 – 08 – 1998, 1200 UTC. 168
Figure C.9 : The same as Figure C.4, but 12 hours forecast for 25 – 08 – 1998, 1200 UTC. 169
Figure C.10: The same as Figure C.5, but 12 hours forecast for 25 – 08 – 1998, 1200 UTC. 170
Figure C.11: The same as Figure C.1, but 24 hours forecast for 26 – 08 – 1998, 0000 UTC. 171
Figure C.12: The same as Figure C.2, but 24 hours forecast for 26 – 08 – 1998, 0000 UTC. 172
Figure C.13: The same as Figure C.3, but 24 hours forecast for 26 – 08 – 1998, 0000 UTC. 173
Figure C.14: The same as Figure C.4, but 24 hours forecast for 26 – 08 – 1998, 0000 UTC. 174
Figure C.15: The same as Figure C.5, but 24 hours forecast for 26 – 08 – 1998, 0000 UTC. 175
Figure C.16: The same as Figure C.1, but 36 hours forecast for 26 – 08 – 1998, 1200 UTC. 176
Figure C.17: The same as Figure C.2, but 36 hours forecast for 26 – 08 – 1998, 1200 UTC. 177
Figure C.18: The same as Figure C.3, but 36 hours forecast for 26 – 08 – 1998, 1200 UTC. 178
Figure C.19: The same as Figure C.4, but 36 hours forecast for 26 – 08 – 1998, 1200 UTC. 179
Figure C.20: The same as Figure C.5, but 36 hours forecast for 26 – 08 – 1998, 1200 UTC. 180
Figure C.21: The same as Figure C.1, but 48 hours forecast for 27 – 08 – 1998, 0000 UTC. 181
Figure C.22: The same as Figure C.2, but 48 hours forecast for 27 – 08 – 1998, 0000 UTC. 182
Figure C.23: The same as Figure C.3, but 48 hours forecast for 27 – 08 – 1998, 0000 UTC. 183
Figure C.24: The same as Figure C.4, but 48 hours forecast for 27 – 08 – 1998, 0000 UTC. 184

Figure C.25: The same as Figure C.5, but 48 hours forecast for 27 – 08 – 1998, 0000 UTC. 185
Figure C.26: The same as Figure C.1, but 60 hours forecast for 27 – 08 – 1998, 1200 UTC. 186
Figure C.27: The same as Figure C.2, but 60 hours forecast for 27 – 08 – 1998, 1200 UTC. 187
Figure C.28: The same as Figure C.3, but 60 hours forecast for 27 – 08 – 1998, 1200 UTC. 188
Figure C.29: The same as Figure C.4, but 60 hours forecast for 27 – 08 – 1998, 1200 UTC. 189
Figure C.30: The same as Figure C.5, but 60 hours forecast for 27 – 08 – 1998, 1200 UTC. 190
Figure C.31: The same as Figure C.1, but 72 hours forecast for 28 – 08 – 1998, 0000 UTC. 191
Figure C.32: The same as Figure C.2, but 72 hours forecast for 28 – 08 – 1998, 0000 UTC. 192
Figure C.33: The same as Figure C.3, but 72 hours forecast for 28 – 08 – 1998, 0000 UTC. 193
Figure C.34: The same as Figure C.4, but 72 hours forecast for 28 – 08 – 1998, 0000 UTC. 194
Figure C.35: The same as Figure C.5, but 72 hours forecast for 28 – 08 – 1998, 0000 UTC. 195
Figure C.36: The same as Figure C.1, but 84 hours forecast for 28 – 08 – 1998, 1200 UTC. 196
Figure C.37: The same as Figure C.2, but 84 hours forecast for 28 – 08 – 1998, 1200 UTC. 197
Figure C.38: The same as Figure C.3, but 84 hours forecast for 28 – 08 – 1998, 1200 UTC. 198
Figure C.39: The same as Figure C.4, but 84 hours forecast for 28 – 08 – 1998, 1200 UTC. 199
Figure C.40: The same as Figure C.5, but 84 hours forecast for 28 – 08 – 1998, 1200 UTC. 200
Figure C.41: The same as Figure C.1, but 96 hours forecast for 29 – 08 – 1998, 0000 UTC. 201
Figure C.42: The same as Figure C.2, but 96 hours forecast for 29 – 08 – 1998, 0000 UTC. 202
Figure C.43: The same as Figure C.3, but 96 hours forecast for 29 – 08 – 1998, 0000 UTC. 203
Figure C.44: The same as Figure C.4, but 96 hours forecast for 29 – 08 – 1998, 0000 UTC. 204
Figure C.45: The same as Figure C.5, but 96 hours forecast for 29 – 08 – 1998, 0000 UTC. 205
Figure C.46: The same as Figure C.1, but 108 hours forecast for 29 – 08 – 1998, 1200 UTC. 206
Figure C.47: The same as Figure C.2, but 108 hours forecast for 29 – 08 – 1998, 1200 UTC. 207
Figure C.48: The same as Figure C.3, but 108 hours forecast for 29 – 08 – 1998, 1200 UTC. 208
Figure C.49: The same as Figure C.4, but 108 hours forecast for 29 – 08 – 1998, 1200 UTC. 209

Figure C.50: The same as Figure C.5, but 108 hours forecast for 29 – 08 – 1998, 1200 UTC. 210
Figure C.51: The same as Figure C.1, but 120 hours forecast for 30 – 08 – 1998, 0000 UTC. 211
Figure C.52: The same as Figure C.2, but 120 hours forecast for 30 – 08 – 1998, 0000 UTC. 212
Figure C.53: The same as Figure C.3, but 120 hours forecast for 30 – 08 – 1998, 0000 UTC. 213
Figure C.54: The same as Figure C.4, but 120 hours forecast for 30 – 08 – 1998, 0000 UTC. 214
Figure C.55: The same as Figure C.5, but 120 hours forecast for 30 – 08 – 1998, 0000 UTC. 215
Figure C.56: 96 hours backward trajectory plot at sigma level 0.998. ... 216
Figure C.57: 96 hours backward trajectory plot at sigma level 0.990. ... 217
Figure C.58: 96 hours backward trajectory plot at sigma level 0.900. ... 218
Figure C.59: 96 hours backward trajectory plot at sigma level 0.850. ... 219
Figure C.60: 96 hours backward trajectories at 3000 m AGL for Antalya, Izmir, Istanbul and Ankara plotted by HYSPLIT and RIP 220
Figure C.61: Multiple backward trajectory plot for Antalya at 100 m AGL. Trajectories are plotted at 3 hour interval between 0000 UTC, 30 Aug. 1998 and 0000 UTC, 26 Aug. 1998. 221
Figure C.62: The same as in Figure C.61 but at 1000 m AGL. 222
Figure C.63: The same as in Figure C.61 but at 1500 m AGL. 223
Figure C.64: The same as in Figure C.61 but at 3000 m AGL. 224
Figure D.1 : 24 hours forecast versus observed Sea level, temperature and horizontal wind velocity, valid at 0000UTC, 26 – 08 – 1998. ... 226
Figure D.2 : 24 hours forecast versus observed 850 hpa geopotential height, temperature and horizontal wind velocity, valid at 0000UTC, 26 – 08 – 1998. 227
Figure D.3 : 24 hours forecast versus observed 700 hpa geopotential heights, temperature and horizontal wind velocity, valid at 0000UTC, 26 – 08 – 1998. 228
Figure D.4 : 24 hours forecast versus observed NW – SE vertical cross section of the potential vorticity, potential temperatures and the wind circulation, valid at 0000UTC, 26 – 08 – 1998. 229
Figure D.5 : 24 hours estimated versus observed Skew – T Plot diagram for Antalya (36.70 °N, 30.73 °E), valid at 0000UTC, 26-08-1998. 230
Figure D.6 : The same as Figure D.1 but 72 hours forecast and valid at 0000UTC, 28 – 08 – 1998. 231
Figure D.7 : The same as Figure D.2 but 72 hours forecast and valid at 0000UTC, 28 – 08 – 1998. 232
Figure D.8 : The same as Figure D.3 but 72 hours forecast and valid at 0000UTC, 28 – 08 – 1998. 233
Figure D.9 : The same as Figure D.4 but 72 hours forecast and valid at 0000UTC, 28 – 08 – 1998. 234
Figure D.10: The same as Figure D.5 but 72 hours forecast and valid at 0000UTC, 28 – 08 – 1998. 235
Figure D.11: The same as Figure D.1 but 120 hours forecast and valid at 0000UTC, 30 – 08 – 1998. 236

Figure D.12: The same as Figure D.2 but 120 hours forecast and valid at 0000UTC, 30 – 08 – 1998. 237
Figure D.13: The same as Figure D.3 but 120 hours forecast and valid at 0000UTC, 30 – 08 – 1998. 238
Figure D.14: The same as Figure D.4 but 120 hours forecast and valid at 0000UTC, 30 – 08 – 1998. 239
Figure D.15: The same as Figure D.5 but 120 hours forecast and valid at 0000UTC, 30 – 08 – 1998. 240
Figure E.1 : Simulation of sulfate and sulfur dioxide concentration during 26 August 1998, a) 00:00 Z, b) 03:00 Z, c) 06:00 Z, d) 09:00 Z, e) 12:00 Z, f) 15:00 Z, g) 18:00 Z and h) 21:00 Z.... 242
Figure E.2 : The same as Fig. E.1 but for 27 Aug. 1998. 250
Figure E.3 : The same as Fig. E.1 but for 28 Aug. 1998. 268
Figure E.4 : The same as Fig. E.1 but for 29 Aug. 1998. 266
Figure E.5 : Dry deposition simulation of sulfate and sulfur dioxide during 26 August 1998; a) 00:00 Z, b) 03:00 Z, c) 06:00 Z, d) 09:00 Z, e) 12:00 Z, f) 15:00 Z, g) 18:00 Z and h) 21:00 Z. 274
Figure E.6 : The same as Fig. E.5 but for 27 Aug. 1998. 282
Figure E.7 : The same as Fig. E.5 but for 28 Aug. 1998. 290
Figure E.8 : The same as Fig. E.5 but for 29 Aug. 1998. 298
Figure E.9 : Wet deposition simulation of sulfate and sulfur dioxide during the episodic period 26 – 29 August 1998; a) 26 August 1998 00:00 Z, b) 26 August 1998 12:00 Z, c) 27 August 1998 00:00 Z, d) 27 August 1998 12:00 Z, e) 28 August 1998 00:00 Z, f) 28 August 1998 12:00 Z, g) 29 August 1998 00:00 Z, h) 29 August 1998 12:00 Z, i) 29 August 1998 23:00 Z..... 306

LIST OF SYMBOLS

A : Total scavenging rate for gases
A_a : Aqueous-phase scavenging rate
Ag : Silver
A_g : Gas-phase scavenging rate
Al : Aluminum
As : Arsenic
Au : Gold
α : Specific volume
Ba : Barium
β_M, β_T : Transitional correction factors for the mass and heat transfer
γ : Temperature lapse rate
C : Concentration
Ca : Calcium
$CaSO_4$: Calcium Sulfate
Cd : Cadmium
Cl : Chlorine
CO : Carbon Mono Oxide
CO_2 : Carbon Dioxide
Co : Cobalt
Cr : Chrome
Cs : Cesium
Cu : Copper
c_p : Specific heat in constant pressure
c_v : Specific heat in constant volume
D_p : Brownian diffusivity
E : Local species emission rate (μmol/s for gasses, μg/s for aerosols)
Eu : Europium
Fe : Iron
Ga : Gallium
g : The gravitational acceleration
Hf : Hafnium
HO_2 : Hydroperoxyl
HONO : Nitrous Acid
H2O2 : Hydrogen Peroxide
H_2S : Hydrogen Sulfide
H_2SO_4 : Sulfuric Acid
I : Iodine
In : Indium
K : Potassium
K : Diffusivity Coefficient
K_0 : Henry's Law constant
K_V : Vertical Diffusivity Coefficient
Kn : Knudsen Number

k : Brownian constant (1.38 x 10^{-23} J/K)
k : Von Karman's constant
k_B : Boltzmann Constant
L : Latent heat of condensation
La : Lanthanum
Lu : Lutetium
M : Mass
M : Molecular weight
Mg : Magnesium
Mn : Manganese
Mo : Molybdenum
m : Meter
m : Map scale factor
mg : Milligram
µm : Micrometer
µg : Microgram
µmol : Micromole
μ : Kinematic viscosity of air (1.8×10^{-5} kg/ms)
μ_w : Kinematic viscosity of water (10^{-3} kg/ms)
NA : Sodium Ion
Na : Sodium
Ni : Nickel
NH_3 : Ammonia
NH_4^+ : Ammonium Ion
NO : Nitric Oxide
NO_2 : Nitrous Oxide
NO_3^{1-} : Nitrates
NOx : Nitrogen Oxides
N_2O_5 : Nitrogen Peroxide
η : The net vertical "entrainment rate",
O_3 : Ozone
OH : Hydroxyl
P : Atmospheric Pressure
Pb : Lead
pH : Cloud or rain water acidity
PCL : Chloride ion
PH_2O : Water in Aerosol Phase
PNH_4 : Particulate Ammonium Ion
PNO_3 : Particulate Nitrate Ion
PSO_4^{2-} : Particulate Sulfate
Q, q : Heat content
R : The ideal gas constant ($8.206.10^{-2}$ l·atm/mol K)
R2 : Correlation coefficient
Re : Reynold's number
RO_2 : Peroxyalkyl
r : Radius of the particle
ρ : Density
ρ_v : Density of condensable vapor
S : Saturation ratio of the gas
SO_2 : Sulfur Dioxide

SO_3 : Sulfite
SO_4^{-2} : Sulfate
Sb : Antimony
Sc : Scandium
Sc : Schmidt number
Se : Selenium
Sm : Samarium
St : Stokes number
s : Second
σ : Terrain following vertical coordinate
T : Temperature
Tg : Terragram
Th : Thorium
Ti : Titanium
t : Time
UV : Ultra Violet
u, v, w : Horizontal and vertical wind velocities in x, y and z directions .
V : Vanadium
W : Watt
W : Tungsten
Zn : Zinc

AVRUPA HAVA KİRLETİCİLERİNİN DOĞU AKDENİZ BÖLGESİNE UZUN MENZİL TAŞINIMININ MODELLENMESİ: ANTALYA İÇİN BİR EPİSODİK ANALİZ

ÖZET

Doğu Akdeniz bölgesinde yapılan ölçümlere göre, PSO_4^{2-} gibi bazı hava kirleticilerinin, Orta ve Doğu Avrupa'dakilerle karşılaştırılabilecek kadar yüksek derişimlere sahip oldukları görülmüştür. Kirlilik kaynaklarından uzak olarak yerleştirilen istasyonlarda ölçülen yüksek derişimli kirleticilerin, Doğu ve Güneydoğu Avrupa gibi kirleticilerin yoğun olarak bulunduğu bölgelerden, taşınma yoluyla transfer edildiğine inanılmıştır. Doğu Akdeniz sahillerinde (Türkiye'nin Güneybatısı) yer alan Antalya ölçüm istasyonunda (36.47° K, 30.34° D), 1992 – 2000 yıllarında yapılan ölçümler arasında, 4 günlük 26 – 29 Ağustos 1998 periyodu en yüksek sülfat derişimine sahip olan ve birkaç ardışık günden oluşan en belirgin episod periyodu olarak görülmüştür. Bu episod dönemini analiz etmek amacıyla, Güney-Doğu Avrupa ve Doğu Akdeniz'de siklojenez ve antisiklojenez ile birlikte kritik hava kirliliği durumlarının oluşumuna yardımcı olan mevsimsel sinoptik klimatolojik paternler de incelenmiş, Doğu Akdeniz bölgesindeki kirliliğin Avrupa'daki olası kaynağı olarak nitelendirilebilecek ana kirlilik emisyon kaynakları belirlenmiştir. Doğu Akdeniz bölgesinde gözlenen yüksek derişimli hava kirleticilerinin (en başta sülfat olmak üzere) kaynak ve taşınım yörüngelerinin belirlenmesi ve simülasyonlarının yapılabilmesi için, kirleticilerin hareketini etkileyen hava sirkülasyonunun ve üç boyutlu meteorolojik değişkenlerin tahmininde, mezo-ölçekli meteorolojik model, MM5 kullanılmıştır. Bu model 26–29 Ağustos 1998 episod periyodunda 50x50 km'lik çözünürlükteki bir alana uygulanmıştır. Hava parsellerinin ve buna bağlı olarak hava kirleticilerinin hareketini kontrol eden yörünge simülasyonu değişik iki modelle tahmin edilmiştir. Bu iki model MM5/RIP ve HYSPLIT modelleridir. Sonuç olarak 3 ana yörünge kaynağı sektörü bulunmuştur. A sektörü: Doğu Avrupa – Türkiye, B sektörü: Orta Avrupa – Türkiye ve C sektörü: Güney Avrupa – Akdeniz olarak bulunmuştur. PSO_4^{2-} ve SO_2 gibi türlerin derişiminin, birikiminin ve taşınımının simülasyonunu elde etmek için MM5 modelinin çıktısı olarak üretilen meteorolojik değişkenler üç boyutlu Eulerian CAMx modelinde kullanılmıştır. Hava kalitesi modelinin sonuçları olan derişim, birikim ve taşınım simülasyonlarının, HYSPLIT ve MM5 modelleriyle üretilen hava parseli yörünge simülasyonlarıyla büyük bir uyum sağladığı görülmüştür. Sülfatın Avrupa'dan Doğu Akdeniz bölgesine taşınması sırasında iki ana geçidi izlediği saptanmıştır. Bunlardan birincisi İtalya'dan kaynaklanan ve Yunanistan ile Ege Denizi üzerinden geçerek Güneybatı Türkiye'ye uzanan geçit iken, ikincisi Orta ve Doğu Avrupa'dan kaynaklanan sülfatın Türkiye'nin Kuzeybatısına ulaşmasını sağlayan geçit olmaktadır. Bu çalışmada uygulanan modelleme sistemi performansının yüksek olduğu ortaya çıkarılmıştır. MM5 modeli oldukça iyi bir doğrulukla meteorolojik değişkenleri tahmin etmiştir. RIP ve HYSPLIT modelleriyle

hesaplanan geriye doğru yapılan yörünge simülasyonlarının birbiriyle büyük ölçüde uyum halinde olduğu bulunmuştur. Hava kalitesi modeli CAMx'in, Ankara Çubuk istasyonu için PSO_4^{2-}'ün derişim ve birikim tahmininde iyi bir performans gösterdiği, ancak Antalya için PSO_4^{2-}'ü 8 faktörüyle ve Ankara için SO_2'yi 6 faktörüyle daha yüksek tahmin ettiği bulunmuştur. Ayrıca CAMx modeline uygulanan duyarlılık analizi, modelin SO_2'nin emisyon envanterlerindeki değişimlere oldukça iyi bir duyarlılık gösterdiği de ortaya çıkarılmıştır.

MODELING LONG RANGE TRANSPORT OF EUROPEAN AIR POLLUTANTS TO THE EAST MEDITERRANEAN REGION: AN EPISODIC ANALYSIS FOR ANTALYA

SUMMARY

Measurements of some air pollution species, mainly PSO_4^{2-} in some rural locations in the Eastern Mediterranean revealed high concentrations which are comparable or higher than those of Central and Eastern Europe. Since the area is free of any source of pollution, it is believed that such high concentration of various pollution species are transported from other regions, such as Eastern or Southeastern Europe. The Antalya measurement station (36.47° N, 30.34° E) which is located on the Mediterranean coasts (southwest Turkey) has recorded high concentrations of PSO_4^{2-} during the years 1992 – 2000. One of the best recognized episodic periods of highest sulfate concentrations in successive few days is the 4 day episode of 26 – 29 August 1998. This study is aiming to determine cyclogenesis and anticyclogenesis conditions in addition to the seasonal synoptic climatological patterns that probably assist to create episodic pollution conditions in the study area. And to identify the major sources in Europe that probably contribute to the air pollution transport phenomenon to the East Mediterranean. For this purpose, Mesoscale Meteorological Modeling system, MM5 was applied to forecast the hourly general circulation conditions and three dimensional meteorological variables that steer the air pollution transport, in a 50 km x 50 km grid mesh domain during the episodic period 26 – 29 August 1998. Backward trajectory simulations which illustrate the particle movement of the air and consequently the air pollutants throughout the region during the episodic period are also predicted by two models; MM5/RIP (Read/Interpolate/Plot) modeling system and Hybrid Single Particle Lagrangian Integrated Trajectory (HYSPLIT) model. Consequently three main sectors of air mass trajectory origins were found; Sector A: Turkey and Eastern Europe, sector B: Turkey and central Europe, and Sector C: Southern Europe and the Mediterranean Sea. MM5 model outputs were used together with other inputs in the three-dimensional Eulerian model CAMx (Comprehensive Air Quality Model with Extension) to calculate and simulate the concentration deposition and the long range transport of the air pollution species PSO_4^{2-} and SO_2 in the entire study domain over the study period. The air quality model simulations of sulfate concentration and deposition have revealed a great agreement with the air mass trajectory simulations produced by HYSPLIT and RIP/MM5 models. Simulations have demonstrated that sulfate transport from Europe to the Eastern Mediterranean region has two main paths: the first is the transport of sulfate originated from Italy through Greece and the Aegean Sea to the southwestern parts of Turkey. The second one is the sulfate transport track which is apparently originated from central and Eastern Europe through the northwestern part of Turkey. The performance of the modeling system was found to be high, MM5 model revealed superior performance in forecasting meteorological variables. RIP and HYSPLIT

trajectory simulations were almost identical. The air quality model CAMx revealed a high performance in predicting PSO_4^{2-} concentration and deposition for Ankara and overestimated PSO_4^{2-} for Antalya by a factor of 8, and also overestimated SO_2 by a factor of 6. Furthermore sensitivity analysis that was applied to CAMx model has shown that the model revealed a good response to the changes of the emission inventories of SO_2.

1. INTRODUCTION

The excessive increase of anthropogenic activities in the previous century, together with the use of coal, have lead to the production of anthropogenic pollutants that have often generated locally unhealthful air quality and, sometimes, lethal air pollution concentrations, as during the well-known London episode of December 1952. Once pollutant is emitted to the atmosphere it is deposited continuously on to surfaces (e.g., vegetation, soils, surface waters and materials) by dry deposition. This dry deposition is mediated by diffusion, Brownian motion, interception, impaction and sedimentation **(Legge and Krupa, 1990)**. At the same time depending on the physical and chemical climatology, emissions of primary pollutants such as sulfur dioxide (SO_2) and nitrogen dioxide (NO_2) undergo chemical transformations in the atmosphere that generate hundreds of pollutants called secondary pollutants such as sulfate (SO_4^{-2}), nitrate (NO_3^{1-}) and ozone (O_3). The secondary pollutants are responsible for new adverse effect such as acidic deposition. These secondary species are generated in dense populated urban and industrial areas. Again depending on the meteorological characteristics pollutants are transported from a few to thousands of kilometers away from their sources to create pollution problems in other locations by either dry or wet deposition.

In addition to transport, transformation and dry deposition, pollutants such as sulfur dioxide (SO_2) and fine particulate sulfate (PSO_4^{2-}) are also incorporated into clouds. During precipitation events these pollutants within the cloud (rainout) and to a degree what is in the air below the clouds (washout), are deposited on to surfaces by wet deposition. Of the major concern in this context is the phenomenon of "acidic precipitation".

Certain pollutants such as sulfur dioxide (SO_2) and hydrogen sulfide (H_2S) are of environmental concern on local scale, while others such as SO_4^{2-} are of regional scale concern.

A number of gaseous sulfur compounds are emitted into the atmosphere through natural and/or anthropogenic activities. Of these SO_2 is the most important species of environmental concern. Once in the atmosphere SO_2 is oxidized by homogeneous (gas to gas phase) and heterogeneous (gas to particle phase) reactions resulting in formation of SO_4^{2-}.

Because of the larger population concentration and the excessive human activities in the northern hemisphere with comparison to the southern hemisphere, it is found that most of the pollution emissions are produced in the northern hemisphere. Of the total emissions of sulfur, 56% are anthropogenic emissions in the northern hemisphere, while only 8% of the anthropogenic emissions are produced in the southern hemispheres. Of the global anthropogenic emissions of sulfur, 94% are produced in the northern hemisphere while the southern hemisphere produced only 6% of the anthropogenic sulfur emissions **(Cullis and Hirschler, 1980)**.

Among the overall industrial activities, power plants are considered as the greatest sulfur emitter activity. It is found that the rates of production of SO_4^{2-} from SO_2 are much higher during the summer compared to the winter **(Richards et al., 1981)**. According to **Forrest et al. (1981)**, noontime SO_2 conversion rates at a power plant plume are larger than that at nighttime (1 – 4% h^{-1} and < 0.5% h^{-1} at noontime and night time respectively).

Air quality and meteorological field measurement programs supporting air pollution modeling and data analysis studies have revealed a spectacular development throughout the world during the last two decades. The profusion of researches that have taken place in the last decade, in particular, indicates the obvious progress that has been achieved. The goal of these modeling studies is: (i) to provide improved understanding of the chemical and physical processes that lead to the accumulation of ozone, aerosol, air pollutants or acidic precipitation, above quality standards based on health and (ii) to provide tools to air quality managers and decision makers in government and industry that will help them develop equitable and effective emission management for attaining and maintaining ambient air quality standards of hazardous air pollutants.

A preliminary distinction between the different transport scales of air pollution phenomena can be made as follows **(Zannetti, 1990)**:

i. Near-field phenomena (less than 1 km from the source); e.g., downwash effects of plume caused by building aerodynamics.

ii. Short-range transport (less than 10 km from the source); e.g., the area in which maximum ground level impact of primary pollutants from the elevated source is generally found.

iii. Intermediate transport (between 10 km and 100 km from the source); e.g., the area in which chemical reactions become important and must be taken into account.

iv. Long-range (regional or interstate) transport (more than 100 km from the source); e.g., the area in which large-scale meteorological effects and, deposition and transformation rates play key roles.

v. Global transport; i.e., phenomena affecting the entire earth atmosphere; e.g., CO_2 accumulation.

A general review of a variety of approaches and methods have been applied to long-range air pollution transport modeling has been provided by **Eliassen (1980)**. He classified models for long-range into two types; (i) models providing hourly or daily concentrations and (ii) models of a statistical nature which give longer-term average concentrations.

The first type of models (which is the type adopted in this study) attempts to use observed meteorological conditions on an hour-by-hour basis to calculate the short-term transport and dispersion of pollutants. Such models cover a wide range of complexity depending upon the detail with which they treat atmospheric structure, land surface characteristics, and pollutants transformation and depletion. However all such models have relatively large computing requirements because of the number of computations needed to treat spatially varying fields over many small time steps. Several models of the both types are discussed in detail by **Zannetti (1990), Seinfeld and Pandis (1998) and Pielke (2002).**

Long-range air pollution transport implies a necessity of international level cooperation to avoid or minimize the effects of the transferred pollutants. The **U**nited **N**ations **E**conomic **C**ommission for **E**urope's **C**onvention on **L**ong-**R**ange **T**ransboundary **A**ir **P**ollution (**UNECE-CLRTAP**) cooperates with the Cooperative Programme for Monitoring and Evaluation of the Long-range Transmission of Air Pollutants in Europe (**EMEP**) and with other organizations (such as: **WMO, WHO**), environmental agencies (such as: **EPA**), universities and research centers to establish models to estimate the fate of pollutants and to understand the effects of changes in emissions.

The phenomenon of long-range transport of air pollution received increasing attention since the 1970's and interest seems to persist at a high level through the later decades. A three dimensional model in a regional scale has been presented by **Shir and Shieh (1974)**. The problem with such three-dimensional dispersion model is the requirement of detailed information about the wind and turbulence in the atmospheric boundary layer as input. Eulerian models with some vertical resolution have been applied to the long-range transport of sulfur; a three-layer model has been developed by **Hidy et al. (1978). Nordlund (1975)** has developed a simple Lagrangian trajectory model in which a configuration of lagrangian cells is initiated on the upwind side of the emission area and the concentration associated with the cells are calculated as they move along trajectories. **Eliassen and Saltbones (1975), Eliassen (1978)** and **Ottar (1978)** have introduced an approach used in the connection with the OECD Program Long Range Transport of Air Pollutants, where trajectories arriving every 6 h at grid points in 127 km grid covering estimated concentration fields of sulfur dioxide and sulfate at these hours.

The contemporary development of measurement technology and sampling techniques as much as remote sensing and satellite products, associated to the development of computation technology have supplied researchers with tremendous amounts of aerosol and pollution data. Consequently a spectacular progress in modeling air pollution transport has taken place in the current and the past two decades.

The last years there is an extensive research focus on particulate matter (PM) **(EPA, 1996; EU, 1996; EMEP-WHO, 1997)**. Aerosol concentration measurements in Eastern Mediterranean have been evaluated by many researchers to investigate the air pollution

problems, identify the probable sources of these pollutants and to estimate scenarios to the future air pollution situations. Appreciated studies have analyzed the concentration data of aerosol species those were collected from several locations in different seasons in the Eastern Mediterranean. In one of these studies **Kubilay et al. (2000)** analyzed the aerosol samples and deposition (wet) measurements during August 1991–December 1992 at Erdemli (36°N, 34°E) located on the Turkish coast of the eastern Mediterranean. The analyses have shown higher dust concentration and total deposition during transitional seasons (spring and autumn) compared to summer and winter seasons.

Wet deposition measurements during the winter of the Eastern Mediterranean region indicate that the North African Sahara desert is the main source of the aerosol pollution in the region **(Herut et al., 2000; Ozsoy and Saydam, 2000; Zerefos et al., 2001; Shaka' and Saliba, 2004).**

Middle East desert originated episodic aerosol and dust events may be seen in the Eastern Mediterranean during the late summer and autumn season probably due to the extension of the Indian summer Monsoon low pressure and for a less extent during spring season probably due to the extension of the Red Sea trough. But the most effective Saharan dust events may happen at any time during the year but are often seen during the spring time due to the Saharan depressions that form in the lee of the Atlas Mountains and move east or northeastward through the Libyan Desert and Mediterranean and finally center near Cyprus.

Aerosol and dust concentration measurements in the atmosphere and their estimated sources and trajectories are statistically discussed by many scientists. But long-range pollution transport modeling and simulation tracks of the pollutants with conceptual mesoscale meteorological circulation studies in the East Mediterranean are still uncommon and rare

The last two decades have been characterized by a growing interest in long-range transport of biogenic and anthropogenic aerosol and other air pollutants, mainly because of serious public health risks for susceptible members of the population and risks to sensitive ecosystems in local, regional or either in global scales **(Draxler, 1987;**

Galperin, 1991; Syrakov and prodnova, 2002; Chen et al., 2002; Sciare et al., 2002; Park and Lee, 2003; Cakmur and Miller, 2004; Kallos et al., 2004).

Because of its unique topographic and climatic diversity and its location in the mid-latitudes, the Mediterranean region is considered as one of the most attractive regions in the world for studying mesoscale and long-range transport of dust **(Kubilay et Al., 2000; Israelevich et al., 2002)**, aerosol **(Dogan and Tuncel, 2003; Kocak et al., 2004a)** and other pollutants such as acidic sulfate and nitrate deposition **(Gullu et al., 2000; Ozturk et al., 2003)**. The non sea source aerosol and dust is transported mainly from the Saharan desert in northern Africa and from the Middle East and the Arabian Desert, while sulfate, nitrate and other anthropogenic pollutants are transported to the Mediterranean region chiefly from Europe **(Lupu and Maenhaut, 2002; Kocak et al., 2004b)**.

Measurements of SO_4^{2-}, NO_3^- and NH_4^+ in Eastern Mediterranean revealed high concentrations, which are comparable or higher than those of Eastern and Western Europe. Statistics showed that the application of effective precautions have achieved a 70% reduction of sulfate (SO_4^{2-}) emissions in Western Europe, while a little decrease was noticed during the last few years in the Eastern Europe, whereas no changes have occurred in the Eastern Mediterranean sulfate concentrations **(Gullu et al., 2000; Luria et al., 2002; Ozturk et al., 2003; Dogan and Tuncel, 2003)**. Accordingly the high concentrations can be attributed to the transfer from Eastern Europe. This allegation was proved by a statistical back trajectory identification method, the potential source contribution function.

Tuncel and Erduran (2001) have employed the aerosol measurements through a six-month period that includes August, September and October 1995 and February, March and April 1996 in order to identify the air pollution characteristics in the Eastern Mediterranean region. The wind analysis in the region has shown that the source of the pollution is probably from the Aegean and central Regions of Turkey as much as from the southern sector. The seasonal variation of the sulfate revealed a concentration maximum in summer and a minimum in winter in spite of the minimum concentration of SO_2 in summer and maximum concentration in winter.

Similar founding was introduced by **MINOS (2002)** which is an international team of eight scientists from eight countries aimed to investigate atmosphere. The study provides evidence for a remarkably high level of air pollution from the surface to the top of the troposphere at 11-15 km altitude. The greatest amount of pollution was observed in the lower 4 km, originating from both western and Eastern Europe. Industrial activity, traffic, forest fires, agricultural and domestic burning are the source of this pollution. Since the Mediterranean region has relatively few clouds in summer, the solar radiation levels are high so that noxious reaction products are formed in a photochemical smog. The resulting air pollution includes ozone and microscopic particles called aerosols.

Comparison among locations that have similar rural environments in Turkey, e.g.: Antalya on the Mediterranean Sea and Amasra on the Black Sea reveals similar anthropogenic measurements. This similarity demonstrates that these locations are influenced by the same pollution transport **(Dogan and Tuncel, 2003).**

Hybrid Single Particle Lagrangian Integrated Trajectory (HYSPLIT) back trajectory model was used to determine the pathway of air pollution of maximum SO_2 concentrations in Izmir city, Turkey **(Dincer et al., 2003).** Wind direction is used to indicate the air mass propagation source and consequently backward trajectory of the pollutants. In this limited area model application it is found that the polluted air is transformed to the city from the northern sector, where the major industrial activities in the district are located.

During the last decade aerosol samples have been collected in various locations of the Eastern Mediterranean region. Wet and dry deposition of natural and anthropogenic aerosol components, besides their composition and concentrations have been analyzed owing to characterize air pollution potential and control the air quality. Assessment of the source origin and transport tracks of some air pollution species was one of the major goals of the recent researches. A statistical back trajectory method has been applied by **Tuncel (2002)** to identify the origin sources and tracks of SO_4^{2-} pollution in the Eastern Mediterranean. The method identifies the air masses in the related study period, then detects their propagation tracks and consequently determines the pollution transport source and track.

Kubilay et al. (2002) showed that the non-sea-salt SO_4^{2-} mean concentrations of samples which had air mass back trajectories originated from the Black Sea region were about twofold higher than the mean concentrations of samples of which had their air mass origin over Europe and former Soviet Union. Moreover the samples which had air mass trajectory from the Mediterranean Sea have greater concentration values of non-sea-salt SO_4^{2-} than those in the above both two cases.

The latest three studies mentioned above, are regarded as good attempts as much as **Kocak et al. (2004b)** for identification the local and regional air pollution transport in Turkey and the Eastern Mediterranean region.

The seasonality of the regional and mesoscale circulation of the Mediterranean atmosphere plays a chief role in determining the tracks and the air pollutants potential in the region. Measurements of SO_4^{2-} and other aerosol species that collected by an aircraft from a 180 km flight path about 70 km to the west of the Israeli coast in September 1993 and June 1994 have shown that the air mass sampled in June is too much deteriorated than that sampled in September **(Luria et al., 2002).** The Regional Atmospheric Modeling System (RAMS) for meteorological simulations and the Hybrid Particle and Concentration Transport Package (HYPACT) for dispersion modeling systems were used to examine the air mass source and the transport. The model's simulations showed that during the 1993 measurement period, the pollution sources in southern Europe and the Balkans did not affect the eastern coasts of the Mediterranean. The synoptic conditions and simulation results for the June 1994 period indicated that the winds over the Eastern Mediterranean tended to be northwesterly and thus forcing the polluted air masses towards the coast of Israel.

Although they are very important in the air pollution inventory of any region, the chemical composition of the rain water, the rain acidity and the chemical characteristics of the contaminated air will not be substantially discussed in this study. These topics are thoroughly investigated in many studies. As example; **Al-Momani et al. (1995a), Tuncel and Ungor (1996)** and **Topcu et al. (2002)** have investigated the chemical composition of the precipitation samples collected from industrial area of Izmir, METU station – Ankara and EMEP station – Ankara respectively. They have shown that the

rainwater is not acidic and most of the $SO4^{2-}$ in rainwater was in the form of $CaSO_4$. Wet and dry deposition, aerosol and precipitation chemical composition in Eastern Mediterranean region have been reported by **Al-Momani et al. (1995b and 1997).**

The mesoscale meteorological model MM5 and three dimensional photochemical grid models system was performed in Turkey for the first time in few pioneer studies that essentially handled the urban air pollution in Istanbul city; **Anteplioglu et al. (2002)** have employed a three dimensional photochemical model, UAM – V to predict and simulate the temporal and spatial variations of the surface ozone concentration in Istanbul urban area. **Anteplioglu et al. (2003)** have used the PSU/NCAR mesoscale meteorological model, MM5 with a three dimensional photochemical model, CAMx to investigate the temporal and spatial dynamics of the photochemical air pollution in urban atmosphere of Istanbul for selected high ozone days. Non-hydrostatic terrain following sigma-coordinate mesoscale meteorological model (MM5 version 3.5) was used to simulate the mesoscale atmospheric circulation and the wind field in the limited study area, while the CAMx was used to predict the ozone concentrations during the related episodic period. **Topcu et al. (2003)** have used a three dimensional mesoscale prognostic meteorological model called System Applications International Mesoscale Model (SAIMM) for the first time in the region to predict the wind and temperature fields in Istanbul owing to simulate the ozone distribution over the city. The CAMx model has also been used by **Andreani-Aksoyoglu et al. (2001)** to simulate the air quality in Switzerland during July 28 – 30, 1993.

Anthropogenic emissions of sulfur dioxide (SO_2) and other pollutants such as NOx have obviously increased with industrialization and anthropogenic fuel use during the previous century. When deposited, SO_2 and NOx lead to acidification of soil and surface waters. Deposition of nitrogen containing compounds may contribute to the eutrophication of terrestrial and marine echo system. Atmospheric residence time of SO_2 and NOx are of order of several days **(Fournier et al., 2004).** As a result and depending on the atmospheric circulation, the acidic deposition and air pollution problems are regional issues rather than local ones with pollutants found hundreds or thousands kilometers from the source.

The long-range transport of PM contributes significantly in the background particle mass and number size distribution. However, there is still considerable debate among the scientific community regarding the vertical exchange processes involved and the spatial and temporal scales of atmospheric particle transport.

In Turkey, there are many studies handled aerosol concentrations and investigated their sources using observed wind field **(Tuncel and Erduran, 2001),** statistical back trajectory method **(Tuncel, 2002)**, by analyzing the air mass trajectories **(Kubilay et al., 2002)** or by applying a trajectory model to a limited region, such as Izmir city, where **Dincer et al. (2003)** applied HYSPLIT back trajectory model to determine the pathway of SO_2 pollution in the city. But the transboundary long range air pollution transport modeling is still an absent topic in the Turkish literature. In this study a modeling system consists of Mesoscale Meteorological Model, MM5, Comprehensive Air Quality Model with Extension, CAMx and the Hybrid Single Particle Lagrangian Integrated Trajectory (HYSPLIT) model was used to predict the atmospheric condition in large domain that includes the European continent, Turkey and the Mediterranean region, to predict the gridded concentrations and depositions of air pollutants, and to simulate their trajectories using the gridded wind field predicted by MM5 during the episodic period 26 – 29 August 1998. This modeling system is used for the first time in Turkey to handle the probable long range air pollution transport phenomenon from Europe to the eastern Mediterranean region represented by Antalya.

This study is aiming to develop a model system in order to address the anthropogenic emissions in a large area including the entire Europe, Turkey and southeastern Mediterranean region, to predict the gridded concentrations distribution of the anthropogenic pollutants and to identify the long-range transport and trajectories of the major pollutants movement to the eastern Mediterranean region.

1.1 Objectives

The major goals of the study are:

a) To select episodic periods during spells conductive to the existence of poor air quality in the Eastern Mediterranean region. For this purpose SO_4^{2-} concentration values measured in Antalya on the Southeastern Mediterranean during the period 1992 – 2000 were evaluated. As a result the period "26 – 29 August 1998" was selected to be the episodic period of the study which is characterized by the highest sulfate concentration values.

b) To determine cyclogenesis and anticyclogenesis conditions in addition to the seasonal synoptic patterns which steer the air pollution transmission and dispersion, and/or assist to create episodic pollution conditions in the study area.

c) To determine the seasonal synoptic climatological patterns in the study area in general, and during the selected study period in particular.

d) To identify the major anthropogenic sources of sulfur in 28 countries in Europe and the East Mediterranean region that probably contribute to the air pollution transport phenomenon to the Eastern Mediterranean.

e) To develop a computer-based model system to handle the following issues:

   i. Forecasting and simulating the mesoscale and regional-scale atmospheric circulation in the selected study area and period.

   ii. Identification of the backward trajectory and source of air masses propagate the East Mediterranean region during the study period.

   iii. Prediction of a four dimensional simulation of pollutant species concentrations, mainly sulfate concentration in the study region.

   iv. Simulation of the long-range trajectories of the pollution species that were recorded in the eastern Mediterranean region during the episodic period.

   v. And finally to emphasize whether the high concentrations of pollutant species in the eastern Mediterranean are transported to the region from other places.

1.2 Methodology

The Fifth-Generation NCAR/Penn State Mesoscale Model MM5-Version 3.61 modeling system is performed in this study to simulate and predict mesoscale and regional-scale atmospheric circulation and trajectory patterns of air pollution transport. MM5 is a 34 vertical layer limited area, nonhydrostatic, terrain-following sigma-coordinate model.

The study domain is 35° Lat. x 40° Lon., between 25 – 60° N and 5 – 45° E in a horizontal spatial resolution of 50 km x 50 km and 89 x 78 grid-points in the E-W and in the N-S directions respectively.

The terrain data at 10 minutes (18.5 km) spatial resolution for the study domain were ftp'ed from the NCAR server. A 24 category USGS vegetation/land-use and land-water mask data have been used to determine the vegetation distribution and land-water mask over the domain. The NCEP/NCAR reanalysis data of a 2.5° Lat. x 2.5° Lon. spatial resolution and 12 hours temporal resolution are used as initial and boundary data to forecast the first guess which is used by the objective analyses program LITTLE_R. While the NCEP surface and upper observational girded binary (GRIB) data were used in the LITTLE_R program for the objective analysis purpose. The numerical weather prediction procedures are done by the model's sub-program, MM5. Various meteorological fields, such as: temperature, wind velocity pressure or geopotential height ... etc, at the mandatory levels from the surface up to 100 hpa were predicted for a 5 days period, 25 – 29 August 1998 in hourly time steps. Furthermore a NW – SE vertical cross section of the wind circulation, potential vorticity and potential temperature fields through the domain was predicted for each time step. Backward trajectory simulations which illustrate the particle movement of the air and consequently the air pollutants throughout the region during the episodic period are also predicted by MM5 modeling system. The outputs of the mesoscale meteorological modeling system, MM5 were plotted in graphs using the plot programs GRAPH and **RIP** which stands to **R**ead **I**nterpolate and **P**lot. Furthermore the Hybrid Single Particle Lagrangian Integrated Trajectory (HYSPLIT) model is also used to calculate and simulate the backward trajectories for the same episodic time period to be compared with MM5/RIP products.

Coupling with the MM5 modeling system the **C**omprehensive **A**ir Quality **M**odel with e**x**tension (**CAMx**) photochemical model was employed. Version 4.11s which is the latest version of the model is applied to simulate the predicted concentration, deposition, transport and source origins of anthropogenic pollutants in the domain during the selected episodic period of the study. The photochemical model, CAMx is employed in the same domain as of MM5, with a horizontal resolution of 0.59 ° x 0.45 ° in the E-W and N-S directions respectively, and 14 layers vertical resolution. The vertical layers start at 50 meters above the ground and extend up to 4000 meters. To solve the pollutant continuity equation which includes the terms of: horizontal advection/diffusion, vertical transport/diffusion, chemistry, dry deposition and wet deposition, the CAMx model requires a wide and well organized set of input data that includes:

(i) Meteorology: 3 dimensional gridded fields supplied by the mesoscale meteorological model, MM5 including: horizontal wind components, temperature, pressure, water vapor, vertical diffusivity, cloud and rain.

(ii) Air quality: Time/space constant top concentration data, gridded initial concentrations and boundary concentration data, calculated by a preprocessor for the entire grid domain.

(iii) Emissions: Gridded emission inventory of each pollutant species for each day of the episode, calculated by a preprocessor for the whole domain.

(iv) Geography: Gridded landuse/surface vegetation cover and gridded surface UV albedo codes, each of these data is calculated by a separate model.

(v) Other inputs such as: Gridded haze opacity codes, gridded ozone column codes and photolysis rates lookup tables, calculated by a radiative model.

The chemistry mechanism No. 4 is chosen to be implemented in CAMx model which includes 100 reactions, 46 gas species (34 state gases and 12 radicals), and 16 aerosol species.

2. CLIMATOLOGY OF THE MEDITERRANEAN AND SOUTHEASTERN EUROPE

2.1 Topography

The Eastern Mediterranean may be geographically regarded as the eastern basin that is bounded from the west by the peninsula of Italy and the island of Sicily, with the Adriatic and Aegean Seas as northward extension. The eastern basin of the Mediterranean is bordered on the north and east by ranges of mountains over 1000 m height above Mean Sea Level (MSL). The Dinaric Alps lie on the east of the Adriatic Sea with heights exceed 2000 m above MSL, this mountain range continues south as the Pindus range of Albania and Greece and reaches a height of 3000 m in Greece. North of the Aegean Sea Rhodope Mountains rise to over 2500 m. Between the Rhodope Mountain Range and the mountains of Turkish Anatolia; there is a break between 80 and 160 km wide, where the land seldom exceeds 200 m above MSL. Here the Dardanelles open into the Aegean and provide an outlet from the Black Sea (Fig. 2.1).

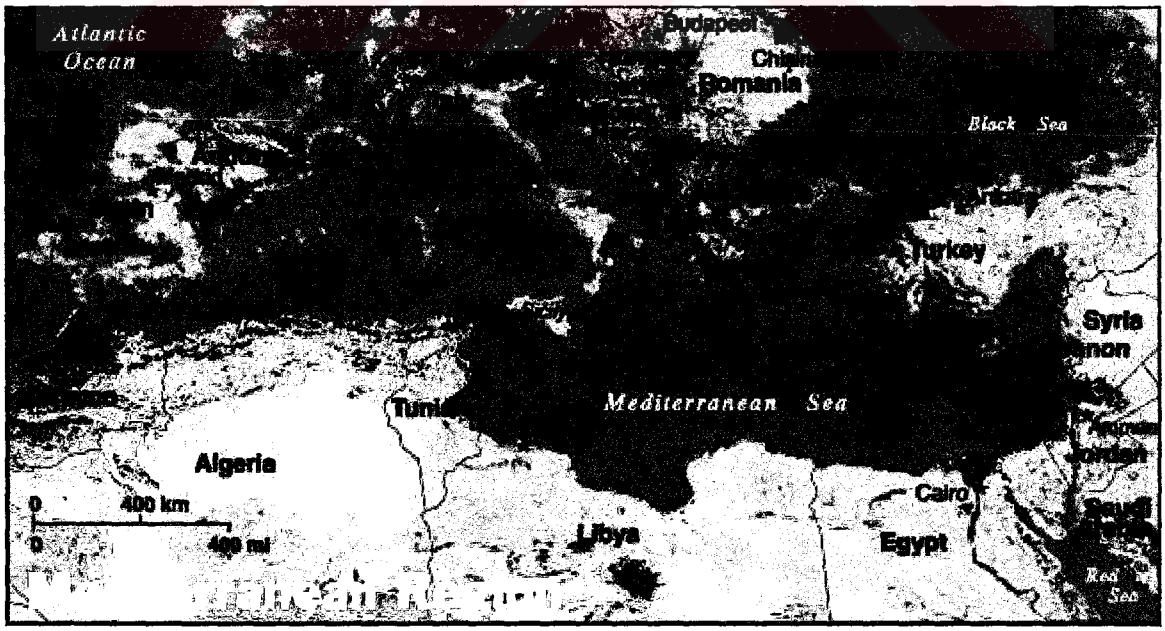

Figure 2.1: The Mediterranean region (National Geography, 2004).

The Anatolian Plateau rises in places to over 2500 m, while the Taurus range which backs the southern coast of Turkey is more than 2000 m, with several peaks over 3500 m above MSL.

To the east, the East Mediterranean is bounded by mountains with heights of 1500 to 2000 m having tops rises to over 3000 m above MSL in Lebanon and borders of Syria.

The north coast of Africa bordering the East Mediterranean is low-lying, being less than 200 m above MSL except some heights that rise to above 500 m to the east of the Gulf of Sidra.

A flow of air directed toward a mountain range is partially deflected sideways by the range. In a stable air mass most of the air below the level of the summit is turned aside, while in unstable air mass the proportion of deflected air is very much smaller, and the rest being lifted over the range **(HMSO, 1962).** In such cases the upward motion may extends to heights many times that of the crest of the range and be apparent strong winds near the summit and in turbulence wave motion downstream. Due to the former case a cross wind flow toward the Dinaric Alps in stable air mass diverts eastward to the Eastern Mediterranean through the Vardar Gap and the Aegean Sea. This kind of flow is of some importance for pollution transport in the lower troposphere from Southeastern Europe to the Eastern Mediterranean region.

2.2 Cyclogenesis

Cyclogenesis and cyclone formation have been precisely discussed by many scientists. Broad and detailed discussions handling the development and structure of cyclones and theories of cyclone formation can be found in **Pettersson (1956 and 1969), Donn (1975)** and **Ahrens (2000)** while the dynamics of their properties are thoroughly investigated by **Holton (1992).**

Satellite imagery has revealed that cyclogenesis takes place on a continuum of scales from large semi-permanent cyclones to vortices within mesoscale cyclones, each of which form within a range of physical environments. Possible physical mechanisms that

influence these developments and which is dominant in a particular situation are questions of active investigation. Several mechanisms exist in current instability theory that in combination or alone might explain the formation of cyclones. They include: baroclinic instability, conditional instability of the second kind (CISK), air-sea interaction instability and barotropic instability **(Businger, 1994).**

In this study we are concern of the area of cyclogenesis and anticyclogenesis, intensity, movement tracks and the seasonal variability of cyclones and anticyclones rather than their formation theories and mechanisms.

Studies focused on the Mediterranean area such as **HMSO (1962)** and **Flocass (1988)** presented cyclone climatologies based on the analysis of pressure charts, while **Alpert et al. (1990a)** introduced objective methods to detect and track Mediterranean cyclones for a five-year climatology using European Center for Medium Range Weather Forecast (ECMWF) dataset. **Alpert et al. (1990b)** have employed the same technique that was used in **Alpert et al. (1990a)** to investigate the month to month variations in cyclonic routes in the Mediterranean Sea. More recently **Trigo et al., 1999** employed an 18 years European Center for Medium Range Weather Forecast (ECMWF) dataset which is in higher spatial and temporal resolution to detect and track Mediterranean cyclones. The long dataset and high temporal and spatial resolution assisted to detect subsynoptic scale systems which were undetectable in the previous studies. Using similar techniques to those have been used in **Alpert et al. (1990a and 1990b), Maheras et al. (2001)** have carried out a climatological analysis of the synoptic scale cyclones that occur in the Mediterranean region for an extended period of 40 years (1958 - 1997). The study focused on the diurnal and seasonal variations of the frequency of cyclonic occurrences.

2.2.1 Spatial and temporal variability of cyclogenesis

The major areas of cyclogenesis in the Western Mediterranean are:

i. The Western Mediterranean represented mainly by the Gulf of Genoa, where cyclogenesis form mostly in the lee of the Alps **(Buzzi and Tibaldi, 1978)** is apparently persistent through the year.

ii. The area to the south of the Atlas Mountains; where Saharan cyclones seem to be the dominant features of the Mediterranean spring. The cyclogenesis over the western part of Africa is dominant all over the year reaching its peak in May – June **(HMSO, 1962; Egger et al., 1995).**

iii. The relatively warm land and sea-land contrast also favors the formation of thermal lows over the Iberian Peninsula from late spring through the summer.

The major areas of cyclogenesis in the Eastern Mediterranean are as follows:

i. The Aegean Sea is one of the major winter and spring cyclone sources. Due to its subcyclonic scale, Aegean cyclogenesis has not been estimated in most of the previous studies. But recently studies applying higher spatial and temporal resolution managed to detect such subcyclonic scale cyclogenesis **(Trigo et al., 1999).**

ii. Cyprus.

iii. The Middle East, mainly over Syria and Iraq.

Both of these two cyclone maxima areas (ii and iii) constitute the major summer characteristic of the Eastern Mediterranean, chiefly as a result of the semi permanent extension of the Indian Monsoon low. The Middle East cyclogenesis area shows high cyclone frequency between July and September **(Trigo et al., 1999).**

In addition to the depressions form over the Mediterranean region due to various mechanisms such as: lee side cyclogenesis, baroclinicity, sea-land temperature contrast and heating either over land or water; depressions may inter the Mediterranean area chiefly from the Atlantic either through the Strait of Gibraltar or from farther north through the Garonne Carcassonne Gap. The position of the blocking anticyclone over Europe identifies the tracks of such depressions. In both cases depressions propagate the Western Mediterranean from the west having an eastward or northeastward track.

The origins of depressions penetrate the Eastern Mediterranean region are summarized as follows:

i- Depressions having Atlantic origin penetrate the Western Mediterranean and propagate east to northeast through southeastern Europe.

ii- Depressions from the same origin also penetrate the Western Mediterranean and propagate southeast to east and center over Cyprus then move towards east, northeast or even southeast.

iii- Saharan depressions that form in the lee side of the Atlas Mountains show three distinguished tracks toward:

a) Northeast through the northern Libyan coasts to the Central Mediterranean.

b) Eastward through the Gulf of Sidra, along the Egyptian coasts then to Cyprus.

c) Eastward through the Libyan Desert and Egypt then northward to Cyprus.

2.3 Anticyclogenesis

The southeastern Europe and the Mediterranean regions are influenced by the semi permanent large scale anticyclones; the Azores anticyclone in the west and the Eurasiatic (Siberian) anticyclone in the northeast (Figures 2.2 and 2.3).

In addition the region is affected by mobile anticyclones generated over Scandinavia, The Atlantic or North Africa **(HMSO, 1962; Wallen, 1977).**

Synoptic climatological aspects, cyclonicity and anticyclonicity in the Mediterranean and the southern Europe have been discussed owing to detect areas of cyclogenesis and anticyclogenesis in the region **(Karalis, 1969; Makrogiannis, 1974; Katsoulis, 1982; Makrogiannis et al., 1989).**

Katsoulis et al. (1998) analyzed the monthly and seasonal frequencies of anticyclone immobility and their geographical distribution in the Mediterranean and Southern Europe using the daily surface synoptic charts published by German Meteorological Service for a period of 13 years (1981 - 1993).

The Mediterranean Sea has maxima in summer (when the water is colder than the surrounding land) and minima in winter. The west to east pattern is clearly indicated in the extreme seasons. Although the average pressure over the surrounding lands is

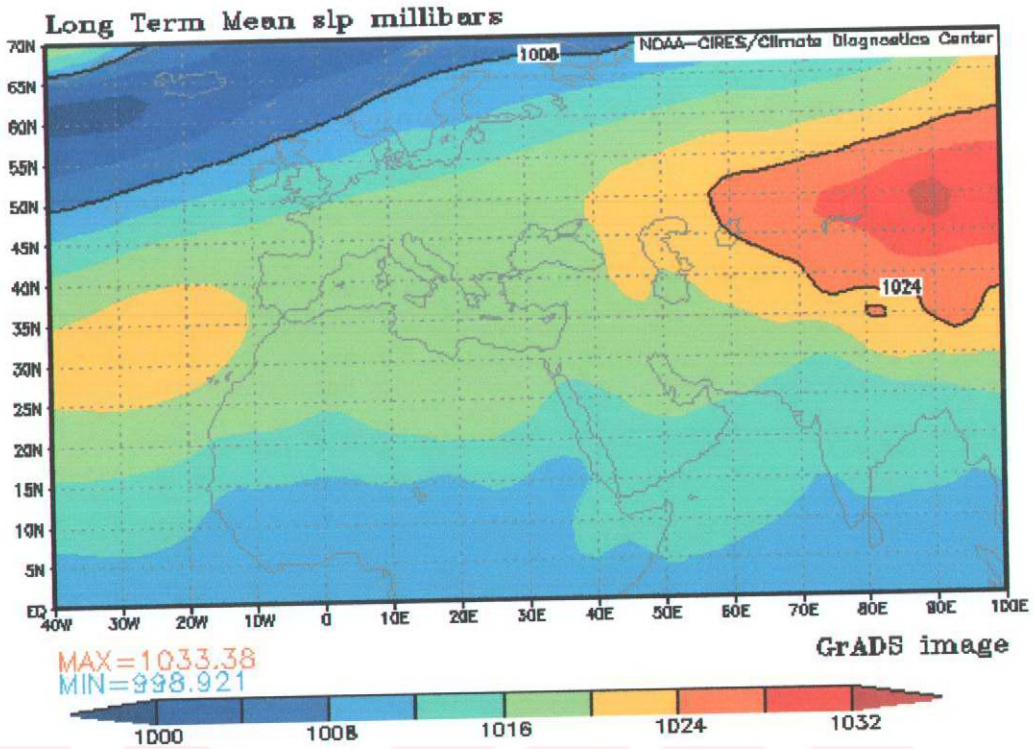

Figure 2.2: The average synoptic pattern represented by MSL pressure during winter months, November – March (NCEP/NCAR Reanalysis Project, 2004).

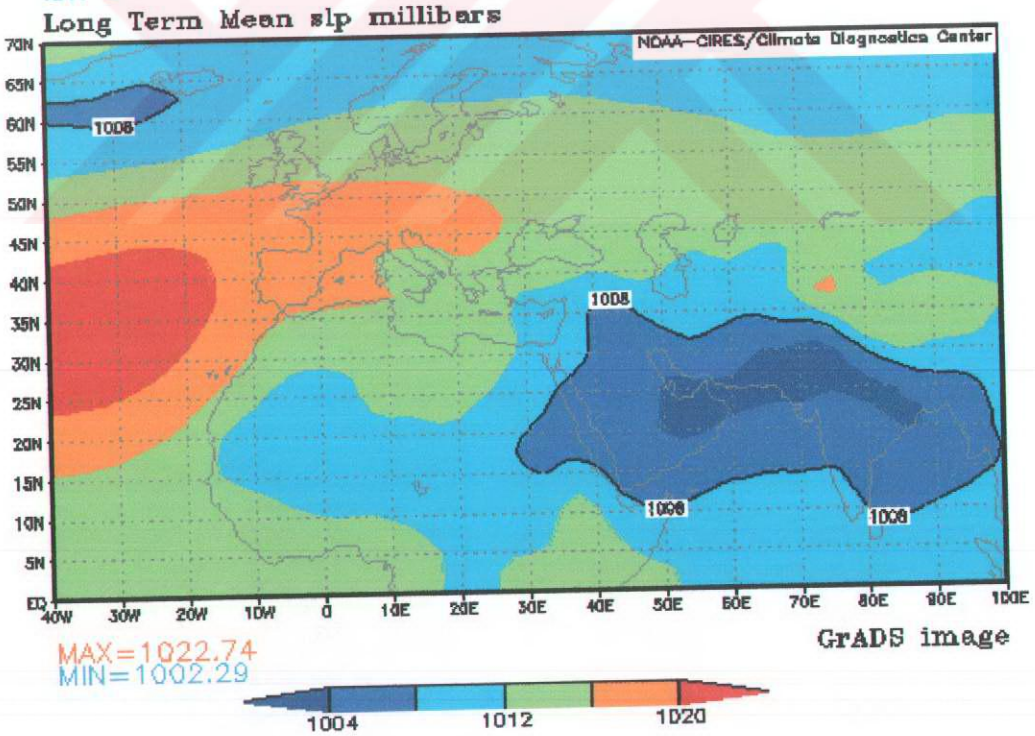

Figure 2.3: The average synoptic pattern represented by MSL pressure during summer months, June – October (NCEP/NCAR Reanalysis Project, 2004).

relatively low during the warm season, the frequency of anticyclones is appreciable. This is due to the fact that the summer anticyclones are, on the whole, relatively weak pressure configurations. Generally, land areas are characterized by higher pressure during winter and lower pressure during summer, while sea areas display an annual cycle with the opposite phase.

Hence, during winter (Fig. 2.2), the Siberian high is much more pronounced than in the annual average. In contrast, the highs over the Mediterranean Sea tend to be most pronounced during summer, and weak or nonexistent during winter. In the winter season, sometimes, a coupling occurs between the upper air warm ridge and the anticyclone stretching from Siberia towards southeastern Europe and created by strong radiational cooling. In the summer season, the Azores high pressure system dominates the circulation (Fig. 2.3) as the upper air jet stream is transferred to the north. In this area the high index circulation gives rise to warm and stable summer weather created by the subsiding air in the high pressure area. Consequently, summer circulation conditions over the region show much greater regularity than do the winter conditions. With the gradual warming up of the Eurasian continent the subtropical high pressure belt and the temperate westerlies are displaced northwards, so that in summer the subtropical high pressure system always extends over the Mediterranean region and in the majority of cases, also over the southern part of Europe. Winds then become weak and mainly from the northwesterly direction over the Mediterranean. Weather is in general sunny and stable.

The seasonal variation of the positions of anticyclone centers is of great importance for the weather conditions over the area. In winter, their centers prefer to locate at approximately 10 ± 5 W and 20 ± 25 E; in summer, at about 0 ± 15 E. Also the variability of the anticyclonicity following the seasonal shifting of the Azores high with the sun and the changes of the intensity of the Eurasiatic high pressure extension is similar.

Kassomenos et al., 1998 have studied the relationship between the synoptic condition derived from synoptic scale circulation and the mesoscale patterns over Athens urban

area. The objective of their study was: a) to examine and classify the day by day synoptic conditions, b) to create a classification scheme of the mesoscale flows, and

c) To identify and examine the day by day relationship between the synoptic scale atmospheric circulation in the lower troposphere and the mesoscale patterns over an urban Mediterranean basin. An attempt has been made to create a methodology of classification of mesoscale patterns based on surface observations. In addition, eight synoptic categories were distinguished that classify the atmospheric circulation in the lower troposphere and were examined with respect to their distinction. Furthermore, a day by day cross tabulation of the mesoscale with the synoptic categories has been carried out in order to examine the relationship between the synoptic scale circulation and the mesoscale flows.

The understanding of the association of large scale atmospheric behavior with the mesoscale flows is considered to be crucial for further investigations of the air quality over the Eastern Mediterranean.

2.4 Analysis of Sulfate Measurements in Antalya and Episode Selection

The Antalya measurement station is located 20 km to the west of Antalya city on the Eastern Mediterranean coast at elevation of about 20 m above MSL and coordinates of 36° 47'N and 30° 34'E (Fig. 2.4).

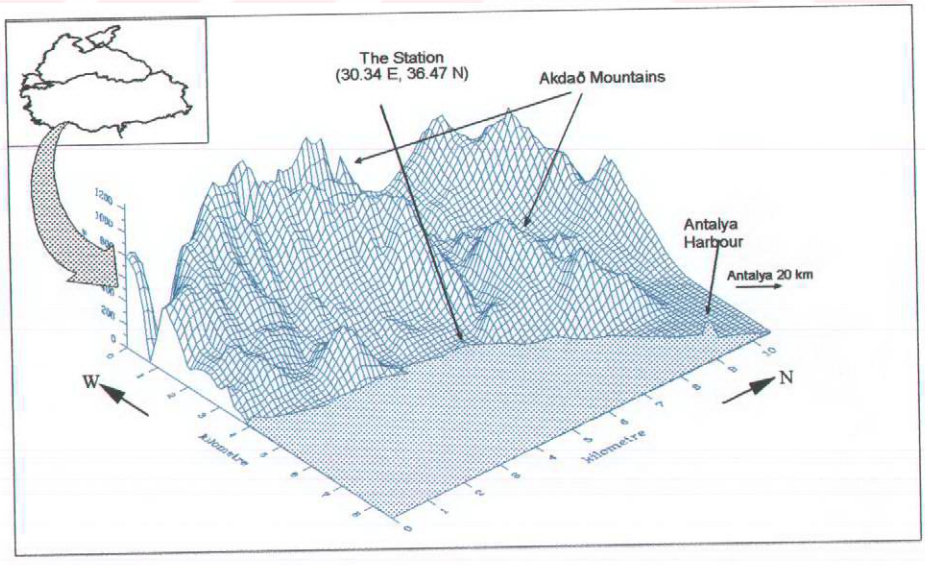

Figure 2.4: The location and topography of the Antalya station (Tuncel, 2005).

The station is too close to the coast (30 m) and just behind it the Taurus Mountains elevated to about 1200 m above MSL. The station has been in operation since 1992. Aerosol measurements are done by sensors that are located 1.5 m above the ground.

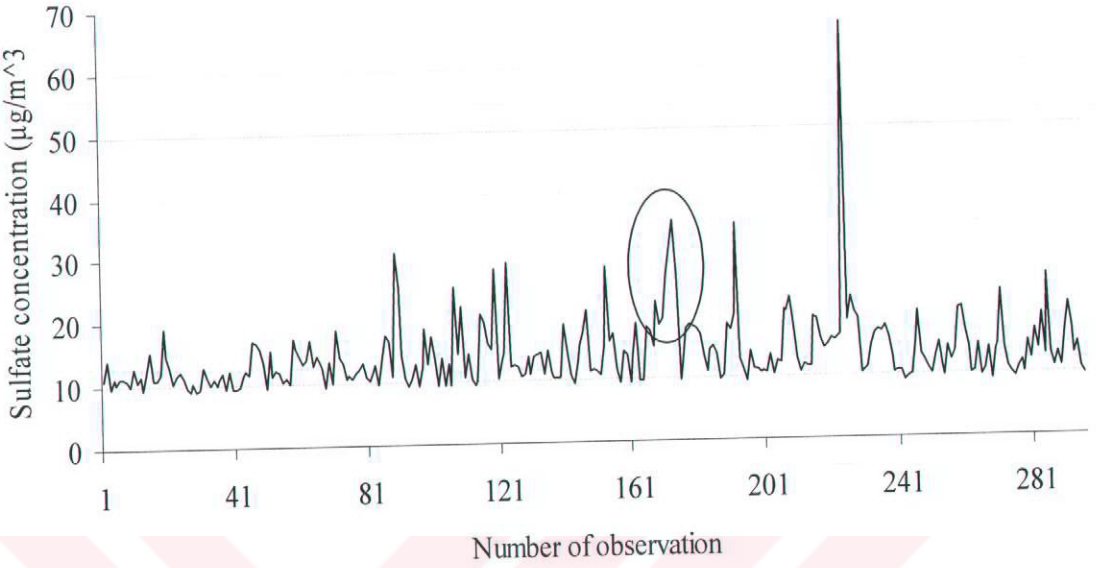

Figure 2.5: The highest 20% discrete measurements of sulfate concentration in Antalya.

1480 individual values of daily SO_4^{2-} concentration measurements have been picked at this station through the years 1992 – 2000 **(Tuncel, 2004).** The average concentration of SO_4^{2-} through the overall period was found to be 6 µg/m^3. Of the 1480 concentration measurements, the highest 20% (296 values) were chosen (Fig. 2.5). Again of the 296 values the ones that less than 10 µg/m^3 were eliminated. The rest 262 values that have concentrations equal to or larger than 10 µg/m^3 were analyzed and the following results were derived:

1. The years 1998, 1999 and 2000 have the greatest annual concentration averages of SO_4^{2-} (15.8, 14.4 and 14.3 µg/m^3 respectively).
2. The years 1998, 1999, 1993 and 2000 have the largest number of days with SO_4^{2-} concentration greater than 10 µg/m^3 (56, 54, 48 and 47 days respectively).
3. High concentration values are mostly measured in summer months between May and September, and rarely in April and March.

4. The longest episode that has concentration values greater than 20 $\mu g/m^3$ is a four-day episode which occurred through the days 26 – 29 August 1998 with concentration values of: 26.3, 30.7, 35.1 and 26.5 $\mu g/m^3$ respectively.

5. Furthermore, two days before and two days after this four day episode (26 – 29 August 1998) are added to constitute the comprehensive investigation period of the study (24 – 31 August 1998).

2.5 Climatological Characteristics of the Study Period, 24 – 31 August 1998

The climatology of the Eastern Mediterranean region during the last eight days (24 – 31) of August 1998 can be summarized as follows:

2.5.1 Climatology during the two days prior the episode, 24 and 25 August 1998

It is obvious from the Mean Sea Level Pressure chart and from the 850 hPa level contour map of 24 August that the Eastern Mediterranean region is influenced by a combination of three systems. The first is the extension of the Indian Summer Monsoon from the southeast through the Arabian Peninsula; the second is the Azores anticyclone extension through the western part of the Mediterranean and central Europe; while the last system is a cyclone centered over the Scandinavia and northern Europe (Fig. B.1, (a) and (b)). In the upper levels, 700 and 500 hpa, the typical subtropical anticyclone covers northern Africa, Mediterranean Sea and the Arabian Peninsula, while a low pressure system lies over the northern parts of Europe (Fig. B.1 (c) and (d)). This situation produces northeasterly to northerly light winds on the surface (Fig. B.1 (a)) and also at the 850 and the 700 hPa levels a negative sign of the both U and V components of the wind are dominant in the Eastern Mediterranean region (Fig. B.2).

The vorticity is defined as the tendency of the air to rotate in either a cyclonic or anticyclonic manner. Positive relative vorticity indicates areas of cyclonic (counterclockwise) rotation of the winds, and/or lateral shear of the wind with stronger flow to the right of the direction of flow. While negative relative vorticity indicates areas of anticyclonic (clockwise) rotation of the winds, and/or lateral shear of the wind with stronger flow to the left of the direction of flow. Areas of positive relative vorticity are

also associated with rising motion and stormy weather, while areas of negative relative vorticity are associated with sinking motion and fair weather. Positive vorticity at 500mb level (in the Northern Hemisphere) is associated with cyclones or storms at upper levels, and will tend to coincide with troughs in the geopotential height field and negative vorticity at 500 hpa level (in the Northern Hemisphere) is associated with calm weather, and will tend to coincide with ridges in the geopotential height field. Furthermore positive vorticity areas are usually characterized by upward motion, while negative vorticity areas are usually characterized by downward motion.

Figure B.3 shows that the relative vorticity at the 850 and 500 hpa levels are very small values (changing between $-2x10^{-5}$ and $+2x10^{-5}$ s^{-1}) with either positive or negative sign. Such values, in the light of the assumptions in the above paragraph, indicate that no well developed system of low or high pressure is seen to take place in the Eastern Mediterranean region. In the other hand there are pronounced centers of maximum relative vorticity such as those over central Europe and over Russia associated to the remarkable upper troughs over these regions, and many minimum relative vorticity centers associated to the ridges of high pressure such as the one that centers over the Black Sea (Fig. B.3).

On the 25th of August, one day prior the onset of episode, the Monsoon trough started to extend to the west through Turkey and the Azores ridge of high pressure started to stretch to the southeast through the southern Mediterranean and Sinai Desert (Fig. B.4) resulting in increasing the westerly and northerly components of the wind which is apparently can be seen from the wide coverage of the positive components – except very small pockets of negative values – of both U and V in Figure B.5. At the same time a slight deepening in the trough at 700 and 500 hPa levels is noticed over the Aegean Sea which leads to more northwesterly flow over the east Mediterranean region (Fig. B.4 (c) and (d)). This result can be explained by the positive relative vorticity values that are associated to the minor upper trough that started to appear in the region (Fig. B.6). As a result of this condition the southeastern Europe and the Aegean Sea regions are characterized by an unstable air associated with upward motion that produce a suitable environment to force the air pollutants in the region to travel vertically to levels higher than the planetary boundary layer where they may be easily transported to other areas.

2.5.2 Climatology of the episodic period, 26 – 29 August 1998

The frontal depression that centered over Scandinavia and northern Europe during the two days prior the episode moved to the east and a ridge of high pressure started to take place instead, covering western Europe and western Mediterranean Sea during the first two days of the episode, the 26th and the 27th of August 1998 (Fig. B.7 and B.10, (a) and (b)). At the same time the Indian summer Monsoon trough has extended beyond Greece to reach the Italian peninsula. The upper trough over the Aegean Sea has become more pronounced on 26 August (Fig. B.7 (c) and (d)). The positive vorticity has increased to values like $+4x10^{-5}$ s^{-1} over the eastern Mediterranean in both 850 and 500 hpa levels (Fig. B.8 and B.12), which indicates the increasing instability conditions over the area and the deepening of the associated upper trough that is obviously seen over the eastern Mediterranean (Fig. B.10, (c) (d)). Additionally a northwesterly polar frontal jet stream over central Europe has started to dig out towards the eastern Mediterranean region which helps to increase the cyclogenesis in the region. Consequently, as a result of the above conditions, obvious completely positive U, and completely negative V components of the wind at 850 and 700 hpa levels (Fig. B.9 and B.11) reflect the permanent northwesterly flow to the eastern Mediterranean region during the two days mentioned above.

On 28 August, the third day of the episode (the day of the largest sulfate concentration in Antalya among the 4 days of the episode) the Monsoon trough has withdraw to the east of Turkey and the eastern coasts of the Mediterranean Sea (Fig. B.13, (a) and (b)), while a Genoa low pressure center started to take place instead, to extend to the east and finally centered over Greece on 29 August, the last day of the episode (Fig. B.16, (a) and (b)). An upper trough has also deepened over Genoa and the subtropical high pressure started to be more pronounced over the southeastern Mediterranean North Africa and Middle East (Fig. B.16, (c) and (d)). This situation deflected the winds at the 850, 700 and 500 hPa levels over the eastern Mediterranean from northwesterly on 28 August (Fig. B.14 and B.15) to southwesterly on 29 August (Fig. B.17 and B.18). The positive relative vorticity values associated to the upper trough and the cyclone over Genoa reveal a remarkable increase reached to $+8 \times 10^{-5}$ s^{-1} (Fig. B.15 and B.18). This area is characterized by a well developed upward motion and consequently precipitation. While

the eastern Mediterranean region show a small relative vorticity values that change between $-2x10^{-5}$ and $+2x10^{-5}$ s^{-1}. These values of relative vorticity are too small to identify a typical pressure system or a permanent upward or downward motion. Therefore both weak upward and downward motion can be experienced in such areas. Thus the situation that prevailed in 29 August 1998 can be considered as the beginning of the end of the episode of the high sulfate concentration in the eastern Mediterranean region. In addition the relative humidity in the eastern Mediterranean region was relatively low and no precipitation has been recorded during the 4 days of the episode, which means that no washout and no wet deposition of sulfate have been occurred.

2.5.3 Climatology during the two days after the episode, 30 and 31 August 1998:

On 30 and 31 August, the two days after the episode, a thermal trough that is known as the Red Sea trough extended over the Middle East and the east of Turkey (Fig. B.19 (a) and B.22 (a)), which creates a northeasterly flow on the surface over the eastern Mediterranean. On the upper levels 850, 700 and 500 hpa levels, a minor upper trough deepened over the Adriatic Sea and Greece and a remarkable high pressure area has covered North Africa and the southern Mediterranean Sea (Fig. B.19 and B.22 (b), (c) and (d)) that leads to westerly to southwesterly flow over the eastern Mediterranean region. This can be obviously seen from the positive U and negative V wind components at the 850 and 700 hpa levels from Fig. B.20 and B.23, and from the wind vector graphics at the 850 and 500 hpa levels in Fig. B.21 and B.24. Obvious negative vorticity areas are also noticed in Fig. B.21 and B.24 over North Africa, Eastern Mediterranean and Middle East regions associated to the huge subtropical anticyclone that covers these regions. These pronounced negative vorticity values indicate a stable weather and the downward motion.

3. ATMOSPHERIC CHEMISTRY AND PHYSICS OF AEROSOLS

Airborne particulate matter is a complex mixture of many different chemical species originating from a variety of sources. Composition, morphology, physical and thermodynamic properties of PM varies in different geographical places and has a seasonal variability **(Alpert and Hopke, 1981).** Sources of PM can be either primary or secondary in nature. Primary particles can be furthermore divided as anthropogenic or natural depending on their origin. Secondary formed particles in the atmosphere are from both natural and anthropogenic origin and are originating from chemical transformations of gaseous precursors such as sulfur dioxide, nitrogen oxides and VOCs.

In Europe anthropogenic sources are dominant because of the urbanization of many countries and the large number of vehicles and combustion sources (industrial and residential). Natural sources of primary aerosols in Europe include sea spray, fugitive dust (e.g. soil resuspension by the wind), long-range transport of Sahara dust, volcanic and biogenic emissions.

An important characteristic of atmospheric particulate matter is the tremendous variation in size ranging from tens of micrometers to a nanometer size **(EPA, 1996).** For example combustion-generated particles (vehicle emissions, power generation) are ranging in size between 0.003 to 1 μm. Pollens and soil dust is composed of particles mainly above 2 μm, whereas fly ash from coal combustion produces particles ranging from 0.1 to 50 μm. In addition, aerosols in the atmosphere undergo changes in their chemical composition and size. This is due to a variety of physical and chemical processes such as nucleation (new particle formation), condensation, evaporation, coagulation, deposition (both wet and dry), activation due to water and other gaseous species and aqueous phase reactions **(Finlayson-Pitts and Pitts, 1986; Seinfeld and Pandis, 1998).**

The dynamics of the particulate matter in the atmosphere involve various physical and chemical processes under different time scales. Furthermore, aerosol dynamics involve

wide range of particle sizes ranging from few nanometers to several hundred micrometers, different compositions and chemical reactivity and undergo complex physical transformations (nucleation, condensation, coagulation and deposition processes). Aerosols arise from natural and anthropogenic sources and are mixture of primary emissions and secondary species. Crustal material, biogenic matter and sea-salt comprise the majority of natural aerosols. Anthropogenic aerosols are composed of primary emitted soot (elemental carbon) and secondary formed carbonaceous material (organic carbon) and inorganic matter (nitrates, sulfates, ammonium and water). Therefore modeling or measuring atmospheric aerosols involves many challenging tasks and is a fast evolving scientific area **(Lazaridis and Melas, 1998; Seigneur et al., 1999).** Meteorological processes affect substantially the physical and chemical processes of atmospheric aerosols as well as the geographical and temporal variation of their sources.

3.1 Physical and Chemical Processes in the Atmosphere

The determination of the aerosol size distribution is one of the most important aspects involved both in measuring and modeling aerosol dynamics. However, the size distribution is a time and spatial evolving property of atmospheric aerosols and involves transfer of material through the gas phase, vapor phase and particle phase. Based on a modal classification by **Whitby (1978)** the aerosol size distribution can be viewed as an addition of several lognormal distributions. These include the Coarse Mode (aerosol mass aerodynamic diameter larger than 3 μm), the Fine Mode (between 1 and 3 μm), the Accumulation Mode (from 0.1 to 1 μm) and the Nuclei Mode (below 0.1 μm). The aerosol behavior in the atmosphere is controlled by internal and external processes. Processes that act within the system boundaries are called internal processes whether processes that at act across system boundaries are called external processes. Internal processes include the coagulation, condensation, evaporation, adsorption/desorption, heterogeneous chemistry and nucleation mechanisms. External processes involve convection, diffusion and the effect of external forces.

3.1.1 Physical processes

3.1.1.1 Nucleation

Nucleation (new particle formation) in the atmosphere has been observed in the vicinity of polluted sources **(Hegg et al., 1985)** and in clean, remote regions **(Clarke et al., 1998).** Nucleation bursts (homogeneous nucleation) may be responsible for the occurrence of new particle formation in clean environment where the background aerosol concentration is low **(Lazaridis and Melas, 1998; Clement and Ford, 1999 a, b).**

Nucleation is the initial stage of a first-order phase transition that takes place in various energetically metastable or unstable systems **(Clement and Ford, 1999 a, b).** In the atmosphere, where various condensable vapors exist in low concentrations, binary (two-component) or multicomponent nucleation is the predominant particle-formation mechanism **(Kulmala et al., 1995).** Even though the homogeneous nucleation process is not an important mechanism for determining the aerosol mass size distribution contributes a large amount of newly formed particles in the atmosphere and shapes the number size distribution. Nucleation on the surface of pre-existing aerosol particles (heterogeneous nucleation) is also a favorable process in the atmosphere, since in the formation of critical clusters it is not necessary to have such a high super saturation as in the homogeneous case **(Lazaridis et al., 1998).**

Several modeling studies have investigated the new particle formation of sulfate particles under various atmospheric conditions **(Clarke et al., 1998; Kulmala et al., 1995; Lazaridis and Melas, 1998; Clement and Ford, 1999 a, b).** These modelling studies are based on the classical model of homogeneous nucleation **(Abraham, 1974)** or on semi-empirical functions **(Binkowski and Shankar, 1995).** A serious uncertainty in modeling new particle formation for the sulfuric acid-water system is that there are no consistent available experimental data in the whole range of water and acid activities, and temperature; neither current available models for binary nucleation agree closely with experimental results. One reason for the disagreement between theory and experimental results is the conditions under which the experiments were performed, since the system presents intrinsic experimental difficulties related to its corrosive

properties and extremely low vapor pressures. However, the classical theory of binary nucleation follows the experimental trend of the measurements at high relative humidities and these at high acid activities.

The classical theory of nucleation is based on the phenomenological concept of a droplet that is viewed as a group of molecules which interact strongly among themselves and weakly with the rest of the system. According to the classical theory, the nucleating cluster is treated with equilibrium thermodynamics as a macroscopic droplet whose free energy of formation depends crucially on the bulk surface tension. The kinetics by which small clusters of the new phase gain or loose molecules is based on ideas developed in chemical kinetics. It is assumed that clusters grow or shrink via the gain or loss of single molecules, an approximation that is reasonable for condensation at low pressures. However, the classical theory being a phenomenological approach lacks a sound microscopic foundation **(Lazaridis and Drossinos, 1997).**

The nucleation rate according the classical theory can be expressed as:

$$J = J_0 \exp\left(-\beta F^*\right) \qquad \textbf{(3.1)}$$

Where:

J_0 : is a kinetic prefactor,

βF^* : is the free energy of formation of the critical droplet, and

$\beta = 1/k_B T$ where, k_B: is the Boltzmann constant and T is the temperature.

The expression for the kinetic prefactor for the binary nucleation may be written in a form similar to the one used in one-component nucleation as follows **(Lazaridis and Drossinos, 1997)**:

$$J_0 = \rho_v ABZ \qquad \textbf{(3.2)}$$

Where:

ρ_v : is the total density of condensable vapors,

A: is the surface area of the droplet,

B: is the average growth rate, and

Z: is the Zeldovich non-equilibrium factor.

From the modeling point of view there are available models for binary and unary nucleation in the literature that are already integrated in regional and mesoscale transport models **(Binkowski and Shankar, 1995; Lazaridis and Melas, 1998).** In addition, various parameterizations have been used for the nucleation rate in atmospheric modeling based on experimental. The problem of new particle formation in the atmosphere is an active field and there are still many unresolved questions to be answered **(Clarke et al., 1998; Clement and Ford, 1999 a, b).**

3.1.1.2 Particle growth

Particle growth is occurring through the mass and energy transfer from/to the vapor to the particle phase. Vapor condensation/evaporation and heterogeneous reactions on the surface or inside the particles are the main mechanisms for particle growth. The condensation mechanism is a rate-limiting process and the ratio of the mean free path in air to the particle radius (Knudsen number, Kn) is an important factor. When particles are much smaller that the mean free path of the surrounding air (free molecular regime) the transport is controlled by the molecular impingement on the particle surface. When particles are larger than the mean free path (continuum regime) the diffusion is the limiting control mechanism. When the Knudsen number is close to one, the regime is called transition regime. The Boltzmann equation can be used for solving rigorously the condensation problem in the transition regime but since there is not a full solution of the Boltzman equation in the whole regime of Knudsen numbers there have been flux matching approximations such as the Fuchs and Sutugin approach **(Fuchs, 1964).** In the flux matching approximations the noncontinuum effects are limited to a region close to the particle and outside the continuum theory applies **(Seinfeld and Pandis, 1998).**

One approach to model binary condensation is the use of the Mason equation **(Mason, 1971).** However, other approaches use an equilibrium method to distribute the mass of inorganic matter between the vapor and particle phase and also inside the particle phase. A simplified method which is used in modeling urban and regional aerosols with the Urban Airshed Model (UAMAERO) adopted the equilibrium method together with a mass allocation method to the size distribution.

The condensation rate of vapor species j onto pre-existing aerosol particles using a modified Mason equation, where the transitional correction factors are included can be expressed as:

$$\frac{dm}{dt} = \frac{4\pi r\left(S_\infty - S_{r,j}\right)}{\frac{N_M}{\beta_M} + \frac{N_T}{\beta_T}} \tag{3.3}$$

With:

$$N_M = \frac{R_g T_\infty}{D_\infty M P_S\left(T_\infty\right)} \tag{3.4}$$

And

$$N_T = \frac{L}{K_B T_\infty}\left(\frac{LM}{K_B T_\infty} - 1\right) \tag{3.5}$$

Where:

β_M and β_T are the transitional correction factors for the mass and heat transfer,

D_∞: is the binary diffusion coefficient,

M: is the molecular weight of the liquid,

L: is the latent heat of condensation,

S_∞: is the saturation ratio of the gas far from the particle and

$S_{r,j}$: is the saturation ratio of gas species *j* at the particle surface.

In addition to the direct condensation on aerosols there are other important mechanisms responsible for their growth as aqueous phase reactions of activated soluble particles in fogs and clouds **(Lurmann et al., 1997).** Aqueous phase reaction mechanisms are in agreement with experimental observations of the aerosol size distribution.

The mechanism of gas-to-particle conversion of sulfur dioxide to sulfate aerosol may take place in two phases:

1- The aqueous phase, which occurs in a solution if droplets are present. The oxidation of SO_2 in aqueous solution, mainly rain or fog droplets, tend to

produce large sulfate containing particles in the presence of NH_3 **(Mason, 1971).** The formation of aerosol-sized particles results from evaporation of the droplets. Condensation and evaporation may take place many times in the atmosphere before the sulfate finally precipitate as rain.

2- The dry phase, which possibly occurs on the surface of solids. The oxidation of SO_2 may be also catalyzed by surface reactions. This is the mechanism by which sulfuric acid is produced industrially over platinum catalysts **(Novakov et al., 1974).**

3.1.1.3 Coagulation

Aerosols in the atmosphere can collide due to their Brownian motion or due to hydrodynamic, electrical or gravitational forces. This is called coagulation (or agglomeration) mechanism and is very crucial in the development of the size distribution in the atmosphere. The collision of particles in the atmosphere is given by the Smoluchowski equation that is normally expressed in terms of particle volume coordinates **(Williams and Loyalka, 1991).** Furthermore, the coagulation equation can be written in continuous or discrete forms **(Williams and Loyalka, 1991; Seinfeld and Pandis, 1998).**

Following the discrete representation, as a result of coagulation between particles, particles are both removed from and added to size bins **(Lazaridis and Koutrakis, 1997).** If two particles of masses m1 and m2 coagulate, the mass of the particle formed is m3 = m1+m2. If K1,2 n1 n2 is the coagulation rate between particles of masses m1 and m2, then : dn1/dt = - K1,2 n1 n2, dn2/dt = - K1,2 n1 n2 and dn3/dt = K1,2 n1 n2. There is a net loss of one particle per coagulation but the total mass is conserved. Generalizing the above equations we can obtain:

$$\frac{dn_k}{dt} = \frac{1}{2}\sum_{i+j=k} K(m_i, m_j) n_i n_j - n_k \sum_{i=1}^{\infty} K(m_i, m_k) n_j \qquad \textbf{(3.6)}$$

Where: i+j = k means that the summation is taken over those grid points for which Mk = mi+mj.

The complexity of integrating detailed aerosol dynamics in air quality models resulted to the exclusion of coagulation processes (e.g. **Lurmann et al., 1997**). However, in regional aerosol modeling studies where the effect of number size distribution is crucial in radiative forcing explicit modeling of coagulation processes is included **(Binkowski and Shankar, 1995).**

3.1.1.4 Deposition

Aerosols and gaseous species are removed from the atmosphere through the mechanisms of dry and wet deposition. It is a common practice to parameterize the deposition process using the concept of deposition velocity. The deposition velocity is defined as the ratio of the deposition flux of the specified pollutant **(Seinfeld and Pandis, 1998)** to the pollutant concentration. There are two general approaches to determine the dry deposition velocity. In the first method available experimental data for different aerosol and gaseous species are used. The second method is based on the transfer of material from the atmosphere to the earth's surface through different resistance mechanisms, the aerodynamic resistance, the surface resistance and the transfer resistance **(Slinn and Slinn, 1980).** The process is discussed in detail in chapter five, section 5.4.

3.1.2 Chemical processes

3.1.2.1 Gas phase reactions

Atmospheric chemistry involves a large number of reactive species which are in ppm and ppb levels. For example the formation of ozone and nitrogen dioxide involves a large number of non-linear chemical reactions (e.g. **Simpson, 1995; Gery et al., 1989**). Furthermore, the chemical reaction rates depend also on the background concentration of the various chemical species that is determined from the emission and meteorological characteristics. The modeling of gaseous chemical reactions in the atmosphere is a difficult task because of the complex chemical reactions and the stochastic mixing processes due to turbulence. Several simplifications are adopted in describing the gaseous phase chemical reactions in air quality models.

The gas-phase chemical mechanisms included in air quality models do not include an explicit reaction scheme for all chemical reactions but instead use "lumped" categories

such as the SAPRC and RADM mechanisms (including lumped mechanisms for alkanes, alkenes etc.) and the CBM-IV mechanism (lumped bonds such as C-C, C=C).

3.1.2.2 Vapor-particle equilibrium

The simulation of the vapor/particle equilibrium in the atmosphere involves the prediction of the main primary and secondary components of atmospheric aerosols in the whole range of the particle size distribution. The main components of aerosols include sulfate, nitrate, ammonium, chloride, elemental carbon, organic carbon, water, chloride and crustal material **(Lurmann et al., 1997).**

The formation of sulfuric acid in the gaseous phase is mainly concentrated on the oxidation of sulfur dioxide by certain free radicals **(Friedlander, 1978).** The most important such radicals are thought to be:

(i) The hydroxyl, OH: $SO_2 + OH + M \rightarrow HSO_3 + M$

(ii) The hydroperoxyl, HO_2: $SO_2 + HO_2 \rightarrow SO_3 + OH$

(iii) Peroxyalkyl, RO_2 $SO_2 + RO_2 \rightarrow SO_3 + RO.$

The SO_3 is then rapidly converted to H_2SO_4 by combination with water vapor

$SO_3 + H_2O \rightarrow H_2SO_4$

The produced sulfuric acid mainly condenses on pre-existing aerosol particles or leads to new particle formation due to homogeneous nucleation. The production of secondary organic particulate matter and of gaseous low-volatility organic products is generally described using condensed lumped reactions including an oxidant reactant (e.g. OH, O_3, and NO3) **(Seinfeld and Pandis, 1998):**

$HC + Oxidant \rightarrow xX + yY + \ldots + gG$

Where: X, Y are the gaseous phase organic products and G refers to condensable organic gas that forms secondary organic aerosols. The low case characters (x,y,…,g) are the corresponding stoichiometric coefficients that correspond to aerosol yields.

3.2 Chemical Composition

3.2.1 Acid aerosols (sulfates-nitrates)

Aerosol acidity is defined as acids and their precursors residing in the atmosphere in the gas and aqueous phase **(Sioutas and Koutrakis, 1996).** Strong acidity refers mainly to sulfuric acid or partly neutralized acid particles, whereas weak acidity includes a number of inorganic (e.g. nitrous acid, hydrogen phosphates, hydrochloric acids) and organic species (e.g. phenols, carboxylic acids).

The production of sulfuric acid in the atmosphere occurs mainly through photo oxidation of sulfur dioxide with hydroxyl radicals in the gaseous phase. Aqueous phase reactions of SO2 with hydrogen peroxide (H_2O_2) are also a very important pathway for sulfuric acid production since it occurs also at nighttime. Further neutralization of the aerosol particles occur with the diffusion of ammonia (NH_3) in the liquid phase **(Sioutas and Koutrakis, 1996).** Sulfate formation takes place in clouds and fogs, where aqueous phase reactions are dominant process. High production rates of aerosol particles are observed in the vicinity of clouds suggesting homogeneous nucleation of H_2SO_4/H_2O particles **(Hegg et al., 1993; Clarke et al., 1998; Clement and Ford, 1999 a, b).**

Nitric acid is mainly formed through the photo-oxidation reaction between NO_2 and OH. During night time there is a reaction between NO_2 and O_3 to form NO_3 which is further reacts with NO_2 to form nitrogen peroxide (N_2O_5). Furthermore, N_2O_5 can react with water vapor to form aqueous nitric acid. Even though this is a slow reaction it can be reaction of N_2O_5 with condensed water (cloud or fog droplets) that is considerably faster **(Tuazon et al., 1983).** Nitric acid can be neutralized when it is reacting with ammonia and forms particulate ammonium nitrate. Nitric acid can be also react with salts of chlorine or carbonate and forms particulate salt solution. In addition the reactions in the atmosphere between NO and OH leads to the production of nitrous acid (HONO). Calculations for the inorganic portion of the atmospheric aerosols are mainly performed using multicomponent equilibrium models. An example of this kind is the SEQUILIB equilibrium model that calculates the total quantities of ammonium, chloride, nitrate and water components of the atmospheric aerosols 19 **(Pilinis and Seinfeld, 1987).** The

SEQUILIB model I, also integrated in the mesoscale air quality model UAM-AERO **(Lurmann et al., 1997).**

3.2.2 Carbon-containing aerosols

3.2.2.1 Elemental carbon- primary organic carbon

Elemental carbon (EC) has a chemical structure similar to impure graphite and is emitted as primary particles mainly during combustion processes (wood-burning, diesel engines) **(EPA, 1996).** Elemental carbon both absorbs and scatters light and contributes significantly to the total light extinction **(Finlayson-Pitts and Pitts, 1986).** Much higher concentrations of EC are found in urban areas compared to rural and remote locations. In rural and remote locations the EC concentration varies between 0.2 and 2.0 $\mu g\ m^{-3}$, and between 1.5 – 20 $\mu g\ m^{-3}$ in urban areas **(Rau, 1989).**

The organic carbon is a complex mixture of thousands of different organic compounds and a very small portion of it is molecular characterized (around 10%). Organic compounds that have been characterized include among others n-alkanes, n-alkanoic acids and polycyclic aromatic compounds. Due to difficulty in measuring organic compounds our current knowledge about organic matter is limited and incomplete. Primary emission sources for organic carbon include combustion processes, geological (fossil fuels) and biogenic sources.

3.2.2.2 Secondary organic matter formation (secondary organic carbon)

An important part of secondary aerosol particles in the atmosphere is composed by secondary formed organic matter produced from oxidation of organic compounds. Partitioning of gas-particle organic compounds in the atmosphere is an important task for determining their association with the fine particulate matter. Understanding the mechanisms that control the conversion of organic matter from the vapor to particulate matter will provide valuable information for determining future control strategies for reducing the partition of organic matter in the particulate phase. However, there is a great complexity of the number of different chemical forms of organic matter and absence of direct chemical analysis which resulted to use mainly experimentally determined fractional aerosol yields, fractional aerosol coefficients and adsorption/

absorption methodologies to describe the incorporation of organic matter in the aerosol phase.

An important pathway for secondary organic particle formation is arising from biogenic hydrocarbons. There are very large quantities of biogenic hydrocarbons that are globally emitted which are also highly reactive. Annual global emissions of biogenic hydrocarbons are estimated to be between 825 and 1150 Tg C per year, whereas the anthropogenic emissions are estimated to be less than 100 Tg C per year **(Hoffmann et al., 1997).**

An empirical approach to describe secondary organic aerosol (SOA) formation is based on the fractional aerosol coefficient (FAC) method that is defined as **(Grosjean and Seinfeld, 1989):**

FAC (dimensionless) = [SOA] (mg m^{-3}) / [VOC] o (mg m^{-3})

Where: [VOC]o is the initial VOC concentration. The VOC concentration is expected to be obtained by experimental data and the SOA mass concentration from available smog chamber experiments (based on VOC-NOx irradiation and VOC-O_3 reaction in dark). Therefore, the FAC is defined through a number of empirical parameters which is not taking into account SOA variations based for example on VOC/NOx ratio. Application of FAC for individual VOC is estimated by **Grosjean (1992).**

3.2.2.3 Metal and other trace elements

Trace metals in atmospheric particulate matter are mainly from anthropogenic sources such as residential wood combustion, forest fires, combustion of coal and oil, waste incineration and metal smelting **(Chow et al., 1992).** In the fine particle size range there have been found various trace metals including mainly Pb, Zn, Cd, As, Sb, Ag, In, La, Mo, I, and Sm **(EPA, 1996).** In the coarse mode there have been found mainly Ca, Al, Ti, Mg, Sc, La, Lu, Hf and Th (Klee, 1984). Furthermore, in both the fine and coarse modes there have been found Na, K, Fe, V, Cr, Co, Ni, Mn, Cu, Se, Ba, Cl, Ga, Cs, Eu, W, and Au **(EPA, 1996).** Emissions, meteorology and photochemistry are important aspects which control the ambient concentration of trace species in the particulate phase **(Finlayson-Pitts and Pitts, 1986).**

3.3 Biological Aerosols

A definition of the primary biological aerosol particles (PBAP) can be written as: "Primary Biological Aerosol Particles describe airborne solid particles (dead or alive) that are or were derived from living organisms, including microorganisms and fragments of all varieties of living things". PBAP include viruses (0.005 μm < r < 0.25 μm) (r, refers to particle radius), bacteria (r ≥0.2 μm), algae, spores of lichen mosses, ferns and fungi (r ≥0.5 μm), pollen (r ≥5 μm), plant debris like leaf litter, part of insects, human and animal epithelial cells (usually r > 1 μm) **(Lazaridis et al., 1999).**

The composition of the PBAP is changing through the year as following:

- Spring: microorganism, pollen, some spores, a few fragments,
- Summer: microorganism, pollen, spores, a few fragments,
- Autumn: microorganism, fragments, spores, a few pollen,
- Winter: microorganism, fragments, spores, some pollen.

3.4 Status of Modeling Aerosol Processes

There are currently several three-dimensional Eulerian air quality models that include a PM module. The modeling of particulate matter is mostly concentrated in a revised chemistry module and deposition module. There is no available aerosol dynamics modeling, no cloud chemistry and no sub-grid treatment of subgrid modeling. However, the RPM model has the ability to model detailed aerosol dynamic processes using a modal method to describe the aerosol size distribution **(Binkowski and Shankar, 1995).**

The description of the pollutant transport in the 3-D air quality models is performed using the atmospheric diffusion equation including a source term and a scavenging term. The atmospheric diffusion equation can be written as **(Seinfeld and Pandis, 1998):**

$$\frac{\partial C_i}{\partial t} + u_j \frac{\partial C_i}{\partial x_j} = \frac{\partial}{\partial x_j}\left(K_{jj} \frac{\partial C_i}{\partial x_j} \right) + R_i(x,t) + S(x,t) \qquad (3.7)$$

Where:

C_i: is the mean concentration of species i,

x_j: the space coordinate at the direction j (j=1-3),

Kjj: is the eddy diffusivity at the direction j,

Ri(x,t): denotes the scavenging of species during chemical reactions and deposition, and

Si(x,t): is the source term (emissions).

The numerical evaluation of the atmospheric diffusion equation is usually performed using an operator splitting technique, which employs a separation of the horizontal and vertical transport terms from the chemical reaction and emission terms so that each term is solved separately.

The available 3-D air quality models including modeling of aerosol processes (in addition to EMEP work) are presented in the next subsections **(Seigneur et al., 1999).**

3.4.1 Mesoscale models

(1) The California Institute of Technology model (CIT)

(2) The Denver Air Quality Model (DAQM)

(3) The Gas, Aerosol, Transport and Radiation model (GATOR)

(4) The Regional Particulate Model (RPM)

(5) The SARMAP Air Quality Model with aerosols (SAQM-AERO)

(6) The Urban Airshed Model Version IV with aerosols (UAM-AERO)

3.4.2 Long range transport models

(1) The Regulatory Modeling System for Aerosols and Deposition (REMSAD)

(2) The Urban Airshed Model Version IV with linearized chemistry (UAM-LC)

(3) The Visibility and Haze in the Western Atmosphere model (VISHWA)

In the European level the EUTREND model has been also used for calculating primary PM_{10}. However, the model has not the possibility to include the formation of secondary aerosols.

Currently, the EMEP model is the main regional regulatory modeling tool in studying photochemical pollutants and acidification Europe and treats the PM10 and PM2.5 fractions of the atmospheric sulfate and nitrate aerosol using a simplified approach. The

EMEP Lagrangian model calculates the air concentrations of sulfate, nitrate, ammonium sulfate and ammonium nitrate secondary formed particles using lumped reaction rates.

3.5 Effects of Aerosols on Ecosystems, Climate and Materials

3.5.1 Acidification-Eutrophication

Pollutants emitted to the atmosphere such as SO_2 and NO_x are oxidized to sulfate and nitrate through gaseous and aqueous phase reactions. These particle species are removed by both dry and wet deposition to the earth's surface leading to effects such as acidification and eutrophication (mostly due to fertilizers and particle deposition). The deposition of sulfate and nitrate particles is dependent on their size that is controlled by the aerosol dynamic processes in the atmosphere. Eutrophication is becoming a serious threat to coastal environments and seems to be a global problem in the next decades. Water enriched with nutrients leads to higher production of organic matter and results to oxygen deficiency which kills marine life **(EMEP-WMO, 1997; Spengler et al., 1989; Pelley, 1998).**

3.5.2 Visibility reduction

Visibility degradation is one of the most readily perceived impacts of fine particulate matter. Fine particles absorb and scatter the light and therefore reducing visibility. The process can be described with the Mie theory **(Seinfeld and Pandis, 1998).** For example in many parts of the United States the visual range has been reduced 70% from natural conditions. In the eastern part of US, the current range is 14-24 miles vs. a natural visibility of 90 miles. In the western US the current range is 33-90 miles vs. a natural visibility of 140 miles. Fine particles (mainly in the accumulation mode, with diameter between 0.3-1.0 μm) make the major contribution to visibility reduction **(EPA, 1996).**

3.5.3 Radiative Forcing

Particulate matter influences the climate directly (through scattering and absorption of the solar radiation) and indirectly through the formation of cloud condensation nuclei. The direct aerosol contribution to radiative forcing is due to sulfate aerosols, fossil fuel soot and biomass burning. The radiative forcing due to sulfate aerosols is estimated to be -0.4 W m^{-2}, with a factor of 2 uncertainty **(Houghton, 1996).** The effect of soot aerosols

is + 0.1 W m^{-2} with a factor of 3 uncertainty and the contribution from biomass burning is estimated to be -0.2 W m^{-2} with a factor of three uncertainty. Therefore the total direct forcing is estimated to be -0.5 W m^{-2} with a factor of 3 uncertainty. The indirect effect of aerosols is still uncertain with an estimated effect from 0 to -1.5 W m^{-2} **(Houghton et al., 1995).** In addition, aerosols can result to considerable changes of soil moisture which can have impacts in the hydrological cycle on vegetation **(Houghton et al., 1995).**

3.5.4 Soiling and damage to materials

An important effect of particulate matter pollution is the soiling of man-made surfaces. The process of cleaning, painting and repairing exposed surfaces becomes an economic burden. Acid particles can severely deteriorate art works and historic monuments (cultural heritage) and results to the reduction of their aesthetic appeal and life span. Chemical degradation of materials due to deposition of atmospheric acid particles is an important aspect of material damage **(Hamilton and Mansfield, 1993).**

4. THE MESOSCALE METEOROLOGICAL MODEL, MM5

4.1 Brief Description

The PSU/NCAR **M**esoscale **M**odeling System, 5th generation (**MM5**) version 3.61 is a limited-area, nonhydrostatic, terrain-following sigma-coordinate model designed to simulate or predict mesoscale and regional-scale atmospheric circulation. It has been developed at Penn State and NCAR as a community mesoscale model and is continuously being improved by contributions from users at several universities and government laboratories.

The Fifth-Generation NCAR/Penn State Mesoscale Model (MM5) version 3.61 is the latest in a series that developed from a mesoscale model used by Anthes at Penn State in the early 70's that was later documented by **Anthes and Warner (1978).** Since that time, it has undergone many changes designed to broaden its usage. These include (i) A multiple-nest capability, (ii) Nonhydrostatic dynamics, which allows the model to be used at a few-kilometer scale, (iii) Multitasking capability on shared and distributed-memory machines, (iv) A four-dimensional data-assimilation capability, and (v) More physics options.

The model (known as MM5) is supported by several auxiliary programs, which are referred to collectively as the MM5 modeling system. A schematic diagram (Fig. 4.1) is intended to show the order of the programs and the flow of the data, and to briefly describe their primary functions. A brief description for each of these programs is given in section 4.10.

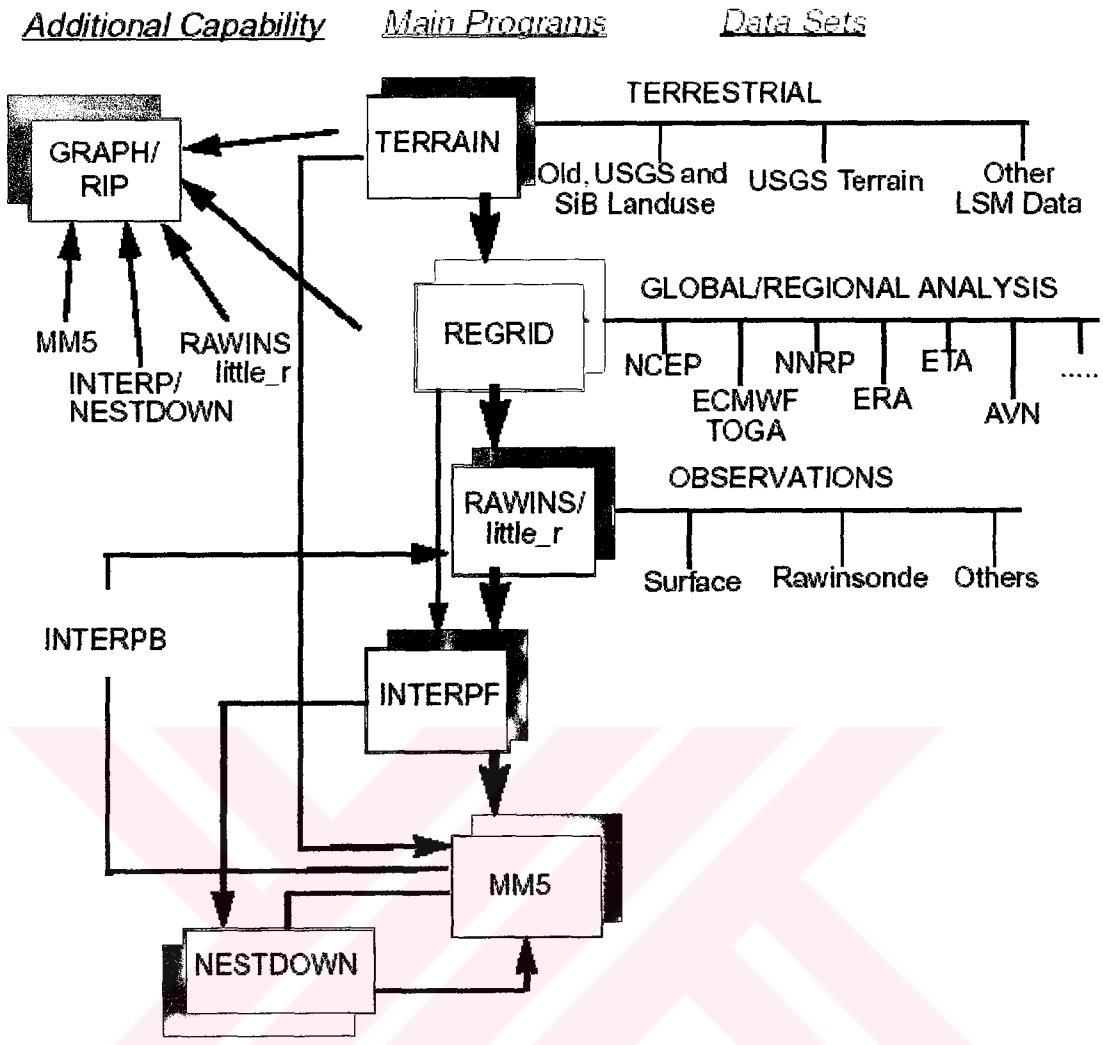

Figure 4.1: A schematic representation of the MM5 modeling system (Dudhia et al., 2004).

4.2 Some Features of MM5 Modeling System – Version 3.61, the Latest Release

I. Globally re-locatable

- Three map projections:
  - Polar stereographic;
  - Lambert conformal;
  - Mercator.
- Support different true latitudes.
- Variable resolution terrain elevation, landuse, soil type, deep soil.

temperature, vegetation fraction, and land-water mask datasets are provided.

II. Flexible and multiple nesting capability

- Can be configured to run from global scale down to cloud scale in one model.
- Can be run in both 2-way and 1-way nesting mode:
  - 2-way: multiple nests and moving nests
  - 1-way: fine-mesh model driven by coarse-mesh model
- Nest domain can start and stop at any time.
- Nest terrain file may be input at the time of nest start-up in the model.

III. Real-data inputs

- Use routine observations

  Upper air and surface reports, including wind, temperature, relative humidity, sea-level pressure, and sea surface temperature.
- Couple with global models and other regional models

  Use other model's output either as first guess for objective analysis, or as lateral boundary conditions, e.g. NCEP and ECMWF global analysis, NCEP/NCAR and ECMWF reanalysis, NCEP ETA model.

V. Non-hydrostatic dynamic frameworks.

VI. Terrain-following vertical coordinates.

VII. Choices of advanced physical parameterization.

VIII. Four-dimensional data assimilation system via nudging.

4.3 The MM5 Model Horizontal and Vertical Grid

The modeling system usually gets and analyzes its data on pressure surfaces, but these have to be interpolated to the model's vertical coordinate before being input to the model. The vertical coordinate is terrain following (see Fig. 4.2), meaning that the lower grid levels follow the terrain while the upper surface is flat. Intermediate levels progressively flatten as the pressure decreases toward the chosen top pressure. A dimensionless quantity σ is used to define the model levels

$$\sigma = (p - p_t)/(p_s - p_t) \tag{4.1}$$

Where:

P: is the pressure, p_t: is a specified constant top pressure and p_s: is the surface pressure.

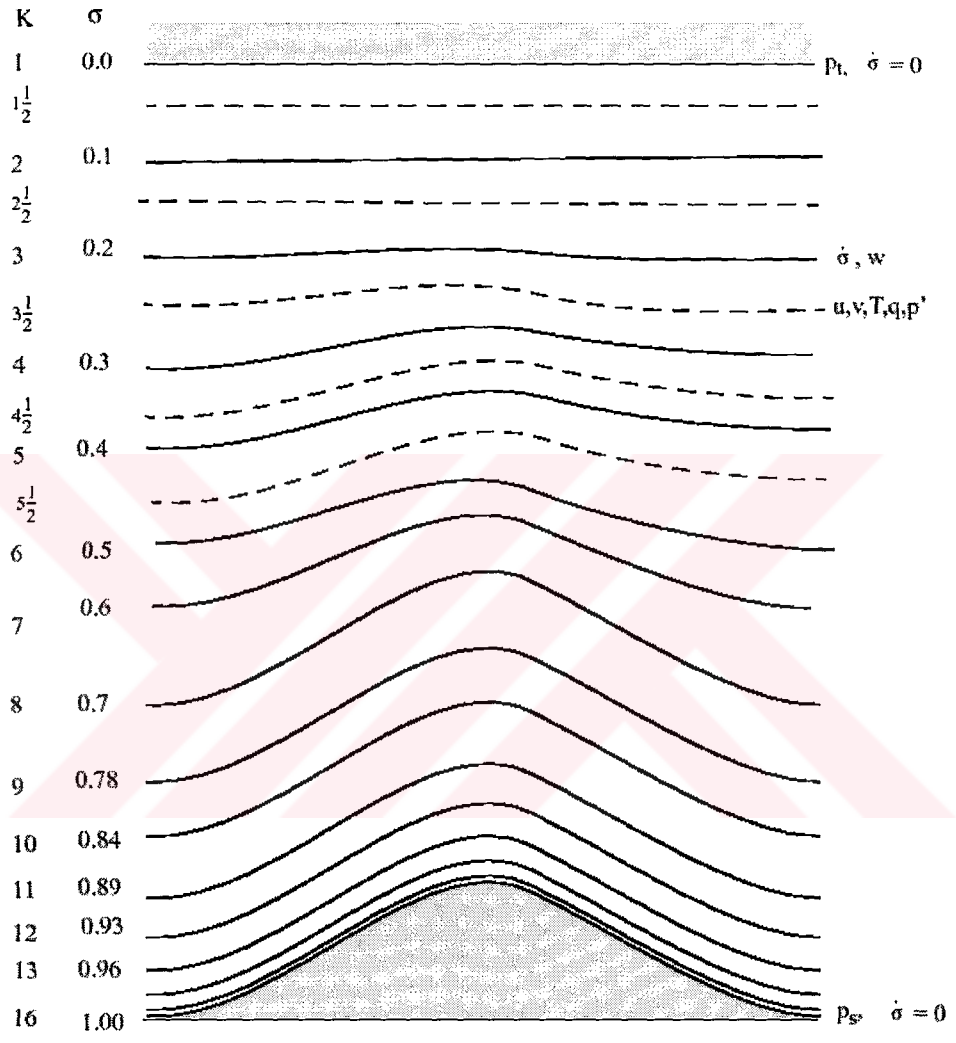

Figure 4.2: The vertical structure of MM5 model. The scheme represents an example for 15 vertical layers. Dashed lines denote half-sigma levels; solid lines denote full-sigma levels (Dudhia et al., 2004).

The nonhydrostatic model coordinate uses a reference-state pressure to define the coordinate rather than the actual pressure which is used in the hydrostatic model. It can be seen from equation (4.1) and Fig 4.2 that σ is zero at the top and one at the surface, and each model level is defined by a value of σ. The model vertical resolution is defined

by a list of values between zero and one. Commonly the resolution in the boundary layer is much finer than above, and the number of levels may vary from ten to forty, although there is no limit in principle.

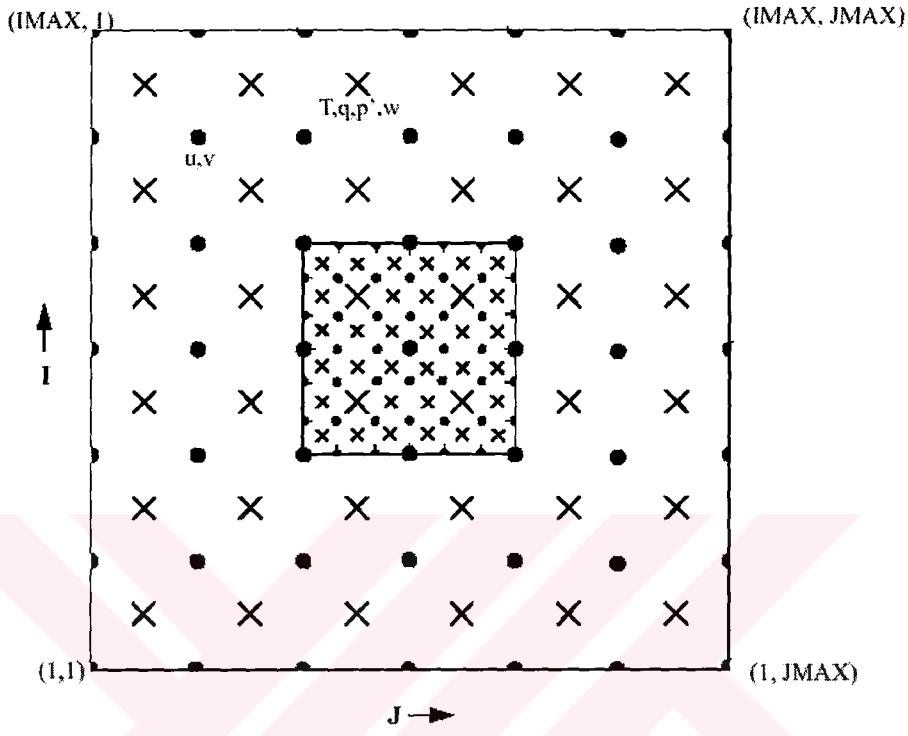

Figure 4.3: Schematic representation showing the horizontal Arakawa B-grid staggering of the dot and cross (x) grid points. The smaller inner box is a representative mesh staggering for a 3:1 course-grid distance to fine-grid distance ratio (Dudhia et al., 2004).

The horizontal grid has an Arakawa-Lamb B-staggering of the velocity variables with respect to the scalars. This is shown in Fig 4.3 where it can be seen that the scalars (T, q etc.) are defined at the center of the grid square, while the eastward (u) and northward (v) velocity components are collocated at the corners. The center points of the grid squares will be referred to as cross points and the corner points are dot points. Hence horizontal velocity is defined at dot points, for example, and when data is input to the model the preprocessors do the necessary interpolations to assure consistency with the grid.

All the above variables are defined in the middle of each model vertical layer, referred to as half-levels and represented by the dashed lines in Fig 4.2. Vertical velocity is carried at the full levels (solid lines). In defining the sigma levels it is the full levels that are listed, including levels at 0 and 1. The number of model layers is therefore always one less than the number of full sigma levels. Note also the I, J, and K index directions in the modeling system.

The finite differencing in the model is, of course, crucially dependent upon the grid staggering wherever gradients or averaging are required to represent terms in the equations, and more details of this can be found in the model description document **(Grell et al., 1994).**

4.4 Nesting

MM5 contains a capability of multiple nesting with up to nine domains running at the same time and completely interacting. The nesting ratio is always 3:1 for two-way interaction. "Two-way interaction" means that the nest's input from the coarse mesh comes via its boundaries, while the feedback to the coarser mesh occurs over the nest interior.

One-way nesting is also possible in MM5. Here the model is first run to create an output that is interpolated using any ratio (not restricted to 3:1), and a boundary file is also created once a one-way nested domain location is specified. Typically the boundary file may be hourly (dependent upon the output frequency of the coarse domain), and this data is time-interpolated to supply the nest. Therefore one-way nesting differs from two-way nesting in having no feedback and coarser temporal resolution at the boundaries. The one-way nest may also be initialized with enhanced-resolution data and terrain.

4.5 Lateral Boundary Conditions

To run any regional numerical weather prediction model requires lateral boundary conditions. In MM5 all four boundaries have specified horizontal winds, temperature, pressure and moisture fields, and can have specified microphysical fields (such as cloud)

if these are available. Therefore, prior to running a simulation, boundary values have to be set in addition to initial values for these fields.

The boundary values come from analyses at the future times, or a previous coarser-mesh simulation (1-way nest), or from another model's forecast (in real-time forecasts). For real-time forecasts the lateral boundaries will ultimately depend on a global-model forecast. In studies of past cases the analyses providing the boundary conditions may be enhanced by observation analysis (Rawins or little_r) in the same way as initial conditions are. Where upper-air analyses are used the boundary values may only be available 12-hourly, while for model-generated boundary conditions it may be a higher frequency like 6-hourly or even 1-hourly.

The model uses these discrete-time analyses by linearly interpolating them in time to the model time. The analyses completely specify the behavior of the outer row and column of the model grid. In the next four rows and columns in from the boundary, the model is nudged towards the analyses, and there is also a smoothing term. The strength of this nudging decreases linearly away from the boundaries. To apply this condition, the model uses a boundary file with information for the five points nearest each of the four boundaries at each boundary time. This is a rim of points from the future analyses described above. The interior values from these analyses are not required unless data assimilation by grid-nudging is being performed, so disk-space is saved by having the boundary file just contain the rim values for each field.

Two-way nest boundaries are similar but are updated every coarse-mesh time-step and have no relaxation zone. The specified zone is two grid-points wide instead of one.

4.6 Nonhydrostatic Dynamics versus Hydrostatic Dynamics

Historically the Penn State/NCAR Mesoscale Model has been hydrostatic because typical horizontal grid sizes in mesoscale models are comparable with or greater than the vertical depth of features of interest. Therefore the hydrostatic approximation holds and the pressure is completely determined by the overlying air's mass. However when the scale of resolved features in the model have aspect ratios nearer unity, or when the

horizontal scale becomes shorter than the vertical scale, nonhydrostatic dynamics should not be neglected.

Miller (1974) has derived a set of equations that is nonhydrostatic but uses pressure as the vertical coordinate. A nonhydrostatic numerical model suitable for simulating mesoscale meteorological phenomena was developed by **Xue and Thorpe (1991).** The model was the first to exploit the nonhudrostatic equation system in σ (normalized pressure) coordinates. The nonhydrostatic version of the Penn State/NCAR Mesoscale Meteorological Model has been developed by **Dudhia (1993).** The version employs reference pressure as the basis for a terrain following vertical coordinate and the fully compressible system of equations.

The only additional term in nonhydrostatic dynamics is vertical acceleration that contributes to the vertical pressure gradient so that hydrostatic balance is no longer exact. Pressure perturbations from a reference state (described in the next section) together with vertical momentum become extra three-dimensional predicted variables that have to be initialized.

In addition to increasing the resolution beyond that of hydrostatic model simulations, a nonhydrostatic model can be used for much more localized by resolving topographical, urban and coastal effects, and deep convection through modeling their interactions with longer scale weather systems on a nested grid model **(Dudhia, 1993).** Thus the range of simulation capability would be substantially increased.

According to **Pielke (2002)** the advantages of using nonhydrostatic dynamics to compute pressure include the following:

1. The horizontal wave length of the mesoscale system, L_x can be of any size without concern for when the hydrostatic assumption is valid.
2. Sound waves which in general are not expected to be meteorologically important on the mesoscale are excluded.

While the disadvantages include the following:

1. The required computation time is increased since pressure must be evaluated from the involved formulation.

2. The mathematical operation of differentiation magnifies errors.

4.6.1 Reference state in the nonhydrostatic model

The reference state is an idealized temperature profile in hydrostatic equilibrium. It is specified by the equation:

$$T = T_{S0} + ALog_e(P_0/(P_{00})) \tag{4.2}$$

T_0 (p_0) is specified by 3 constants: p_{00} is sea-level pressure taken to be 10^5 Pa, T_{S0} is the reference temperature at p_{00}, and A is a measure of lapse rate usually taken to be 50 K, representing the temperature difference between p_{00} and p_{00}, e = *36788* Pa. These constants are chosen in the INTERP program. Usually just T_{S0} needs to be selected based on a typical sounding in the domain. The reference profile represents a straight line on a T-log p thermodynamic diagram. The accuracy of the fit is not important, and typically T_{S0} is taken to the nearest 10 K (e.g. 270, 280, 290, and 300 in polar, midlatitude winter, midlatitude summer, and tropical conditions, respectively). A closer fit however does reduce the pressure gradient force error associated with sloped coordinate surfaces over terrain, so T_{s0} should be selected by comparison with the lower tropospheric profile.

The surface reference pressure therefore depends entirely upon the terrain height. This can be derived from (1.2) using the hydrostatic relation,

$$Z = -\frac{RA}{2g}\left[\ln\frac{P_0}{P_{00}}\right]^2 - \frac{RT_{S0}}{g}\left[\ln\frac{P_0}{P_{00}}\right] \tag{4.3}$$

and this quadratic can be solved for p_0 (surface) given Z, the terrain elevation. Once this is done, the heights of the model σ levels are found from

$$P_0 = P_{S0}\sigma + P_{top} \tag{4.4}$$

Where:

$$P_{S0} = P_0(surface) - P_{top} \tag{4.5}$$

and then (4.3) is used to find Z from p_0 .

It can be seen that since the reference state is independent of time, the height of a given grid point is constant.

Since Version 3.1 the reference state can include an isothermal layer at the top to better approximate the stratosphere. This is defined by a single additional temperature (Tiso) which acts as a lower limit for the base-state temperature. Using this effectively raises the model top height.

4.7 Four-Dimensional Data Assimilation

Four-dimensional data assimilation (FDDA) is the option that allows the data over an extended time period to be input to the model. Essentially FDDA allows the model to be run with forcing terms that "nudge" it towards the observations or an analysis. The benefit of this is that after a period of nudging the model has been fit to some extent to all the data over that time interval while also remaining close to a dynamical balance. This has advantages over just initializing with an analysis at a single synoptic time because adding data over a period effectively increases the data resolution. Observations at a station are carried downstream by the model and may help fill data voids at later times.

4.8 Land-Use Categories

Land-use categorizations are used to describe the status of the surface (type of vegetation, desert, urban, water, ice, etc.). Each grid cell of the model is assigned one of the categories, and this determines surface properties such as albedo, roughness length, long wave emissivity, heat capacity and moisture availability.

4.9 Map Projections and Map-Scale Factors

The modeling system has a choice of several map projections.

I. Lambert Conformal is suitable for mid-latitudes,

II. Polar Stereographic for high latitudes and

III. Mercator for low latitudes.

The x and y directions in the model do not correspond to west-east and north-south except for the Mercator projection, and therefore the observed wind generally has to be rotated to the model grid, and the model u and v components need to be rotated before comparison with observations.

The map scale factor, m, is defined by

m = (distance on grid) / (actual distance on earth)

and its value is usually close to one varying with latitude. The projections in the model preserve the shape of small areas, so that dx=dy everywhere, but the grid length varies across the domain to allow a representation of a spherical surface on a plane surface. Map-scale factors need to be accounted for in the model equations wherever horizontal gradients are used.

4.10 The Auxiliary Programs of the Mesoscale Modeling System, MM5

TERRAIN:

It is the program that begins any complete forecast simulation in MM5 modeling system (Fig. 4.1). This program horizontally interpolates (or analyzes) the regular latitude - longitude terrain elevation and vegetation (land use) onto the chosen mesoscale domains (Fig. 4.4).

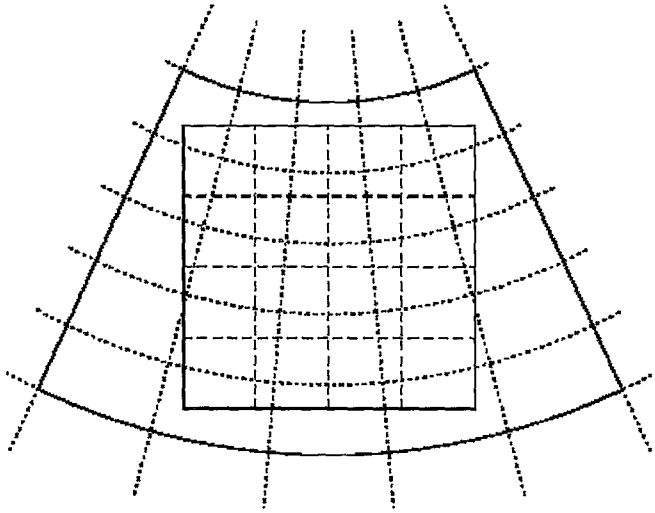

Figure 4.4: Horizontal interpolation of regular latitude longitude onto mesoscale domain (Dudhia et al., 2004).

There are essentially two tasks the program TERRAIN performs:

1. Set up mesoscale domains: coarse and fine grids (except for moving nests).
2. Produce terrestrial data fields for all of the mesoscale domains, which will first be used by REGRID, and later by MM5 (optionally) and NESTDOWN.

The program also computes a few constant fields required by the modeling system: latitude and longitude, map scale factors, and Coriolis parameter.

REGRID

The purpose of REGRID is to read archived gridded meteorological analyses and forecasts on pressure levels and interpolate those analyses from some native grid and map projection to the horizontal grid and map projection as defined by the MM5 preprocessor program TERRAIN. REGRID handles pressure-level and surface analyses.

REGRID is the second step in the flow diagram of the MM5 modeling system (Fig. 4.1). It expects input from the TERRAIN program, and creates files ready for LITTLE_R or INTERPF. These files are generally used as the first guess to an objective analysis (LITTLE_R), or as analyses which are to be directly interpolated to the MM5 model levels for initial and boundary conditions for MM5 (INTERPF).

LITTLE_R

LITTLE_R is the program responsible to objective analysis of direct observations. The goal of objective analysis in meteorological modeling is to improve meteorological analyses (the first guess) on the mesoscale grid by incorporating information from observations.

INTERPF

The INTERPF program handles the data transformation required to go from the analysis programs to the mesoscale model. This entails vertical interpolation, diagnostic computation, and data reformatting. INTERPF takes REGRID, LITTLE_R, or INTERPB output data as input to generate a model initial, lateral boundary condition and a lower boundary condition (see Fig. 4.1).

NESTDOWN

The NESTDOWN program horizontally interpolates σ-coordinate data, from a coarse grid to a fine grid.

INTERPB

The INTERPB program handles the data transformation required to go from the mesoscale model on σ-coordinates back to pressure levels. This program only handles vertical interpolation and a few diagnostics. The output from this program is suitable for input to REGRIDDER (to re-grid a model forecast), LITTLE_R (for pressure-level re-analysis), INTERPF (for pressure to *s* interpolation for generating model input) and GRAPH (for visualization and diagnostic computation).

GRAPH

The GRAPH program generates simple diagnostics and plots for some standard meteorological variables. The GRAPH code will process multiple times and vertical levels, computing the same diagnostics for each time and level. The GRAPH code will provide simple vertical interpolation capability, cross-section figures, and skew-T plots. The GRAPH program can overlay two plots. The GRAPH code is written to be used as a batch processor, so that all graphical choices are made from tables. The GRAPH code can process data from TERRAIN, REGRID, little_r and RAWINS, INTERPF, MM5, NESTDOWN, LOWBDY, and INTERPB. But GRAPH code cannot plot boundary condition data. The GRAPH code does not produce any standard output for use by a subsequent program.

MM5

- This is the numerical weather prediction part of the modeling system.
- MM5 can be used for a broad spectrum of theoretical and real-time studies, including applications of both predictive simulation and four-dimensional data assimilation to monsoons, hurricanes, and cyclones.
- On the smaller meso-beta and meso-gamma scales (2-200 km), MM5 can be used for studies involving mesoscale convective systems, fronts, land-sea breezes, mountain-valley circulations, and urban heat islands.

RIP

RIP (which stands for **R**ead/**I**nterpolate/**P**lot) is a Fortran program that invokes NCAR Graphics routines for the purpose of visualizing output from the Mesoscale Modeling System, MM5.

4.11 The Basic Equations of MM5

In terms of terrain following coordinates (x, y, σ), these are the equations for the nonhydrostatic model's basic variables excluding moisture **(Dudhia, 1993; Dudhia et Al., 2004).**

Pressure:

$$\frac{\partial p'}{\partial t} - \rho_0 g w + \gamma p \nabla \cdot \mathbf{V} = -\mathbf{V} \cdot \nabla p' + \frac{\gamma p}{T}\left(\frac{\dot{Q}}{c_p} + \frac{T_0}{\theta_0} D_\theta\right) \quad \textbf{(4.6)}$$

Momentum (x-component):

$$\frac{\partial u}{\partial t} + \frac{m}{\rho}\left(\frac{\partial p'}{\partial x} - \frac{\sigma}{p^*}\frac{\partial p^*}{\partial x}\frac{\partial p'}{\partial \sigma}\right) = -\mathbf{V} \cdot \nabla u + v\left(f + u\frac{\partial m}{\partial y} - v\frac{\partial m}{\partial x}\right) - ew\cos\alpha - \frac{uw}{r_{earth}} + D_u \quad \textbf{(4.7)}$$

Momentum (y-component):

$$\frac{\partial v}{\partial t} + \frac{m}{\rho}\left(\frac{\partial p'}{\partial y} - \frac{\sigma}{p^*}\frac{\partial p^*}{\partial y}\frac{\partial p'}{\partial \sigma}\right) = -\mathbf{V} \cdot \nabla v - u\left(f + u\frac{\partial m}{\partial y} - v\frac{\partial m}{\partial x}\right) + ew\sin\alpha - \frac{vw}{r_{earth}} + D_v \quad \textbf{(4.8)}$$

Momentum (z-component):

$$\frac{\partial w}{\partial t} - \frac{\rho_0 g}{\rho p^*}\frac{\partial p'}{\partial \sigma} + \frac{g p'}{\gamma p} = -\mathbf{V} \cdot \nabla w + g\frac{p_0}{p}\frac{T'}{T_0} - \frac{g R_d}{c_p}\frac{p'}{p} + e(u\cos\alpha - v\sin\alpha) + \frac{u^2 + v^2}{r_{earth}} + D_w \quad \textbf{(4.9)}$$

Thermodynamics:

$$\frac{\partial T}{\partial t} = -\mathbf{V}\cdot\nabla T + \frac{1}{\rho c_p}\left(\frac{\partial p'}{\partial t} + \mathbf{V}\cdot\nabla p' - \rho_0 g w\right) + \frac{\dot{Q}}{c_p} + \frac{T_0}{\theta_0} D_\theta \tag{4.10}$$

Advection terms can be expanded as

$$\mathbf{V}\cdot\nabla A \equiv mu\frac{\partial A}{\partial x} + mv\frac{\partial A}{\partial y} + \dot{\sigma}\frac{\partial A}{\partial \sigma} \tag{4.11}$$

$$\dot{\sigma} = -\frac{\rho_0 g}{p^*} w - \frac{m\sigma}{p^*}\frac{\partial p^*}{\partial x} u - \frac{m\sigma}{p^*}\frac{\partial p^*}{\partial y} v \tag{4.12}$$

Where:

Divergence term can be expanded as:

$$\nabla\cdot\mathbf{V} = m^2\frac{\partial}{\partial x}\left(\frac{u}{m}\right) - \frac{m\sigma}{p^*}\frac{\partial p^*}{\partial x}\frac{\partial u}{\partial \sigma} + m^2\frac{\partial}{\partial y}\left(\frac{v}{m}\right) - \frac{m\sigma}{p^*}\frac{\partial p^*}{\partial y}\frac{\partial v}{\partial \sigma} - \frac{\rho_0 g}{p^*}\frac{\partial w}{\partial \sigma} \tag{4.13}$$

4.12 Derivation of the Basic Equations of MM5

First Law of thermodynamics:

$$dQ = c_v dT + p d\alpha = c_p dT - \alpha dp \tag{4.14}$$

Since from the gas law:

$$RdT = p d\alpha + \alpha dp$$

and

$$c_p - c_v = R$$

Temperature tendency therefore is given by:

$$c_p \frac{DT}{Dt} = \frac{1}{\rho}\frac{Dp}{Dt} + \dot{Q} \tag{4.15}$$

Derivation of pressure tendency equation:

$$\frac{1}{p}\frac{Dp}{Dt} = \frac{1}{\rho}\frac{D\rho}{Dt} + \frac{1}{T}\frac{DT}{Dt} \tag{4.16}$$

From Gas Law

Continuity and thermodynamics lead to:

$$\frac{1}{p}\frac{Dp}{Dt} = \frac{1}{\rho}\frac{D\rho}{Dt} + \frac{1}{T}\frac{DT}{Dt} \tag{4.17}$$

However, $c_p \rho T = \left(\frac{c_p}{R}\right) p$, so

$$\frac{1}{p}\frac{Dp}{Dt}\left(1 - \frac{R}{c_p}\right) = -\nabla \cdot \mathbf{v} + \frac{\dot{Q}}{c_p T} \tag{4.18}$$

But $1 - \frac{R}{c_p} = \frac{c_v}{c_p} = \frac{1}{\gamma}$, therefore

$$\frac{Dp}{Dt} = -\gamma p \nabla \cdot \mathbf{v} + \frac{\gamma p \dot{Q}}{c_p T} \tag{4.19}$$

Forms of the vertical momentum equation:

$$\frac{Dw}{Dt} + \frac{1}{\rho}\frac{\partial p}{\partial z} + g = D_w \tag{4.20}$$

$$\frac{Dw}{Dt} + \alpha\frac{\partial p}{\partial z} + g = D_w \tag{4.21}$$

Defining $\alpha = \frac{1}{\rho}$,

Defining hydrostatic reference and perturbation,

$$\alpha = \alpha_0 + \alpha', p = p_0 + p',$$

$$\frac{Dw}{Dt} + (\alpha_0 + \alpha')\left(\frac{\partial p_0}{\partial z} + \frac{\partial p'}{\partial z}\right) + g = D_w \tag{4.22}$$

By definition, $\alpha_0 \frac{\partial p_0}{\partial z} = -g$, so

$$\frac{Dw}{Dt} + \alpha'\frac{\partial p'}{\partial z} + \alpha_0\frac{\partial p'}{\partial z} + \alpha'\frac{\partial p_0}{\partial z} = D_w \tag{4.23}$$

Which can be written as:

$$\frac{Dw}{Dt} + \alpha\frac{\partial p'}{\partial z} - g\frac{\alpha'}{\alpha_0} = D_w \tag{4.24}$$

This can be expanded as:

$$\frac{Dw}{Dt} + \alpha\frac{\partial p'}{\partial z} - g\frac{\alpha - \alpha_0}{\alpha_0} = D_w \tag{4.25}$$

In terms of ρ, this is:

$$\frac{Dw}{Dt} + \frac{1}{\rho}\frac{\partial p'}{\partial z} - g\frac{\frac{1}{\rho} - \frac{1}{\rho_0}}{\frac{1}{\rho_0}} = D_w \tag{4.26}$$

Which is:

$$\frac{Dw}{Dt} + \frac{1}{\rho}\frac{\partial p'}{\partial z} + g\frac{\rho'}{\rho} = D_w \tag{4.27}$$

This can be expressed in terms of temperature and pressure perturbations for the buoyancy term because:

$$-\frac{\rho'}{\rho} = \frac{\rho_0}{\rho} - 1 = \frac{p_0 T}{p T_0} - 1 = \frac{p_0}{p}\left(\frac{T}{T_0} - \frac{p}{p_0}\right) = \frac{p_0}{p}\left(\frac{T'}{T_0} - \frac{p'}{p_0}\right) \tag{4.28}$$

So:

$$\frac{Dw}{Dt} + \frac{1}{\rho}\frac{\partial p'}{\partial z} - g\frac{p_0}{p}\left(\frac{T'}{T_0} - \frac{p'}{p_0}\right) = D_w \tag{4.29}$$

Coordinate Transformation:

General coordinate transformation $(x, y, z) \rightarrow (x, y, \sigma)$

$$\left(\frac{\partial}{\partial x}\right)_z \rightarrow \left(\frac{\partial}{\partial x}\right)_\sigma - \left(\frac{\partial z}{\partial x}\right)_\sigma \frac{\partial}{\partial z} \tag{4.30}$$

but $\delta z = \dfrac{-\delta p_0}{\rho_0 g} = -\dfrac{(p^*\delta\sigma + \sigma\delta p^*)}{\rho_0 g}$, so

$$\left(\frac{\partial}{\partial x}\right)_z \rightarrow \left(\frac{\partial}{\partial x}\right)_\sigma - \frac{\sigma}{p^*}\frac{\partial p^*}{\partial x}\frac{\partial}{\partial \sigma} \tag{4.31}$$

Derivation of $\dot{\sigma}$ Relation:

$$\sigma = \frac{p_0 - p_{top}}{p_{surf} - p_{top}} = \frac{p_0 - p_{top}}{p^*} \tag{4.32}$$

Where: p_{top} and p_{surf} are the values of p_0 at the top and surface and

$$p^* = p_{surf} - p_{top}$$

$$\dot{\sigma} = \frac{D\sigma}{Dt} \tag{4.33}$$

Therefore:

$$\dot{\sigma} = \frac{1}{p^*}\frac{Dp_0}{Dt} - \frac{(p_0 - p_{top})}{(p^*)^2}\frac{Dp^*}{Dt} \tag{4.34}$$

Expanding total derivatives noting that

$$p_0 = p_0(z) \quad \text{and} \quad p^* = p^*(x,y)$$

and also that P_0 is hydrostatic.

$$\dot{\sigma} = -\frac{\rho_0 g}{p^*} w - \frac{\sigma}{p^*}\left(u\frac{\partial p^*}{\partial x} + v\frac{\partial p^*}{\partial y}\right) \tag{4.35}$$

5. THE AIR QUALITY MODELING SYSTEM

5.1 The Comprehensive Air Quality Model with Extension (CAMx)

5.1.1 Description of the model

CAMx is an Eulerian photochemical grid model that allows for integrated assessment of gaseous and particulate air pollution over many scales ranging from urban to super regional. It is designed to unify all of the technical features required for "state-of-the-science" air quality models into a single system (ENVIRON, 2004). CAMx simulates the emissions, dispersions, chemical reactions, and removal of pollutants in the lower troposphere by solving the pollutant continuity equation for each chemical species (l) on a system of nested three-dimensional grids. The Eulerian continuity equation describes the time dependency of the average species concentration (c_l) within each grid cell volume as a sum of all of the physical and chemical processes operating on that volume. This equation is expressed mathematically in terrain-following height (z) coordinates:

$$\frac{\partial c_l}{\partial t} = -\nabla_H . V_H c_l + \left[\frac{\partial (c_l \eta)}{\partial z} - c_l \frac{\partial}{\partial z}\left(\frac{\partial h}{\partial t}\right)\right] + \nabla . \rho K \nabla \left(\frac{c_l}{\rho}\right) + \\ + \left.\frac{\partial c_l}{\partial t}\right|_{Chemistry} + \left.\frac{\partial c_l}{\partial t}\right|_{Emission} + \left.\frac{\partial c_l}{\partial t}\right|_{\mathrm{Re}moval} \qquad (5.1)$$

Where:

V_H: is the horizontal wind vector,

η : is the net vertical "entrainment rate",

h: is the layer interface height,

ρ : is atmospheric density, and

K: is the turbulent exchange (or diffusion) coefficient.

The first term on the right-hand side represents horizontal advection; the second term represents net resolved vertical transport across an arbitrary space- and time-varying height grid; and the third term represents sub-grid scale turbulent diffusion. Chemistry is treated by simultaneously solving a set of reaction equations defined from specific chemical mechanisms. Pollutant removal includes both dry surface uptake (deposition) and wet scavenging by liquid precipitation.

The continuity equation is numerically marched forward in time over a series of time steps. At each step, the continuity equation is replaced by an operator-splitting approach that calculates the separate contribution of each major process (advection, diffusion, chemistry, etc.) to concentration change within each grid cell. Although advection is performed separately in the x (east-west), y (north-south), and z (vertical) directions, the numerical linkage between these components has been developed in a mass consistent fashion to preserve the density field at each time step. This maintains the flexibility to allow many types of meteorological models, and modeling grid resolutions, projections, and layer structures, to characterize transport in CAMx.

A master time step for the model is internally determined during the simulation to ensure numerical stability for horizontal advection in the largest and coarsest (master) grid. Time steps typically range from 5-30 minutes for grid cell sizes of 10-50 km, to a minute or less for small cell sizes of 1-2 km. As a result, transport calculations on nested grids require multiple time steps per master step depending on their grid sizes relative to the master grid spacing. Furthermore, multiple chemistry time steps per transport step are used as necessary to ensure accurate solution of the very numerically stiff chemical reaction equations. The first process in each time step for a given grid is the injection of emissions from all sources. CAMx then performs horizontal advection, but alternates the order of advection in the x and y directions each master time step. This alleviates any potential numerical biases that can develop when the x/y advection order is constant. Vertical advection is performed after horizontal advection, followed by vertical diffusion, horizontal diffusion, wet scavenging, and finally chemistry. The specific equations that are solved individually in the operator-splitting process are shown in order below **(ENVIRON, 2004):**

$$\left.\frac{\partial c_l}{\partial t}\right|_{Emission} = m^2 \frac{E_l \Delta t}{\partial x \partial y \partial z} \tag{5.2}$$

$$\left.\frac{\partial c_l}{\partial t}\right|_{x-advection} = -\frac{m^2}{A_{yz}} \frac{\partial}{\partial x}\left(\frac{u A_{yz} c_l}{m}\right) \tag{5.3}$$

$$\left.\frac{\partial c_l}{\partial t}\right|_{y-advection} = -\frac{m^2}{A_{xz}} \frac{\partial}{\partial y}\left(\frac{v A_{xz} c_l}{m}\right) \tag{5.4}$$

$$\left.\frac{\partial c_l}{\partial t}\right|_{z-transport} = \frac{\partial (c_l \eta)}{\partial z} - c_l \frac{\partial}{\partial z}\left(\frac{\partial h}{\partial t}\right) \tag{5.5}$$

$$\left.\frac{\partial c_l}{\partial t}\right|_{z-diffusion} = \frac{\partial}{\partial z}\left[\rho K_v \frac{\partial (c_l / \rho)}{\partial z}\right] \tag{5.6}$$

$$\left.\frac{\partial c_l}{\partial t}\right|_{xy-diffusion} = m\left\{\frac{\partial}{\partial x}\left[m \rho K_x \frac{\partial (c_l / \rho)}{\partial x}\right] + \frac{\partial}{\partial y}\left[m \rho K_y \frac{\partial (c_l / \rho)}{\partial y}\right]\right\} \tag{5.7}$$

$$\left.\frac{\partial c_l}{\partial t}\right|_{Wet-Scavening} = -A_l c_l \tag{5.8}$$

$$\left.\frac{\partial c_l}{\partial t}\right|_{Chemistry} = \text{Mechanism} - \text{Specific Reaction Equation} \tag{5.9}$$

Where:

C_l: is species concentration (μmol/m^3 for gasses, μg/m^3 for aerosols),

E_l: is the local species emission rate (μmol/s for gasses, μg/s for aerosols),

Δt : is time step length (s),

u and v: are the respective east-west (x) and north-south (y) horizontal wind components (m/s),

A_{yz} and A_{xz}: are cell cross-sectional areas (m^2) in the y-z and x-z planes, respectively,

m: is the ratio of the transformed distance on the various map projections to true distance (m=1 for curvi-linear latitude/longitude coordinates),

E_l: is the wet scavenging rate (s^{-1}).

Dry deposition is an important removal mechanism, but it is not explicitly treated as a separate process in the time-splitting approach. Instead, deposition velocities for each species are calculated based on species chemical properties and local meteorological surface conditions, and used as the lower boundary condition for vertical diffusion. This appropriately couples the surface removal of pollutants through each column of cells via the vertical mixing process.

5.1.1.1 CAMx grid configuration

CAMx carries pollutant concentrations at the center of each grid cell volume, representing the average concentration over the entire cell. Meteorological fields are supplied to the model to quantify the state of the atmosphere in each grid cell for the purposes of calculating transport and chemistry. CAMx internally carries these variables in an arrangement known as an "Arakawa C" grid configuration (Fig. 5.1) which is somewhat different from that of "Arakawa B" in MM5 model (Fig. 4.3).

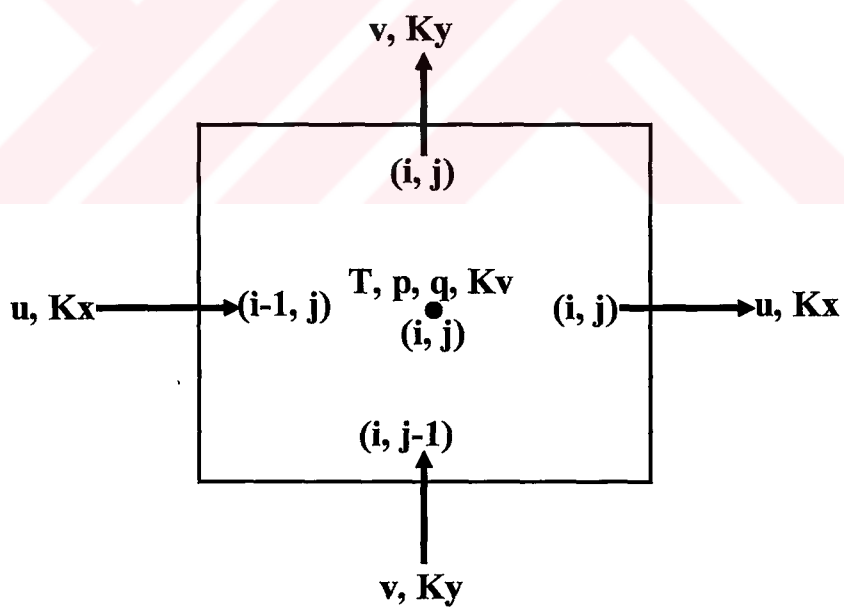

Figure 5.1: A horizontal representation of the Arakawa C variable configuration used in CAMx.

State variables such as temperature, pressure, water vapor, and cloud water are located at cell center along with pollutant concentration, and represent grid cell average conditions.

Wind components and diffusion coefficients are carried at cell interfaces to describe the transfer of mass in and out of each cell face. That horizontal wind components u and v are staggered from each other. This facilitates the solving of the transport equations in "flux form".

In the horizontal cell indexing convention used in CAMx, each cell is defined by the index pair (i,j), where i ranges from 1 to nx (the number of cells in the east-west direction), and j ranges from 1 to ny (the number of cells in the north-south direction). The eastern and northern faces of the cell are indexed (i,j), while the western and southern faces are indexed $(i\text{-}1,j)$ and $(i,j\text{-}1)$, respectively.

In the vertical, most variables are carried at each layer midpoint (defined as exactly half way between layer interfaces). Again the exceptions are those variables that describe the rate of mass transport across the layer interfaces, which include the vertical diffusion coefficient K_V and the vertical entrainment rate η. These variables are carried in the center of each cell horizontally, but are located at the top of the layer (i.e., the interface) vertically.

5.1.2 Transport fundamentals

The approach to solving pollutant transport in CAMx provides both mass conservation and mass consistency. Mass conservation refers to the ability to accurately account for all sources and sinks of mass in the model, with no spurious loss or gain of mass during model integration. To be mass conservative, CAMx internally carries concentrations of each species as a density ($\mu mol/m^3$ for gases, $\mu g/m^3$ for aerosols), and solves the advection equations in flux form. This also serves to simplify mass budget accounting, which is used by the various source apportionment and process analysis options. Gas concentrations are internally converted to volumetric mixing ratio (parts per million, or ppm) for the chemistry and diffusion steps, and when they are written to the average output files.

Mass consistency refers to the model's ability to transport pollutant mass exactly equivalent to the input atmospheric momentum field. For example, a model that is perfectly mass consistent will preserve a unity pollutant mixing ratio field given constant unity boundary and initial conditions and zero sources and sinks.

To account for all sources of error while maintaining flexibility on input requirements and grid configuration, CAMx internally minimizes the sources of mass inconsistency as the model integrates forward in time. The model does this in several ways:

1. The transport equations are written and solved in "flux" form. Gridded meteorological inputs are carried in an "Arakawa C" arrangement, which optimizes the calculation of mass flux divergences while ensuring mass conservation. These points are important for the calculations described below. Solutions based on the alternative "advective" form cannot guarantee mass conservation or consistency.

2. CAMx can accept input meteorological fields (horizontal wind components, pressure, temperature, moisture, vertical diffusion coefficients and cloud parameters) for each individual nested grid, if available from a meteorological model. This reduces errors stemming from internal interpolations from coarse to fine grids. Input gridded fields of layer heights, temperature, pressure, and horizontal winds are then interpolated in time to the unique timesteps for each modeling grid.

3. Third, and most importantly, the grid- and timestep-specific horizontal momentum fields are used to determine a vertical velocity field that balances the local atmospheric continuity equation for the specific grid configuration employed. Since the vertical grid structure is defined via external inputs, layer interface heights may be specified as any arbitrary function of space and/or time. This allows the CAMx vertical grid system to exactly match all or a subset of any meteorological model layer structures, whether they are defined in terms of physical height above ground, normalized height coordinates (i.e., "sigma-z"), or normalized pressure coordinates (i.e., "sigma-p"). Therefore, total vertical transport is the combination of resolved vertical advection and mass exchange across undulating layer interfaces.

   The total vertical transport rate is referred to as the local "entrainment rate" η, which is defined as the combination of net vertical velocity w and the local time-rate of change in layer interface heights:

$$\eta = \frac{\partial h}{\partial t} - w \tag{5.10}$$

To calculate a vertical velocity profile for a given grid column, the atmospheric continuity equation is locally integrated through the depth of the column. Most air quality models perform this integration by assuming an incompressible atmosphere and either a non-divergent wind field ($\nabla .V=0$), or a non-divergent momentum field ($\nabla .\rho V=0$). Both of these approaches presume that the three dimensional divergence components exactly balance to result in a zero net change in local atmospheric density. The non-divergent wind assumption is not valid for model applications spanning a significant fraction of the atmospheric scale height (8 or 9 km). In either case, the presumption of zero density tendency in an air quality model is usually invalid since the externally supplied wind and density fields are often not balanced in the first place. In CAMx, such a density-momentum balance obviously does not exist since a linear rate of temperature, pressure and horizontal wind change is imposed at each time step between meteorological update times. Thus, the vertical velocity profile at each time step is determined from vertical integration of the divergent incompressible continuity equation:

$$\frac{\partial \rho}{\partial t} = -\nabla .\rho V \tag{5.11}$$

Which is:

$$\rho w(z) = -\int_0^z \left(\frac{\partial \rho}{\partial t} + \nabla_H .\rho V_H \right) dz \tag{5.12}$$

Where: the local time-rate change of atmospheric density ρ in each grid cell is known from the input meteorological fields. In this approach, a vertical velocity profile is constructed that provides a balance between the imposed density tendency and the resolved horizontal momentum divergence in each grid cell at

each time step. This vertical velocity is used for subsequent vertical transport calculations for all pollutants.

4- The fourth way CAMx ensures mass consistency is to calculate the horizontal flux divergence of atmospheric density in a manner that is numerically consistent with the procedure used to horizontally transport pollutants. Atmospheric density is advected in and out of each cell using the same equation as for pollutants:

$$\nabla_H \cdot \rho V_H = \frac{m^2}{A_{yz}} \frac{\partial}{\partial x}\left(\frac{uA_{yz}\rho}{m}\right) + \frac{m^2}{A_{xz}} \frac{\partial}{\partial y}\left(\frac{uA_{xz}\rho}{m}\right) \qquad \textbf{(5.13)}$$

The resulting horizontal advective fluxes include resolved momentum convergence/ divergence rates as well as any artificial divergences caused by the horizontal and vertical grid specifications (e.g., spatially varying vertical grid structure, or systematic distortions associated with the map projections). In simple tests in which a uniform pollutant field of unity mixing ratio is transported throughout a single regional grid over several days using actual episodic meteorological inputs, this approach has been shown to provide nearly exact (to 10^{-3} - 10^{-4}%) consistency between the density and pollutant fields.

5.1.3 Chemistry

5.1.3.1 Gas phase chemistry

The chemical mechanisms supported in version 4 of CAMx are based on the Carbon Bond mechanism version 4 (CB4) **(Gery et. al. 1989)** and the SAPRC99 mechanism **(Carter, 2000)**. There are five specific mechanisms currently supported:

Mechanism I: 110 reactions and 48 species (34 state gasses and 14 radicals). This mechanism extends the CB4 by adding reactive chlorine chemistry (Cl_2, Cl and ClO reactions) to mechanism III **(Tanaka et al., 2000).**

Mechanism II: 91 reactions and 36 species (24 state gasses and 12 radicals). **CB4 (Gery et al., 1989)** with revised radical-radical termination reactions that are necessary for regional modeling

Mechanism III: 96 reactions and 37 species (25 state gasses and 12 radicals). Mechanism II with updated isoprene chemistry based on **Carter (1996)** as implemented for the Ozone Transport Assessment Group (OTAG) by **Whitten et al. (1996).**

The choice between II and III depends upon whether the user wishes to use the original CB4 isoprene chemistry or the newer Carter "one product" isoprene chemistry **(Carter, 1996).** Compared to the original isoprene chemistry, the Carter chemistry is generally less reactive at low to medium VOC/NOx ratios, but under NOx-limited conditions may produce more ozone because it has weaker NOx removal pathways. Most users who don't need to simulate aerosols choose mechanism III because it was established as the "default" mechanism in the US during the OTAG modeling.

Mechanism IV: 100 reactions and 46 gas species (34 state gasses, 12 radicals). This mechanism includes aerosol chemistry. It is Mechanism III with extensions for aerosol modeling, including a biogenic olefin (OLE2) for terpenes, four condensable organic gasses, secondary organic aerosol formation, and inorganic aerosol chemistry/ thermodynamics. Number of aerosol species is 16 for the CF scheme and 13 for the CMU scheme.

Mechanism V: 211 reactions and 74 species (56 state gasses and 18 radicals). It is the SAPRC99 chemistry adapted mechanism for photochemical grid modeling by selecting a specific "fixed parameter" lumping scheme **(Carter, 2000).**

Photolysis rates are derived for each grid cell assuming clear sky conditions as a function of five parameters: (i) Solar zenith angle, (ii) Altitude, (iii) Total ozone column, (iv) Surface albedo, and (v) Atmospheric turbidity. The rates are taken from a large lookup table that spans the range of conditions for each of the five dimensions. This table may be developed using the accompanying TUV photolysis preprocessor **(Madronich, 1993, 2002).** The CAMx version of TUV is modified to output information in a format directly compatible with CAMx for either the CB4 or SAPRC99 chemical mechanisms.

Photolysis rates can be significantly affected by the presence of clouds. CAMx treats the impact of clouds on photolysis based upon the RADM approach **(Chang, et al., 1987).** This approach requires information on cloud optical depth for each cell. Optical depth is

used to scale down photolysis rates for layers within or below clouds to account for UV attenuation, or to scale up the rates for layers above clouds to account for UV reflection.

5.1.3.2 Aerosol chemistry

CAMx has model structures in place for modeling aerosols. In CAMx version 4, aerosol processes have been linked to the CB4 gas-phase chemical mechanism and are selected by choosing mechanism IV. Aerosol processes also could be linked to the other chemical mechanisms (e.g., SAPRC99) but this has not been completed to date. Mechanism IV provides two options for treating aerosol size distributions: the CF scheme and CMU scheme.

The CF scheme divides the size distribution into two modes (coarse and fine), as originally released in V4.00. Primary species are modeled as fine and/or coarse particles, while all secondary species are modeled as fine particles. The CMU scheme employs a sectional approach that models the size evolution of each aerosol constituent among a number of fixed size sections. Aerosol water has also been explicitly added to both CF and CMU treatments and affects aerosol size and density.

The gas-phase photochemistry in mechanism IV forms aerosol precursors via the OH initiated oxidation of SO2 to sulfate, production of nitric acid, and formation of condensible organic gasses. These aerosol precursors are supplied to aerosol chemistry, which performs the following processes:

1. Aqueous sulfate and nitrate formation in resolved cloud water using the RADM aqueous chemistry algorithm **(Chang et al., 1987).**
2. Partitioning of condensible organic gases (CG1-CG4) to secondary organic aerosols (SOA1-SOA4) to form a condensed "organic solution phase" using a semi-volatile, equilibrium scheme called SOAP **(Strader et. al., 1999).**
3. Partitioning of inorganic aerosol constituents (sulfate, nitrate, ammonium, sodium, and chloride) between the gas and particle phases using the ISORROPIA thermodynamic module **(Nenes et. al., 1998, 1999).**

The yields and properties of the condensible organic gases (CGs) are shown in table 2-4. The CG yields are expressed as ppm of aerosol precursor formed per ppm of VOC

reacted so that CG concentrations follow the CAMx convention for gasses and are in ppm. The secondary organic aerosols (SOAs) formed from the CGs are in units of μg/m3 as are all other aerosol species.

It is a limited number of aerosol species that can be run with the CF scheme. Only few of these species are mandatory (PSO_4, PNO_3, PNH_4, PH_2O, SOAl-4) to the CAMx run with the CF scheme and the rest are optional (NA, PCL, POA, PEC, FPRM, FCRS, CPRM, CCRS). While the CMU scheme requires that the complete list of all aerosol species be present in the chemistry parameters file (i.e., none are optional).

5.1.4 Pollutant removal

Trace gases and small particles are removed from the atmosphere via deposition to the surface. Dry deposition refers to the direct sedimentation and/or diffusion of material to various terrestrial surfaces and uptake into biota. Wet deposition refers to the uptake of material via chemical absorption (gases) or nucleation/impaction (particles) into cloud water, and the subsequent transfer to the Earth's surface by precipitation. The efficiency with which wet and dry deposition processes can remove pollutants from the air depends on: (i) the physical and chemical properties of the pollutants, (ii) local meteorological conditions, (iii) the type of surface on which they are being deposited, and on (iv) the frequency, duration, and intensity of precipitation events.

5.1.4.1 Pollutant removal by precipitation (wet deposition)

Wet deposition is an important removal process for particles. Particles act as cloud condensation nuclei; the cloud droplets grow and collect into sufficiently large sizes to fall as precipitation. A fraction of particles that are subsequently entrained into the cloud, and those exist within sub-cloud layers, are scavenged by liquid precipitation via impaction. The rates of nucleation and impaction depend upon: cloud type (e.g., prolonged stratiform vs. vigorous convective development), rainfall rate and particle size distribution.

Wet deposition is an important removal process for relatively soluble gaseous pollutants and this occurs through the following series of steps:

- Mixing of trace gas and condensed water in common air space;

- Absorption of gas molecules by water droplets;
- Possible aqueous-phase reactions of the pollutant within water droplets;
- Precipitation of droplets to the earth's surface;
- Diffusion of ambient gases into falling precipitation.

It is important to note that each of the above steps may be reversible, so that the overall wet deposition rate depends on the net results of the forward and backward processes at each step.

The wet scavenging of pollutants by liquid precipitation is improved in CAMx with the introduction of the new full-science PM chemistry package. The basic model implemented in CAMx is a scavenging approach in which the local rate of concentration change $\frac{\partial c}{\partial t}$ within or below a precipitating cloud depends on a scavenging coefficient A:

$$\frac{\partial c}{\partial t} = Ac \tag{5.14}$$

The scavenging coefficient is determined separately for gases and particulates, based upon relationships described by **Seinfeld and Pandis (1998)**. For gasses, two components are calculated: (i) the uptake of ambient gas concentration into falling precipitation, which can occur within and below clouds; and (ii) the collection by precipitation of cloud droplets that contain dissolved gas species.

For particles, separate in-cloud and below-cloud scavenging coefficients are determined. Within clouds, all aerosol mass is assumed to exist in cloud droplets (all particles are activated as condensation nuclei), so scavenging is due to the efficient collection of cloud droplets by precipitation. Below clouds, dry particles are scavenged by falling precipitation with an efficiency that is dependent upon particle size.

The following general assumptions are made in this scavenging model:

1. Only liquid cloud water and precipitation are effective at removing pollutants;
2. Rain drops and cloud droplets are each represented by a single mean size; rain drop size is an empirical function of rainfall intensity;

3. Within clouds, dissolved pollutants in liquid cloud water droplets and are in equilibrium with ambient concentrations according to Henry's Law;
4. Cloud water acidity is non-evolving and is set to a representative cloud pH as established by the model's list of Henry's Law equilibrium constants for each species (pH ~ 5);
5. All gas species behave as ideal gases;
6. All PM species and sizes are hygroscopic and internally mixed;
7. All in-cloud PM mass exists in cloud water (i.e., no "dry" aerosols exist in the interstitial air between cloud droplets), so in-cloud scavenging results from scavenging of cloud droplets by falling precipitation.

5.1.4.1.1 Wet scavenging of ambient gasses

Wet scavenging of gases occurs within and below precipitating clouds. Below the cloud, the total gas concentration in a given grid cell is subject to precipitation scavenging. Within a cloudy cell, the total gas concentration must first be partitioned into an aqueous fraction c_{aq} within cloud water and the remaining gaseous fraction c_g within the interstitial air; this split is determined by Henry's Law thereby assuming that steady-state equilibrium exists between the two.

The Henry's Law constant for a given gas species k_0 (M/atm) specifies the ratio of pollutant mass in aqueous solution (M or mol/lH_2O) to its equilibrium partial pressure (atm). This constant is adjusted for temperature T (°K) and converted to a dimensionless molar ratio:

$$H = k_0 RT \exp\left[A\left(\frac{1}{298} - \frac{1}{T}\right)\right] \qquad \textbf{(5.15)}$$

Where:

R: is the ideal gas constant ($8.206.10^{-2}$ l·atm/mol K),

A: is the temperature dependence factor (K).

The aqueous concentration (mass per volume of water) can thus be determined from the equilibrium gas concentration (mass per volume of air):

$$c_{aq} = Hc_g \tag{5.16}$$

Given the relatively short residence times of falling rain drops through a given grid cell, aqueous equilibrium between ambient gas and precipitation water cannot be assumed and so the transfer of ambient gas into precipitation is explicitly calculated. The rate of transfer W of a gas to a water drop is:

$$w = K_c\left(Hc_g - c_{aq}\right) \tag{5.17}$$

Where: K_c is the mass transfer coefficient.

For a falling rain drop with speed v_d (m/s) and diameter d_d (m), the mass transfer coefficient is given by:

$$K_c = \frac{D_g}{d_d}\left[2 + 0.6\left(\frac{v_d d_d}{v}\right)^{\frac{1}{2}}\left(\frac{v}{D_g}\right)^{\frac{1}{3}}\right] \tag{5.18}$$

Where:

D_g and v are the molecular diffusivity of the gas species and air, respectively.

The mean raindrop diameter and fall speed are taken from the empirical estimates of **Scott (1978).** The drop diameter is related to rainfall rate P (mm/hr), and the fall speed relationship has been modified to better agree with data provided by **Seinfeld and Pandis (1998):**

$d_d = 9.0 \times 10^{-4} P^{0.21}$ and $v_d = 3100\, d_d$

The rate of c_{aq} increase can be represented by a mass balance with the rate of transport to the drop:

$$\frac{1}{6}\pi d_d^3 \frac{dc_{aq}}{dt} = \pi d_d^2 W \tag{5.19}$$

The expression for W is substituted into the equation above, rearranged, and expressed in terms of rainfall velocity. Then assuming that through a given model layer the ambient gas concentration, pH, and raindrop size is constant, and specifying $c_{aq}^{\,0}$ *at* the top of the

layer, integration through a layer depth Δz (m) is performed. After falling through the layer each drop will have scavenged a species mass m_{aq} equal to:

$$m_{aq} = \frac{1}{6}\pi d_d^3 \left(Hc_g - c_{aq}^0\right)\left[1 - \exp\left(-\frac{6K_c \Delta z}{d_d v_d H}\right)\right] \quad \textbf{(5.20)}$$

Multiplying this mass by the number density of falling raindrops (N_d, m^{-3}) yields the gas concentration scavenged by all drops falling through the layer. The number density can be expressed in terms of rainfall rate, fall velocity, and drop size:

$$N_d = \frac{2.8x10^{-7} P}{\pi d_d^3 v_d / 6} \quad \textbf{(5.21)}$$

Finally, to obtain a gas-phase scavenging rate, the mass equation above is multiplied by N_d, and divided by the total ambient concentration c and by the time it takes for rain to fall through the layer depth:

$$A_g = \frac{2.8x10^{-7} P}{c\Delta z}\left(Hc_g - c_{aq}^0\right)\left[1 - \exp\left(-\frac{6K_c \Delta z}{d_d v_d H}\right)\right] \quad \textbf{(5.22)}$$

For below-cloud scavenging, cg in the difference term is replaced with c so that all ambient gas is subject to scavenging.

5.1.4.1.2 Wet scavenging of gasses dissolved in cloud water

The fraction of gases present in cloud water can be removed by precipitation via collection/impaction. As a rain drop falls, it sweeps a cylindrical volume per unit time equal to

$$V = \frac{\pi}{4}\left(d_d + d_c\right)^2 v_d \quad \textbf{(5.23)}$$

Where: d_c is the size of cloud droplets.

This implies that the motion of cloud droplets is insignificant compared to the rain drop fall speed. Due to aerodynamic perturbations of air flow around the falling drop, a

collection efficiency is applied, i.e., the fraction of cloud droplets within the collection volume that are scavenged by precipitation. For large raindrops with sizes greater than 0.5 mm and droplets 10-20 μm, the efficiency is taken as 0.9 **(Seinfeld and Pandis, 1998).** Also, it can be asserted that $(d_d + d_c)^2 \sim d_d$. Assuming then that a monodisperse distribution of rain drops are falling through a monodisperse distribution of cloud water droplets, the scavenging coefficient for rain collecting cloud water is:

$$A_c = \frac{\pi}{4} d_d^2 v_d E N_d \qquad \textbf{(5.24)}$$

Where: E is the collection efficiency (0.9) and N_d is the rain drop number density described earlier. Substituting the relationship between N_d and rainfall parameters, then:

$$A_c = 4.2x10^{-7} \frac{EP}{d_d} \qquad \textbf{(5.25)}$$

The cloud water scavenging coefficient is scaled by the ratio of aqueous concentration to total grid cell concentration to achieve the aqueous-phase scavenging coefficient:

$$A_a = A_c \frac{c_{aq} L_c}{c \rho_w} \qquad \textbf{(5.26)}$$

Within cloud layers, the gas-phase and aqueous-phase scavenging coefficients are added to provide the total in-cloud scavenging rate for gases, $A = A_c + A_a$.

5.1.4.1.3 Wet scavenging of in-cloud aerosols

All aerosols within cloudy layers are assumed to be in cloud water. Therefore, the scavenging coefficient for aqueous aerosols is exactly the same as for the scavenging of cloud droplets: $A = A_c$.

5.1.4.1.4 Wet scavenging of dry particles

Wet scavenging of dry particles only occurs below precipitation cloud (equation 5.25). In this case, however, the collection efficiency E is a function of particle size d_p, and is given by **Seinfeld and Pandis (1998)** as:

$$E(d_p) = \frac{4}{R_e S_c}\left(1 + 0.4R_e^{\frac{1}{2}}S_c^{\frac{1}{3}} + 0.16R_e^{\frac{1}{2}}S_c^{\frac{1}{2}}\right) + 4\phi\left[\frac{\mu}{\mu_w} + \phi\left(1 + 2R_e^{\frac{1}{2}}\right)\right] + \left(\frac{S_t - S^*}{S_t - S^* + \frac{2}{3}}\right)^{\frac{3}{2}} \quad \textbf{(5.27)}$$

Where μ and μ_w are the kinematic viscosity of air (1.8×10^{-5} kg/ms) and water (10^{-3} kg/ms), respectively, $\varphi = d_p/d_d$ is the ratio of particle size to rain drop size, *Re* is the Reynolds number for the rain drop, *Sc* is the Schmidt number for the collected particle, and *St* is the Stokes number of the collected particle.

The Reynolds number is given by: $Re = D_d\, v_d / 2v$

The Schmidt number is: $Sc = v / D_p$

Where D_p is the particle Brownian diffusivity: $D_p = \frac{kTC}{3\pi\mu d_p}$

Here k is the Brownian constant (1.38×10^{-23} J/K) and C is the Cunningham correction factor for small particles:

$$C = 1 = \frac{2\lambda}{d_p}\left[1.257 + 0.4\exp\left(-\frac{0.55d_p}{\lambda}\right)\right] \quad \textbf{(5.28)}$$

Where λ is the mean free path of air (6.5×10^{-8} m). The Stokes number is given by:

$$S_t = \frac{v_d d_p^2 \rho_p C}{9\mu d_d} \quad \textbf{(5.29)}$$

Where ρ_p is the particle density. And the S^* is given by:

$$S^* = \frac{1.2 + \ln(1 + R_e)/12}{1 + \ln(1 + R_e)} \quad \textbf{(5.30)}$$

5.1.4.2 Dry deposition

For many compounds, dry deposition can be as important as wet deposition as a removal process. Due to the difficulty of making direct measurements of dry deposition and the need for a suitable model parameterization, dry deposition is often treated as a

first-order removal mechanism, where the flux of a pollutant to the surface is the product of a characteristic deposition velocity and its concentration in the "surface layer" (i.e., the lowest model layer). Deposition velocities are derived from models that account for the reactivity, solubility, and diffusivity of gases, the sizes of particles, local meteorological conditions, and surface characteristics.

For a given species, particle size, and grid cell, CAMx determines a deposition velocity for each landuse type in that cell and then linearly combines them according to the fractional distribution of landuse **(ENVIRON, 2004).** The deposition flux is used as the lower boundary condition in the vertical diffusion algorithm. Aerosol size spectra and species-dependent properties needed for the deposition velocity calculations are externally supplied to CAMx for all pollutant species via the chemistry parameters file, gridded landuse is also externally supplied to the master grid and the season is determined by the simulation date.

Movement of material along a path from the atmosphere, through any plant canopy, and onto the various plant and ground surfaces within and below the canopy is typically modeled by analogy to an electrical circuit. Resistances in serial and parallel arrangements are used to represent the relative ease with which material moves through different portions of the deposition pathway **(Wesely, 1989).** Each branch of the circuit represents a different path by which material may be deposited. For example, gaseous pollutants may transfer through the lowest layers of the atmosphere partially into a plant canopy, through the stomatal openings on plant leaves and into the plant mesophyll tissue. Alternatively, the material may travel all the way through the plant canopy and deposit on the ground surface.

5.1.4.2.1 Dry deposition of gasses

Wesely (1989) has developed a resistance model that incorporates the major elements described above. Deposition velocity v_d is calculated from three primary resistances r (s/m) in series:

$$v_d = \frac{1}{r_a + r_b + r_s} \tag{5.31}$$

The aerodynamic resistance r_a represents bulk transport through the lowest model layer by turbulent diffusion, and operates equivalently for all gases and small particles. The magnitude of this resistance depends on the intensity of turbulent motion, which in turn depends on solar insolation, wind speed, surface roughness, and near-surface temperature lapse rate. In CAMx it is calculated from:

$$r_a = \frac{1}{ku_*}\left[\ln\left(\frac{1}{z}\right) - \phi_h\right] \tag{5.32}$$

Where u_* is friction velocity (m/s), k is Von Karman's constant, z and z_0 are the lowest model layer midpoint height (m) and landuse-dependent surface roughness length (m), respectively, and ϕ_h is a stability correction term. The surface layer parameterization of **Louis (1979)** is used to supply friction velocity and stability function. In general, aerodynamic resistance is at a minimum on warm, sunny days with strong mixing due to surface heating and mechanical turbulence, and at a maximum on cool, calm nights when turbulent mixing is suppressed.

The quasi-laminar sub-layer (or boundary) resistance, r_b represents molecular diffusion through the thin layer of air directly in contact with the particular surface to which material is being deposited. It is usually assumed to depend only on the molecular diffusivity of each pollutant species, and is given by:

$$r_b = \frac{2S_c^{\frac{2}{3}}}{ku_*} \tag{5.33}$$

Where: S_c, is the Schmidt number, or the ratio of air viscosity to species molecular diffusivity.

Over land, surface resistance r_s is further expressed as several more serial and parallel resistances that depend upon the physical and chemical properties of the surface in question:

$$r_s = \frac{1}{\frac{1}{r_{st}+r_m} + \frac{1}{r_{uc}} + \frac{1}{r_{dc}+r_{cl}} + \frac{1}{r_{ac}+r_{gs}}} \quad (5.34)$$

Where the first serial resistance set represents the pathway into the stomatal and mesophyllic portions of active plants, the second is the pathway into the upper canopy, the third is the pathway into the lower canopy, and the fourth is the pathway to the ground surface. Many of these resistances are season and landuse-dependent, and are built into Wesely's model; some in turn are adjusted within CAMx for solar insolation, moisture stress, and surface wetness. A few others have been developed by Wesely for SO_2 and ozone, and so are scaled for each gaseous species based on the following pollutant properties:

1. Molecular diffusivity;
2. Henry's law solubility;
3. Chemical reactivity toward oxidation of biological substances.

This allows the resistance approach to be used to estimate deposition velocities for a wide range of gaseous pollutants.

Over water, the surface resistance is based on some improvements adopted by **Kumar et al. (1996)** in UAM-AERO, following **Sehmel (1980):**

$$r_s = \frac{1}{3.9x10^{-5} HT_s u_*} \quad (5.35)$$

Where: *Ts:* is surface temperature (°K).

The surface resistance for strong acids such as nitric and hydrochloric acid is set to zero given their strong rates of update by biota and other surfaces. The species for which surface resistance is to be zeroed are defined in the CAMx chemistry parameters file.

5.1.4.2.2 Dry deposition of aerosols

Surface deposition of particles occurs via diffusion, impaction, and/or gravitational settling. Particle size is the dominant variable controlling these processes. The resistance approach of **Slinn and Slinn (1980),** as implemented in UAM-AERO **(Kumar et al.,**

1996), has been adopted in CAMx. Particle deposition velocity for a given aerosol size is calculated using the following resistance equation:

$$v_d = v_{sed} + \frac{1}{r + r_b + r_a r_b v_{sed}} \quad \textbf{(5.36)}$$

Where: v_{sed} is the gravitational settling (or sedimentation) velocity. This velocity is dependent on aerosol size and density:

$$v_{sed} = \frac{D^2 g C \rho_p}{18v} \quad \textbf{(5.37)}$$

Where:

D: is the log-mean particle diameter (m) of a given size section,

ρ_p: is particle density (g/m^3),

g: is the gravitational acceleration,

v: is the viscosity of air, and

C: is the Cunningham correction for small particles, as described earlier for wet scavenging of particles in section 5.4.1.4.

Aerodynamic resistance r_a is identical to the value used for gaseous dry deposition. Resistance to diffusion through the quasi-laminar sub-layer layer depends on aerosol Brownian diffusion and inertial impaction. Particles are assumed to remain on a surface once they impact, so resuspension effects are ignored. Boundary resistance r_b is given by:

$$r_b = \frac{1}{u_* \left(S_c^{-2/3} + 10^{-3/S_t} \right)} \quad \textbf{(5.38)}$$

Where: St is the stokes number which is calculated from:

$$S_t = \frac{v_{sed} u_*^2}{vg} \quad \textbf{(5.39)}$$

5.2 European Anthropogenic Sulfur Emissions

28 countries represent western, central and eastern Europe, the western countries of the former USSR and Turkey (Fig. 5.2) were chosen to investigate their anthropogenic sulfur emissions. The total national anthropogenic sulfur emissions during the years 1990 – 1999 in the countries included to the study are given in Table 5.1 and illustrated in Fig. 5.3. It is obviously noticed from the mentioned table and figure that the majority of the sulfur emissions in Eastern Europe and Eastern Mediterranean region are produced by Poland, Ukraine, Romania, Bulgaria and Turkey respectively.

According to the CORINAIR/UNECE source category split of emissions, the major anthropogenic sulfur emission sectors can be classified with respect to their emission percentages in the following categories **(Vestreng, 2001):**

a- Combustion in energy and transformation industries 63%
b- Combustion in manufacturing industry 17%
c- Production processes 9%
d- Non-industrial combustion plants 6%
e- Extraction and distribution of fossil fuels and geothermal energy 2%
f- Road transport 2%
g- Other mobile source and machinery 1%

The percentage of the reduction in the total yearly sulfur production in the 10 years 1990 – 1999 is given in Table 5.2. It is apparent that countries that have signed the Gothenburg Protocol were capable to reduce sulfur emissions to an appreciable extent. While the countries that have not signed the Gothenburg Protocol have increased emitting sulfur emissions. Turkey shows the greatest increase percentage of 76.1%.

The point sources of the anthropogenic emissions of SO_2 are allocated to four principal categories **(Barrett and Protheroe, 1995):**

a- Power stations.
b- Industries (processes such as smelters).
c- Refineries, and
d- District heating plant, which do not produce electricity.

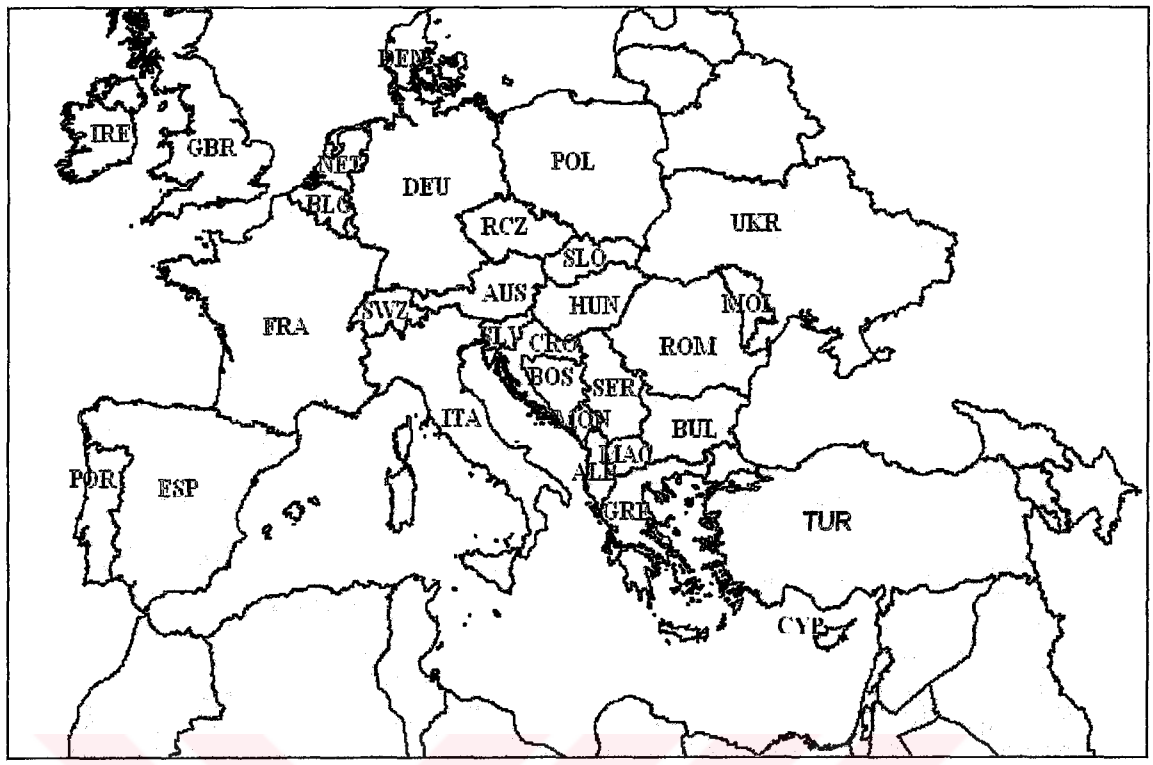

Figure 5.2: The study domain and the included Countries.

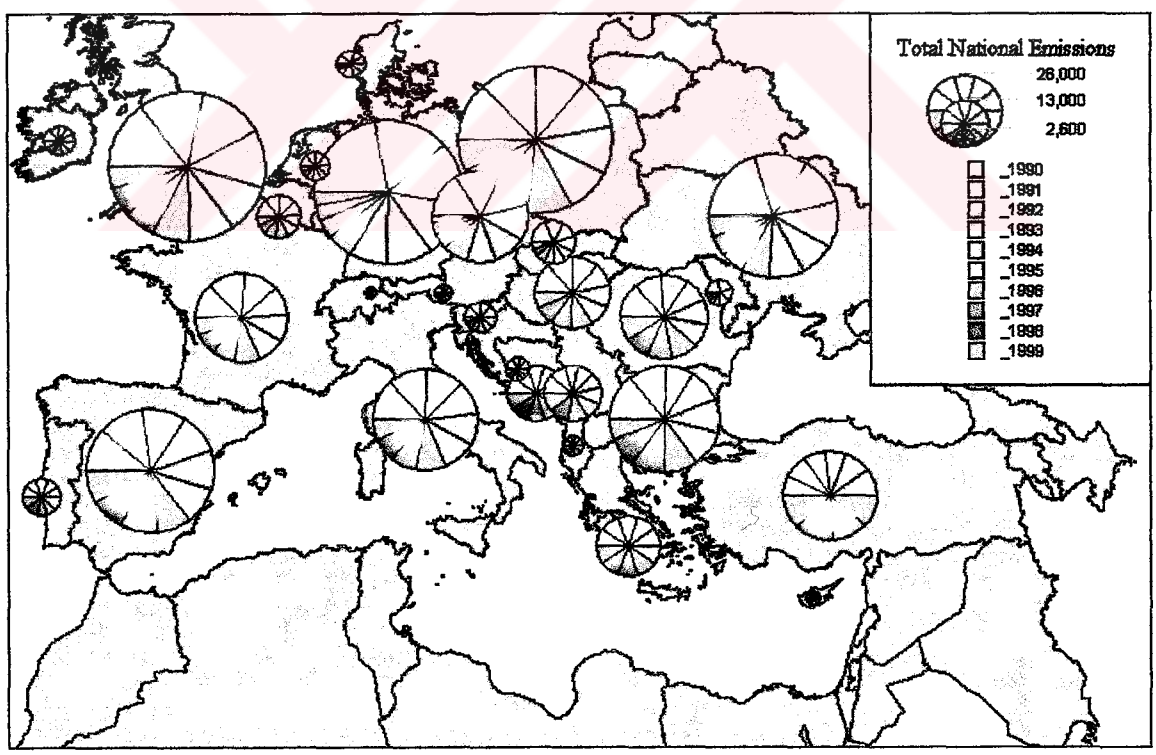

Figure 5.3: Total national anthropogenic sulfur emissions (1000 tones / year) during the years 1990 – 1999.

Table 5.1: Total national emissions of sulfur (1000 tones as SO_2 per year).

Country/year	1990	1991	1992	1993	1994	1995	1996	1997	1998	1999
Albania	72	68	64	59	55	51	52	54	55	57
Austria	80	77	61	59	53	52	49	45	41	38
Belgium	362	330	315	294	252	257	240	219	212	181
Bosnia & Her.	480	480	480	480	480	480	480	480	480	480
Bulgaria	2008	1665	1115	1426	1480	1476	1420	1365	1251	943
Croatia	180	108	107	114	98	70	66	80	89	90
Cyprus	46	33	39	43	42	41	45	47	49	50
Czech Rep.	1881	1780	1543	1424	1275	1089	944	697	438	268
Denmark	177	236	182	147	147	138	174	101	75	55
France	1326	1444	1261	1093	1041	978	954	806	823	705
Germany	5326	3996	3307	2945	2473	1937	1339	1039	836	735
Greece	506	549	556	551	526	551	540	531	540	540
Hungary	1010	913	827	757	741	705	673	659	592	590
Ireland	222	192	172	161	175	161	147	166	176	157
Italy	1748	1635	1533	1414	1332	1263	1203	1063	1002	893
Netherlands	191	173	172	164	146	130	135	118	108	103
Poland	3210	2995	2820	2725	2605	2376	2368	2181	1897	1719
Portugal	229	227	281	240	217	249	186	195	241	248
Rep. Moldava	265	260	168	156	108	64	67	36	32	12
Romania	1311	1041	951	928	912	912	912	912	912	912
Slovakia	542	445	380	325	238	239	227	202	179	171
Slovenia	196	180	186	183	177	125	112	118	123	104
Spain	2098	2091	2068	1946	1902	1754	1540	1709	1577	1606
Switzerland	42	41	38	34	31	34	30	26	28	26
Turkey	765	841	821	768	992	1016	1172	1234	1361	1347
Ukraine	3782	2538	2376	2194	1715	1639	1293	1132	1028	1029
United Kingdom	3721	3537	3463	3117	2676	2363	2028	1670	1607	1229
Yugoslavia	508	446	348	401	424	462	434	522	521	521

The largest thousand such point sources of sulfur emission in Europe (the region includes Europe, Scandinavia, the western states of the former USSR, and Turkey) contribute 80% to 90% of total anthropogenic sulfur emission for the region **(Barrett and Protheroe, 1995).** These sources have tall chimneys and so are major contributors to long distance sulfur pollution. Locations, characteristics, types, productions and sulfur emissions of the largest 100 sulfur emitters in Europe have been defined (Tab. A.1) and the spatial distribution of these emitters and the annual rates of their sulfur emission productions are shown in Figure 5.4.

Table 5.2: Percentage of sulfur reduction (1990 – 1999) of 1990 level (negative number indicates an increase, * and † indicate percentages calculated from 1998 and 1994 emissions respectively) (Vestreng, 2001)

Country	**Year**		
Signatories to the Gothenburg Protocol	**1990**	**1999**	**%**
Albania	72	57	21.0
Austria	91	42	53.9
Belgium	372	186	50.0
Bulgaria	2008	943	53.0
Croatia	180	90.7	49.6
Czech Republic	1876	269	85.7
Denmark	183	56	69.4
France	1278	682	46.6
Germany	5321	831	84.4
Greece	506	540	-6.7 *
Hungary	1010	590.15	41.6
Ireland	186	157	15.6
Italy	1651	923	44.1
Netherlands	202	100	50.5
Poland	3210	1719	46.5
Portugal	359	248	30.9
Rep. of Moldava	265	12.6	95.5
Romania	1311	912	30.4 †
Slovakia	543	171	68.5
Slovenia	196	104	46.9
Spain	2049	1606	21.6
Switzerland	42	26	39.3
United Kingdom	3754	1187	68.4
Non Signatories to the Gothenburg Protocol			
Bosnia and Herzegovina	480	480	0.0
Cyprus	46	50	-8.7
Turkey	764.7	1346.7	-76.1
Ukraine	3782	1132	70.07*
Yugoslavia	508	521	-2.6 *

The three largest sources, Maritsa (Bulgaria), Afsin-Elbistan (Turkey) and Puentes Garcia Rodriguez (Spain), are power stations and they make up 13% of the total

emission from the top 100. Of the largest 100 sources, 93 are power stations. Of these, the largest two emitters, which are power plants, are located in Turkey and the neighboring country, Bulgaria being the closest sources to the measurement station, Antalya.

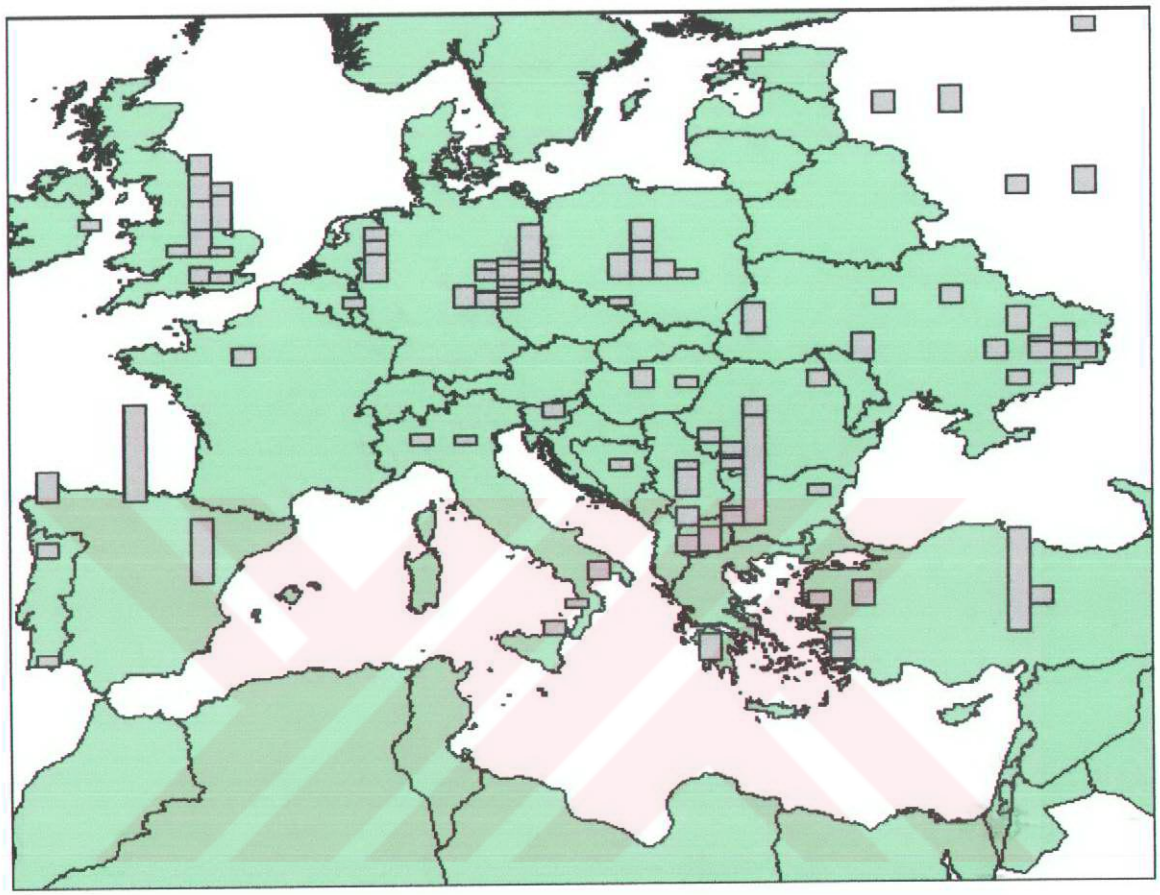

Figure 5.4: Distribution of the largest 100 Sulfur emitters in Europe (Emission rates are 1000 tones per year).

6. RESULTS AND DISCUSSION

6.1 The Mesoscale Meteorological Model, MM5

The auxiliary program TERRAIN is the first step in the application of the MM5 modeling system. The task of the program TERRAIN is to set up the mesoscale domain and to produce the terrestrial data fields for this domain, which will be used by the other programs in the model system. The mesoscale domains are defined to the TERRAIN program as follows:

1- The coarse domain: This domain is chosen to cover the region between latitudes 15° N – 65° N and longitudes 5° W – 55° E in a horizontal spatial resolution of 50 km x 50 km and 141 x 121 grid mesh.

2- The nested fine domain: The finer domain covers an area lies between latitudes 25° N – 60° N and longitudes 5° E – 45° E in a horizontal spatial resolution of 16.667 km x 16.667 km and 262 x 232 grid mesh.

The anthropogenic sulfur emission inventory for Europe is available only in 50 km x 50 km resolution which restricted the selection of the spatial resolution of the study domain. Thus we were forced to choose the coarse domain in 50 km x 50 km resolution to produce the meteorological data that will be used in the photochemical model in the next stage of the study. Unfortunately we have no chance to employ the higher spatial resolution (16.667 km x 16.667 km) predictions by nesting to a finer domain in the air quality model under the current conditions of emission inventory resolution.

The mandatory input data required for TERRAIN are chosen as follows:

1- The terrain elevation data at 10 minutes (18.5 km) and 5 minutes (9.25 km) spatial resolution for the coarse and the fine domains respectively were ftp'ed from the NCAR server.

2- A 24 category USGS global coverage of vegetation/landuse distribution and land-water mask data at the same resolution as in 1.

The outputs of the TERRAIN program are

1. A binary data file for each domain to be used later by the other MM5 auxiliary programs.
2. Several frames plotted by NCAR GRAPHICS for each of the study domains illustrating the followings: a map background (Fig. 6.1), black/white contour terrain height, color terrain height (Fig. 6.2), map of the land-use/vegetation distribution (Fig. 6.3) and a schematic RAOB station map.

The output of the TERRAIN program is used together with the reanalysis data in the next step as input data to the auxiliary program REGRID.

Program REGRID is the second program in the suite of MM5 system programs. This program creates meteorological fields on the mesoscale grid we designed in program TERRAIN. This is also the first place we select the time period of the case as 25 – 29 August 1998.

REGRID has two sequential programs: pregrid and regridder. Program pregrid pre-processes girdded pressure-level meteorological fields from the 2.5° Lat. x 2.5° Lon. NCEP data files and puts the data in an intermediate-format. Program regridder takes the intermediate-format data and output file from TERRAIN, and creates the "first-guess" for subsequent programs LITTLE_R and INTERPF. The output file from REGRID will have 3-dimensional meteorological fields of wind, temperature, relative humidity, geopotential height, and 2-dimensional fields like sea-level pressure and sea-surface temperature for each domain.

The next program in the MM5 modeling system is INTERPF. This program takes pressure-level meteorological fields produced by REGRID, and the definition of model sigma levels, and interpolates pressure level data to sigma levels. 34 sigma levels were defined in the INTERPF program as follows:

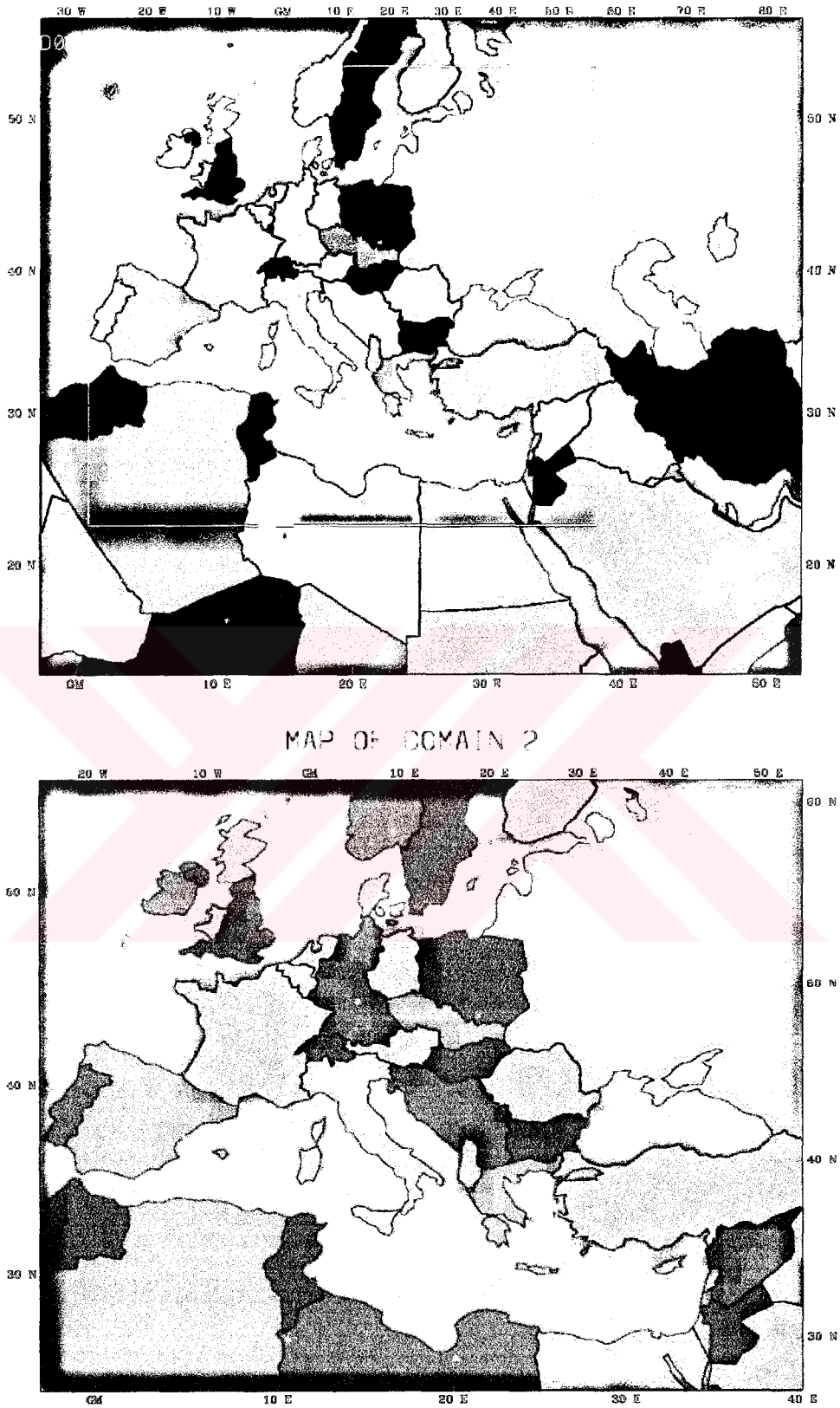

Figure 6.1: The background maps of the coarse domain (upper) and the nest domain (lower) of the study as plotted by the TERRAIN program.

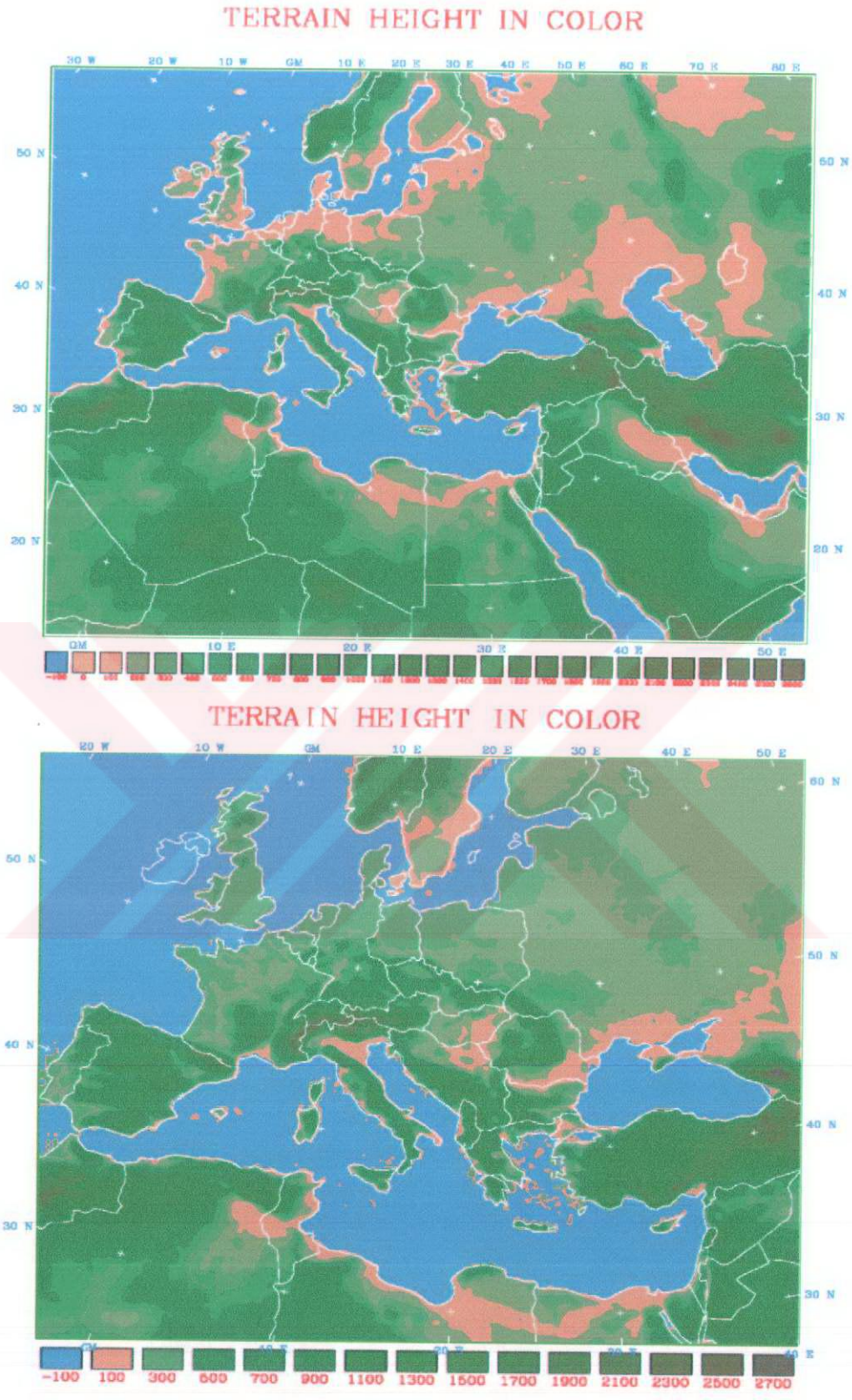

Figure 6.2: The terrain elevation (meter above MSL) in the coarse domain (upper) and the fine domain (lower) of the study as plotted by the TERRAIN program.

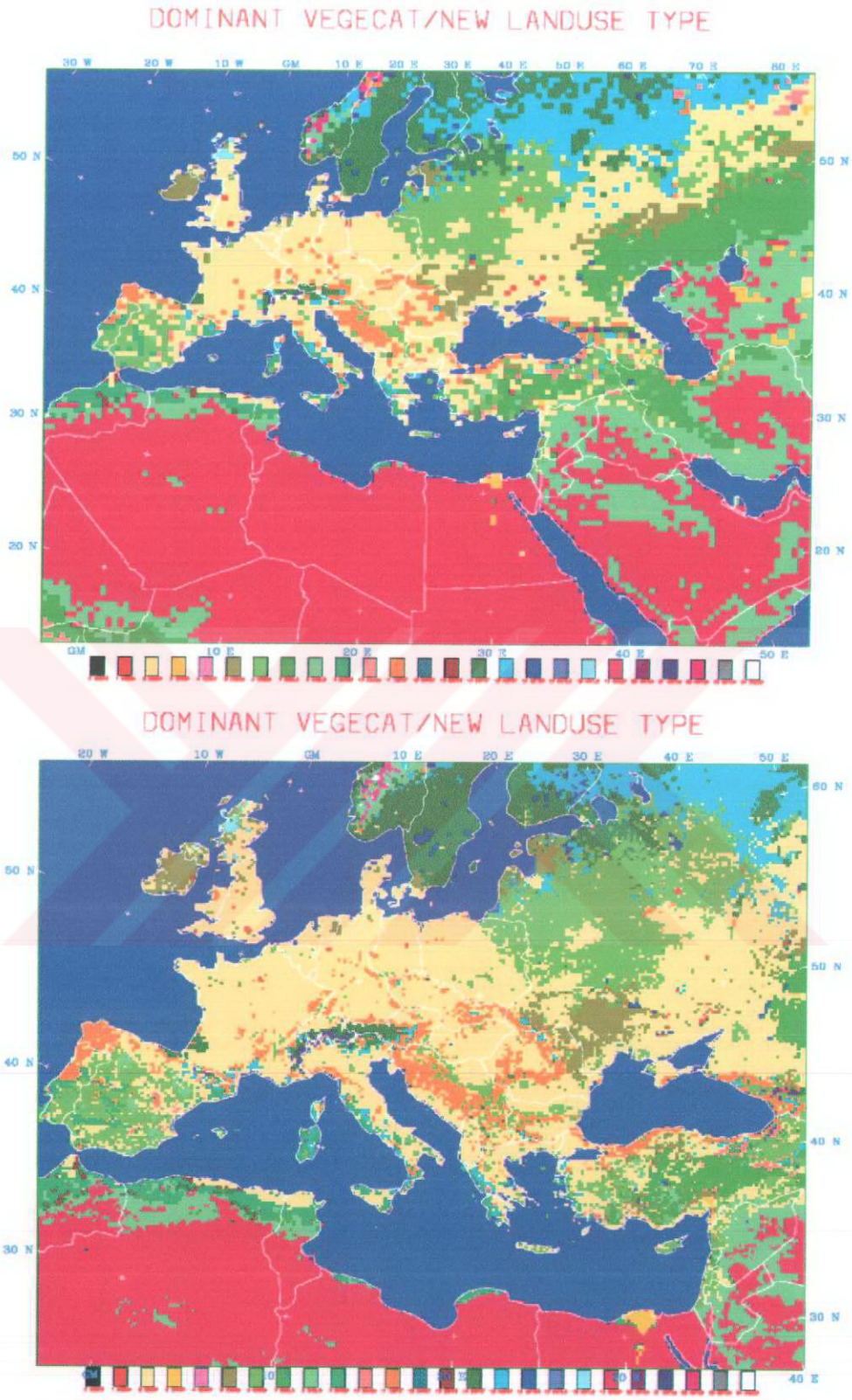

Figure 6.3: The USGS 24 category land-use and vegetation distribution in the coarse domain (upper) and the fine domain (lower) of the study as plotted by the TERRAIN program.

1.00, 0.995, 0.990, 0.985, 0.980, 0.975, 0.970, 0.965, 0.960, 0.950, 0.940, 0.925, 0.900, 0.875, 0.850, 0.825, 0.800, 0.775, 0.750, 0.725, 0.700, 0.650, 0.600, 0.550, 0.500, 0.450, 0.400, 0.350, 0.300, 0.250, 0.200, 0.150, 0.100, 0.050, 0.000

The vertical resolution of the model is defined by the sigma levels. Therefore sigma levels particularly in the boundary layer were carefully selected to idealize the dispersion, diffusion and the complex three dimensional movement of the air.

Three files for each domain are produced by the INTERPF program:

1. MMINPUT_DOMAIN 1, 2, which are the binary initial condition files for the numerical prediction program, MM5. These files contain 3-Dmensional wind, temperature, mixing ratio, vertical motion and perturbation pressure fields on the 34 sigma levels of the model.
2. BDYOUT_DOMAIN 1, 2, which are the binary lateral boundary condition files that contain rows and columns of fields in the MMINPUT_DOMAIN 1, 2 files in the boundary zone.
3. LOWBDY_DOMAIN 1, 2, which are the lower boundary condition files that contain the time-varying, ground temperature and sea-surface temperature fields.

The prediction program in the suite of mesoscale modeling system is MM5. This program requires the above mentioned three output files from INTERPF: MMINPUT_DOMAIN1 or 2, BDYOUT_DOMAIN1 or 2, and LOWBDY_DOMAIN1 or 2.

MM5 generates an output file called MMOUT_DOMAIN 1, 2 which contain the binary history output files from the model that are written at the interval specified earlier in the program script.

For our case MM5 program generated a prediction output files for the 5 days, 25 – 29 August 1998 in one hour time intervals.

The files generated by MM5 were plotted by the visualization program RIP. Temperature, wind vectors, and pressure or geopotential height fields were predicted for each time step in the 5-day period at the levels from the surface up to 100 hpa level. Additionally a NW – SE vertical cross section of the wind circulation, potential vorticity

and potential temperature fields through the domain was predicted for each time step. Furthermore a Skew-T plot for Antalya is also predicted for each time step. Thus the complete simulation of the mesoscale modeling system, MM5 consists of 1092 maps for each domain. Because it is not convenient to include such a large number of plots in the study, only the plots that represent the midday and midnight times of the 5 days period are shown. The model output plots are included in appendix C (Figures C.1 through C.55).

6.1.1 Air mass trajectories to the East Mediterranean Region

6.1.1.1. Definition

There exist two different ways to view air motions, namely the Eulerian and the Lagrangian perspectives **(Dutton, 1986).** The first one focuses on points fixed in the space through which the air flows, the second one on individual air parcels as they move through time and space. The paths of these air parcels are known as **trajectories (Stohl, 1998).**

Trajectory Models are popular tools for describing air mass motions and are applied in several fields of the atmospheric sciences. But their accuracy is limited. Errors in the trajectory calculations result from numerical truncation, interpolation, treatment of the vertical velocity (for instance, use of isobaric or isentropic approximation), errors in the underlying wind field and sometimes inaccurate specification of starting positions and times and subsequent growth of error **(Rolph and Draxler, 1990; Stohl et al., 2001).**

In Principle trajectories can be calculated directly from wind observations by interpolating between the measurements locations. In practice however, trajectory calculations are mostly based on the gridded output of numerical models. In the mesoscale trajectory calculations, prognostic mesoscale models may produce more accurate fields.

6.1.1.2 Trajectory calculation and plot for the East Mediterranean Region

The prognostic hourly wind field produced by the Mesoscale Meteorological Model, MM5 in 50 km x 50 km horizontal resolution was used to calculate air pollution trajectories to the Southeastern Mediterranean region. Two models were employed to

calculate and plot the trajectories using MM5 forecast data through a 96 hour period between 00 UTC, 26 – 08 – 1998 and 00 UTC, 30 – 08 – 1998.

1- The first model is the plot program RIP (Read/Interpolate/Plot).

2- The second is the Hybrid Single Particle Lagrangian Integrated Trajectory (HYSPLIT) model.

Backward trajectories at four sigma levels were plotted for selected 13 points in the Eastern Mediterranean region and western Turkey. The Backward trajectory plots at sigma levels 0.998, 0.990, 0.900 and 0.850 are shown in Figures C.56, C.57, C.58 and C.59 respectively. Trajectories can be easily separated into three main sectors taking in account their tracks to the Eastern Mediterranean as follows:

1. Sector A: East Europe, which includes trajectories originated in Ukraine, Moldavia and Romania through the Black Sea and Turkey to the Eastern Mediterranean that is represented by Antalya.
2. Sector B: Central Europe, which has trajectories originated mainly in Bulgaria, Macedonia, Albania, the former Yugoslavia, Croatia and Slovenia through the northwestern part of Turkey and then the Eastern Mediterranean.
3. Sector C: Southern Europe and the Mediterranean Sea, the trajectories in this sector are originated mainly in the Central and Western Mediterranean Sea, Spain, the southern parts of France, Italy, Greece and the southwestern parts of Turkey to the Eastern Mediterranean, which is represented by Antalya.

Fig. C.56 shows that the trajectories at the lowest level, 0.998 sigma levels (up to 25 m AGL) are mainly originated in sector A (54%), then sector B (31%) and sector C (15%). In a higher level, 0.99 sigma level (approximately 100 m AGL) the contribution of the air mass origin sectors are 38 % for each of sector A and B, while 24% of the trajectories are originated in sector C (Fig. C.57). At sigma level 0.9 (approximately 1000 m AGL) trajectories are originated in sector C (77%) and the rest 23% in sector B, while there is no contribution from section A. At the top of the boundary layer (sigma level 0.85, approximately 1500 m AGL) the majority of trajectories are originated in sector C (84%) while only 8% of the trajectories are originated in each of sector A and B.

These results are obvious evidence to the statement: "In the summer season the source origin of air masses reach the eastern Mediterranean region is from north and northwest" which was derived from the synoptic and climatological analysis during the episodic period in the study area (chapter 2 section 2.5).

The results presented above are in a great agreement with the findings of **Sciare et al. (2002)** regarding to the backward trajectories to Finokalia in the eastern Mediterranean.

In order to confirm the RIP trajectory simulations and to make comparisons with another model, 96 hours backward trajectory plots were produced by both models; the RIP and the HYSPLIT for Antalya, Izmir, Istanbul and Ankara at 3000 m AGL (Fig. C.60). The results are superior; trajectories produced by the two models are completely identical. Fig. C.60 shows that the trajectories to the Eastern Mediterranean and western parts of Turkey are originated from Southeastern Europe and the Mediterranean Sea through Greece and the Aegean Sea.

Furthermore multiple backward trajectory plots for Antalya at levels 100 m, 1000 m, 1500 m and 3000 m AGL are simulated by the HYSPLIT model (Figures C.61, C.62, C.63 and C.64 respectively). In these simulations trajectory generation is renewed every 3 hours all over the entire period that starts at 0000 Z 30 Aug. 1998 and ends at 0000 Z 26 Aug. 1998. As a result 32 trajectories are produced during 96 hour period, the first trajectory starts at Antalya at 0000 Z 30 Aug. 1998 while the last one starts at 0300 Z 26 Aug. 1998 and all trajectories end at the origin source at 0000 Z 26 Aug. 1998.

Fig. C.61, which shows the simulated lowest level (100 m AGL), illustrates that short time trajectories (3 – 48 h) are originated mainly in Western Turkey, while the long time trajectories (48 – 96 h) are originated in the Southern Ukraine, Moldavia through the Black Sea and Western Turkey. The lower part of the same figure shows that trajectories come from location may be elevated up to 2500 m AGL.

In higher levels, 1000 m AGL (Fig. C.62) and 1500 m AGL (Fig. C.63), very few long trajectories have origins at the Southern Ukraine, Moldavia through the Black Sea and Southern Turkey, while the majority is short time trajectories originated in regions closed to Antalya, such as: Greece the Aegean Sea and Western Turkey. The lower part of the both figures show that the short time trajectories come from locations lower than

1000 m AGL (Fig. C.62) and 1500 (Fig. C.63), while long trajectories in both cases have origins located up to 4000 m AGL.

Backward trajectory plots for Antalya station at 3000 m AGL (Fig. C.64) indicate that there are few short range trajectories originated from closed areas to Antalya, such as the southern parts of Turkey at levels below 3000 m AGL. Whereas the medium and long range transport is chiefly originated from Italy and Mediterranean Sea through the southern parts of Greece to Antalya within a layer ranges between 3000 – 6000 m AGL.

6.1.2 Performance verification of the Mesoscale Meteorological Model, MM5

The MM5 model performance was found to be superior in forecasting temperature and wind fields. Figures D.1 through D.15 illustrate the MM5 model predicted plots versus observed ones of temperature, wind velocity and Sea Level Pressure on 0.998 sigma level, and temperature, wind velocity and geopotential heights at 850 and 700 hpa levels, vertical cross section and Skew T plot diagram for Antalya. It is apparently seen from the figures that the model accomplished not only to predict the general pattern of the pressure systems, but also to produce a highly accurate forecast all over the episodic period. The 96 and 120 hours forecasts are as accurate as the 24 and 48 hours, which mean that the model has succeeded to prevent its accuracy and to maintain its performance level during the whole forecast period.

Figures D.5, D.10 and D.15 show that the model has revealed a high performance in forecasting the wind profile in both speed and direction, especially in the lower boundary layer where light and variable winds are dominant, which may be considered as a challenge to any model accuracy.

In order to verify the model performance, a comparison between the model predicted hourly 5 day time series of air temperature and 10 m wind speed and the observed temperature and wind speed time series at three locations (Istanbul, Izmir and Antalya) have been illustrated in Figures 6.4 and 6.5. Furthermore scattered diagram of observed values versus MM5 model prediction values for both temperature and wind speed are also plotted for the same stations (Fig. 6.6). It is obvious from Fig. 6.4 that the model revealed a high accuracy in forecasting the temperature in each of the three stations. The

same result may easily be seen from Fig. 6.6, where the correlation coefficient (R^2) is relatively high (0.59, 0.55 and 0.57) for Istanbul, Izmir and Antalya respectively.

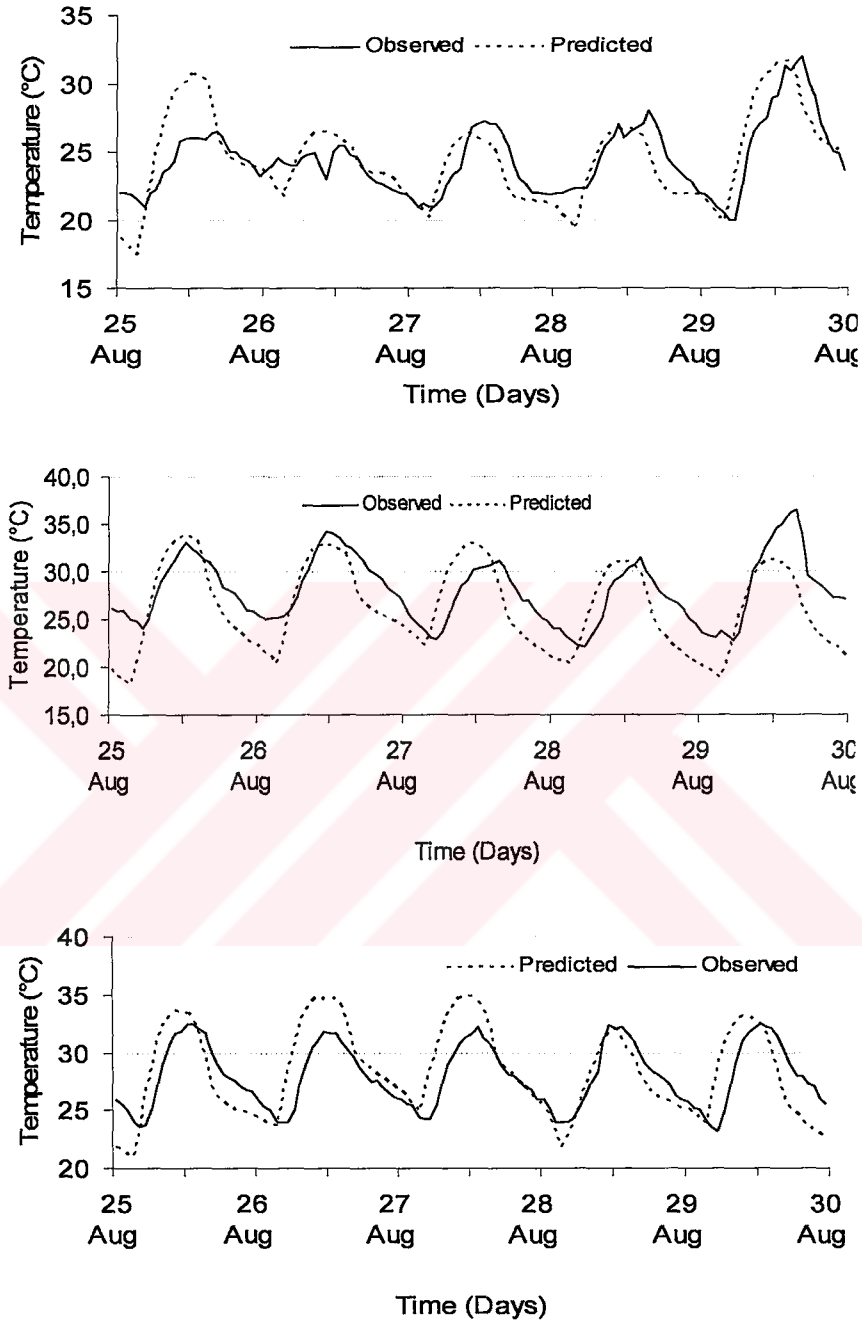

Figure 6.4: Hourly temperatures (°C) observed in meteorological stations of Istanbul (upper), Izmir (middle) and Antalya (lower) versus predicted by MM5 modeling system for the period from 00 Z, 25 – 08 – 1998 to 00 Z, 30 – 08 – 1998.

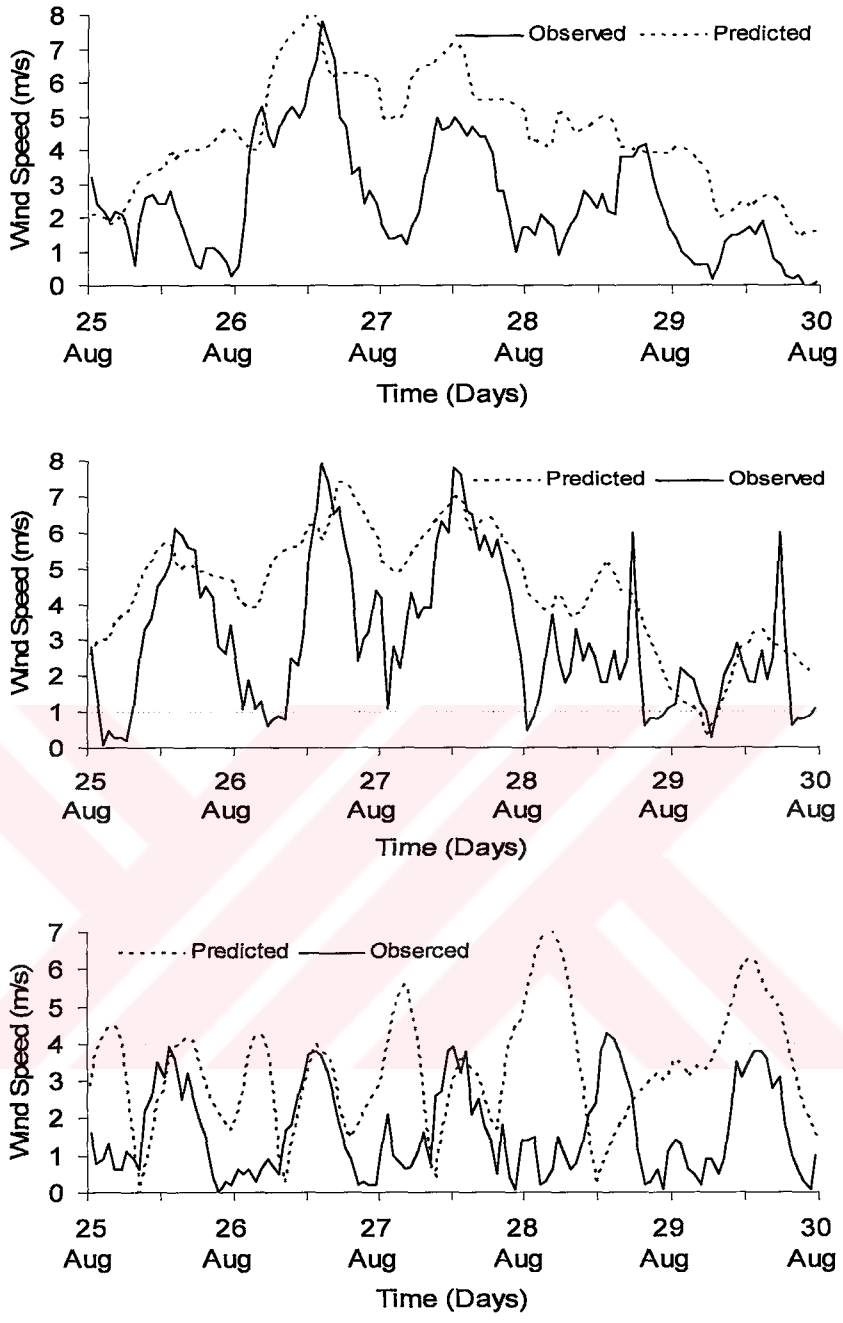

Figure 6.5: Hourly wind speed (m/s) observed at 10m height in Istanbul (upper), Izmir (middle) and Antalya (lower) meteorological stations versus predicted by MM5 modeling system for the period from 00 Z, 25 – 08 – 1998 to 00 Z, 30 – 08 – 1998.

The observed wind speed average over the 120 hour period is 2.5, 3.0 and 1.6 m/s for Istanbul, Izmir and Antalya respectively and the wind speed is below 8 m/s over the entire period in Istanbul and Izmir, while it is bellow 4 m/s in Antakya (Fig. 6.5). The

figure shows that the model overestimate the wind speed when it is low whereas it is accurately estimated when high.

It is noticed that the model exhibits a higher accuracy forecast in the forth and fifth days of the forecast period than the first 24 hours, which might be related to the objective analysis quality that have initialized the model run.

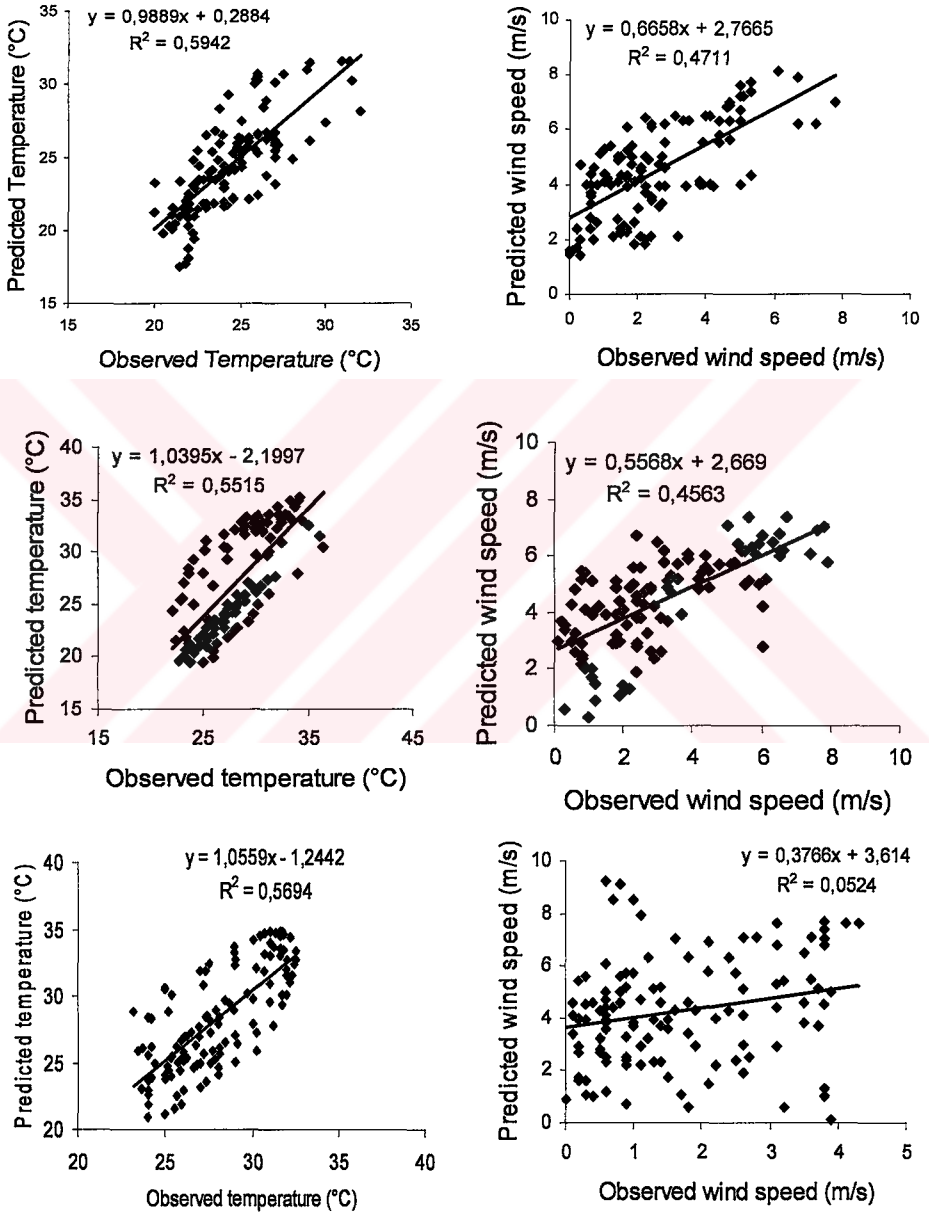

Figure 6.6: Model predicted versus observed hourly temperature (left) and 10m wind speed (right) in Istanbul (Goztepe), Izmir and Antalya meteorological stations for the period from 00 Z, 25 – 08 – 1998 to 00 Z, 30 – 08 – 1998.

6.2 The Air Quality Chemical Model, CAMx

CAMx air quality model, version 4.11s which is the most recent version of the model is applied to simulate the predicted concentration, deposition, transport and source origins of anthropogenic pollutants in the study domain during the selected episodic period 26 – 29 August 1998. The photochemical model, CAMx is applied to a mesoscale domain of 89 x 78 grid points with a horizontal resolution of 0.59° x 0.45° in the E-W and N-S directions respectively, and 14 layers vertical resolution. The first layer is 50 m AGL and the highest level is 4000 m AGL. The detailed vertical structure of the model is shown in Table 6.1.

Table 6.1: Vertical layer structure of CAMx.

CAMx Layer	MM5 Layer	Layer Range (m)	Top (m AGL)	Center (m AGL)	Thickness (m)
14	**22**	3000-4000	4000	3500	1000
13	**20**	2500-3000	3000	2750	500
12	**18**	2000-2500	2500	2250	500
11	**16**	1500-2000	2000	1750	500
10	**14**	1250-1500	1500	1375	250
9	**13**	1000-1250	1250	1125	250
8	**12**	800-1000	1000	900	200
7	**11**	600-800	800	700	200
6	**10**	450-600	600	525	150
5	**9**	300-450	450	375	150
4	**6**	200-300	300	250	100
3	**4**	100-200	200	150	100
2	**2**	50-100	100	75	50
1	**1**	0-50	50	25	50

6.2.1 CAMx Inputs

To solve the pollutant continuity equation including the terms of: horizontal advection/ diffusion, vertical transport/diffusion, chemistry, dry deposition and wet deposition, the CAMx model requires a set of input data that include:

I. Emissions: Substances emitted into the atmosphere by human and natural activities are the cause of many current and potential environmental problems, including: acidification, air quality degradation, global warming/climate change, damage and soiling of buildings and other structures, stratospheric ozone depletion and human and ecosystem exposure to hazardous substances.

There are many types of sources of atmospheric emissions and many examples (often millions) of each type **(EEA, 2002),** for example:

1. Power plants
2. Refineries
3. Incinerators
4. Factories
5. Domestic households
6. Cars and other vehicles
7. Animals and humans
8. Fossil fuel extraction and production sites
9. Offices and public buildings
10. Trees and other vegetation
11. Distribution pipelines
12. Fertilised land
13. Land with biological decay.

It is not possible to measure emissions from all of the individual examples of these sources or, in the short term, from all the different source types. In practice, atmospheric emissions are estimated on the basis of measurements made at selected or representative samples of the (main) sources and source types.

Emission inventories may contain data on three types of source, namely point, line and area.

(i) Point sources: Emission estimates are provided on an individual plant or emission outlet (usually large) usually in conjunction with data on location, capacity or throughput, operating conditions etc. The tendency is for more sources to be provided as point sources as legislative requirements extend to

more source types and pollutants as well as more openness provides more such relevant data.

(ii) Line sources: In some inventories, vehicle emissions from road transport, railways, inland navigation, shipping or aviation etc are provided for sections along the line of the road, railway-track, sea-lane etc.

(iii) Area sources: smaller or more diffuse sources of pollution are provided on an area basis either for administrative areas, such as countries, regions etc, or for regular grids (for example the EMEP 50x50 km grid, which is the inventory used in this study).

The basic model for an emission estimate is the product of (at least) two variables **(EEA, 2002),** for example:

a) An activity statistic and a typical average emission factor for the activity, or
b) An emission measurement over a period of time and the number of such periods emissions occurred in the required estimation period.

For example, to estimate annual emissions of sulfur dioxide in grams per year from an oil-fired power plant you might use, either:

a) Annual fuel consumption (in tones fuel/year) and an emission factor (in grams SO2 emitted/tones fuel consumed), or

b) Measured SO2 emissions (in grams per hour) and number of operating hours per year.

In practice, the calculations tend to more complicated but the principles remain the same. The most challenging part of the study was the preparation of the emission inventories. Emissions of some pollutants are available in yearly totals for most of the European countries. However the model requires the gridded hourly emissions for each modeled species. To obtain these emissions there is a necessity to have a precise knowledge about each pollution source and each emitted pollutant including the emission rates in each single grid of the domain in the light of the above classifications. Currently the emission inventories are not available in Turkey. In some European countries emission inventories are calculated from EMEP emission data using special

preprocessors and models. These inventories are not public. For this study the emission inventories were prepared in Greece **(Kallos and Astitha, 2005).** These inventories contain hourly anthropogenic emissions of: SO_2, NO, NO_2, OLE, PAR, TOL, XYL, FORM, ALD2, ETH, CO and NH_3.

These emission inventories were prepared in LAT/LON Map Projection, while MM5 output files are produced in Lambert Conformal Map Projection. In this case we were forced to run CAMx in LAT/LON and to transform the mm5 output data projection from Lambert Conformal to LAT/LON and also to produce all other input data in the LAT/LON projection.

II. Meteorology: 3 dimensional gridded fields supplied by the mesoscale meteorological model, MM5 including: horizontal wind components, temperature, pressure, water vapor, vertical diffusivity, cloud and rain (converted from Lambert Conformal to LAT/LON projection).

III. Air quality: The average default values of time/space constant top concentrations of all the species were selected to be used in a preprocessor by which the initial concentration and boundary concentration gridded data files were generated.

IV. Geography: Gridded landuse/surface vegetation cover: The landuse / surface vegetation data are obtained from the USGS sever. The data are available in 24 categories in six resolutions ranging from 1° to 30 sec., while CAMx model uses 11 categories. Thus we have converted the USGS 24 categories (Table A.2) at 30 sec. resolution to CAMx 11 categories (Table A.3) at 0.59° x 0.45° resolution.

V. Gridded surface UV albedo codes: The UV albedo codes were calculated by a preprocessor depending on the landuse and vegetation distribution.

VI. Other inputs such as: Gridded haze opacity codes, gridded ozone column codes and photolysis rates lookup tables are calculated by the radiative model, TUV.

The chemistry mechanism No. 4 is chosen to be implemented in CAMx model which includes 100 reactions, 46 gas species (34 state gases and 12 radicals), and 16 aerosol species.

6.2.2 Results of CAMx Model

CAMx version 4.11s with aerosol chemistry mechanism No. 4 has been run for the 4 day episodic period, 26 – 29 Aug. 1998. Hourly gridded concentration and deposition distribution of the gaseous species SO_2 and the aerosol species PSO_4 were generated and the **P**ackage for **A**nalysis and **V**isualization of **E**nvironmental data (**PAVE**) software was used to simulating and mapping the gridded binary outputs of the CAMx model. The outputs include the following issues:

a) Three-dimensional hourly concentrations of gaseous species SO_2 and aerosol species PSO_4 were predicted in PPM and $\mu g/m^3$ respectively. The predicted concentrations of the two species are shown in Figures E.1 to E.4 in 3 hour intervals during the episodic period.

b) The deposition output file includes the followings:

   1. Two-dimensional dry deposition velocity fields for the both species predicted in m/s.
   2. Two-dimensional dry deposited mass field (mol/ha for gaseous species and g/ha for aerosols).
   3. Two-dimensional wet deposited mass field (mol/ha for gaseous species and g/ha for aerosols).
   4. Two-dimensional precipitation liquid concentration for species (mol/l for gasses, g/l for aerosols).

There is no internationally or regionally established methodology for the routine observation of dry deposition. Moreover, research on dry deposition is still limited in comparison with the many research projects and ongoing measurements of wet deposition in Europe. In this study gridded hourly deposition velocity, wet and dry deposition rates are predicted by CAMx model. The dry deposition rates of the PSO_4 and SO_2 are simulated in 3 hour intervals during the study period (Figures E.5 to E.8). It is apparently seen from the concentration and the dry deposition figures in Appendix E that the areas of high concentration of SO_2 and PSO_4 are also areas of large deposition of the

same species and vice versa. Accordingly we can say that the deposited sulfate in the Eastern Mediterranean region is originated from Central and Southeastern Europe.

Although the East Mediterranean region was free of rainfall during the study period and so was a large portion of the domain, the wet deposition of the both species in some other areas revealed a remarkable influence on the transport of the pollutants to the Eastern Mediterranean region. The wet deposition rates of the PSO_4 and SO_2 are simulated in 12 hour intervals during the study period in Fig. E.9. It is obviously noticed from the simulation sequence in Fig. E.9 particularly (f), (g), (h) and (i) that the sulfate and sulfur dioxide were effectively deposited in Southwestern Europe (the former Yugoslavia, Bulgaria and Romania) during the second half of the episode. This effective wet deposition together with the less effective dry deposition lessens the pollution transport to the northwestern parts of Turkey.

The simulation sequence of the SO_2 concentrations during the 4 day episodic period shows that the SO_2 concentration reveals large values only near sources and SO_2 is not transported to long distances from the origin sources. This result is unexpected, since several studies have reported that most of the SO_2 over the Eastern Mediterranean originates from Central and Eastern Europe. The same findings were derived by **Sciare et al. (2002).** This can be probably attributed to the active oxidation of SO_2 to SO_4 in the fume of the power plant and to the rapid transformation of the SO_2 to aerosol sulfate in the troposphere which may occur within a short time (may be several hours). In the other hand the PSO_4 concentration maps (Figures E.1 through E.4) indicate obvious evidence to the sulfate transformation from Central and Southeastern Europe to the Eastern Mediterranean region. Two main tracks are identifiable:

1- The first track is the transport of sulfate originated from Italy through Greece and the Aegean Sea to the Eastern Mediterranean. This result is also emphasized by the backward trajectories discussed in section 6.1.1.2. and illustrated in Fig. C.67. In this case the transport taking place at high levels ranging between 3000 – 6000 m AGL may explain the long range transport of sulfate rather than SO_2.

2- The second is the sulfate transport track which is originated from Central and Eastern Europe through the northwestern part of Turkey. This track is also

identical to sector B of the backward trajectory distributions discussed in section 6.1.1.2.

Similar results related to transport and origin source determination of PSO_4 are reported by **Kouvarakis et al. (2000), Sciare et al. (2002)** and **Kallos et al. (2004).**

6.2.3 Performance verification of the CAMx Model

Several methods exist to verify any model performance:

1. Of these, the most popular method is the comparison between the model estimated and observed values of some species in particular locations. Fig. 6.7 shows the predicted hourly concentration time series of PSO_4 and SO_2 species in Antalya and Cubuk/Ankara during the episodic period, 26 – 29 Aug. 1998. Measurements of SO_2 and SO_4 in EMEP stations are available only in daily intervals and the hourly concentration of these species is not available, and so in Antalya station. Therefore the daily averages of the predicted species concentrations are calculated and compared to the observed ones (Table 6.2).

   The model exhibited a good performance in estimating PSO_4 in Ankara with a small overestimating factor of about 30% and underestimated the sulfate in Antalya by a factor of about 8. The model also overestimated SO_2 by a factor of 6 in Ankara, while no SO_2 observations are available in Antalya. According to **Andreani-Aksoyoglu et al. (2004)** many model applications yield too high SO_2 concentrations which could be caused either by boundary conditions or emissions. In this case sensitivity tests should be applied to the model to achieve the best fit estimations. The sensitivity tests may be reduction of SO_2 emissions by particular factor (e.g., 25%, 50% or 100%), or reduction of the initial and boundary levels of SO_2.

2. The second method is comparison with other studies: there is a remarkable lack in air pollution modeling studies and pollutant transport from Europe to Turkey or to the East Mediterranean. In a recent study **Kindap et al. (2005)** have modeled the long range transport of PM from Europe to Istanbul (the northwestern part of

Turkey) during the period 5 – 12 Jan. 2002. The photochemical model CMAQ has overestimated PM concentrations by a factor of 10 to 20.

3. Sensitivity analysis methods: Sensitivity analysis methods measure the model response to an input change, e.g., the change in sulfate concentration due to a change in SOx emissions. Brute force or direct method, zero-out modeling method and double direct method are sensitivity analysis methods discussed in detail by **Yarwood et al (2004).**

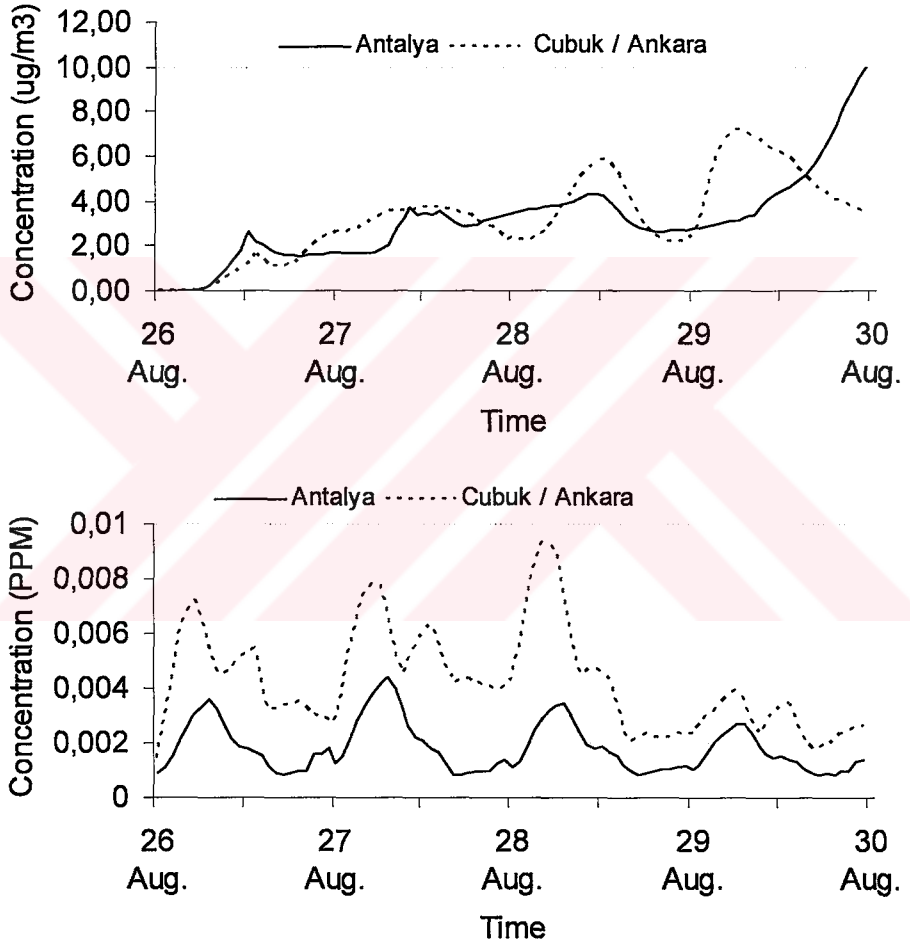

Figure 6.7: The predicted hourly concentration time series of PSO4 (upper) and SO_2 (lower) in Antalya and Cubuk/Ankara during the period between 00 UTC 26 Aug. and 23 UTC 29 Aug. 1998.

Table 6.2: Daily average predicted versus observed concentrations of PSO_4 and SO_2 in Antalya and Cubuk EMEP station during the period between 26 and 29 August 1998.

	PSO_4 Concentration ($\mu g/m^3$)				**SO_2 Concentration ($\mu g/m^3$)**			
	Antalya		**Cubuk/Ankara**		**Antalya**		**Cubuk/Ankara**	
Date	Predicted	Observed	Predicted	Observed	Predicted	Observed	Predicted	Observed
26 - 8	1.11	26.3	0.9	0.9	5.11	Not Available	12.2	2.62
27 - 8	2.74	30.7	3.22	1.56	5.69	Not Available	14.64	2.88
28 - 8	3.44	35.1	3.55	1.14	4.88	Not Available	12.55	2.14
29 - 8	5.04	26.5	5.22	3.84	4.65	Not Available	7.67	0.72

In this thesis sensitivity analysis has been done by running CAMx model twice for each day of the episodic period 26 – 29 August 1998 in order to measure the response of the model to SO_2 input changes. In one run we used emission inventories having SO_2 reduced by 50% while in the other the SO_2 emission inventories were doubled. CAMx model revealed a good response to the input changes of SO_2. Figure 6.8 shows the sulfate concentration time series predicted by CAMx model in Antalya using three different scenarios of SO_2 emission inventory inputs. The average sulfate concentration during the 4 day episode exhibited a reduction of 30% when the SO_2 emissions have been reduced by 50% and exhibited an increase of 65% when the SO_2 emissions have been increased by 100%. This result may emphasize the evidence of long range transport of European pollutants to the East Mediterranean region.

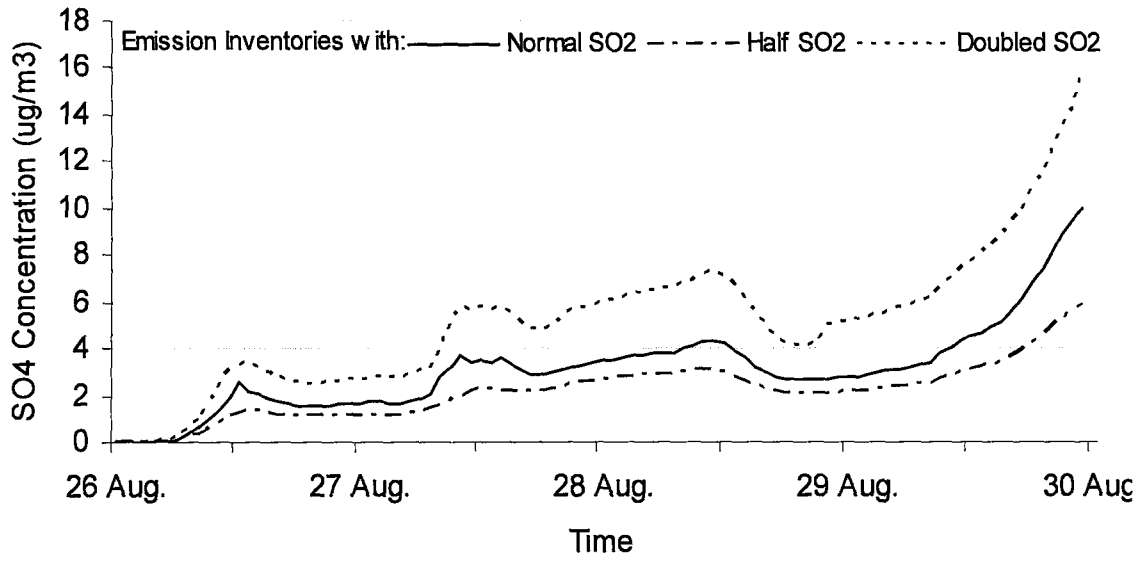

Figure 6.8: Sulfate concentration time series predicted by CAMx model using different emission inventory inputs of SO_2 during the episodic period 26 – 29 August 1998.

7. CONCLUSION

In this thesis, we presented the analysis results of the episodic conditions found in a rural site of Antalya (Southwest of Turkey on the East Mediterranean coast) using a modeling system consists of the Mesoscale Meteorological Model MM5, a three-dimensional Eulerian model CAMx (Comprehensive Air Quality Model with Extension) and the Hybrid Single Particle Lagrangian Integrated Trajectory (HYSPLIT) model. The episodic period, 26 – 29 August 1998 was chosen due to the highest concentration of sulfate from European emissions.

The model system was used to predict the atmospheric condition in large domain which includes Europe, Turkey and East Mediterranean region, to estimate the gridded concentrations of various air pollution species and to simulate their trajectories using the gridded wind field predicted by MM5 model.

For this analysis the seasonal synoptic climatological patterns in the study area in general and for the episodic period in particular were investigated. The modeling system has been conducted for the episodic period in August 1998 with the purpose to identify the reasons of the episodic levels.

Firstly, the air mass backward trajectory simulations by MM5/RIP and HYSPLIT have demonstrated three main sectors of air mass origins and tracks as follows:

Sector A: East Europe, which includes trajectories originated from Ukraine, Moldavia and Romania through the Black Sea to the central and western parts of Turkey and then the Eastern Mediterranean.

Sector B: Central Europe, this sector includes trajectories originated mainly from Bulgaria, Macedonia, Albania, the former Yugoslavia, Croatia and Slovenia to the western part of Turkey and then the Eastern Mediterranean.

Sector C: Southern Europe and the Mediterranean Sea, trajectories in this sector are originated mainly from the Central and Western Mediterranean Sea, Spain, the southern parts of France, Italy and Greece through the Aegean Sea to the southwestern parts of Turkey and then to the Eastern Mediterranean.

The air quality model simulations of sulfate concentration and deposition have revealed a great agreement with the air mass trajectory simulations produced by HYSPLIT and RIP/MM5 models. Simulations have demonstrated that sulfate transport from Europe to the East Mediterranean has two main paths: the first and the most effective one is the transport of sulfate originated from Italy through Greece and the Aegean Sea to the southwestern parts of Turkey. The second and less effective one is the sulfate transport track which is originated from Central and Eastern Europe through the northwestern part of Turkey.

The effective wet deposition together with the less effective dry deposition in the Southeastern Europe lessens the pollution transport to the northwestern parts of Turkey.

Simulations of PSO_4 and SO_2 indicate a remarkable coincidence between concentration and deposition of the both species. The areas of high concentration of SO_2 and PSO_4 are also areas of large deposition of the same species and vice versa. Both SO_2 concentration and deposition have revealed large values only nearby sources which indicate that SO_2 is not transported to long distances from the origin sources and deposited on the same areas. In contrast to SO_2, the deposited sulfate in the Eastern Mediterranean region is mostly originated from Central and Southeastern Europe.

The performance of the mesoscale meteorological model, MM5 was examined. The model results exhibit a higher accuracy in the fourth and fifth days of the forecast period. CAMx model also revealed a better performance in estimating PSO_4 in Ankara, but it underestimated the sulfate in Antalya by a factor of about 8. The model also overestimated SO_2 by a factor of 6. The overestimation of SO_2 concentration may be attributed to either boundary conditions or emissions.

Sensitivity analysis results show that the average sulfate concentration during the 4 day episode exhibits a reduction of 30% when the SO_2 emissions have been reduced by 50% and an increase of 65% when the SO_2 emissions have been increased by 100%. This

result may emphasize the evidence of long range transport of European pollutants to the East Mediterranean region.

The following future works are necessarily should be implemented:

- Sensitivity simulations to examine the features (i.e., day-to-day changes in fossil fuel emissions and meteorology) that control the variations of pathways are needed to be conducted.
- Since the atmospheric circulation is continuously variable and such studies are manipulated in a few days period, similar works are certainly required in the area to better evaluate the long range transport phenomenon in different seasons or even in each month of the year.
- The study should be broadened to investigate the long range transport of further gaseous and aerosol species and ozone.
- The most challenging part of the study is the preparation of a high quality emission inventory. For this purpose the EMEP data are generally used, which is available only in yearly averages and cover the European continent only. Consequently an original national emission model is needed.
- In case emission inventories become available in horizontal resolutions higher than 50 km x 50 km, such studies should be repeated in finer domains.
- Air pollution simulations along with measurements for other locations as well as future data taken from Seferhisar, Izmir, Vize, Kirklareli EMEP stations would allow the generalization of the above conclusions.

REFERENCES

Abraham., F.F., 1974: Homogeneous Nucleation Theory. *Academic Press*, US.

Ahrens, D., 2000: Meteorology Today: An Introduction to Weather, Climate, and the Environment. *Brooks Cole press,* USA

Al-Momani, I. F., Ataman, O. Y, Anwari, M. A., Tuncel, S., Kose, C. And Tuncel, G., 1995a: Chemical composition of precipitation near an industrial area at Izmir - Turkey. *Atmos. Environ.*, **29**, pp. 1131 – 1144.

Al-Momani, I. F., Tuncel, S., Eler, U., Ortel, E., Sirin, G, and Tuncel, G., 1995b: Major ion composition of wet and dry deposition in Eastern Mediterranean Basin. *Sci. Total Environ.,* **164**, pp. 75 – 85.

Al-Momani, I. F., Gullu, G., Olmez, I., Eler, U., Ortel, E., Sirin, G, and Tuncel, G., 1997: Chemical composition of Eastern Mediterranean aerosol and precipitation: Indicators of long range transport. *Pure Appl. Chem.,* **69**, pp. 41 – 46.

Alpert, D.J. and Hopke, P.K., 1981: A determination of the sources of airborne Particles collected during the regional air pollution study. *Atmos. Environ.* **15**, PP. 675-687.

Alpert, P., Neeman, B. U., and Shay-El, Y., 1990a: Climatological analysis of Mediterranean cyclones using ECMWF data. *Tellus*, **42**, 65 – 77.

Alpert, P., Neeman, B. U., and Shay-El, Y., 1990b: Intermonthly variability of cyclone tracks in the Mediterranean. *Journal of Climate*, **Vol. 3**, 1474 – 1478.

Andreani-Aksoyoglu, S., Keller, J., Dommen, J., and Prevot, A.S.H., 2001: Modeling of Air quality with CAMx: *A case study in Switzerland. Proceeding of the 2nd International Symposium on Air Quality Management at Urban, Regional and Global Scales*. 25 – 28 September, Istanbul, Turkey, pp. 306 – 313.

Andreani-Aksoyoglu, S., Pre´vo^t, A. S. H., Baltensperger, U., Keller, J.,and Dommen, J., 2004: Modeling of formation and distribution of secondary aerosols in the Milan area (Italy), *J. Geophys. Res.,* **109**, D05306, doi:10.1029/2003JD004231.

Anteplioglu, U., Incecik, S., and Topcu, S., 2003: Model study with MM5 and CAMx in Istanbul area during high ozone days. *International Symposium on Clean Environment.* 21 – 22 November, Cheonan, Korea.

Anteplioglu, U., Topcu, S., And Incecik, S., 2002: An application of a photochemical model for urban airshed in Istanbul. *The 25th NATO/CCMS International Technical Meeting on Air Pollution Modeling and its Application. Louvain-la-Neuve, Belgium.*

Anthes, R. A., and Warner, T. T., 1978: Development of hydrodynamic models suitable for air pollution and other mesometeorological studies. *Mon. Wea. Rev.*, **106**, 1045-1078.

Barrett, M., and Protheroe, R., 1995: Sulfur emissions from large point sources in Europe, 2nd Edition. Air Pollution and Climate Series NO. 3, *Swedish NGO Secretariat on Acid Rain.*

Binkowski, F.S., and Shankar, U., 1995: The regional particulate model 1. Model description and preliminary results. *J. Geophys. Res.* **100**, 26191-26209.

Businger, S., 1994: Cool season vyclogenesis and associated mesoscale weather: U.S. National Report to International Union of Geodesy and Physics. *Reviews of Geophysics*, 1991 – 1994.

Buzzi, A., and Tibaldi, S., 1978: Cyclogenesis in the lee of Alps: A case study. *Quart. J. Roy. Meteor. Soc.*, **104**, 271 – 287.

Camkur, R. V., and Miller, R. L., 2004: Incorporating the effect of small-scale circulations upon dust emission in an atmospheric general circulation model. *J. Geophys. Res.*, **109**, D07201, doi: 10.1029/2003JD004067.

Carter, W.P.L., 1996: Condensed Atmospheric Photooxidation Mechanisms for Isoprene. *Atmos. Environ.*, **30**, 4275-4290.

Carter, W.P.L, 2000: Programs and Files Implementing the SAPRC-99 Mechanism and its Associates Emissions Processing Procedures for Models-3 and Other Regional Models, http://pah.cert.ucr.edu/~carter/SAPRC99.htm.

Chang, J.S., Brost, R.A., Isaksen, I.S.A., Madronich, S., Middleton, P., Stockwell, W.R., and Walcek, C.J, 1987: A Three-dimensional Eulerian Acid Deposition Model: Physical Concepts and Formulation. *J. Geophys. Res.*, **92**, 14,681-14,700.

Chen, L.-W. A., Doddridge, B. G., Dickerson R. R., Chow, C. C., and Henry, R. C., 2002: Origins of fine Aerosol mass in Baltimore – Washington corridor: implications from observation, factor analysis and ensemble air particle back trajectory. *Atmospheric Environment*, **36**, pp. 4541–4554

Chow, J.C., Watson, J.G., Lowenthal, D.H., Solomon, P.A., Magliano, K.L., Ziman, S.D., and Richards, L.W., 1992: PM10 Source Apportionment in California's San Joaquim Valley. *Atmos. Environ.* **26**, 3335 – 3354.

Christopher Godfrey, 2004: Christopher Godfrey's NCEP Reanalysis Page. Internet Site: *http://weather.ou.edu/~cgodfrey/reanalysis.*

Clarke, A.D., Davis, D., Kapustin, V.N., Eisele, F., Chen, G., Paluch, I., Lenschow, D., Bandy, A.R., Thornton, D., Moore, K., Mauldin, L., Tanner, D., Litchy, M., Carroll, M.A., Collins, J. and Albercook, G., 1998: Particle nucleation in the tropical boundary layer and its coupling to marine sulfur sources. *Science,* **282**, pp. 89 – 92.

Clement, C.F. and Ford, I.J., 1999 a: Gas-to-particle conversion in the atmosphere: I. Evidence from empirical atmospheric aerosols. *Atmos. Environ.* **33**, pp. 475 – 487.

Clement, C.F. and Ford, I.J., 1999 b: Gas-to-particle conversion in the atmosphere: II. Analytical models of nucleation bursts. *Atmos. Environ.* **33**, pp. 489 – 499.

Cullis C. F., and Hirschler, M. M., 1980: Atmospheric Sulfur: Natural and man-made sources. *Atmospheric Environment,* **14**, 1263 – 1278.

Dincer, F., Elbir, T., and Muezzinoglu, A., 2003: Analyzing the impacts of environmental air pollution the air quality in Izmir region using HYSPLIT back trajectory model. *The 6th national symposium on: combustion and air pollution control*, 10 – 12 September, Izmir, Turkey, pp. 161 – 168 (in Turkish).

Dogan G., and Tuncel, G., 2003: Comparison among aerosol concentrations in various regions of Turkey. *The 6th national symposium on: combustion and air pollution control*, 0 – 12 September, Izmir, Turkey (in Turkish).

Donn, W. L., 1975: Meteorology. *McGraw-Hill Book Company*, USA.

Draxler, R. R., 1987: Sensitivity of a trajectory model to the spatial and temporal resolution of the meteorological data during CAPTEX. *Journal of Climate and Applied Meteorology*, **Vol. 26**, No: 11, pp. 1577 – 1588.

Dudhia, J. 1993: A nonhydrostatic version of the Penn State/NCAR mesoscale model: Validation tests and simulation of an Atlantic cyclone and cold front. *Mon. Wea. Rev.*, **121**, 1493-1513.

Dudhia, J., Gill, D., Manning, K., Wang, W., and Bruyere, S., 2004: PSU/NCAR Mesoscale Modeling System Tutorial Class Notes and Users' Guide (MM5 Modeling System Version 3). Internet site: http://www.mmm.ucar.edu/mm5/documents/tutorial-v3-notes.html

Dutton, J. A., 1986: The Ceaseless Wind. An Introduction to the Theory of atmospheric Motion, *Dover,* New York.

EEA, 2002: EMEP/CORINAIR Emission Inventory Guidebook - 3rd edition, Technical report No 30, *European Environment Agency*, Copenhagen K, Denmark

Egger, J., Alpert, P., Tafferner, A., and Ziv, B., 1995: Numerical experiments on the genesis of Sharav cyclones: Idealized simulation. *Tellus*, **47A**, 162 – 174.

Eliassen, A., 1978: The OECD Study of the Long Range transport of Air Pollutants: Long-Range Transport Modeling. *Atmos. Environ.* **12,** pp. 479 – 487.

Eliassen, A., 1980: A Review of Long-Range Transport Modeling. *Journal of Applied Meteorology,* **Vol. 19**, No. 3, pp. 231 – 240.

Eliassen, A., and Saltbones, J., 1975: Decay and Transformation Rates for SO_2 as Estimated from Emission Data, Trajectories and Measured Concentrations. *Atmos. Environ.,* **9**, pp. 425 – 429.

Eliassen, A. and Saltbones, J., 1983: Modelling of long range transport of sulfur over Europe: a two year model run and some model experiments. *Atmos. Environ.* **17**, 1457-1473.

EMEP-WHO, 1997: Workshop on Strategies for Monitoring of Regional Air Pollution in relation to the need within EMEP, GAW and other international bodies. *Aspenäs Herrgård, Lerum, Sweden June 2-4, Kjeller (EMEP/CCCReport).*

ENVIRON, 2004: User's Guide: Comprehensive Air quality Model with extensions (CAMx), **Version 4.10s**, *ENVIRON International Corporation.*

EPA., 1996: Air quality criteria for particulate matter. North Carolina, U.S. *Environmental Protection Agency* (**EPA/600/P-95/001**).

EU, 1996: Ambiant air pollution by particulate matter. *European Commission* Executive Summary.

Finlayson-Pitts, B.J. and Pitts, J.N., 1986: Atmospheric chemistry: fundamentals and experimental techniques. Wiley.

Flocass, A. A., 1988: Frontal depressions over the Mediterranean Sea and Central Southern Europe. *Mediterranêe*, **4**. 43 – 52.

Forrest, J., Garber, R. W., and Newman, L., 1981: Conversion rates in power plant plumes based on filter pack data: The coal-fired Cumberland plume. *Atmospheric Environment*, **15**, 2273 – 2282.

Fournier, N., Dorea, A.J., Vienoa, M., Westonb, K.J., Dragositsa, U., Suttona, M.A., 2004: Modelling the deposition of atmospheric oxidized nitrogen and sulfur to the United Kingdom using a multi-layer long-range transport model. *Atmospheric Environment,* **38**, pp. 683–694.

Friedlander, S. K., 1978: A review of the dynamics of sulfate containing aerosols. *Atmospheric Environment,* **12,** pp. 187 – 195.

Fuchs, N.A., 1964: The mechanisms of aerosols. *Pergamon Press*, Oxford.

Galperin, M., 1991: Routine model for long-range transport calculations of sulfur and nitrogen compounds from continuous sources allowing for non-linear effects. Air Pollution modeling and its Application **VIII**, Edited by H. Van Dop and D.G. Steyn, *Plenum Press*, New York USA

Gery, M.W., Whitten, G.Z., Killus, J.P., and Dodge, M.C., 1989: A Photochemical Kinetics Mechanism for Urban and Regional Scale Computer Modeling. *J. Geophys. Res.*, **94**, 925-956.

Grell, G. A., Dudhia, J., and Stauffer, D. R., 1994: A description of the fifth generation Penn State/NCAR mesoscale model (MM5). *NCAR Technical Note*, NCAR/TN-398+STR, 117 pp.

Grosjean, D., 1992: In Situ-Organic Aerosol Formation during a Smog Episode: Estimated Production and Chemical Functionality. *Atmos. Environ.* **26**, pp. 953 – 963.

Grosjean, D., and Seinfeld, J.H. 1989: Parameterization of the Formation Potential of Secondary Organic Aerosols. *Atmos. Environ.* **23**, 1733 – 1747.

Gullu H.G., Olmez I., and Tuncel G., 2000: Temporal variability of atmospheric trace element concentrations over the Eastern Mediterranean Sea. *Spectrochimica Acta, Part B,* **55,** pp. 1135–1150.

Hamilton, R.S., and Mansfield, T.A., 1993: The Soiling of Materials in the Ambient Atmosphere. *Atmos. Environ.* **27A**, pp. 1369 – 1374.

Hegg, D.A., Hobbs, P.V. and Lyons, J.H., 1985: Field studies of a power plant plume in the arid south-western United States. *Atmos. Environ.* **19**, 1147-1167.

Herut B., Starinsky A., Katz A., and Rosenfeld D., 2000: Relationship between the acidity and chemical composition of rainwater and climatological conditions along a transition zone between large deserts and Mediterranean climate, Israel. *Atmospheric Environment*, Vol. 34, **8**, pp. 1281-1292.

Hidy, G. M., Mueller, P. K., and Tong, E. Y., 1978: Spatial and Temporal Distributions of Airborne Sulfate in Parts of the United States. *Atmos. Environ.,* **12**, pp. 735 – 752.

HMSO, 1962: Weather in the Mediterranean. **Vol. 1**, second edition, *Her Majesty's Stationary Office*, London, UK.

Hoffmann, T., Odum, J.R., Bowman, F., Collins, D., Klockow, D., Flagan, R.C., and Seinfeld, J.H., 1997: Formation of Organic Aerosols from Oxidation of Biogenic Hydrocarbons. *J. Atmos. Chem.* **26**, 189 – 222.

Holton, J. R., 1992: An introduction to dynamical meteorology. *Academic press,* USA.

Houghton, J.T., 1996: Climate Change, 1995: The Science of Climate Change. Contribution of working group I to the second assessment report of the Intergovernmental Panel on Climate Change. *Cambridge University Press,* Cambridge.

Houghton, J.T., Meira Filho, L.G., Bruce, J.P., Lee, H., Callander, B.A., and Haites, E.F., 1995: Climate Change 1994—Radiative Forcing of Climate Change and an Evaluation of the IPCC IS92 Emission Scenarios. *Cambridge University Press,* Cambridge.

Israelevich, P. L., Levin, Z., Joseph, J. H., Ganor, E., 2002: Desert aerosol transport in the Mediterranean region as inferred from the TOMS aerosol index. *J. Geophys. Res.*, **107(D21)**, 4572, doi: 10.1029/2001JD002011.

Kallos, G., Astitha, M., Gofa, F., O'Connor, M., Mihalopoulos, N., and Zlatev, Z., 2004: "Transport and Deposition Patterns of Ozone and Aerosols in the Mediterranean Region". *27th NATO/CCMS International Technical Meeting on Air Pollution Modeling and its Applications*, October 2004, Banff, Canada.

Kallos, G., Astitha, M., 2005: Personal Contact.

Karalis, J. D., 1969: Weather Types of Greece. *University of Athens*: Doctoral Thesis.

Kassomenos, P., Flocas, H. A., Lykoudis, S., and Petrakis, M., 1998: Analysis of mesoscale patterns in relation to synoptic conditions over an urban Mediterranean basin. *Theor. Appl. Climato.*, **59**, 215 – 229.

Katsoulis, B. D., 1982: Climatic and synoptic considerations of the Mediterranean depressions developing and passing over or near the Balkan Peninsula. Athens: *Proceed. 1st Hell-British Climatic Congress (Sept. 1980)*, pp. 73 – 84.

Katsoulis, B. D., Makrogiannis, T. J., Goutsidou, Y. A., 1998: Monthly anticyclonicity in southern Europe and the Mediterranean region. *Theor. Appl. Climatol.*, **59**, 51 – 59.

Kindap, T., Unal, A., Chen, S.H., Hu, Y., Odman, M.T., and Karaca M., 2005: Long Range Aerosol Transport from Europe to Istanbul, Turkey. *Atmospheric Environment,* Submitted.

Klee, A.J., 1984: Source Control-Municipal Solid Waste Iincinerators. In: *Handbook of Airpollution Technology.* Ed. by S. Calvert, H.M. Englund. New York, Wiley. pp. 513 – 550.

Kocak, M., Nimmo, M., Kubilay, N., and Herut, B., 2004a: Spatio-temporal Aerosol trace metal concentrations and sources in Levantine basin of the Eastern Mediterranean. *Atmospheric Environment,* **Vol. 38,** pp, 2133 – 2144.

Kocak, M., Kubilay, N., and Mihalopoulos, N., 2004b: Ionic composition of lower tropospheric aerosol at a Northern Mediterranean site: Implications regarding sources and long-range transport. *Atmospheric Environment*, **Vol. 38,** pp, 2067 – 2077.

Kouvarakis, G., Tsigaridis, K., Kanakidou, M., and Mihalopoulos, N., 2000: Temporal Variation of Surface Regional Background Ozone over Crete Island in the Southeast Mediterranean. *J. Geophys. Res.* **Vol. 105**, No. D4. pp. 4399 – 4407.

Kubilay N., Nickovic S., Moulin C., and Dulac F., 2000: An illustration of the transport and deposition of mineral dust onto the eastern Mediterranean. *Atmospheric Environment,* **Vol. 34,** 8 , pp, 1293-1303.

Kubilay, N., Koçak, M., and Mihalopoulos N., 2002: Chemical composition of aerosols in the atmospheric boundary layer of the Eastern Mediterranean: *Implications regarding sources and transport.* Bi-National Israeli-Turkish **workshop on: Atmospheric deposition of aerosols and gases in the** *Eastern Mediterranean*, Golden Tulip Hotel, Dead Sea, Israel.

Kulmala, M., Kerminen, V.M. and Laaksonen, A., 1995: Simulations on the effect of sulfuric acid formation on atmospheric aerosol concentrations. *Atmos. Environ.* **29**, pp. 377 – 382.

Kumar, N., Lurmann, F.W., Wexler, A.S., Pandis, S., and Seinfeld, J.H., 1996: Development and Application of a Three Dimensional Aerosol Model. *Presented at the A&WMA Specialty Conference on Computing in Environmental Resource Management*, Research Triangle Park, NC, December 2-4.

Lazaridis, M., and Drossinos, Y.,: 1997: Energy fluctuations in steady state binary nucleation. *J. Phys. A – Math. Gen.*, **A30**, 3847 – 3865.

Lazaridis, M., Drossinos, Y. and Georgopoulos, P.G., 1998: Turbulent resuspension of small nondeformable particles. *J. Colloid Interface Sci.* **204**, pp. 24-32.

Lazaridis, M. and Melas, D., 1998: New sulfate particle formation during summer pollution episodes using a 3-D aerosol model. *J. Aerosol Sci.* **29**, 913 – 928.

Lazaridis, M., Semb, A., and Hov, Ø., 1999: Long-Range Transport of Aerosol Particles: A Literature Review, *EMEP/CCC-Report 8/99, O-98134.*

Legge, A. H., and Krupa, S. V., 1990: Acidic Deposition: Sulfur and nitrogen oxides. *Lewis Publishers, INC*, Chelsea, Michigan, USA.

Louis, J.F., 1979: A Parametric Model of Vertical Eddy Fluxes in the Atmosphere. *Bound. Lay. Meteor.* **17**, 187-202.

Lupu, A., and Maenhaut, W., 2002: Application and comparison of two statistical trajectory techniques for identification of source region of atmospheric aerosol species. *Atmospheric Environment*, **36**, pp. 5607 – 5618.

Luria, M., Peleg, M., Vanger, A., Matveiv, V., Dayan, U., Kallos, G., and Alper, D.S. T., 2002: Transport of particulate sulfate to the East *Mediterranean region.* Bi-National Israeli-Turkish workshop on: *Atmospheric deposition of aerosols and gases in the Eastern Mediterranean*, Golden Tulip Hotel, Dead Sea, Israel.

Lurmann, F.W., Wexler, A.S., Pandis, S.N., Mussara, S., Kumar, N. and Seinfeld, J.H., 1997: Modelling urban and regional aerosols-II. Application to California's South Coast Air Basin. *Atmos. Environ.* **31**, pp. 2695 – 2715.

Madronich, S., 1993: UV radiation in the natural and perturbed atmosphere, in Environmental Effects of UV (Ultraviolet) Radiation. *(M. Tevini, ed.), Lewis Publisher*, Boca Raton, pp. 17-69.

Madronich, S., 2002: The Tropospheric Visible Ultra-violet (TUV) model web page. *National Center for Atmospheric Research, Boulder, CO.,* http://www.acd.ucar.edu/TUV/.

Maheras, P., Flocas, H.A., Patrikas, I., and Anagnostopoulou, C., 2001: A 40 year objective climatology of surface cyclones in the Mediterranean region: spatial and temporal distribution. *Int. J. Climatol.*, **21**, 109 – 130.

Makrogiannis, T. J., 1974: Weather Types and Atmospheric Pressure in Thessaloniki. University of Thessaloniki: *Science Annals, Faculty of Physics and Mathematics*, **V. 14**, 237 - 242.

Makrogiannis, T. J., Bloutsos, A. A., Sahsamanoglou, H. S., 1989: Moving anticyclones across the Alps and Balkan Peninsula. *Opatija: Zbornik, 10; XVIII. International Conference for Alpine Meteorology (September 1984)*, 192 - 194.

Mason, B.J., 1971: The physics of clouds. 2. ed., Clarendon Press, Oxford.

Miller, M. J., 1974: On the use of pressure as vertical coordinate in modeling conversion. *Quart. J. Roy. Meteor. Soc.*, **100**, 155 – 162.

MINOS, 2002: Smog over the Mediterranean. *Max Planck Society, News Release*, October 25th 2002.

NCEP/NCAR Reanalysis Project, 2004: Reanalysis data averaged for the years, 1948 - 2004, Internet site: *http://www.cdc.noaa.gov/cdc/reanalysis/.*

Nenes, A, Pilinis, C., and Pandis, S.N., 1998: "ISORROPIA: A New Thermodynamic Model for Multiphase Multicomponent Inorganic Aerosols." *Aquatic Geochemistry*, **4**, 123 - 152.

Nenes, A, Pilinis, C., and Pandis, S.N., 1999: "Continued Development and Testing of A New Thermodynamic Aerosol Module for Urban and Regional Air Quality Models." *Atmos. Environ.*, **33**, 1553-1560.

Nordlund, G. G., 1975: A Quasi-Lagrangian Cell Method for Calculating Long-Distance Transport of Atmospheric Pollution. *J. Appl. Meteor.*, **14**, pp. 1095 – 1104.

Novakov, T., Chang, S. C., and Harker, A. B., 1974: Sulfates as Pollution Particulates: Catalytic on Carbon (soot) Particles. *Science*, **186**, p. 259.

Ottar, B, 1978: An Assesment of the OECD Study on Long-Range transport of Air Pollutants (LRTAP). *Atmos. Environ.*, **12**, pp. 445 – 454.

Ozsoy T., and Saydam A. C., 2000: Acidic and alkaline precipitation in the Cilician Basin, north-eastern Mediterranean Sea. *The Science of the Total Environment,* Vol. 253, **1-3**, pp. 93-109.

Ozturk, F., Soultanov, L., and Tuncel, G., 2003: Determination of the observed high sulfate concentrations in the Eastern Mediterranean Region. *The 6th national symposium on combustion and air pollution control*, 10 – 12 September Izmir, Turkey. pp. 298 – 309 (in Turkish).

Pacyna, J.M., Larssen, S. and Semb, S., 1991: European survey for NOx emissions with emphasis on Eastern Europe. *Atmos. Environ.* **25A**, 425-439.

Park, S.-U., and Lee, E.-H., 2003: Long-range transport contribution to dry deposition of acid pollutants in South Korea. *Atmospheric Environment,* **37**, pp. 3967–3980.

Pelley, J., 1998: Is Coastal Eutrophication out of Control ? *Environ. Sci. Techn.* **32**, 462A-466A.

Pettersson, S., 1956: Weather analysis and forecasting. *McGraw-Hill Book Company*, USA.

Pettersson, S., 1969: Introduction to meteorology. *McGraw-Hill Book Company*, USA.

Pielke, R. A., 2002: Mesoscale Meteorological Modeling. *Academic Press*, Clifornia, USA.

Pilinis, C., and Seinfeld, J.H., 1987: Continued Development of a General Equilibrium Model for Inorganic Multicomponent Atmospheric Aerosols. *Atmos. Environ.* **32**, 2453 – 2466.

Rau, J.A., 1989: Composition and Size Distribution of Residential Wood Smoke Particles. *Aerosol Sci. Technol.* **10**, 181 – 192.

Richards, L. W., Anderson, J. A., Blumenthal, D. L., Brandt, A. A., MacDonald, J. A., Watus, N., Macias, E. S., and Bhardwaja, P. S., 1981: The chemistry, aerosol physics and optical properties of western coal-fired power plant plume. *Atmospheric Environment*, **15**, 2111 – 2134.

Rolph, G. D., and Draxler, R. R., 1990: Sensevity of Three Dimensional Trajectories to the Spatial and Temporal Densities of the Wind Field. *J. Appl. Metorol.,* **59**, pp. 1043 – 1054.

Sciare, J., Bardouki, H., Moulin, C., and Mihalopoulos, N, 2002: Aerosol Sources and their Contribution to the Chemical Composition of Aerosols in the Eastern editerranean Sea during Summertime. *Atmos. Chem. Discuss.*, **2**, pp. 1287 – 1315.

Scott, B.C., 1978: Parameterization of sulfate removal by precipitation. *J. Appl. Meteor.,* **17**, 1375-1389.

Sehmel, G.A. 1980: Particle and Gas Deposition, a Review. *Atmos. Environ.,* **14**, 983 – 1011.

Seigneur, C., Pai, P., Hopke, P. and Grosjean, D., 1999: Modeling atmospheric particulate matter. *Environ. Sci. Technol.* **February 1**, 80A-86A.

Seinfeld, J. H., and Pandis, S.N., 1998: Atmospheric Chemistry and Physics: from air pollution to climate change. *A wiley –Interscience Publication, John Wiley & Sons, INC*, New York, USA.

Shaka' H., and Saliba N. A., 2004: Concentration measurements and chemical composition of PM10-2.5 and PM2.5 at a coastal site in Beirut, Lebanon. *J. of Atmos. Env.*, Vol. 38, February 2004, pp. 523-531.

Shir, C. C., and Shieh, L. J., 1974: A Generalized Urban Air Pollution Model and its Application to the Study of SO_2 Distribution in the St. Louis Metropolitan Area. *J. Appl. Meteor.,* **13**, pp. 185 – 204.

Simpson, D., 1995: Hydrocarbon Reactivity and Ozone Formation in Europe. *J. Atmos. Chem.* **20**, 163-177.

Sioutas, C. and Koutrakis, P., 1996: Methods for Measuring Atmospheric Acidic Particles and Gases. *Ed. by T. Kouimtzis and C. Samara. Springer*, pp. 201 – 231.

Slinn, S.A., and Slinn, W.G.N., 1980: Predictions for particle deposition on natural waters. *Atmos. Environ.*, **24**, 1013-1016.

Spengler, J.D., Keeler, G.J., Koutrakis, P., Ryan, P.B., Raizenne, M. and Franklin, C.A., 1989: Exposures to Acidic Aerosols. *Environ. Health Perspect.* **79**, 43-51.

Stohl, A., 1998: Computation, Accuracy and Applications of Trajectories – A Review and Bibliography. *Atmospheric Environment,* **Vol. 32,** No. 6, pp. 749 – 766.

Stohl. A., Haimberger, L., Scheele, M. P., and Wernli, H., 2001: An Intercomparison of Results from Three Trajectory Models. *Meteorol. Appl.* **8**, pp.127–135.

Strader, R., Lurmann, F., and Pandis, S.N., 1999: Evaluation of secondary organic aerosol formation in winter. *Atmos. Environ.,* **33**, 4849-4863.

Syrakov, D., and Prodanova, M., 2002: Transboundary exchange of sulfur pollution in region southeastern Europe. Air Pollution and its Application **XV**, Edited by Borrego and Schayes, *Kluwer Academic / Plenum Publissers*, New York, USA.

Tanaka, P.L., Allen, D.T., McDonald-Buller, E.C., Chang, S., Kimura, Y., Mullins, C.B., Yarwood, G., Neece, J.D., 2000: Development of a chlorine mechanism for use in the carbon bond IV chemistry model. *Journal of Geophysical Research*, **Vol. 108(D4)**, 4145.

Tarrason, L. and Tsyro, S., 1998: Long-range transport of fine secondary particles, as presently estimated by the EMEP Lagrangian model. Oslo, DNMI *(EMEP/MSC-W Note 2/98) (Research report/Norwegian Meteorological Institute* No. **69**).

Topcu, S., Incecik, S., and Atimtay, A. T., 2002: Chemical composition of rain water at EMEP station in Ankara, Turkey. *Atmospheric Research*, **65**, pp. 77 – 92.

Topcu, S., Anteplioglu, U., and Incecik, S., 2003: Surface ozone concentrations and its relation to wind field in Istanbul. *Water, Air, & Soil Pollution: Focus*, **Vol, 3**, Nos. 5 – 6, pp. 53 – 64.

Trigo, I. F., Davies, T. D., and Bigg, G. R., 1999: Objective climatology of cyclones in the Mediterranean region. *Journal of Climate*, **Vol. 12**, 1685 – 1696.

Tuazon, E.C., Atkinson, R., Plum, C.N., Winer, A.M., and Pitts, J.N. Jr., 1983: The Reaction of Gas Phase N_2O_5 with Water Vapor. *Geophys. Res. Lett.* **10**, 953 – 956.

Tuncel, G., *2002:* Wet and dry deposition of natural and anthropogenic aerosol components to the Eastern Mediterranean. *Bi-National Israeli-Turkish workshop on: Atmospheric deposition of aerosols and gases in the Eastern Mediterranean,* Golden Tulip Hotel, Dead Sea, Israel.

Tuncel, G., 2004: Sulfate concentration data in Antalya during the years 1992 – 2000, Personal communication.

Tuncel, G., 2005: Personal Communication.

Tuncel, S. G., and Erduran, M. S., 2001: Characteristics of air pollutant in the Eastern Mediterranean coast. *The 2nd international symposium on: Air quality management at: urban, regional and global scales*. Istanbul, Turkey.

Tuncel S. G., and Ungor, S., 1996: Rain water chemistry in Ankara – Turkey. *Atmos. Environ.*, **30**, pp. 2721 – 2738.

USGS, 2005: United States Geographical Survey Homepage. *http://www.usgs.gov/*

Vestreng, V., 2001: Emission data reported to UNECE/EMEP: Evaluation of the Spatial Distribution of Emissions. *Norwegian Meteorological Institute*, Rersearch Note **No. 56**, EMEP/MSC-W Status Report.

Wallen, C. C., 1977: Climates of Central and Southern Europe. In: *World Survey climatology*, **V. 6**, Amsterdam, *Elsevier*, 247 pp.

Wesely, M.L., 1989: Parameterization of Surface Resistances to Gaseous Dry Deposition in Regional-Scale Numerical Models. *Atmos. Environ.*, **23**, 1293-1304.

Whitby, K.T., 1978: The physical characteristics of sulfur aerosols. *Atmos. Environ.* **12**, pp. 135 – 159.

Whitten, G., Deuel, H.P., Burton, C.S., and Haney, J.L., 1996: Memorandum to OTAG Participants "Overview of the Implementation of an Updated Isoprene Chemistry Mechanism in CB4/UAM-V." (Revised Memorandum, July 22).

Williams, M.M.R., and Loyalka, S.K., 1991: Aerosol science: theory and practice: *With special applications to the nuclear industry.* Pergamon Press, Oxford.

Xue, M., and Thorpe, A. J., 1991: A mesoscale numerical model using the nonhydrostatic pressure-based sigma-coordinate equations: Model experiment with dry mountain flows. *Mon. Wea. Rev.*, **Vol. 119**, pp. 1168 – 1185.

Yarwood, G., Morris, R. E., and Wilson, G. M., 2004: Particulate Matter Source Apportionment Technology (PSAT) in CAMx Photochemical Grid *Model. Environ International Corporation*, 101 Rowland Way, suite 220, Novato, CA. Internet site: http://www.camx.com/publ/pdfs/Yarwood_ITM_paper.pdf

Zannetti, P., 1990: Air pollution modeling: theories, computational methods and available software. *Van Nostrand Reinhold*, New York. USA.

Zerefos C. S., Kourtidis K. A., Balis D., and Calpini B., 2001: Photochemical activity over the eastern Mediterranean under variable environmental conditions – Physics and Chemistry of the Earth, Part C: *Solar, Terrestrial & Planetary Science* Vol., 26, 7 , 2001, pp, 549-554.

APPENDICES

APPENDIX A

TABLES

Table A.1: The largest 100 sulfur emitters in Europe (Barrett and Protheroe, 1995).

No	Site Name	Country	Lat.	Lon.	Elev.	type	Cap. MWe	Emis. ktS
1	Maritsa East	Bulgaria	42	24	903	PS	2060	350
2	Afsin-Elbistan	Turkey	38	37	1222	PS	1376	288
3	Puentes (As	Spain	43	-4	1130	PS	1400	271
4	Montsegorsk	Russia	67	32	128	Sm		212
5	Nikel	Russia	52	59	305	Sm		211
6	Teruel	Spain	40	-1	995	PS	1050	183
7	Belchatow	Poland	51	19	208	PS	4320	168
8	Janschwalde	Germany	51	14	65	PS	3000	157
9	Boxberg	Germany	51	7	359	PS	3520	149
10	Prunerov	Czech Rep.	50	13	334	PS	1490	137
11	Drax	UK	53	00	4	PS	3960	132
12	Cottam	UK	53	00	19	PS	2018	98
13	Tusimice	Czech Rep.	50	13	264	PS	1130	98
14	Krivorozhskaya	Ukraine	48	38	188	PS	3000	95
15	Burshtynskaya	Ukraine	49	24	211	PS	2400	92
16	Ratcliffe- On- Soar	UK	52	-1	66	PS	2008	90
17	Meirama	Spain	43	-8	428	PS	550	90
18	Yenikoy (Yentes)	Turkey	37	28	706	PS	420	89
19	Ferrybridge	United	53	-1	33	PS	2000	86
20	West Burton	United	54	-1	370	PS	2000	85
21	Fiddler's Ferry	UK				PS	2000	80
22	Novocherkasskaya	Russia	51	58	341	PS	2400	80
23	Lodyzhinskaya	Ukraine	48	29	202	PS	1800	80
24	Isalnita	Romania	44	23	105	PS	985	79
25	Zapoljarnyj	Russia	57	33	284	Sm		79
26	Nikola tesla	Yugoslavia	43	21	326	PS	2890	78
27	Ryazanskaya	Russia	54	39	152	PS	1200	76
28	Megalopolis	Greece	37	22	425	PS	300	76
29	Eggborough	UK				PS	1800	73
30	Irini	Greece	41	22	223	PS	550	72
31	Turow	Poland	51	18	196	PS	2000	72
32	Seyitomer	Turkey	39	29	1147	PS	600	72
33	Zmiyevskaya	Ukraine	49	36	102	PS	2400	70
34	Kurakhovskaya	Ukraine	48	37	110	PS	1470	69

Table A.1: Continued

35	Yatagan	Turkey	37	28	488	PS	630	68
36	Lukomyl	Russia	57	30	56	PS	2400	68
37	Thierbach	Germany	50	11	566	PS	840	65
38	Kashiri	Russia	53	59	413	PS	2070	64
39	Pocerady	Czech Rep.	50	13	215	PS	1200	63
40	Lippendorf(Bohlen)	Germany	51	12	133	PS	600	63
41	Matra	Hungary	47	19	756	PS	800	60
42	Blyth	UK	55	-1	1	PS	660	60
43	Starobeshevo	Ukraine	47	38	117	PS	2000	58
44	Pridneprovskaya	Ukraine	48	35	45	PS	1800	57
45	Brindisi Sud	Italy	40	17	16	PS	2640	57
46	Kangal	Turkey	39	37	1521	PS	300	56
47	Zuevskaya	Ukraine	50	33	116	PS	1200	55
48	Adamow	Poland	51	20	160	PS	600	55
49	Kosovo	Yugoslavia	42	21	653	PS	2618	54
50	Hagenwerder	Germany	51	14	204	PS	1200	54
51	Cherepetskaya	Russia	54	36	164	PS	1500	53
52	Kremikovtsi	Bulgaria	42	23	657	Pl		53
53	Didcot	UK	51	-1	74	PS	2000	51
54	Chemnitz	Germany	50	12	297	PS	255	51
55	Ludus	Romania	46	24	322	PS	800	51
56	Porcheville	France	48	1	20	PS	2340	50
57	Slavyanskaya	Ukraine	48	37	52	PS	2100	49
58	Moldavia	Moldava	47	27	140	PS	2520	47
59	Fortuna	Germany				PS	801	47
60	Bitola	Macedonia	41	21	577	PS	630	46
61	Luganskaya	Ukraine	48	39	133	PS	1600	44
62	Melnik	Czech Rep.	50	13	686	PS	1276	44
63	Turceni	Romania	44	23	122	PS	2310	43
64	Mintia	Romania	45	22	216	PS	1260	43
65	Soma	Turkey	39	27	162	PS	990	43
66	Tisova	Czech Rep.	50	12	715	PS	322	43
67	Milazzo	Italy	38	15	33	Ref		43
68	Bobovdol	Bulgaria	42	23	694	PS	630	43
69	Uglegorskaya	Ukraine	48	38	289	PS	1200	42
70	Sostanj	Slovenia	46	15	374	PS	1389	42

Table A.1: Continued

71	Compostilla	Spain	41	-8	552	PS	1312	42
72	Tripolskaya	Ukraine	50	30	120	PS	1200	41
73	Gerstein	Germany	52	7	26	PS	1698	41
74	Lubbenau	Germany	51	13	49	PS	900	41
75	Belovskaya	Russia	60	39	135	PS	1200	41
76	Zaporozhye	Ukraine	47	36	244	PS	1200	41
77	Kirishi	Russia	54	60	400	PS	2070	40
78	High Marnham	UK				PS	1000	39
79	Espenhaim	Germany	51	12	164	PS	310	39
80	Rosanno	Italy	45	9	87	PS	1280	38
81	Oradea	Romania	47	21	145	PS	380	38
82	Vetschau	Germany	50	6	181	PS	1200	38
83	Varna	Bulgaria	43	27	80	PS	1260	38
84	Balti	Estonia	59	24	28	PS	1435	37
85	Ironbridge	UK	52	-2	81	PS	988	37
86	Tuzla	Yugoslavia	44	18	231	PS	779	37
87	Sines	Portugal	37	-8	0	PS	1256	36
88	Rovinari	Romania	44	23	183	PS	1720	35
89	Schwarze Pumpe	Germany	51	14	115	PS	1275	35
90	Moneypoint	Ireland	53	-6	150	PS	915	34
91	Kingsnorth	UK	51	0	37	PS	2000	34
92	MZRP Plock	Poland	52	19	95	Ref		34
93	Drmno	Yugoslavia	44	21	72	PS	700	33
94	Kozienice	Poland	51	21	122	PS	2600	33
95	Chemopetrol	Czech Rep.	50	13	214	Pro		33
96	Rybnik	Poland	50	18	232	PS	1600	33
97	Ostiglia	Italy	45	11	6	PS	1220	32
98	La Casella	Italy	39	16	9	PS	1200	32
99	Sermide	Italy	45	11	9	PS	1200	32
100	Thorpe Marsh	UK	52	0	56	PS	1000	31

Table A.2: USGS 30 second landuse categories (USGS, 2005).

Land Cover ID	Description
0	Ocean
1	Urban and Built-Up Land
2	Dryland Cropland and Pasture
3	Irrigated Cropland and Pasture
4	Mixed Dryland/Irrigated Cropland and Pasture
5	Cropland/Grassland Mosaic
6	Cropland/Woodland Mosaic
7	Grassland
8	Shrubland
9	Mixed Shrubland/Grassland
10	Savanna
11	Deciduous Broadleaf Forest
12	Deciduous Needleleaf Forest
13	Evergreen Broadleaf Forest
14	Evergreen Needleleaf Forest
15	Mixed Forest
16	Water Bodies
17	Herbaceous Wetland
18	Wooded Wetland
19	Barren or Sparsely Vegetated
20	Herbaceous Tundra
21	Wooded Tundra
22	Mixed Tundra
23	Bare Ground Tundra
24	Snow or Ice

Table A.3: CAMx landuse categories and default surface roughness values (m) assigned to each category within CAMx. (ENVIRON, 2004)

Category ID	Land Cover Category	Surface Roughness (m)	UV Albedo
1	Urban	3.00	0.08
2	Agriculture	0.25	0.05
3	Rangeland	0.05	0.05
4	Deciduous forest	1.00	0.05
5	Coniferous forest including wetland	1.00	0.05
6	Mixed forest	1.00	0.05
7	Water	0.0001	0.04
8	Barren land	0.002	0.08
9	Non-forested wetland	0.15	0.05
10	Mixed agricultural and range	0.10	0.05
11	Rocky (with low shrubs)	0.10	0.05

APPENDIX B

FIGURES

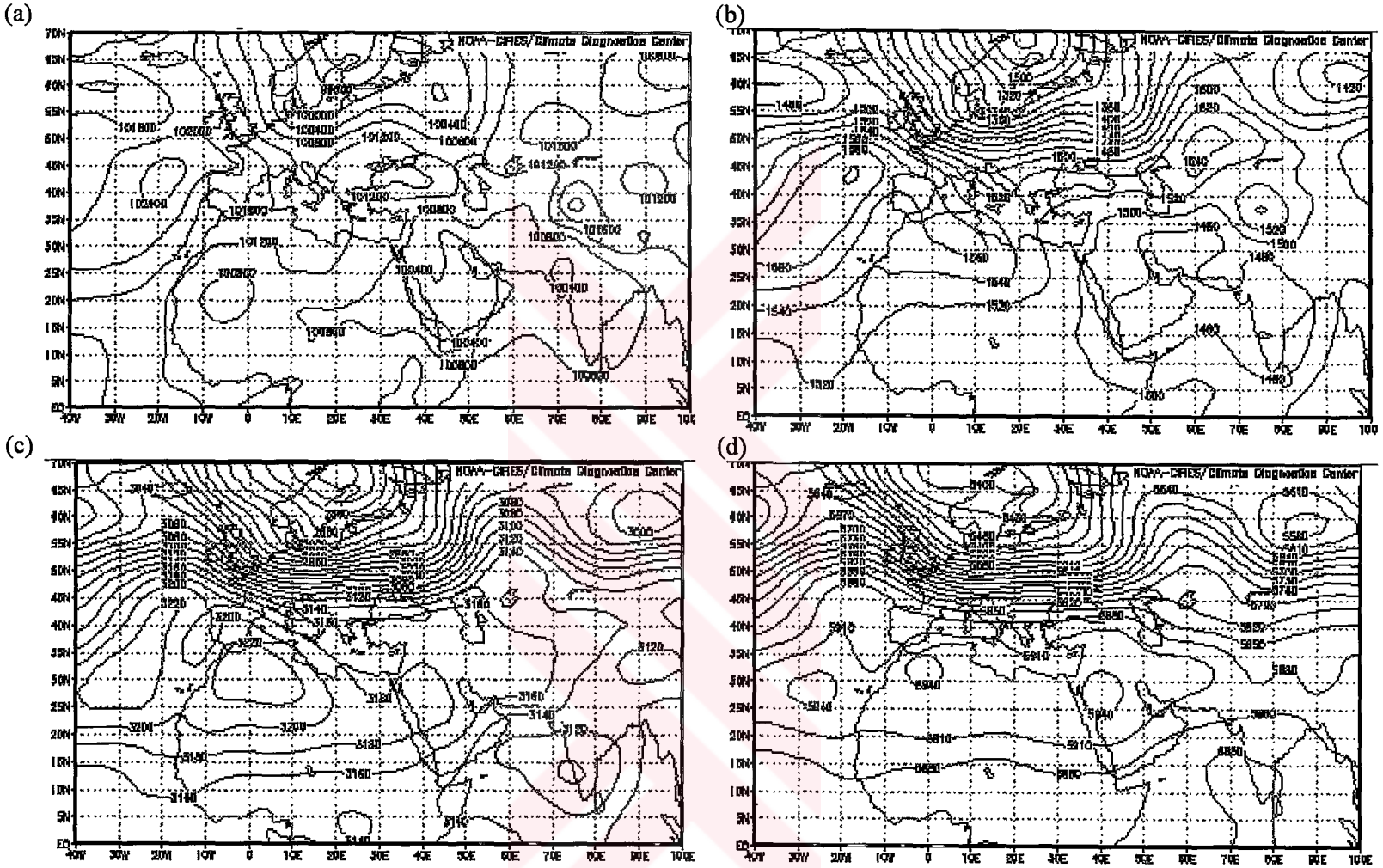

Figure B.1: Synoptic and climatologic situation on 24 August 1998, two days before the episode: a) Daily average Mean Sea Level Pressure in Pascal ($(P_{00}+P06+P_{12}+P_{18})/4$), b), c) and d) show the mean daily geopotantial height (gpm) on 850, 700 and 500 hpa pressure levels respectively (NCEP/NCAR Reanalysis Project, 2004).

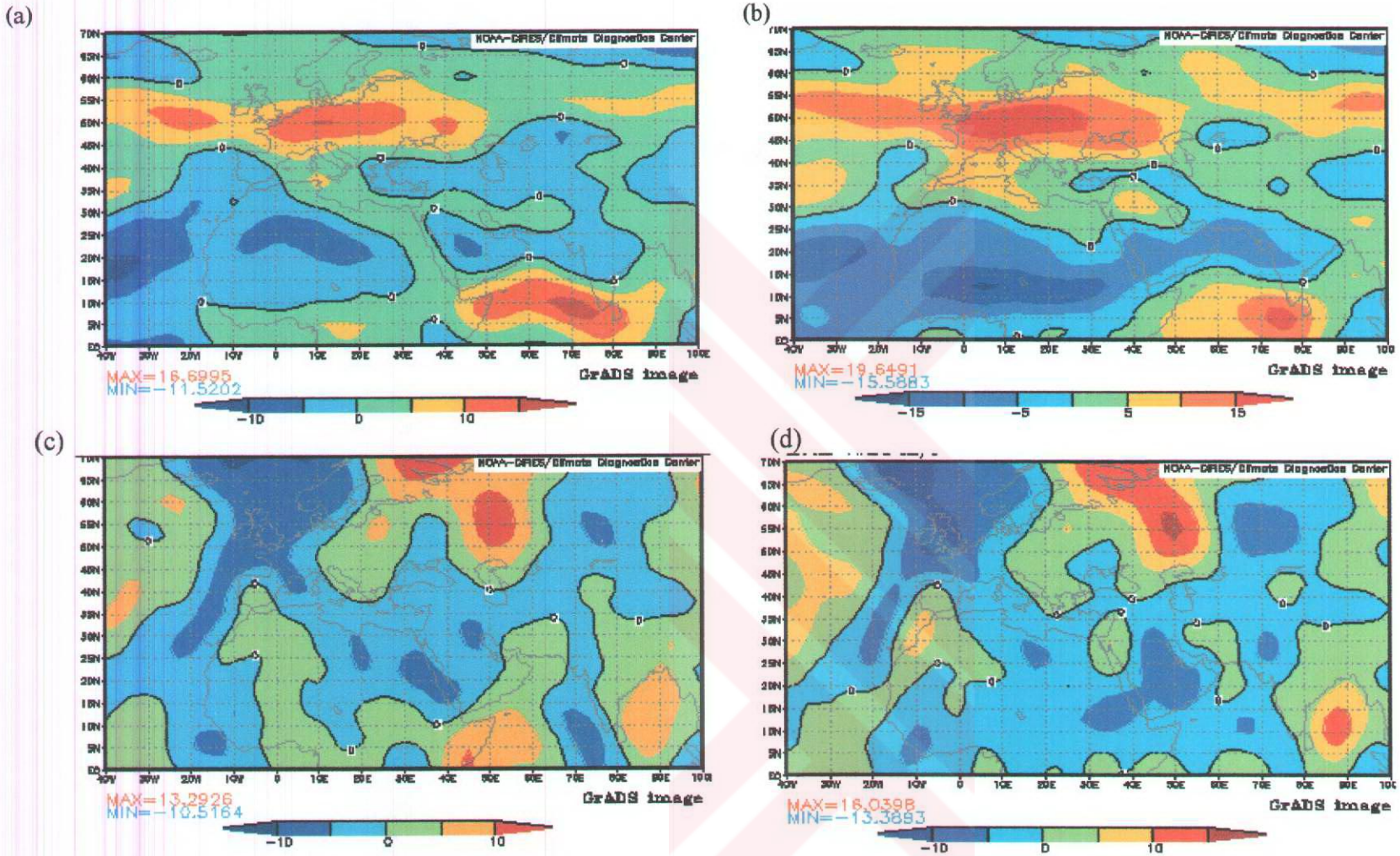

Figure B.2: Daily mean U and V wind components (m/s) on 24 August 1998, two days before the episode: a) and b) represent the U component at the 850 and 700 hPa pressure levels respectively, while c) and d) represent the V component at the same levels (NCEP/NCAR Reanalysis Project, 2004).

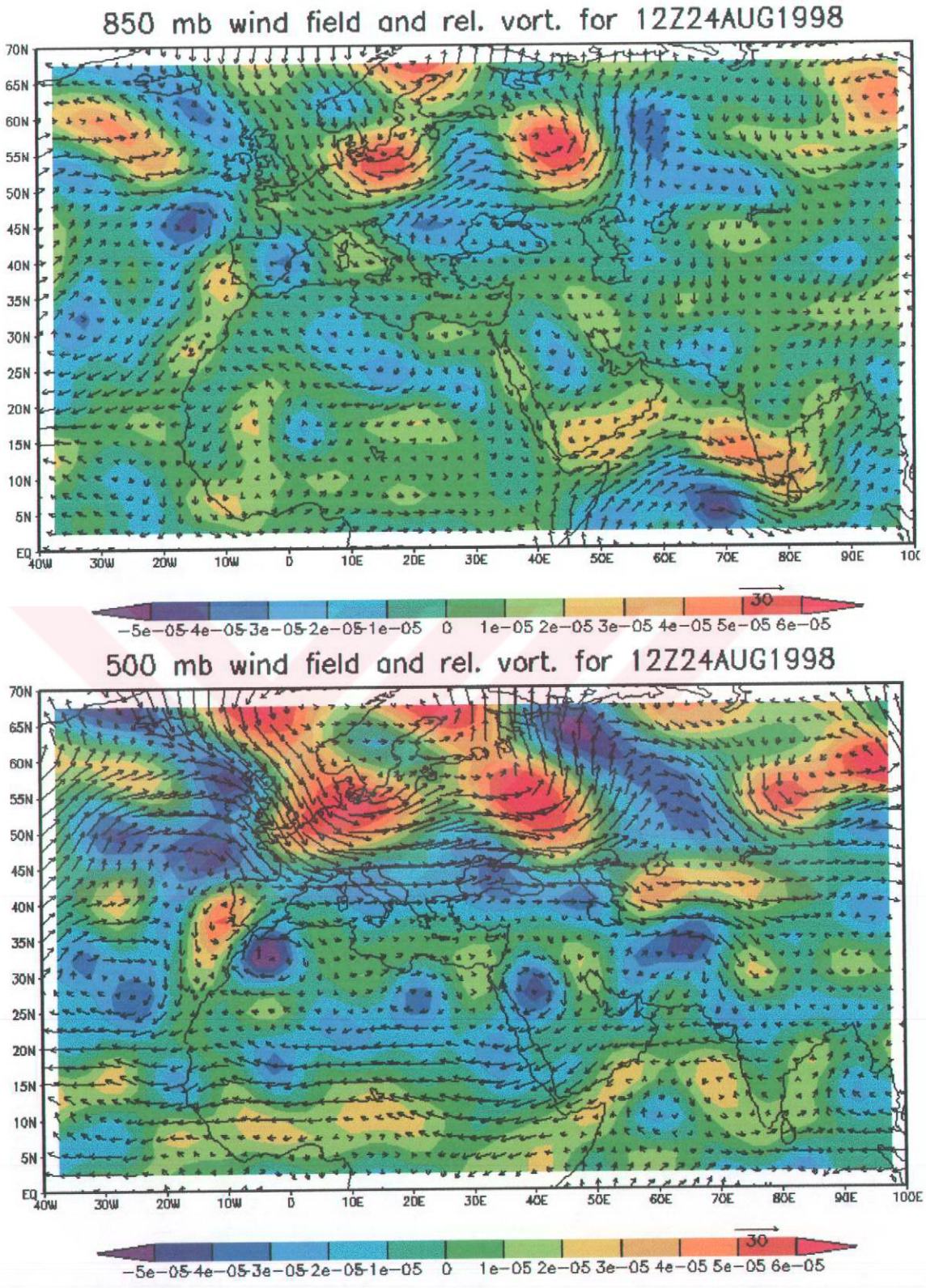

Figure B.3: The wind vector (m/s) and relative vorticity (s^{-1}) on 24 August 1998, two days before the episode, at the 850 hPa pressure level (upper graph) and the 500 hPa pressure level (lower graph) respectively (Christopher Godfrey, 2004).

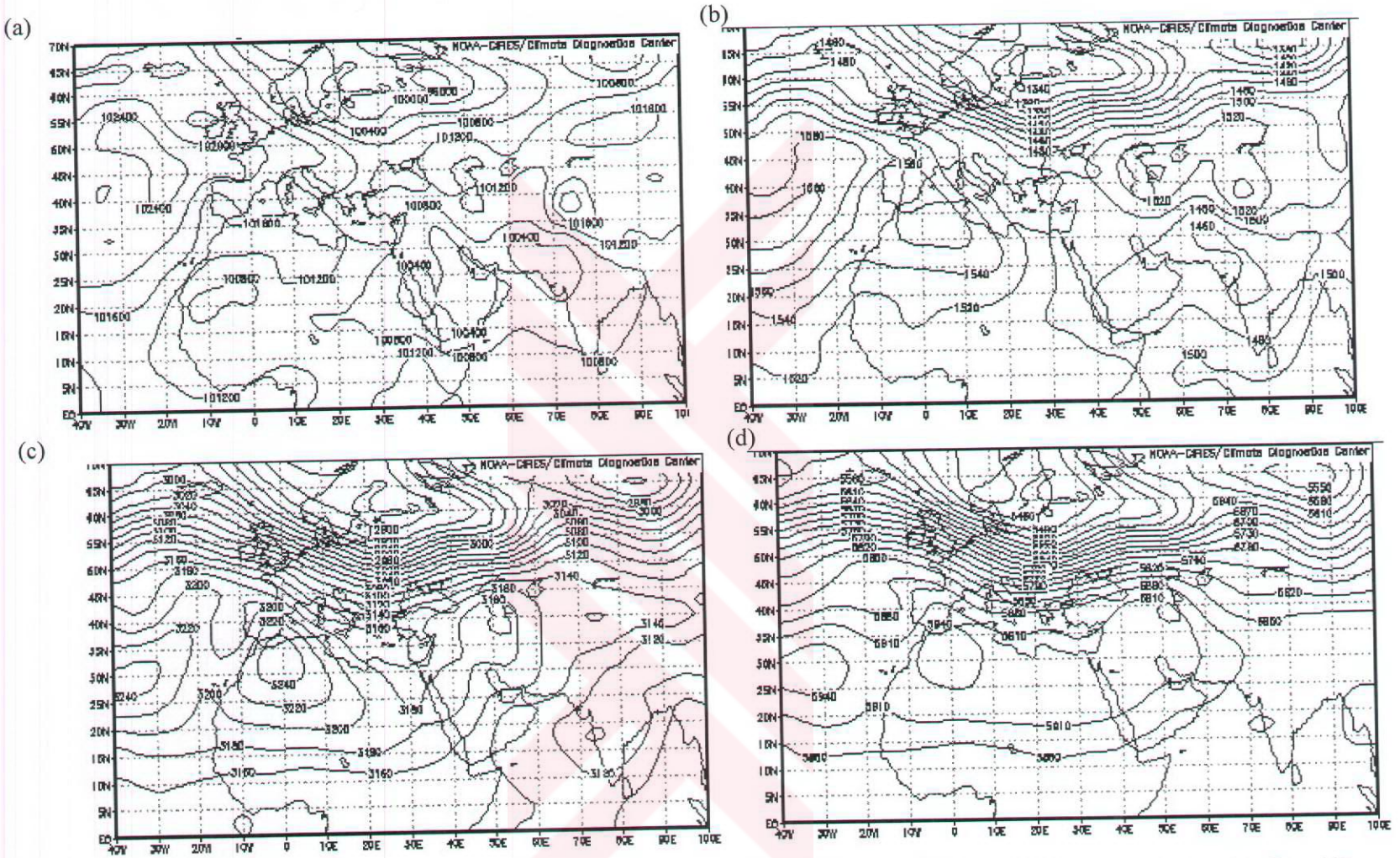

Figure B.4: Synoptic and climatologic situation on 25 August 1998, one day before the episode: a) Daily average Mean Sea Level Pressure in Pascal ($(P_{00}+P06+P_{12}+P_{18})/4$), b), c) and d) show the mean daily geopotantial height (gpm) on 850, 700 and 500 hpa pressure levels respectively (NCEP/NCAR Reanalysis Project, 2004).

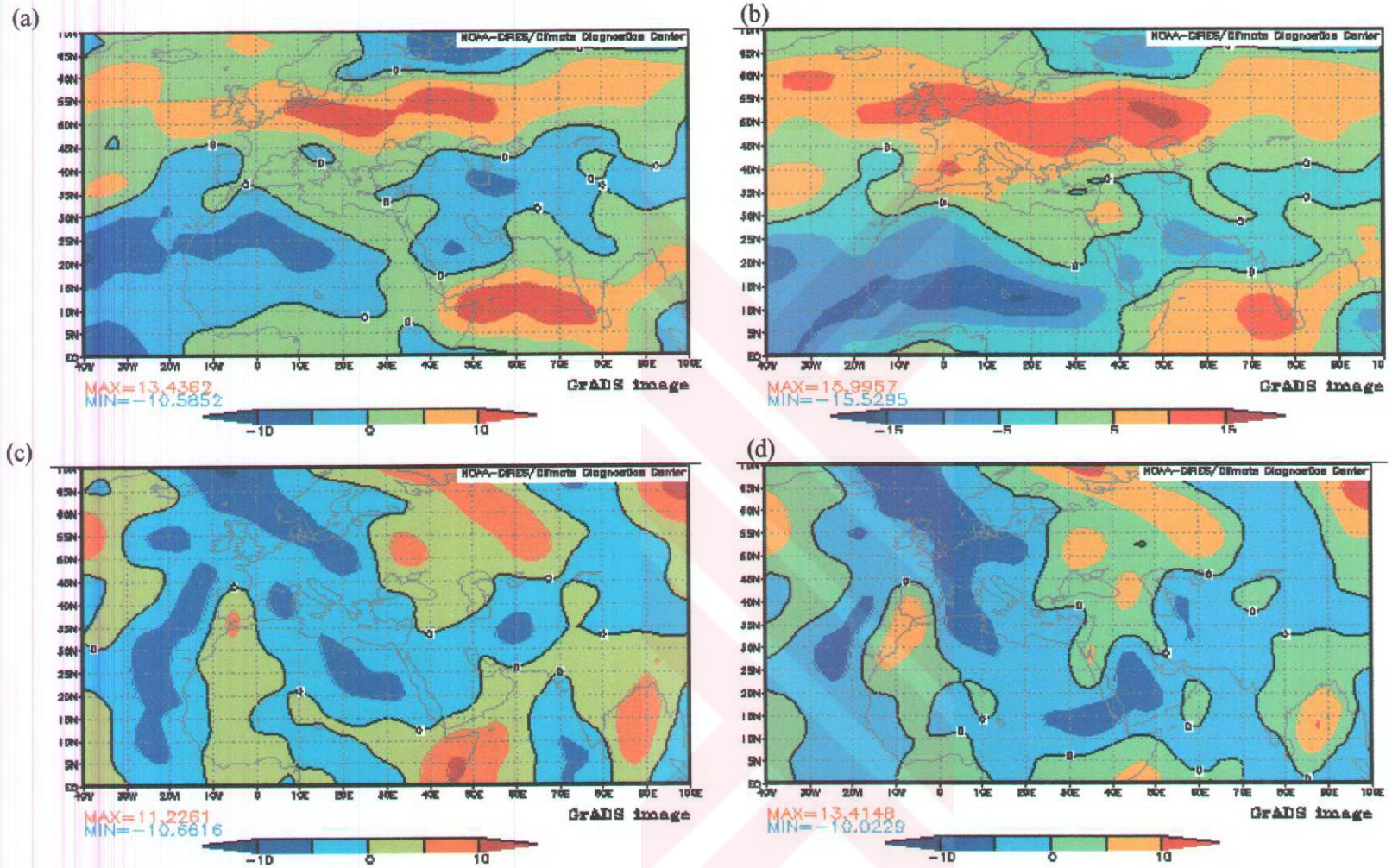

Figure B.5: Daily mean U and V wind components (m/s) on 25 August 1998, one day before the episode: a) and b) represent the U component at the 850 and 700 hPa pressure levels respectively, while c) and d) represent the V component at the same levels (NCEP/NCAR Reanalysis Project, 2004).

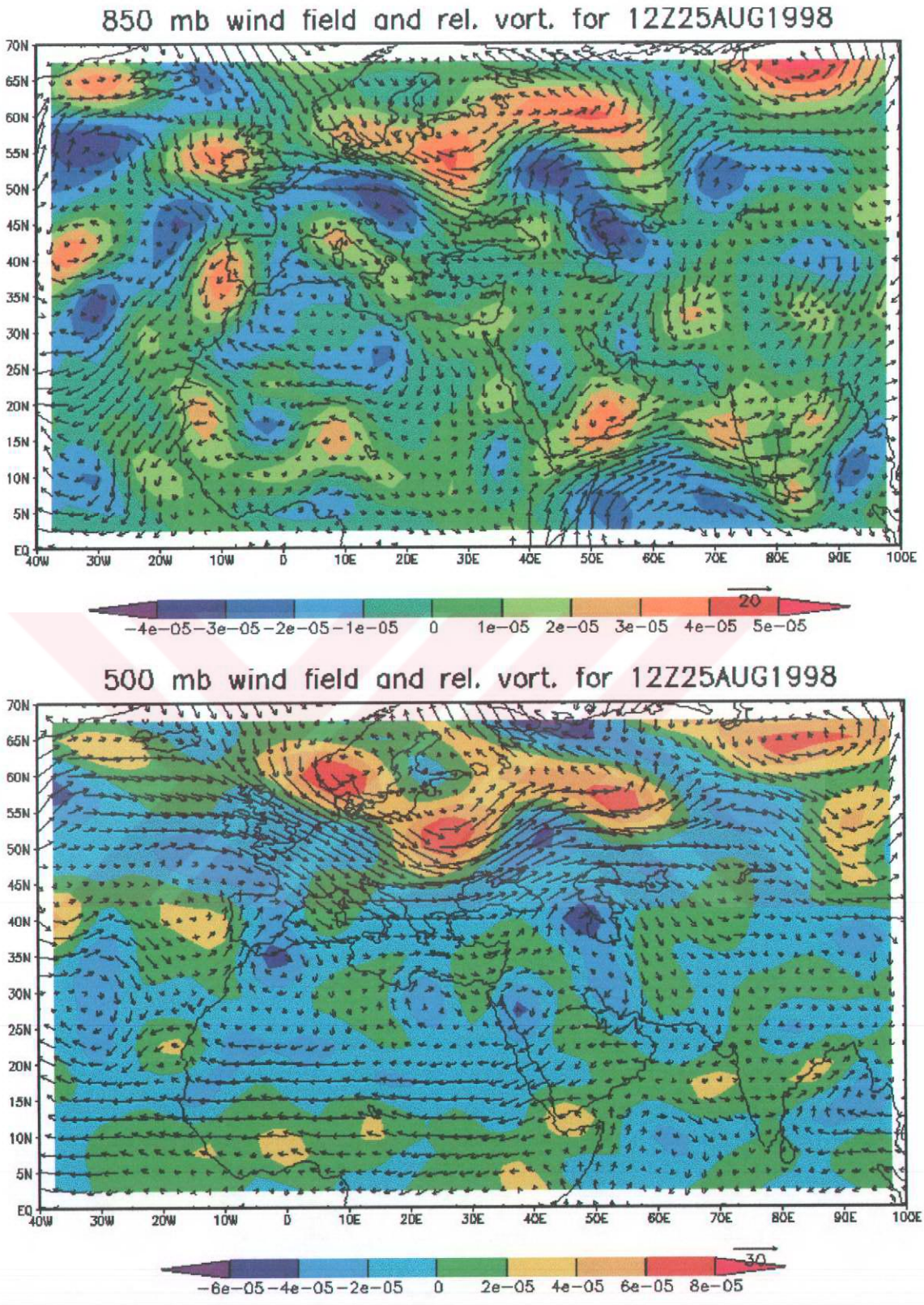

Figure B.6: The wind vector (m/s) and relative vorticity (s^{-1}) on 25 August 1998, one day before the episode, at the 850 hPa pressure level (upper graph) and the 500 hPa pressure level (lower graph) respectively (Christopher Godfrey, 2004).

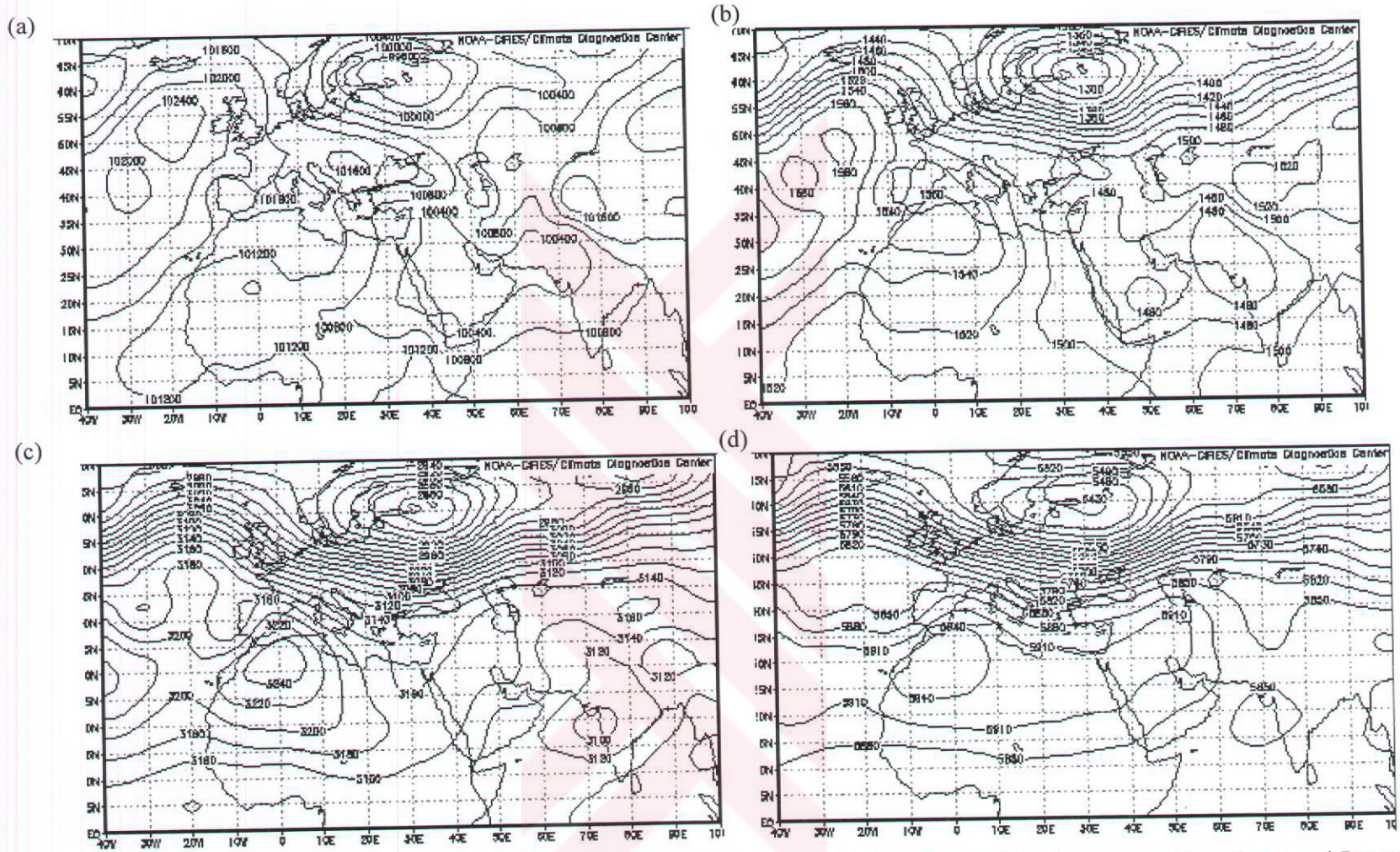

Figure B.7: Synoptic and climatologic situation on 26 August 1998, the first day of the episode: a) Daily average Mean Sea Level Pressure in Pascal ($(P_{00}+P06+P_{12}+P_{18})/4$), b), c) and d) show the mean daily geopotantial height (gpm) on 850, 700 and 500 hpa pressure levels respectively (NCEP/NCAR Reanalysis Project, 2004).

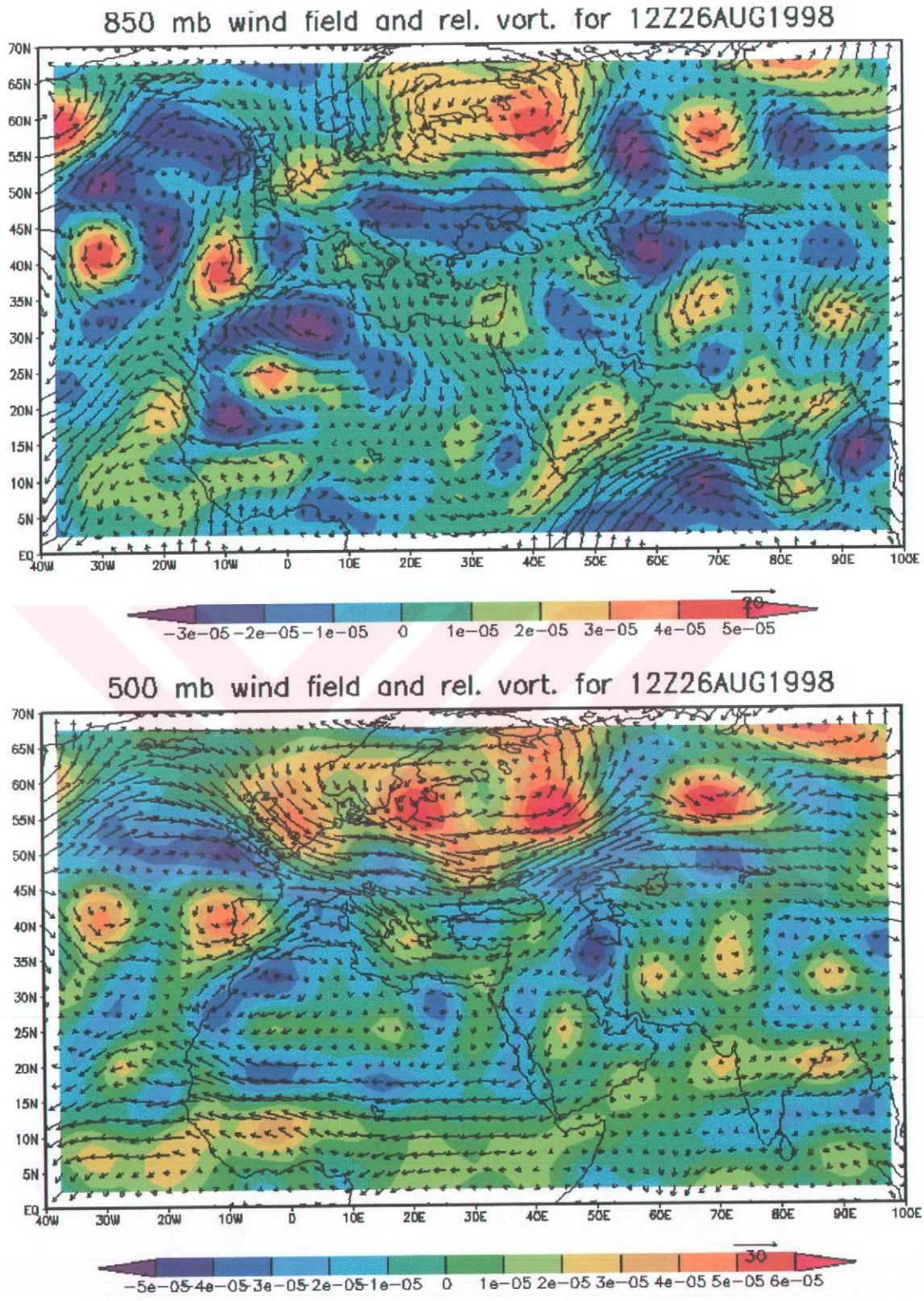

Figure B.8: The wind vector (m/s) and relative vorticity (s^{-1}) on 26 August 1998, the first day of the episode, at the 850 hPa pressure level (upper graph) and the 500 hPa pressure level (lower graph) respectively (Christopher Godfrey, 2004).

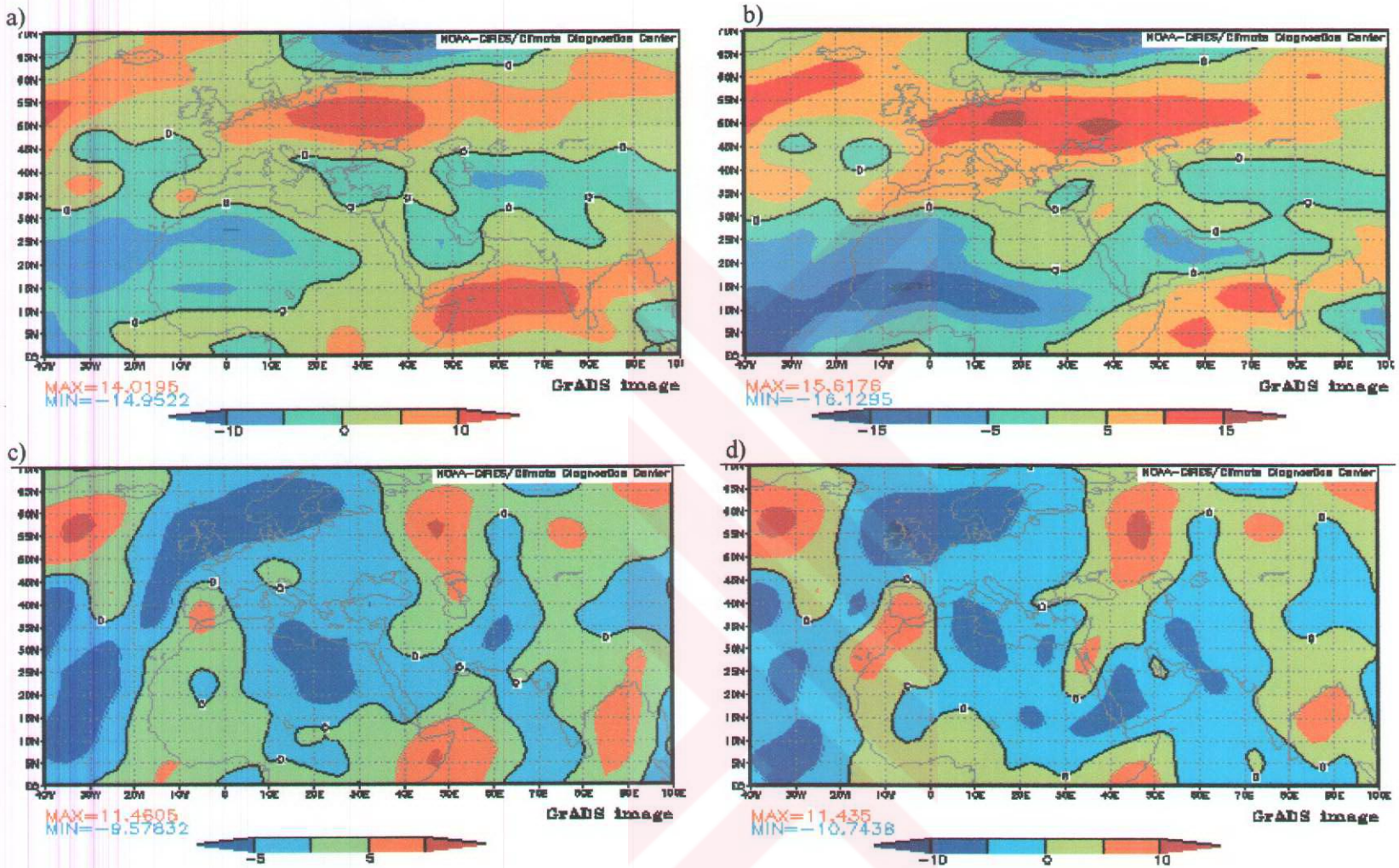

Figure B.9: Daily mean U and V wind components (m/s) on 26 August 1998, the first day of the episode: a) and b) represent the U component at the 850 and 700 hPa pressure levels respectively, while c) and d) represent the V component at the same levels (NCEP/NCAR Reanalysis Project, 2004).

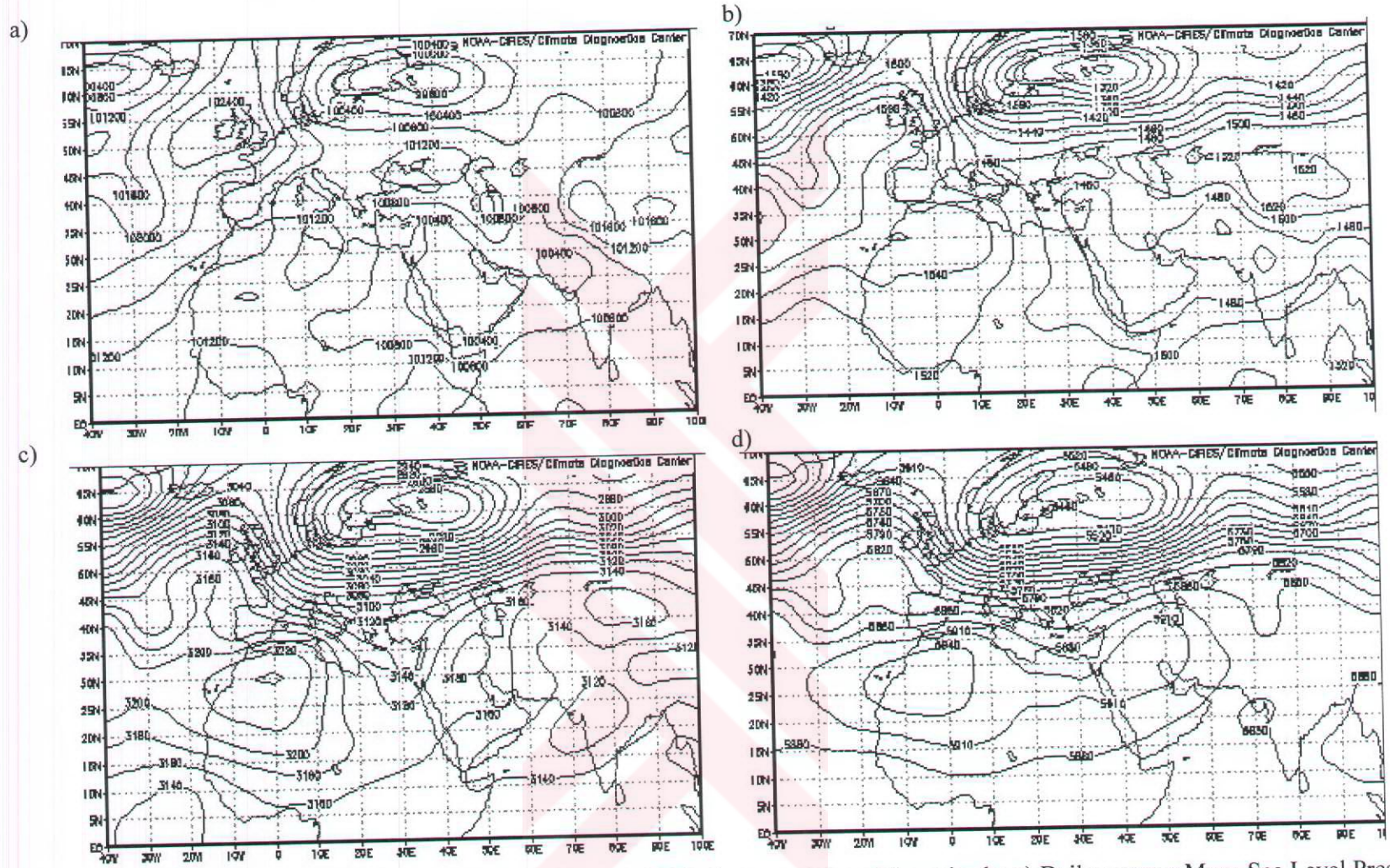

Figure B.10: Synoptic and climatologic situation on 27 August 1998, the second day of the episode: a) Daily average Mean Sea Level Pressure in Pascal ($(P_{00}+P06+P_{12}+P_{18})/4$), b), c) and d) show the mean daily geopotantial height (gpm) on 850, 700 and 500 hpa pressure levels respectively (NCEP/NCAR Reanalysis Project, 2004).

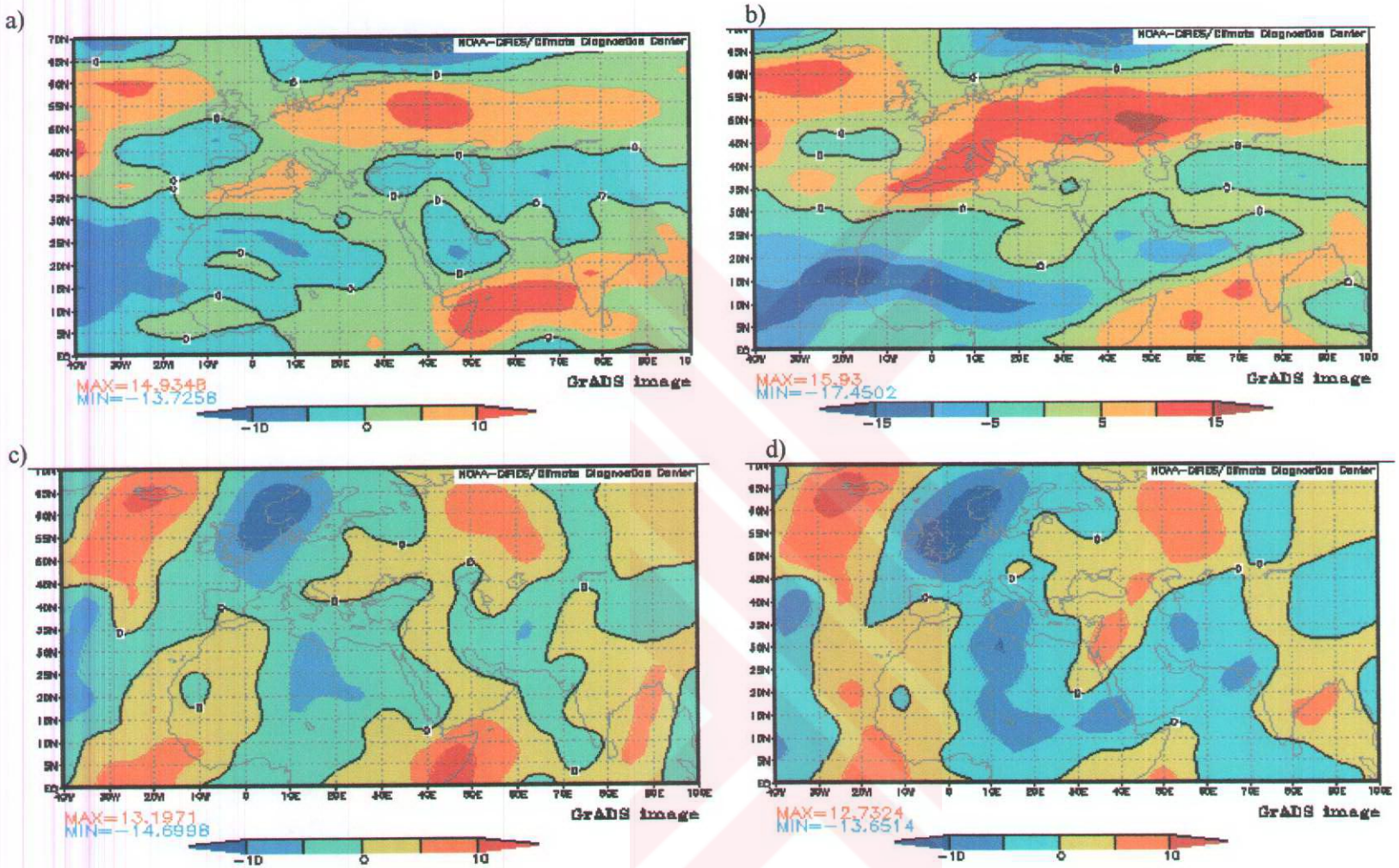

Figure B.11: Daily mean U and V wind components (m/s) on 27 August 1998, the second day of the episode: a) and b) represent the U component at the 850 and 700 hPa pressure levels respectively, while c) and d) represent the V component at the same levels (NCEP/NCAR Reanalysis Project, 2004).

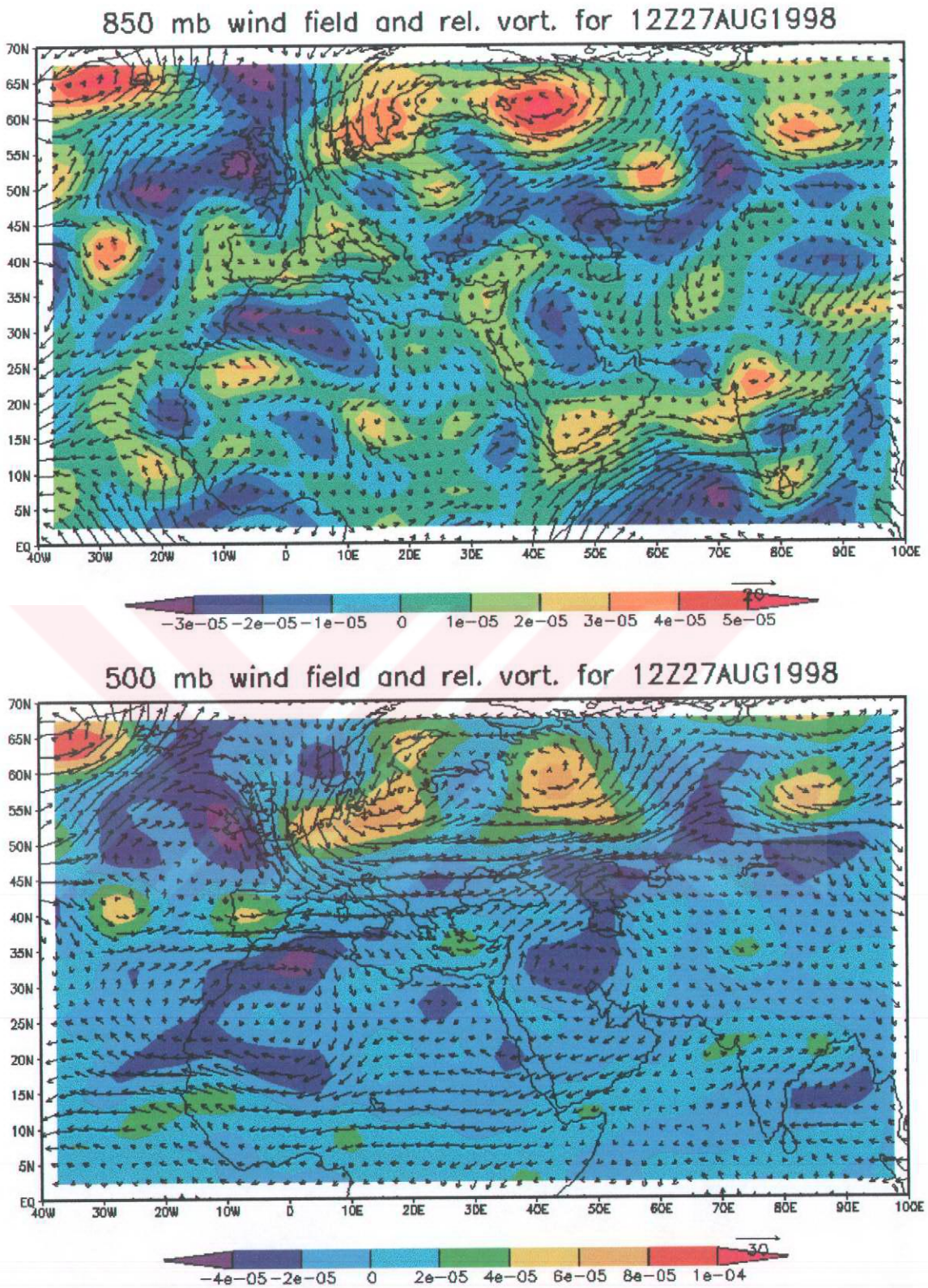

Figure B.12: The wind vector (m/s) and relative vorticity (s^{-1}) on 27 August 1998, the second day of the episode, at the 850 hPa pressure level (upper graph) and the 500 hPa pressure level (lower graph) respectively (Christopher Godfrey, 2004).

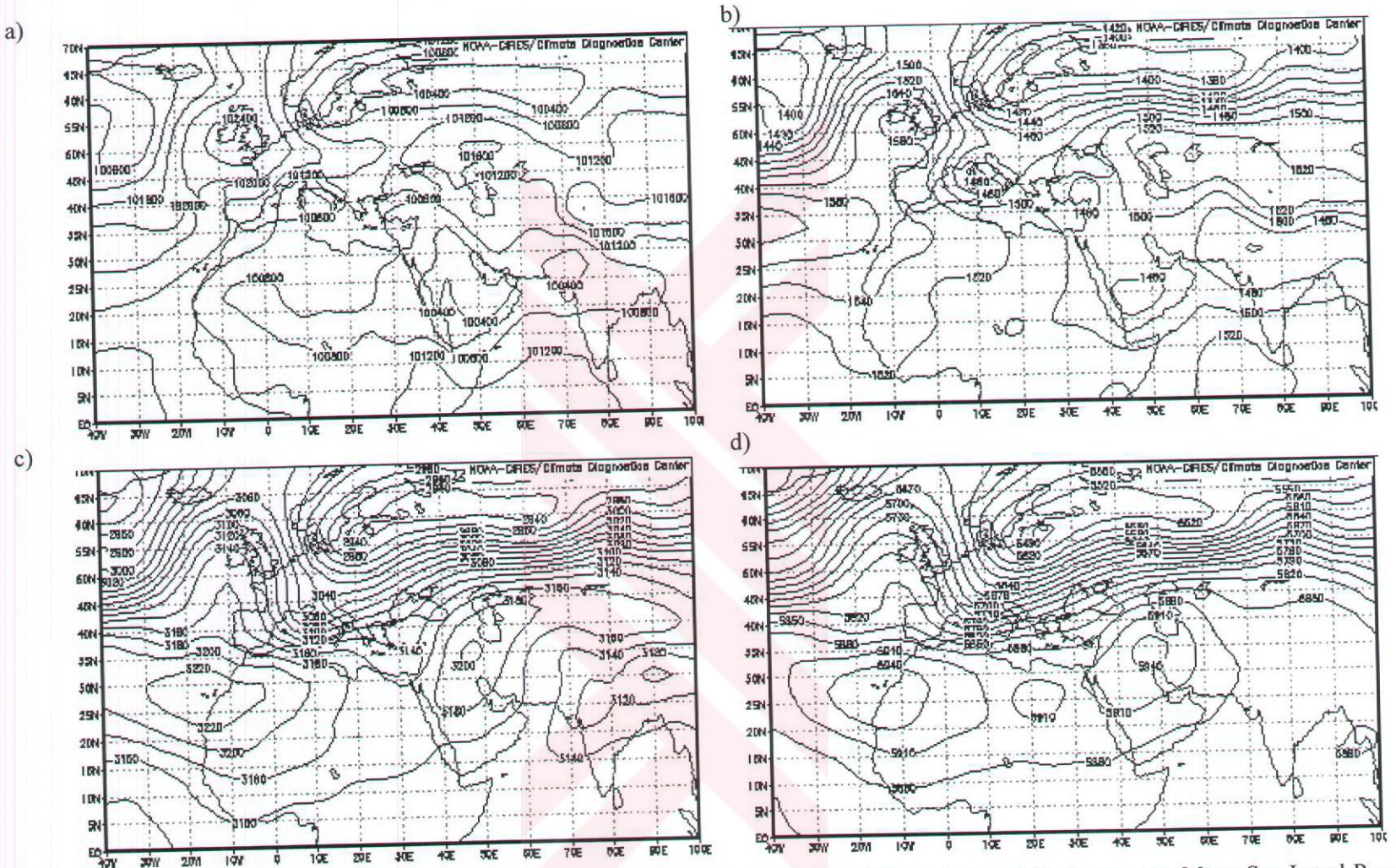

Figure B.13: Synoptic and climatologic situation on 28 August 1998, the third day of the episode: a) Daily average Mean Sea Level Pressure in Pascal $((P_{00}+P06+P_{12}+P_{18})/4)$, b), c) and d) show the mean daily geopotantial height (gpm) on 850, 700 and 500 hpa pressure levels respectively (NCEP/NCAR Reanalysis Project, 2004).

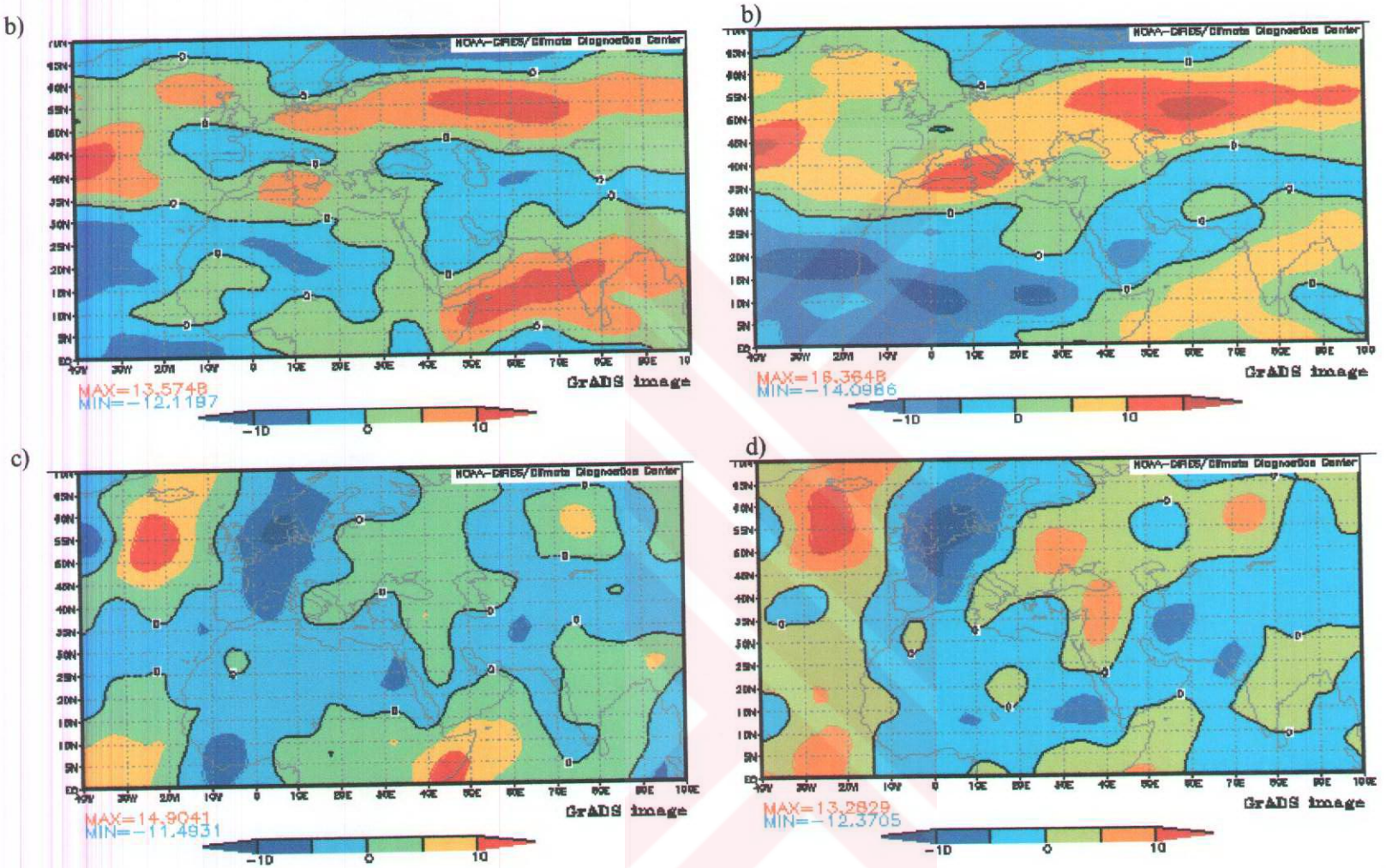

Figure B.14: Daily mean U and V wind components (m/s) on 28 August 1998, the third day of the episode: a) and b) represent the U component at the 850 and 700 hPa pressure levels respectively, while c) and d) represent the V component at the same levels (NCEP/NCAR Reanalysis Project, 2004).

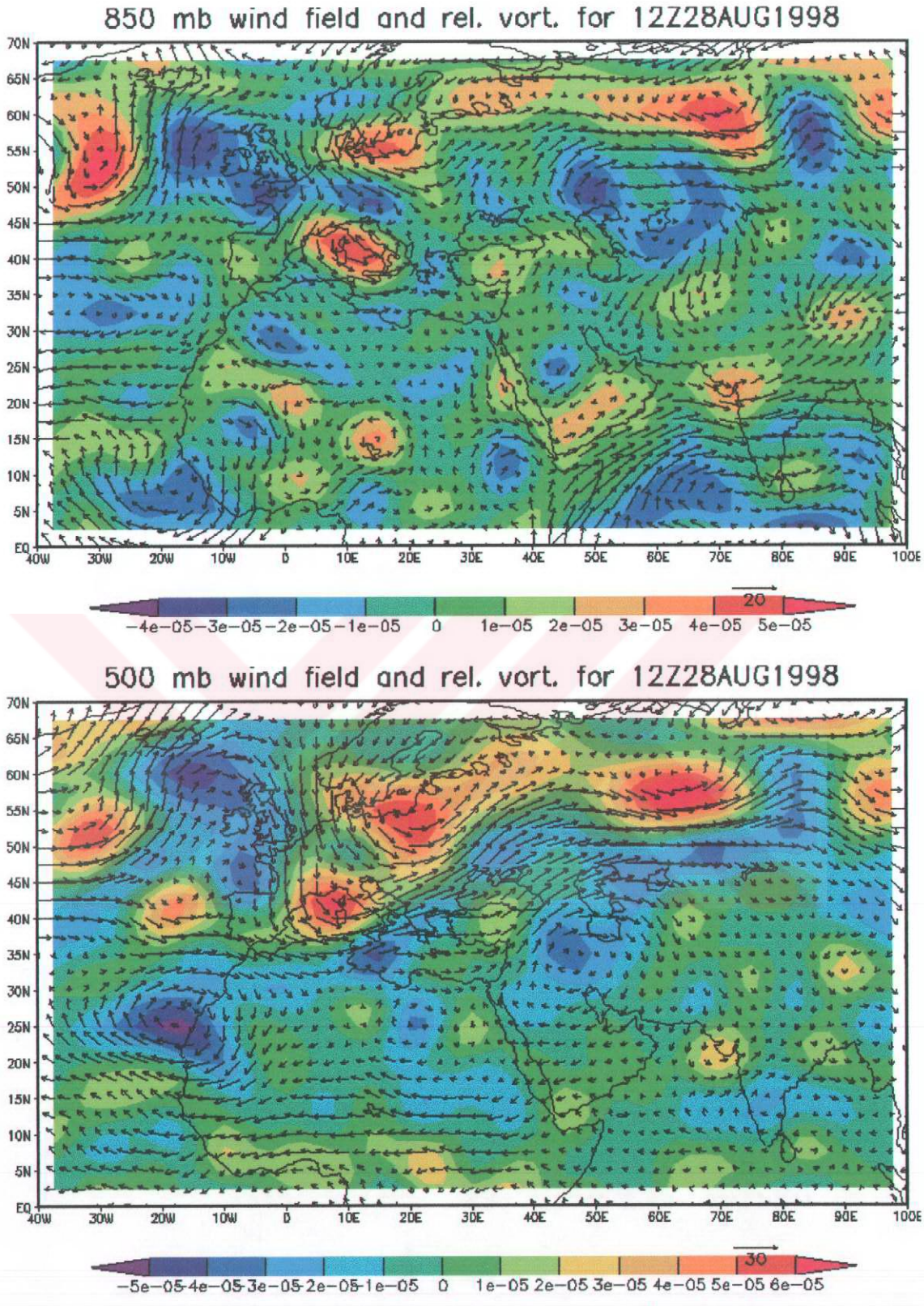

Figure B.15: The wind vector (m/s) and relative vorticity (s^{-1}) on 28 August 1998, the third day of the episode, at the 850 hPa pressure level (upper graph) and the 500 hPa pressure level (lower graph) respectively (Christopher Godfrey, 2004).

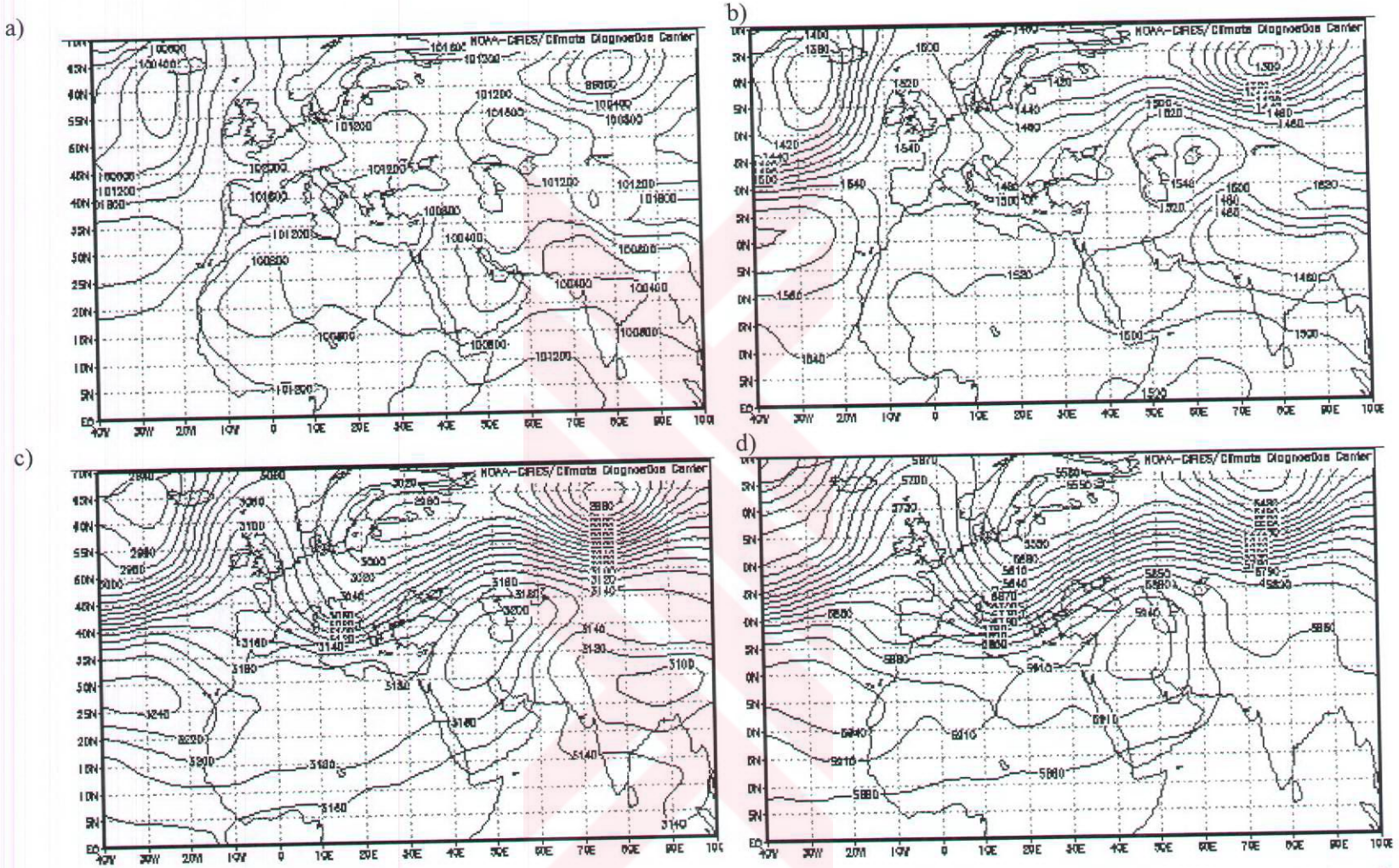

Figure B.16: Synoptic and climatologic situation on 29 August 1998, the fourth and the last day of the episode: a) Daily average Mean Sea Level Pressure in Pascal $((P_{00}+P06+P_{12}+P_{18})/4)$, b), c) and d) show the mean daily geopotantial height (gpm) on 850, 700 and 500 hpa pressure levels respectively (NCEP/NCAR Reanalysis Project, 2004).

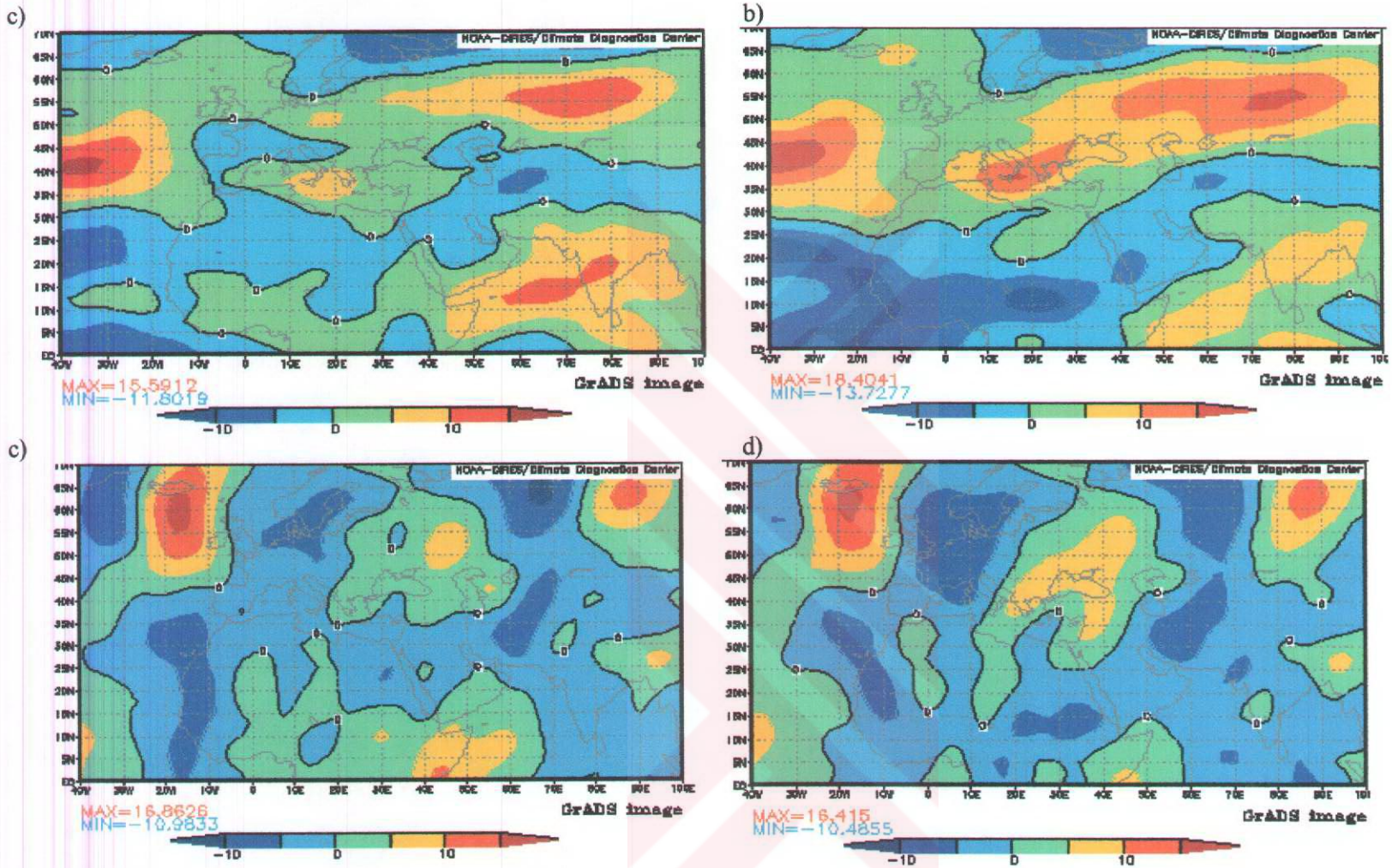

Figure B.17: Daily mean U and V wind components (m/s) on 29 August 1998, the fourth and last day of the episode: a) and b) represent the U component at the 850 and 700 hPa pressure levels respectively, while c) and d) represent the V component at the same levels (NCEP/NCAR Reanalysis Project, 2004).

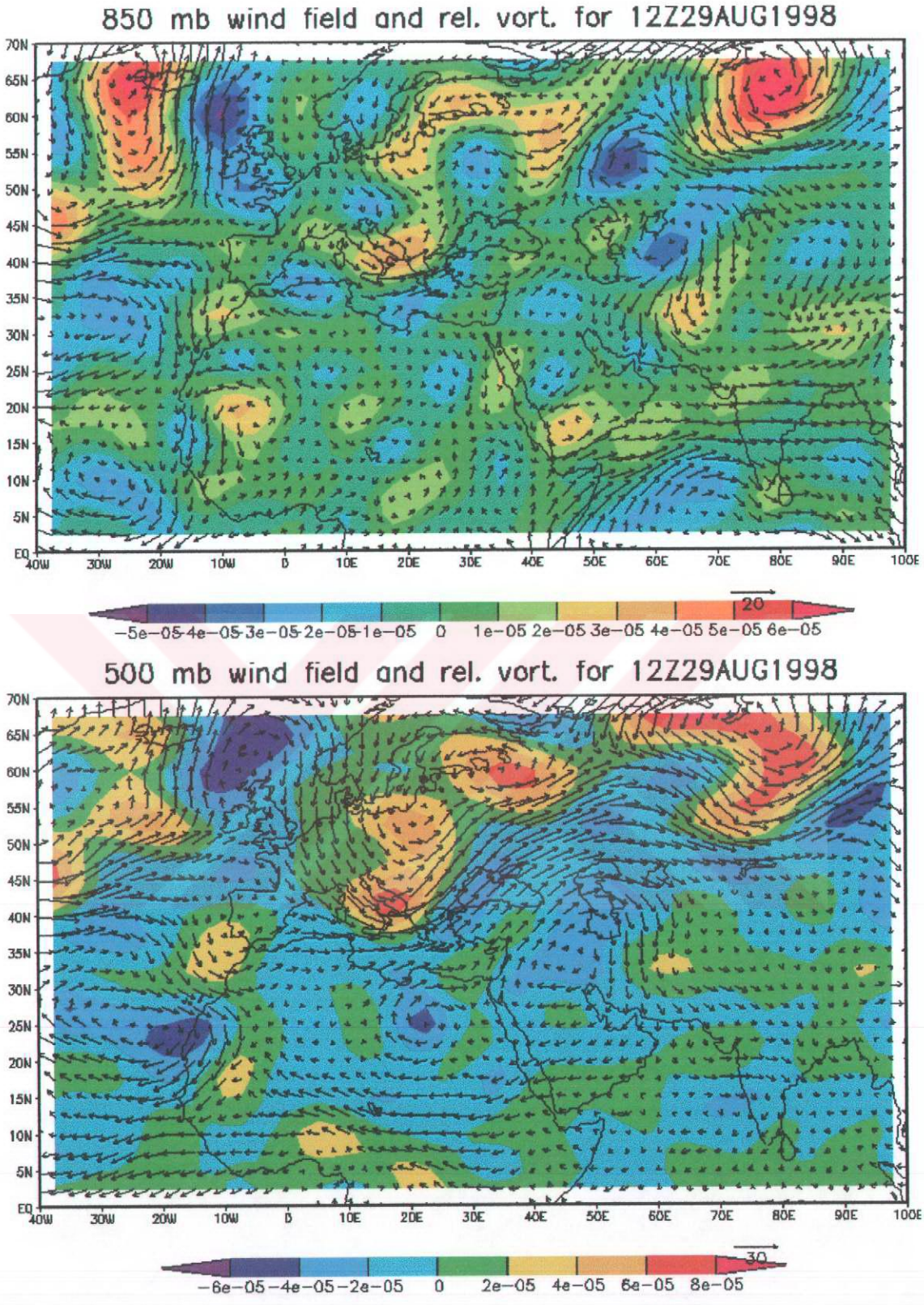

Figure B.18: The wind vector (m/s) and relative vorticity (s^{-1}) on 29 August 1998, the fourth and last day of the episode, at the 850 hPa pressure level (upper graph) and the 500 hPa pressure level (lower graph) respectively (Christopher Godfrey, 2004).

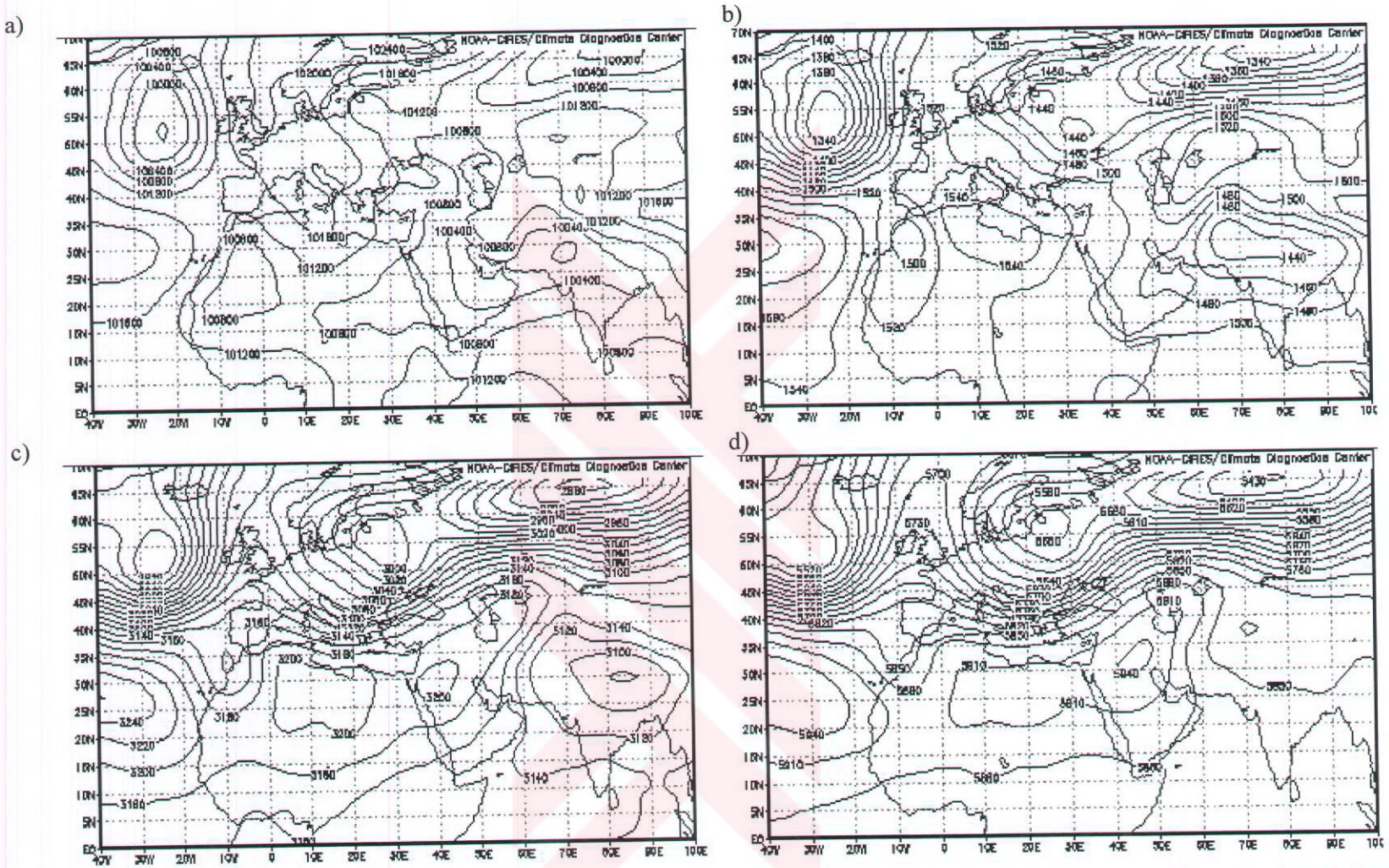

Figure B.19: Synoptic and climatologic situation on 30 August 1998, one day after the episode: a) Daily average Mean Sea Level Pressure in Pascal ($(P_{00}+P06+P_{12}+P_{18})/4$), b), c) and d) show the mean daily geopotantial height (gpm) on 850, 700 and 500 hpa pressure levels respectively (NCEP/NCAR Reanalysis Project, 2004).

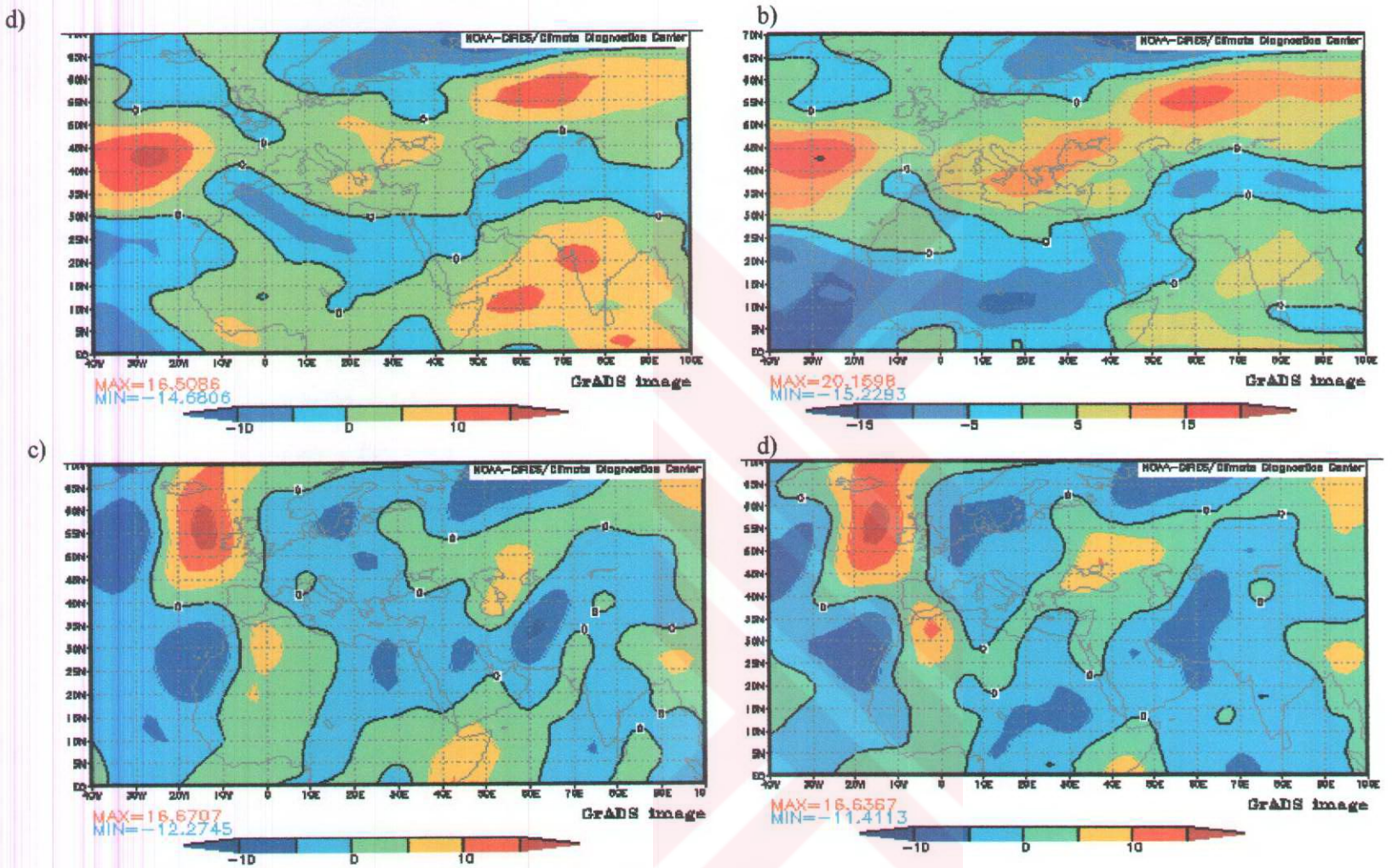

Figure B.20: Daily mean U and V wind components (m/s) on 30 August 1998, one day after the episode: a) and b) represent the U component at the 850 and 700 hPa pressure levels respectively, while c) and d) represent the V component at the same levels (NCEP/NCAR Reanalysis Project, 2004).

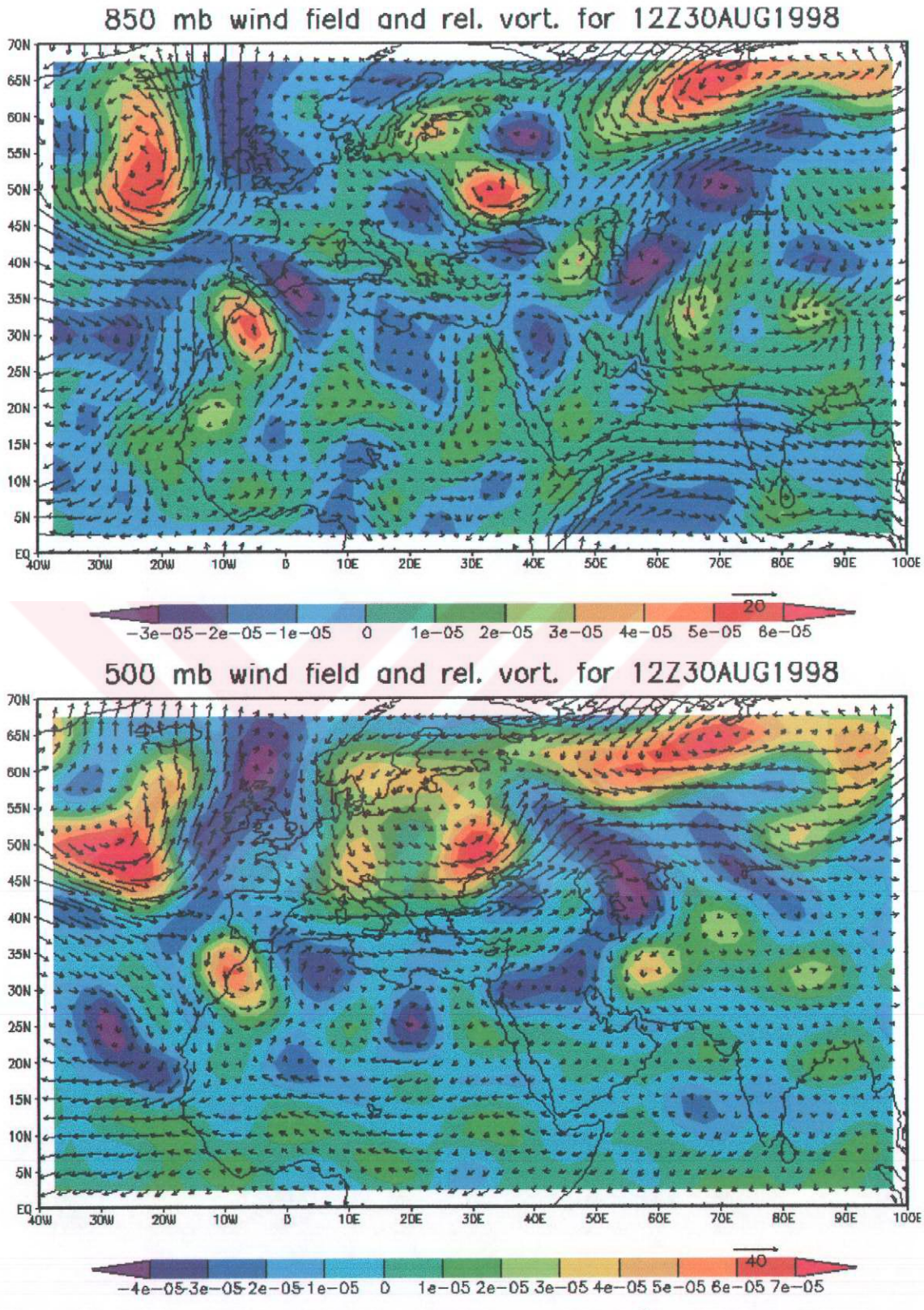

Figure B.21: The wind vector (m/s) and relative vorticity (s^{-1}) on 30 August 1998, one day after the episode, at the 850 hPa pressure level (upper graph) and the 500 hPa pressure level (lower graph) respectively (Christopher Godfrey, 2004).

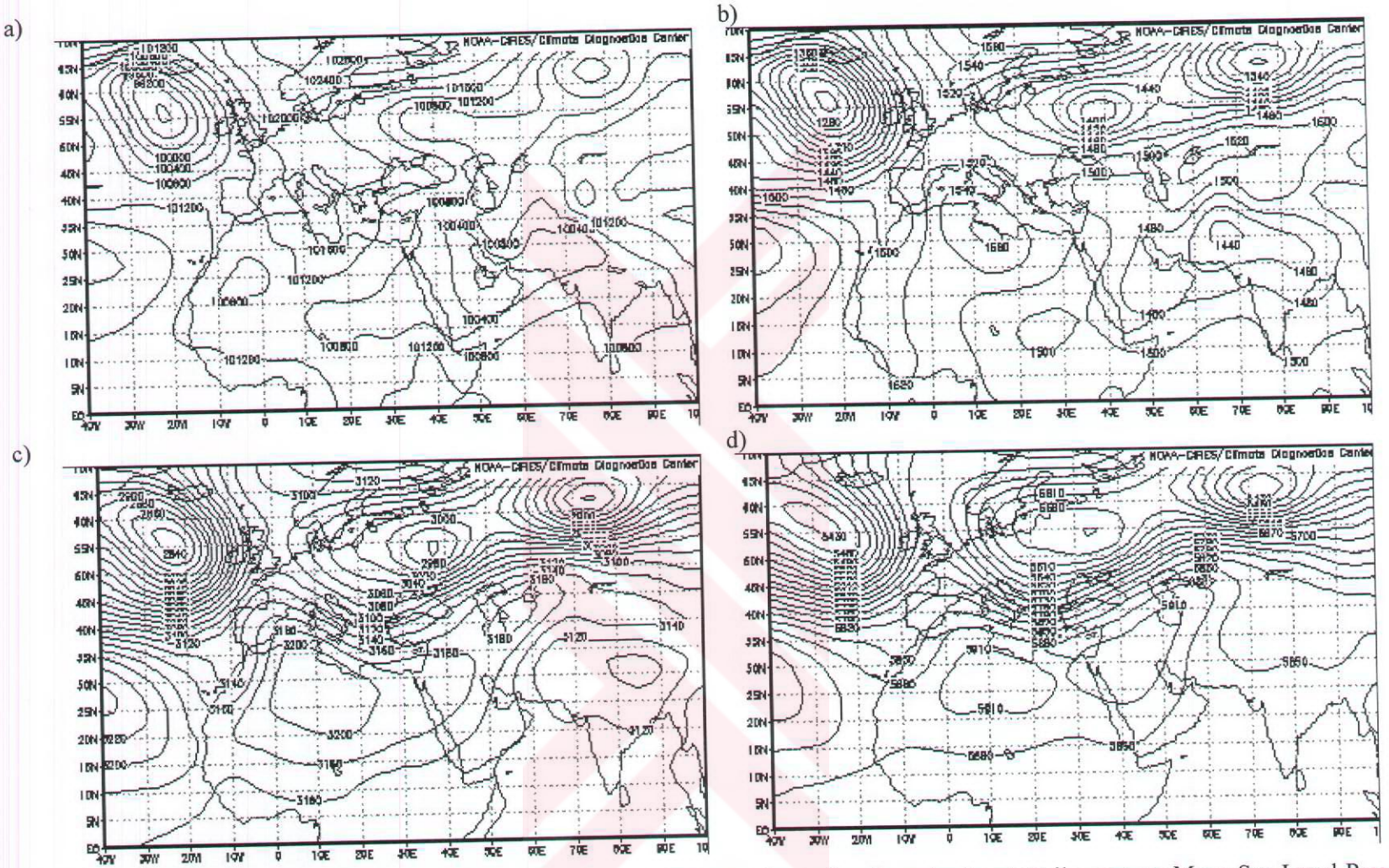

Figure B.22: Synoptic and climatologic situation on 31 August 1998, two days after the episode: a) Daily average Mean Sea Level Pressure in Pascal ($(P_{00}+P06+P_{12}+P_{18})/4$), b), c) and d) show the mean daily geopotantial height (gpm) on 850, 700 and 500 hpa pressure levels respectively (NCEP/NCAR Reanalysis Project, 2004).

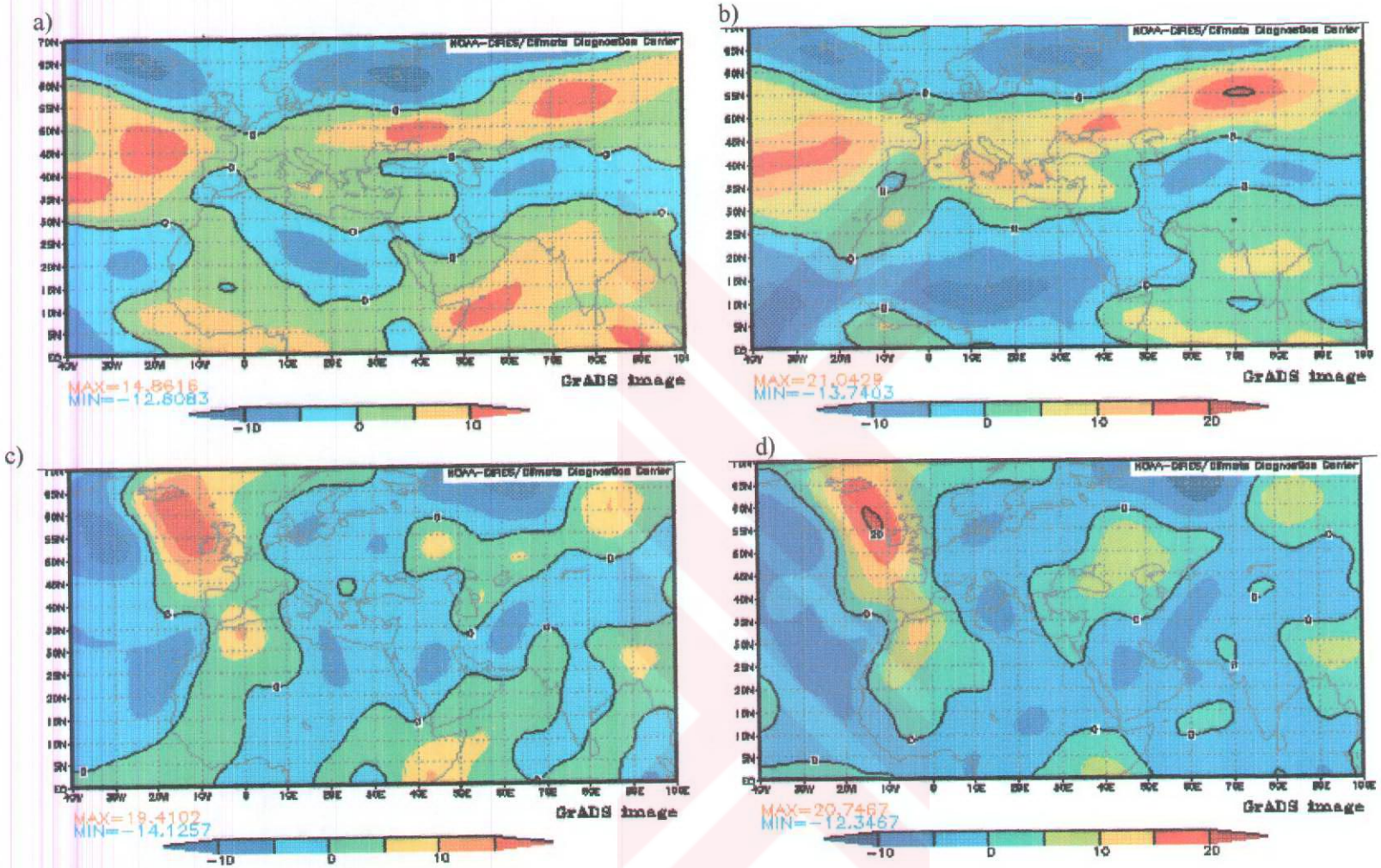

Figure B.23: Daily mean U and V wind components (m/s) on 31 August 1998, two days after the episode: a) and b) represent the U component at the 850 and 700 hPa pressure levels respectively, while c) and d) represent the V component at the same levels (NCEP/NCAR Reanalysis Project, 2004).

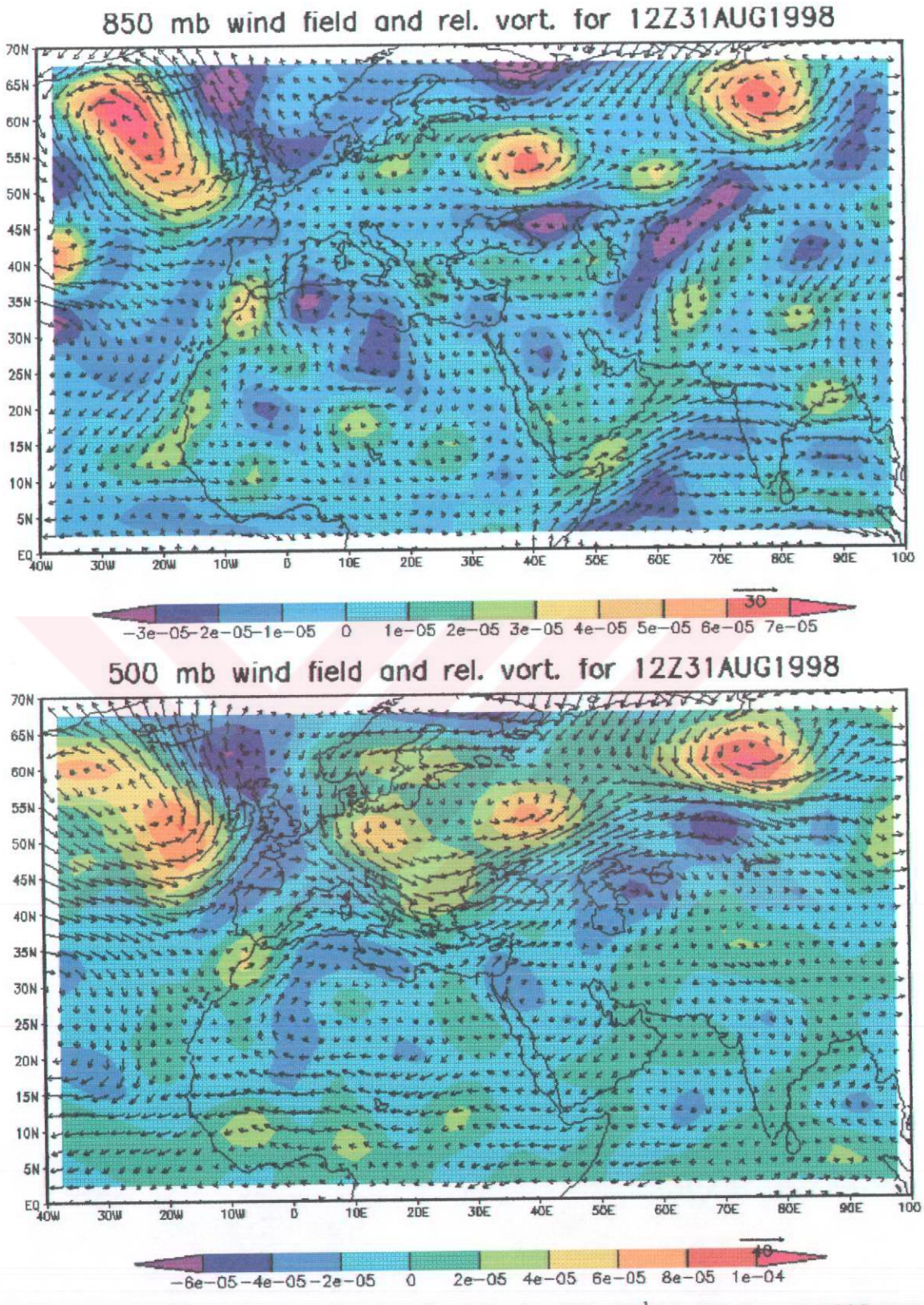

Figure B.24: The wind vector (m/s) and relative vorticity (s^{-1}) on 31 August 1998, two days after the episode, at the 850 hPa pressure level (upper graph) and the 500 hPa pressure level (lower graph) respectively (Christopher Godfrey, 2004).

APPENDIX C

MM5 AND HYSPLIT MODELS OUTPUTS

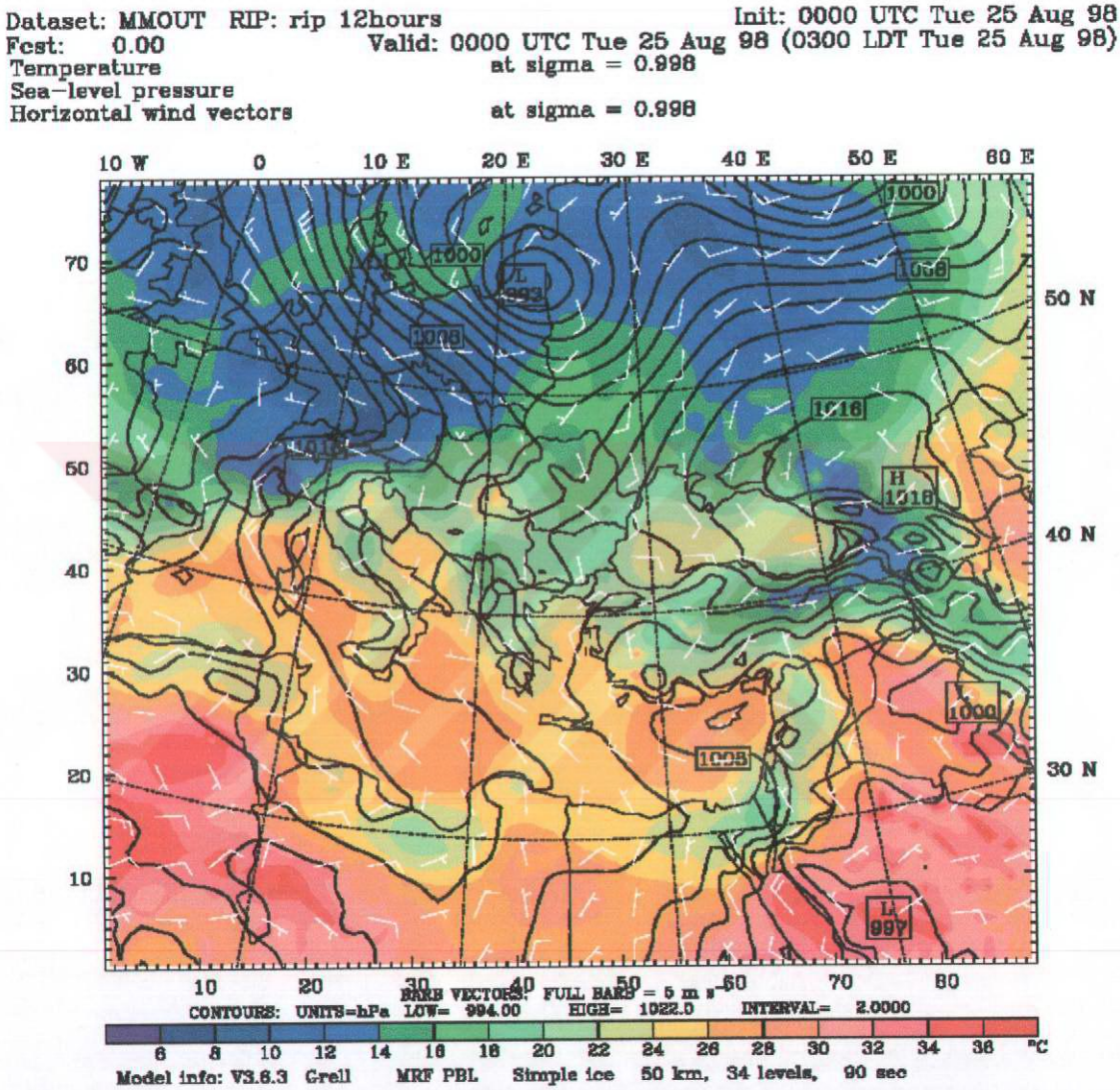

Figure C.1: Predicted Sea level pressure in hpa (black contours), temperature in °C (color shading) and horizontal wind velocity (white vectors). 00 hours forecast on 25 – 08 – 1998, 0000 UTC. (The temperature and the wind vectors are at sigma level 998).

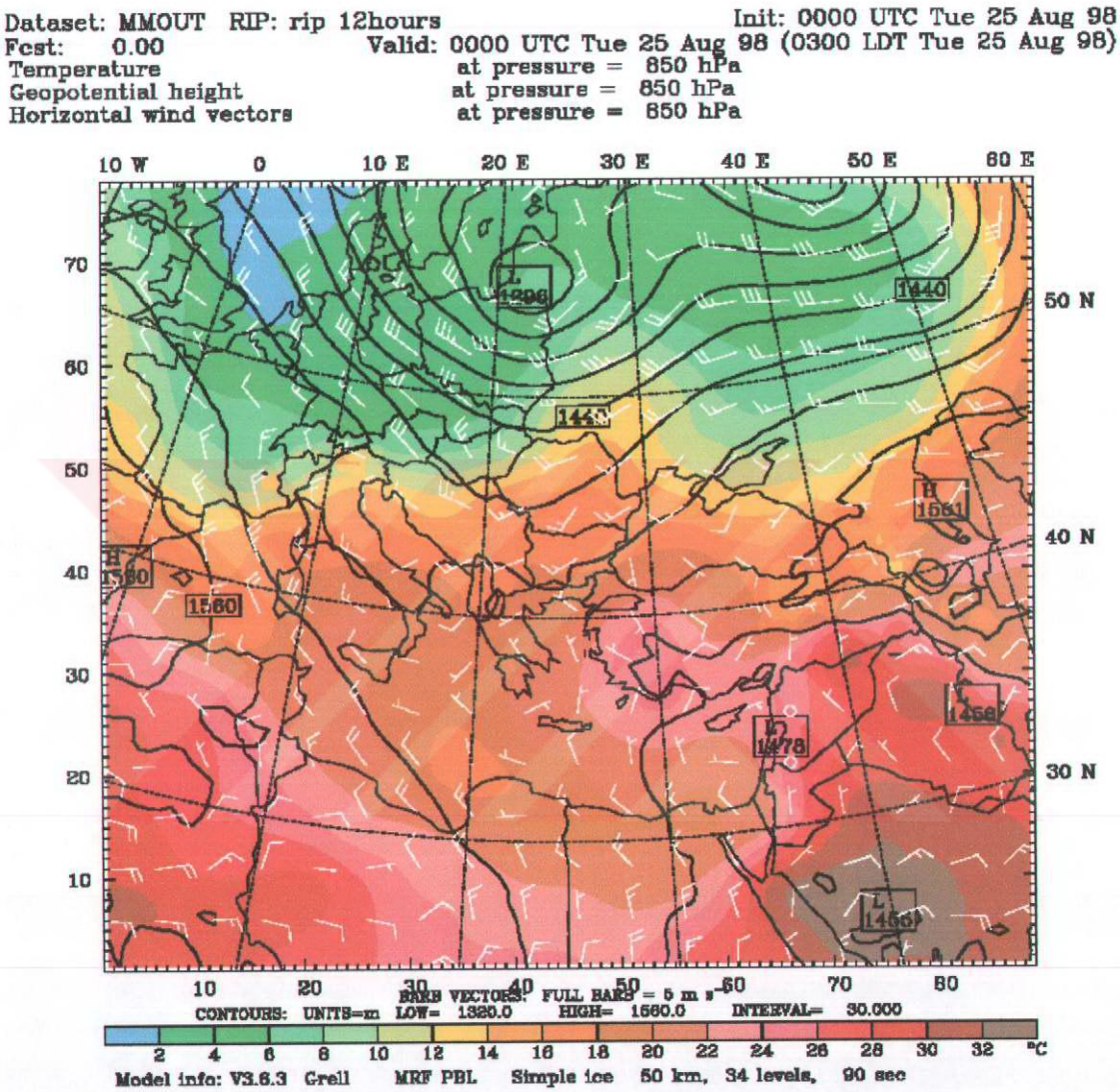

Figure C.2: Predicted 850 hpa geopotential heights in gpm (black contours), temperature in °C (color shading) and horizontal wind velocity (white vectors). 00 hours forecast on 25 – 08 – 1998, 0000 UTC.

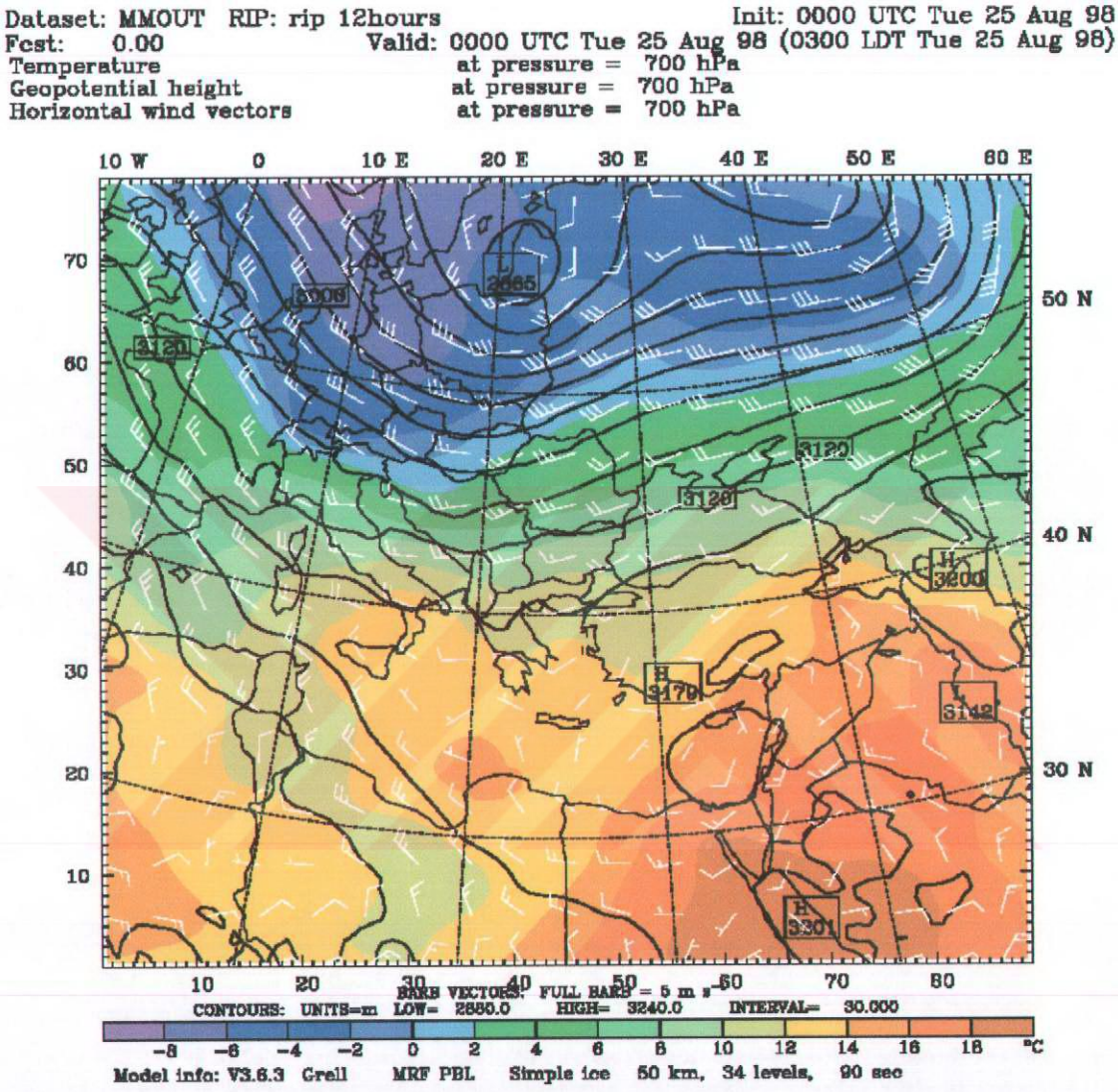

Figure C.3: Predicted 700 hpa geopotential heights in gpm (black contours), temperature in °C (color shading) and horizontal wind velocity (white vectors). 00 hours forecast on 25 – 08 – 1998, 0000 UTC.

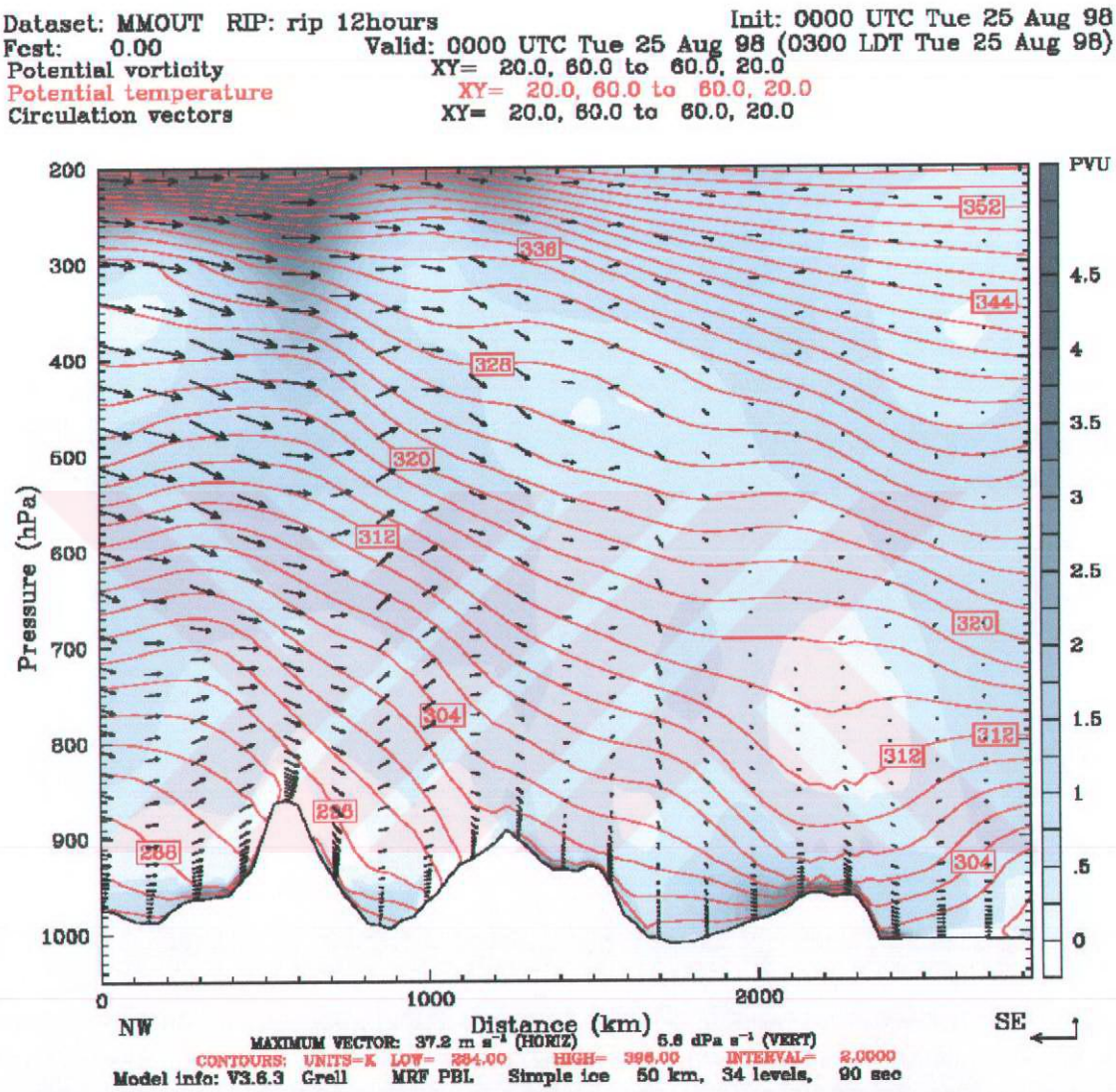

Figure C.4: A vertical cross section of the potential vorticity (black and white shading), potential temperatures (red lines) and the wind circulation (black vectors) predicted over a NW – SE line of length around 3000 km from the south of Poland to Cyprus. 00 hours forecast on 25 – 08 – 1998, 0000 UTC.

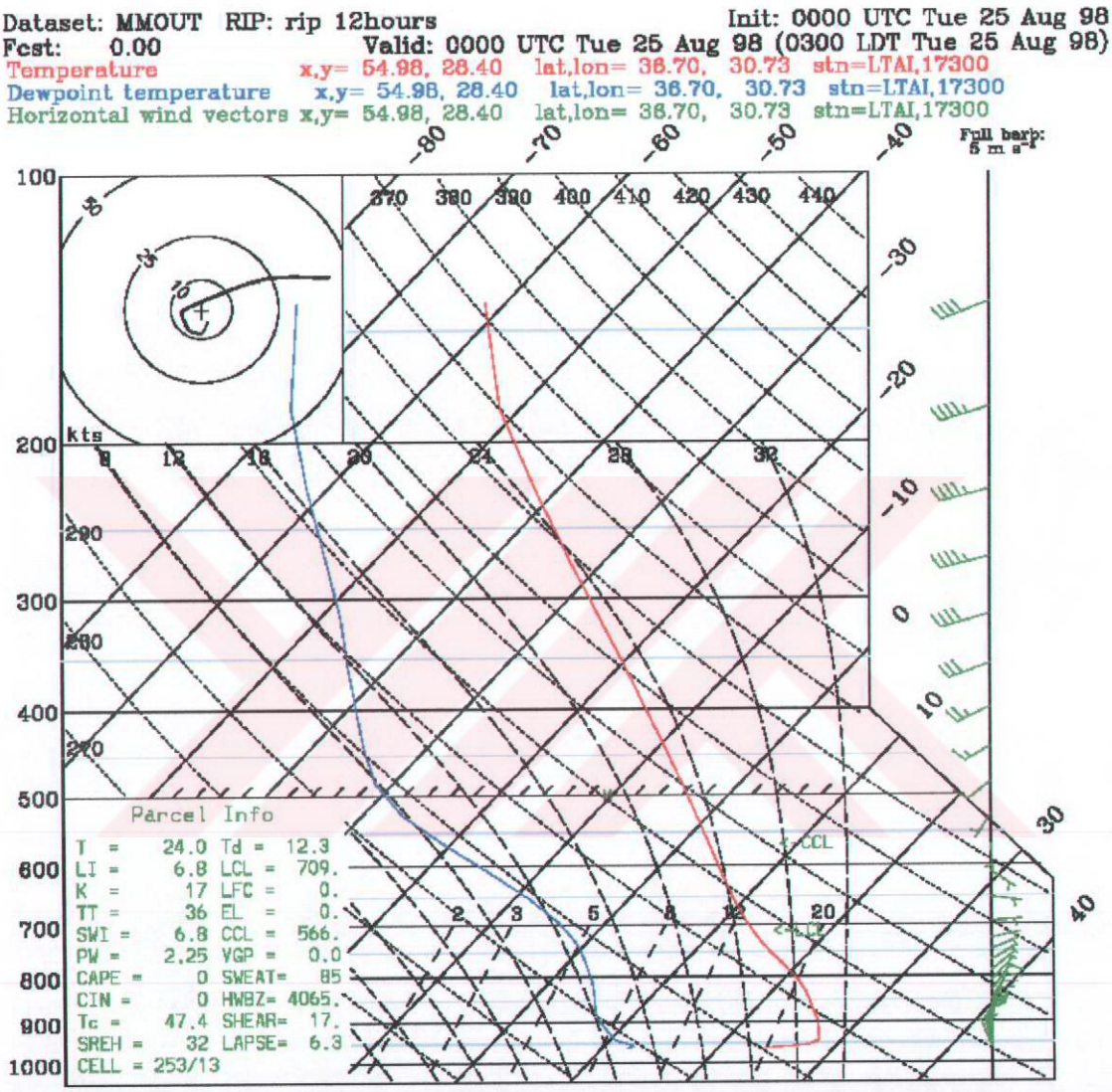

Figure C.5: An estimated Skew – T Plot diagram for Antalya (36.47 °N, 30.34 °E). 00 hours forecast on 25 – 08 – 1998, 0000 UTC.

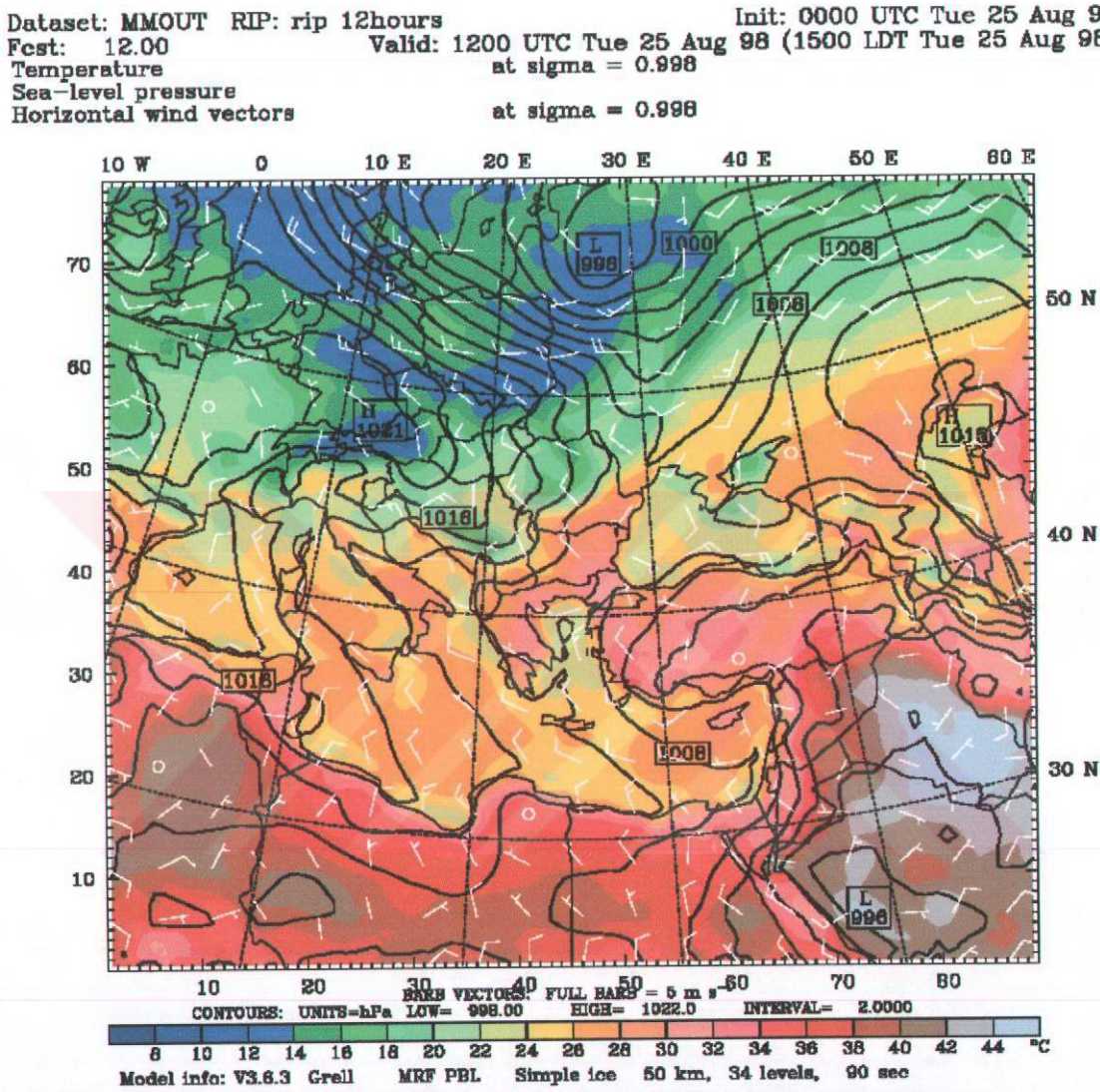

Figure C.6: Predicted Sea level pressure in hpa (black contours), temperature in °C (color shading) and horizontal wind velocity (white vectors). 12 hours forecast for 25 – 08 – 1998, 1200 UTC. (The temperature and the wind vectors are at sigma level 998).

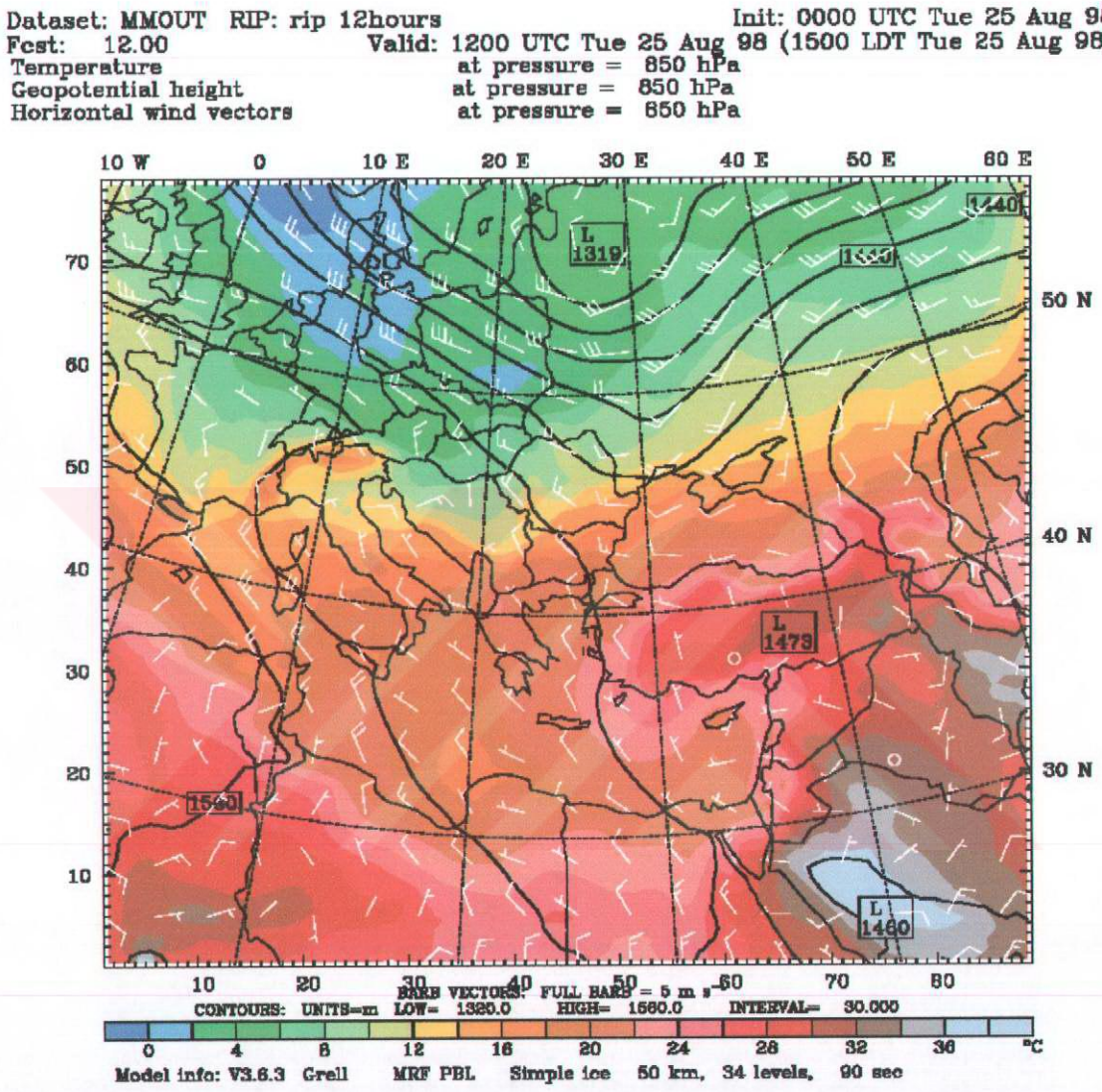

Figure C.7: Predicted 850 hpa geopotential heights in gpm (black contours), temperature in °C (color shading) and horizontal wind velocity (white vectors). 12 hours forecast for 25 – 08 – 1998, 1200 UTC.

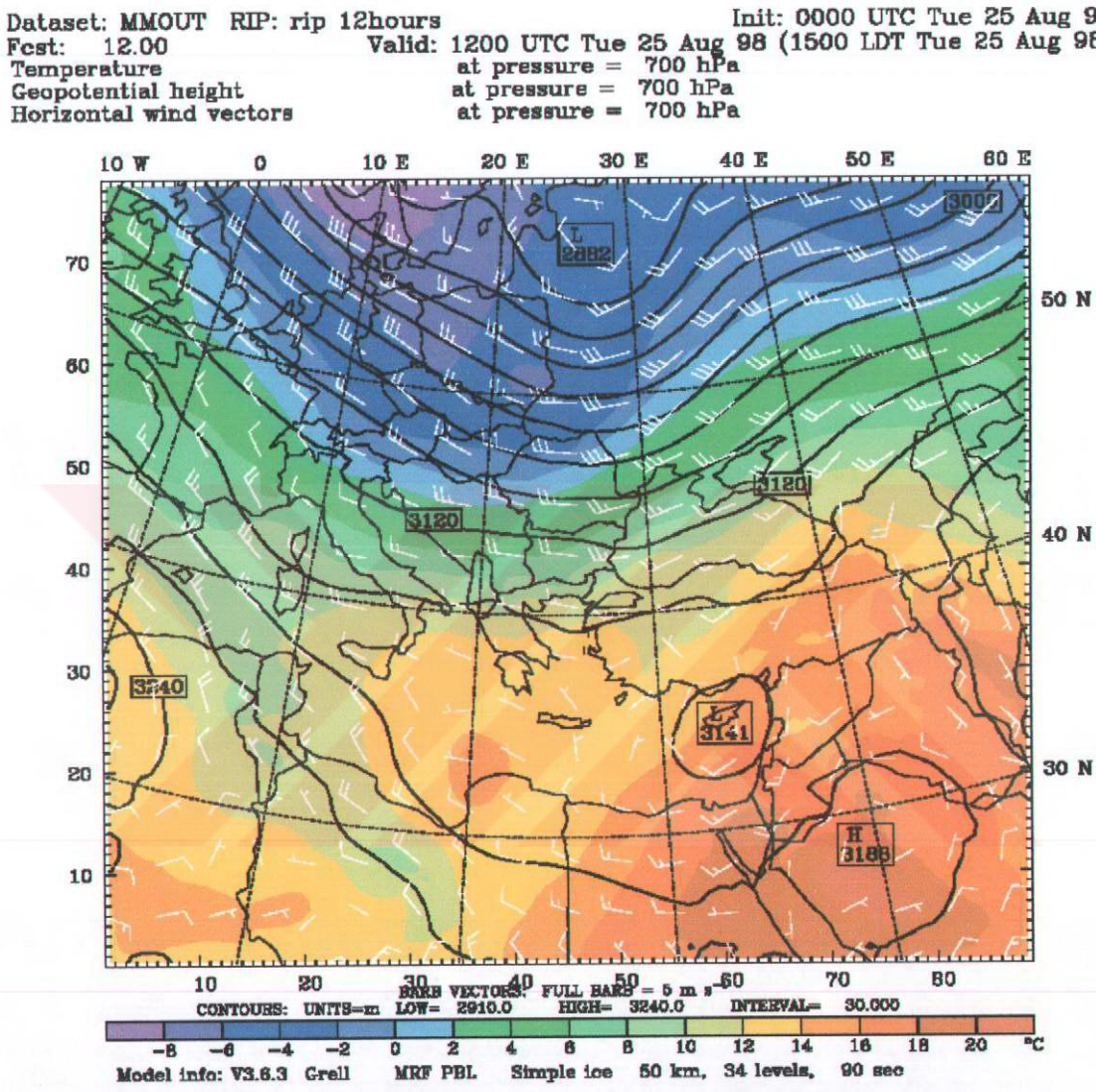

Figure C.8: Predicted 700 hpa geopotential heights in gpm (black contours), temperature in °C (color shading) and horizontal wind velocity (white vectors). 12 hours forecast for 25 – 08 – 1998, 1200 UTC.

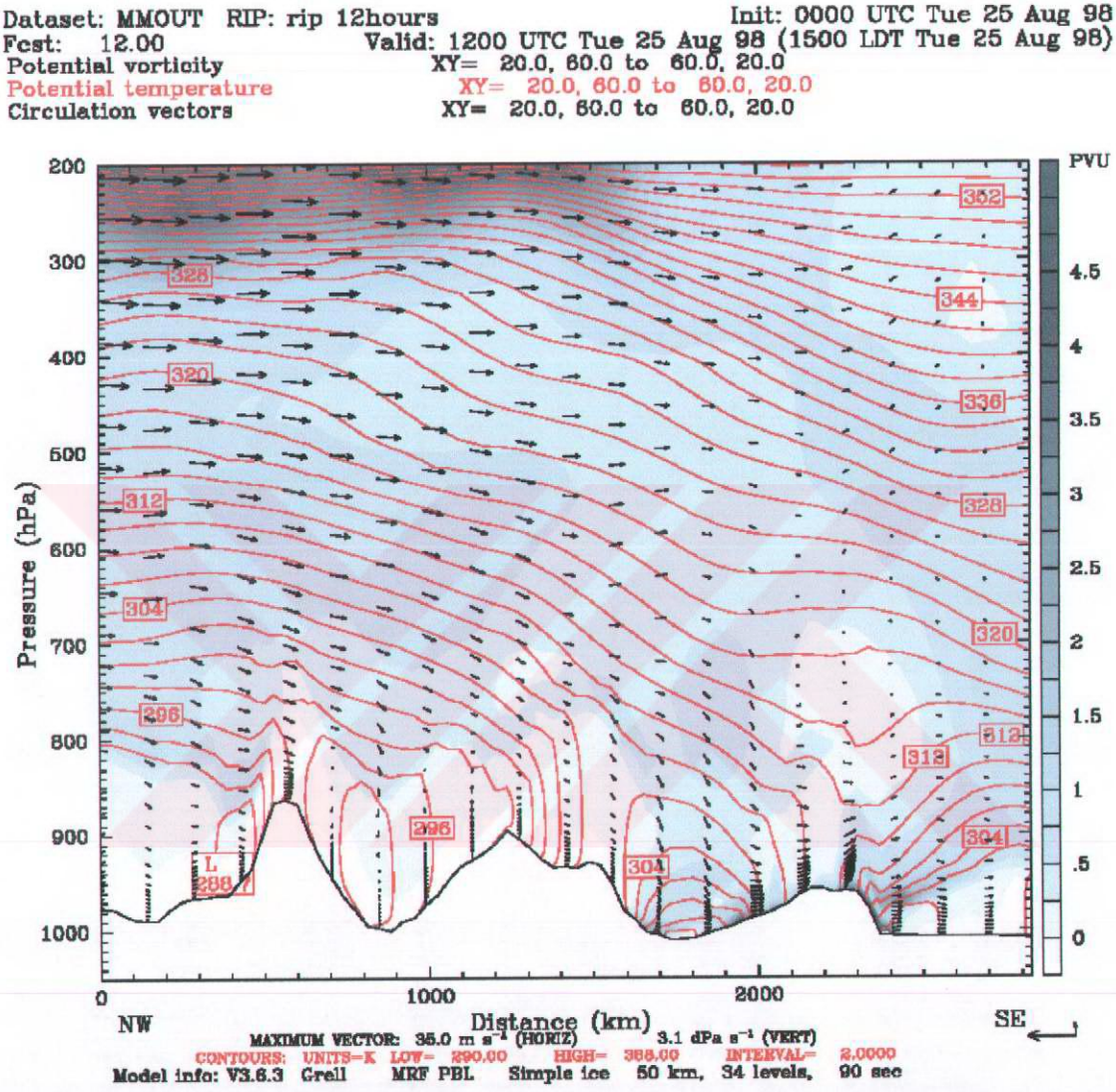

Figure C.9: A vertical cross section of the potential vorticity (black and white shading), potential temperatures (red lines) and the wind circulation (black vectors) predicted over a NW – SE line of length around 3000 km from the south of Poland to Cyprus. 12 hours forecast for 25 – 08 – 1998, 1200 UTC.

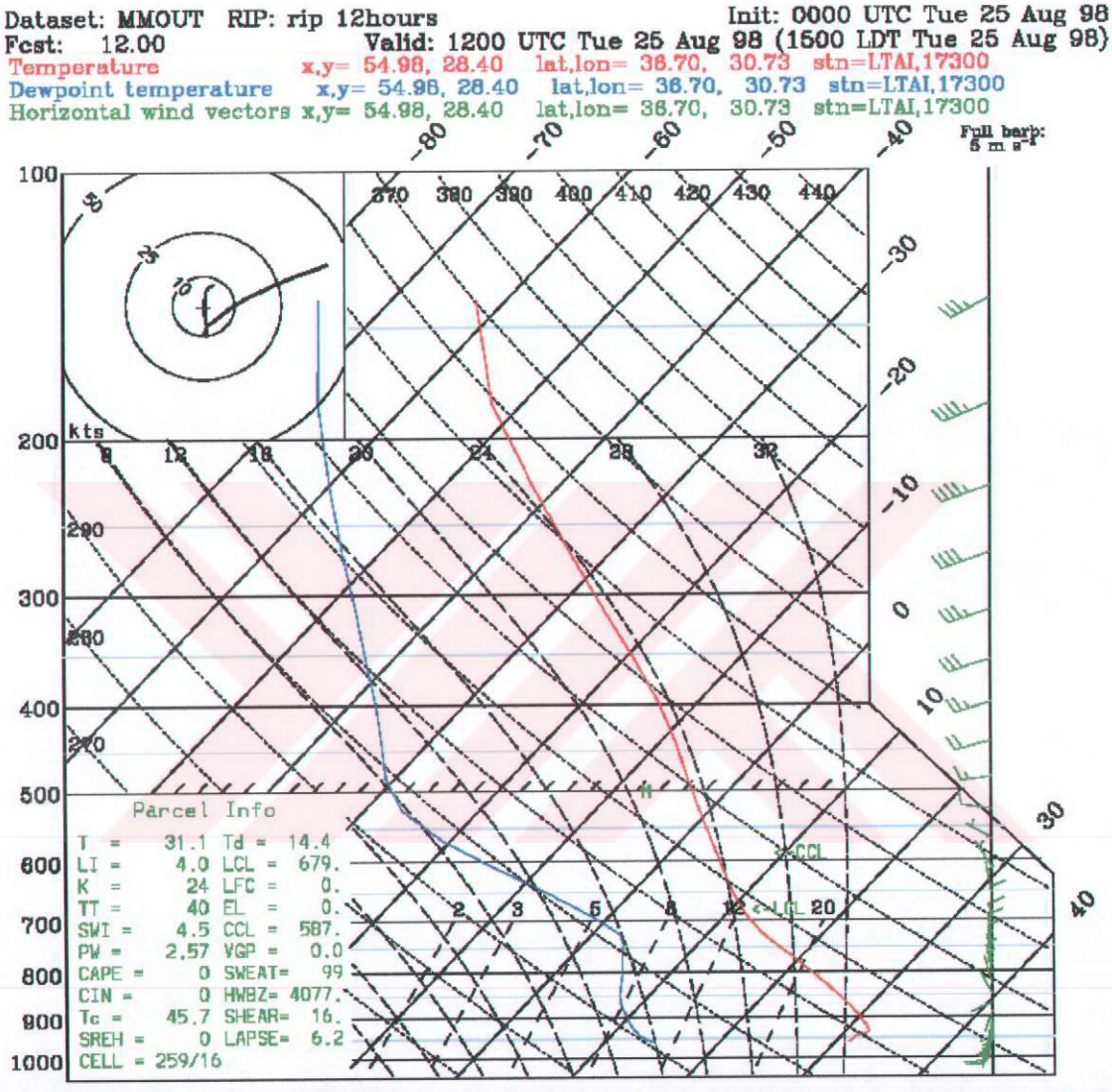

Figure C.10: An estimated Skew – T Plot diagram for Antalya (36.47 °N, 30.34 °E). 12 hours forecast for 25 – 08 – 1998, 1200 UTC.

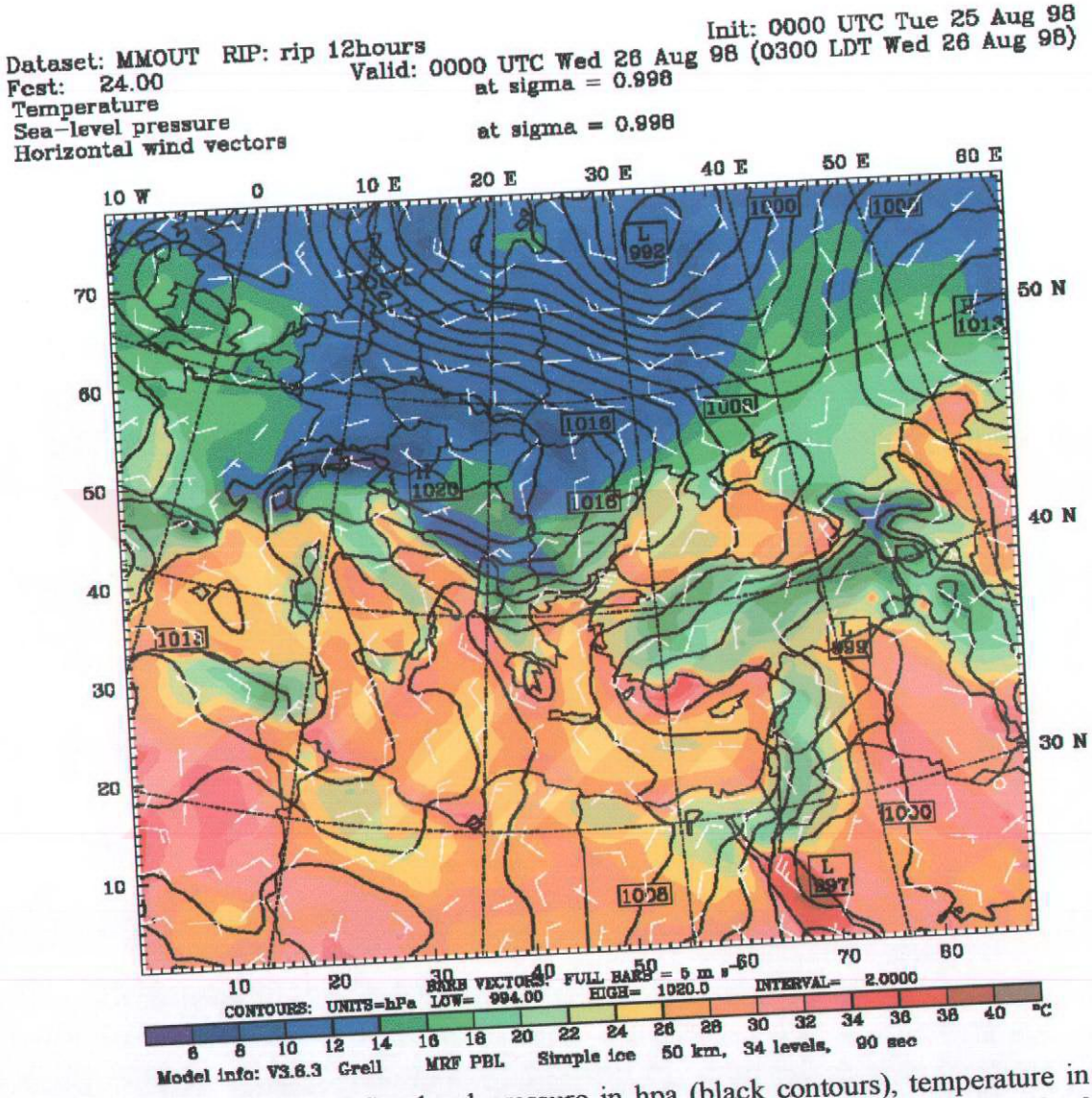

Figure C.11: Predicted Sea level pressure in hpa (black contours), temperature in °C (color shading) and horizontal wind velocity (white vectors). 24 hours forecast for 26 – 08 – 1998, 0000 UTC. (The temperature and the wind vectors are at sigma level 998).

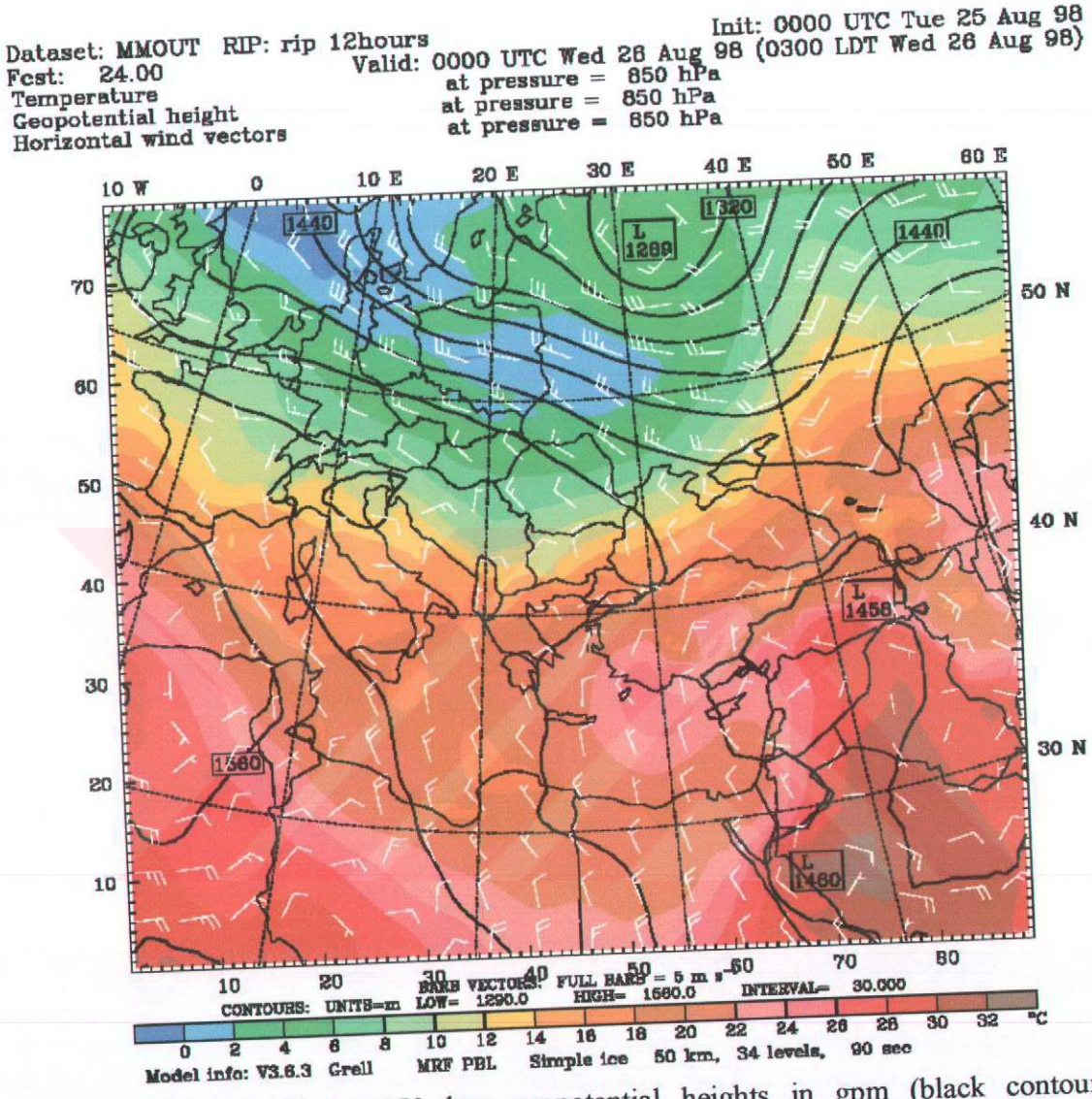

Figure C.12: Predicted 850 hpa geopotential heights in gpm (black contours), temperature in °C (color shading) and horizontal wind velocity (white vectors). 24 hours forecast for 26 – 08 – 1998, 0000 UTC.

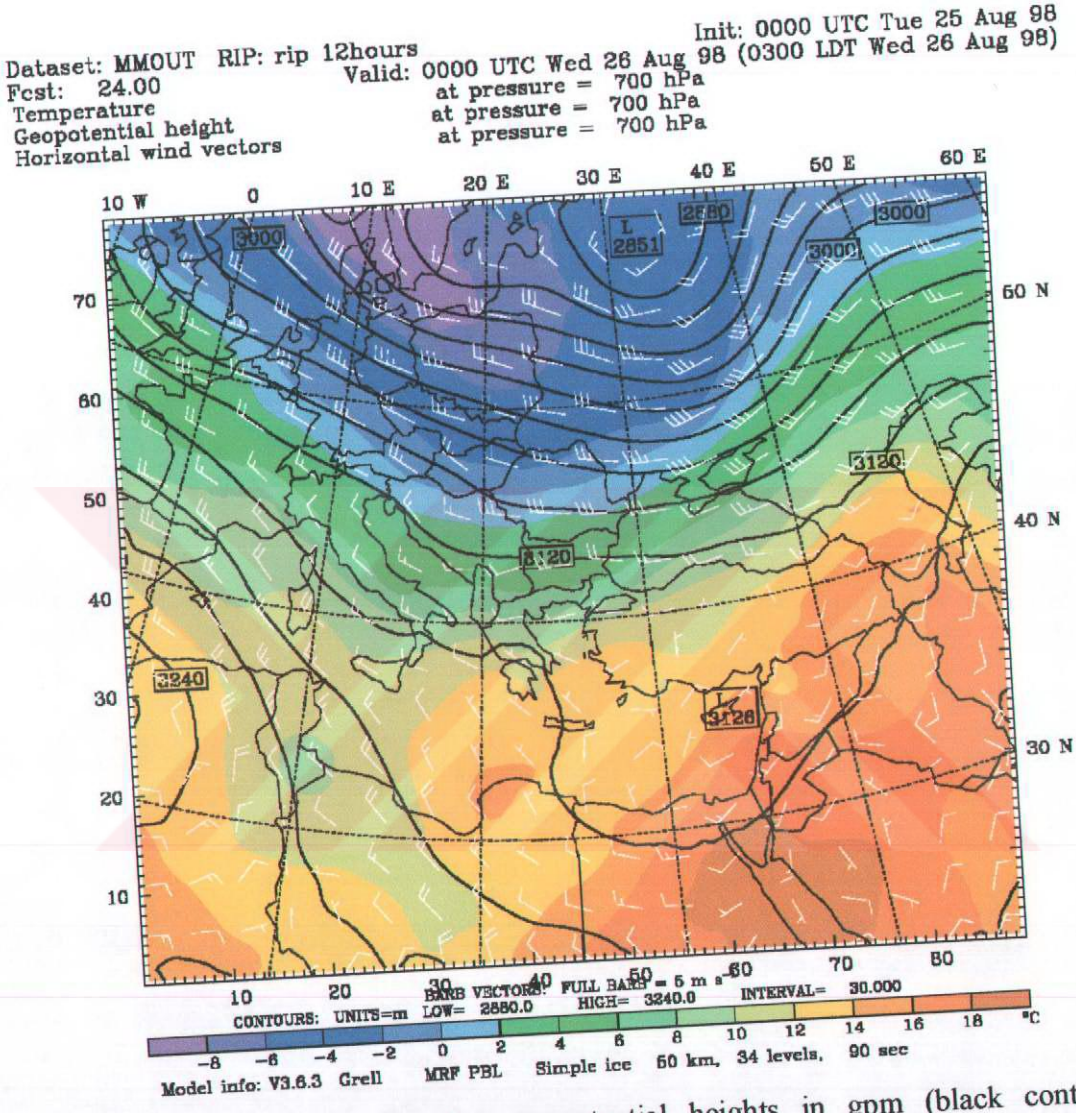

Figure C.13: Predicted 700 hpa geopotential heights in gpm (black contours), temperature in °C (color shading) and horizontal wind velocity (white vectors). 24 hours forecast for 26 – 08 – 1998, 0000 UTC.

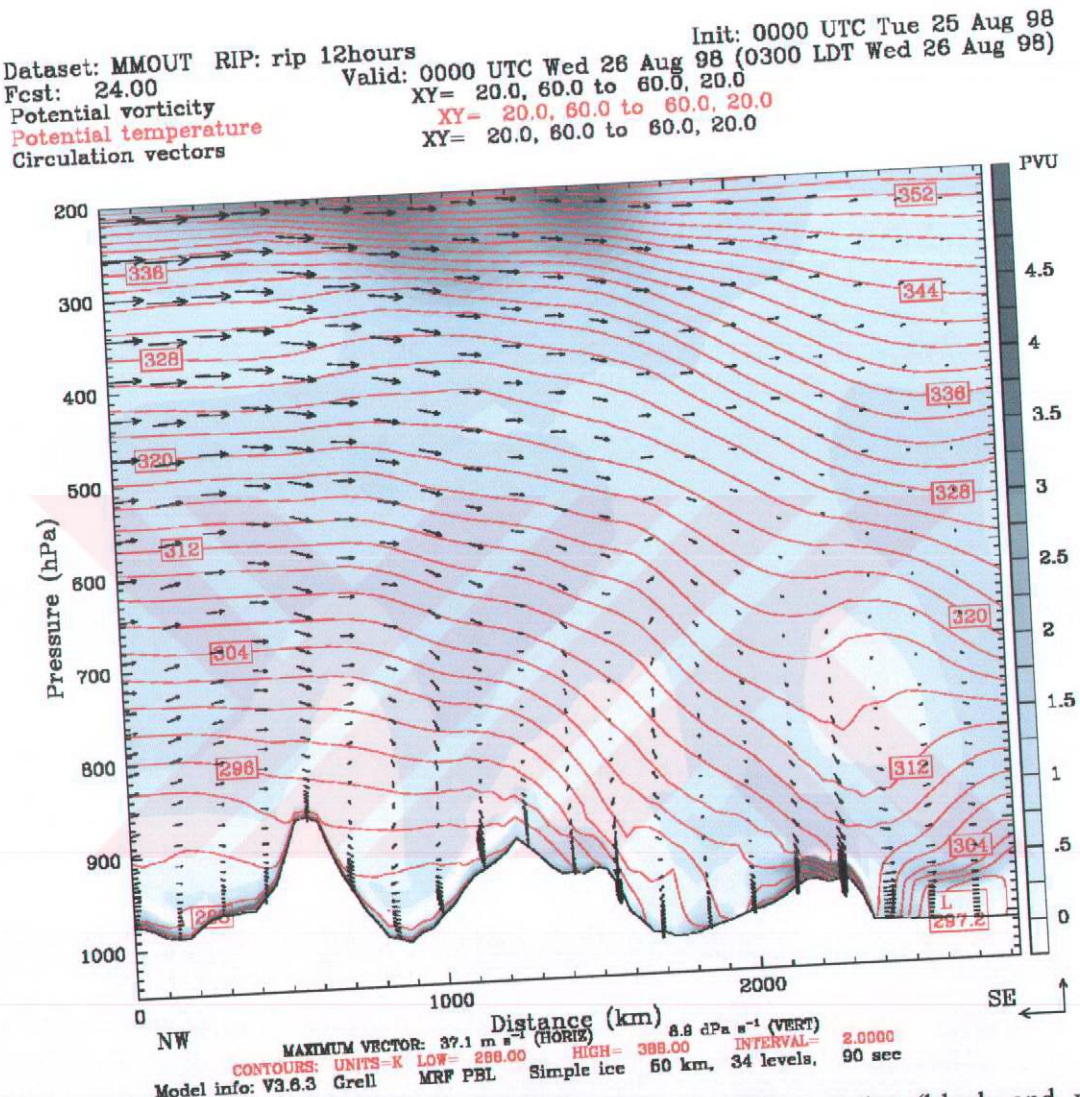

Figure C.14: A vertical cross section of the potential vorticity (black and white shading), potential temperatures (red lines) and the wind circulation (black vectors) predicted over a NW – SE line of length around 3000 km from the south of Poland to Cyprus. 24 hours forecast for 26– 08 – 1998, 0000 UTC.

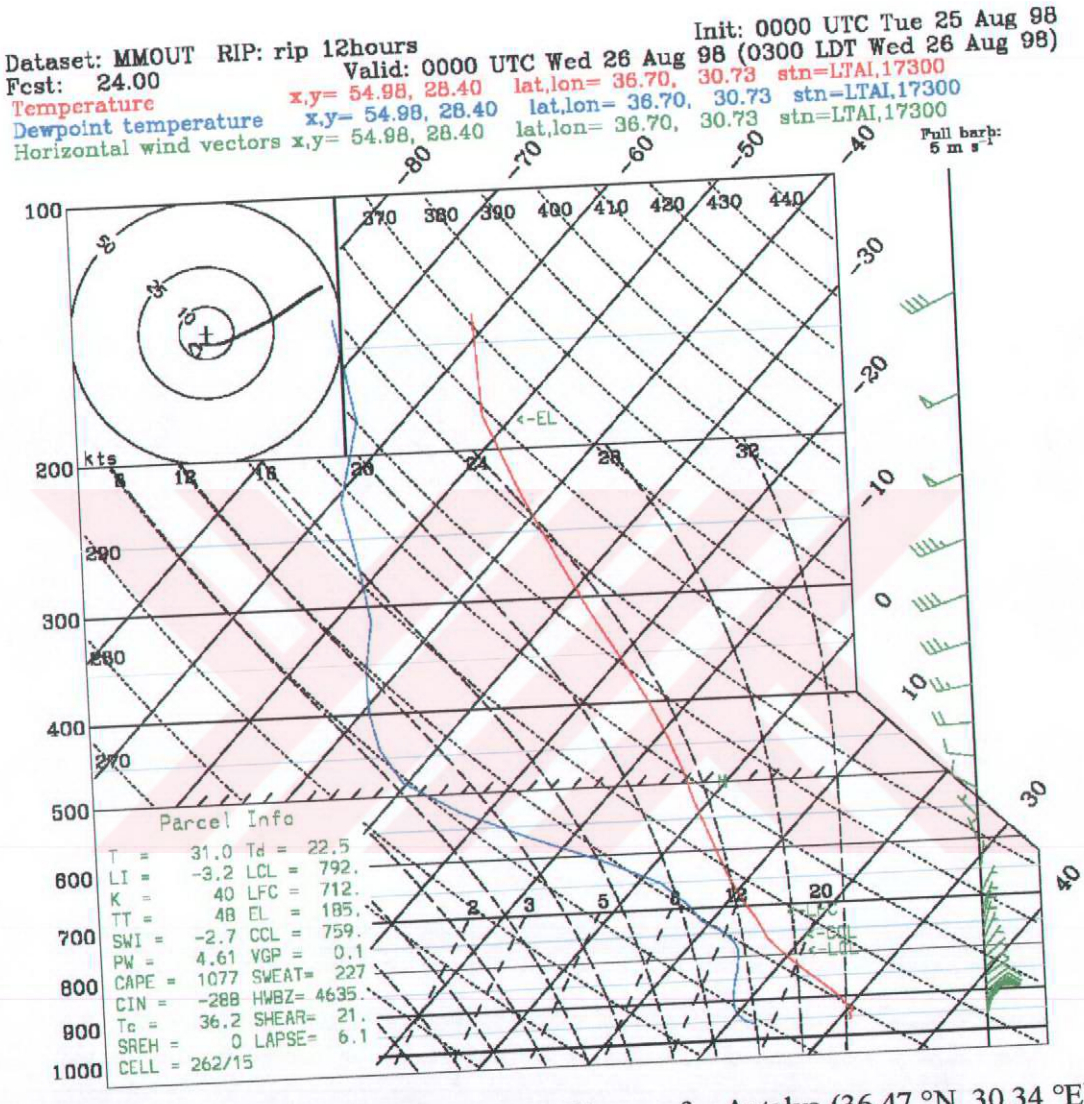

Figure C.15: An estimated Skew – T Plot diagram for Antalya (36.47 °N, 30.34 °E). 24 hours forecast for 26 – 08 – 1998, 0000 UTC.

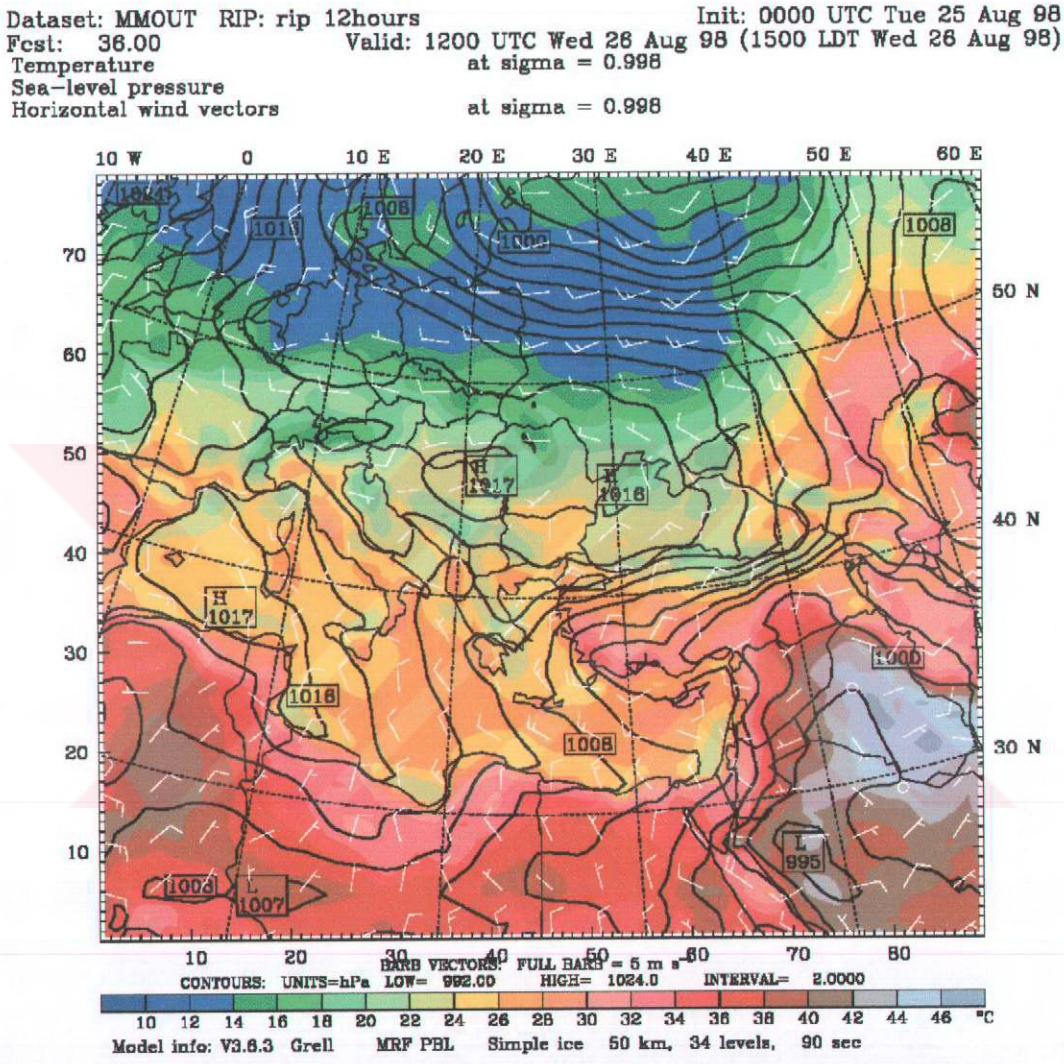

Figure C.16: Predicted Sea level pressure in hpa (black contours), temperature in °C (color shading) and horizontal wind velocity (white vectors). 36 hours forecast for 26 – 08 – 1998, 1200 UTC. (The temperature and the wind vectors are at sigma level 998).

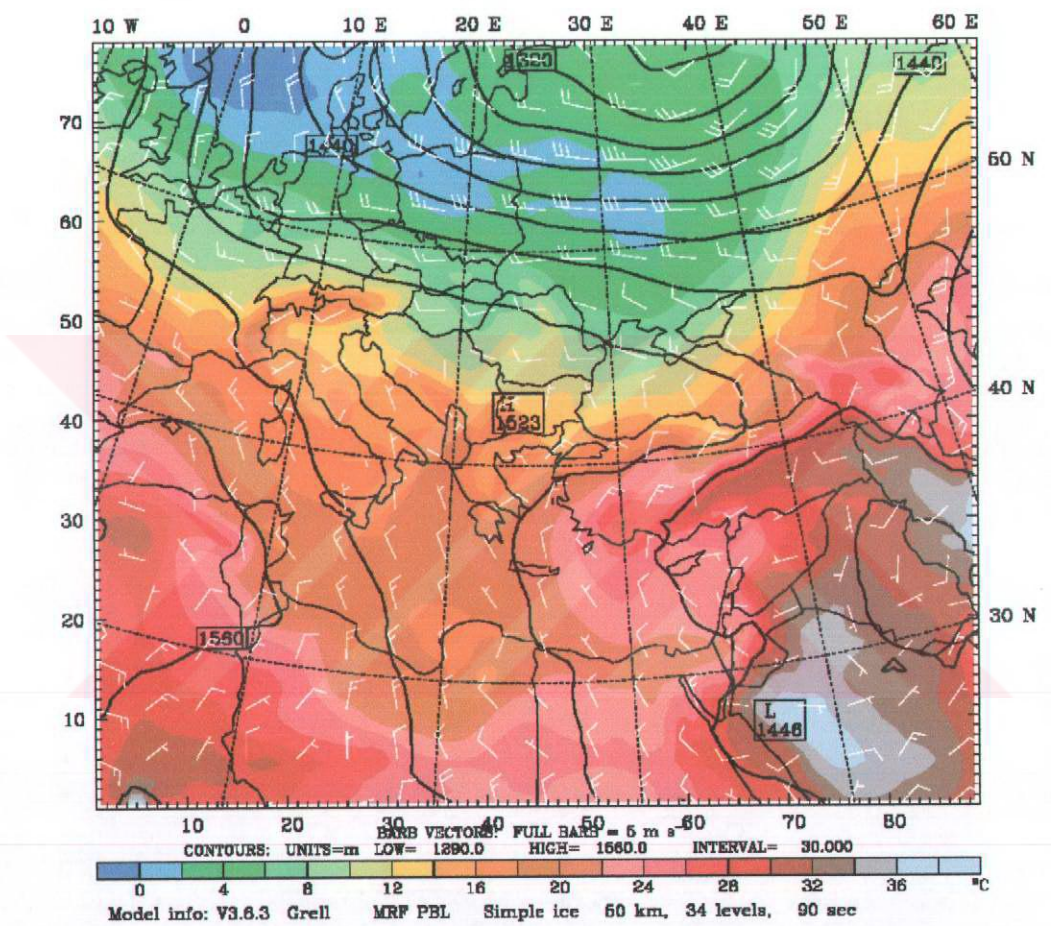

Figure C.17: Predicted 850 hpa geopotential heights in gpm (black contours), temperature in °C (color shading) and horizontal wind velocity (white vectors). 36 hours forecast for 26 – 08 – 1998, 1200 UTC.

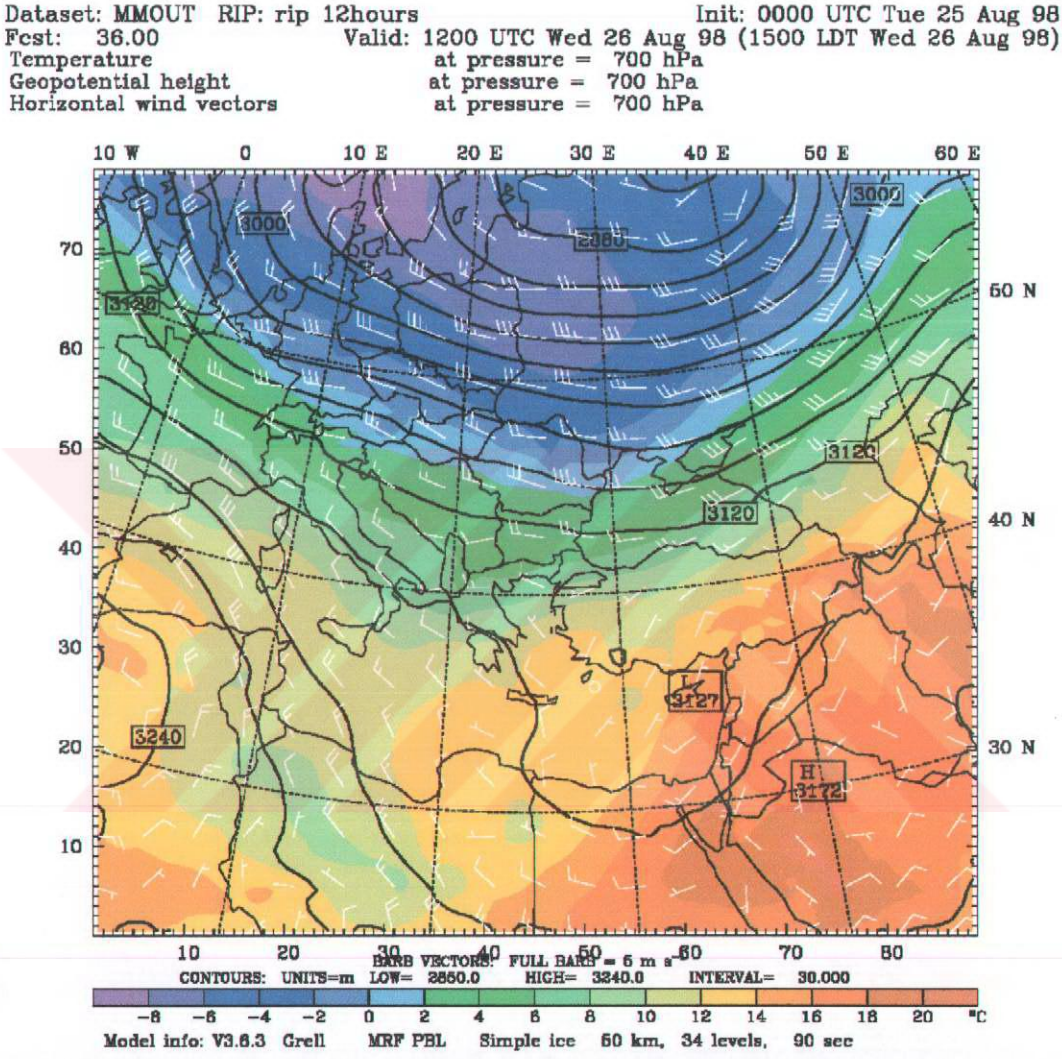

Figure C.18: Predicted 700 hpa geopotential heights in gpm (black contours), temperature in °C (color shading) and horizontal wind velocity (white vectors). 36 hours forecast for 26 – 08 – 1998, 1200 UTC.

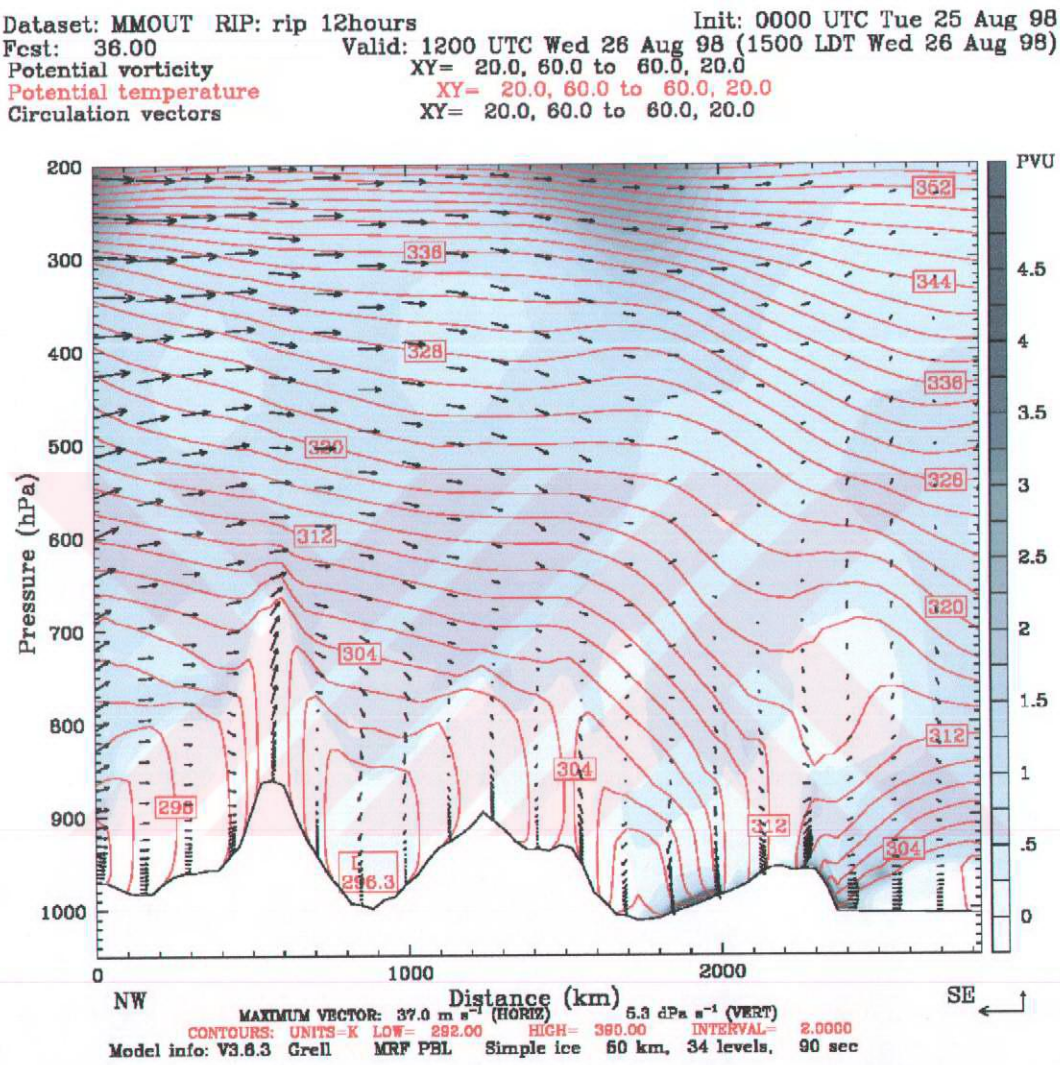

Figure C.19: A vertical cross section of the potential vorticity (black and white shading), potential temperatures (red lines) and the wind circulation (black vectors) predicted over a NW – SE line of length around 3000 km from the south of Poland to Cyprus. 36 hours forecast for 26 – 08 – 1998, 1200 UTC.

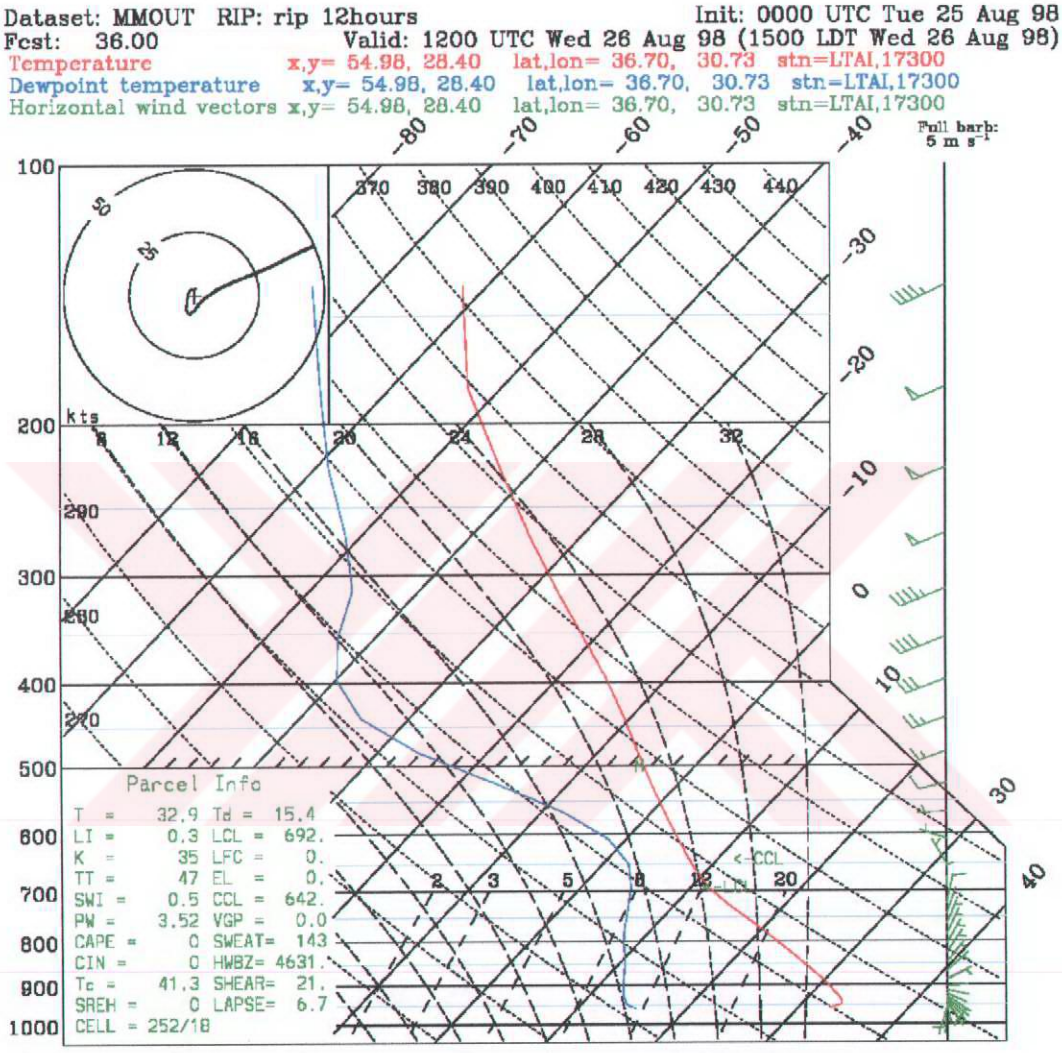

Figure C.20: An estimated Skew – T Plot diagram for Antalya (36.47 °N, 30.34 °E). 36 hours forecast for 26 – 08 – 1998, 1200 UTC.

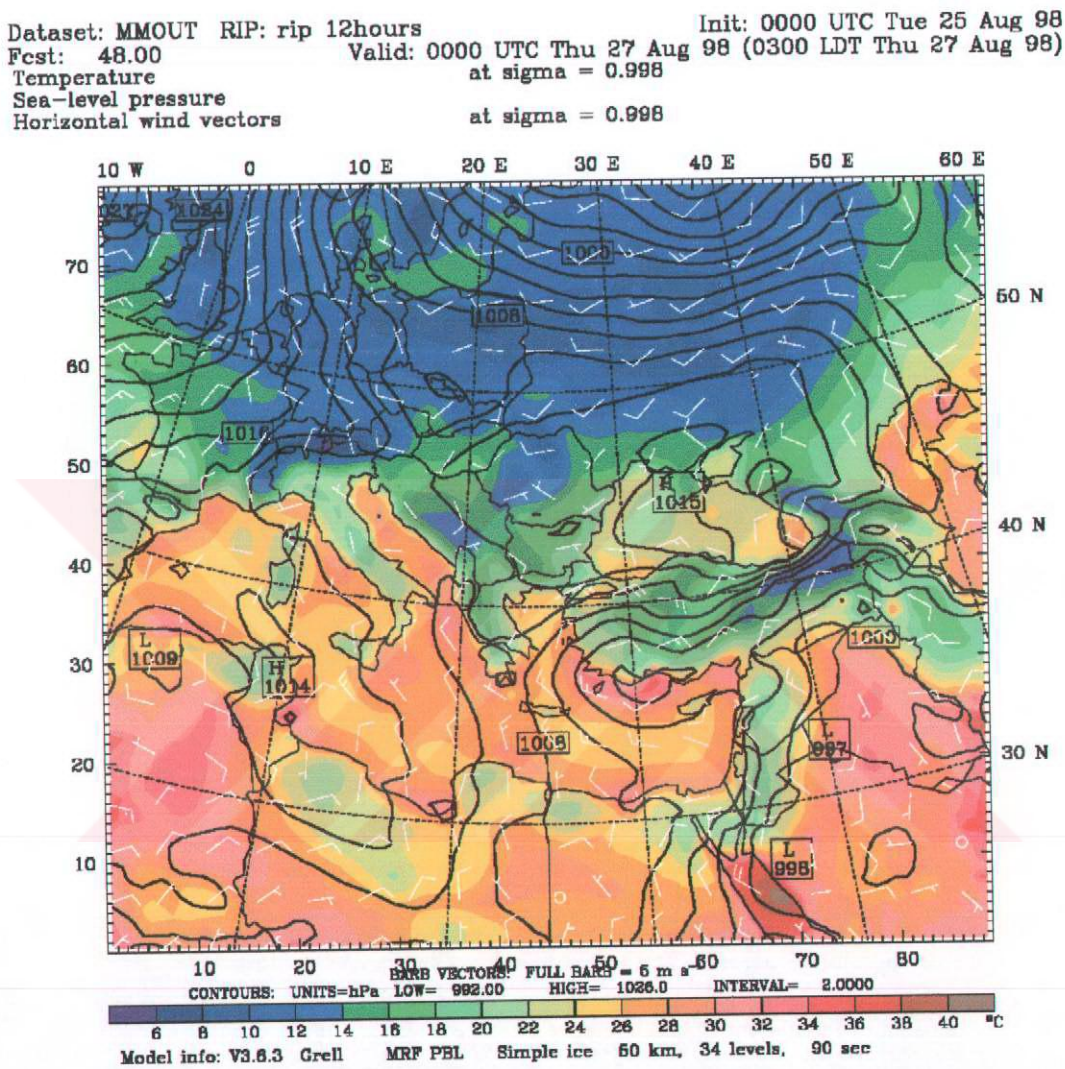

Figure C.21: Predicted Sea level pressure in hpa (black contours), temperature in °C (color shading) and horizontal wind velocity (white vectors). 48 hours forecast for 27 – 08 – 1998, 0000 UTC. (The temperature and the wind vectors are at sigma level 998).

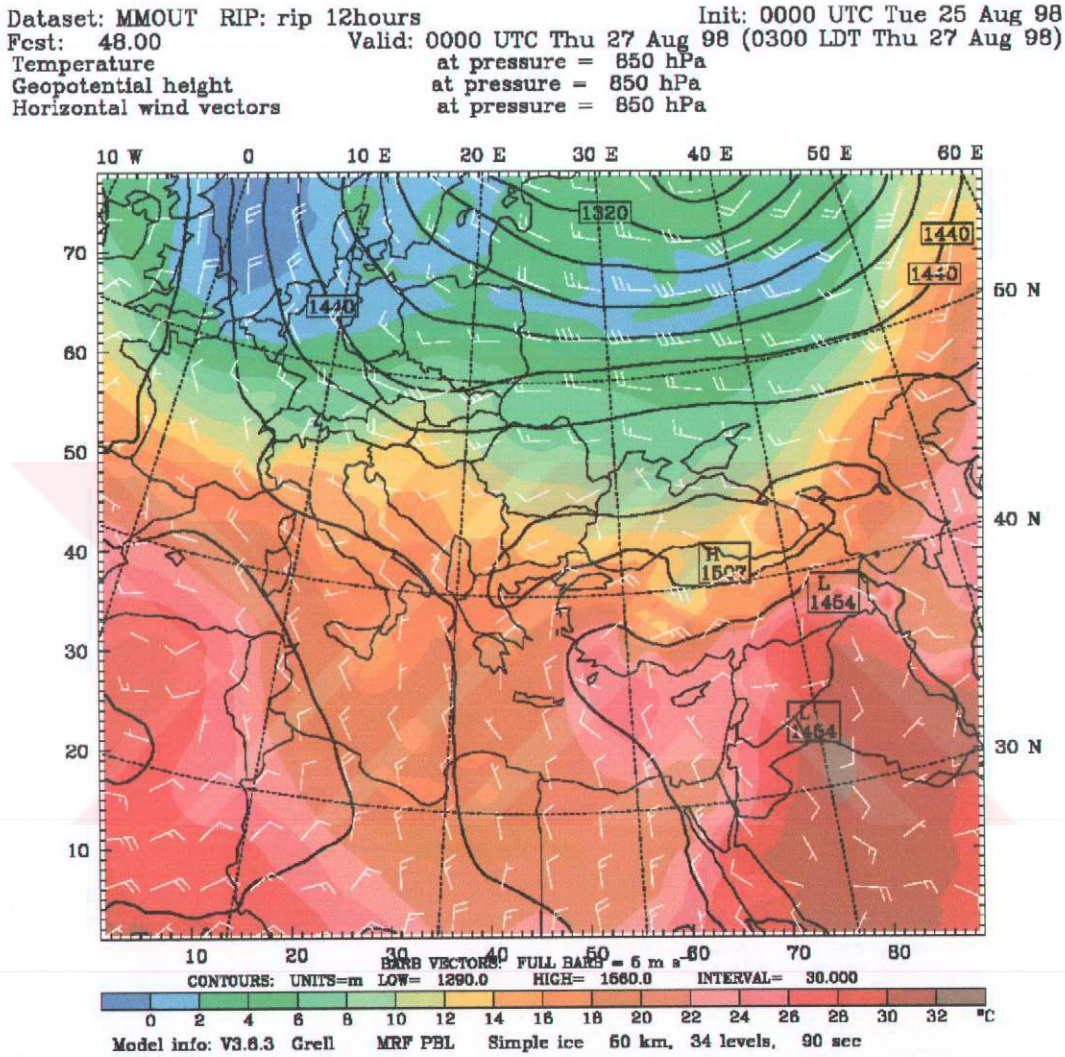

Figure C.22: Predicted 850 hpa geopotential heights in gpm (black contours), temperature in °C (color shading) and horizontal wind velocity (white vectors). 48 hours forecast for 27 – 08 – 1998, 0000 UTC.

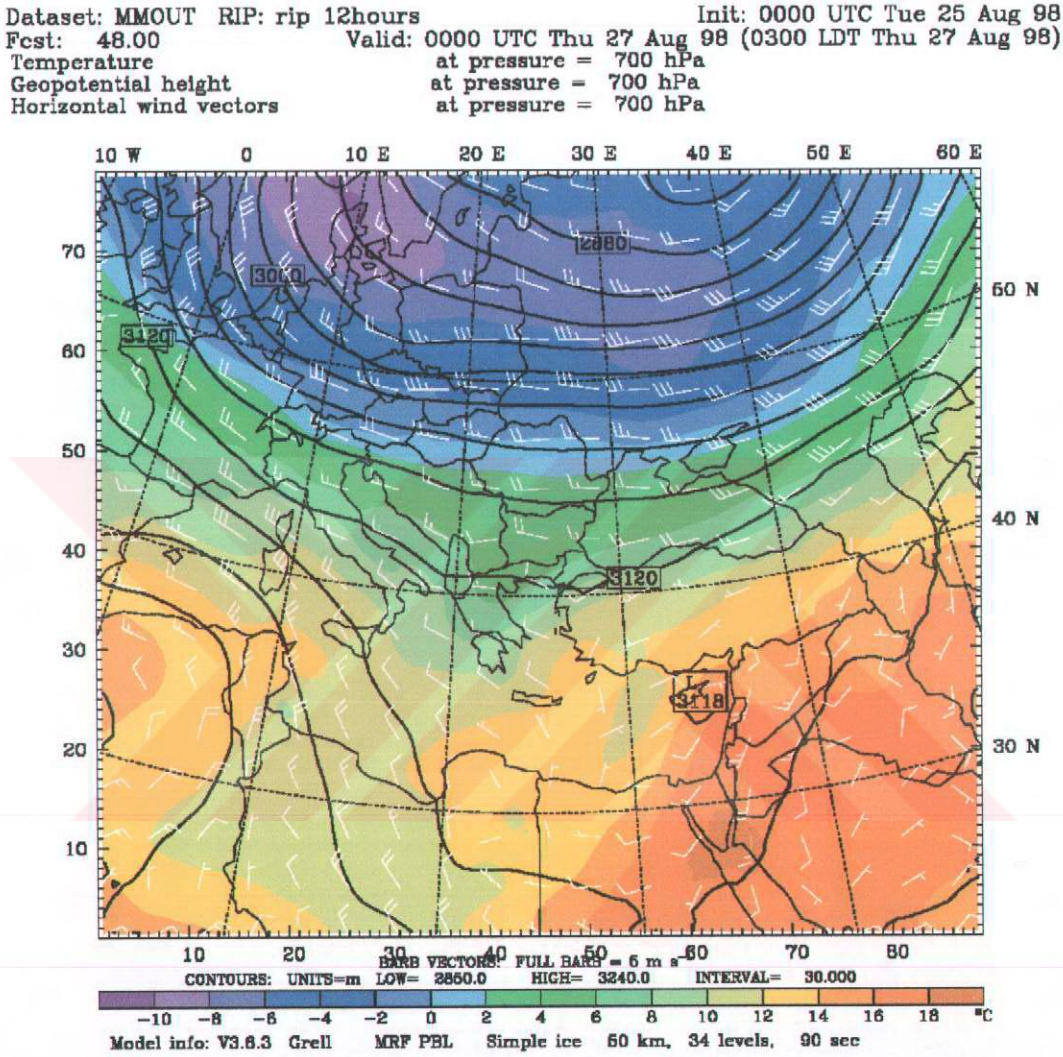

Figure C.23: Predicted 700 hpa geopotential heights in gpm (black contours), temperature in °C (color shading) and horizontal wind velocity (white vectors). 48 hours forecast for 27 – 08 – 1998, 0000 UTC.

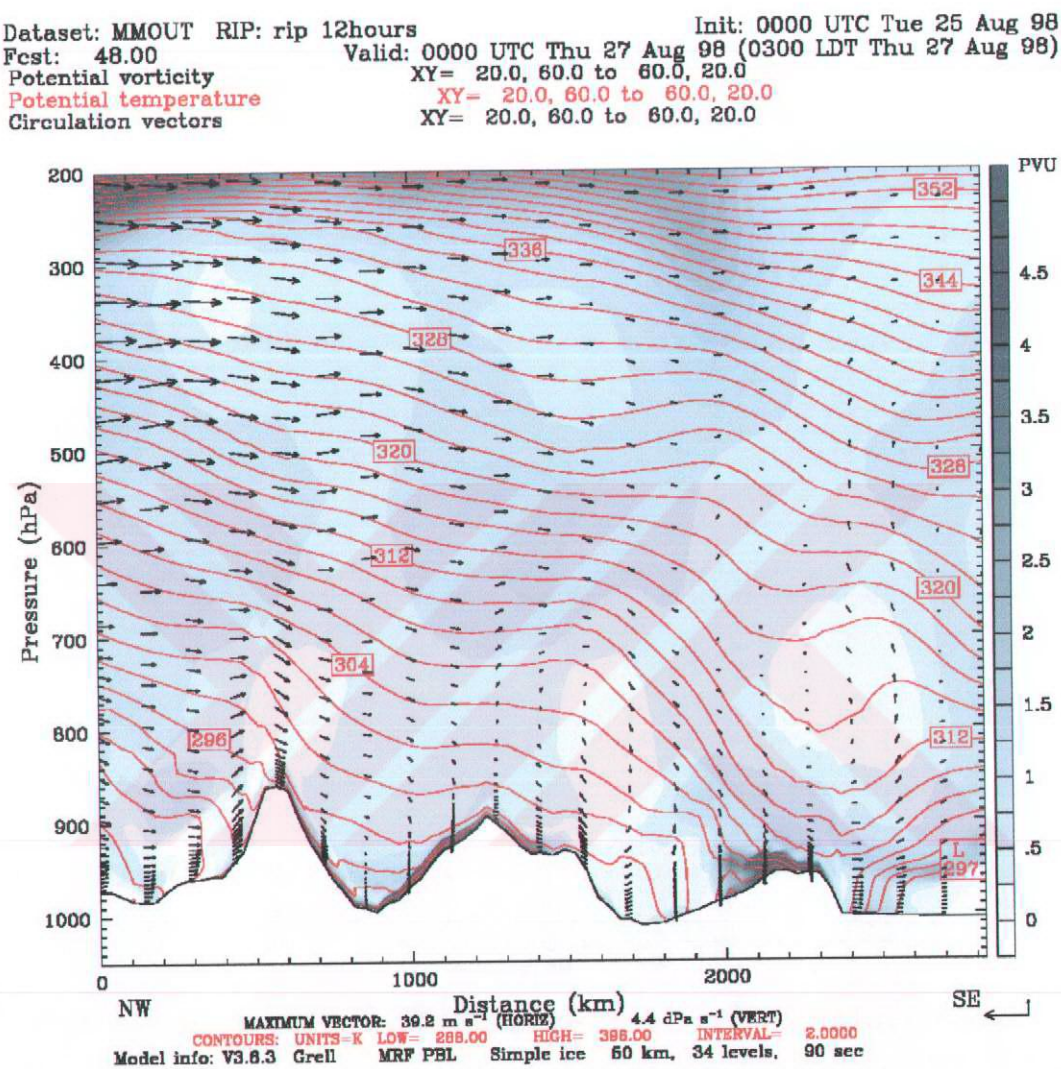

Figure C. 24: A vertical cross section of the potential vorticity (black and white shading), potential temperatures (red lines) and the wind circulation (black vectors) predicted over a NW – SE line of length around 3000 km from the south of Poland to Cyprus. 48 hours forecast for 27 – 08 – 1998, 0000 UTC.

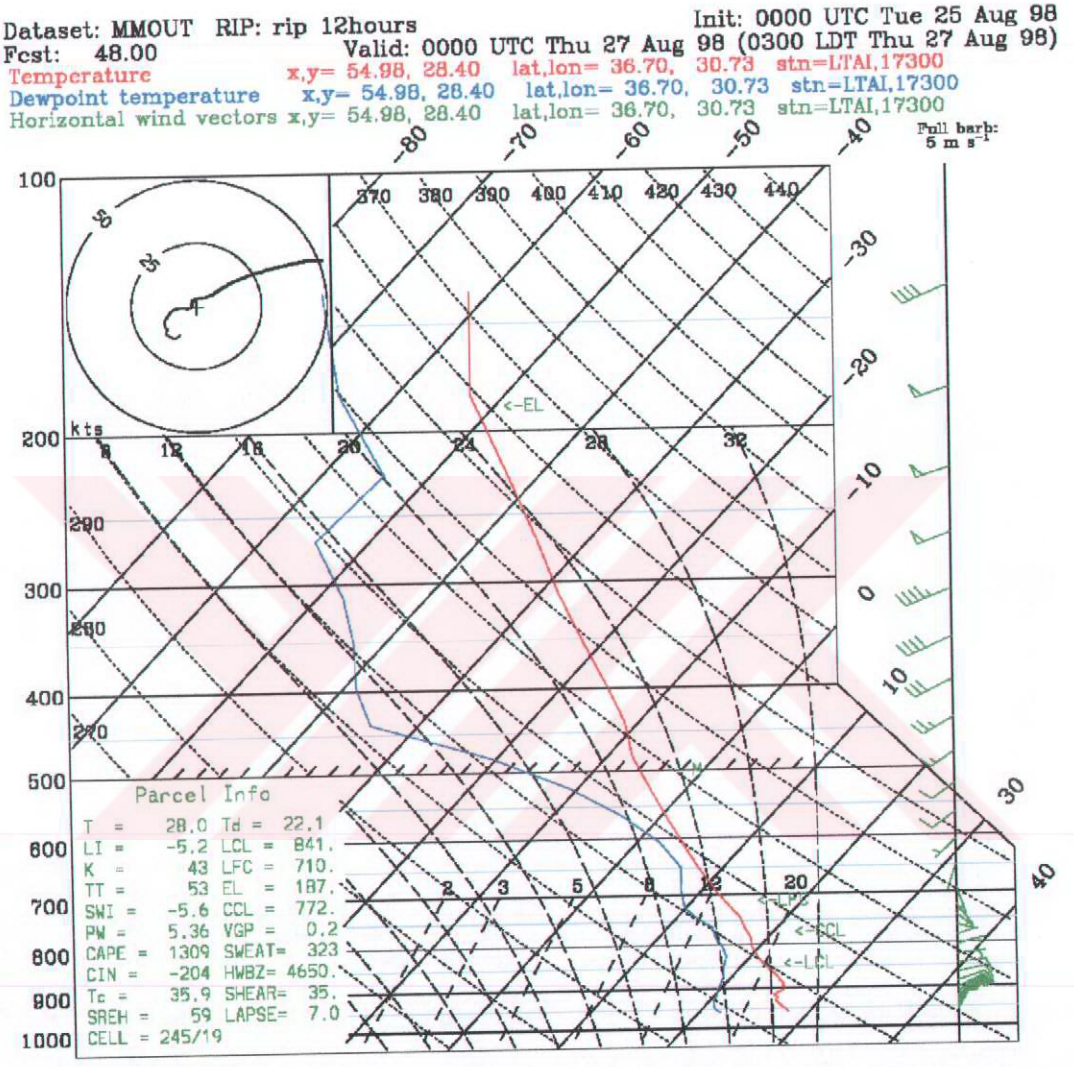

Figure C.25: An estimated Skew – T Plot diagram for Antalya (36.47 °N, 30.34 °E). 48 hours forecast for 27 – 08 – 1998, 0000 UTC.

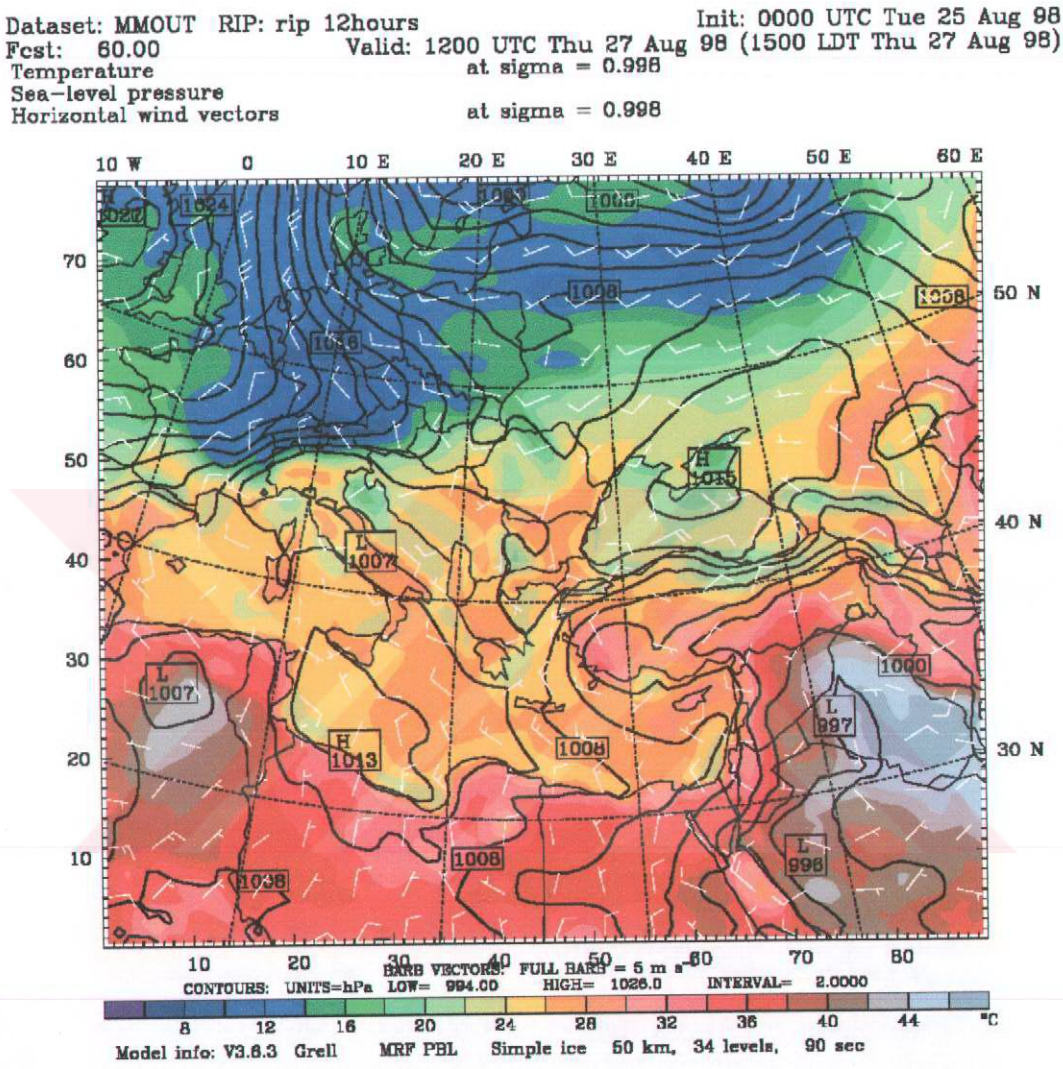

Figure C.26: Predicted Sea level pressure in hpa (black contours), temperature in °C (color shading) and horizontal wind velocity (white vectors). 60 hours forecast for 27 – 08 – 1998, 1200 UTC. (The temperature and the wind vectors are at sigma level 998).

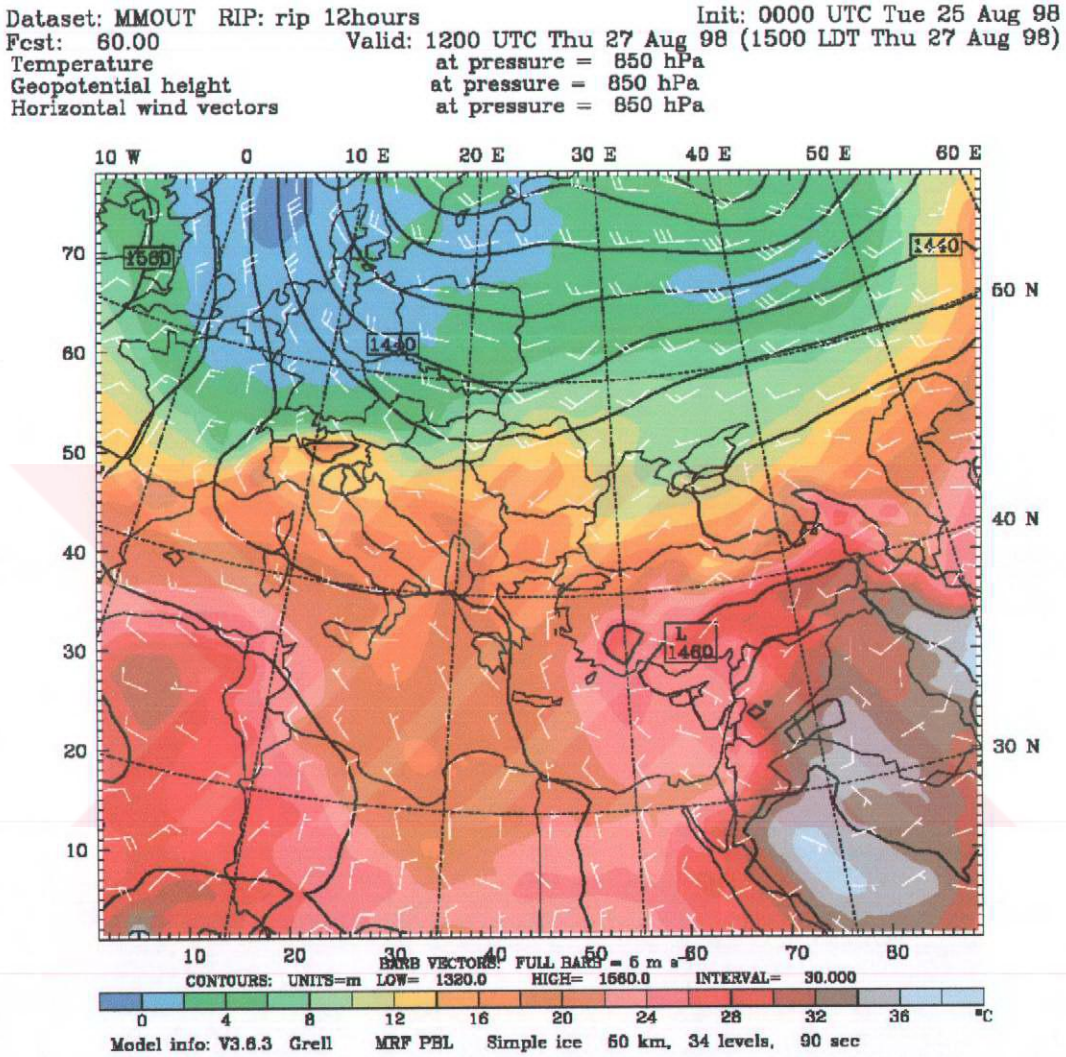

Figure C.27: Predicted 850 hpa geopotential heights in gpm (black contours), temperature in °C (color shading) and horizontal wind velocity (white vectors). 60 hours forecast for 27 – 08 – 1998, 1200 UTC.

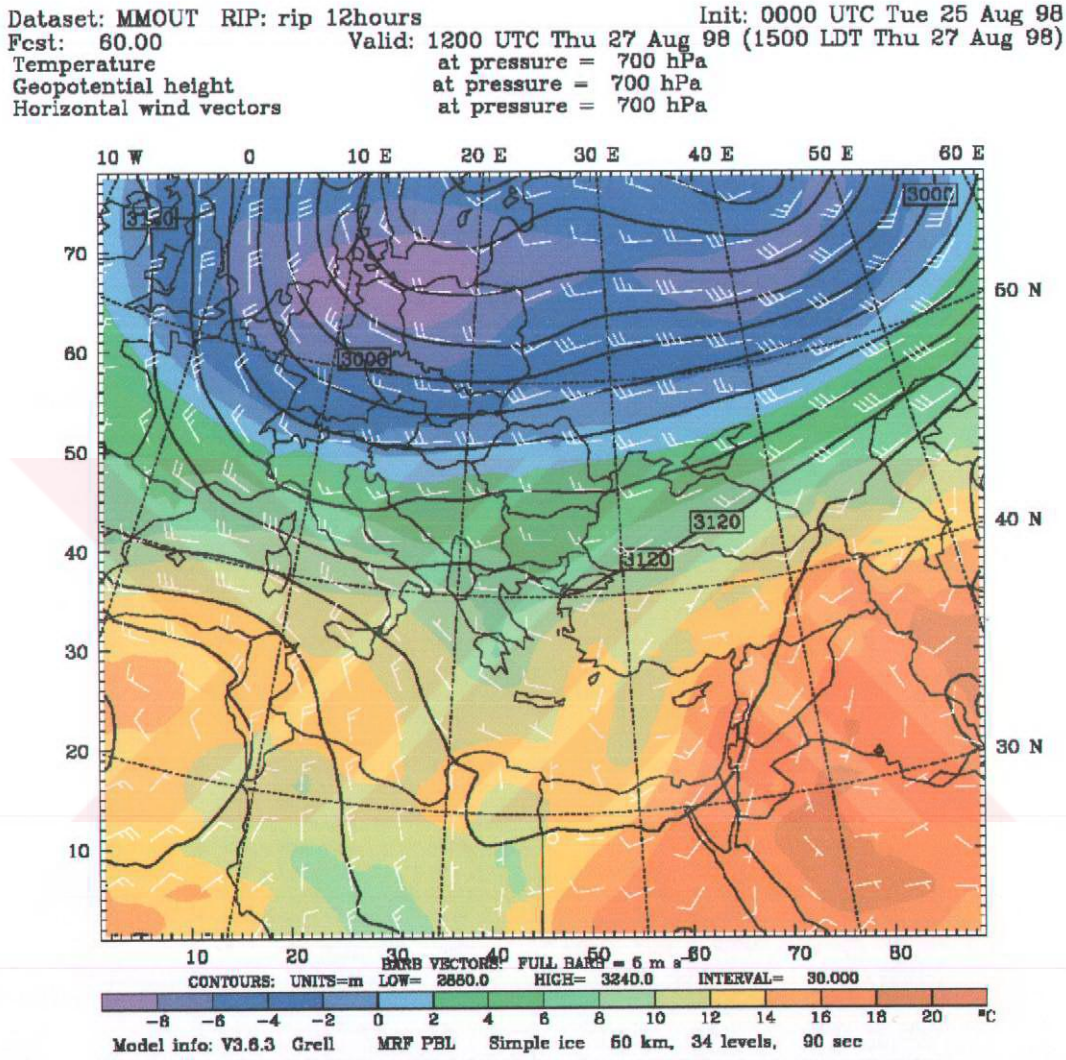

Figure C.28: Predicted 700 hpa geopotential heights in gpm (black contours), temperature in °C (color shading) and horizontal wind velocity (white vectors). 60 hours forecast for 27 – 08 – 1998, 1200 UTC.

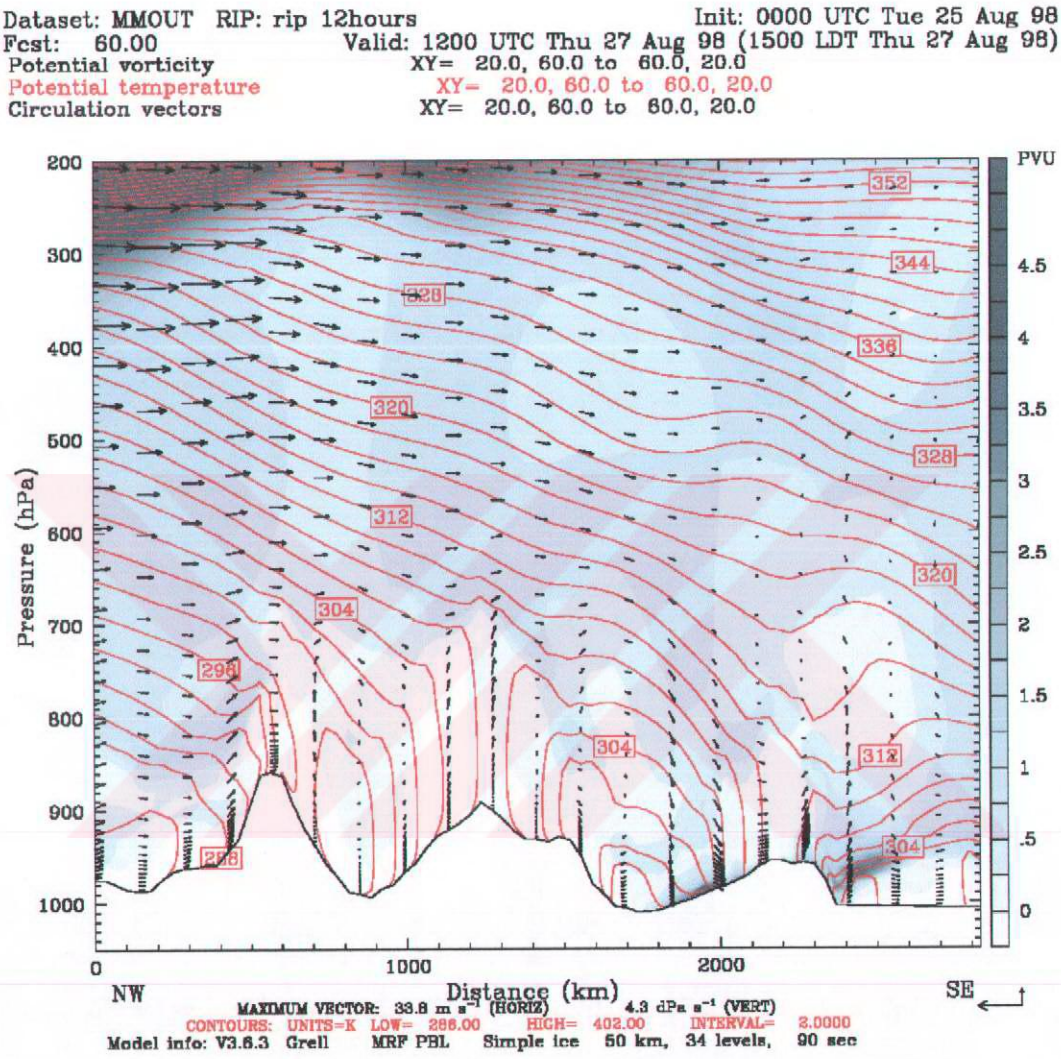

Figure C.29: A vertical cross section of the potential vorticity (black and white shading), potential temperatures (red lines) and the wind circulation (black vectors) predicted over a NW – SE line of length around 3000 km from the south of Poland to Cyprus. 60 hours forecast for 27 – 08 – 1998, 1200 UTC.

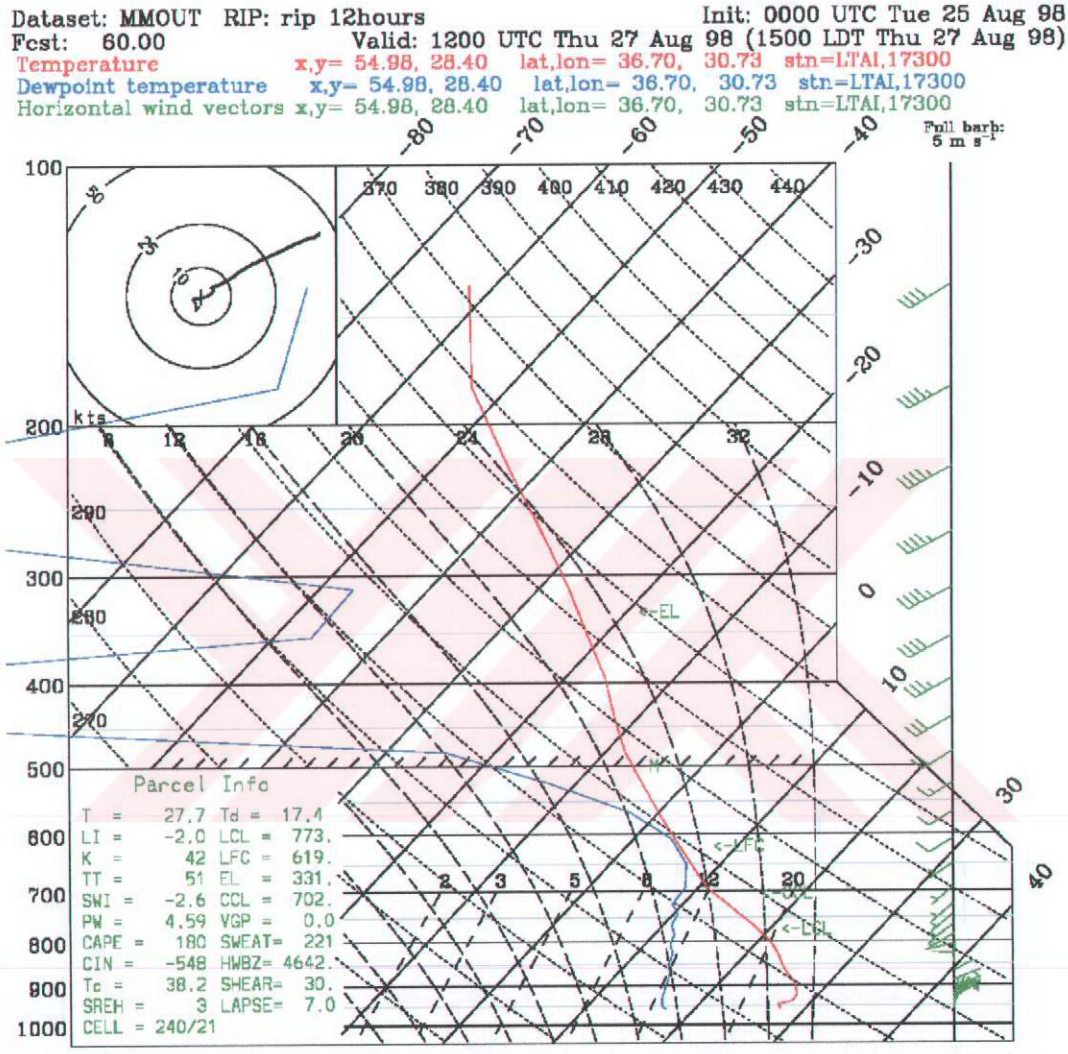

Figure C.30: An estimated Skew – T Plot diagram for Antalya (36.47 °N, 30.34 °E). 60 hours forecast for 27 – 08 – 1998, 1200 UTC.

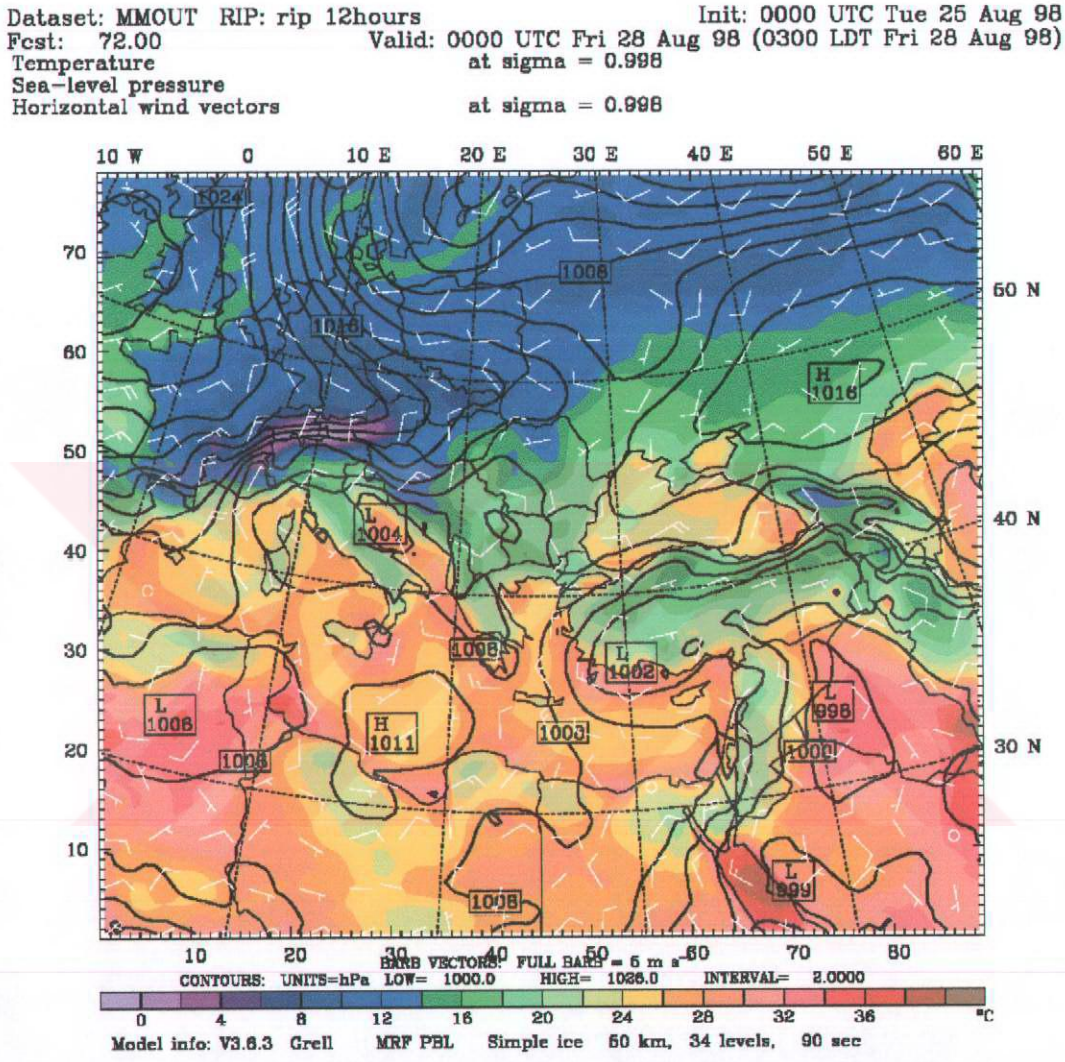

Figure C.31: Predicted Sea level pressure in hpa (black contours), temperature in °C (color shading) and horizontal wind velocity (white vectors). 72 hours forecast for 28 – 08 – 1998, 0000 UTC. (The temperature and the wind vectors are at sigma level 998).

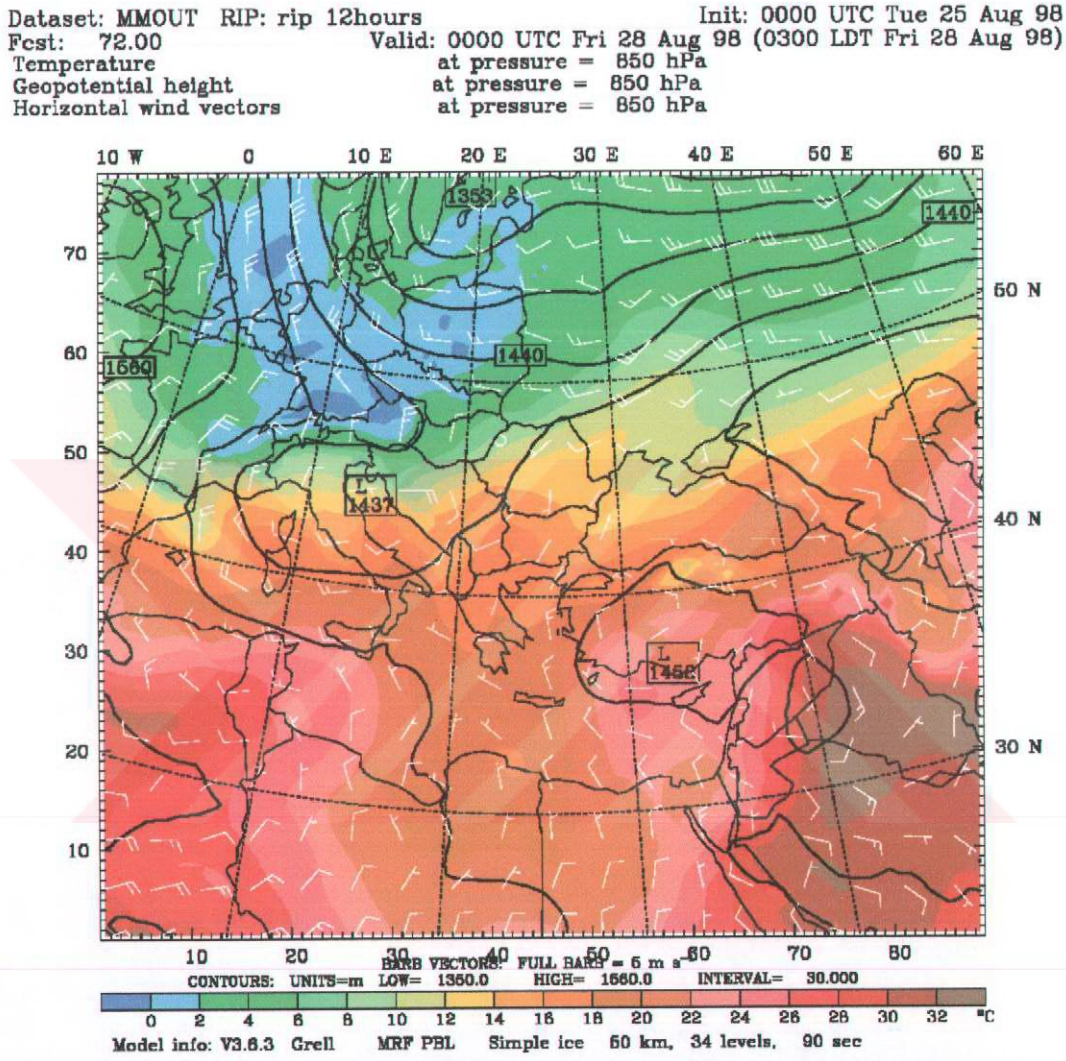

Figure C.32: Predicted 850 hpa geopotential heights in gpm (black contours), temperature in °C (color shading) and horizontal wind velocity (white vectors). 72 hours forecast for 28 – 08 – 1998, 0000 UTC.

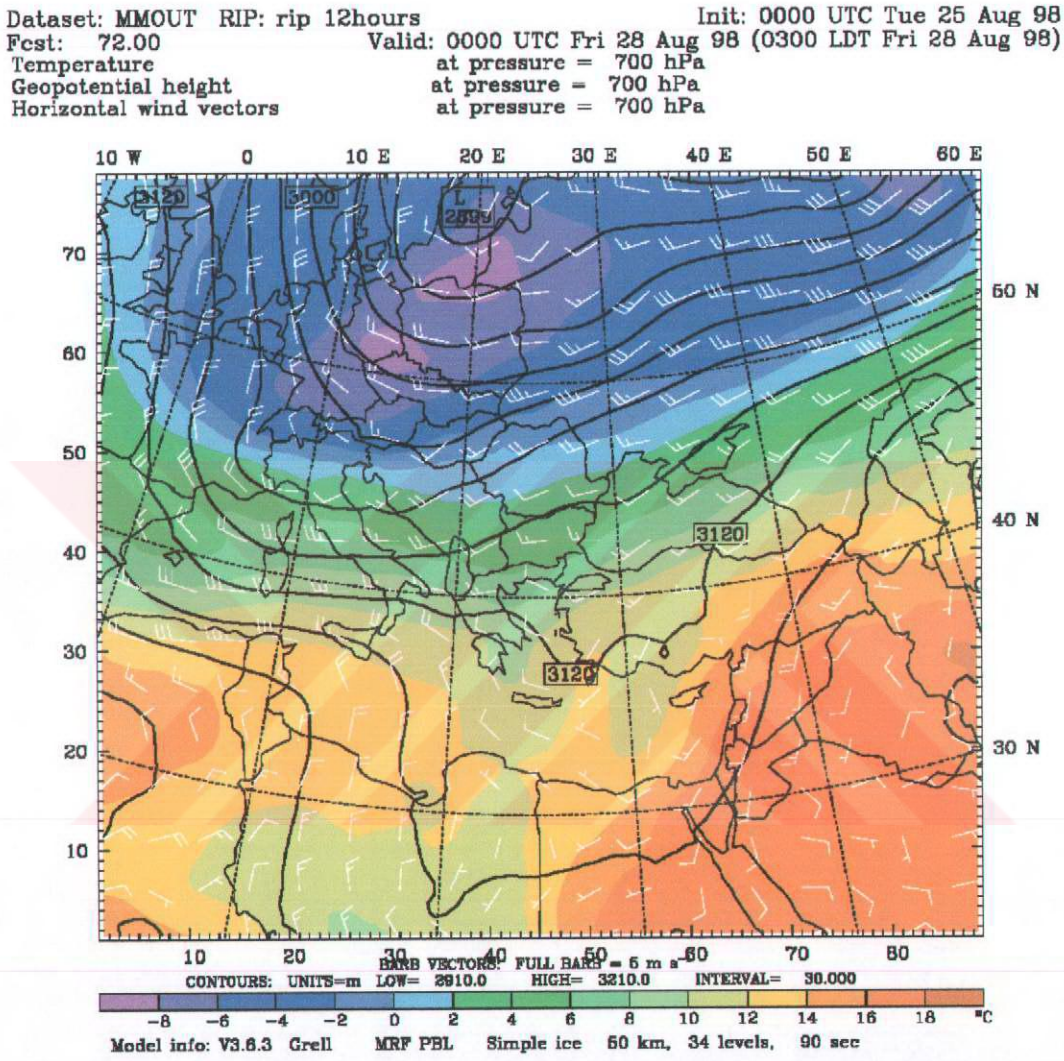

Figure C.33: Predicted 700 hpa geopotential heights in gpm (black contours), temperature in °C (color shading) and horizontal wind velocity (white vectors). 72 hours forecast for 28 – 08 – 1998, 0000 UTC.

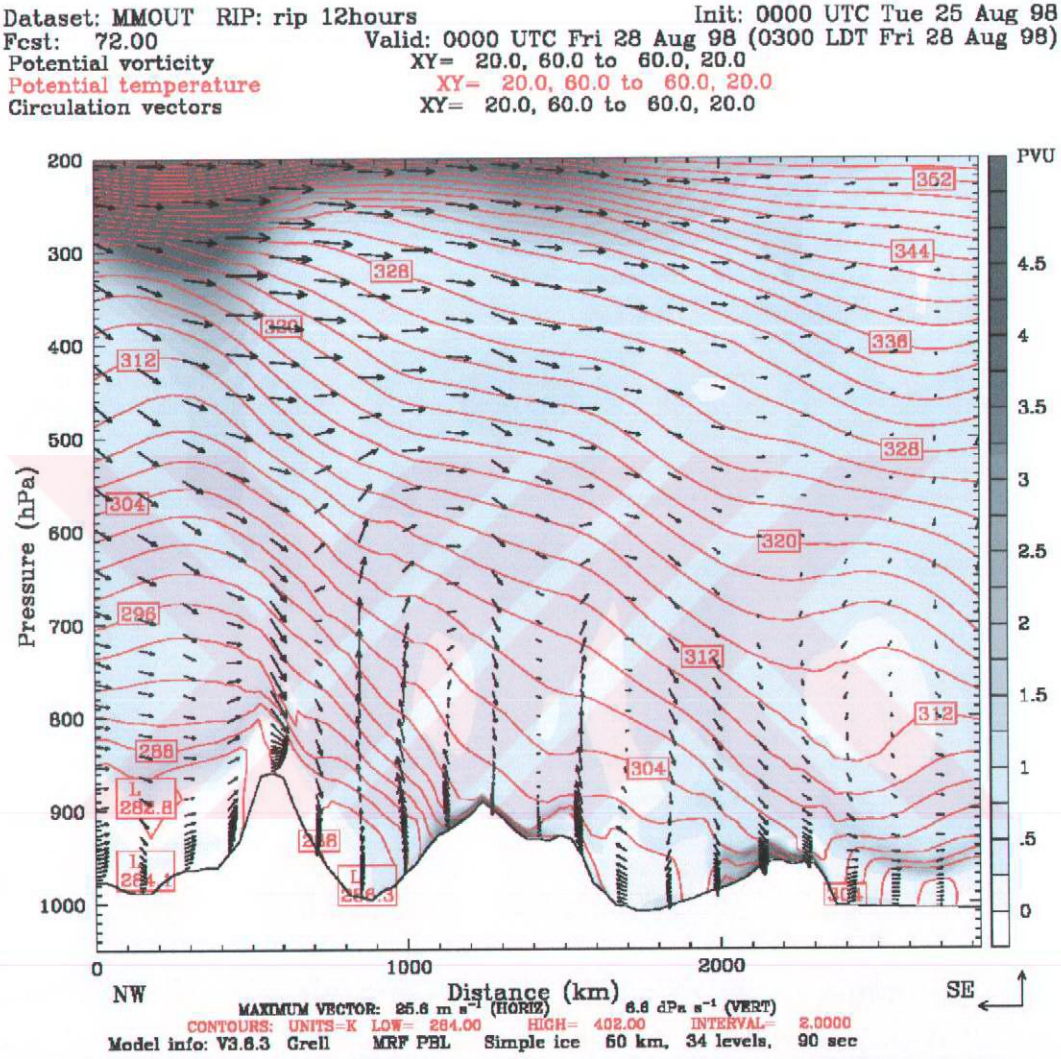

Figure C.34: A vertical cross section of the potential vorticity (black and white shading), potential temperatures (red lines) and the wind circulation (black vectors) predicted over a NW – SE line of length around 3000 km from the south of Poland to Cyprus. 72 hours forecast for 28 – 08 – 1998, 0000 UTC.

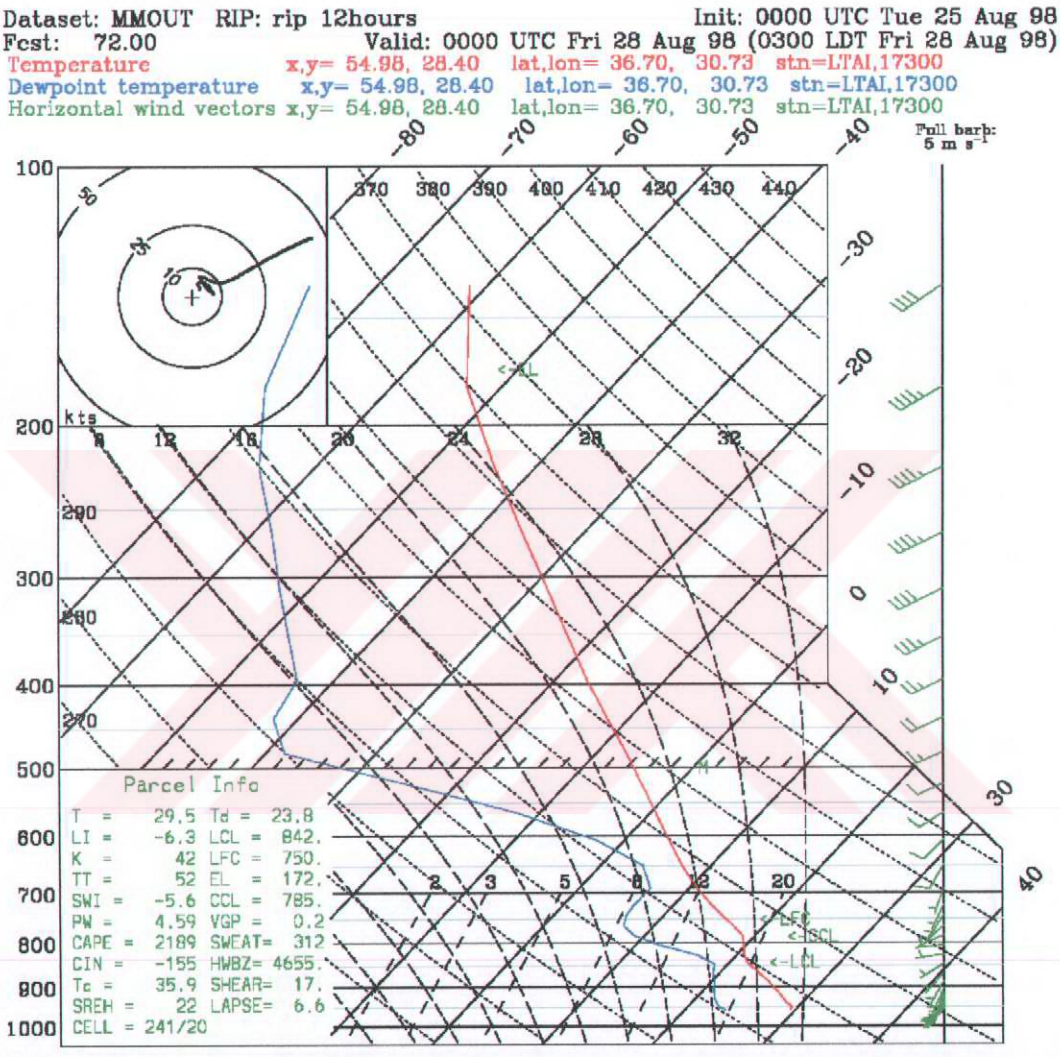

Figure C.35: An estimated Skew – T Plot diagram for Antalya (36.47 °N, 30.34 °E). 72 hours forecast for 28 – 08 – 1998, 0000 UTC.

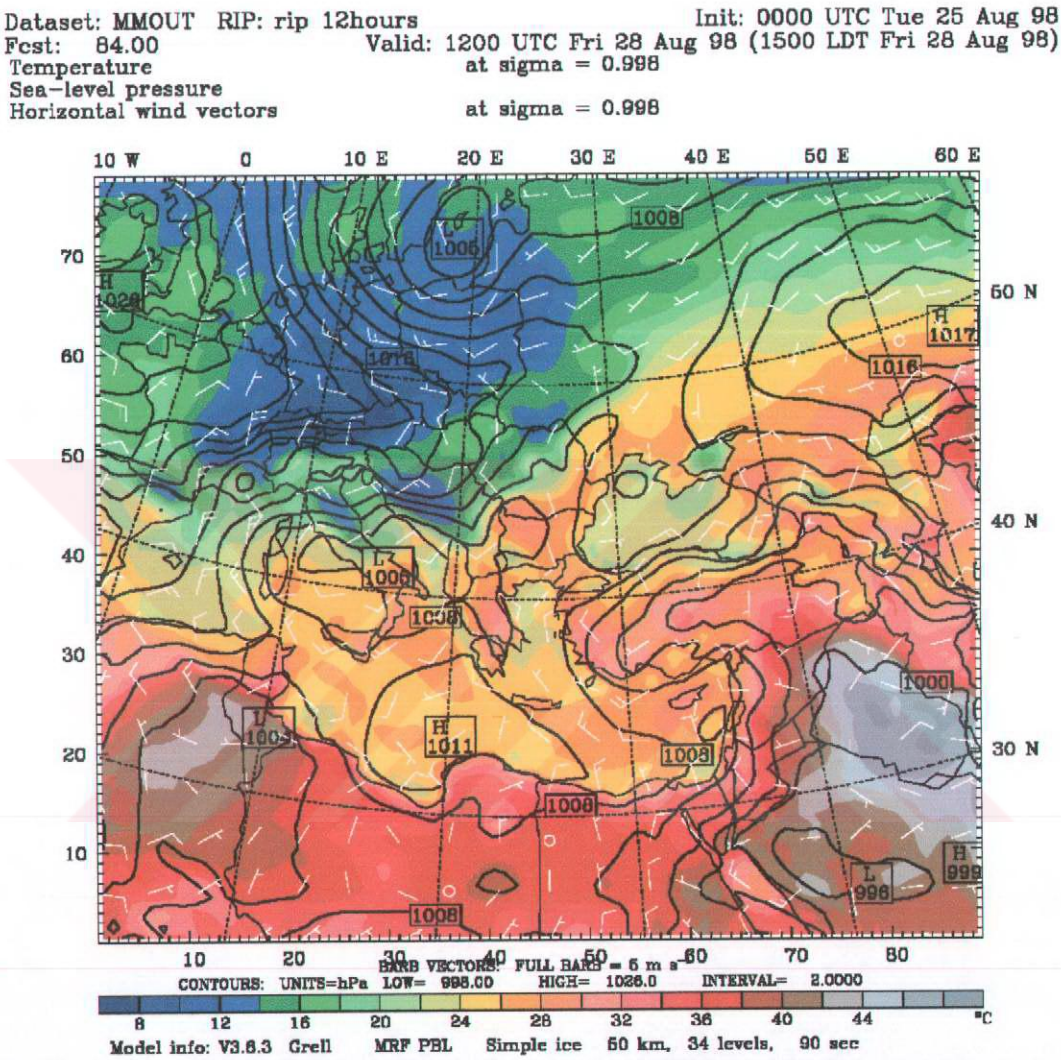

Figure C.36: Predicted Sea level pressure in hpa (black contours), temperature in °C (color shading) and horizontal wind velocity (white vectors). 84 hours forecast for 28 – 08 – 1998, 1200 UTC. (The temperature and the wind vectors are at sigma level 998).

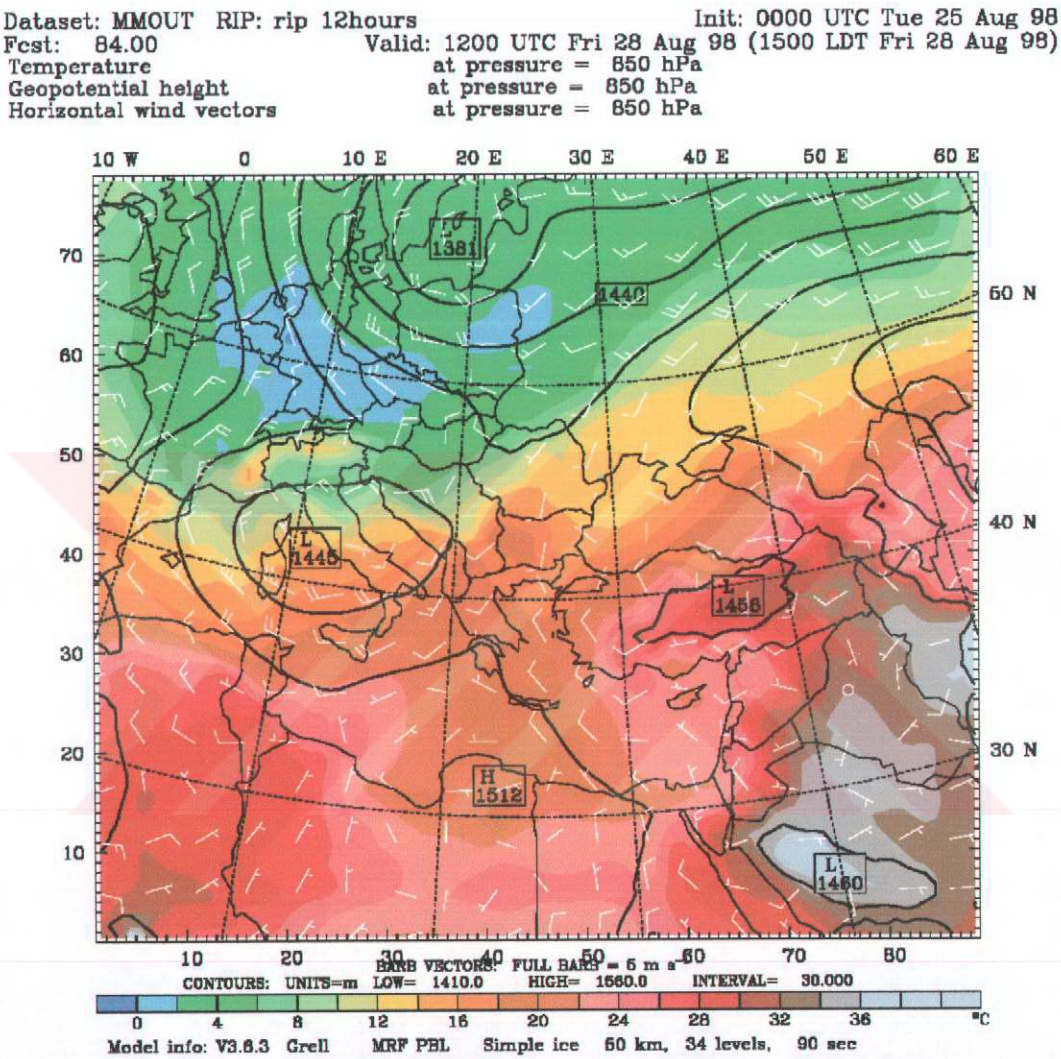

Figure C.37: Predicted 850 hpa geopotential heights in gpm (black contours), temperature in °C (color shading) and horizontal wind velocity (white vectors). 84 hours forecast for 28 – 08 – 1998, 1200 UTC.

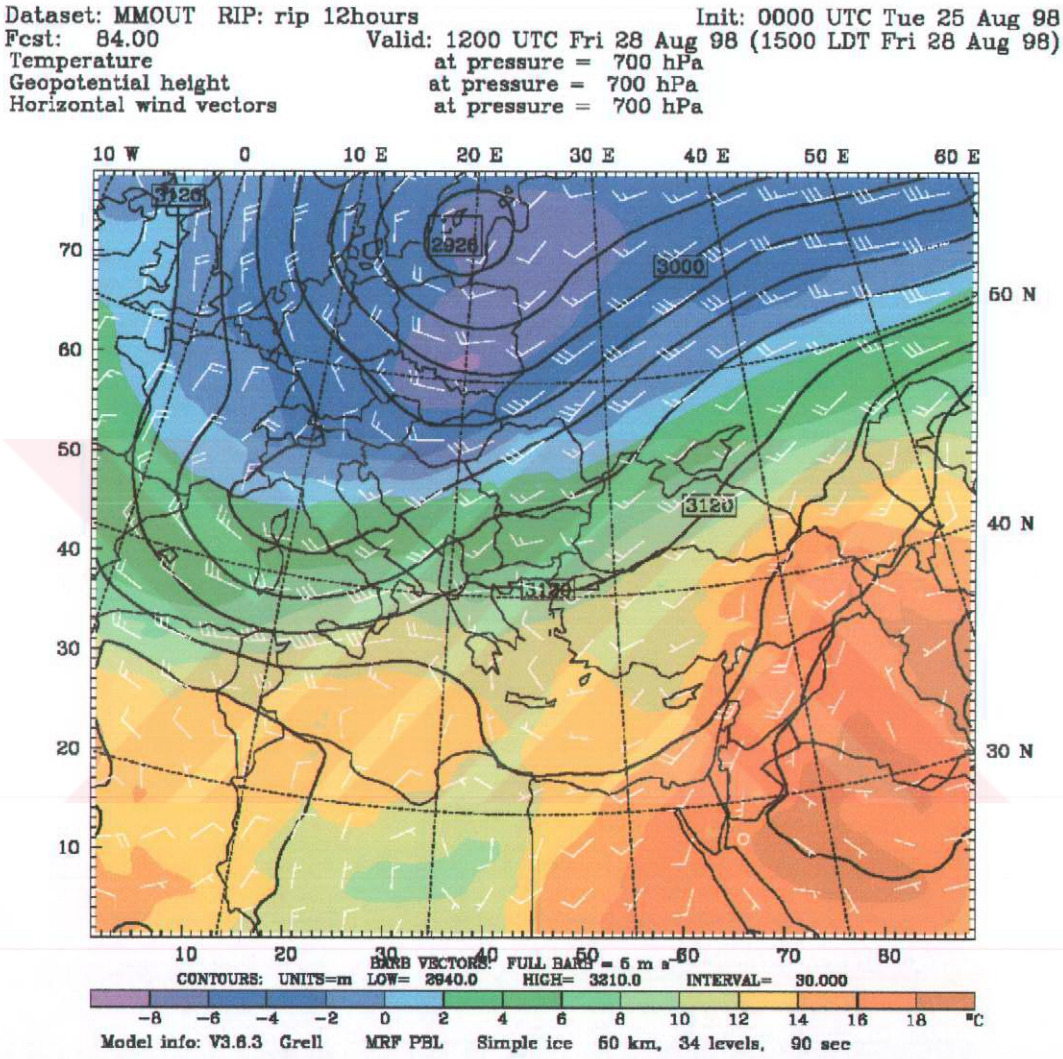

Figure C.38: Predicted 700 hpa geopotential heights in gpm (black contours), temperature in °C (color shading) and horizontal wind velocity (white vectors). 84 hours forecast for 28 – 08 – 1998, 1200 UTC.

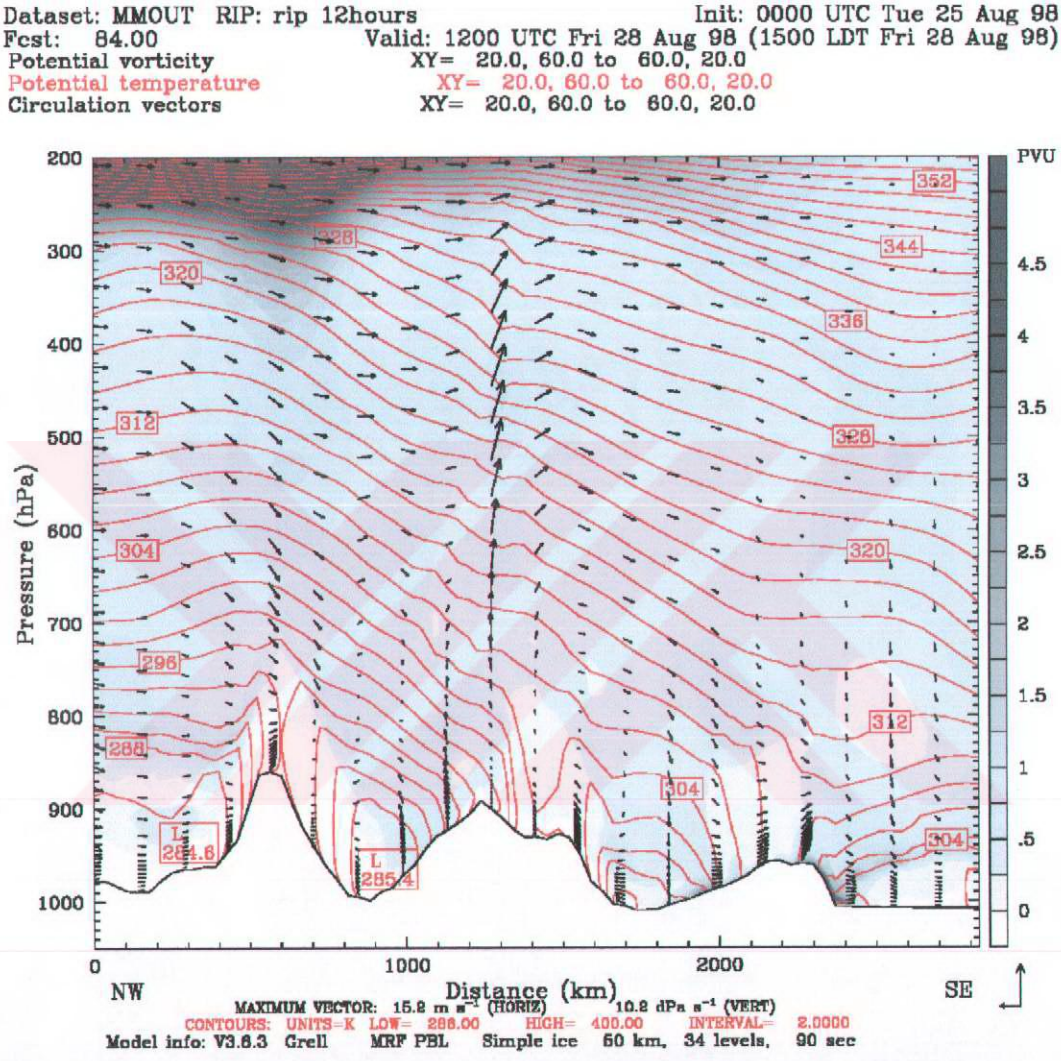

Figure C.39: A vertical cross section of the potential vorticity (black and white shading), potential temperatures (red lines) and the wind circulation (black vectors) predicted over a NW – SE line of length around 3000 km from the south of Poland to Cyprus. 84 hours forecast for 28 – 08 – 1998, 1200 UTC.

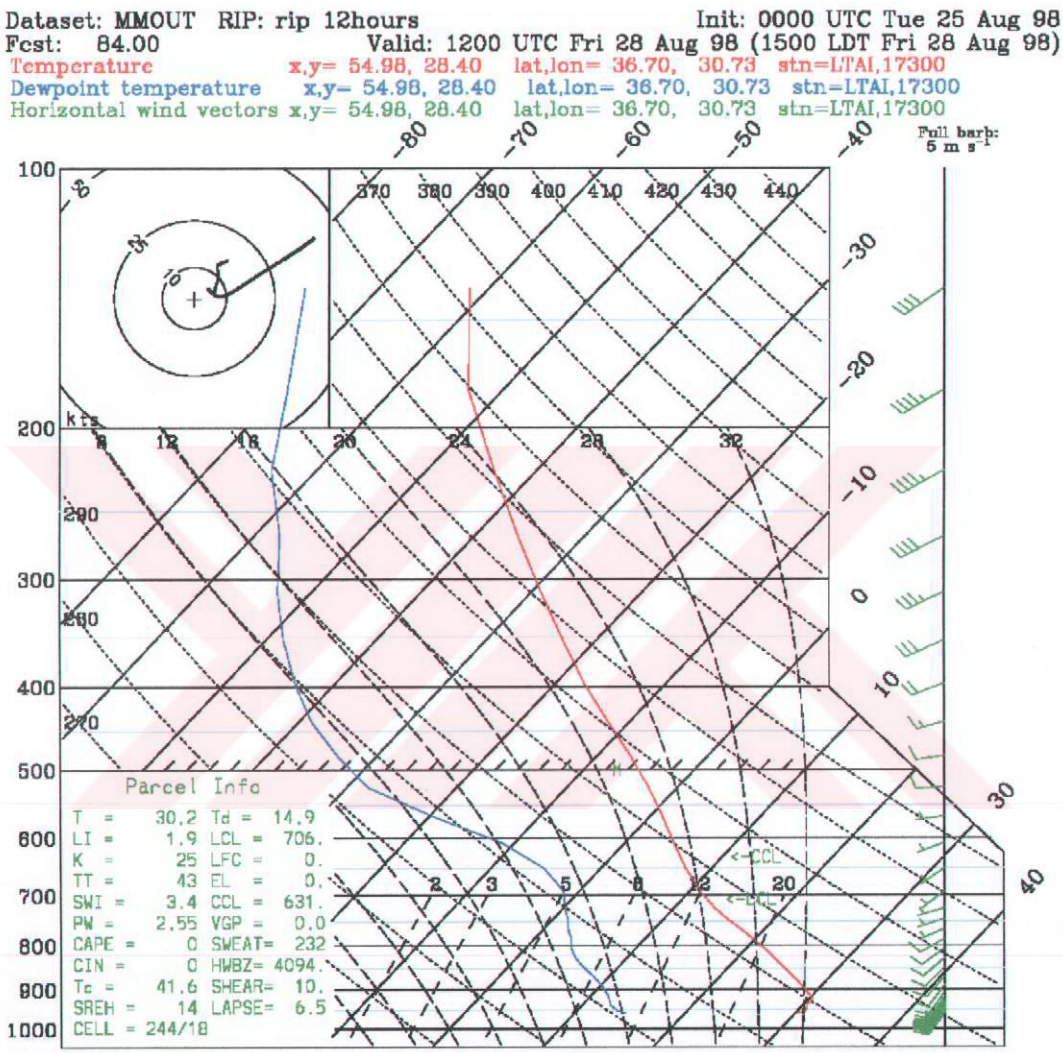

Figure C.40: An estimated Skew – T Plot diagram for Antalya (36.47 °N, 30.34 °E). 84 hours forecast for 28 – 08 – 1998, 1200 UTC.

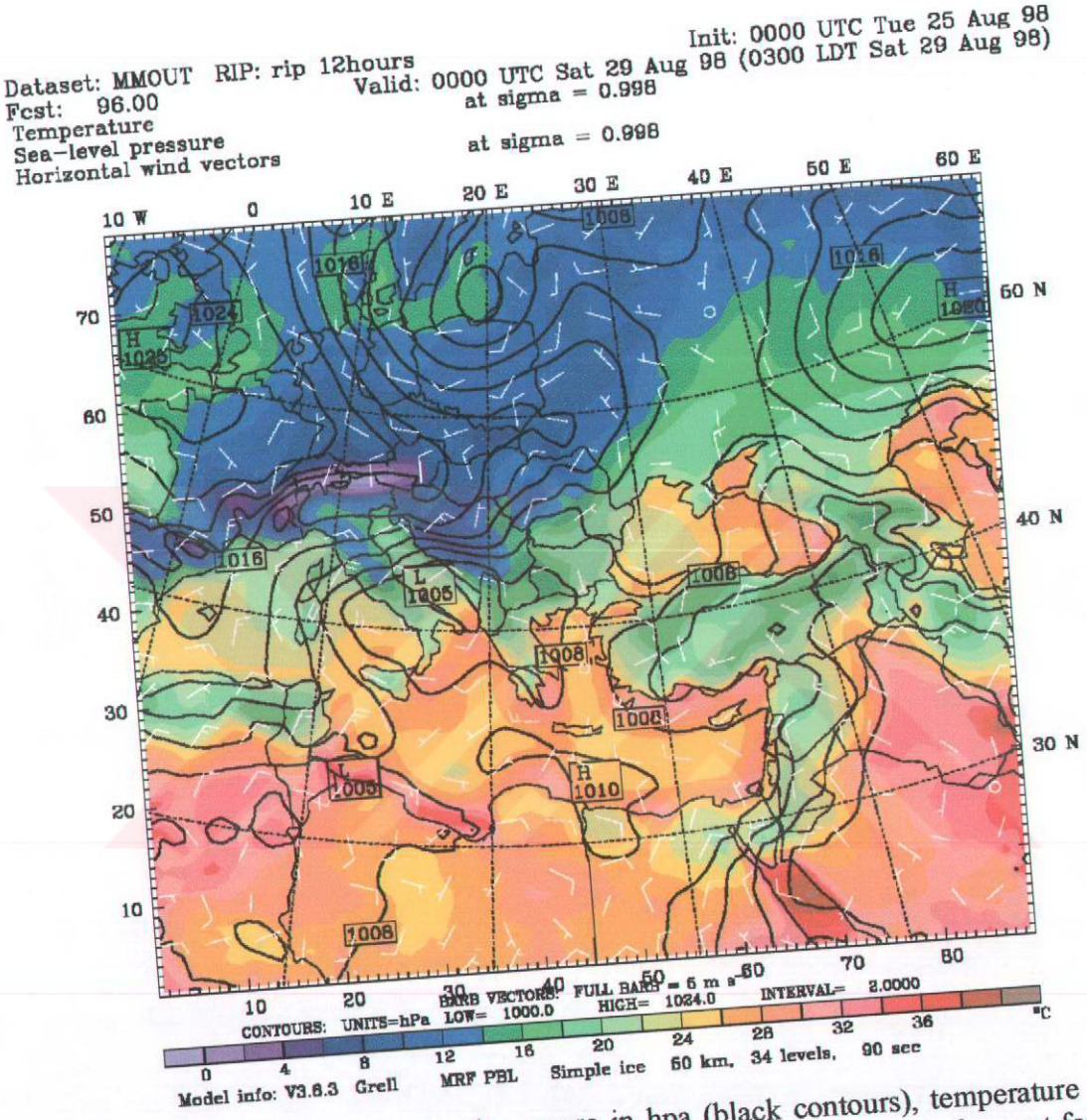

Figure C.41: Predicted Sea level pressure in hpa (black contours), temperature in °C (color shading) and horizontal wind velocity (white vectors). 96 hours forecast for 29 – 08 – 1998, 0000 UTC. (The temperature and the wind vectors are at sigma level 998).

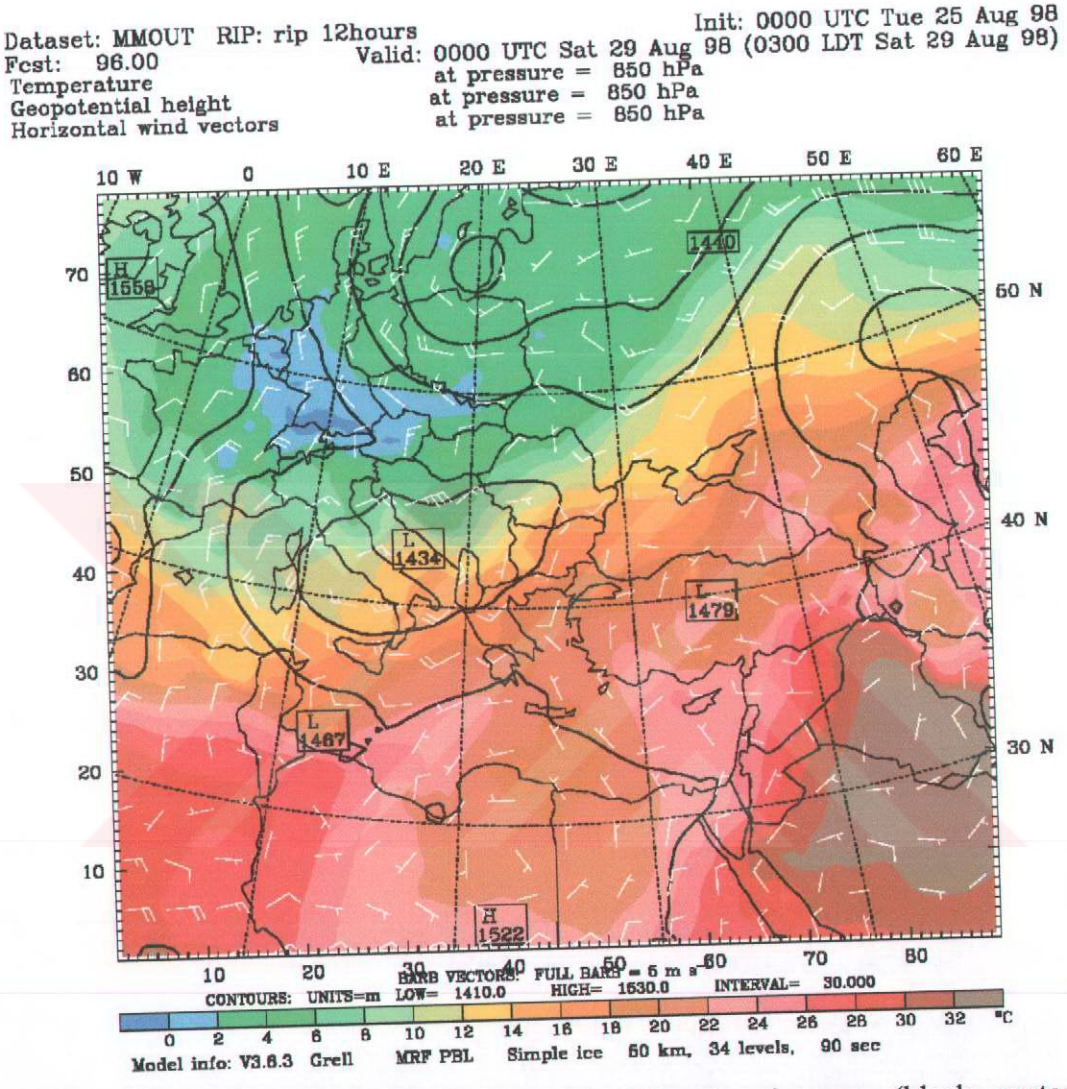

Figure C.42: Predicted 850 hpa geopotential heights in gpm (black contours), temperature in °C (color shading) and horizontal wind velocity (white vectors). 96 hours forecast for 29 – 08 – 1998, 0000 UTC.

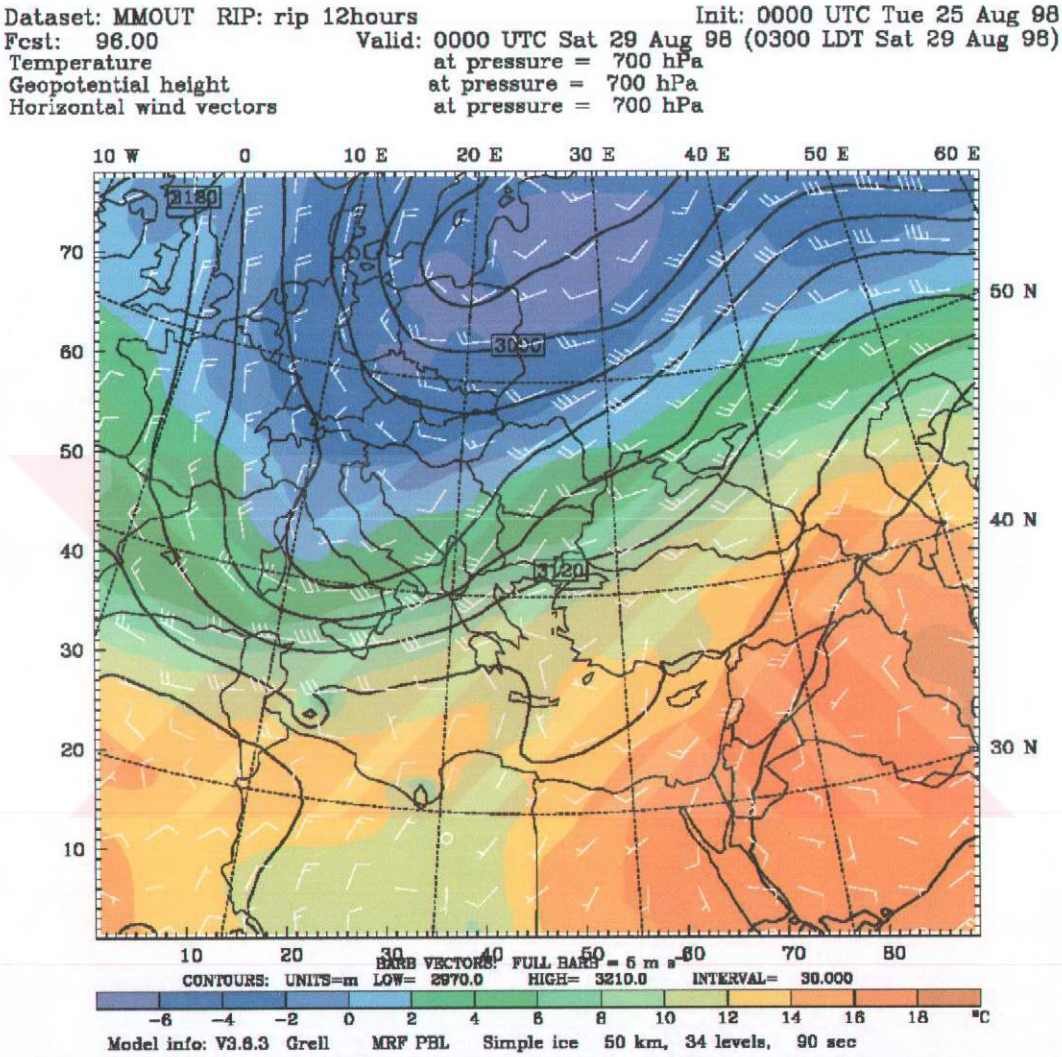

Figure C.43: Predicted 700 hpa geopotential heights in gpm (black contours), temperature in °C (color shading) and horizontal wind velocity (white vectors). 96 hours forecast for 27 – 08 – 1998, 0000 UTC.

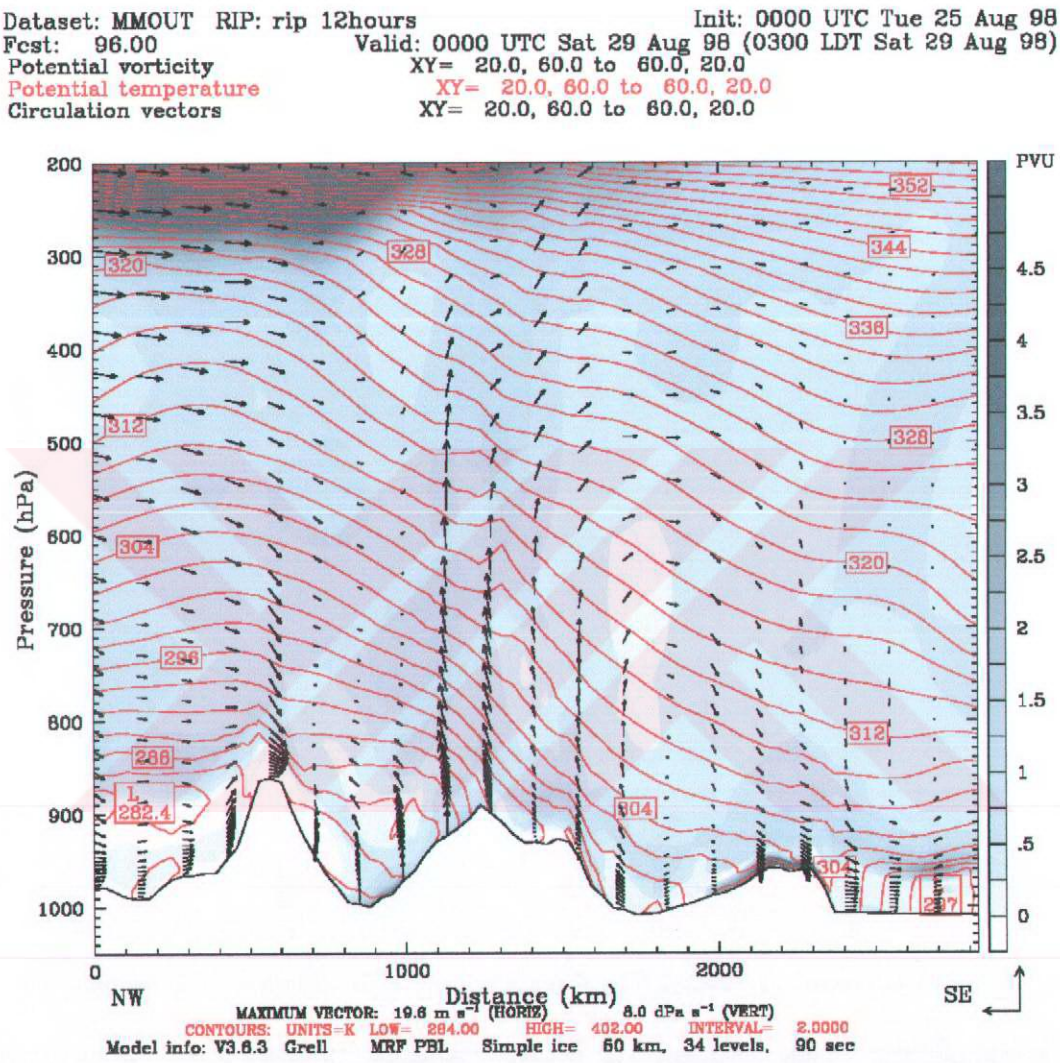

Figure C.44: A vertical cross section of the potential vorticity (black and white shading), potential temperatures (red lines) and the wind circulation (black vectors) predicted over a NW – SE line of length around 3000 km from the south of Poland to Cyprus. 96 hours forecast for 29 – 08 – 1998, 0000 UTC.

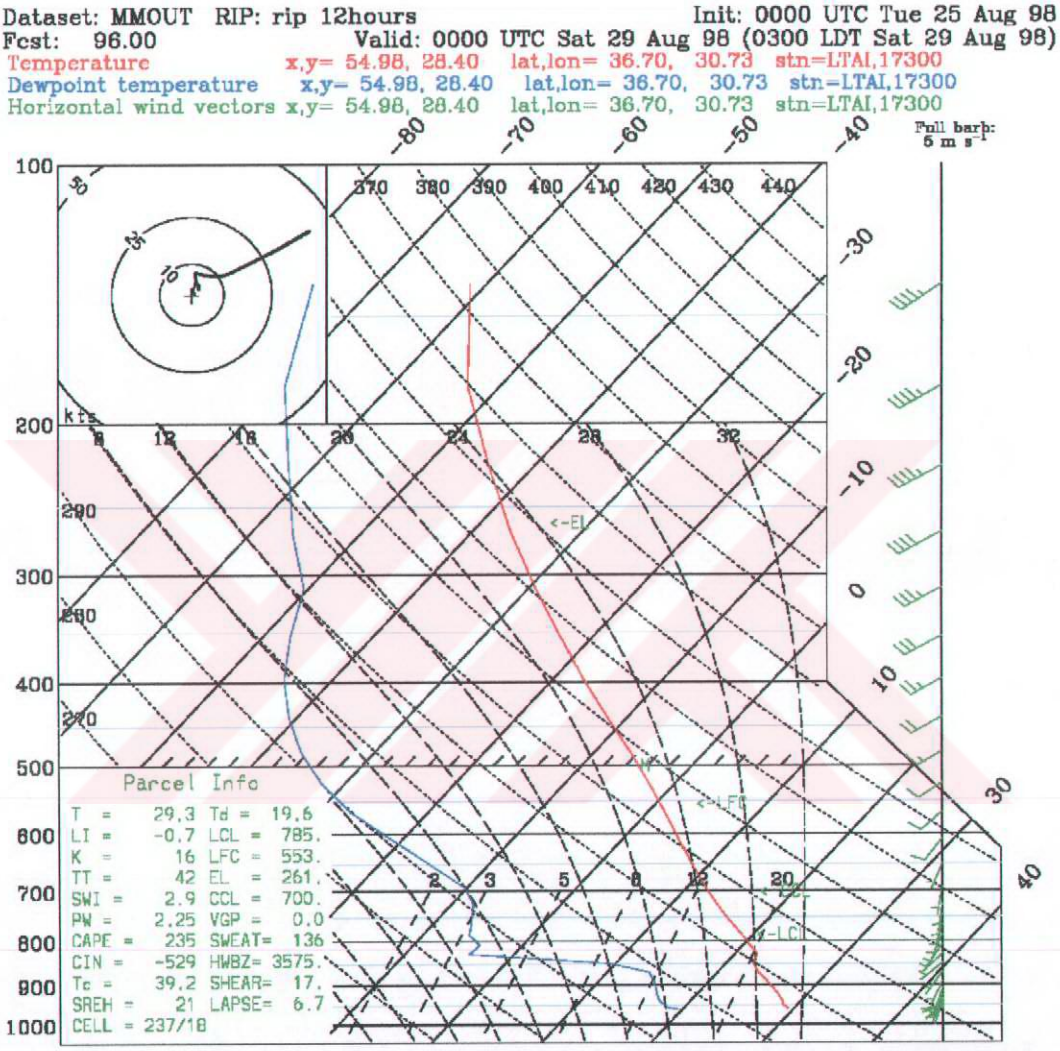

Figure C.45: An estimated Skew – T Plot diagram for Antalya (36.47 °N, 30.34 °E). 96 hours forecast for 29 – 08 – 1998, 0000 UTC.

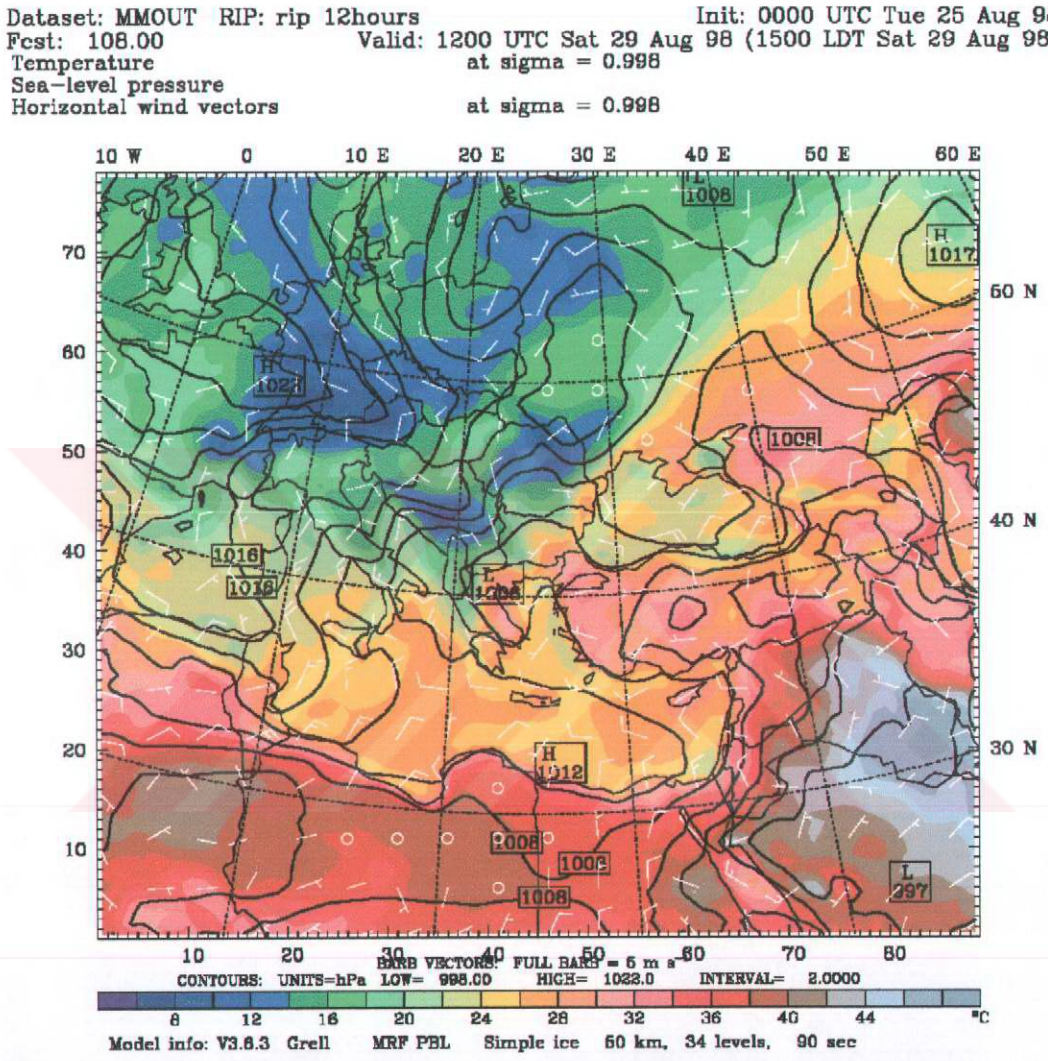

Figure C.46: Predicted Sea level pressure in hpa (black contours), temperature in °C (color shading) and horizontal wind velocity (white vectors). 108 hours forecast for 29 – 08 – 1998, 1200 UTC. (The temperature and the wind vectors are at sigma level 998).

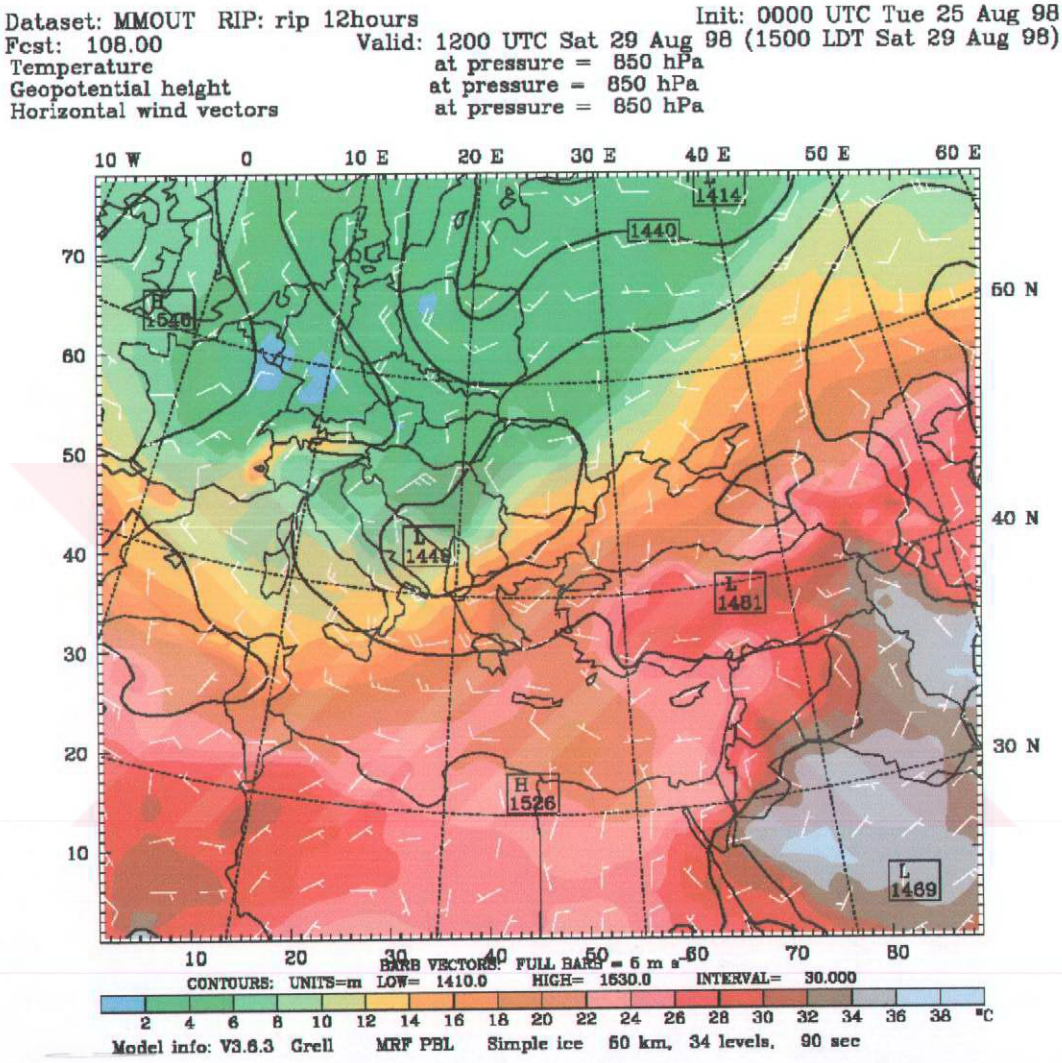

Figure C.47: Predicted 850 hpa geopotential heights in gpm (black contours), temperature in °C (color shading) and horizontal wind velocity (white vectors). 108 hours forecast for 29 – 08 – 1998, 1200 UTC.

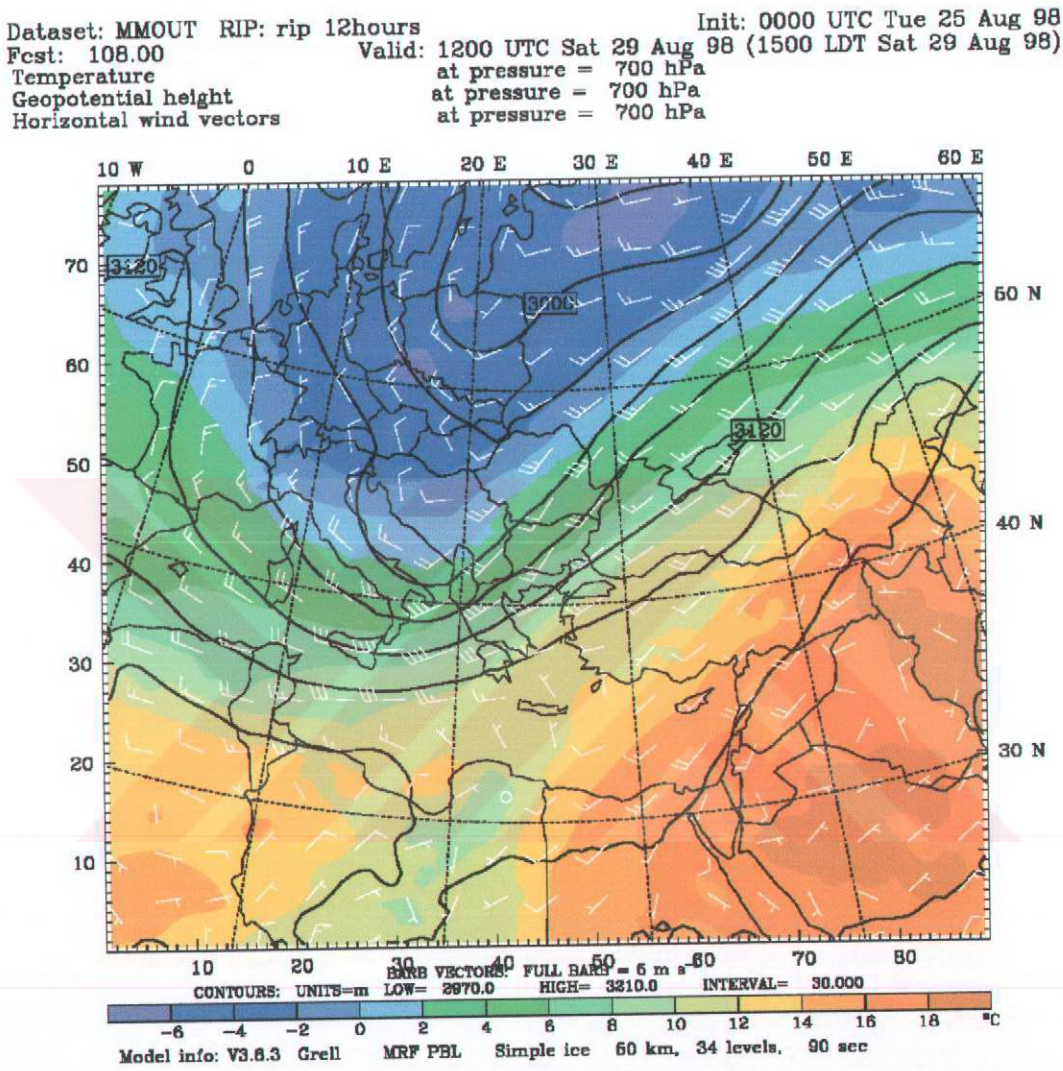

Figure C.48: Predicted 700 hpa geopotential heights in gpm (black contours), temperature in °C (color shading) and horizontal wind velocity (white vectors). 108 hours forecast for 29 – 08 – 1998, 1200 UTC.

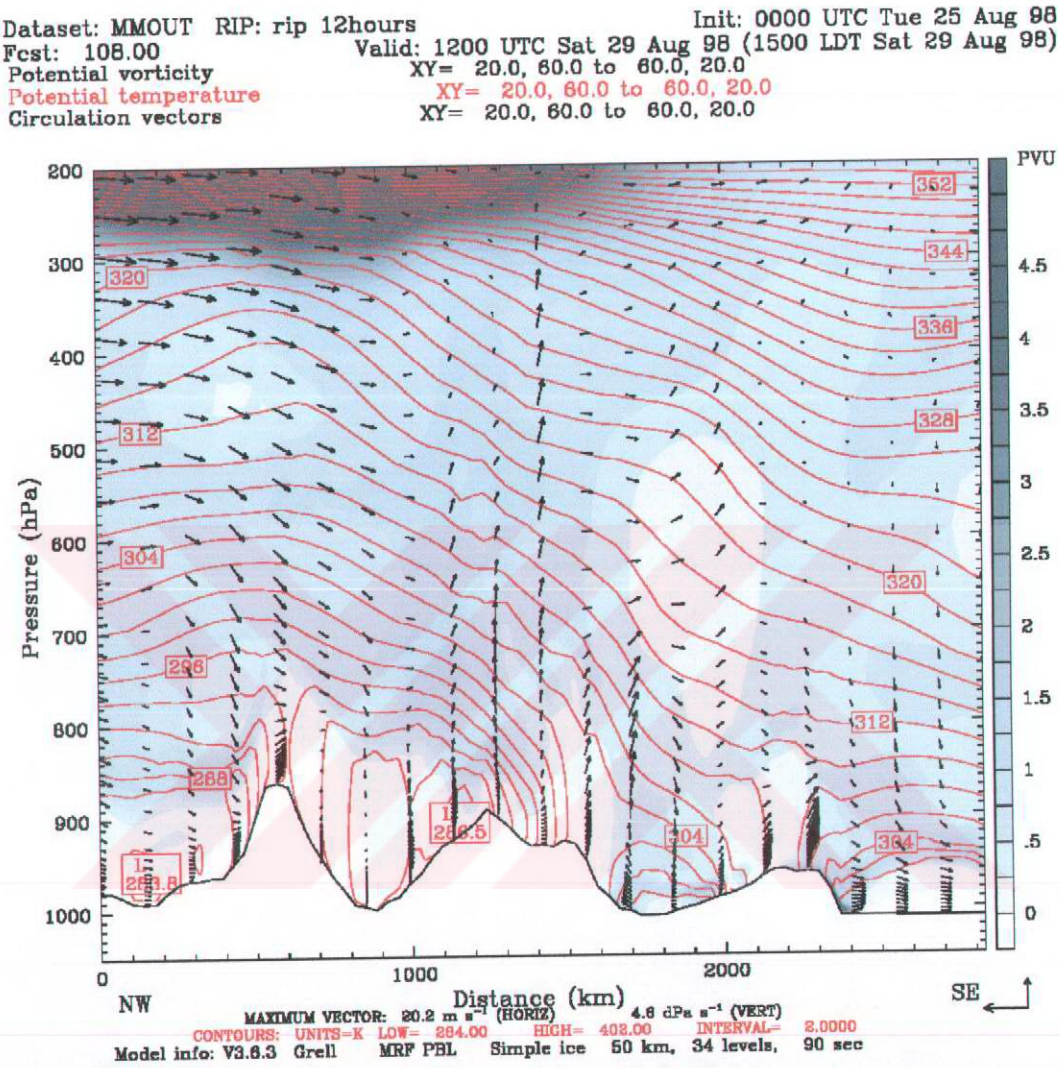

Figure C.49: A vertical cross section of the potential vorticity (black and white shading), potential temperatures (red lines) and the wind circulation (black vectors) predicted over a NW – SE line of length around 3000 km from the south of Poland to Cyprus. 108 hours forecast for 29 – 08 – 1998, 1200 UTC.

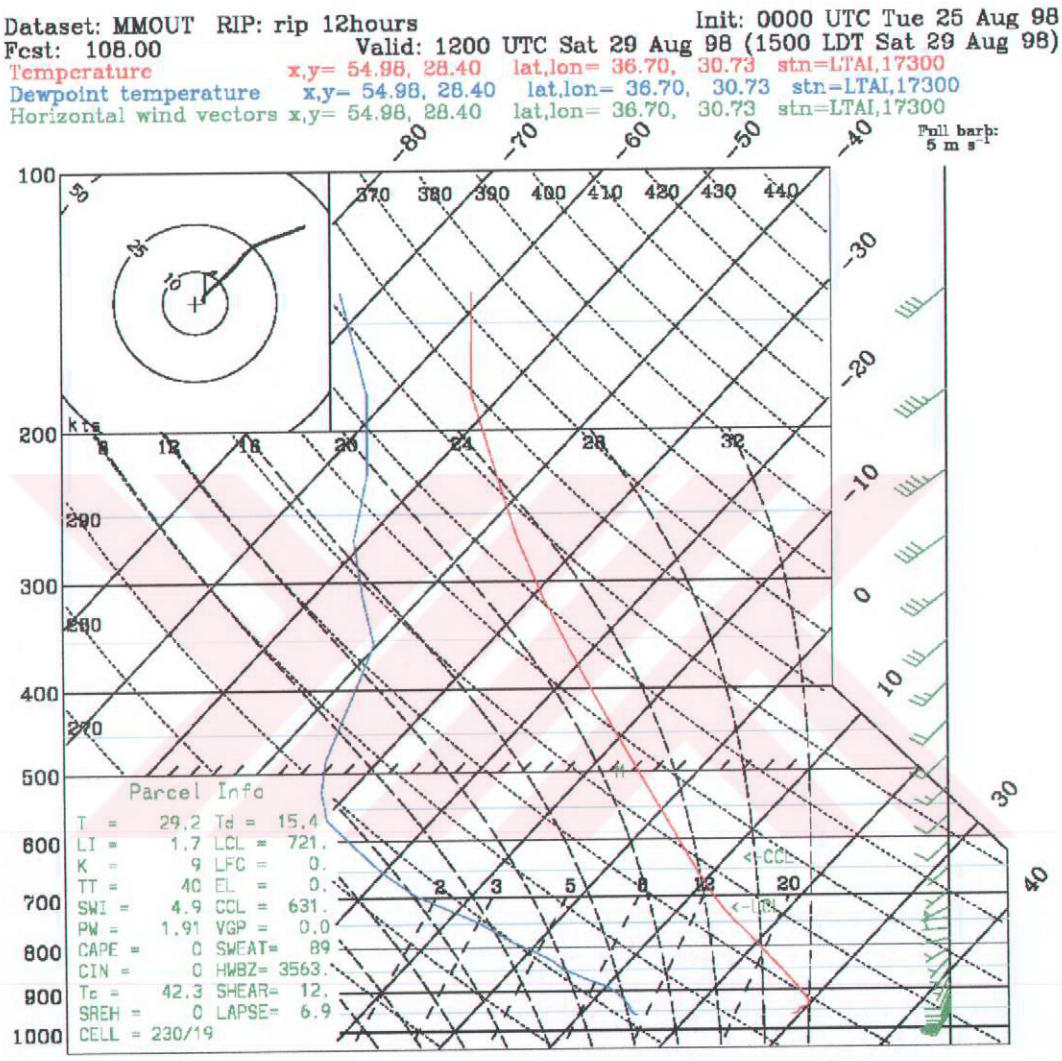

Figure C.50: An estimated Skew – T Plot diagram for Antalya (36.47 °N, 30.34 °E). 108 hours forecast for 29 – 08 – 1998, 1200 UTC.

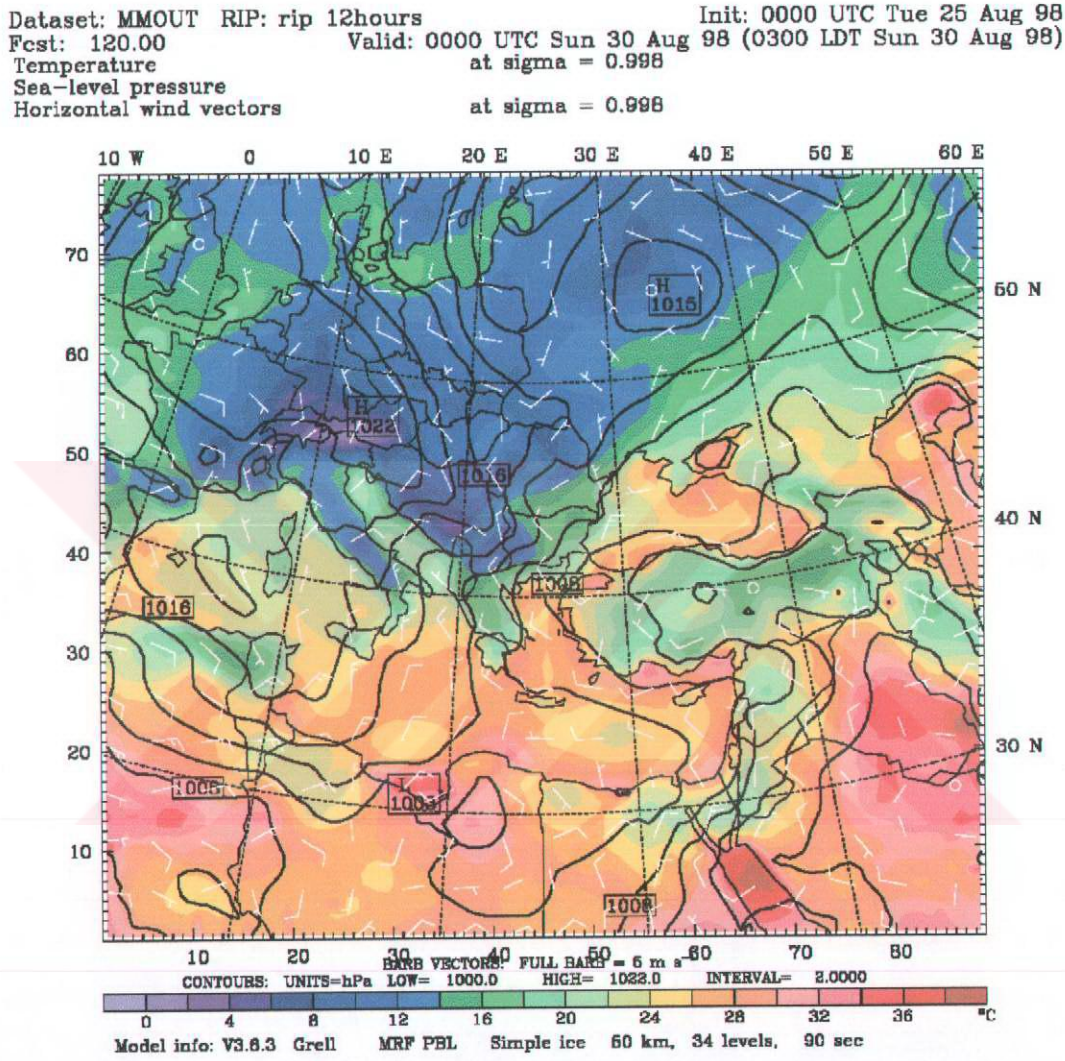

Figure C.51: Predicted Sea level pressure in hpa (black contours), temperature in °C (color shading) and horizontal wind velocity (white vectors). 120 hours forecast for 30 – 08 – 1998, 0000 UTC. (The temperature and the wind vectors are at sigma level 998).

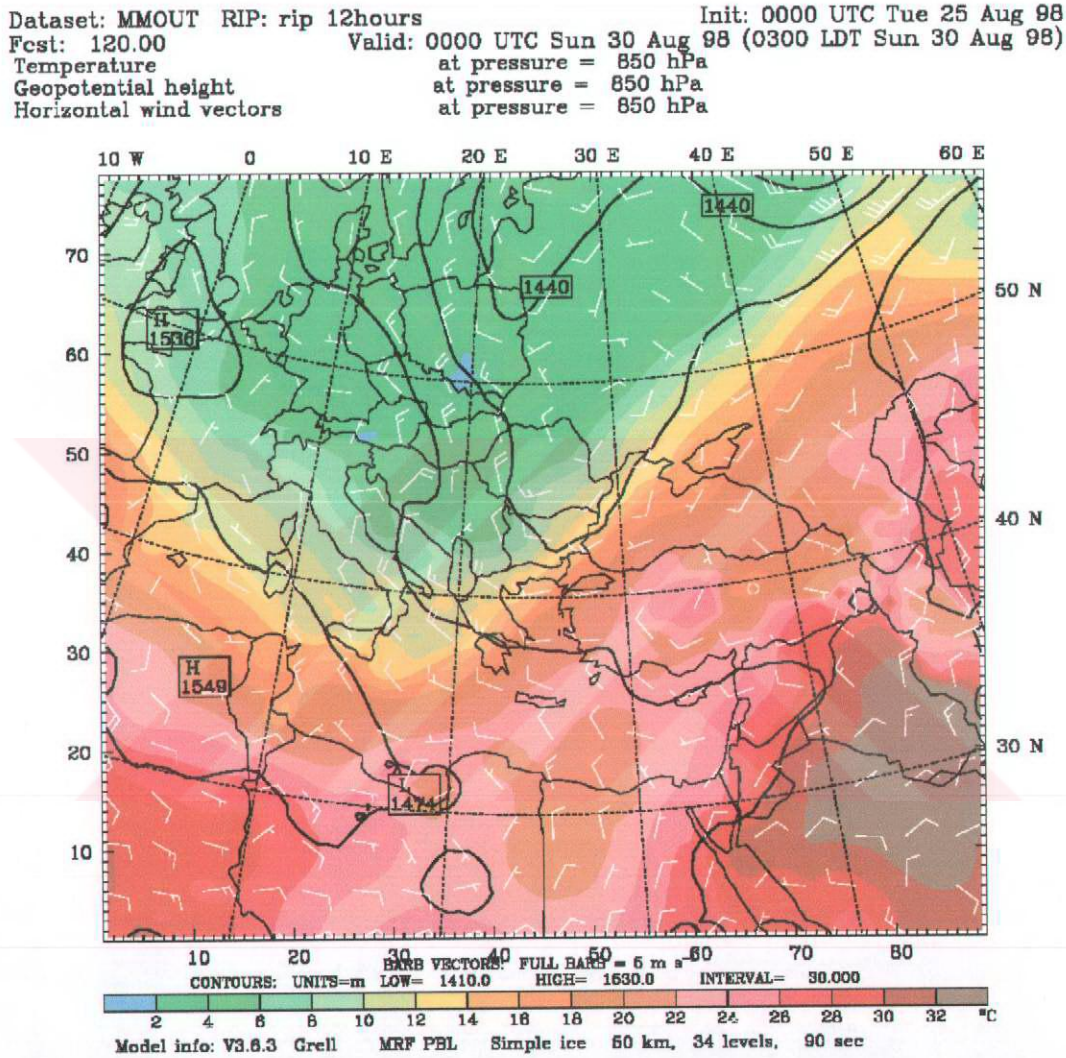

Figure C.52: Predicted 850 hpa geopotential heights in gpm (black contours), temperature in °C (color shading) and horizontal wind velocity (white vectors). 120 hours forecast for 30 – 08 – 1998, 0000 UTC.

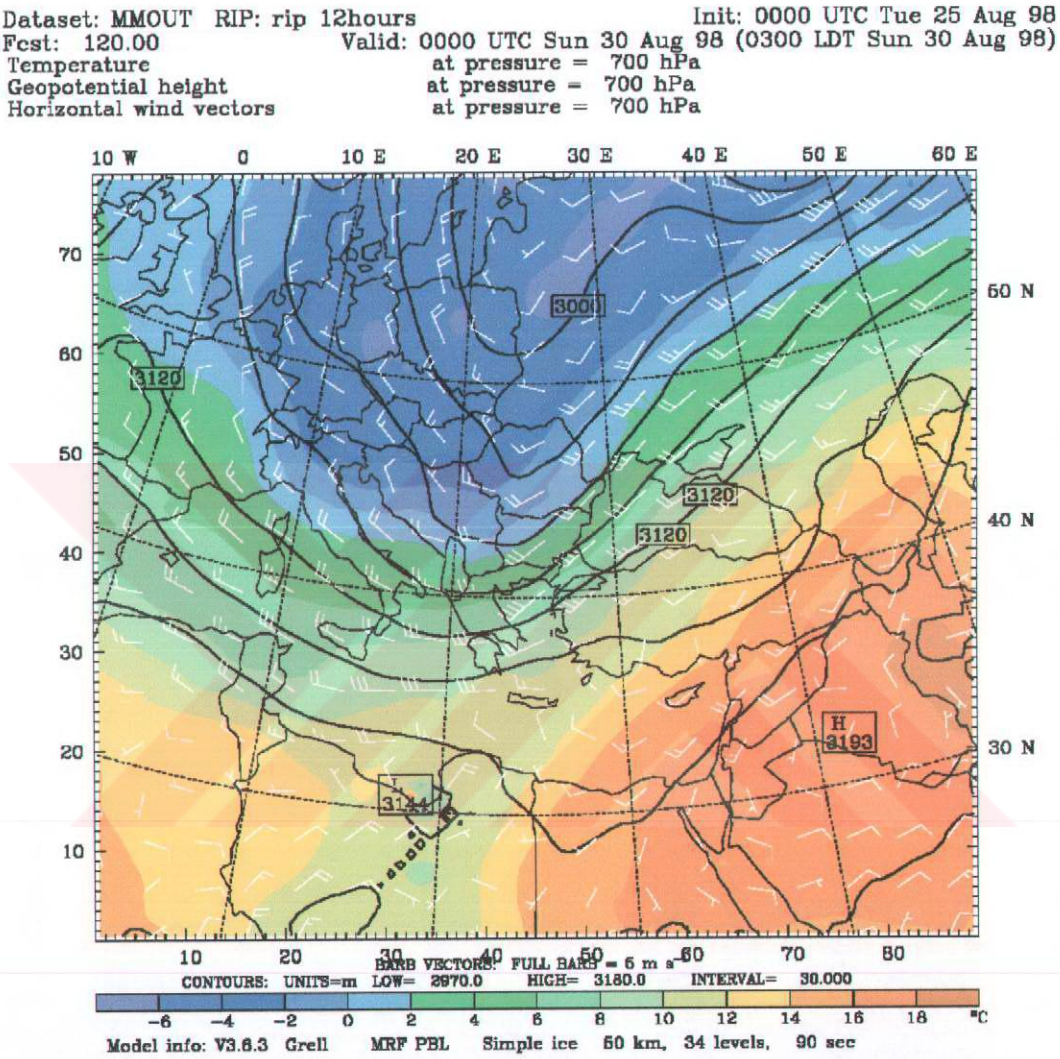

Figure C.53: Predicted 700 hpa geopotential heights in gpm (black contours), temperature in °C (color shading) and horizontal wind velocity (white vectors). 120 hours forecast for 30 – 08 – 1998, 0000 UTC.

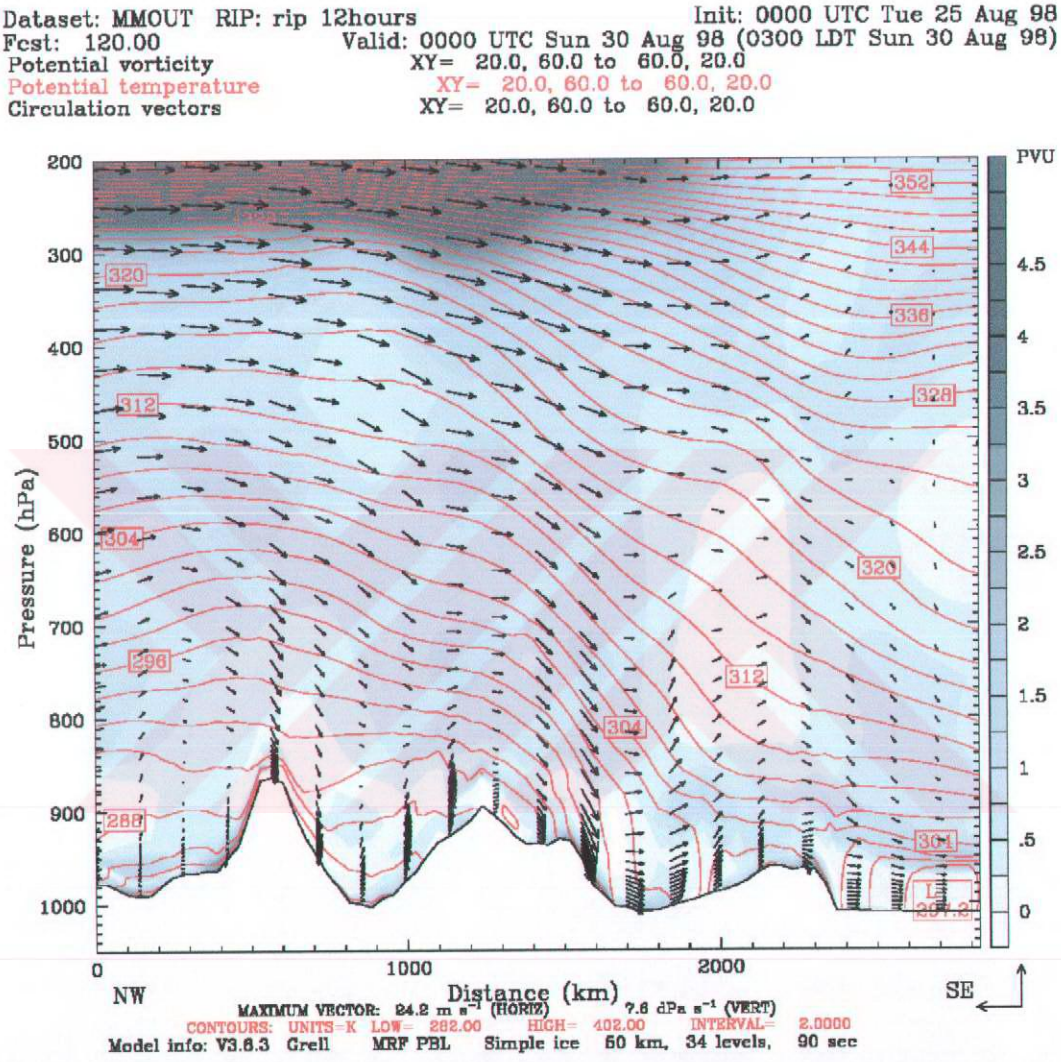

Figure C.54: A vertical cross section of the potential vorticity (black and white shading), potential temperatures (red lines) and the wind circulation (black vectors) predicted over a NW – SE line of length around 3000 km from the south of Poland to Cyprus. 120 hours forecast for 30 – 08 – 1998, 0000 UTC.

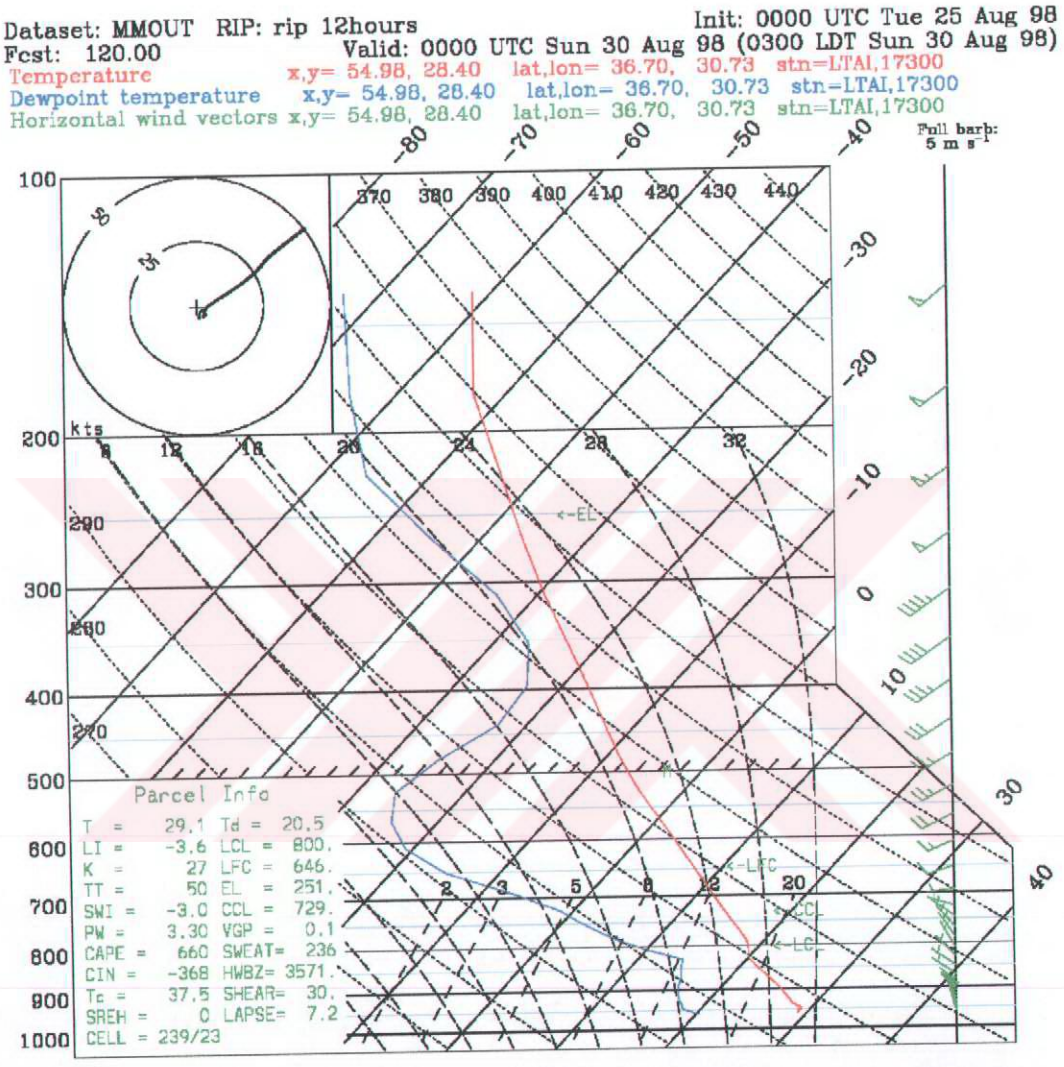

Figure C.55: An estimated Skew – T Plot diagram for Antalya (36.47 °N, 30.34 °E). 120 hours forecast for 30 – 08 – 1998, 0000 UTC.

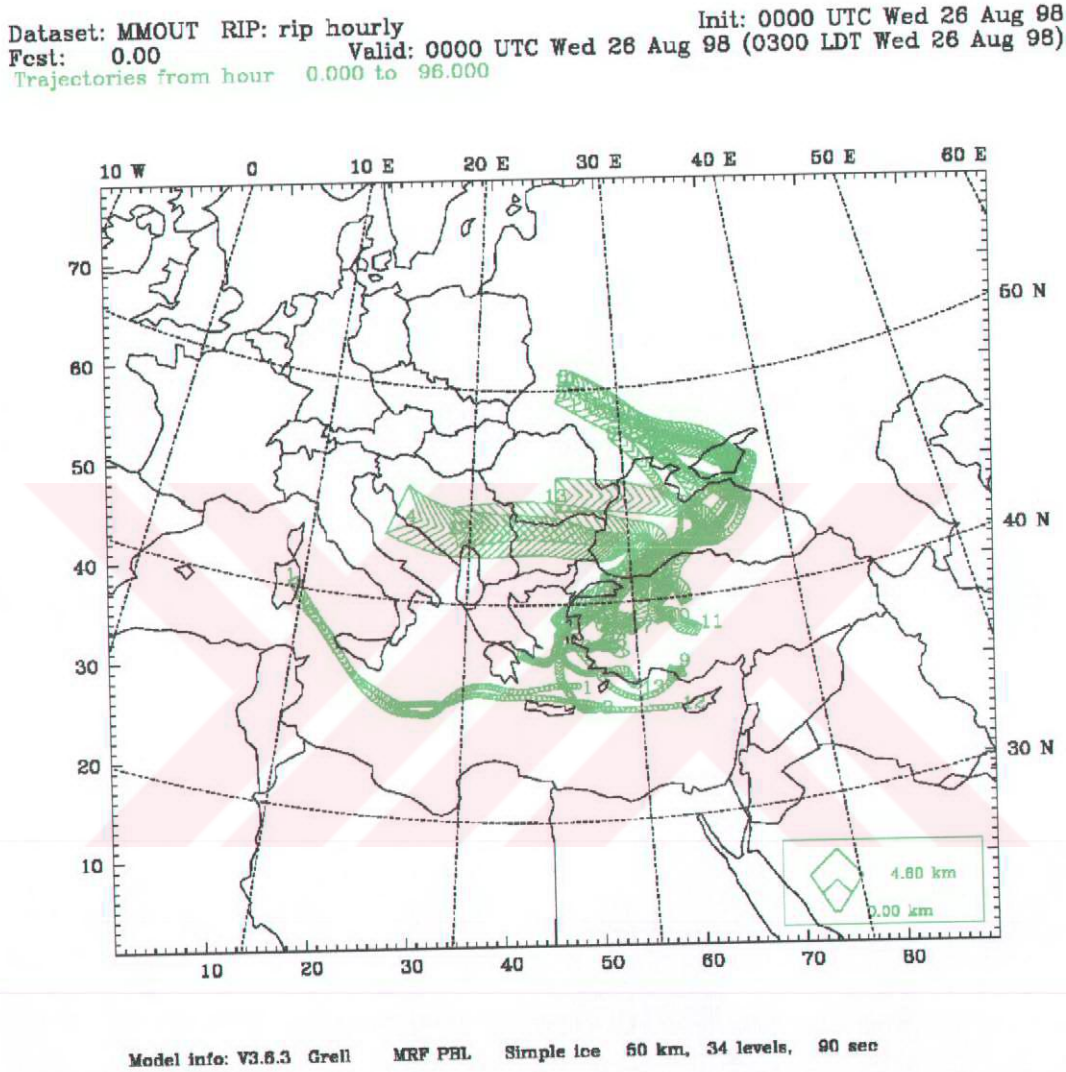

Figure C.56: 96 hours RIP backward trajectory plots (start at 0000 UTC, 30 Aug. 1998 and end at 0000 UTC, 26 Aug. 1998) at sigma level 0.998 for selected 13 locations in the Eastern Mediterranean region and Western Turkey.

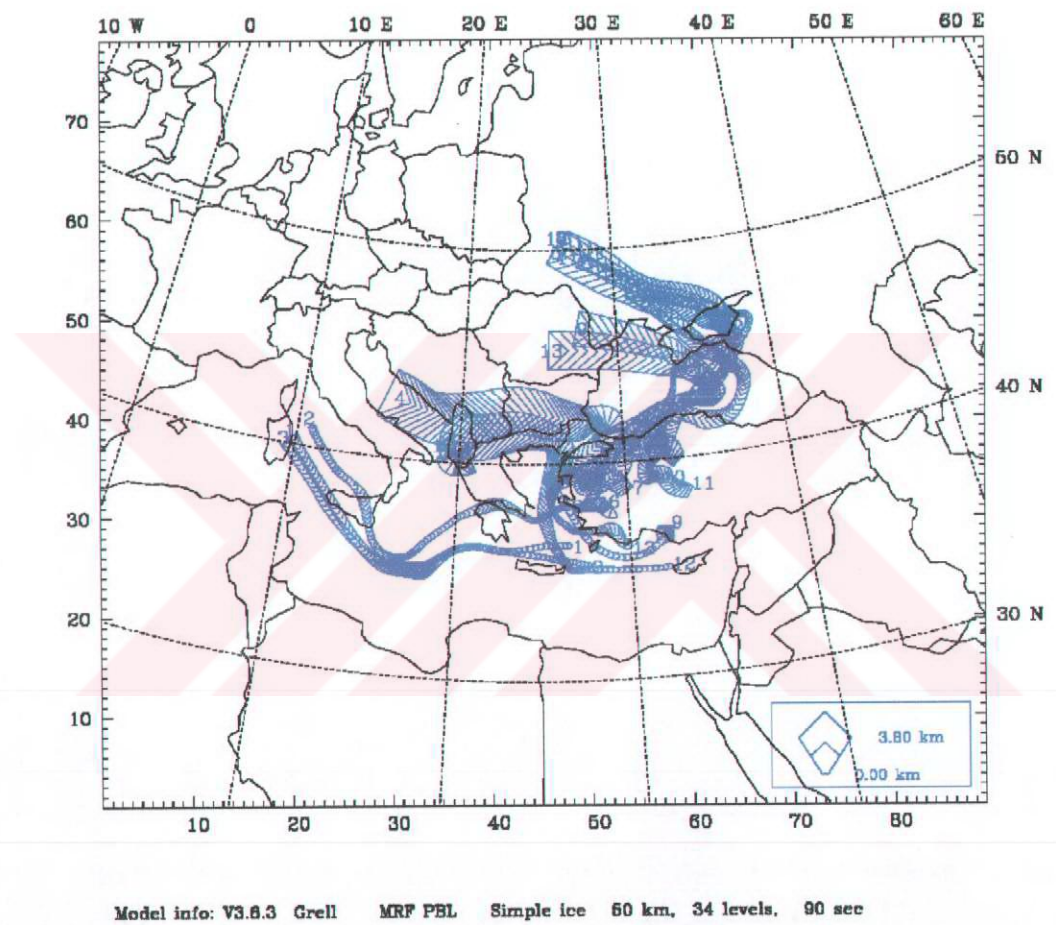

Figure C.57: 96 hours RIP backward trajectory plots (start at 0000 UTC, 30 Aug. 1998 and end at 0000 UTC, 26 Aug. 1998) at sigma level 0.990 for selected 13 locations in the Eastern Mediterranean region and Western Turkey.

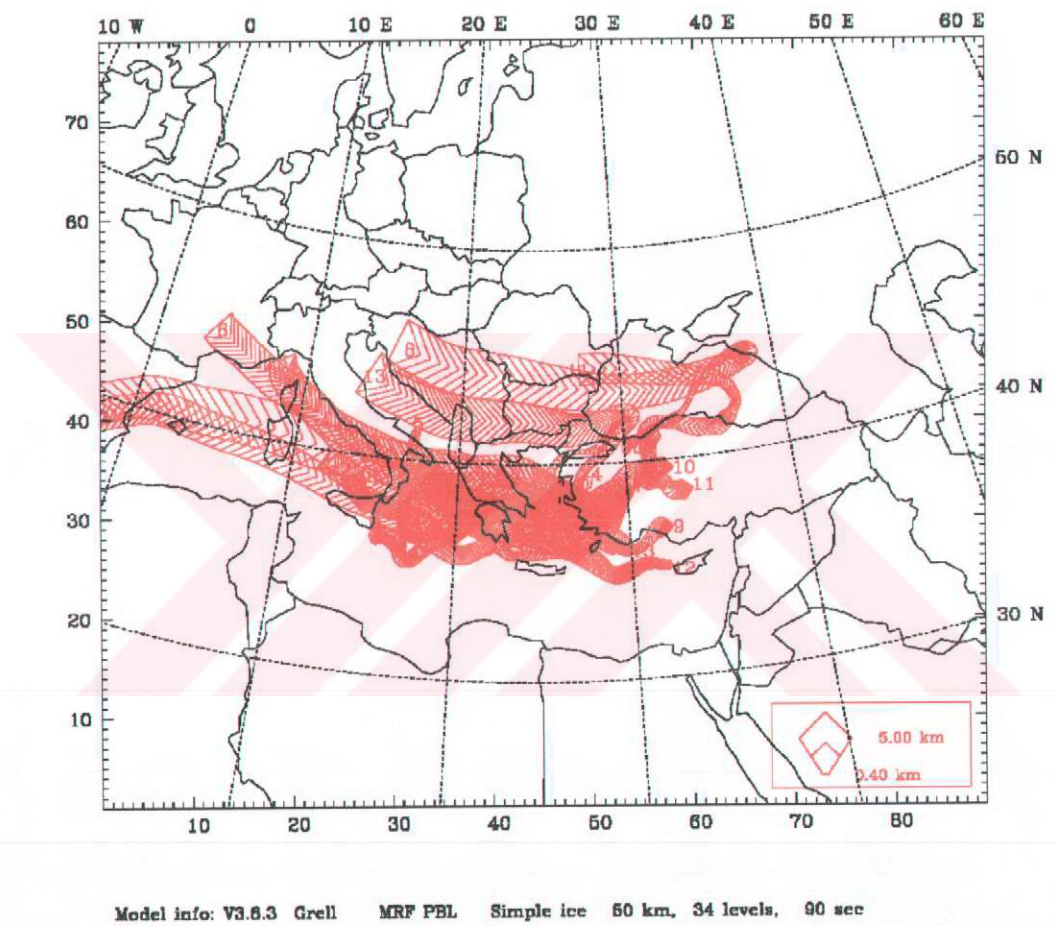

Figure C.58: 96 hours RIP backward trajectory plots (start at 0000 UTC, 30 Aug. 1998 and end at 0000 UTC, 26 Aug. 1998) at sigma level 0.900 for selected 13 locations in the Eastern Mediterranean region and Western Turkey.

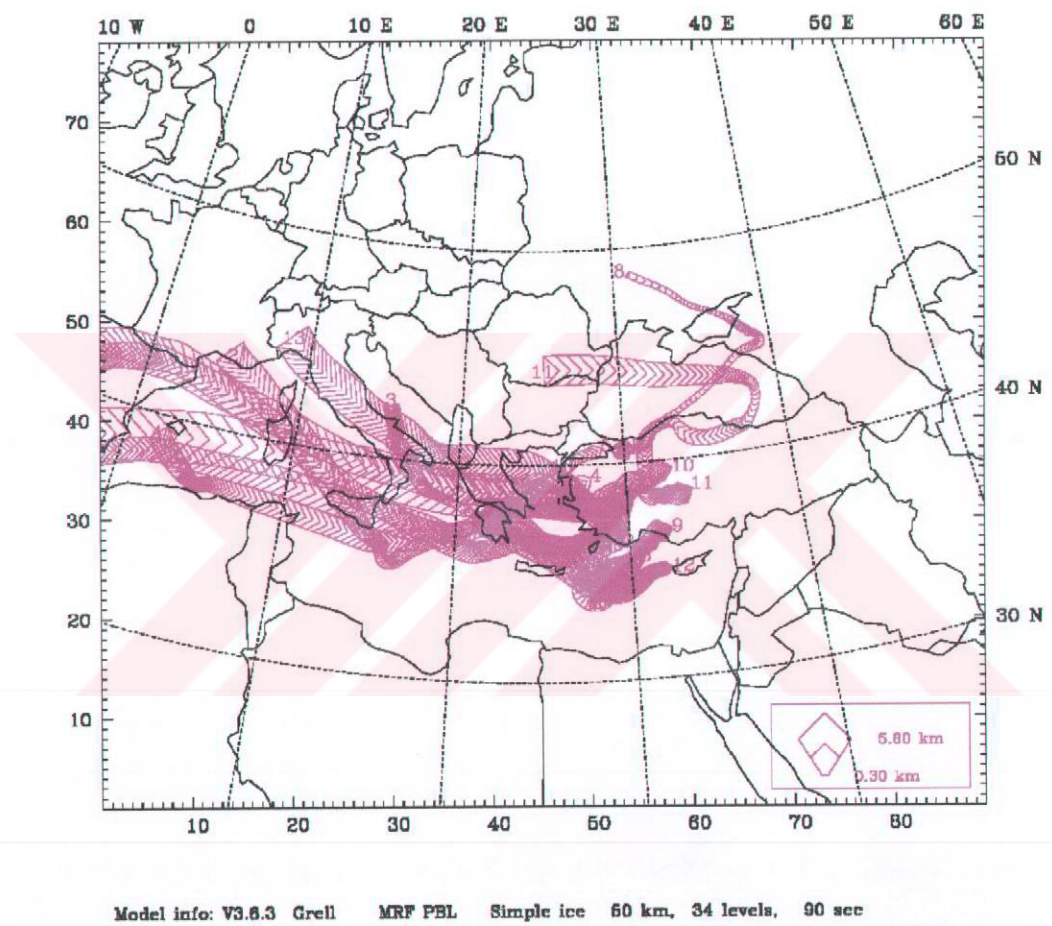

Figure C.59: 96 hours RIP backward trajectory plots (start at 0000 UTC, 30 Aug. 1998 and end at 0000 UTC, 26 Aug. 1998) at sigma level 0.850 for selected 13 locations in the Eastern Mediterranean region and Western Turkey.

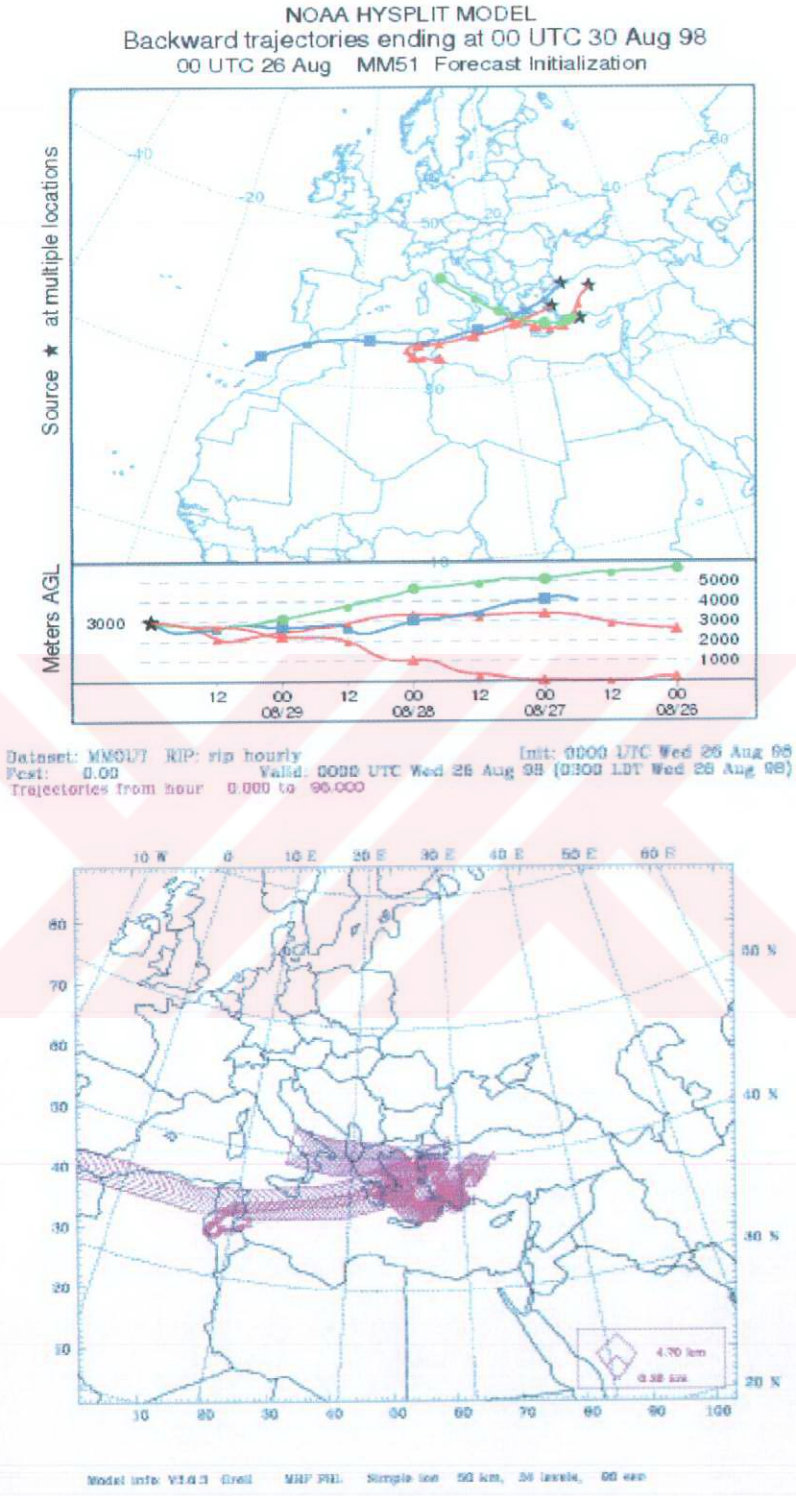

Figure C.60: 96 hours backward trajectories at 3000 m AGL for Antalya, Izmir, Istanbul and Ankara plotted by HYSPLIT (upper) and RIP (lower) using the meteorological data predicted by MM5 model. Trajectories start at 0000 UTC, 30 Aug. 1998 and end at 0000 UTC, 26 Aug. 1998.

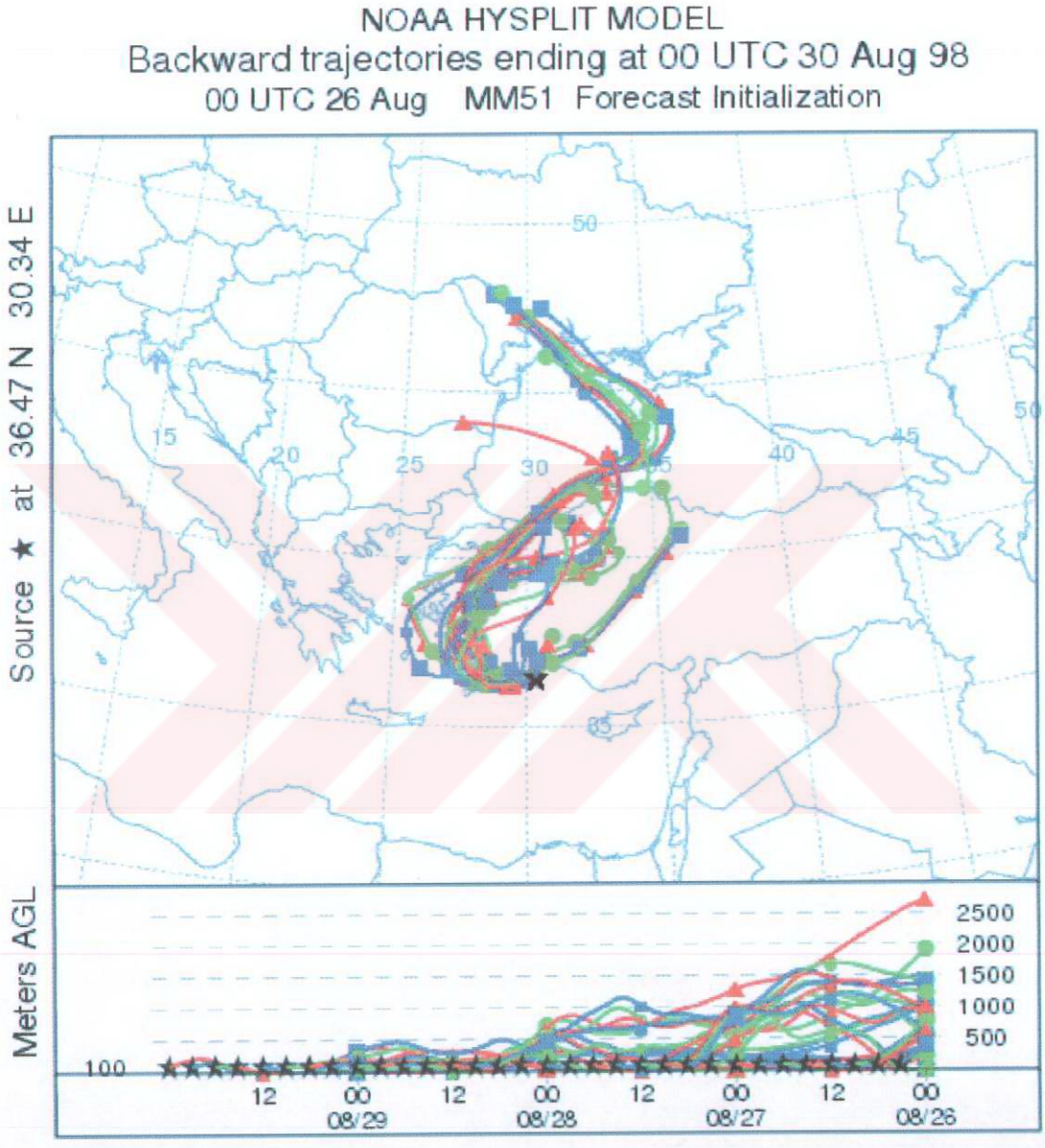

Figure C.61: A multiple backward trajectory plot for Antalya at 100 m AGL. Trajectories are plotted at 3 hour interval between 0000 UTC, 30 Aug. 1998 and 0000 UTC, 26 Aug. 1998.

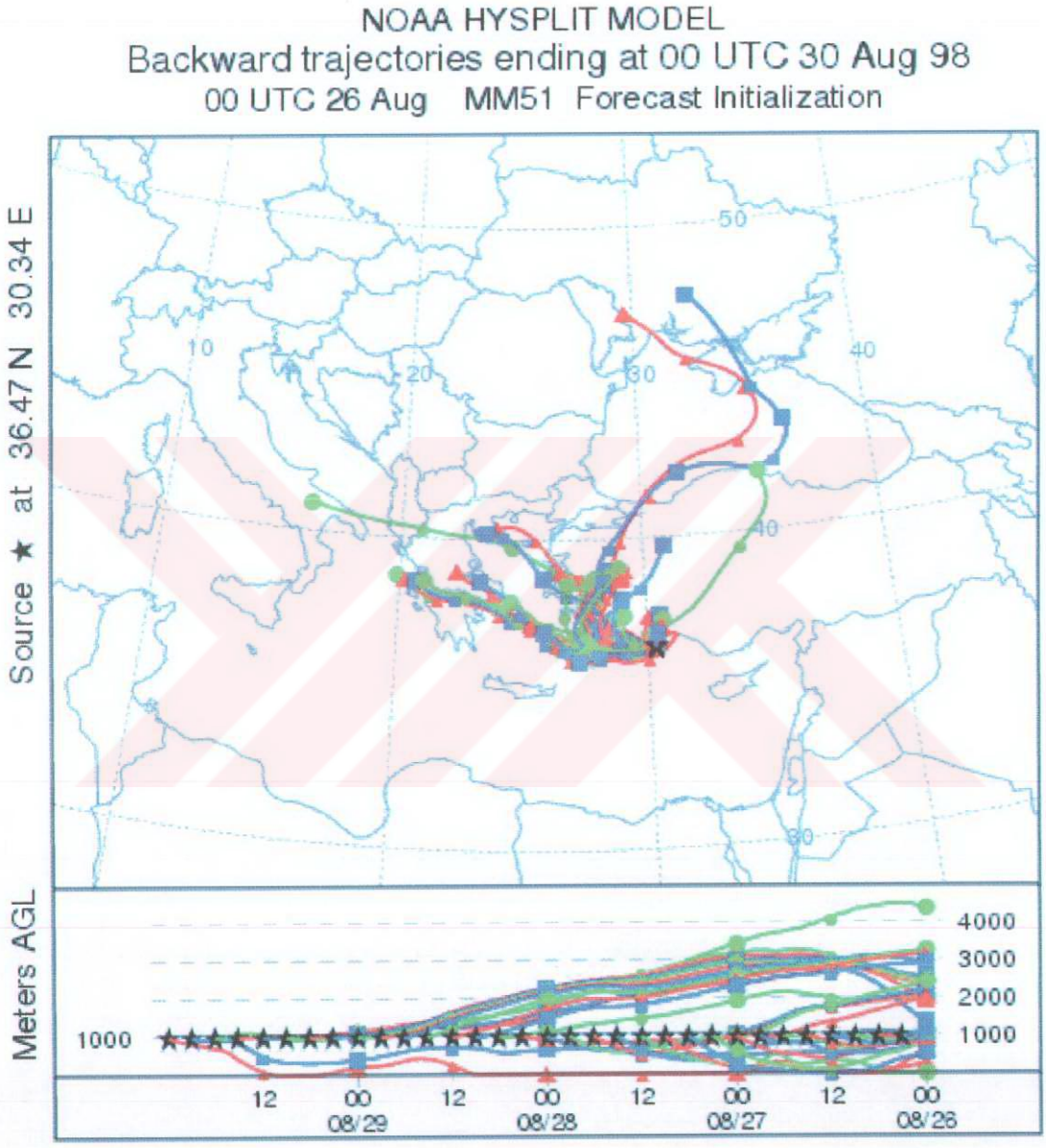

Figure C.62: A multiple backward trajectory plot for Antalya at 1000 m AGL. Trajectories are plotted at 3 hour interval between 0000 UTC, 30 Aug. 1998 and 0000 UTC, 26 Aug. 1998.

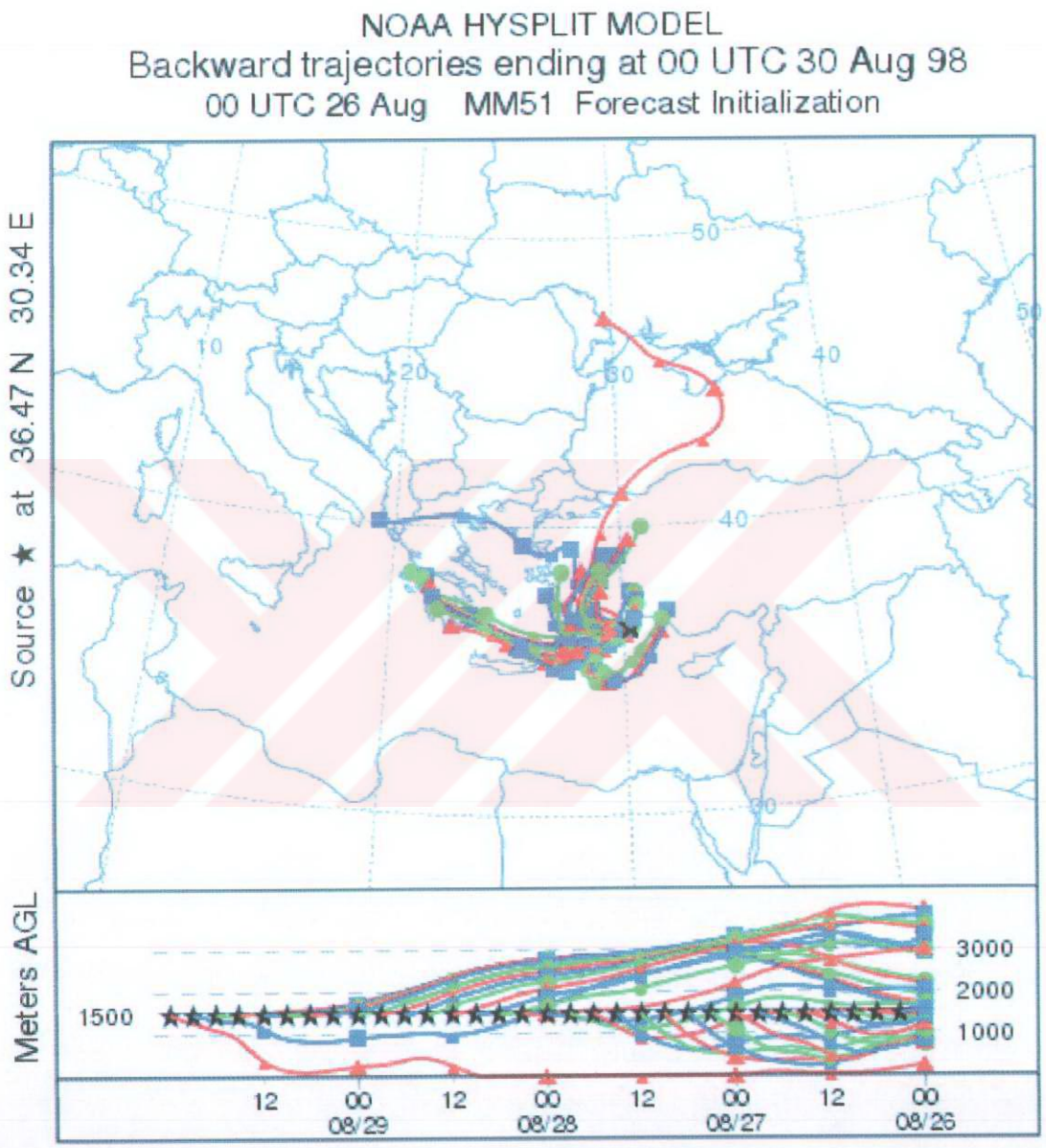

Figure C.63: A multiple backward trajectory plot for Antalya at 1500 m AGL. Trajectories are plotted at 3 hour interval between 0000 UTC, 30 Aug. 1998 and 0000 UTC, 26 Aug. 1998.

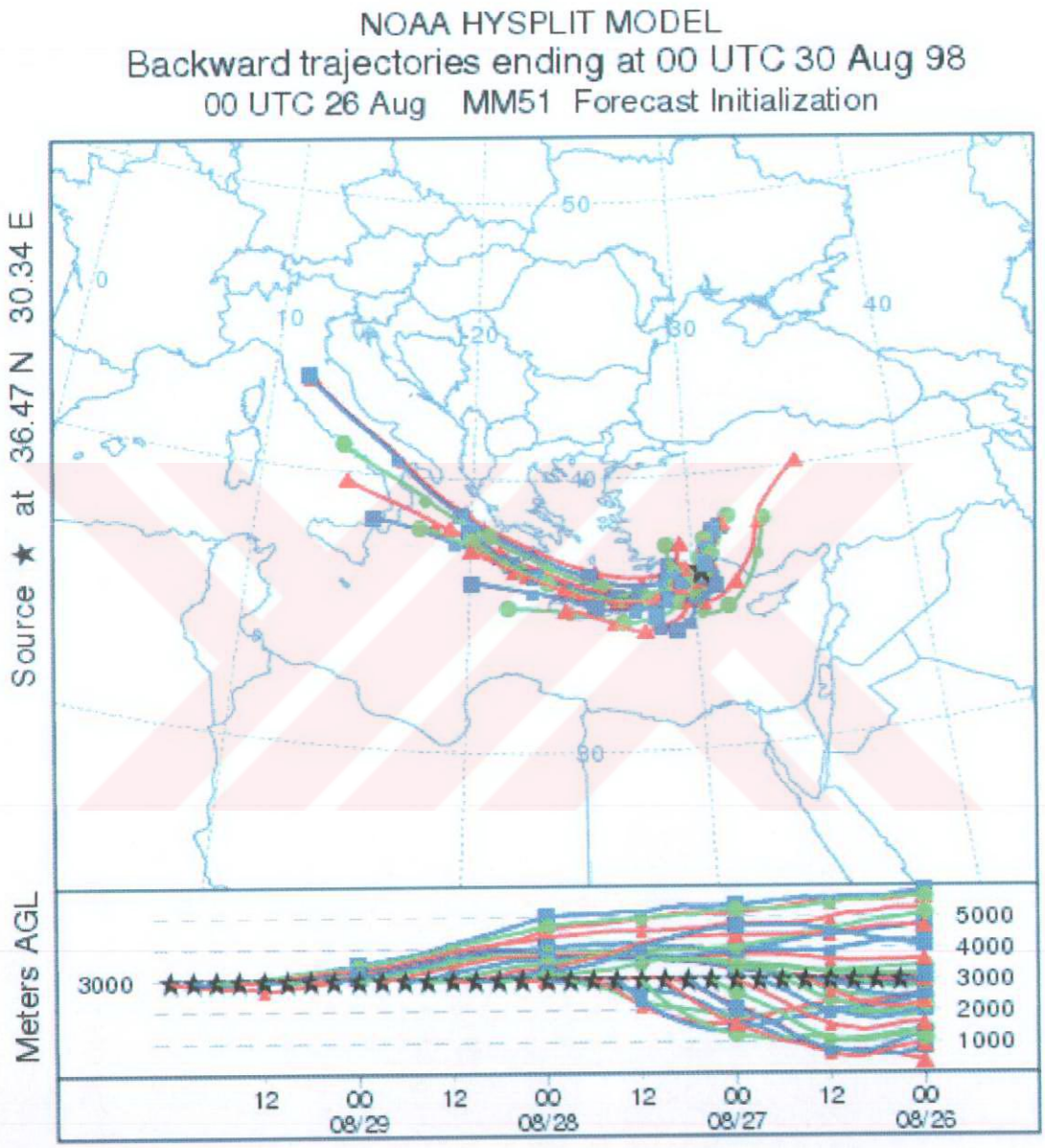

Figure C.64: A multiple backward trajectory plot for Antalya at 3000 m AGL. Trajectories are plotted at 3 hour interval between 0000 UTC, 30 Aug. 1998 and 0000 UTC, 26 Aug. 1998.

APPENDIX D

MM5 MODEL VERIFICATION FIGURES

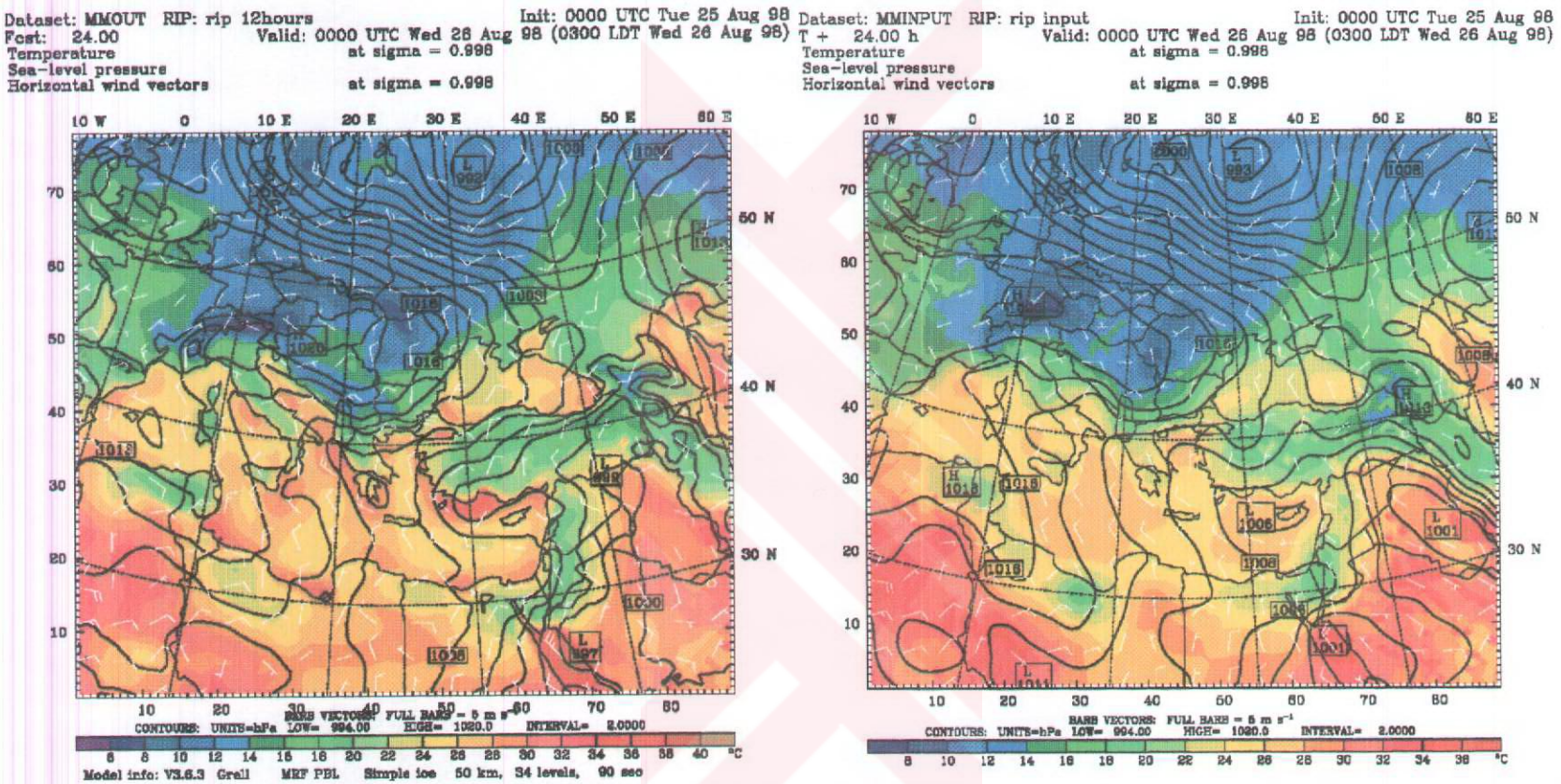

Figure D.1: 24 hours forecast (left) versus observed (right) Sea level pressure in hpa (black contours), temperature in °C (color shading) and horizontal wind velocity (white vectors), valid at 0000UTC, 26 – 08 – 1998.

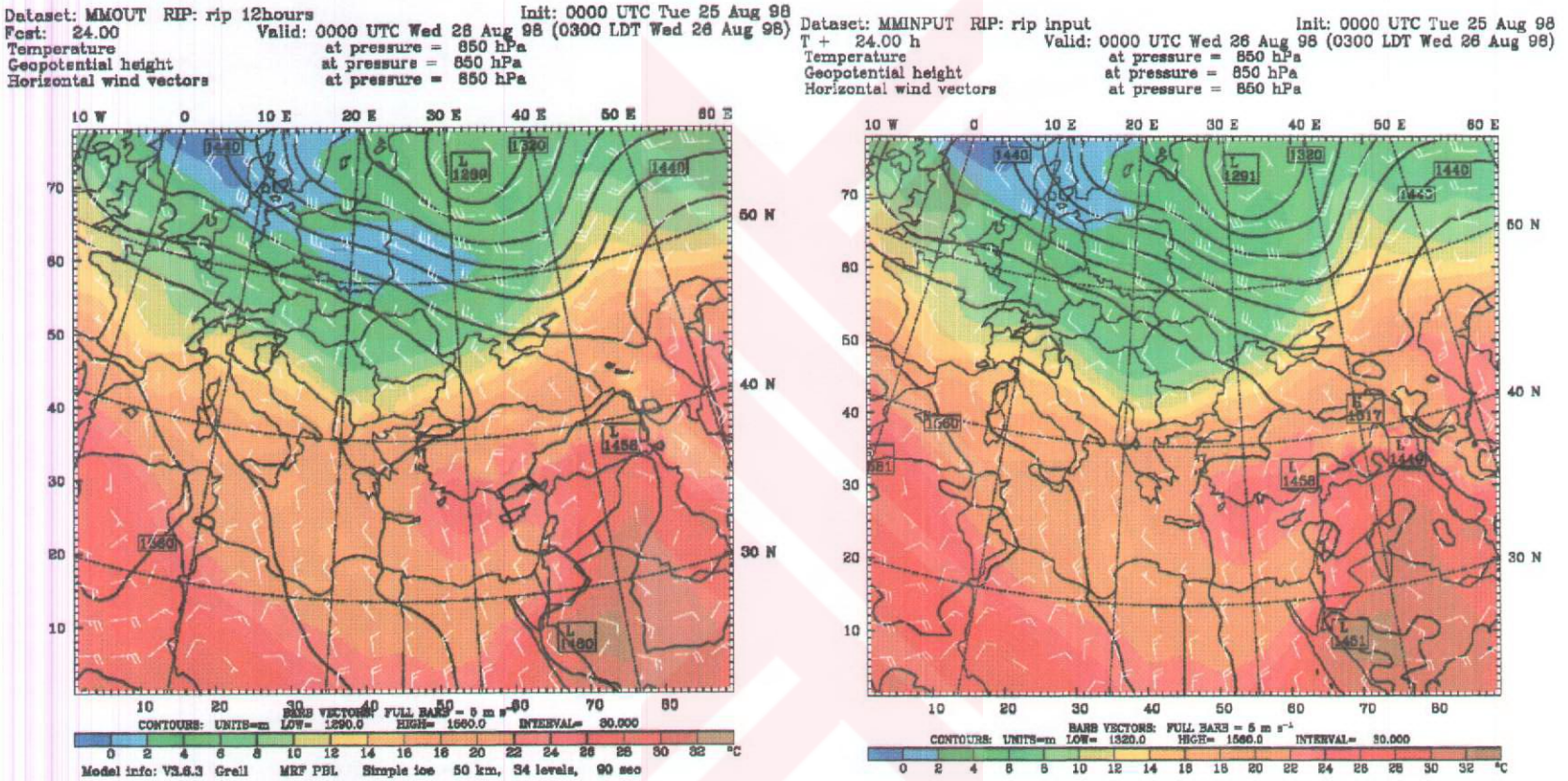

Figure D.2: 24 hours forecast (left) and observed (right) 850 hpa geopotential heights in gpm (black contours), temperature in °C (color shading) and horizontal wind velocity (white vectors), valid at 0000UTC, 26 – 08 – 1998.

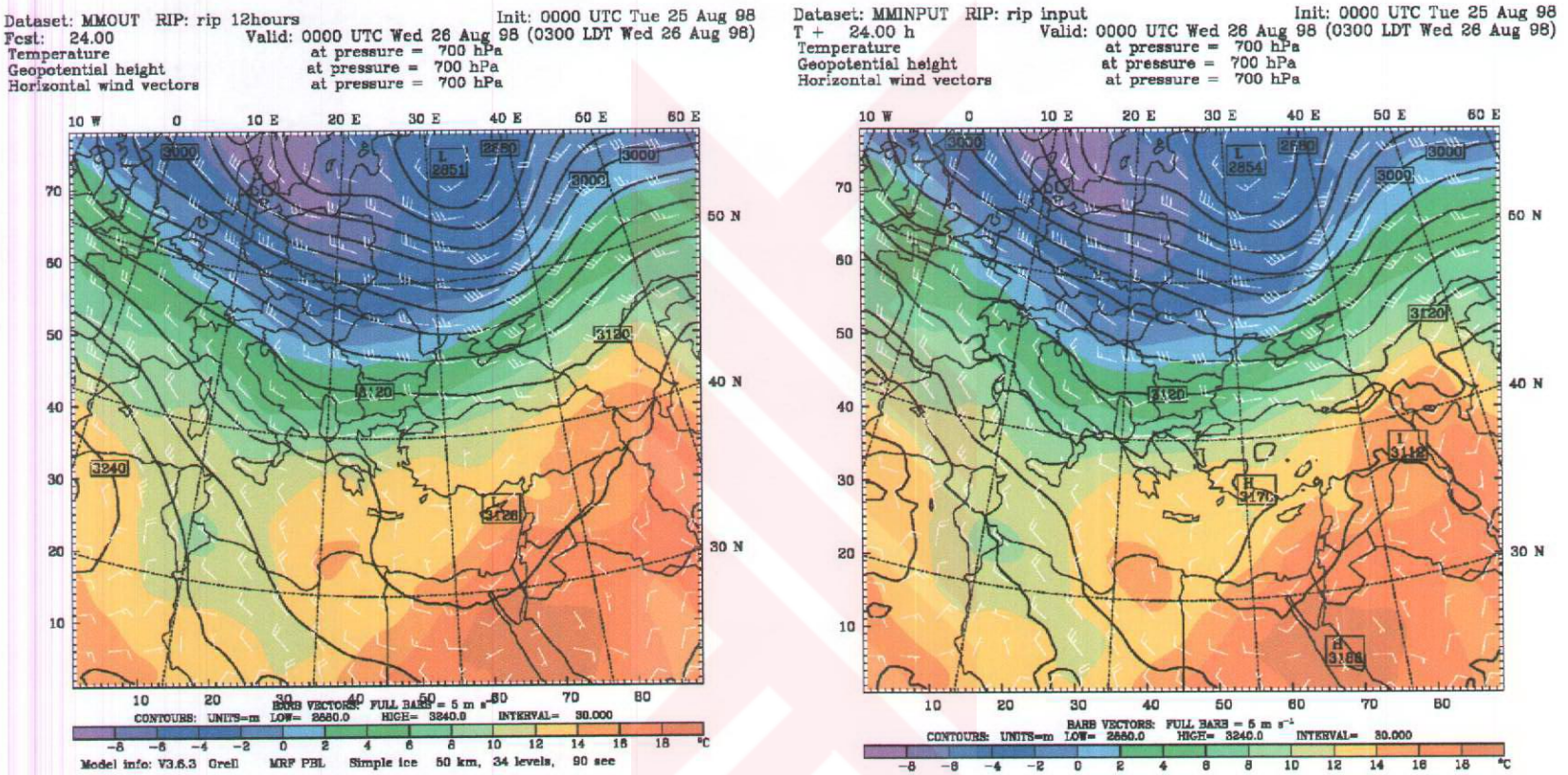

Figure D.3: 24 hours forecast (left) and observed (right) 700 hpa geopotential heights in gpm (black contours), temperature in °C (color shading) and horizontal wind velocity (white vectors), valid at 0000UTC, 26 – 08 – 1998.

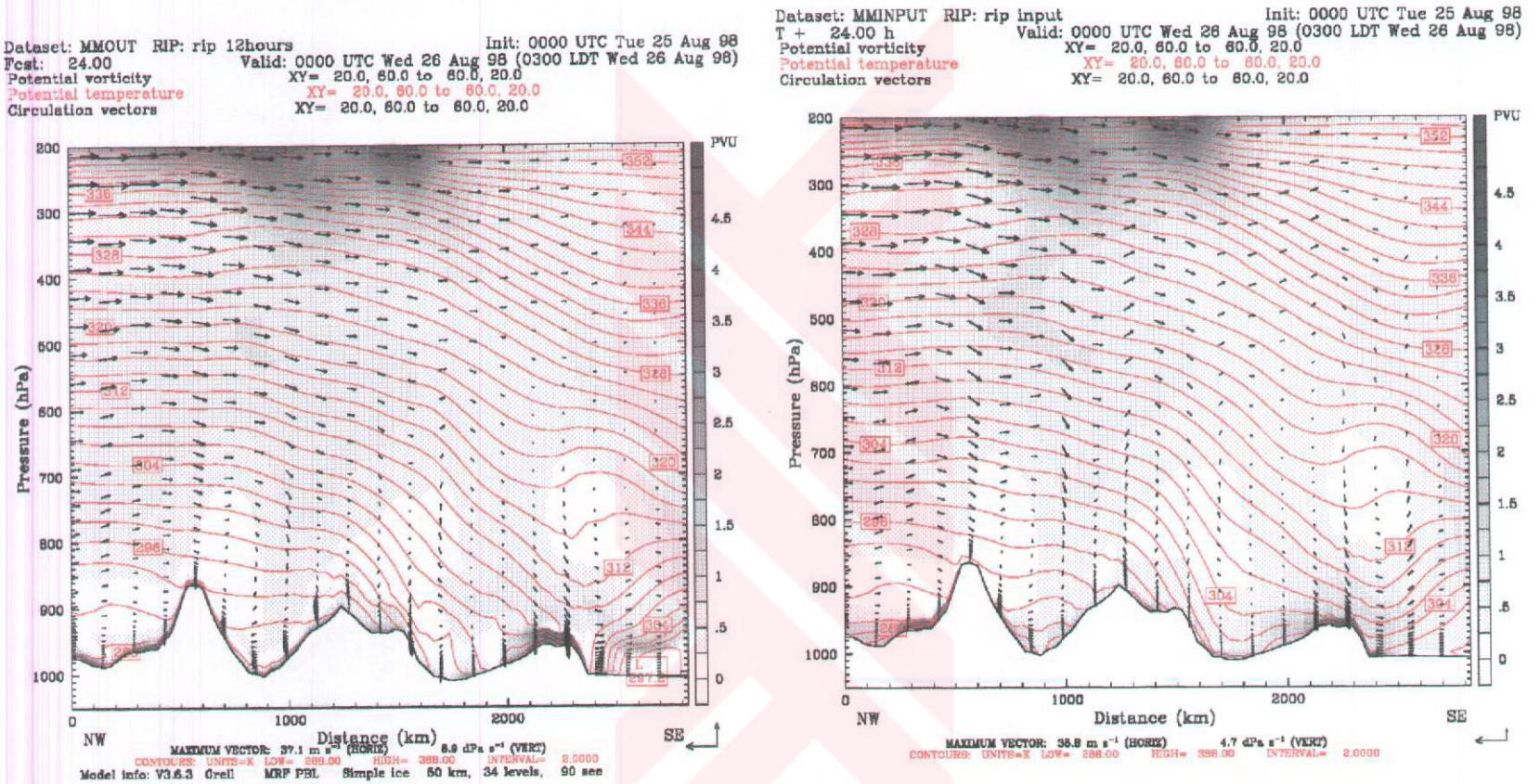

Figure D.4: 24 hours forecast (left) and observed (right) vertical cross section of the potential vorticity (black and white shading), potential temperatures (red lines) and the wind circulation (black vectors) predicted over a NW – SE line of length around 3000 km from the south of Poland to Cyprus, valid at 0000UTC, 26 – 08 – 1998.

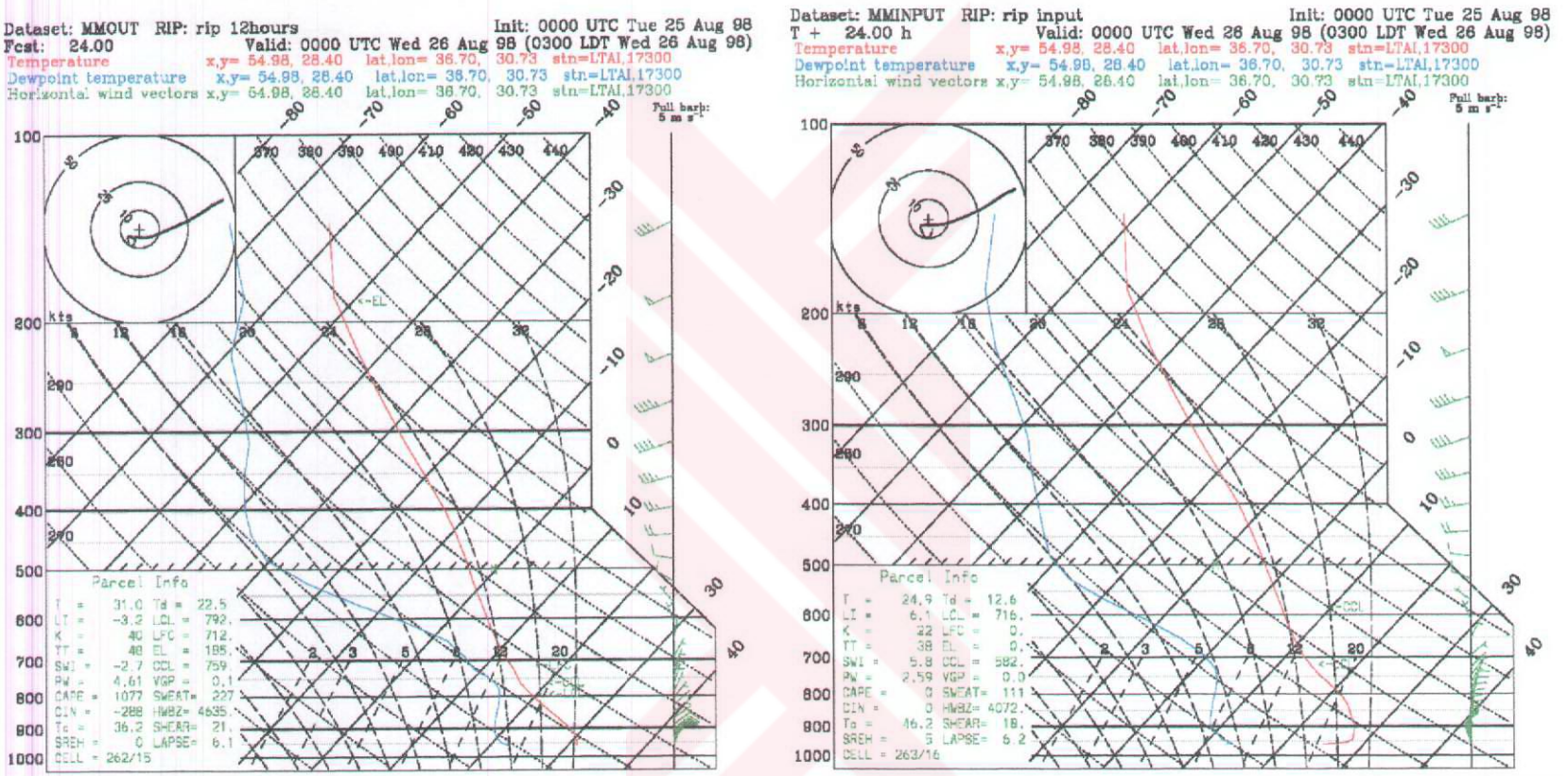

Figure D.5: 24 hours estimated (left) and observed (right) Skew – T Plot diagram for Antalya (36.47 °N, 30.34 °E), valid at 0000UTC, 26 – 08 – 1998.

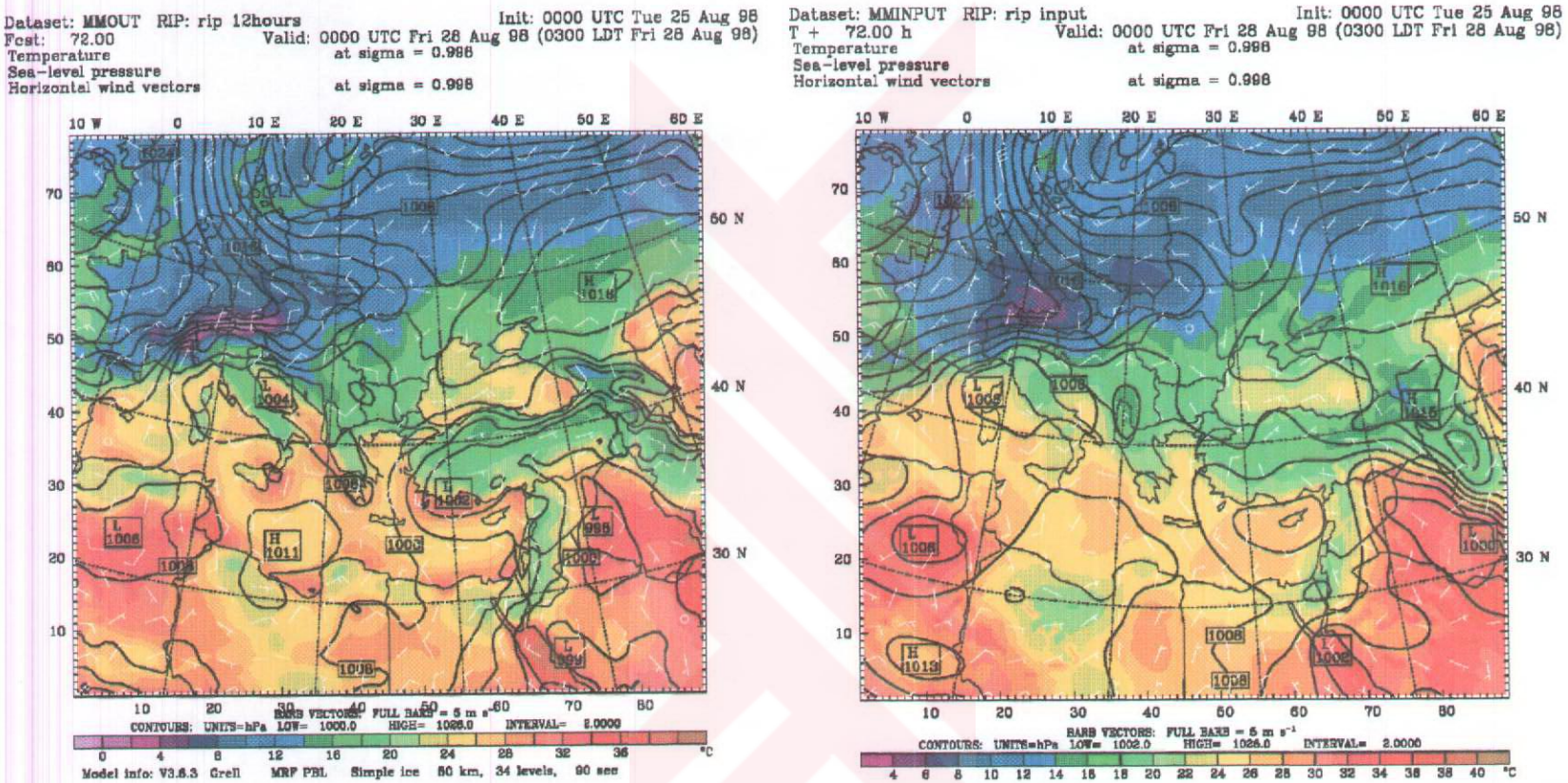

Figure D.6: 72 hours forecast (left) versus observed (right) Sea level pressure in hpa (black contours), temperature in °C (color shading) and horizontal wind velocity (white vectors), valid at 0000UTC, 28 – 08 – 1998.

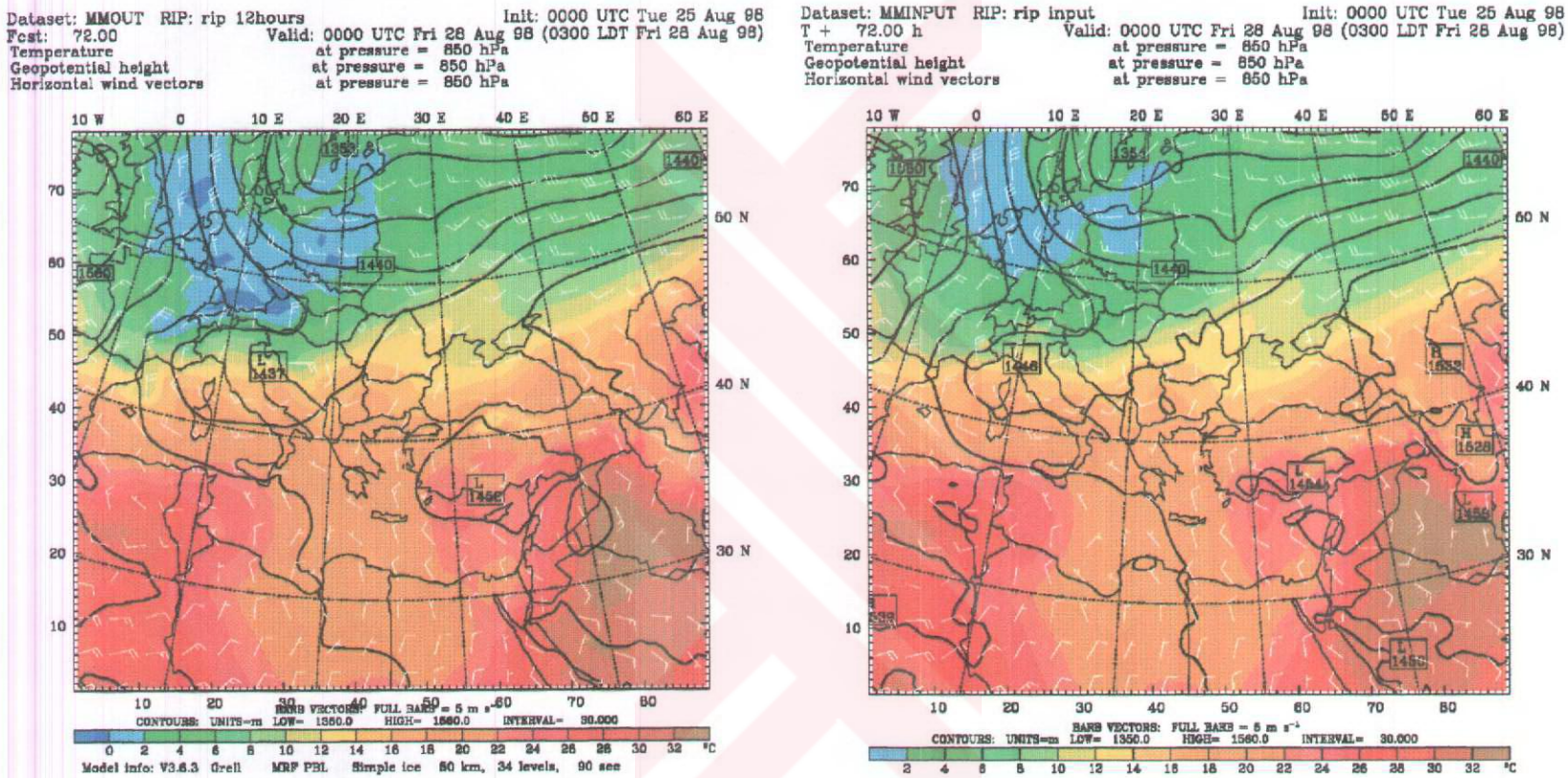

Figure D.7: 72 hours forecast (left) and observed (right) 850 hpa geopotential heights in gpm (black contours), temperature in °C (color shading) and horizontal wind velocity (white vectors), valid at 0000UTC, 28 – 08 – 1998.

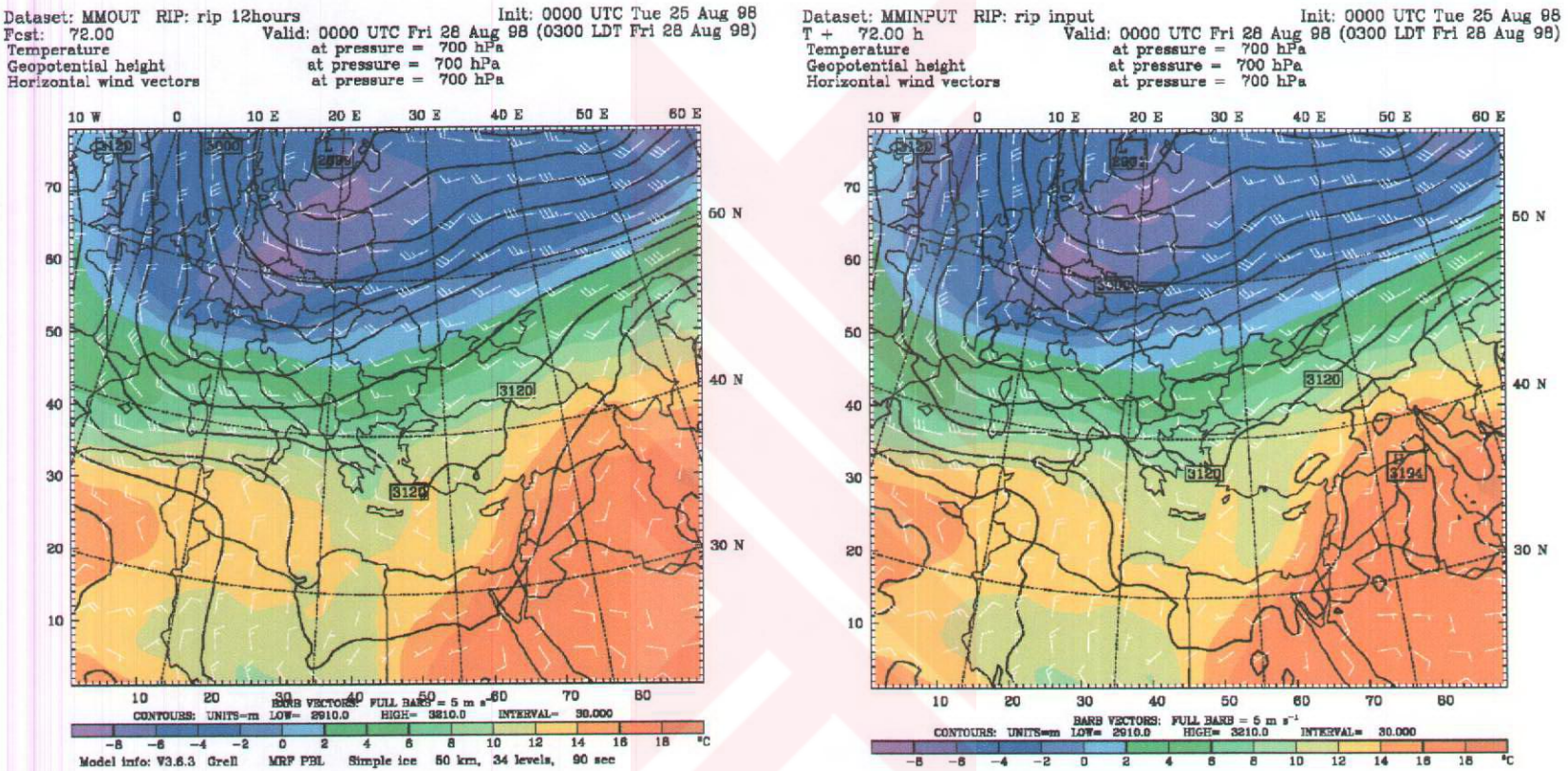

Figure D.8: 72 hours forecast (left) and observed (right) 700 hpa geopotential heights in gpm (black contours), temperature in °C (color shading) and horizontal wind velocity (white vectors), valid at 0000UTC, 28 – 08 – 1998.

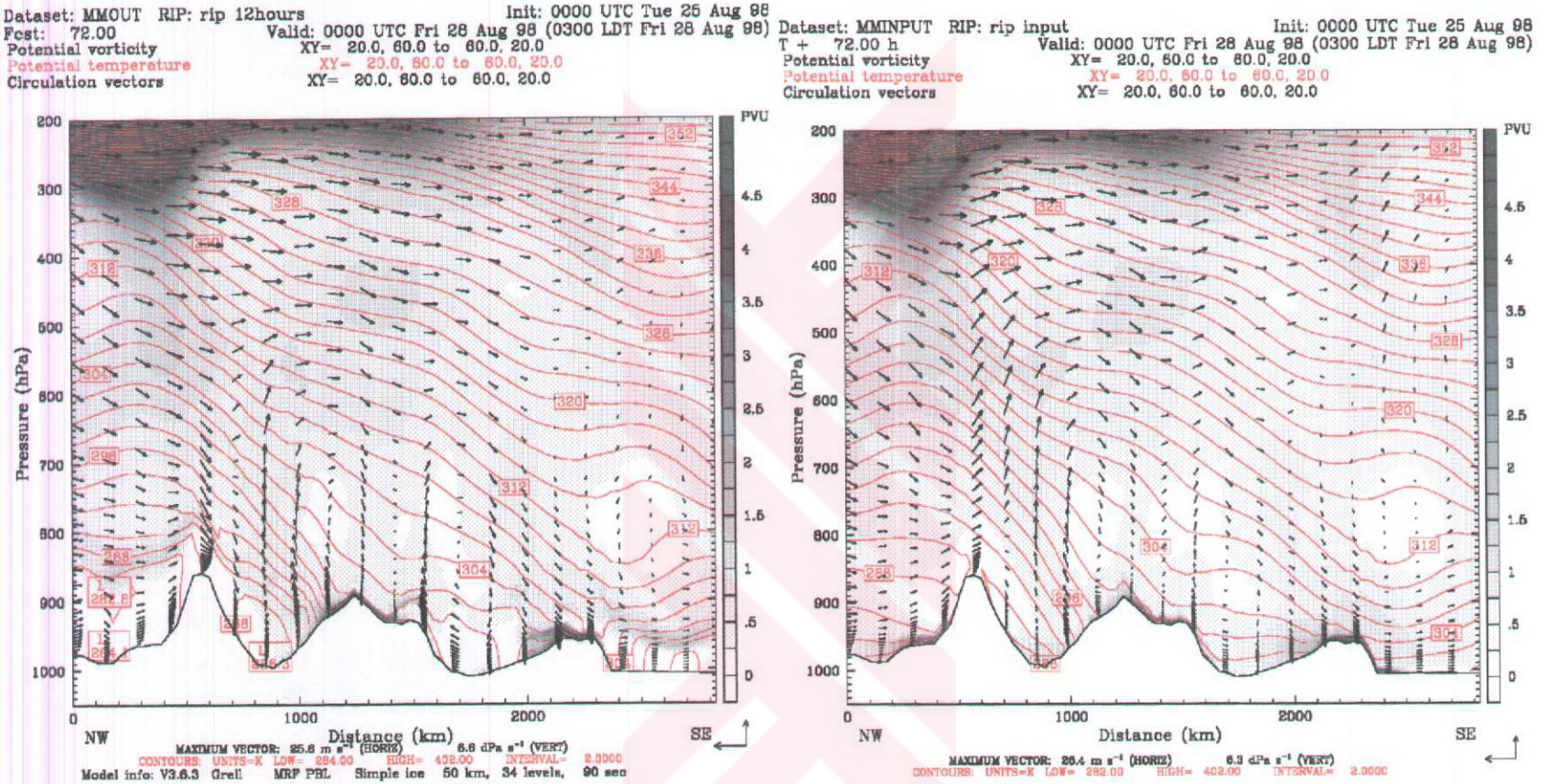

Figure D.9: 72 hours forecast (left) and observed (right) vertical cross section of the potential vorticity (black and white shading), potential temperatures (red lines) and the wind circulation (black vectors) predicted over a NW – SE line of length around 3000 km from the south of Poland to Cyprus, valid at 0000UTC, 28 – 08 – 1998.

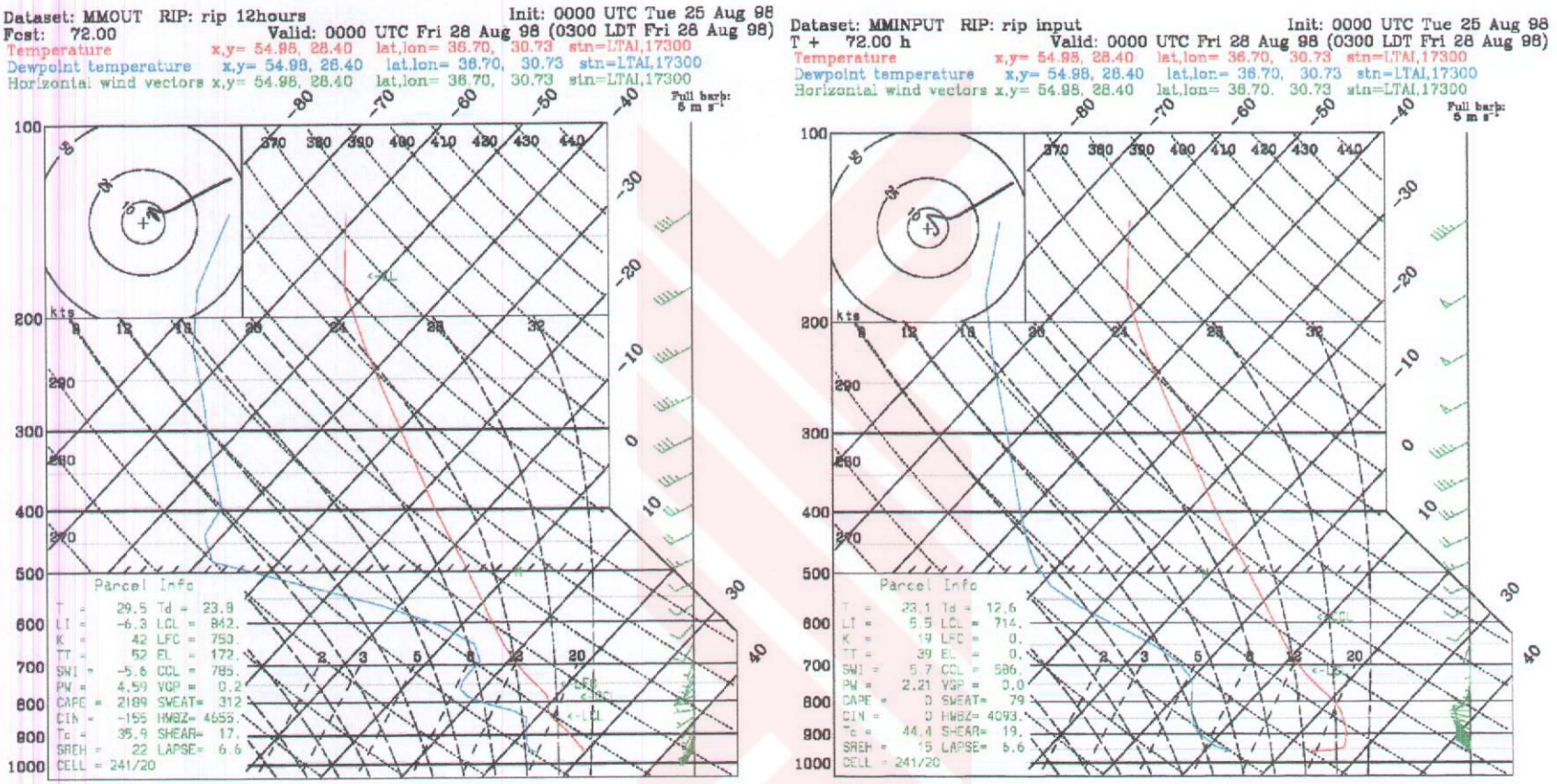

Figure D.10: 72 hours estimated (left) and observed (right) Skew – T Plot diagram for Antalya (36.47 °N, 30.34 °E), valid at 0000UTC, 28 – 08 – 1998.

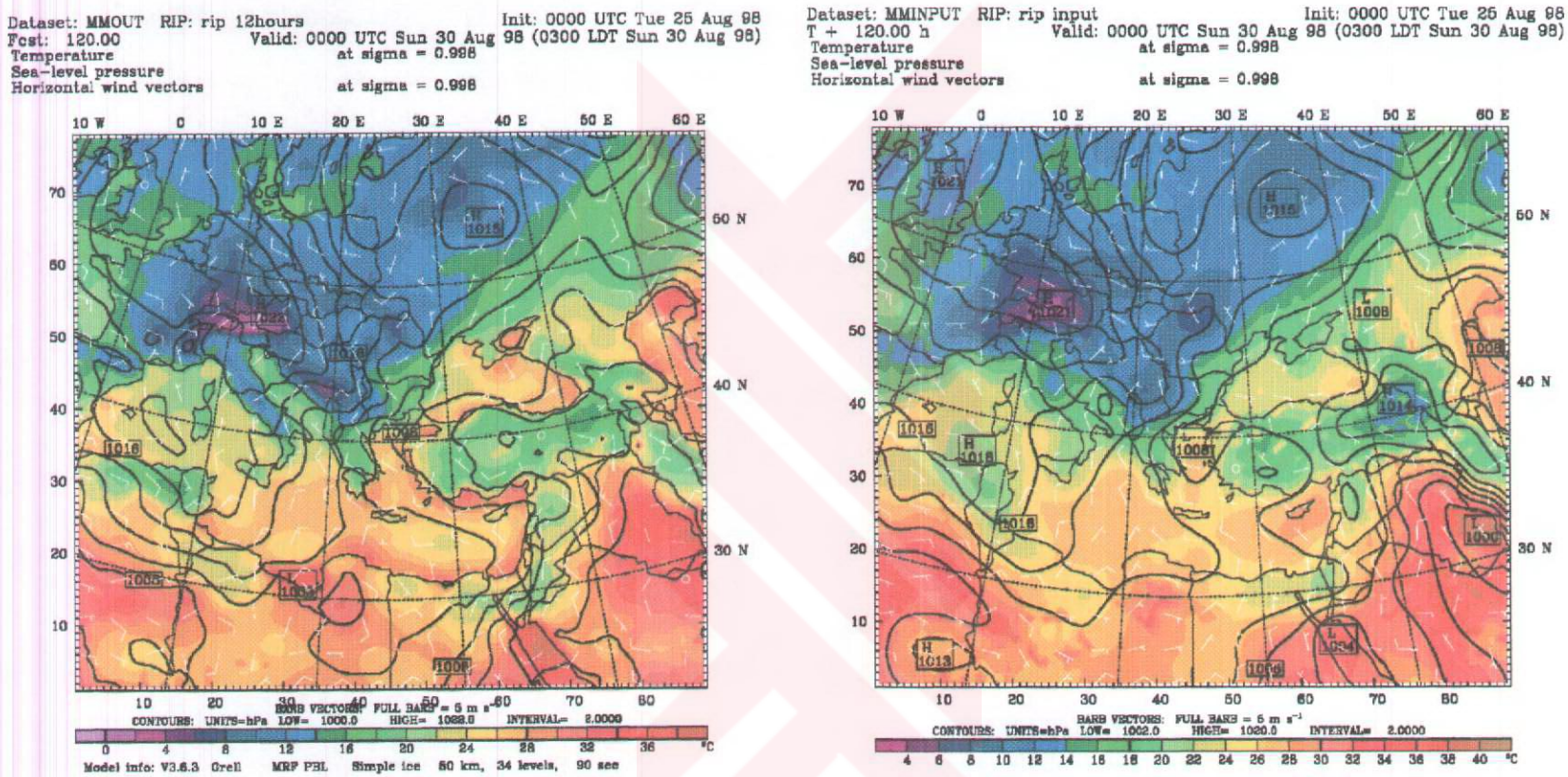

Figure D.11: 120 hours forecast (left) versus observed (right) Sea level pressure in hpa (black contours), temperature in °C (color shading) and horizontal wind velocity (white vectors), valid at 0000UTC, 30 – 08 – 1998.

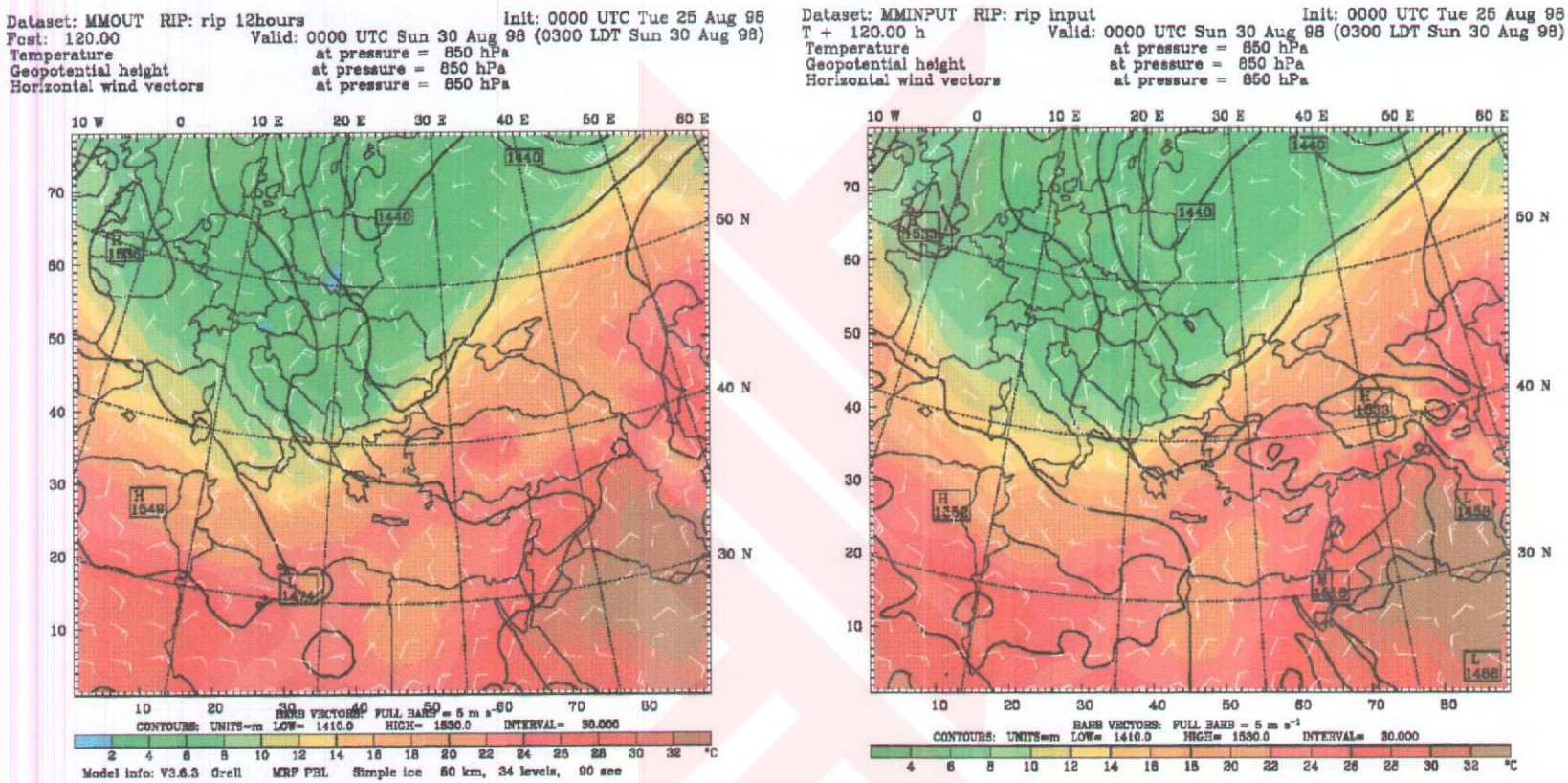

Figure D.12: 120 hours forecast (left) and observed (right) 850 hpa geopotential heights in gpm (black contours), temperature in °C (color shading) and horizontal wind velocity (white vectors), valid at 0000UTC, 30 – 08 – 1998.

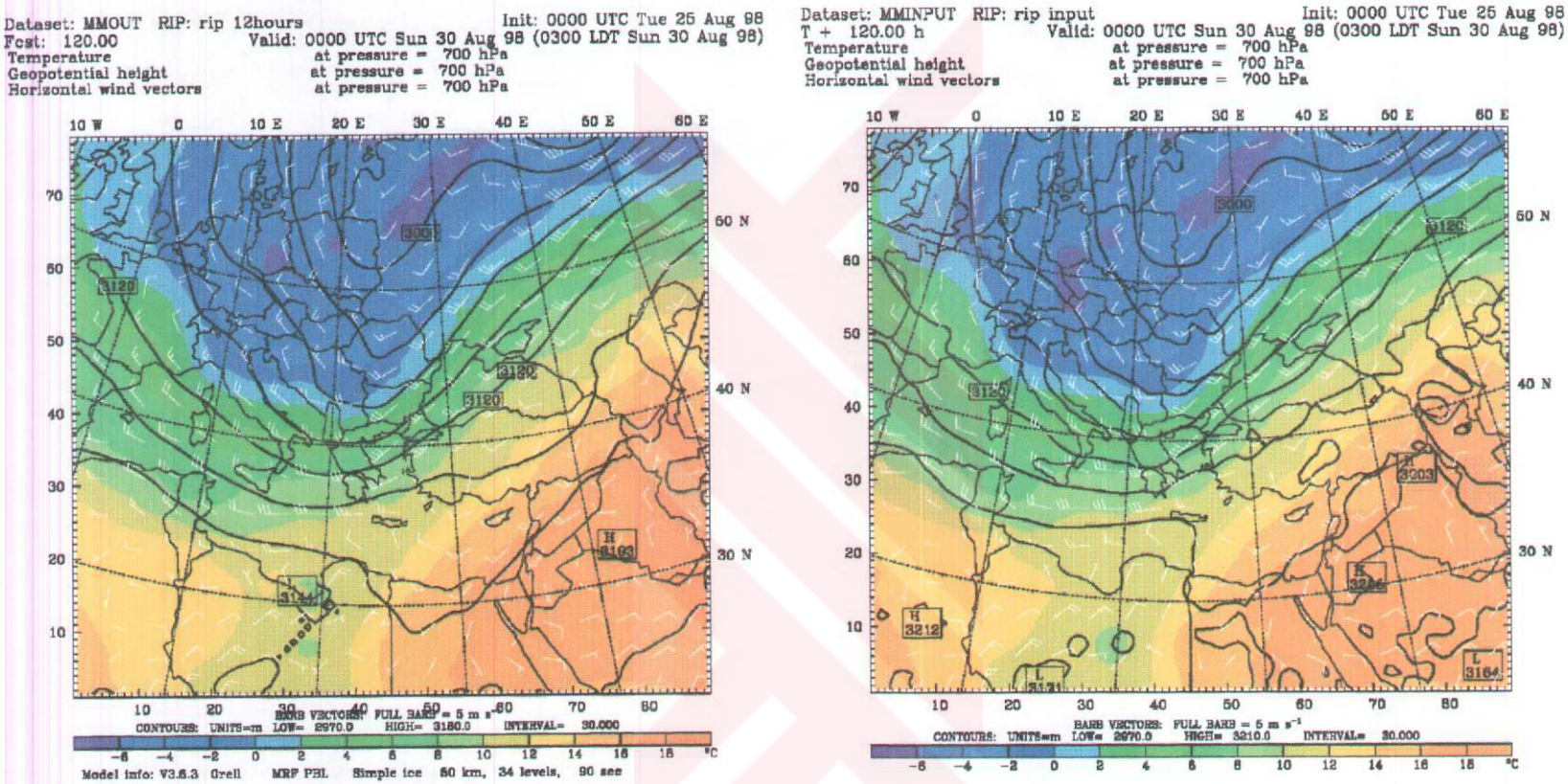

Figure D.13: 120 hours forecast (left) and observed (right) 700 hpa geopotential heights in gpm (black contours), temperature in °C (color shading) and horizontal wind velocity (white vectors), valid at 0000UTC, 30 – 08 – 1998.

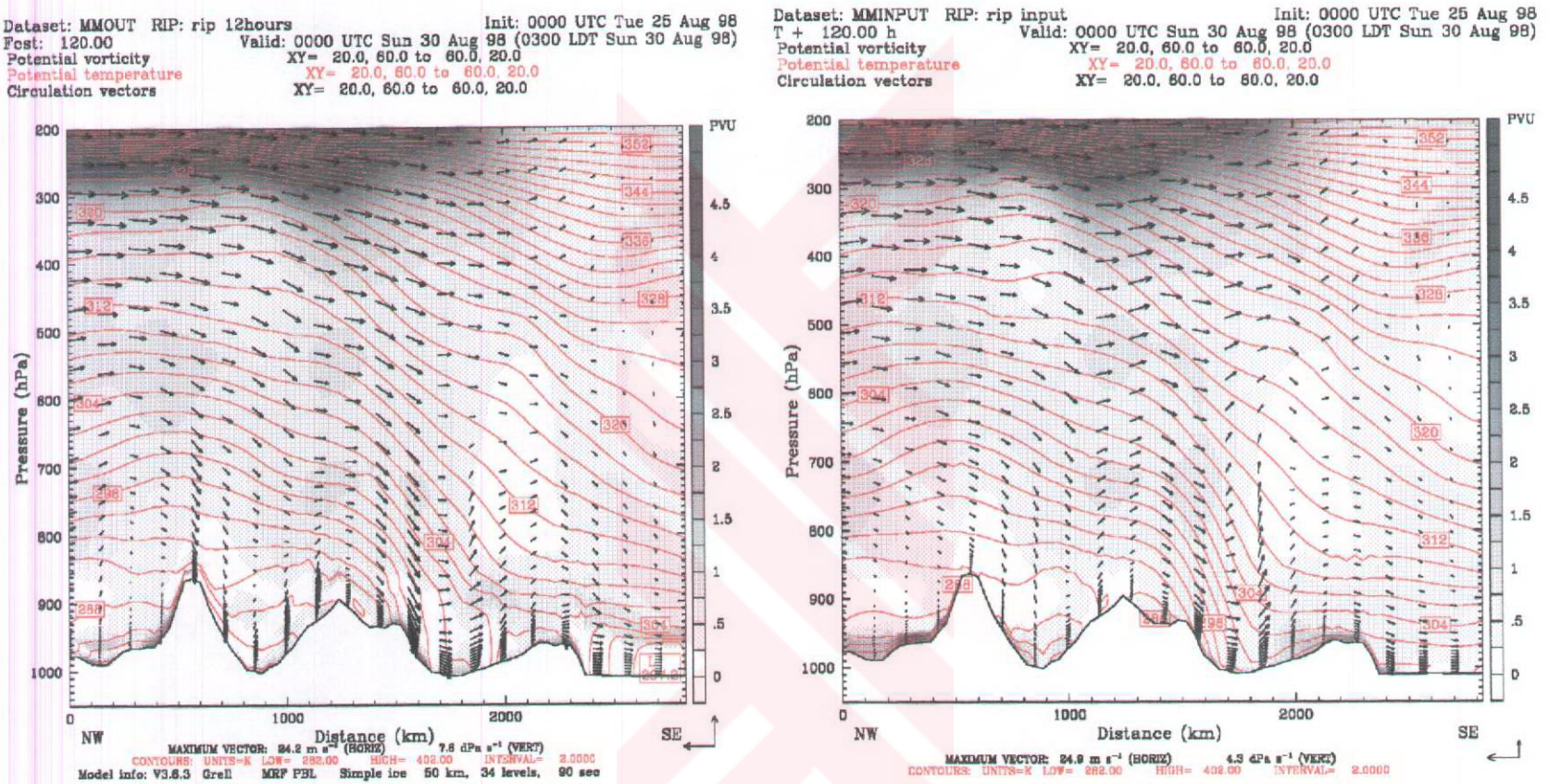

Figure D.14: 120 hours forecast (left) and observed (right) vertical cross section of the potential vorticity (black and white shading), potential temperatures (red lines) and the wind circulation (black vectors) predicted over a NW – SE line of length around 3000 km from the south of Poland to Cyprus, valid at 0000UTC, 30 – 08 – 1998.

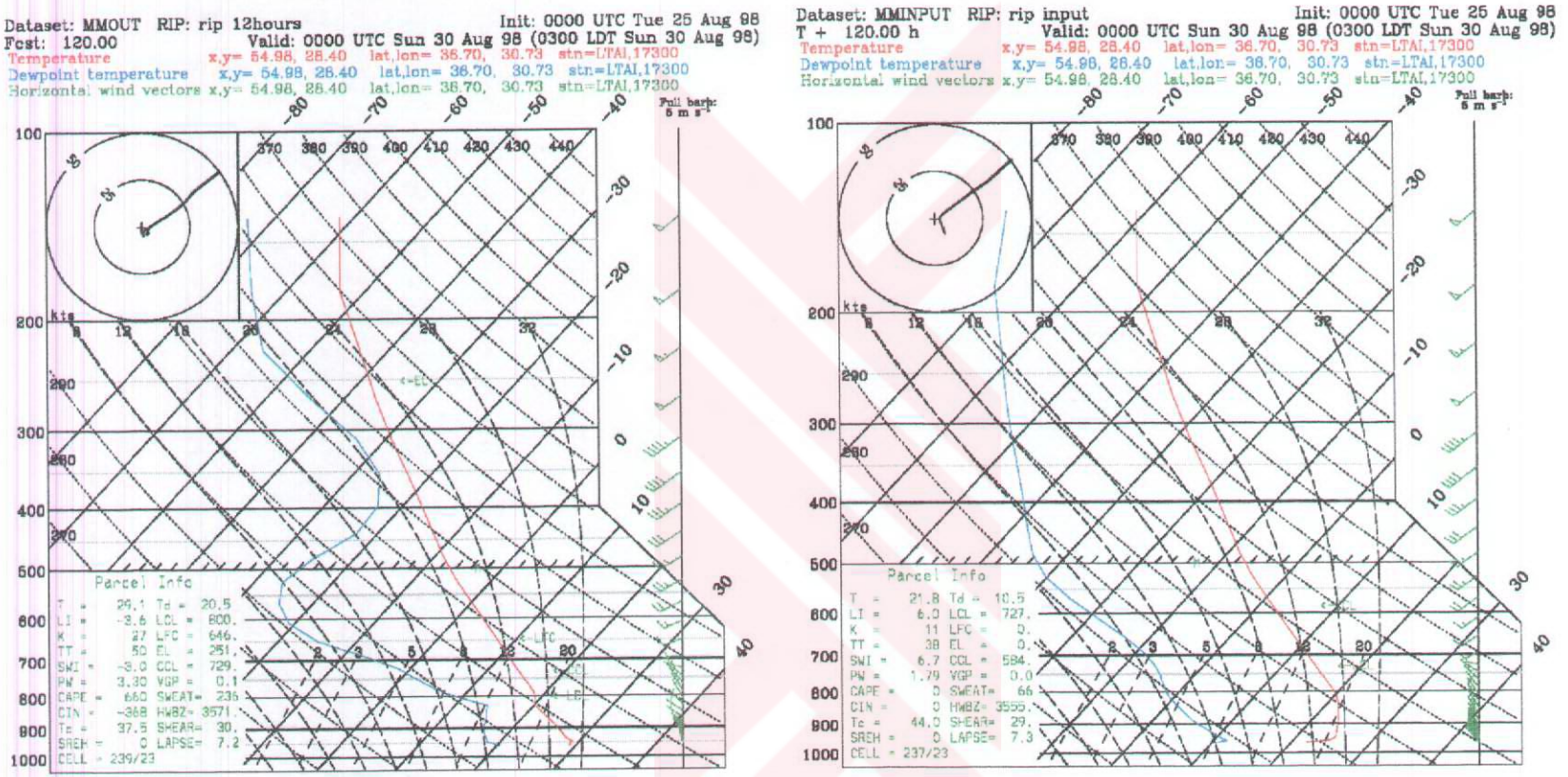

Figure D.15: 120 hours estimated (left) and observed (right) Skew – T Plot diagram for Antalya (36.47 °N, 30.34 °E), valid at 0000UTC, 30 – 08 – 1998.

APPENDIX E

CAMx MODEL FIGURES

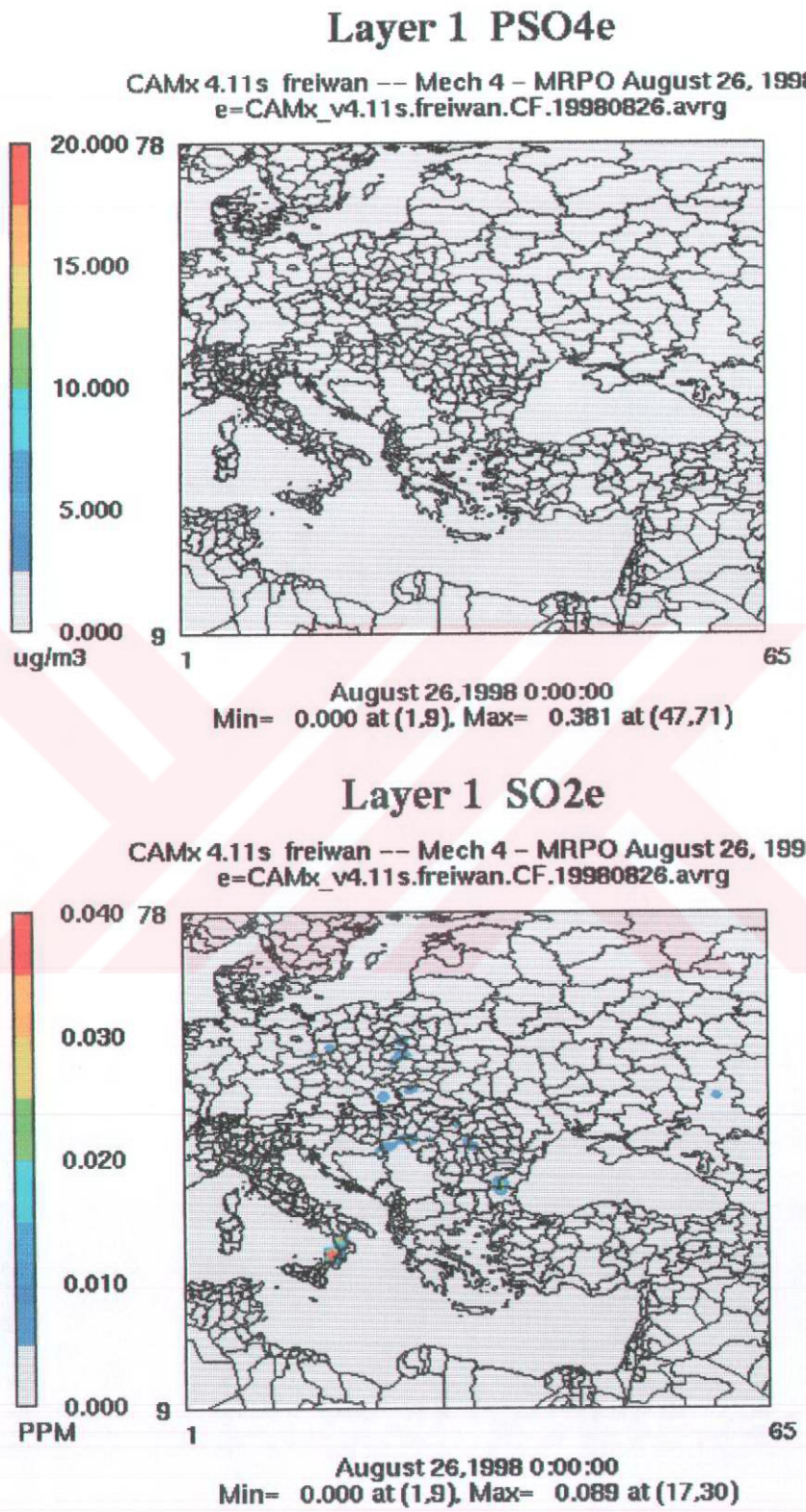

Figure E.1: Simulation of sulfate (upper) and sulfur dioxide (lower) concentration during 26 August 1998; a) 00:00 Z

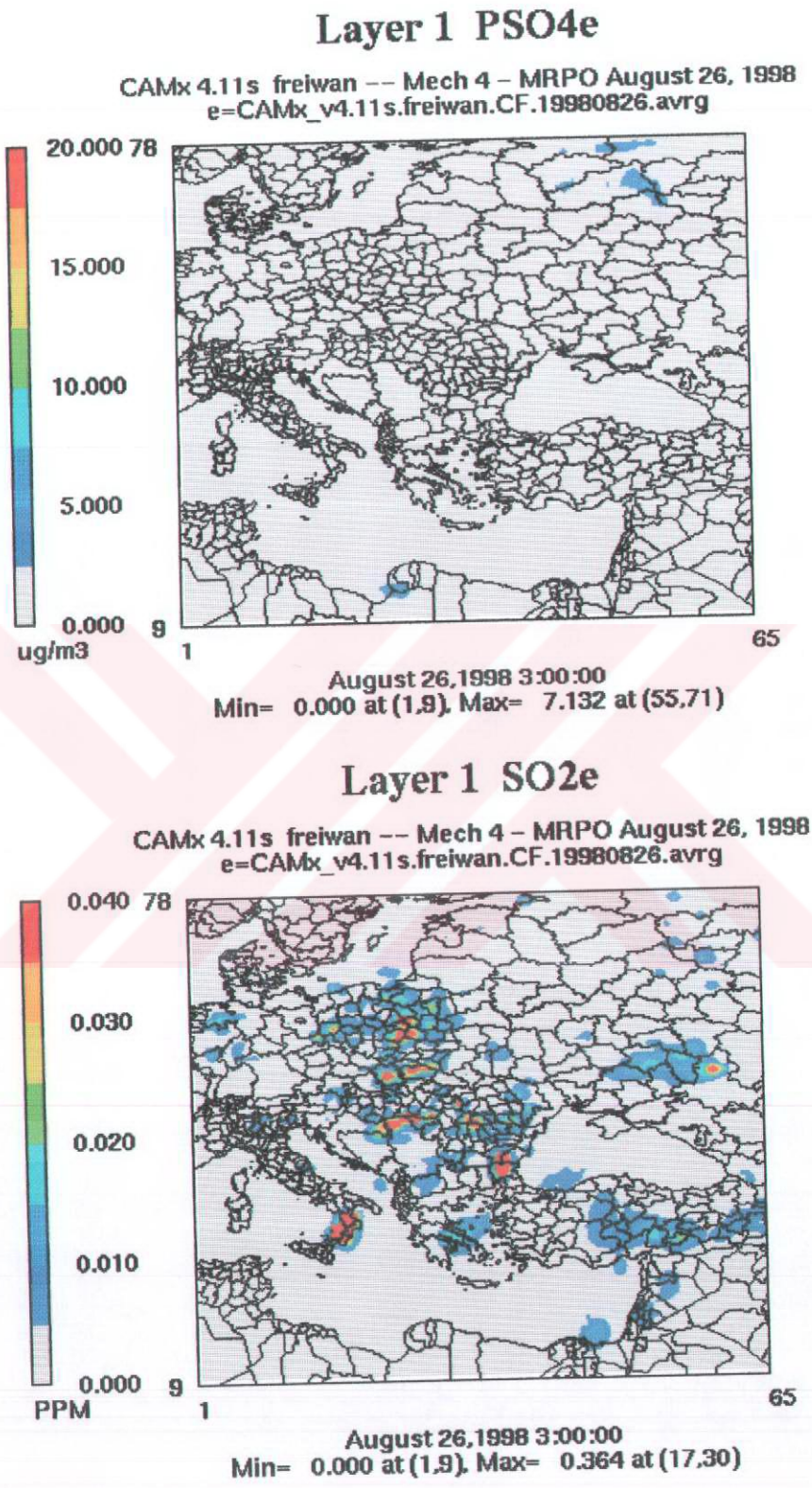

Figure E.1 b) 03:00 Z

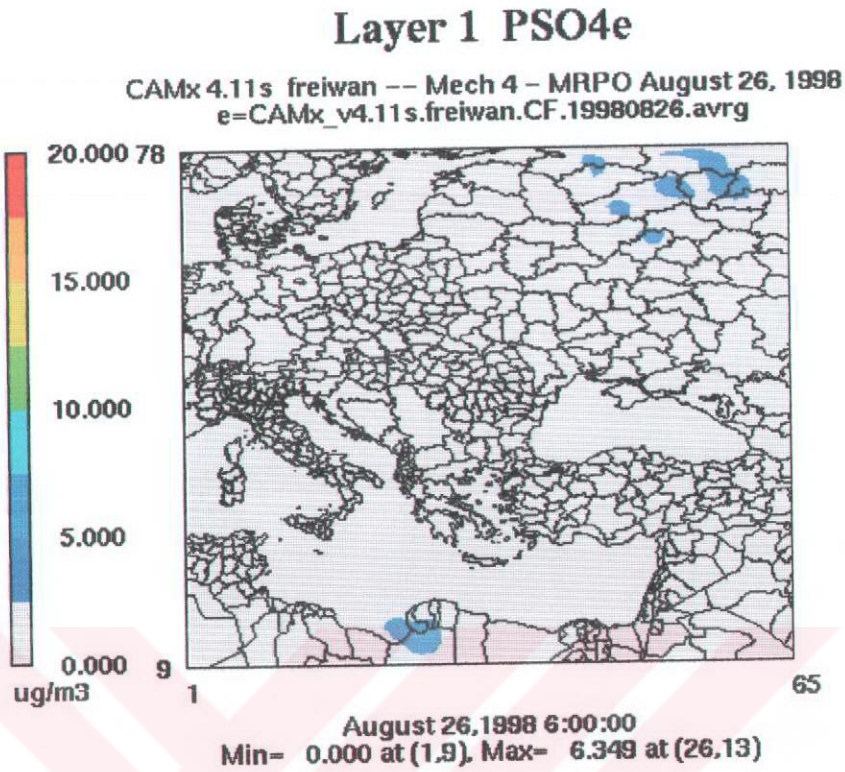

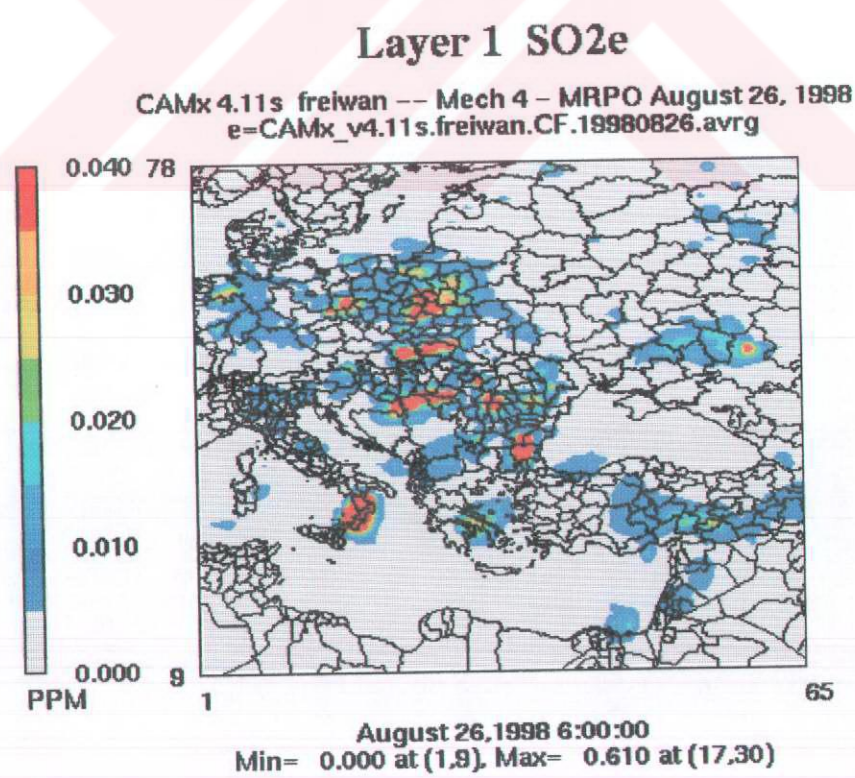

Figure E.1 c) 06:00 Z

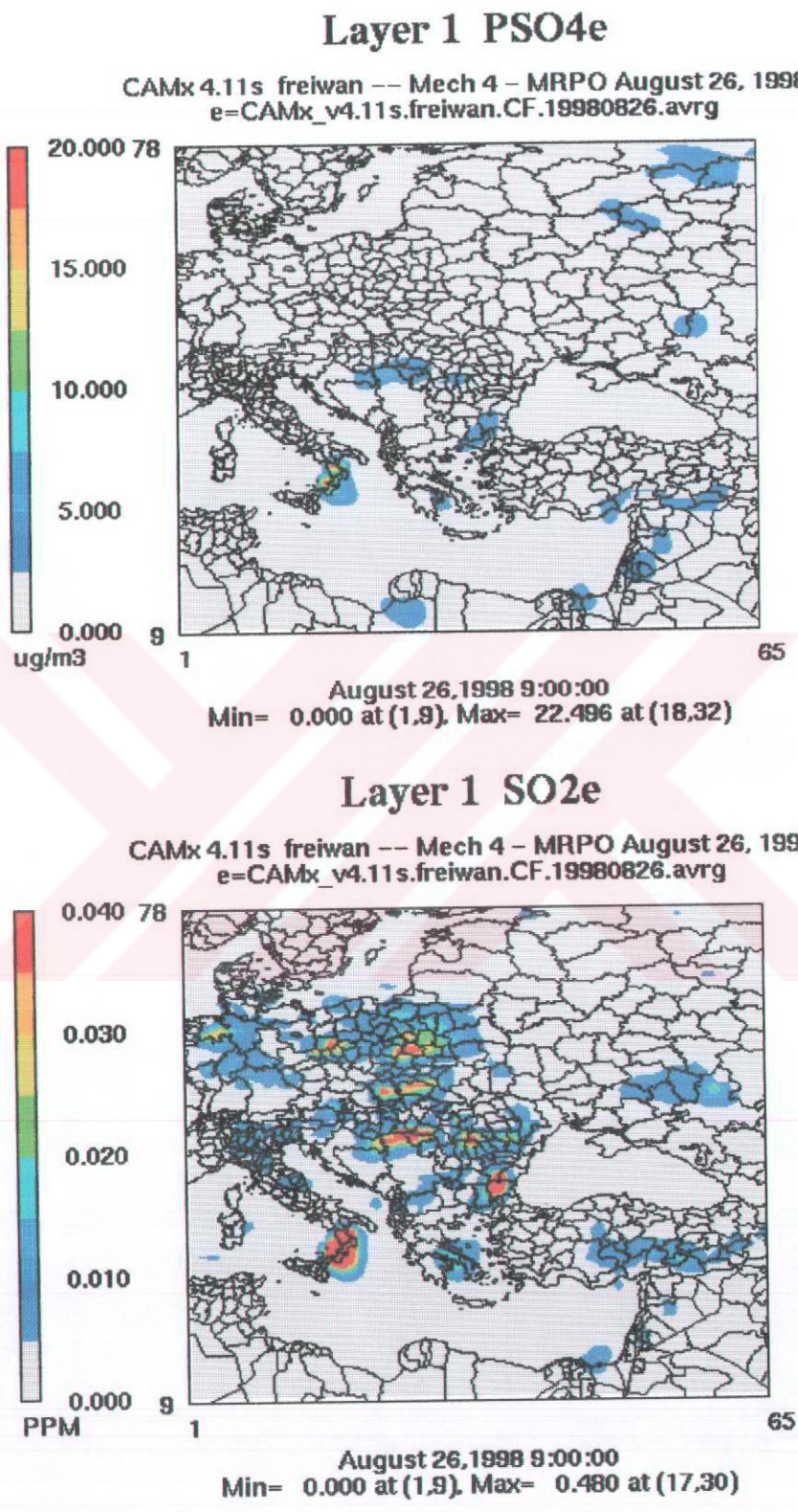

Figure E.1 d) 09:00 Z

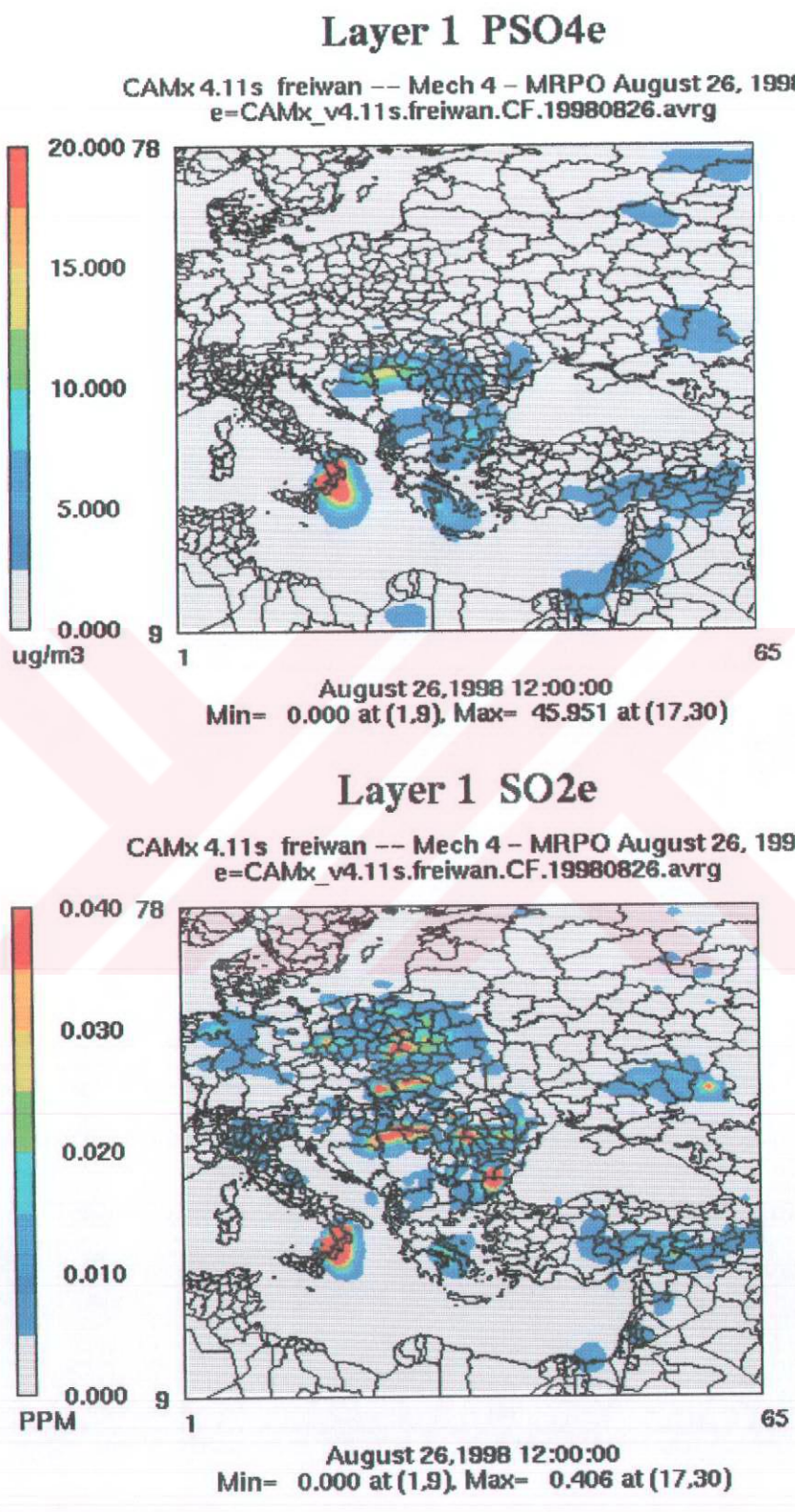

Figure E.1 e) 12:00 Z

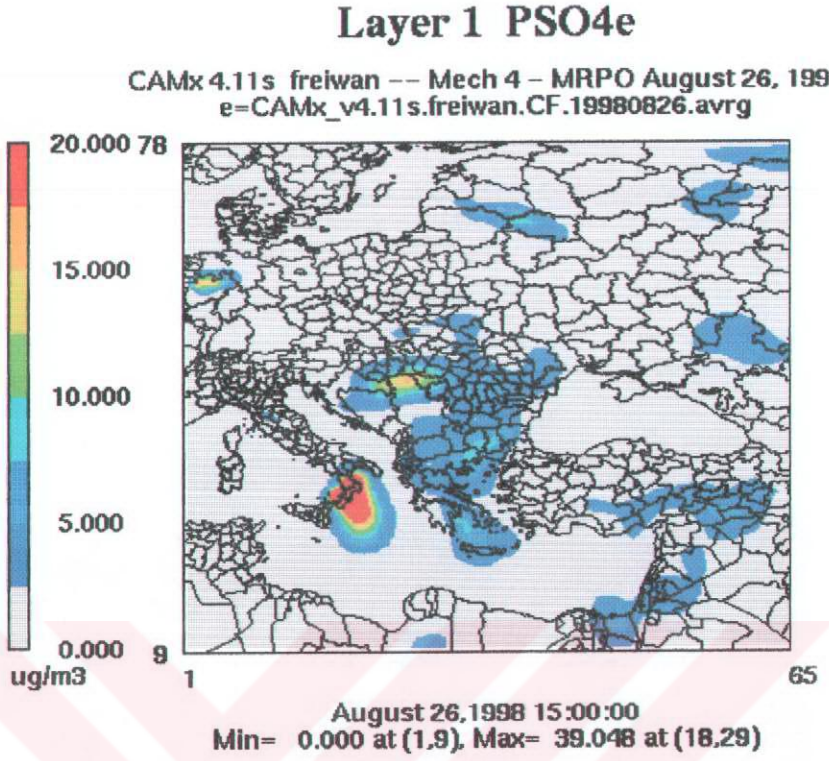

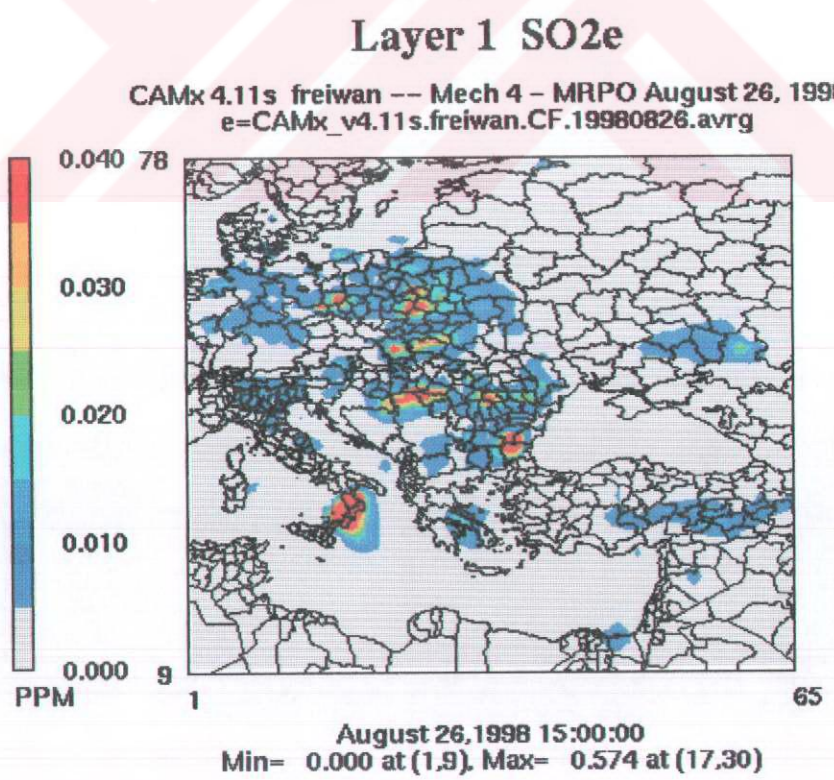

Figure E.1 f) 15:00 Z

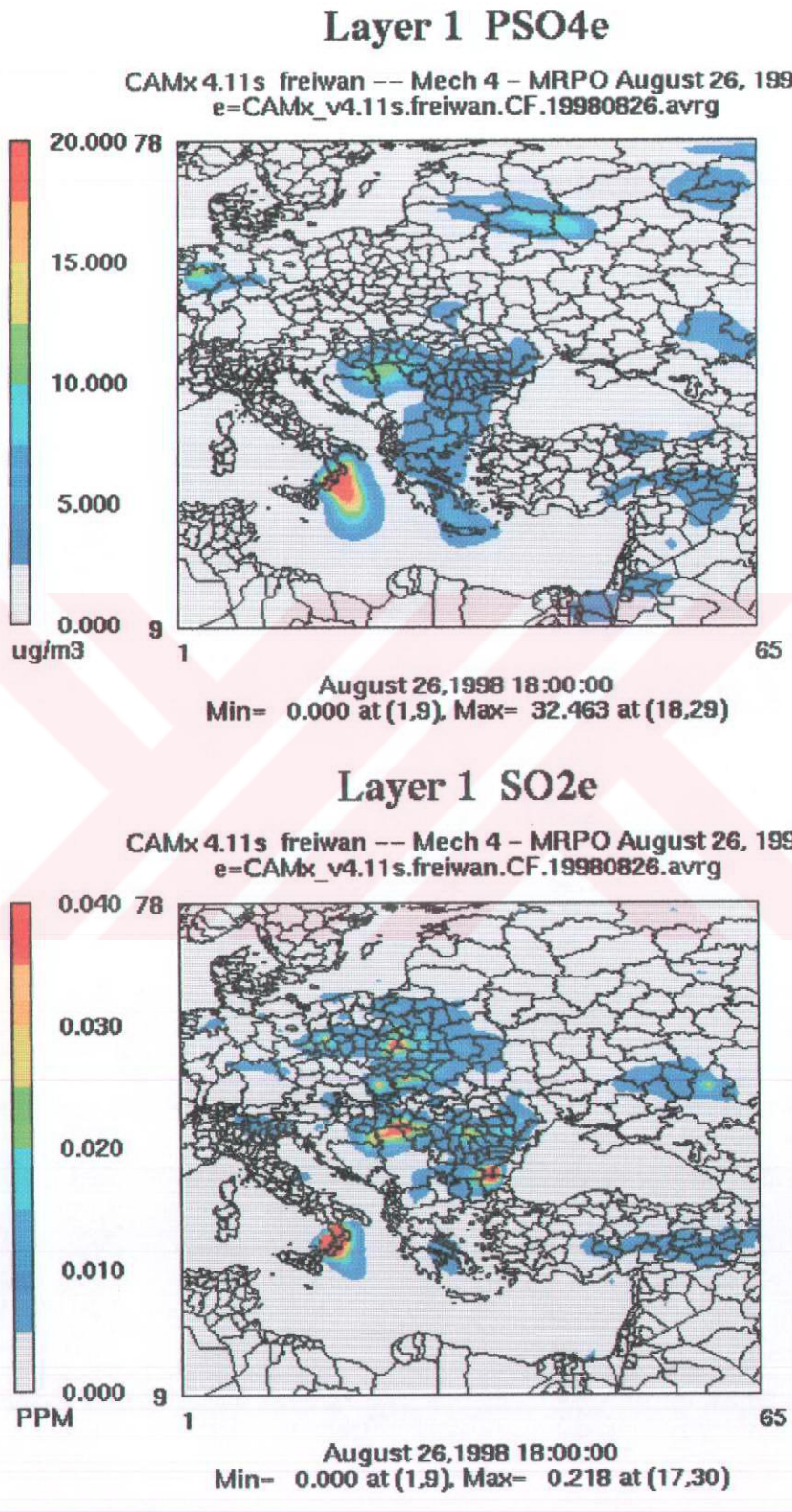

Figure E.1 g) 18:00 Z

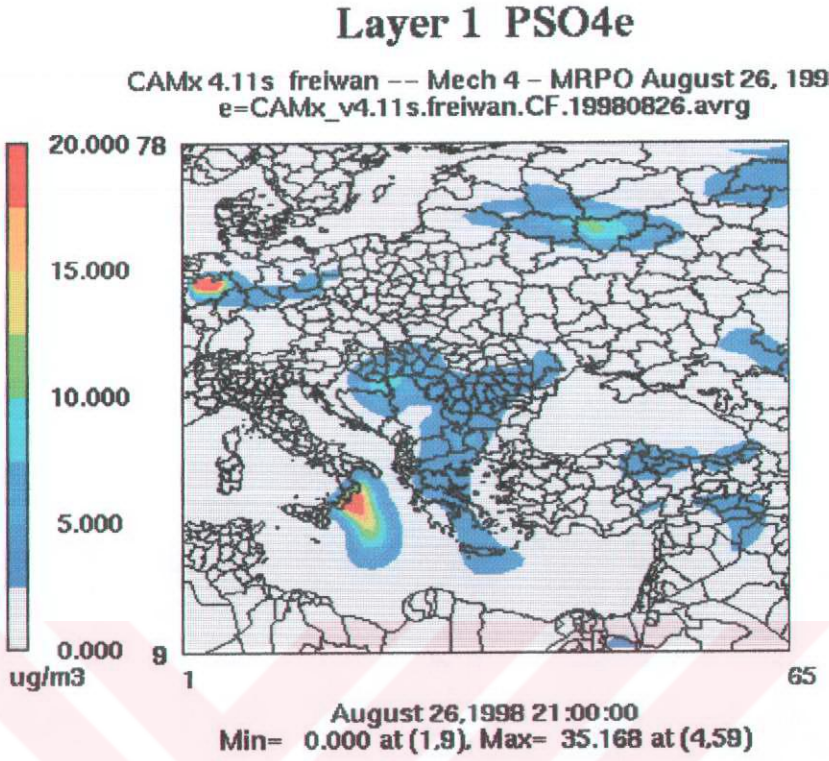

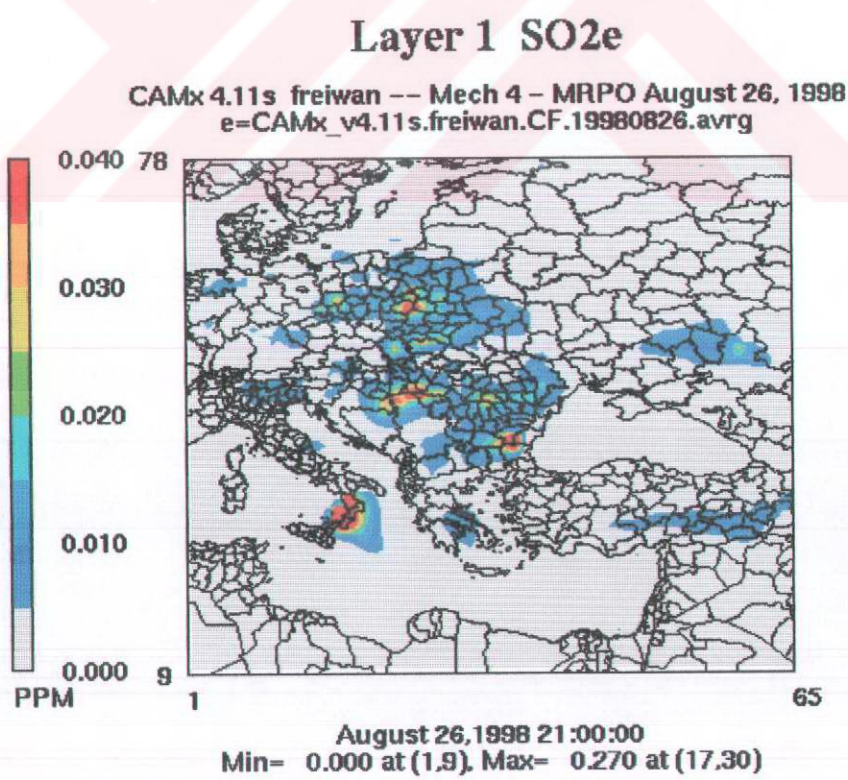

Figure E.1 h) 21:00 Z

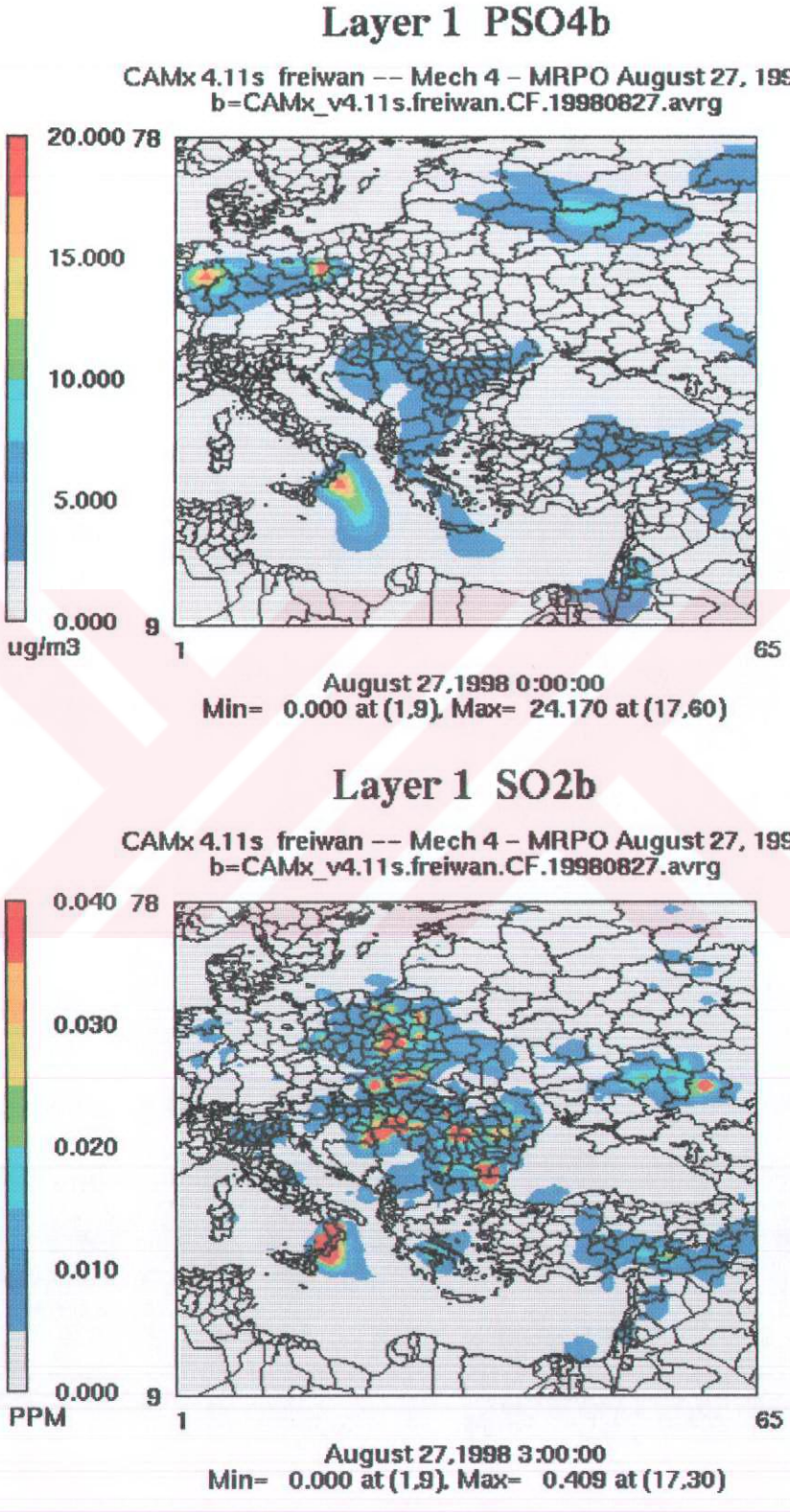

Figure E.2: The same as Fig. E.1 but for 27 Aug. 1998, a) 00:00 Z

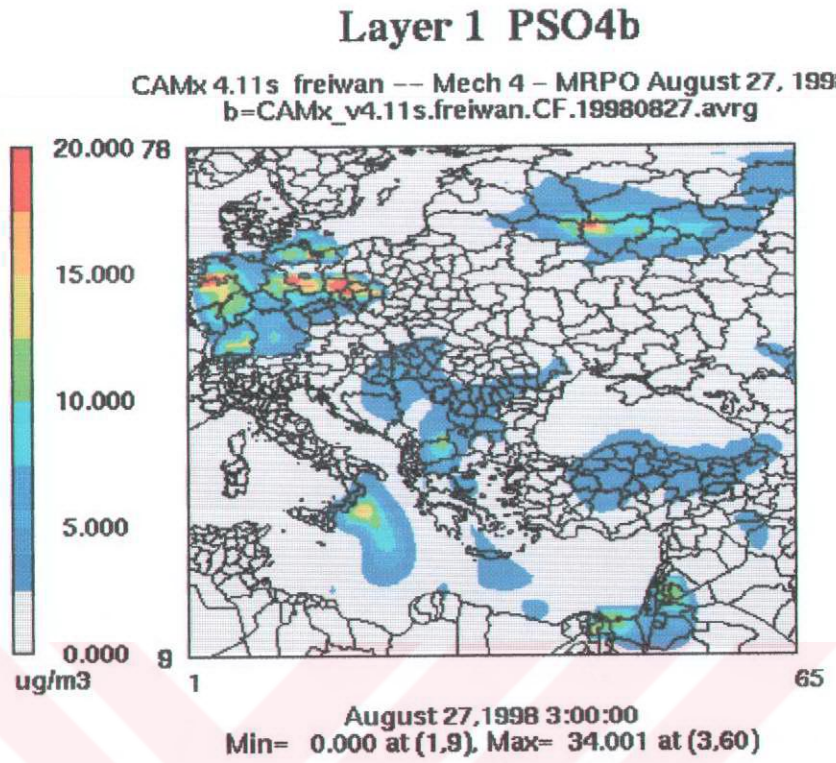

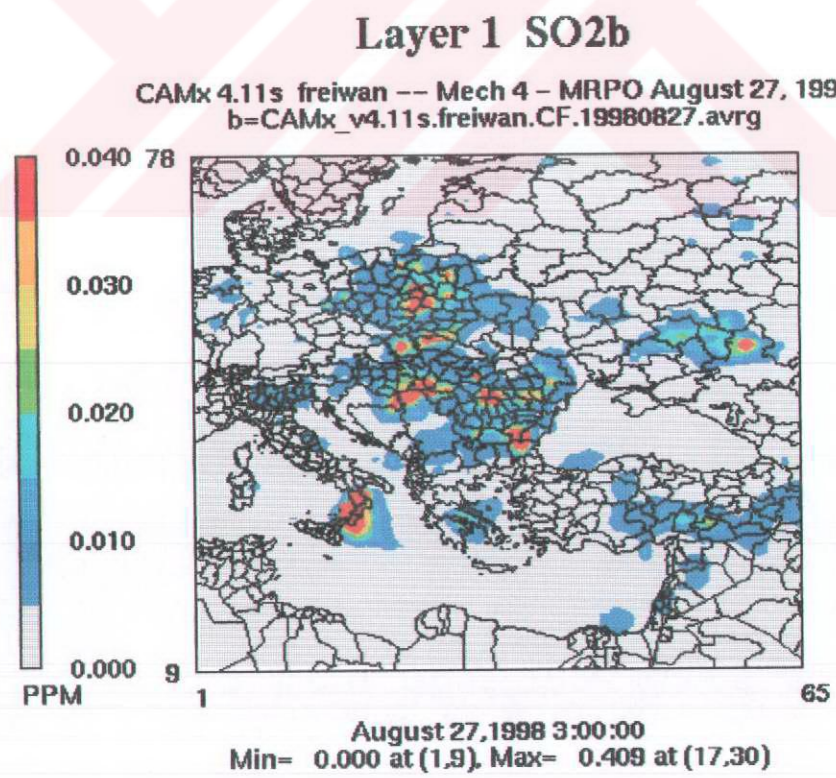

Figure E.2 b) 03:00 Z

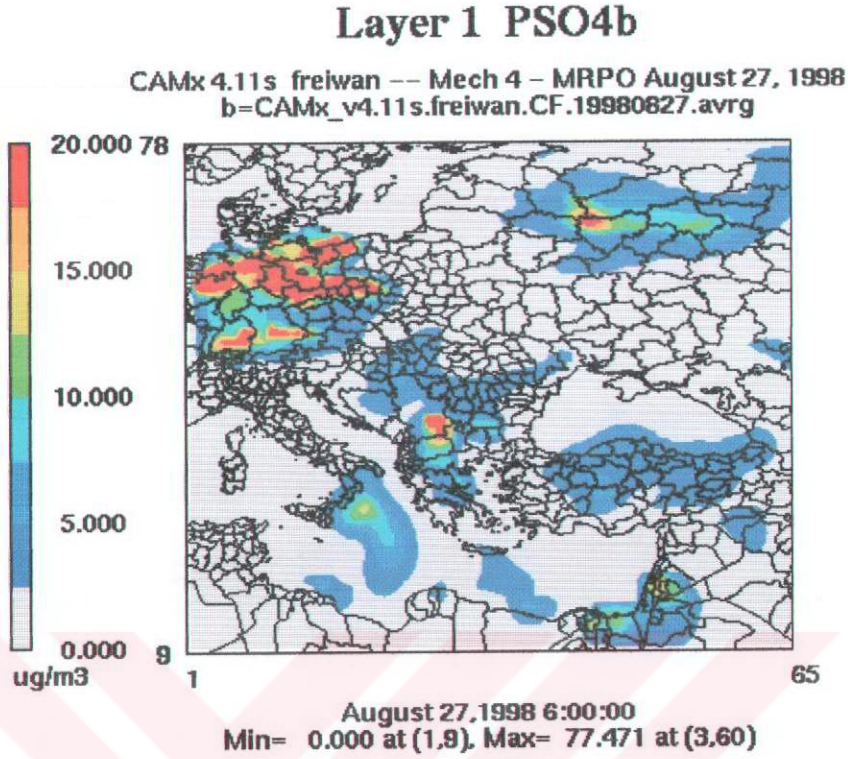

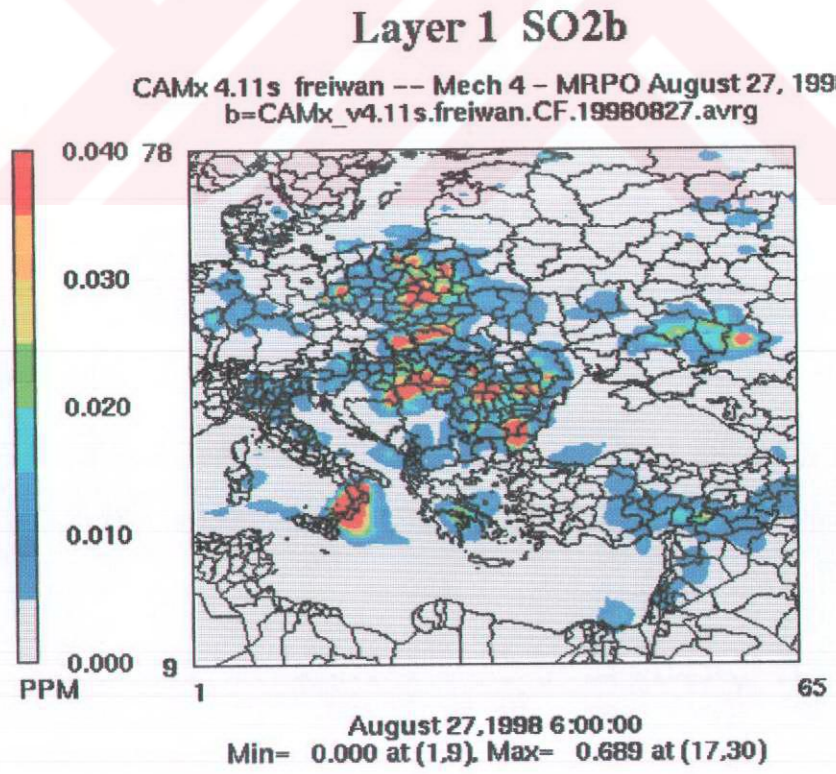

Figure E.2 c) 06:00 Z

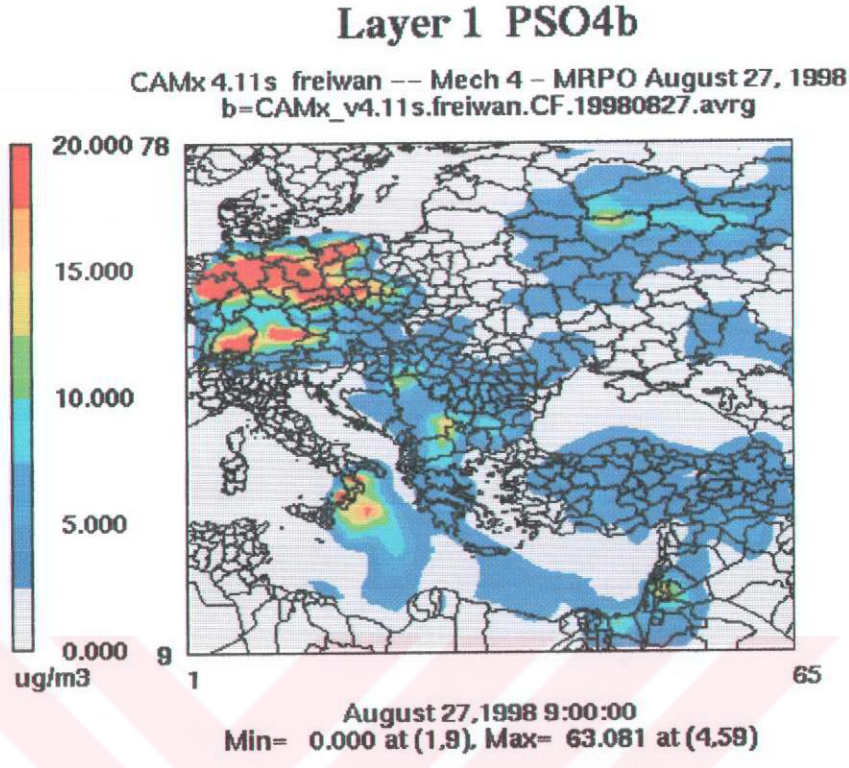

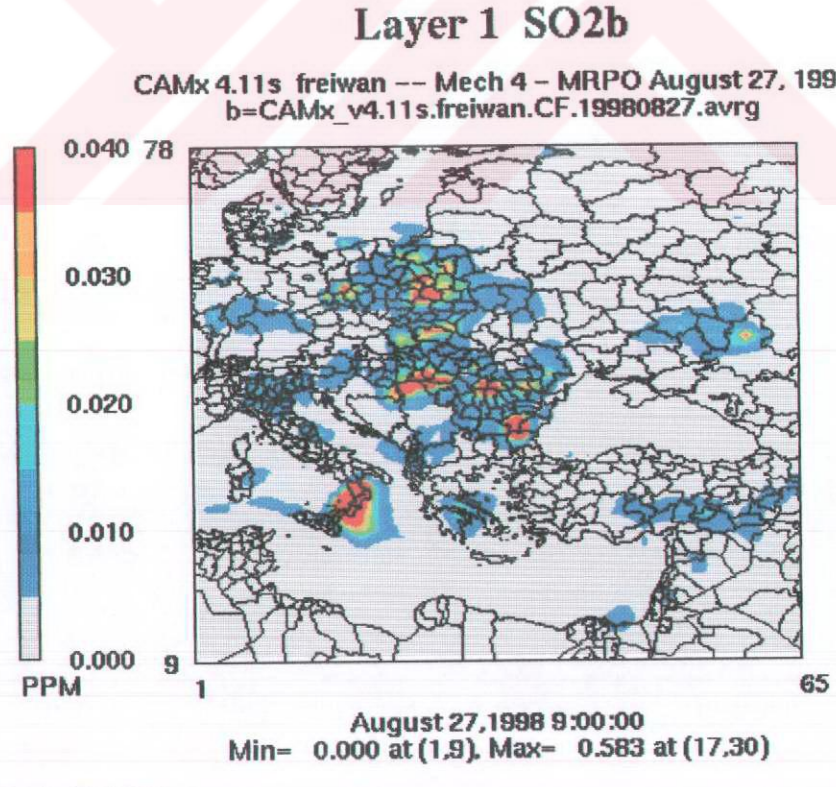

Figure E.2 d) 09:00 Z

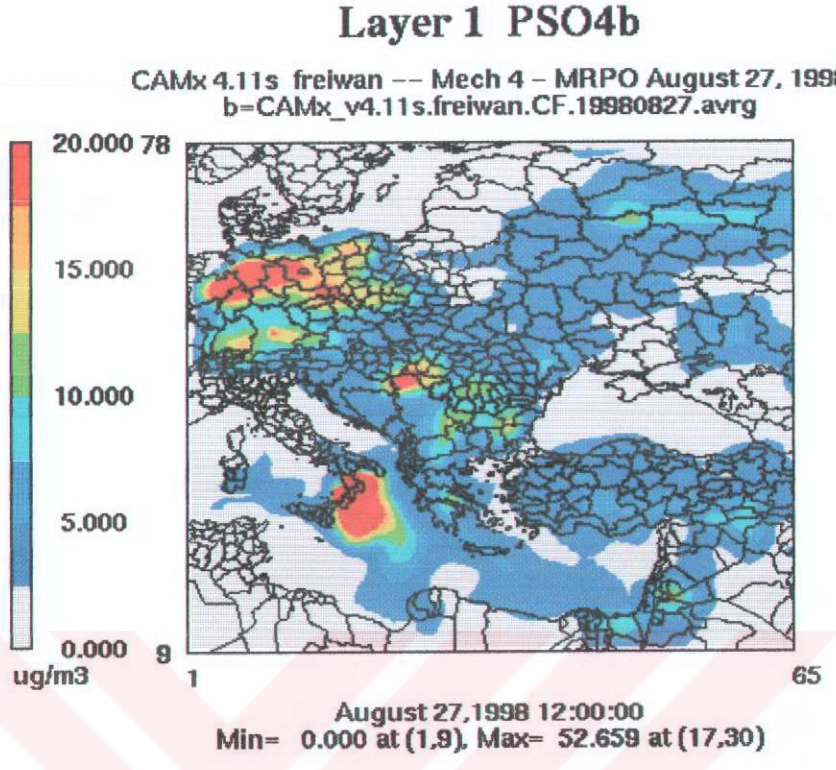

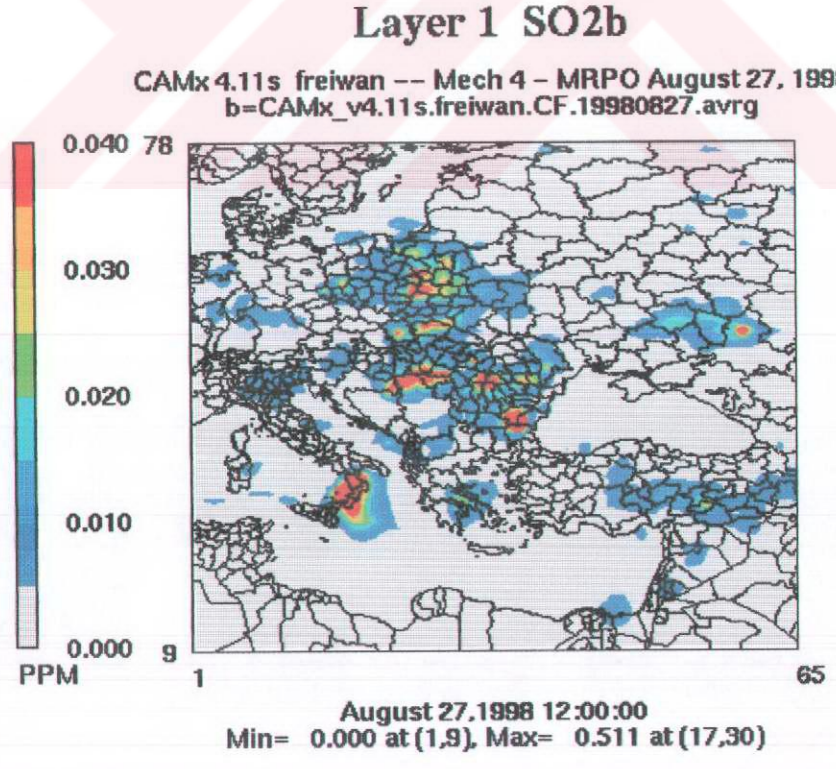

Figure E.2 e) 12:00 Z

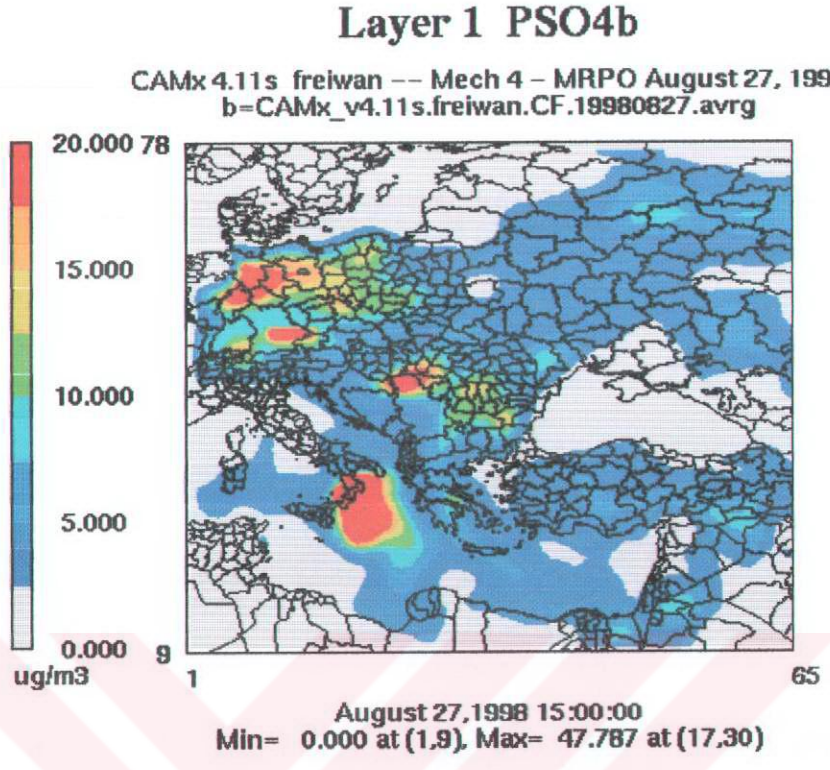

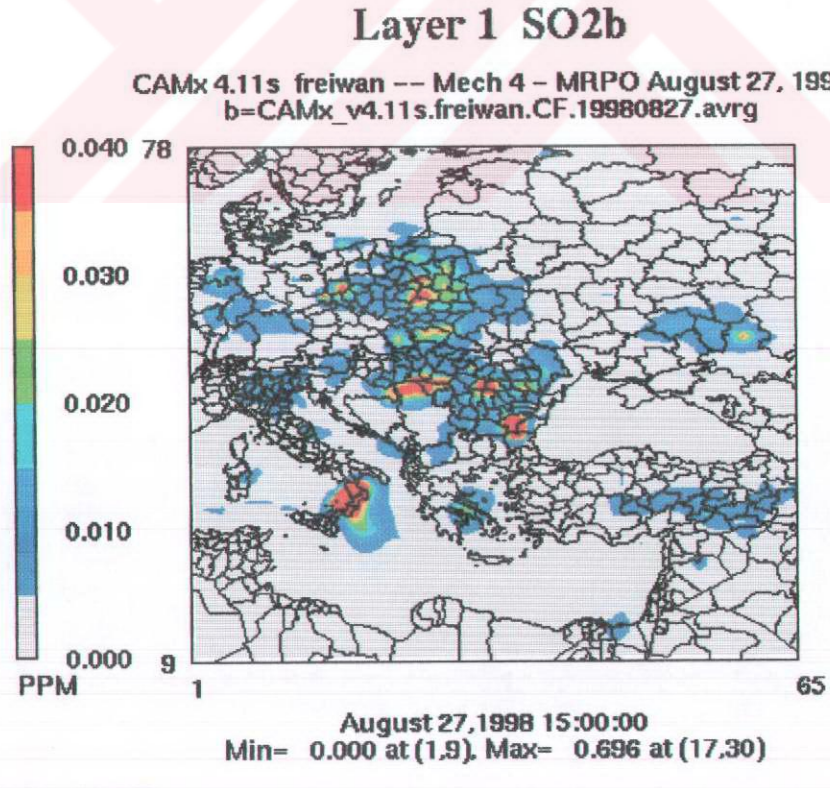

Figure E.2 f) 15:00 Z

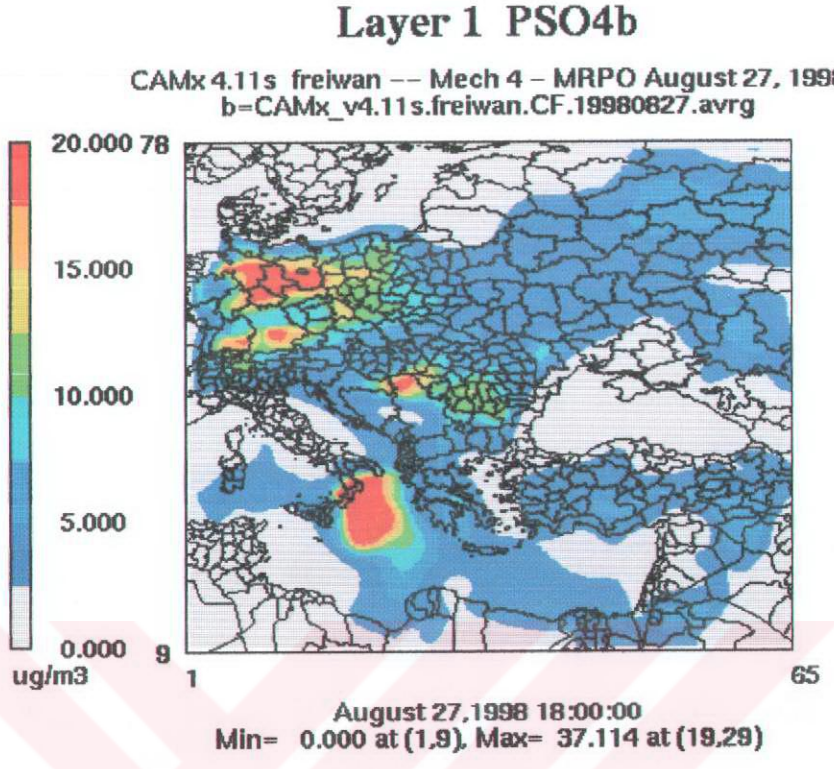

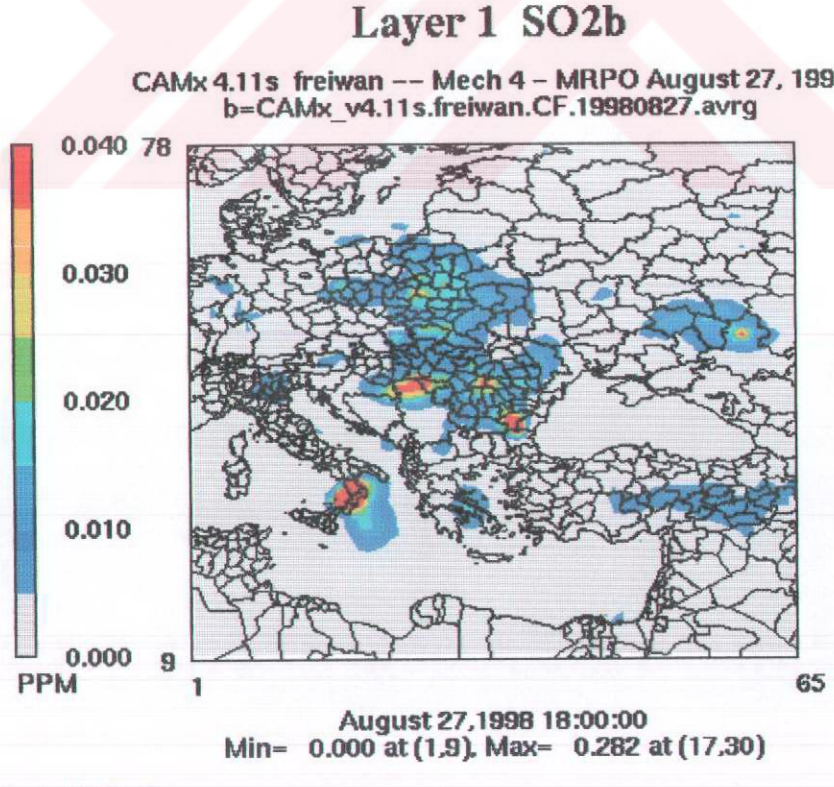

Figure E.2 g) 18:00 Z

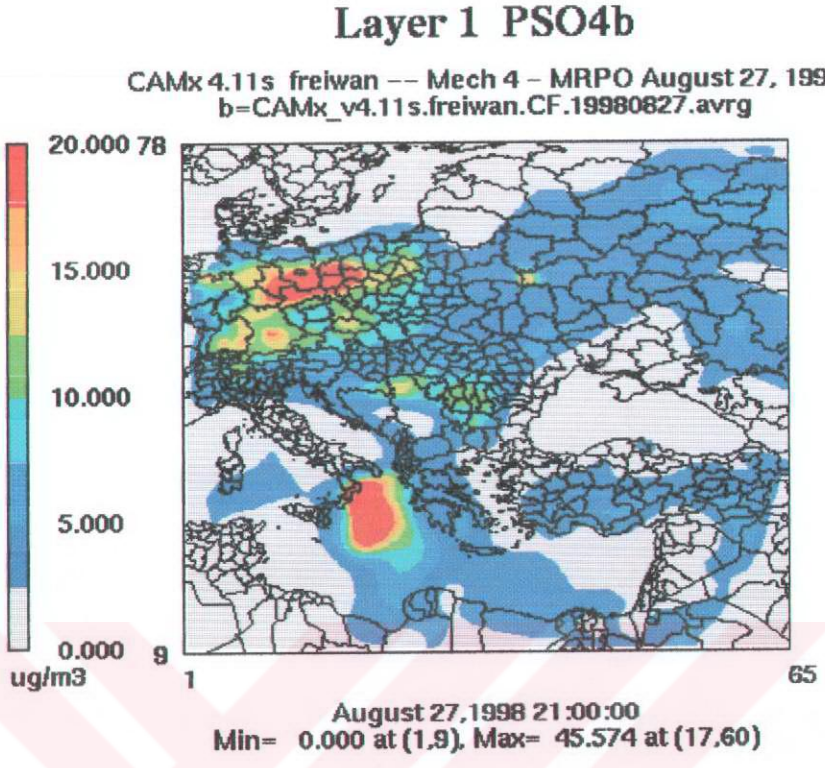

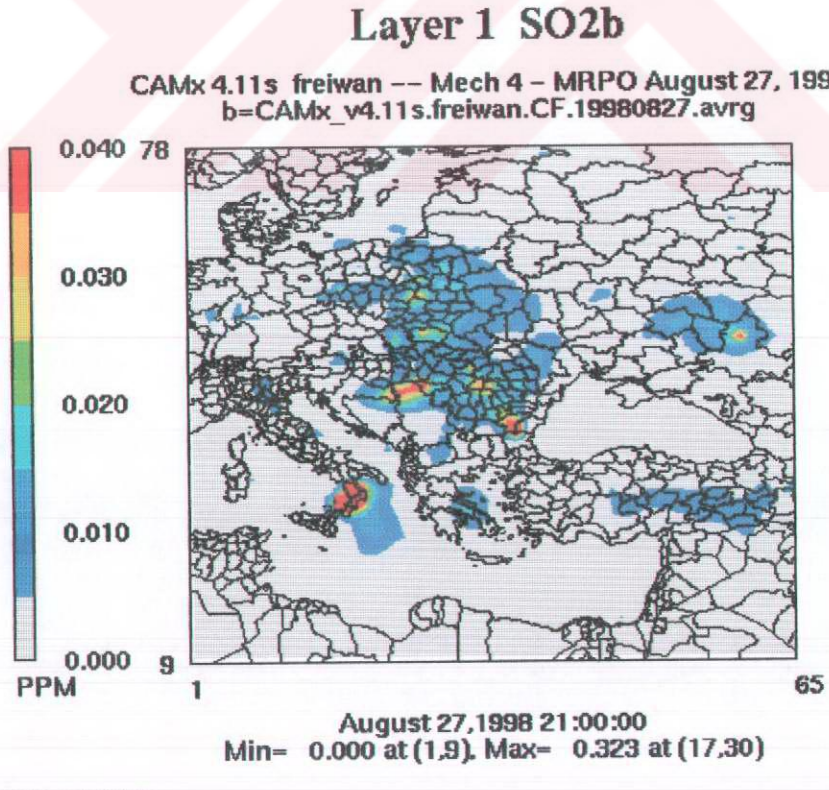

Figure E.2 h) 21:00 Z

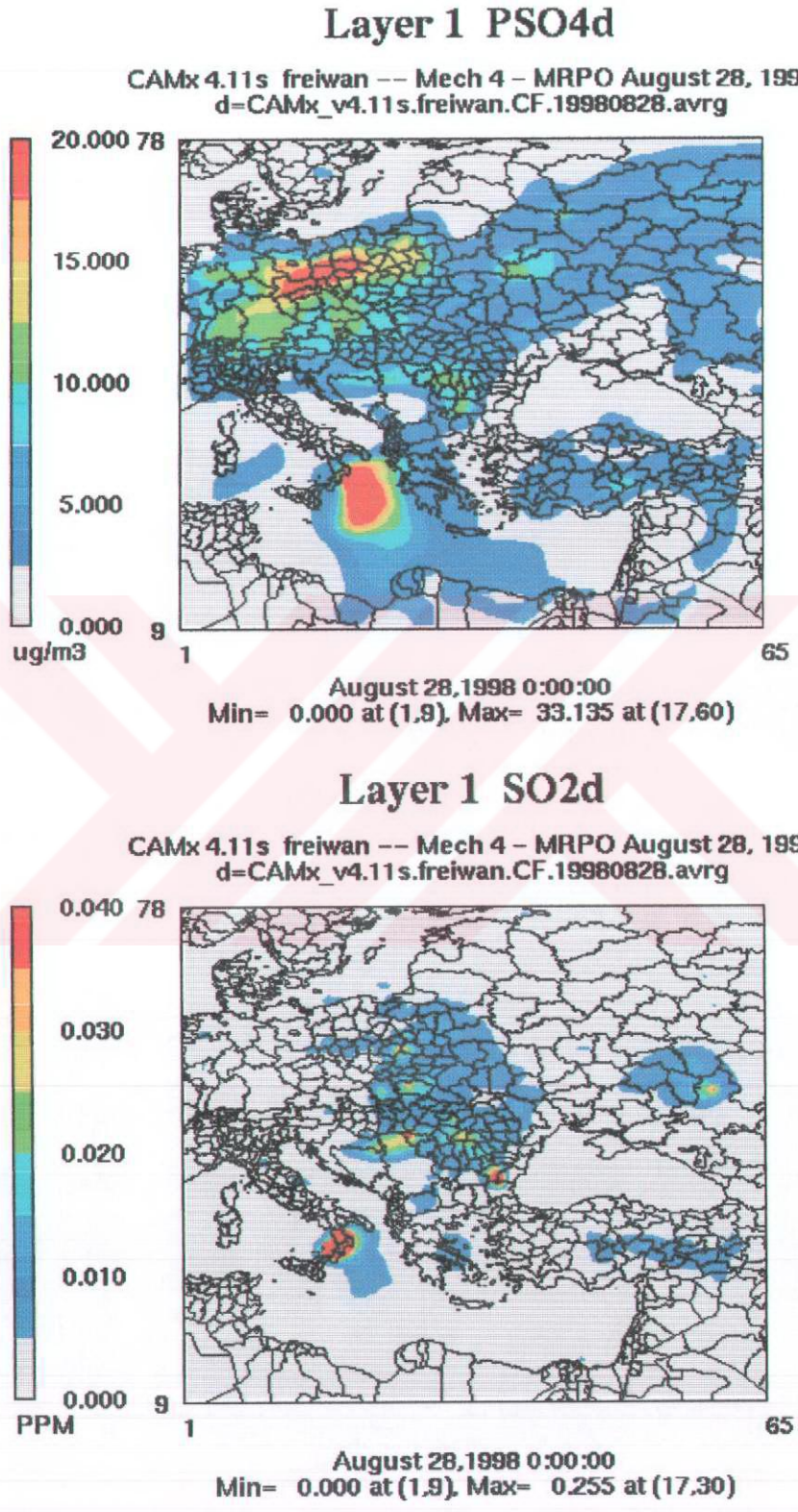

Figure E.3: The same as Fig. E.1 but for 28 Aug. 1998, a) 00:00 Z

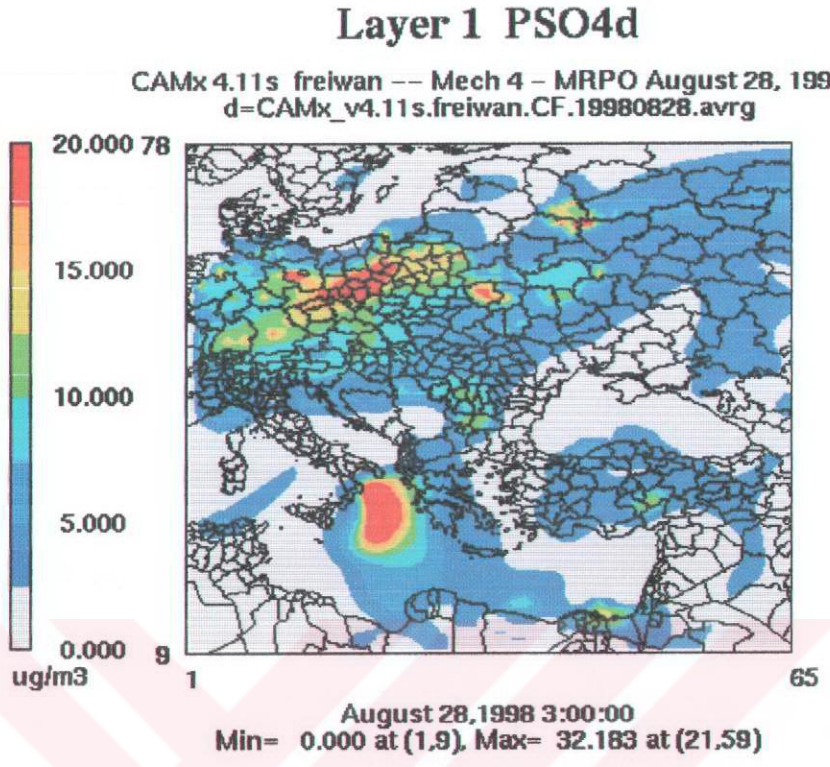

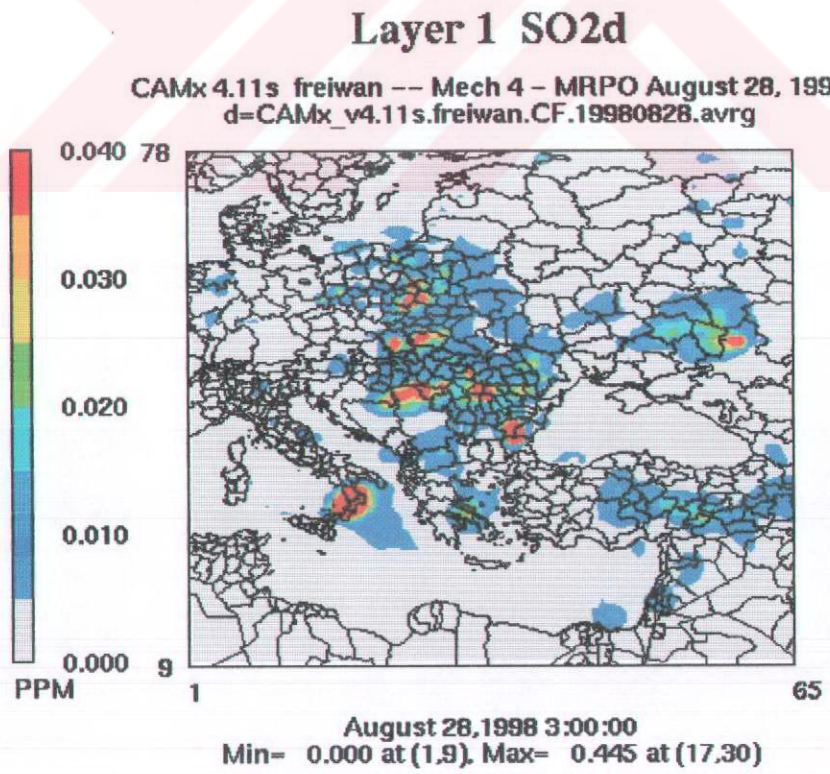

Figure E.3 b) 03:00 Z

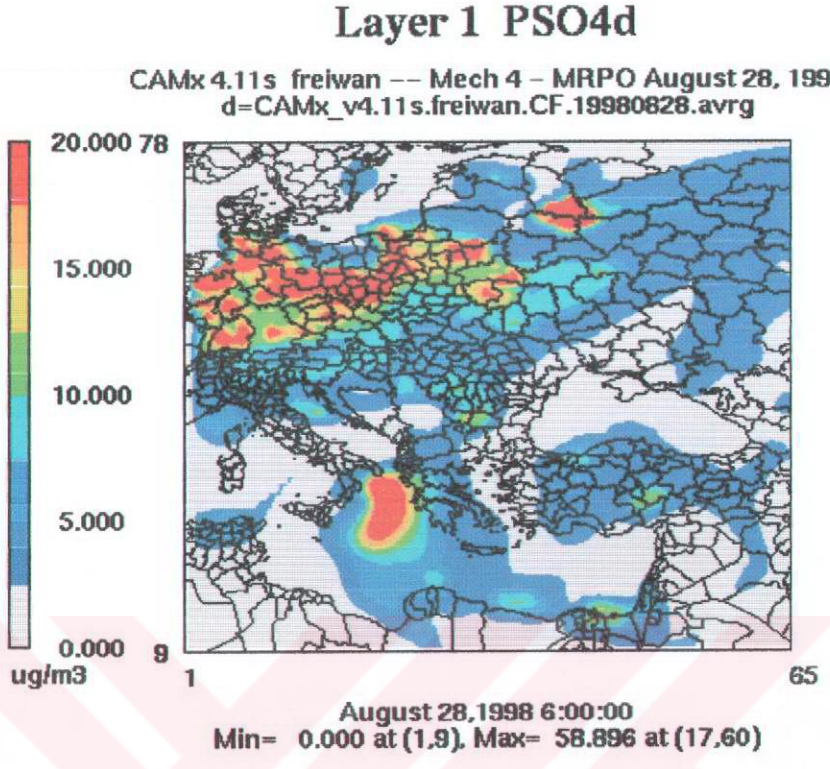

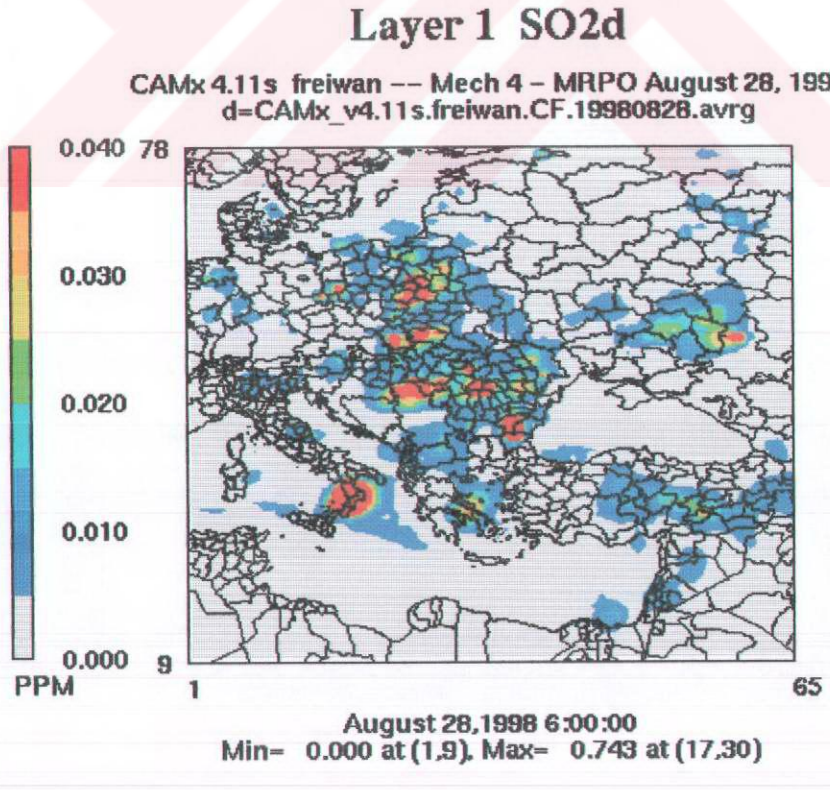

Figure E.3 c) 06:00 Z

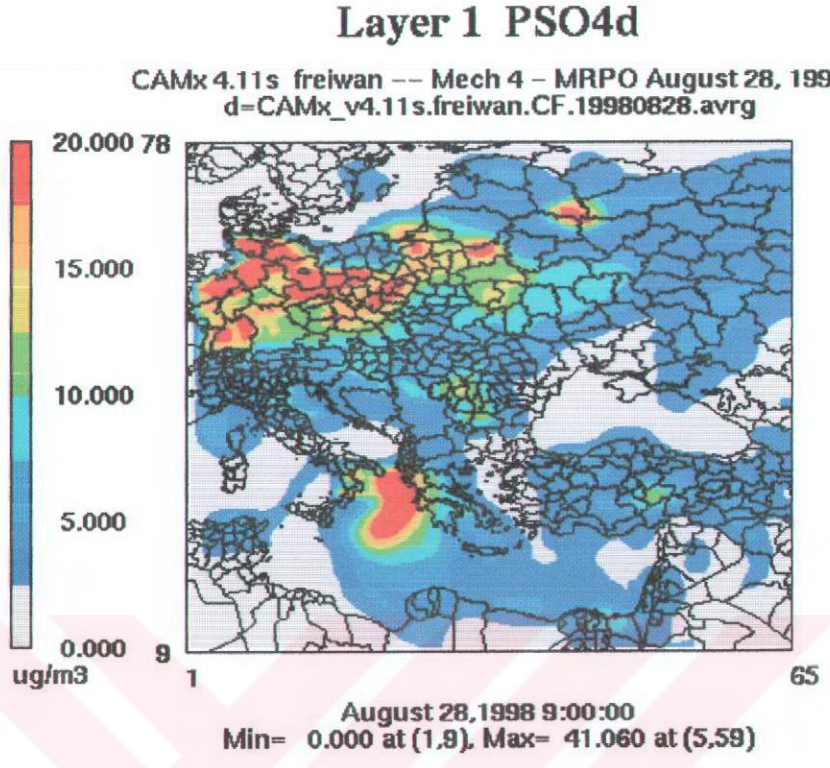

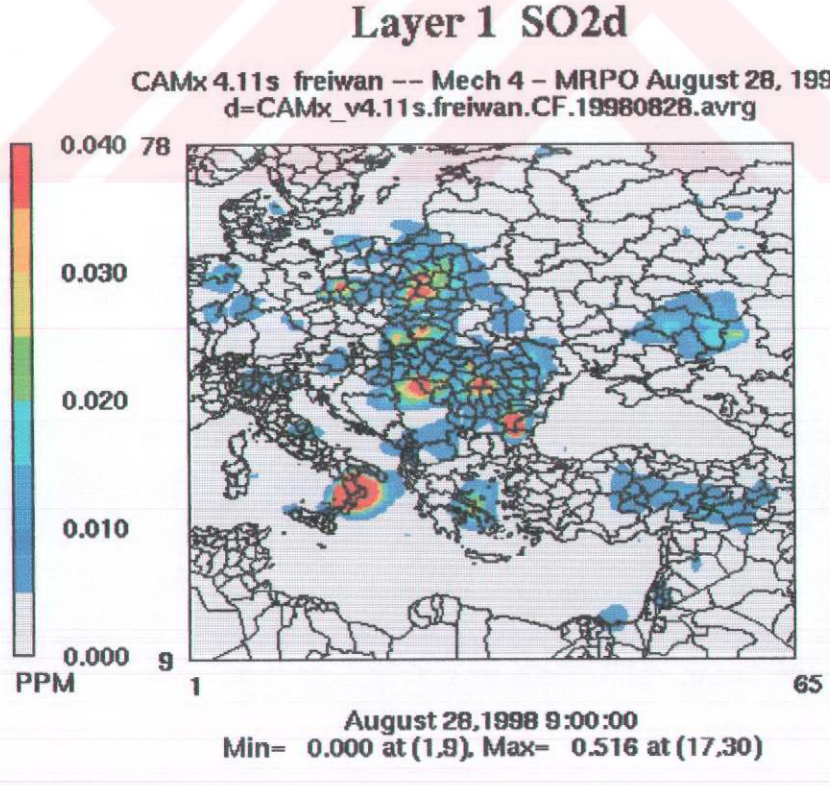

Figure E.3 d) 09:00 Z

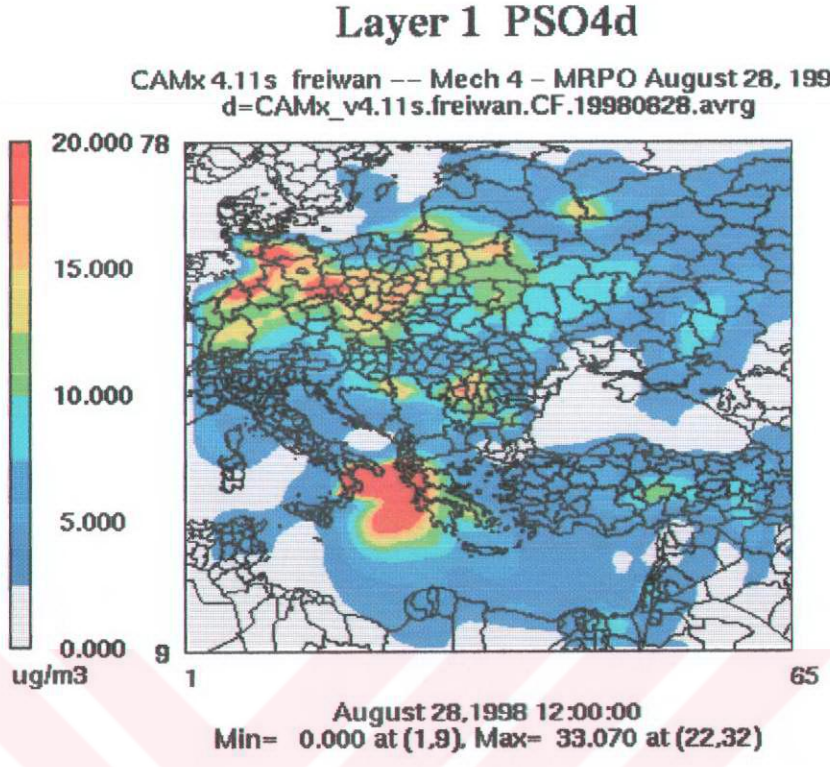

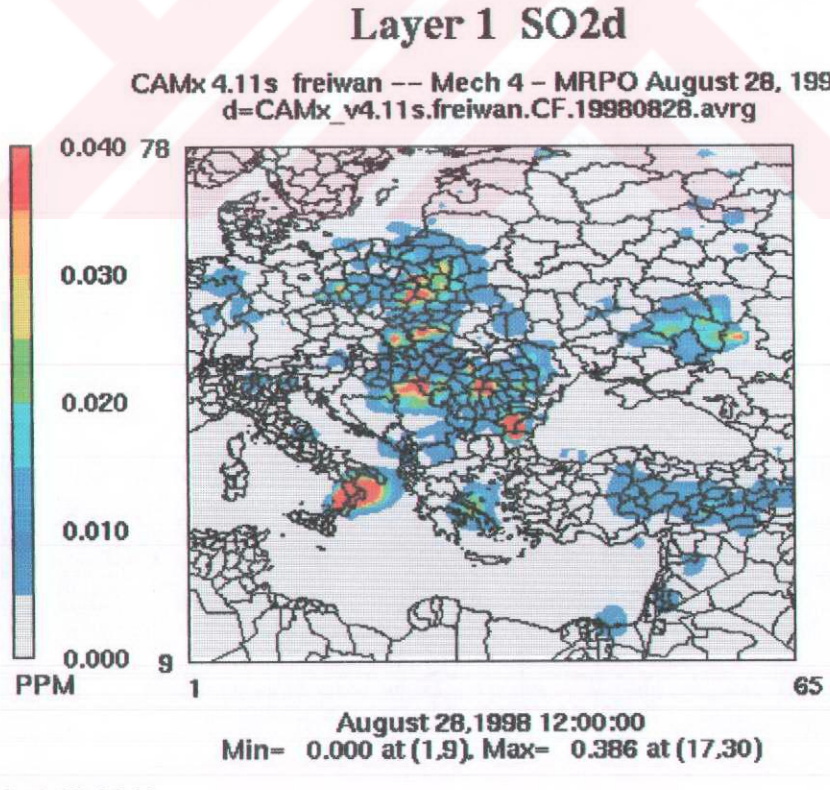

Figure E.3 e) 12:00 Z

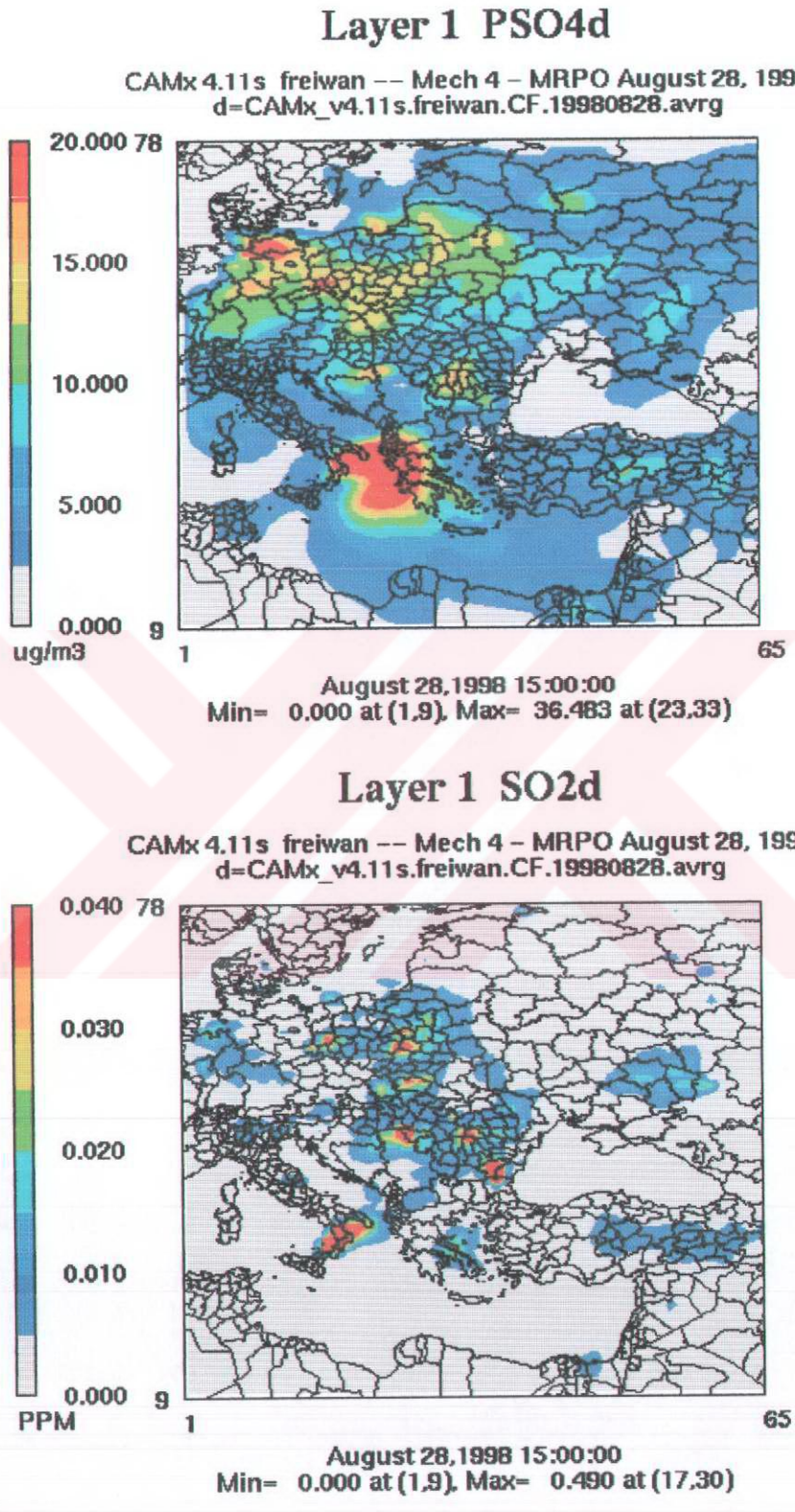

Figure E.3 f) 15:00 Z

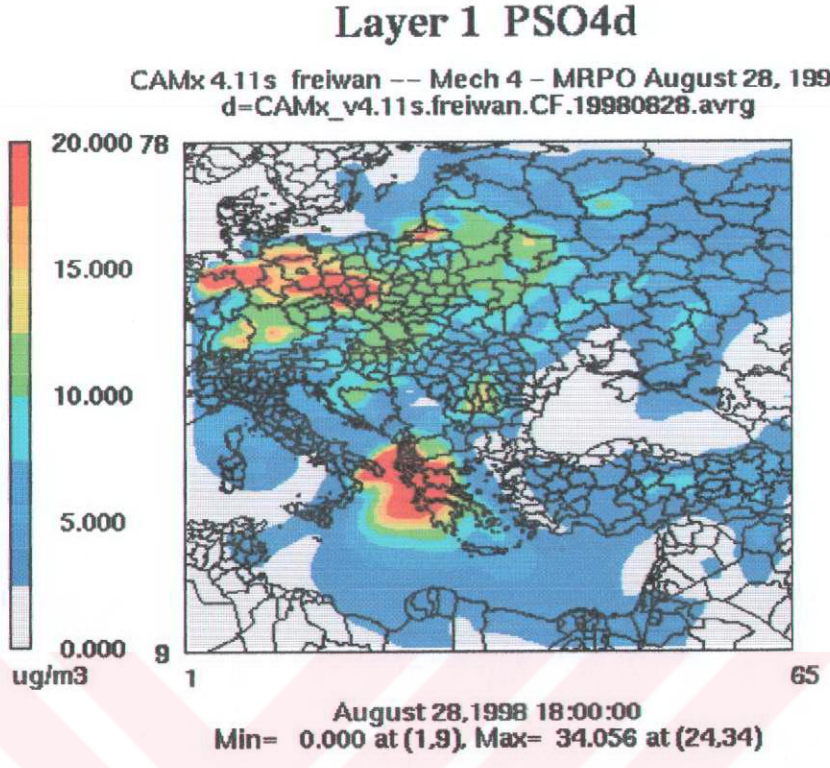

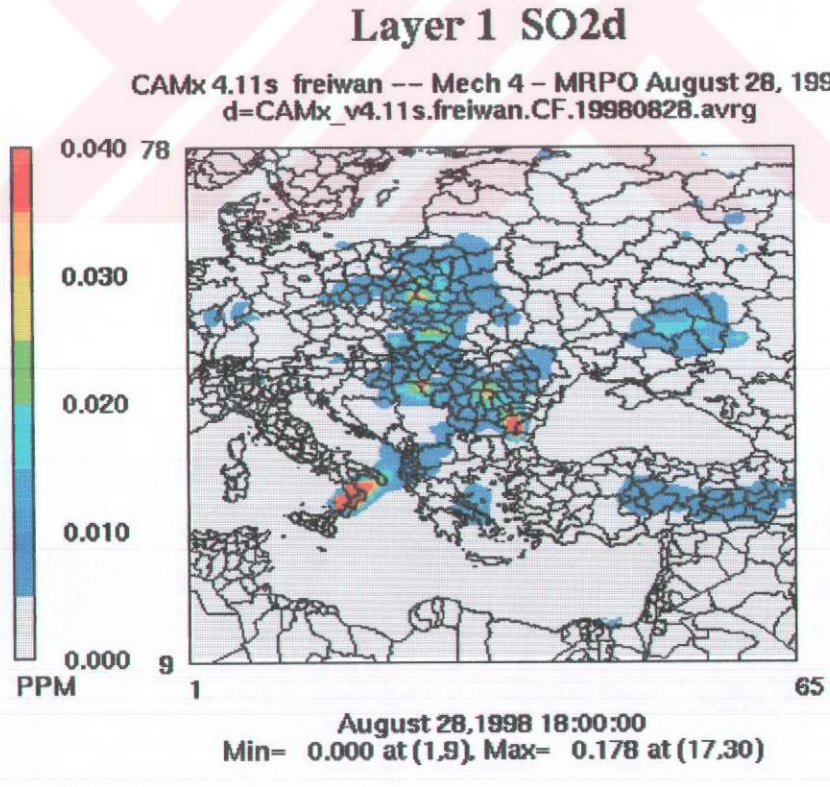

Figure E.3 g) 18:00 Z

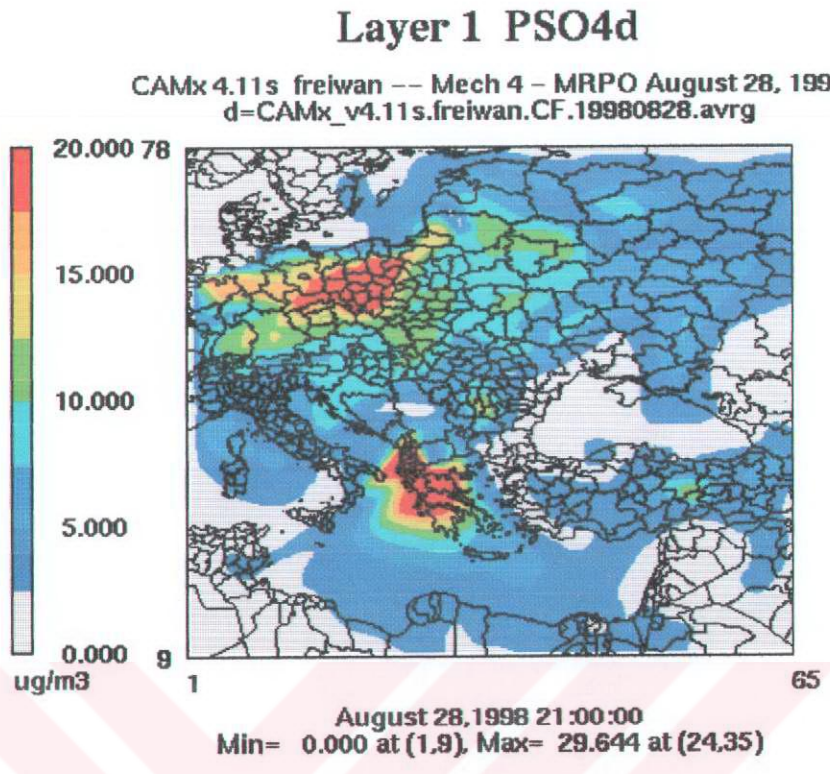

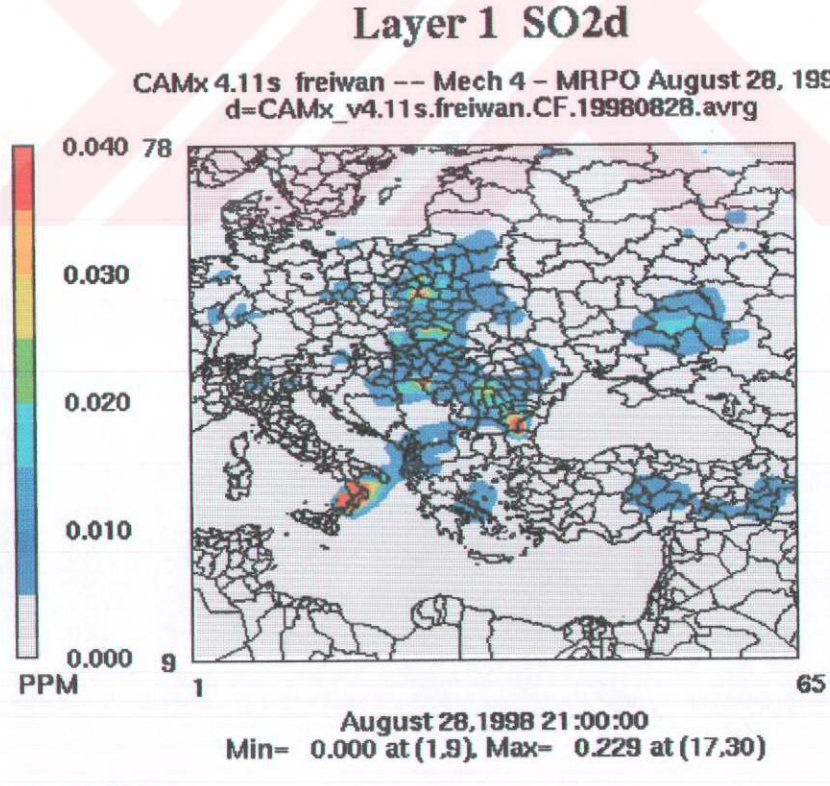

Figure E.3 h) 21:00 Z

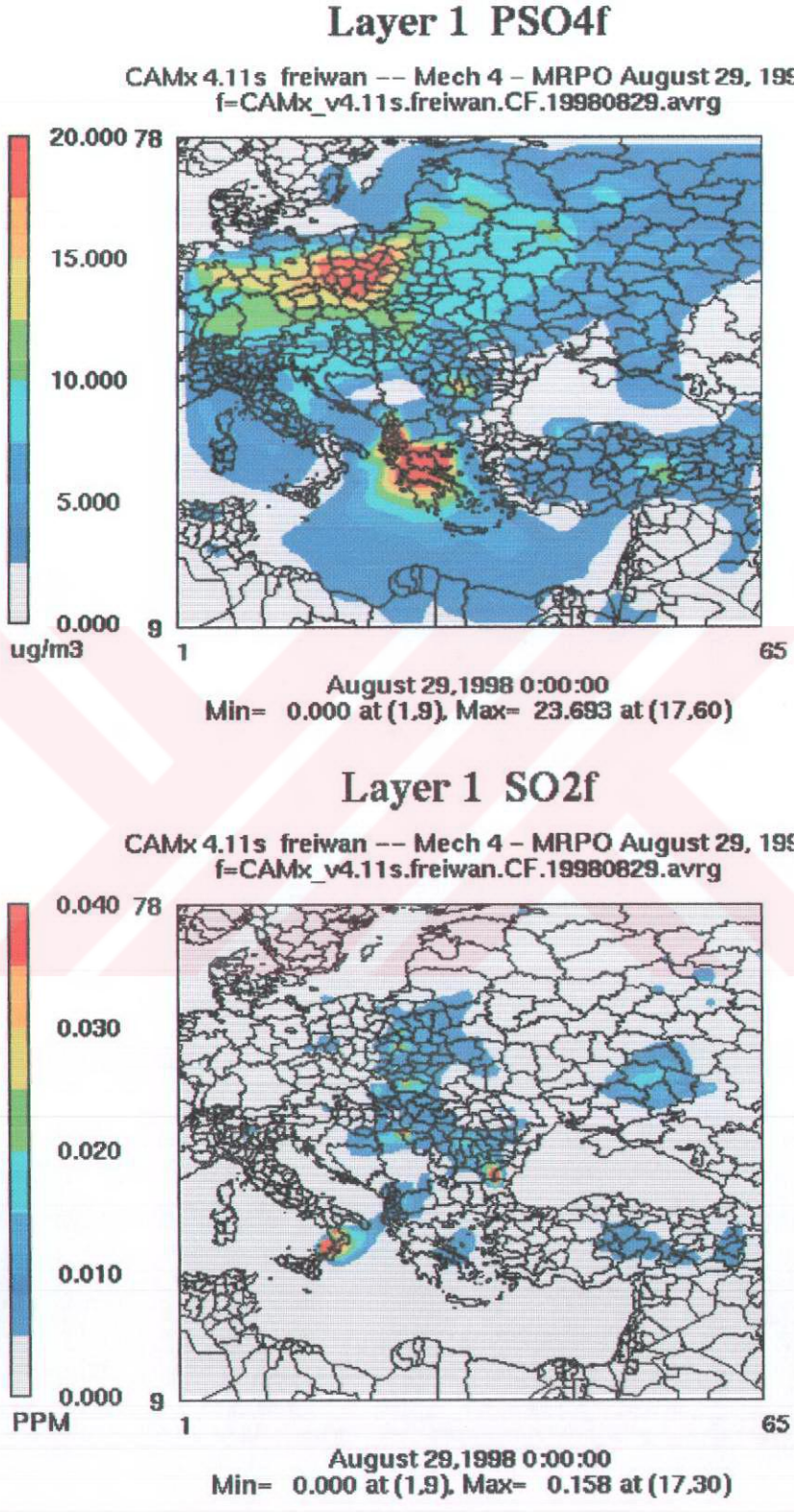

Figure E.4: The same as Fig. E.1 but for 29 Aug. 1998, a) 00:00 Z

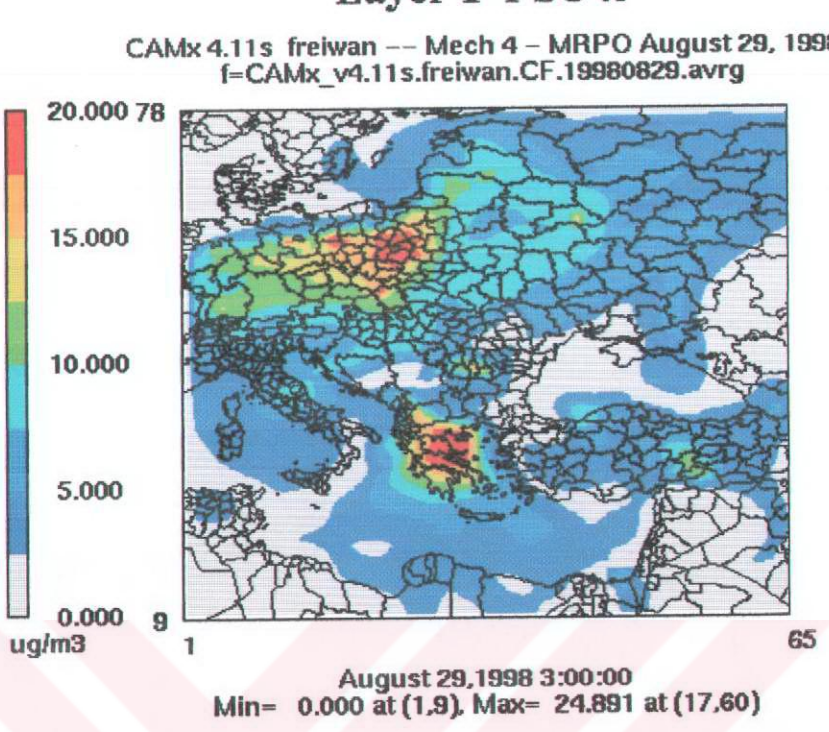

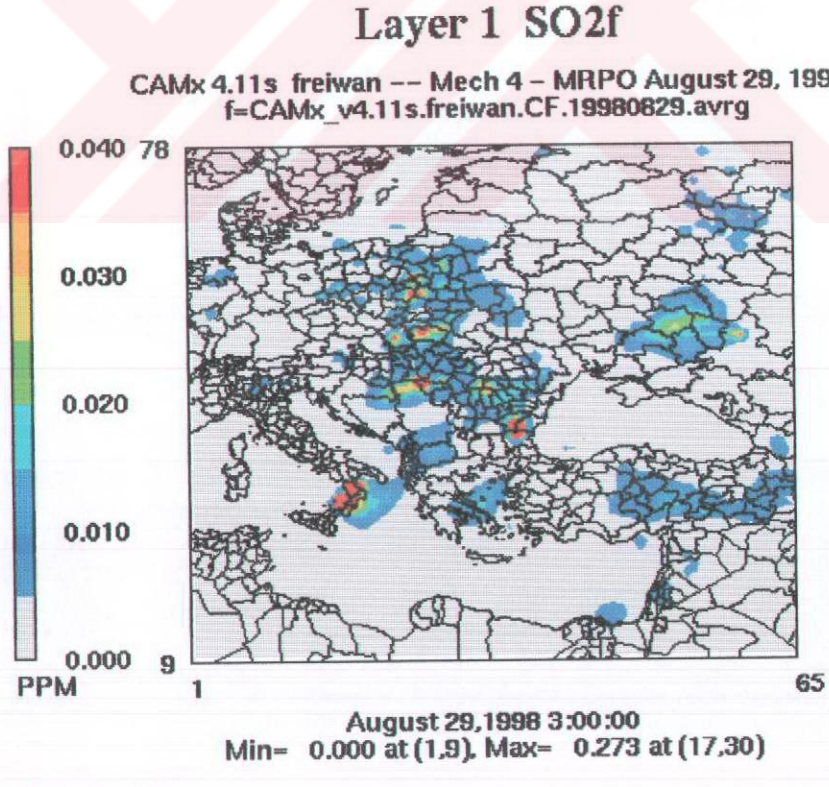

Figure E.4 b) 03:00 Z.

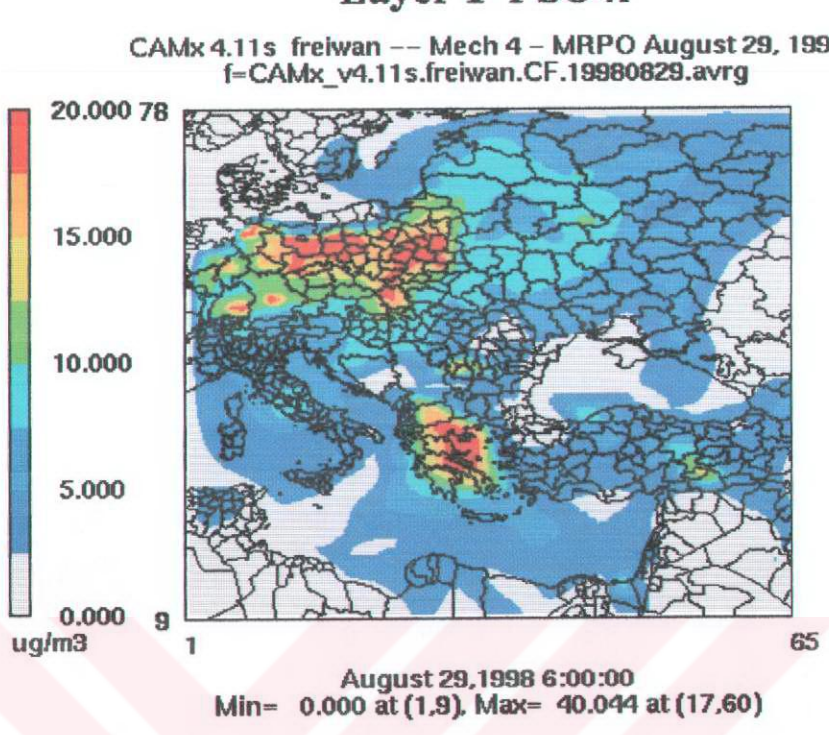

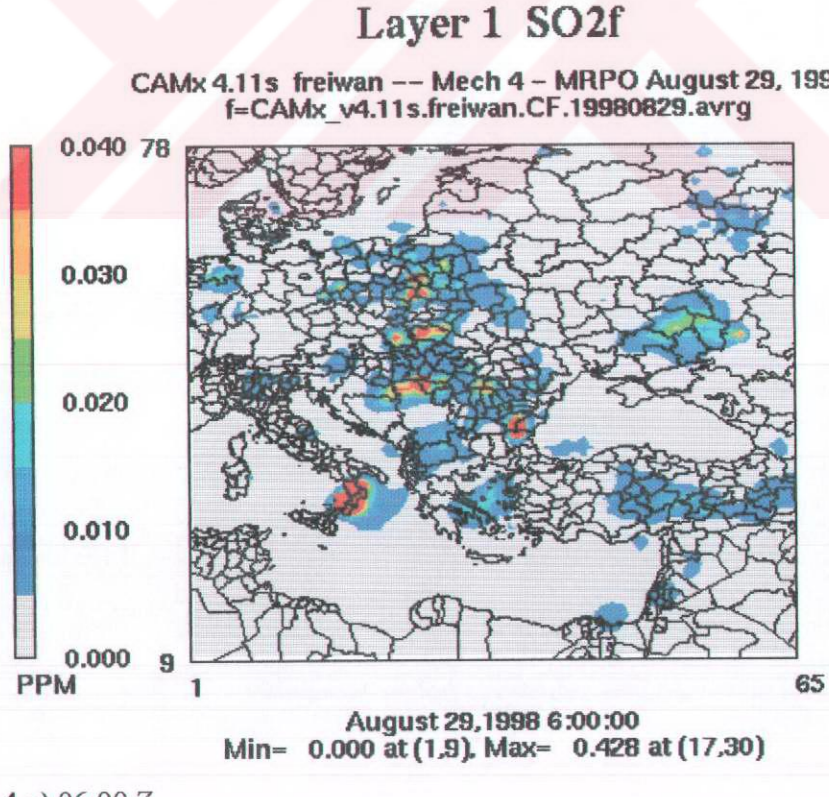

Figure E.4 c) 06:00 Z.

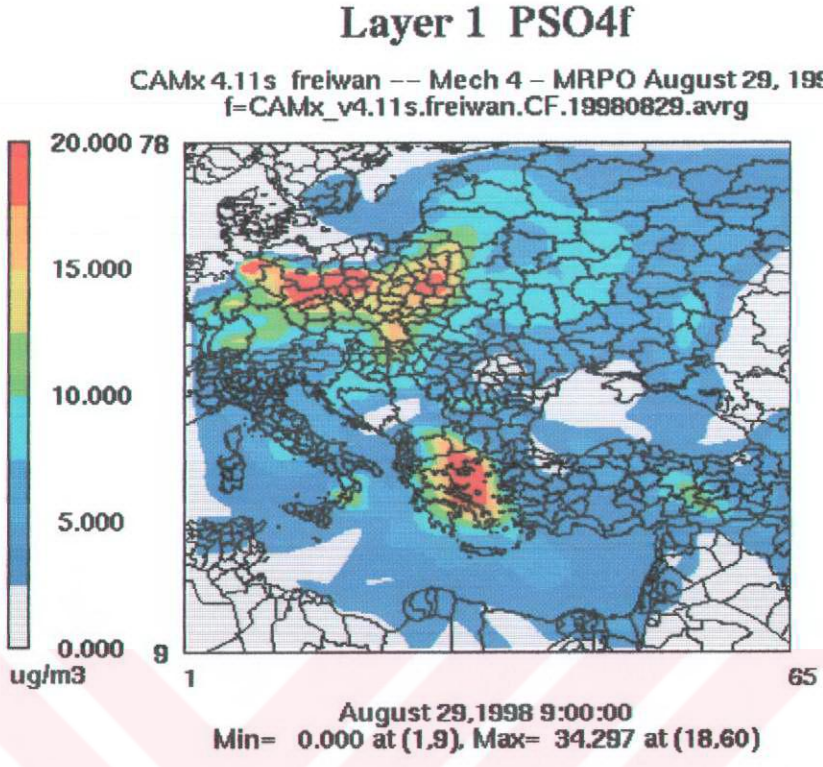

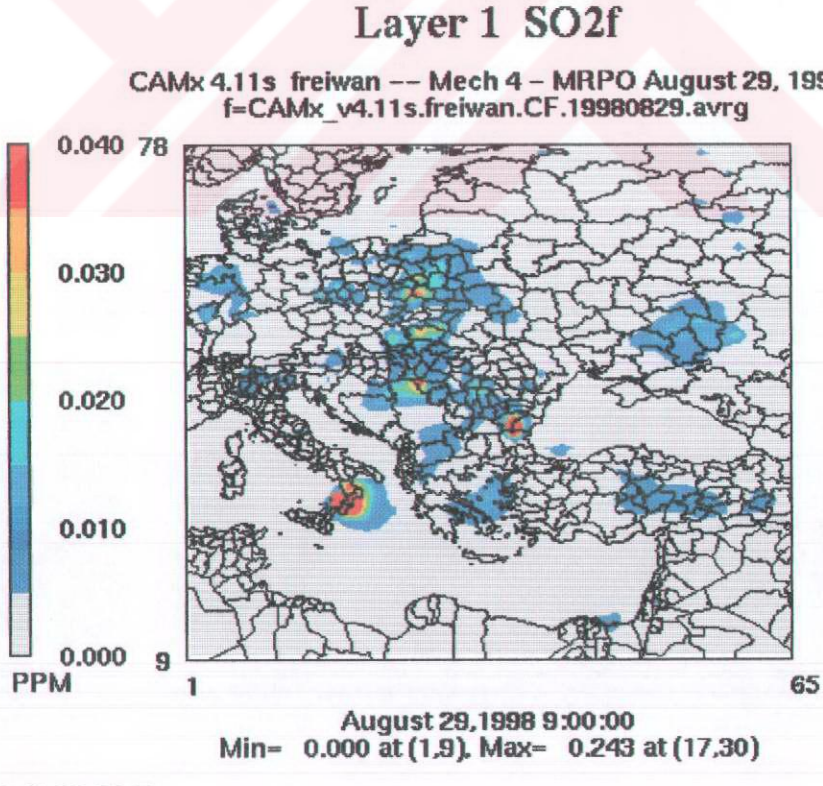

Figure E.4 d) 09:00 Z.

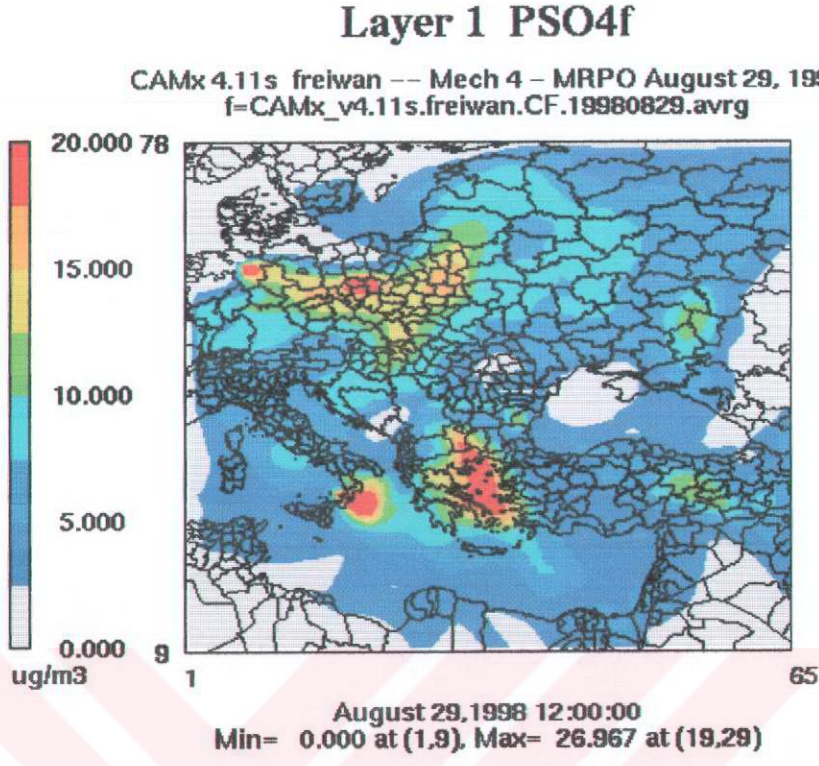

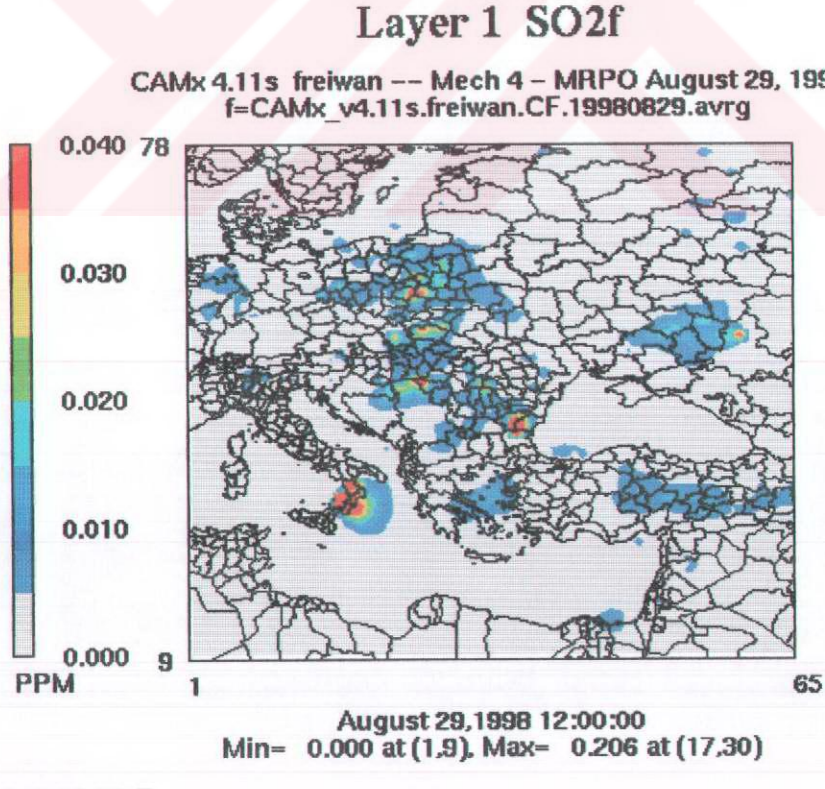

Figure E.4 e) 12:00 Z.

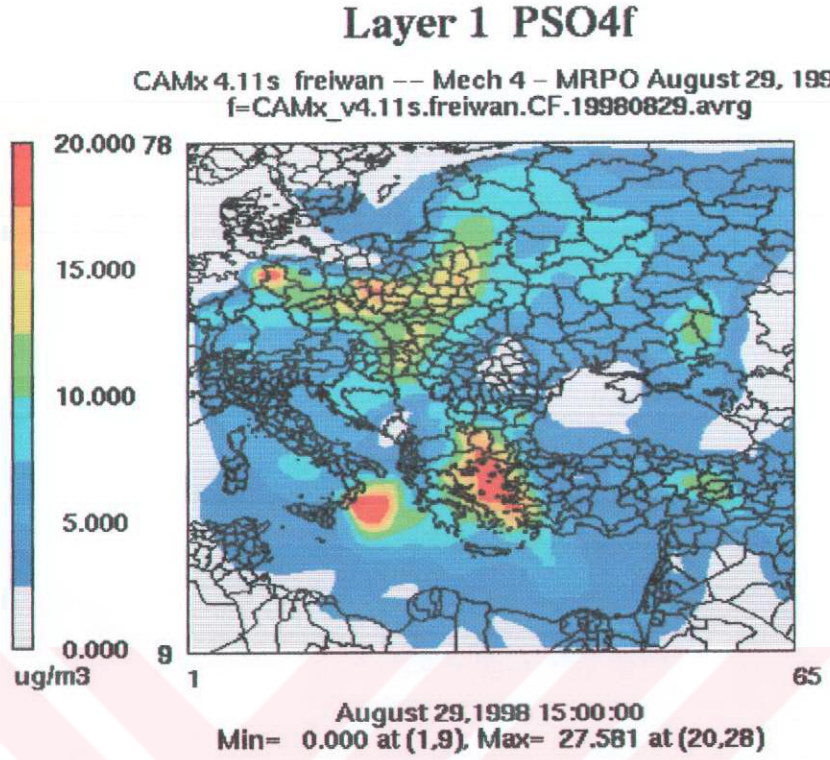

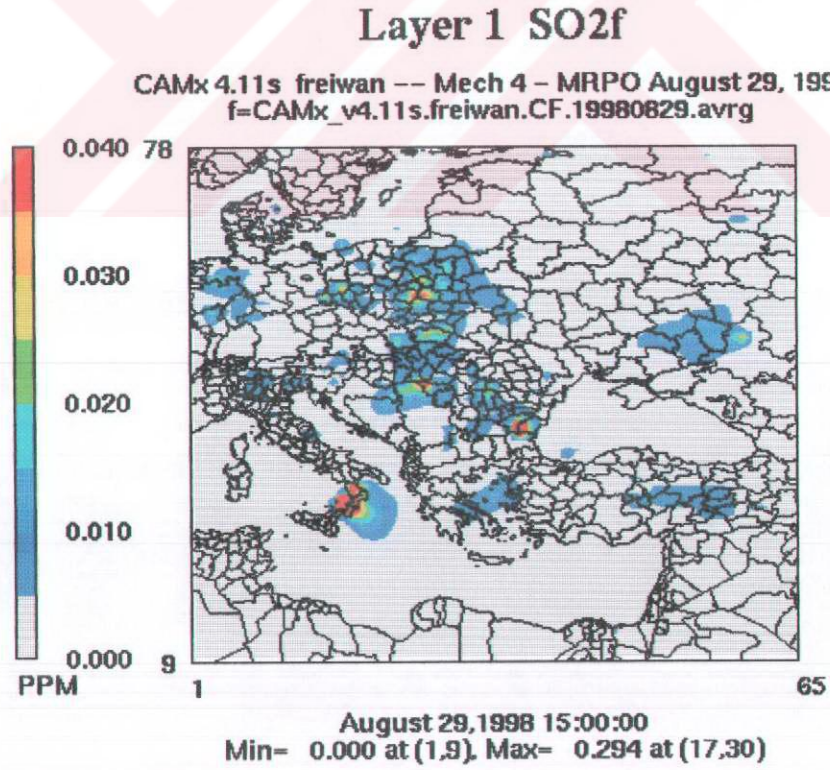

Figure E.4 f) 15:00 Z.

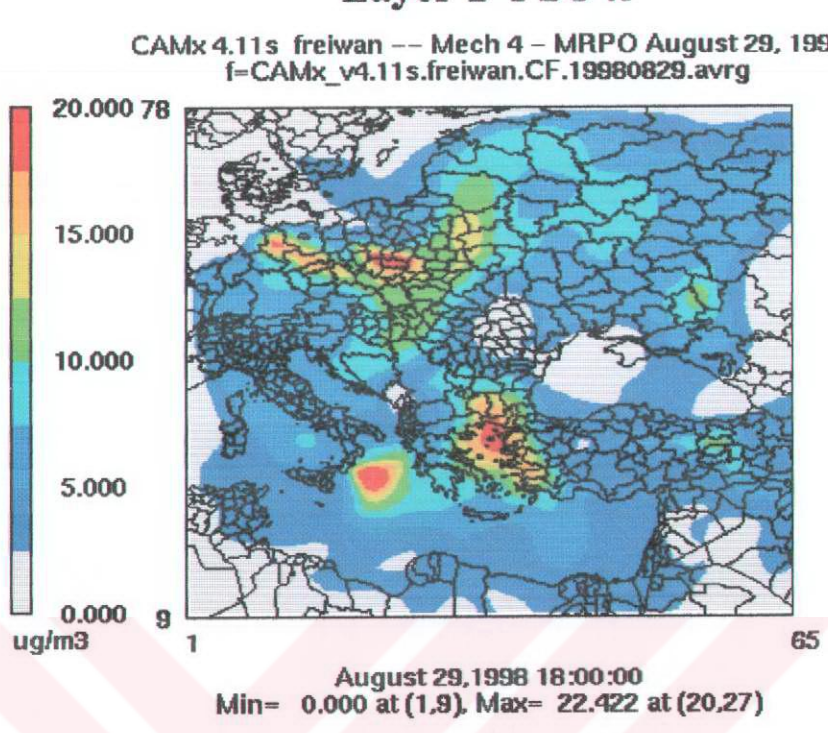

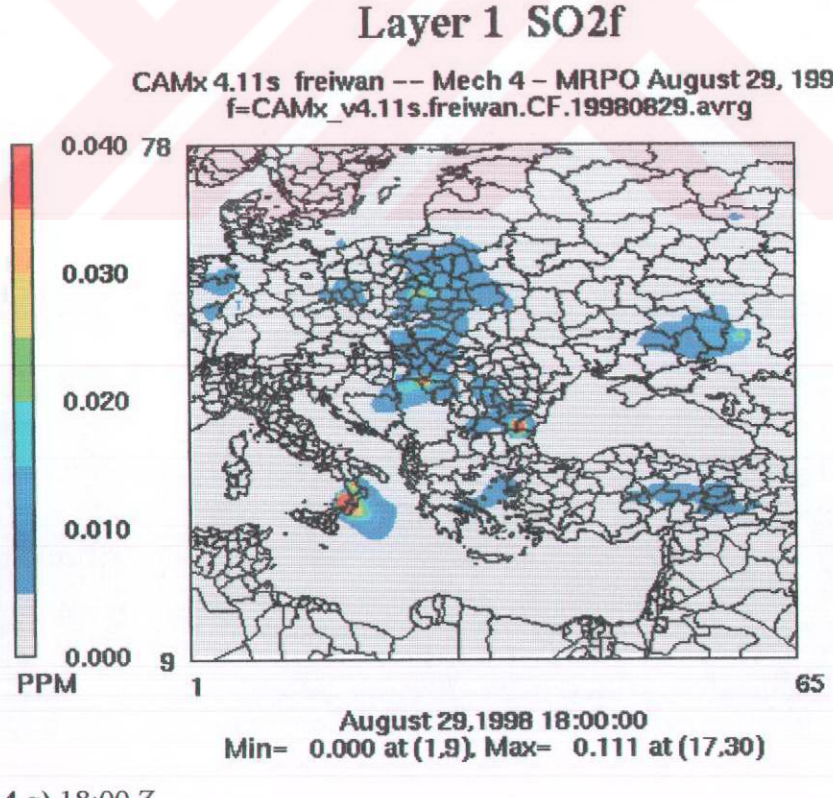

Figure E.4 g) 18:00 Z.

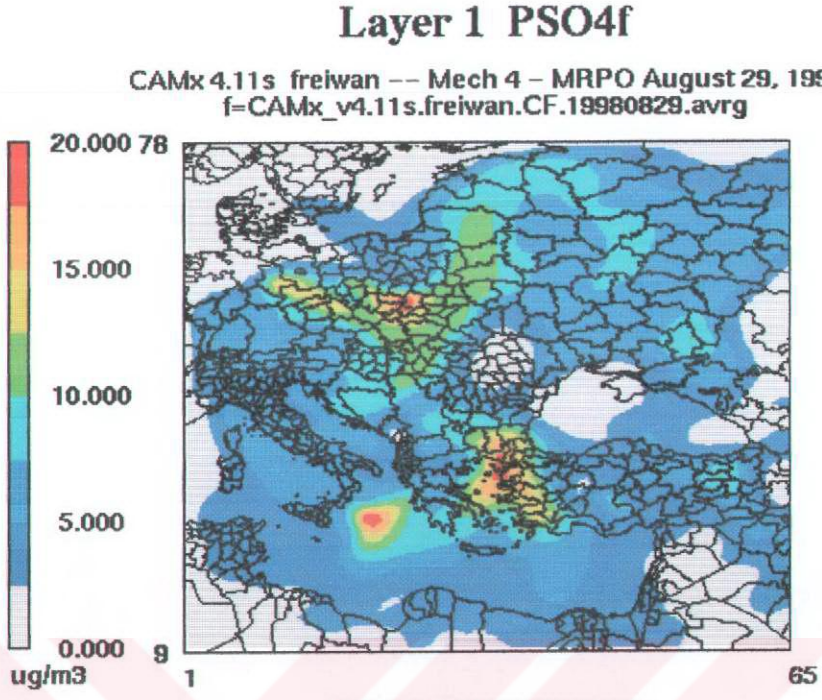

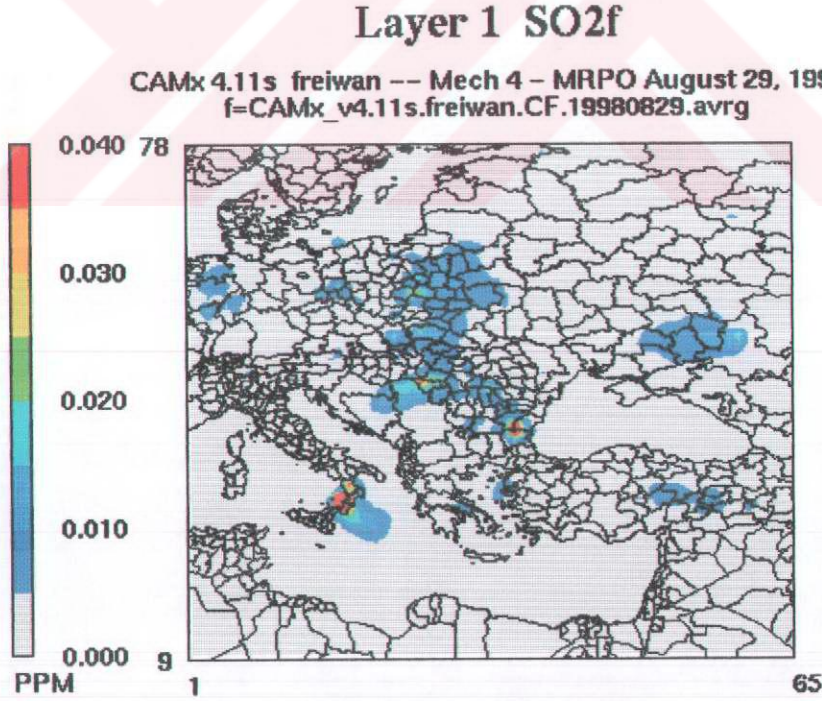

Figure E.4 h) 21:00 Z.

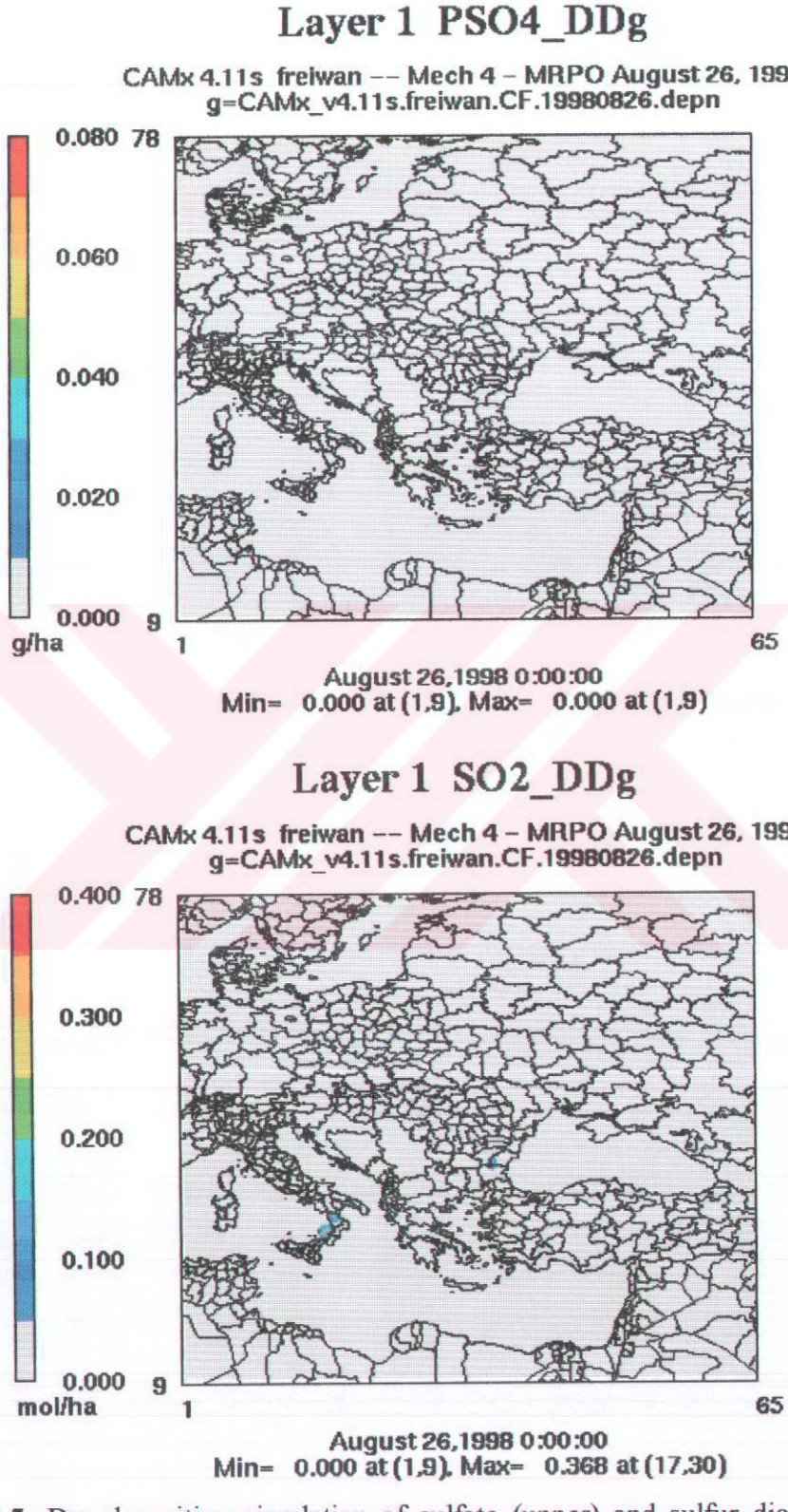

Figure E.5: Dry deposition simulation of sulfate (upper) and sulfur dioxide (lower) during 26 August 1998; a) 00:00 Z.

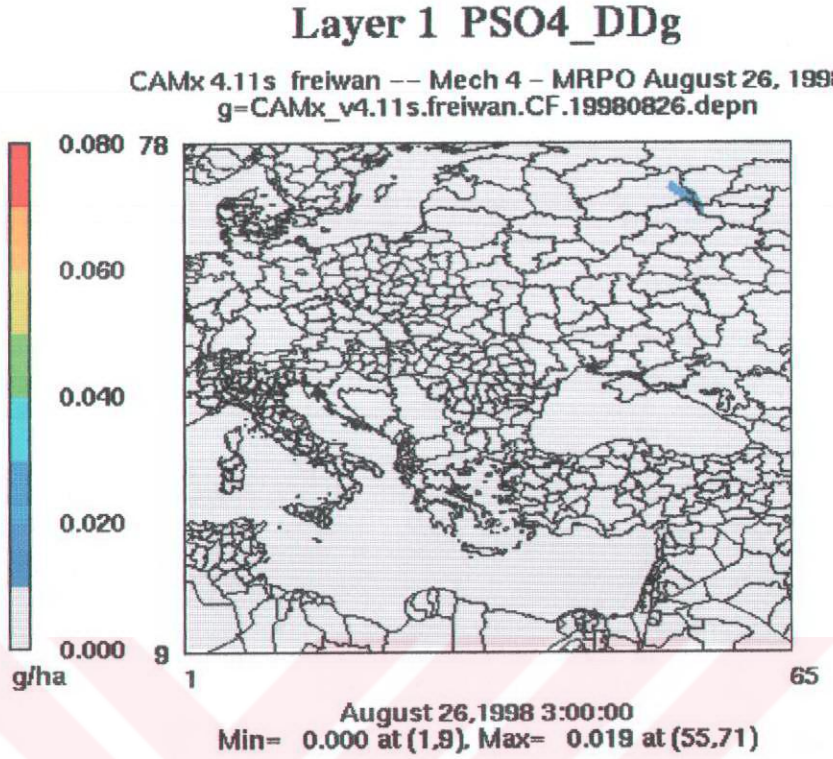

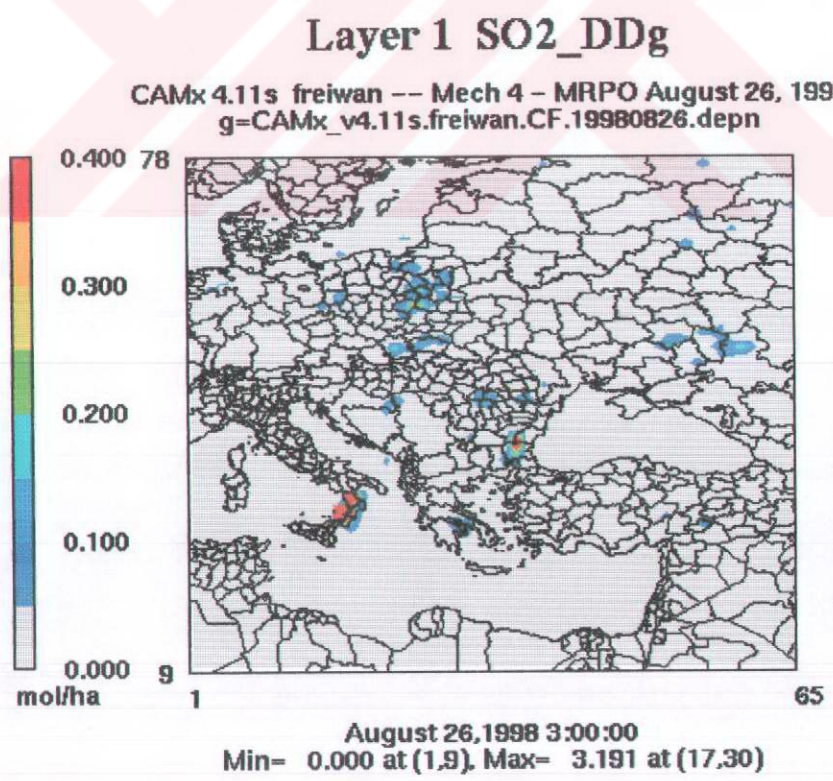

Figure E.5 b) 03:00 Z.

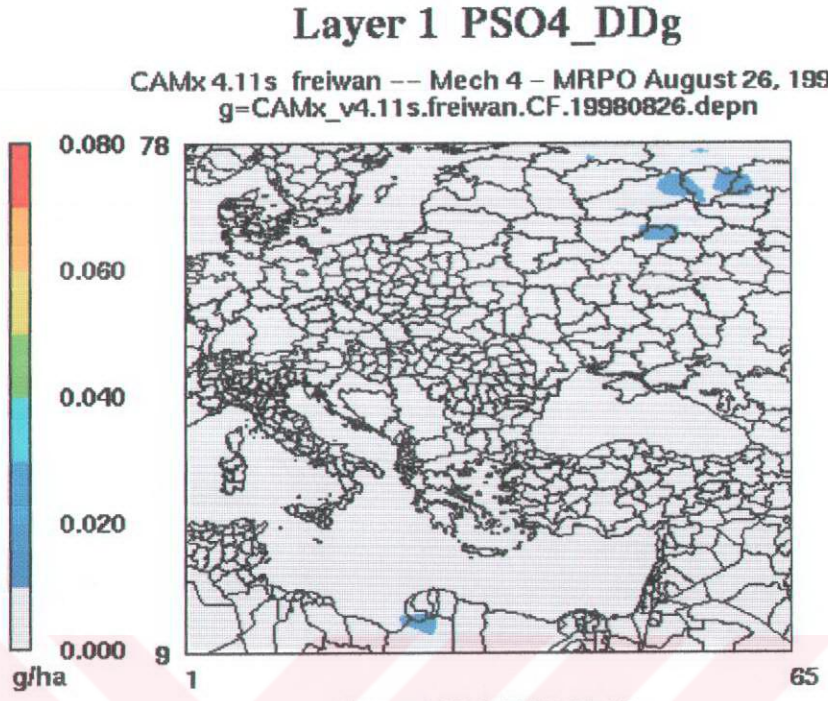

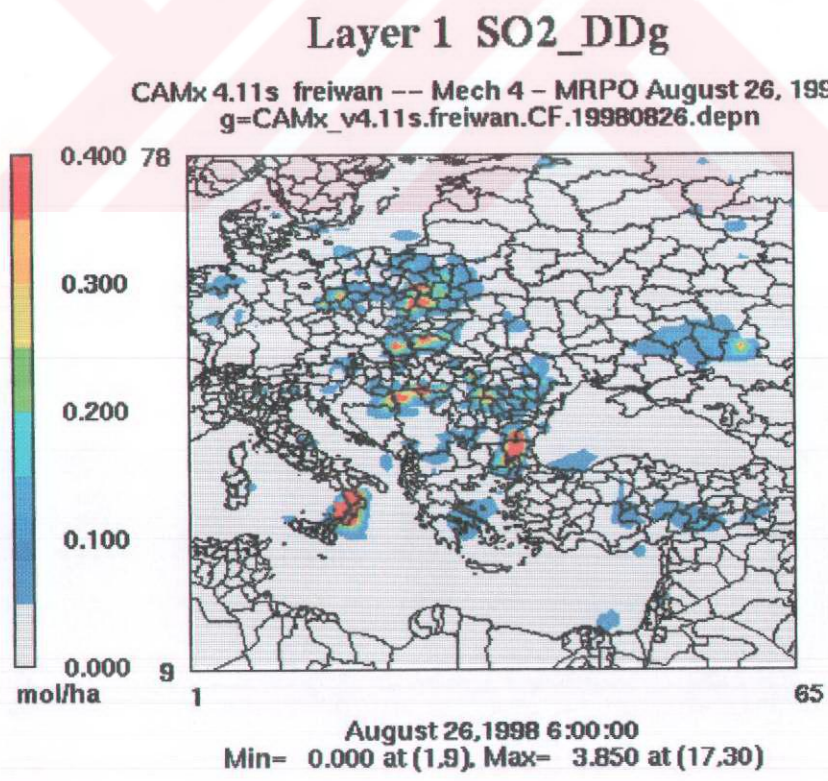

Figure E.5 c) 06:00 Z.

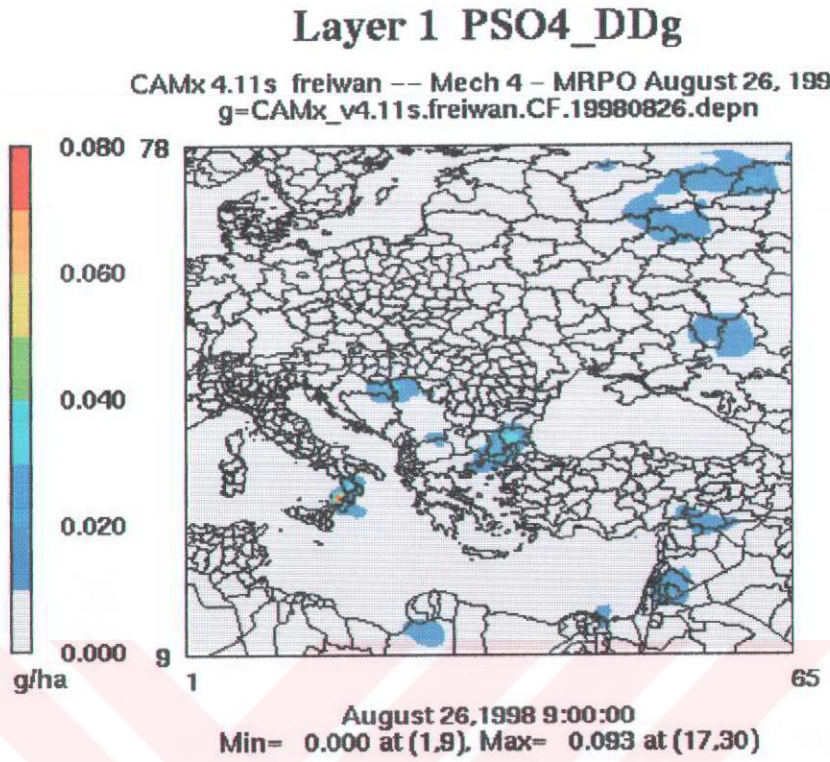

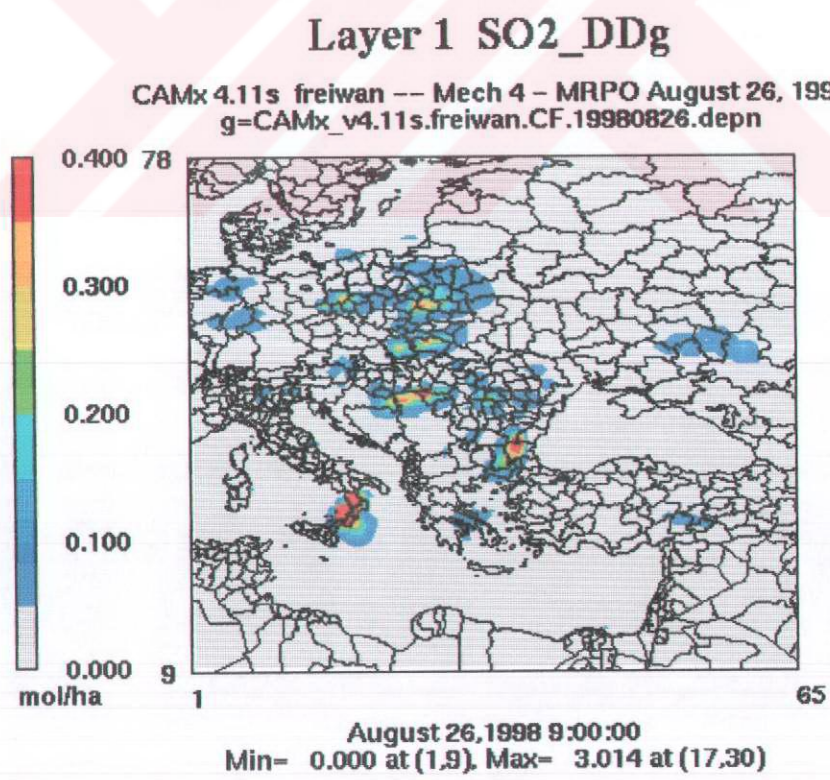

Figure E.5 d) 09:00 Z.

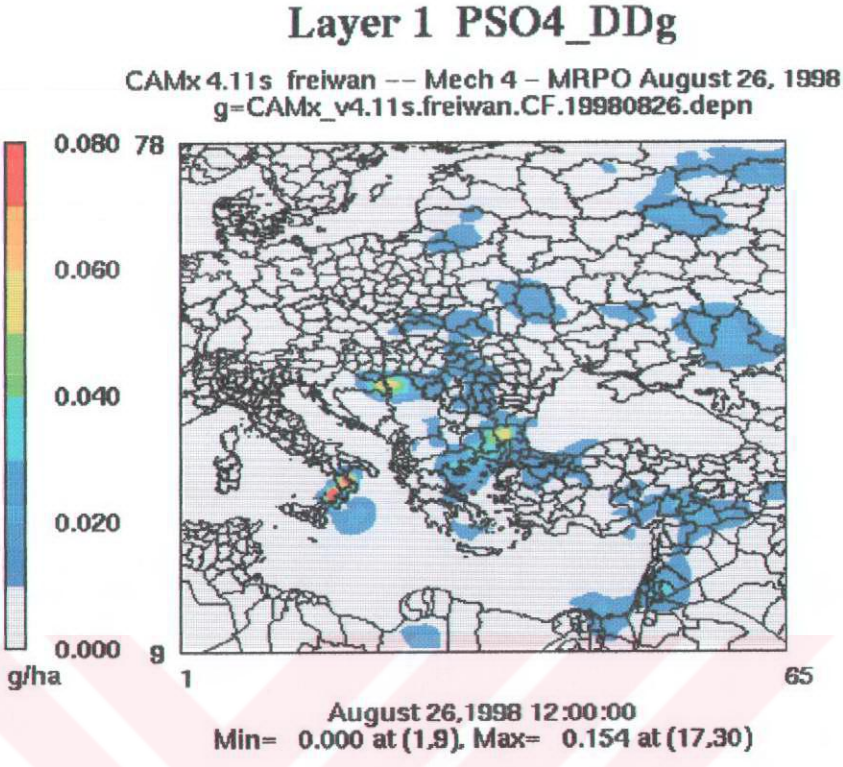

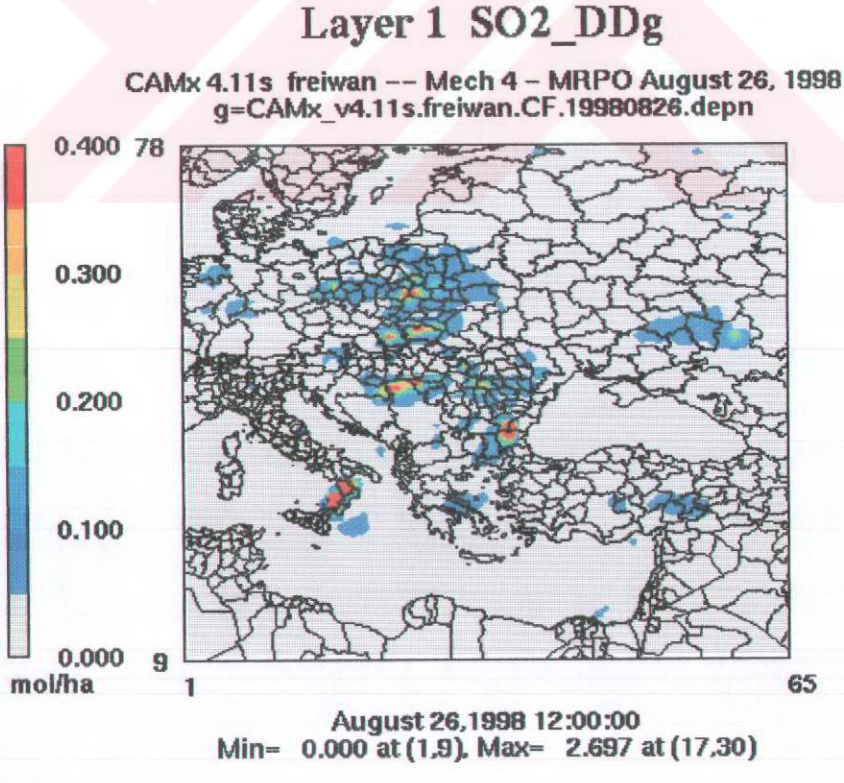

Figure E.5 e) 12:00 Z.

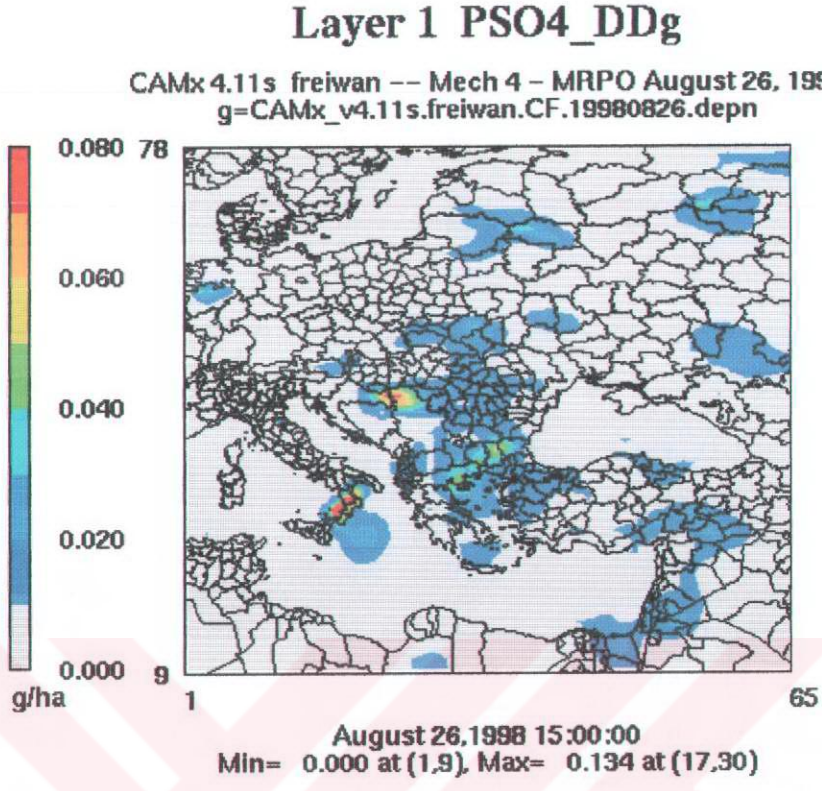

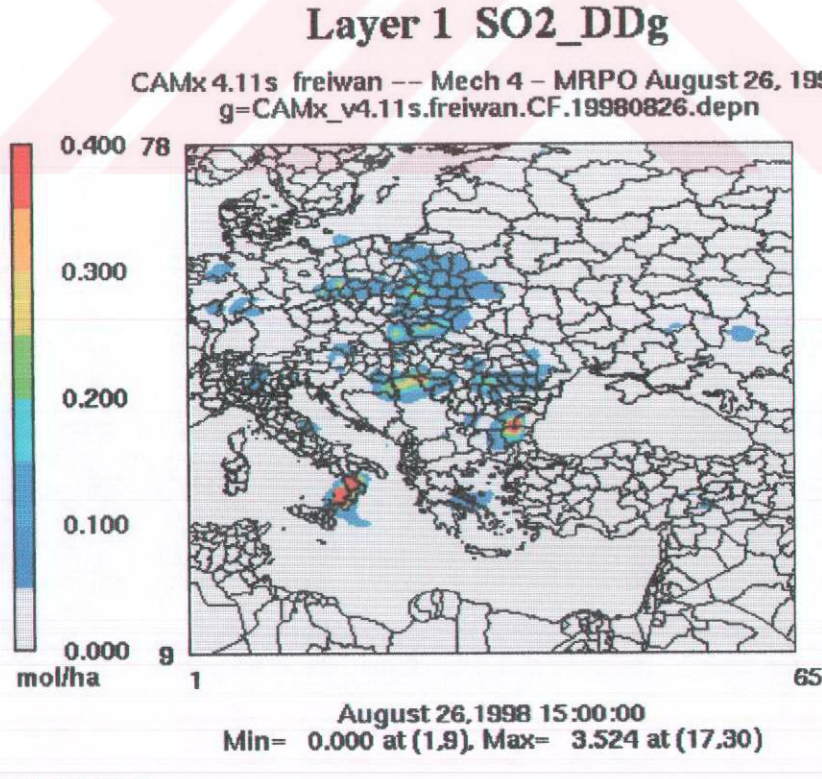

Figure E.5 f) 15:00 Z.

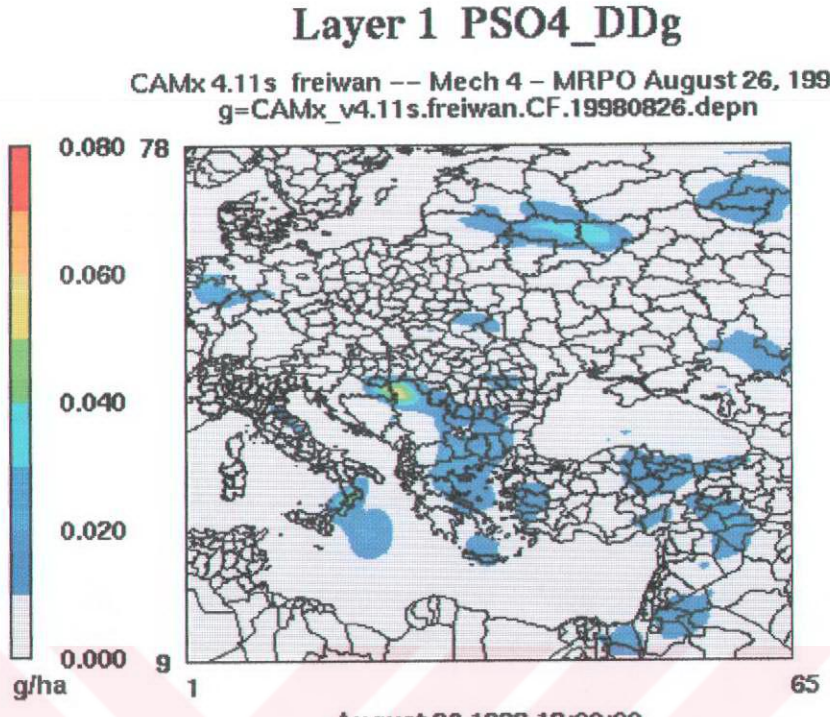

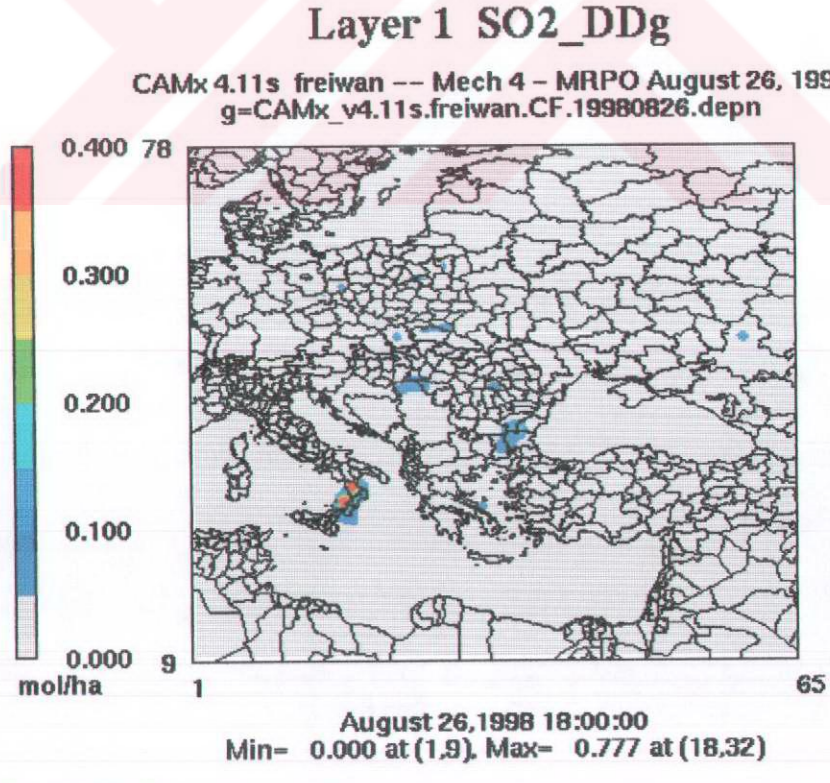

Figure E.5 g) 18:00 Z.

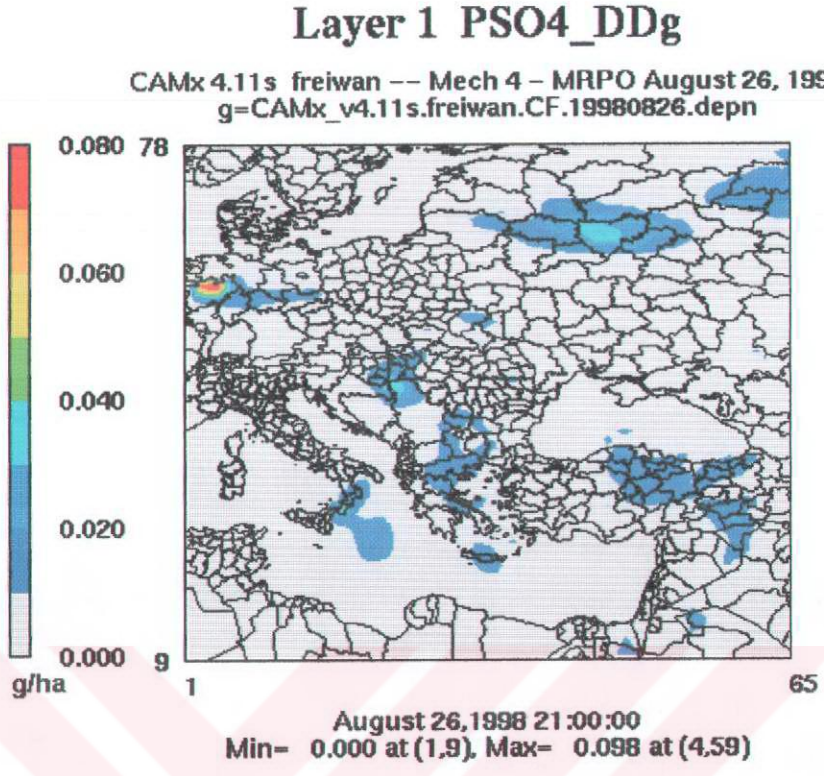

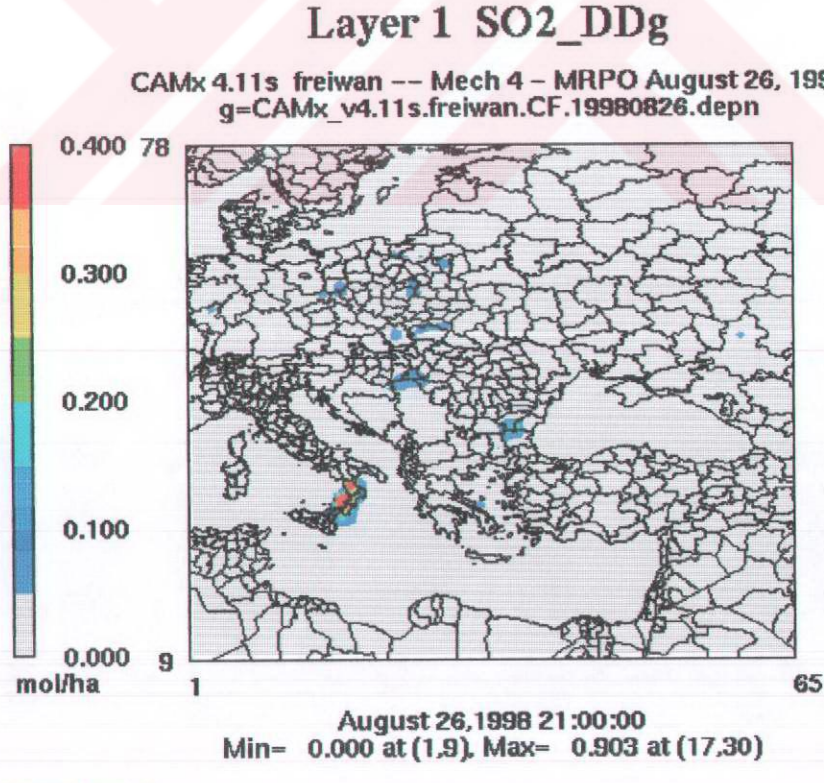

Figure E.5 h) 21:00 Z.

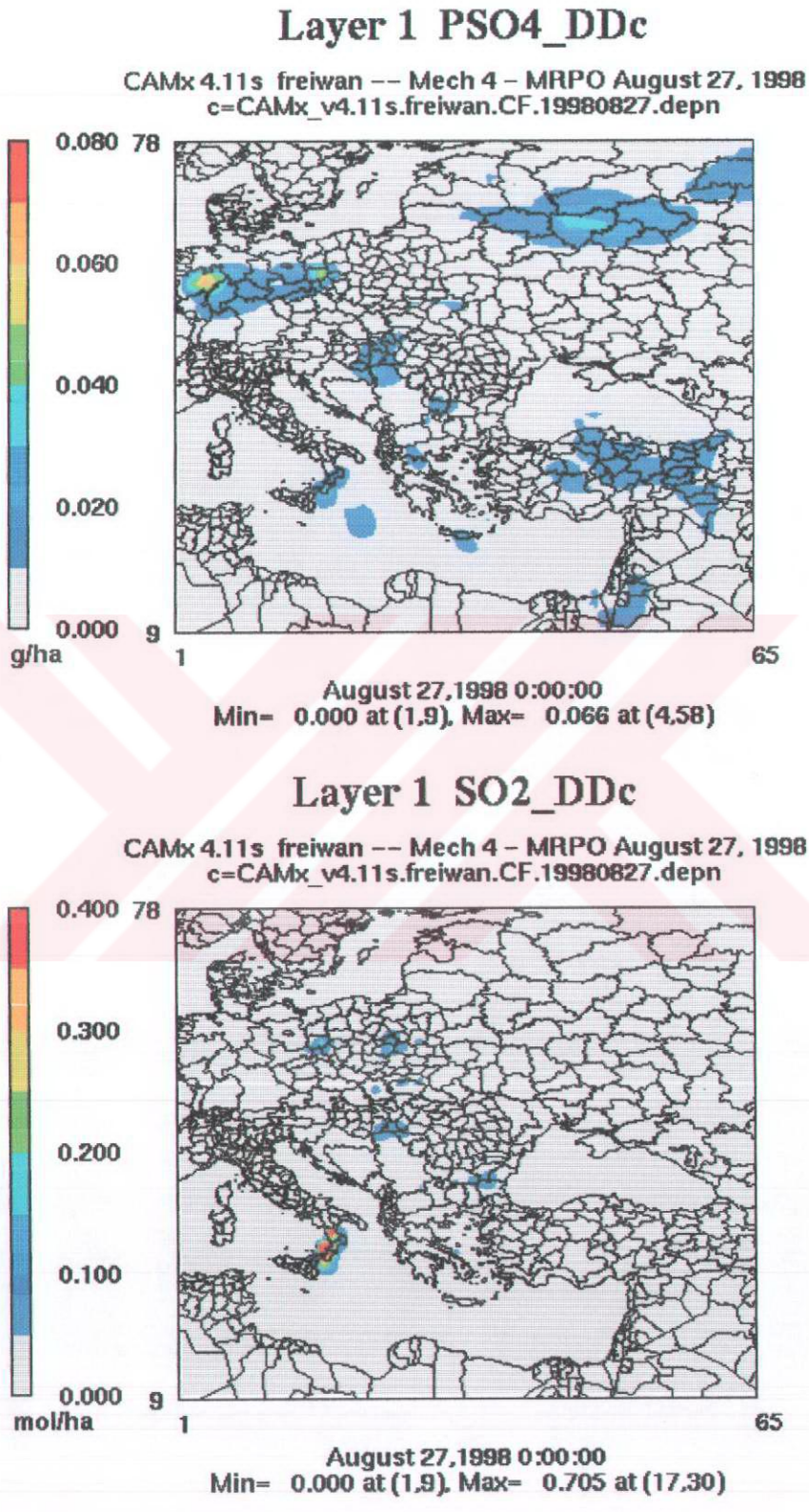

Figure E.6: The same as Fig. E.5 but for 27 Aug. 1998, a) 00:00 Z

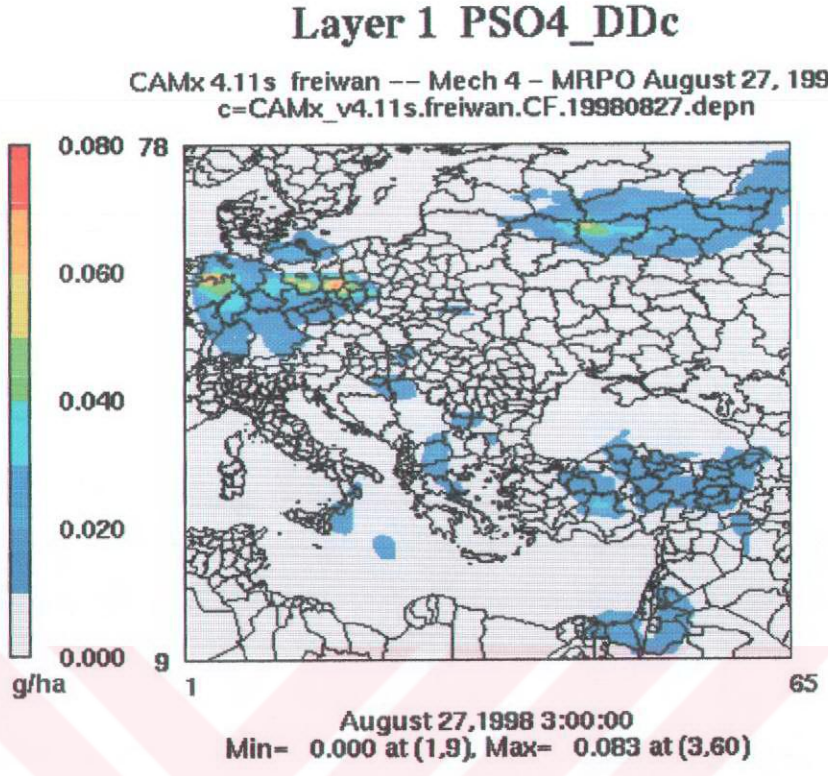

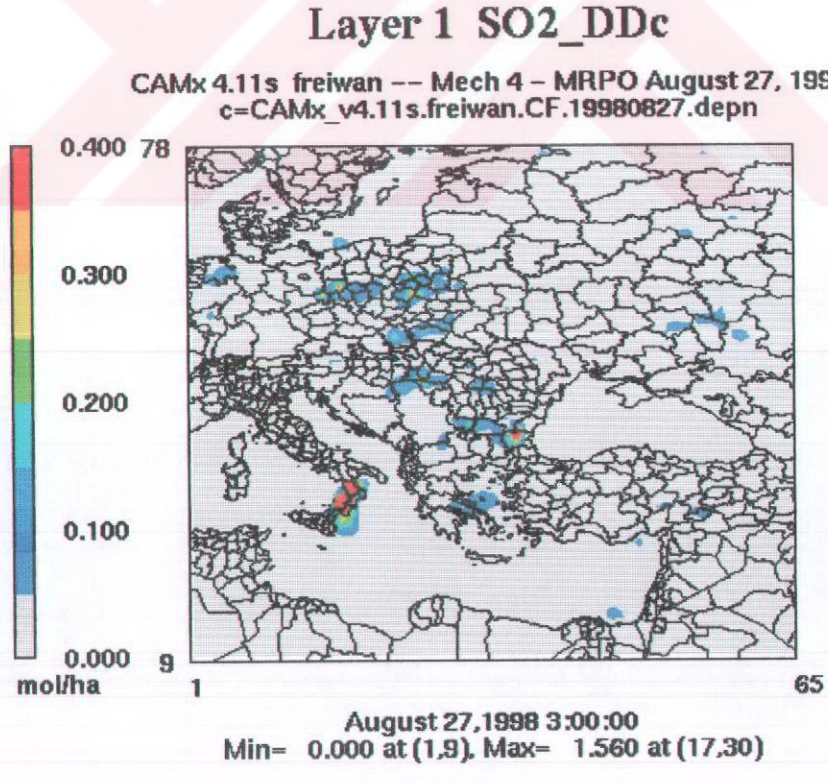

Figure E.6 b) 03:00 Z.

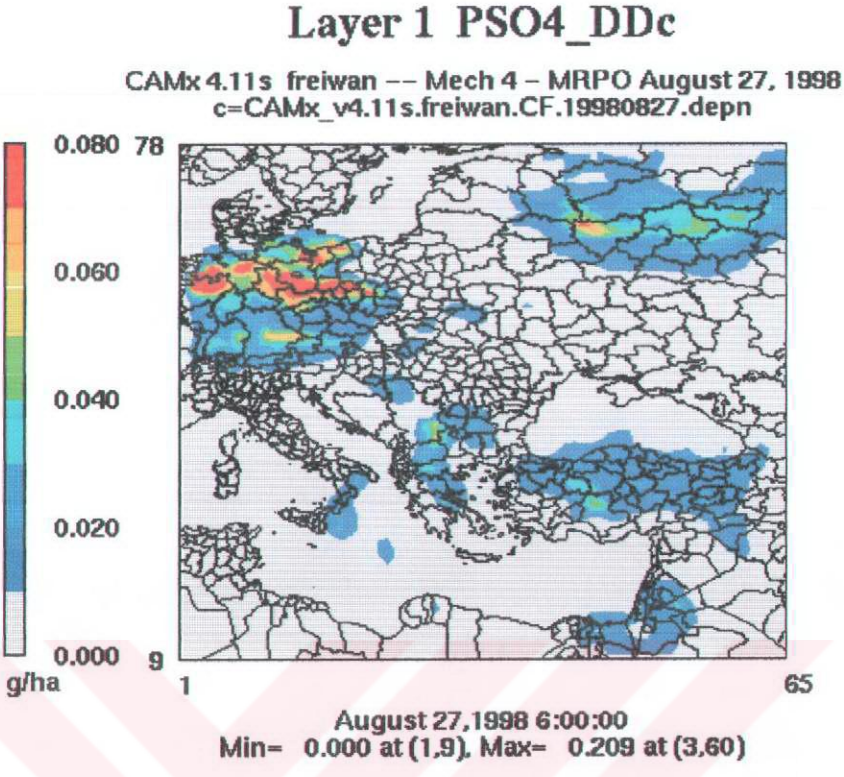

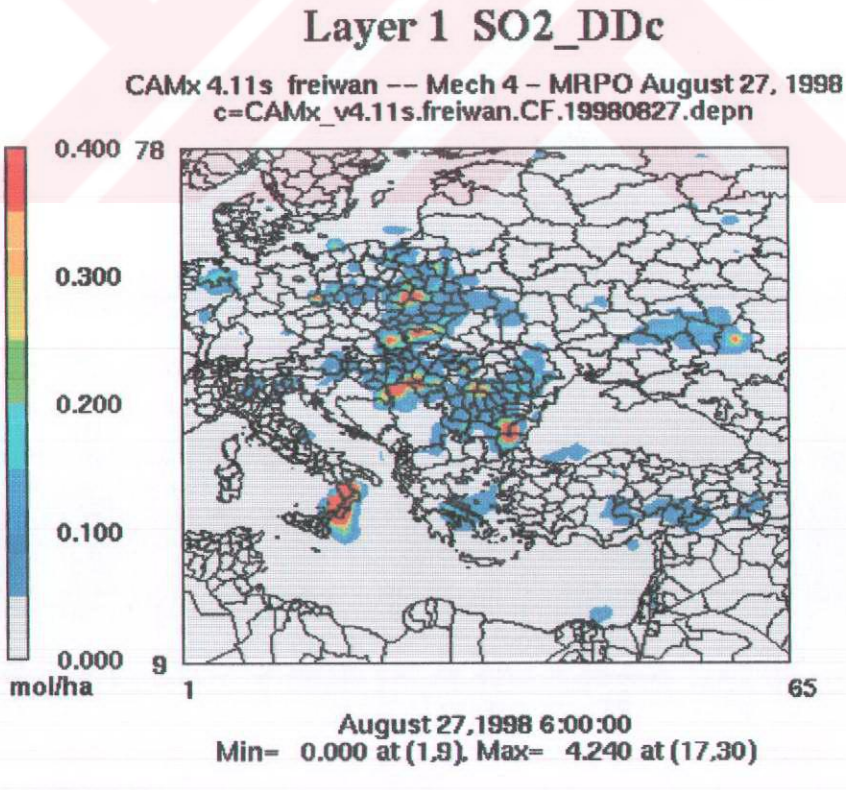

Figure E.6 c) 06:00 Z.

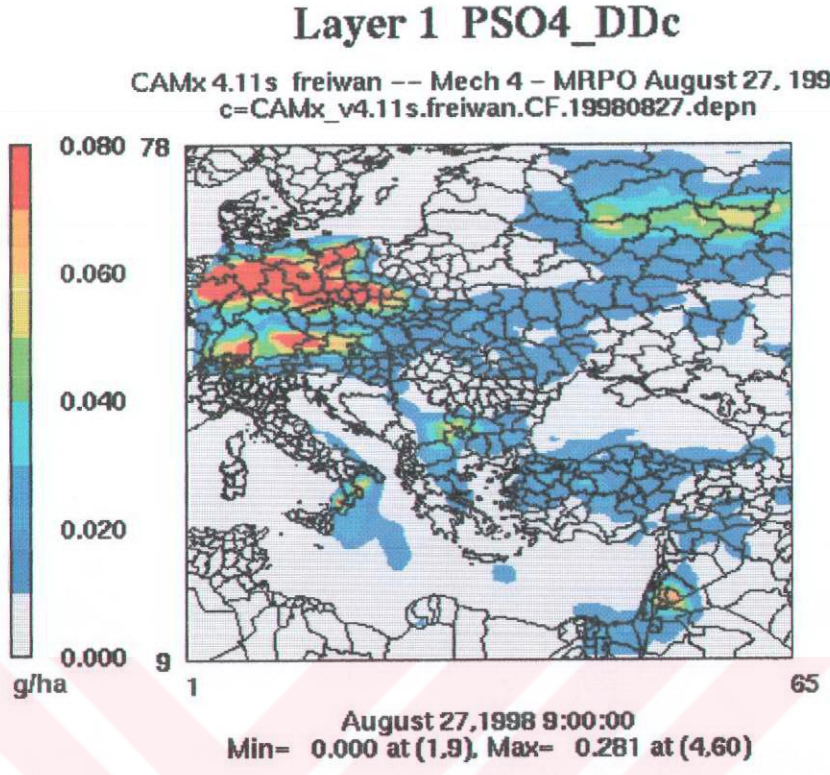

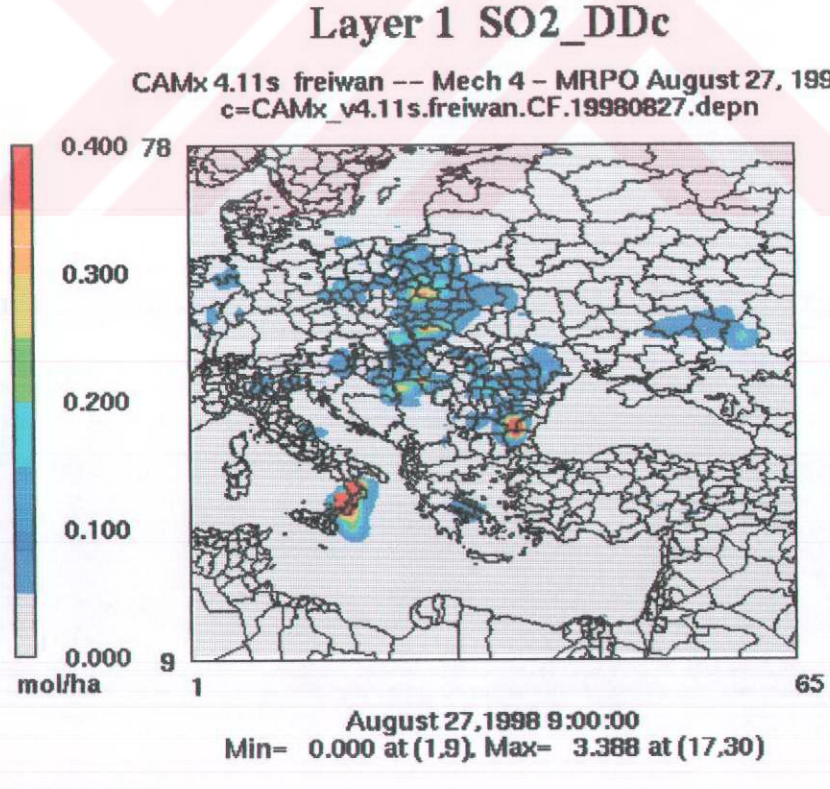

Figure E.6 d) 09:00 Z.

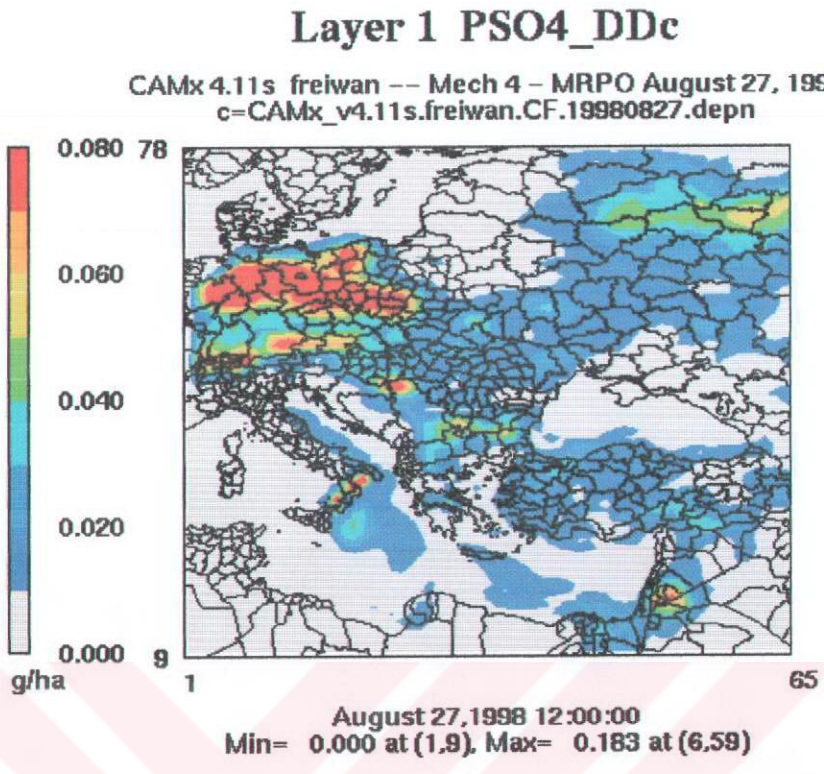

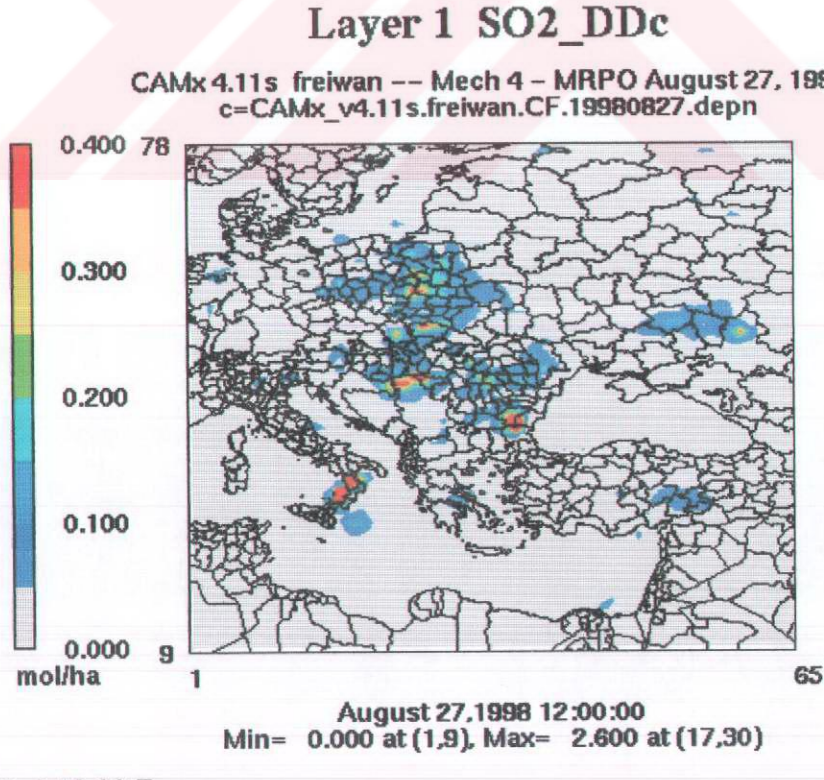

Figure E.6 e) 12:00 Z.

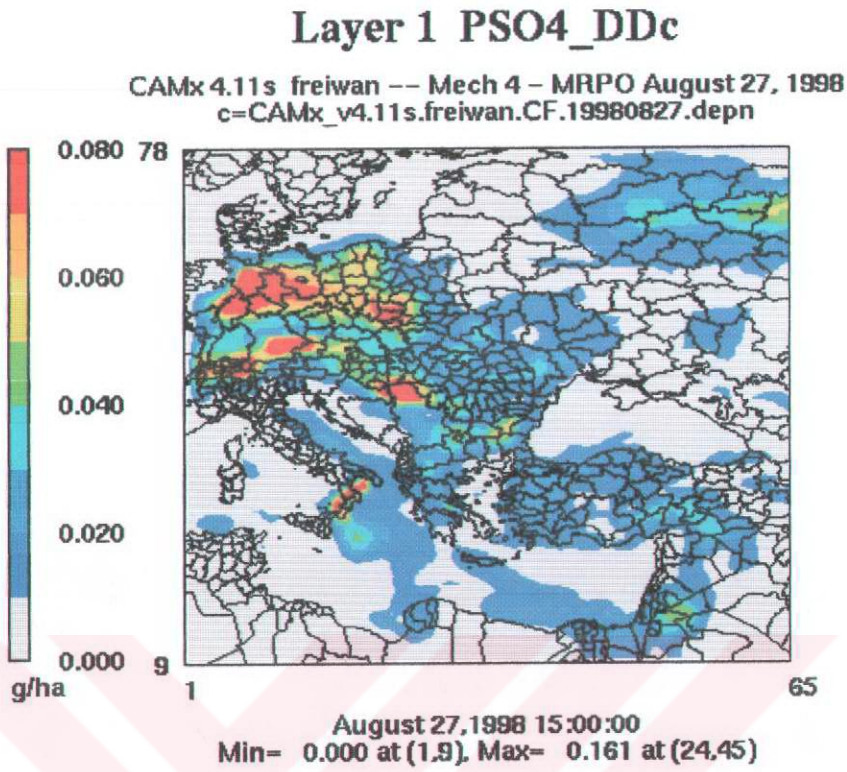

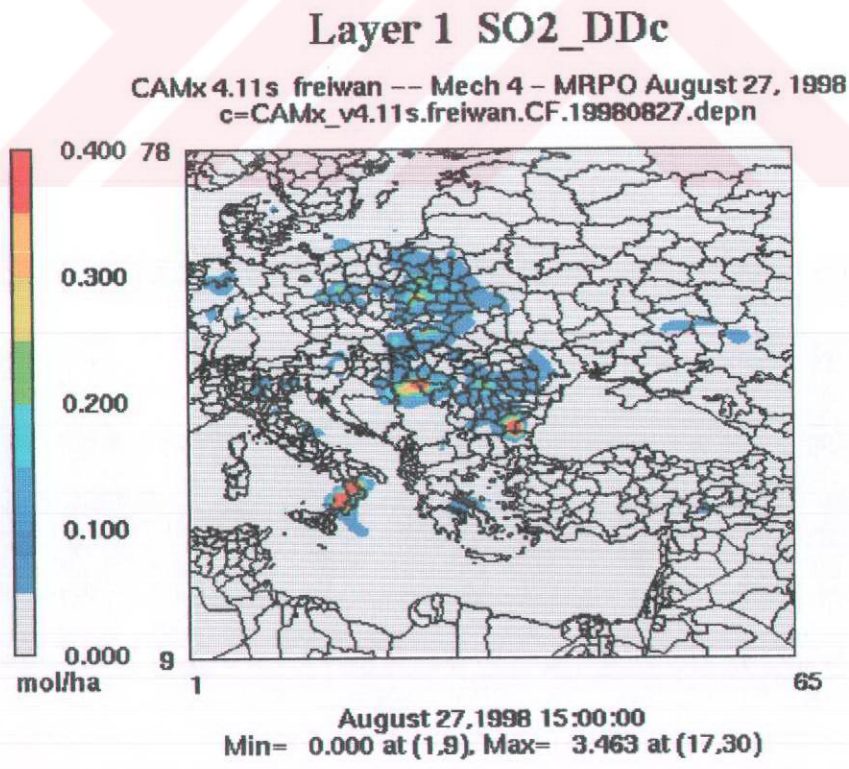

Figure E.6 f) 15:00 Z.

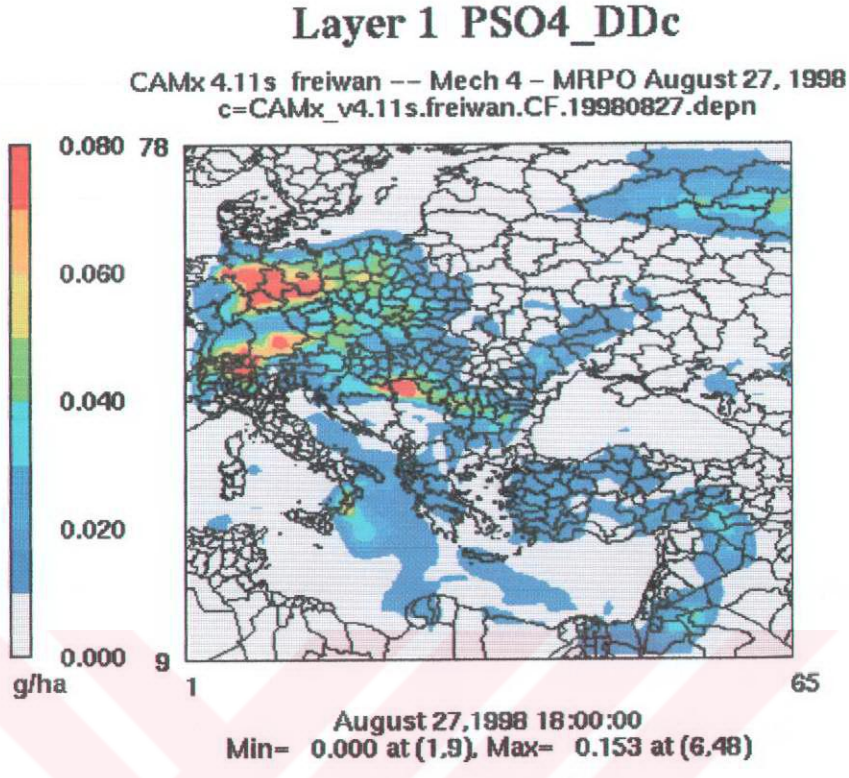

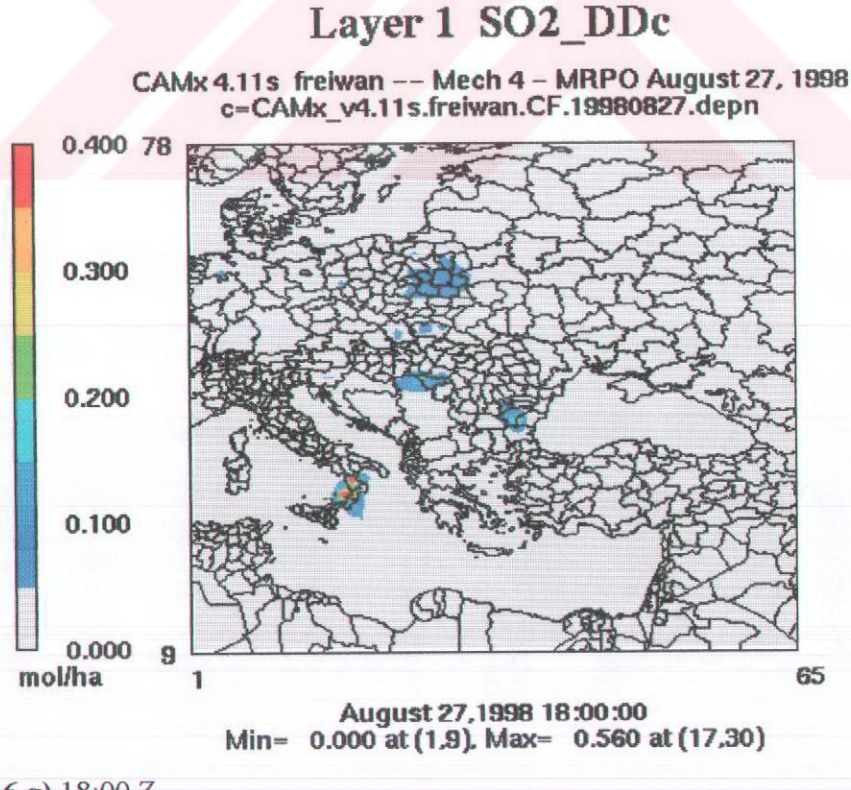

Figure E.6 g) 18:00 Z.

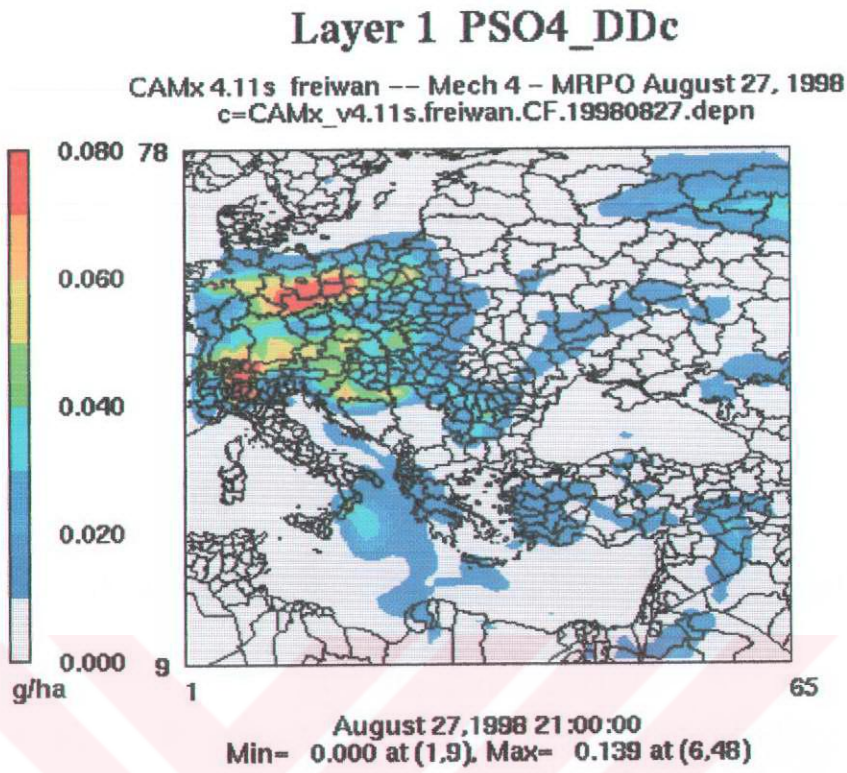

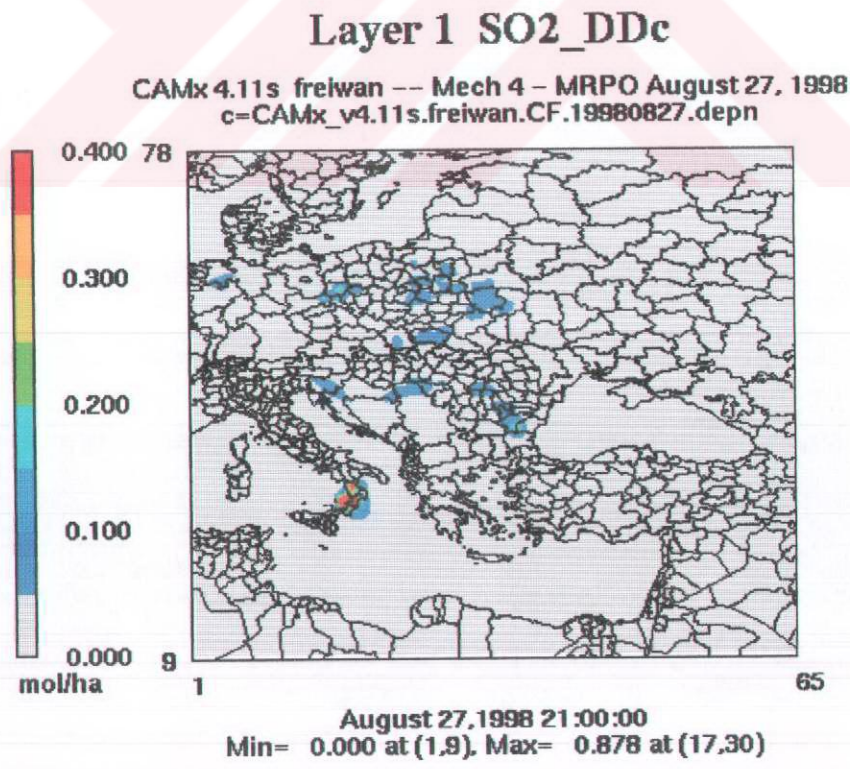

Figure E.6 h) 21:00 Z.

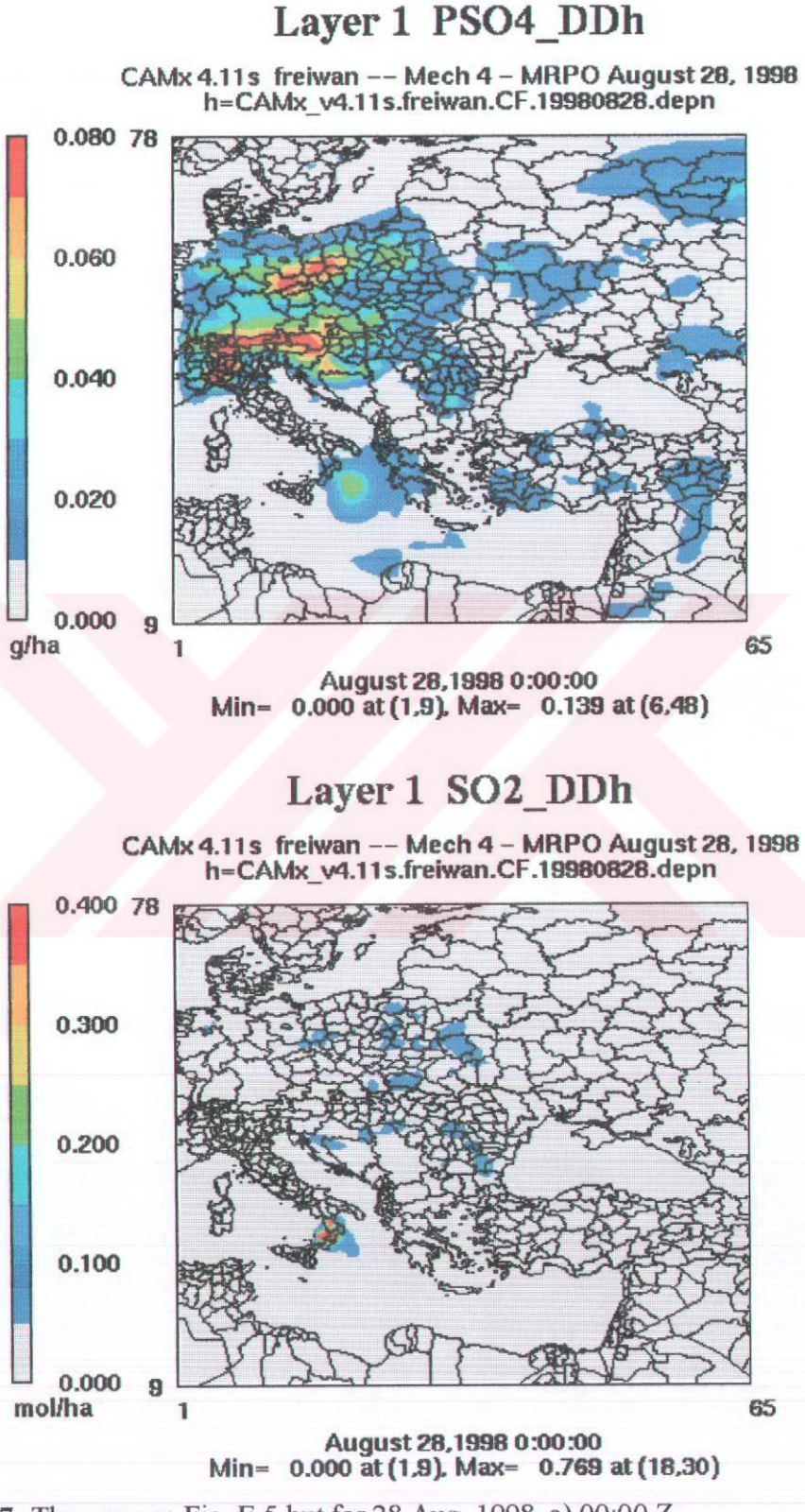

Figure E.7: The same as Fig. E.5 but for 28 Aug. 1998, a) 00:00 Z

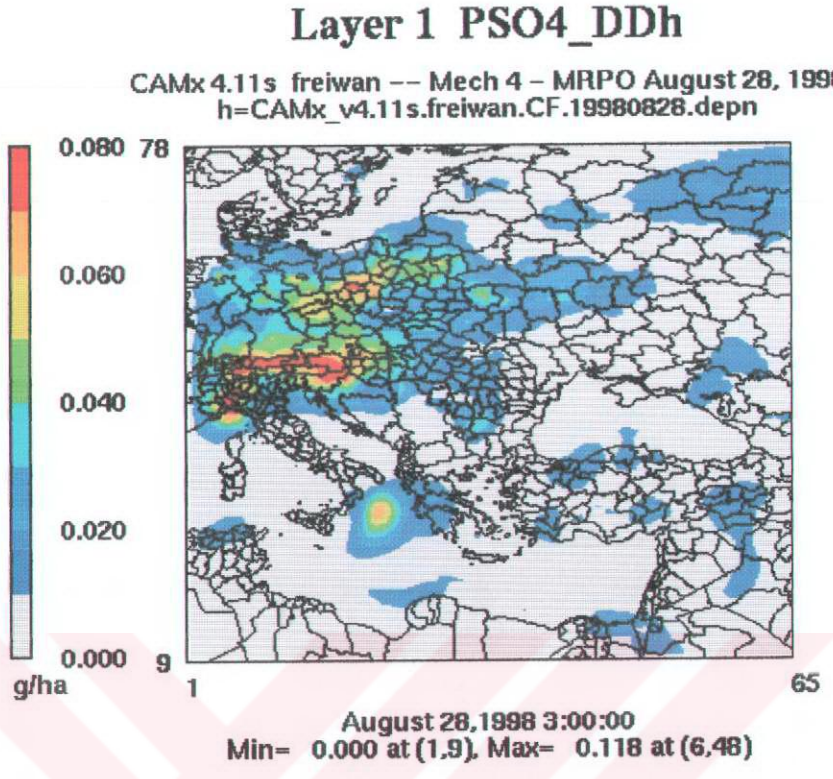

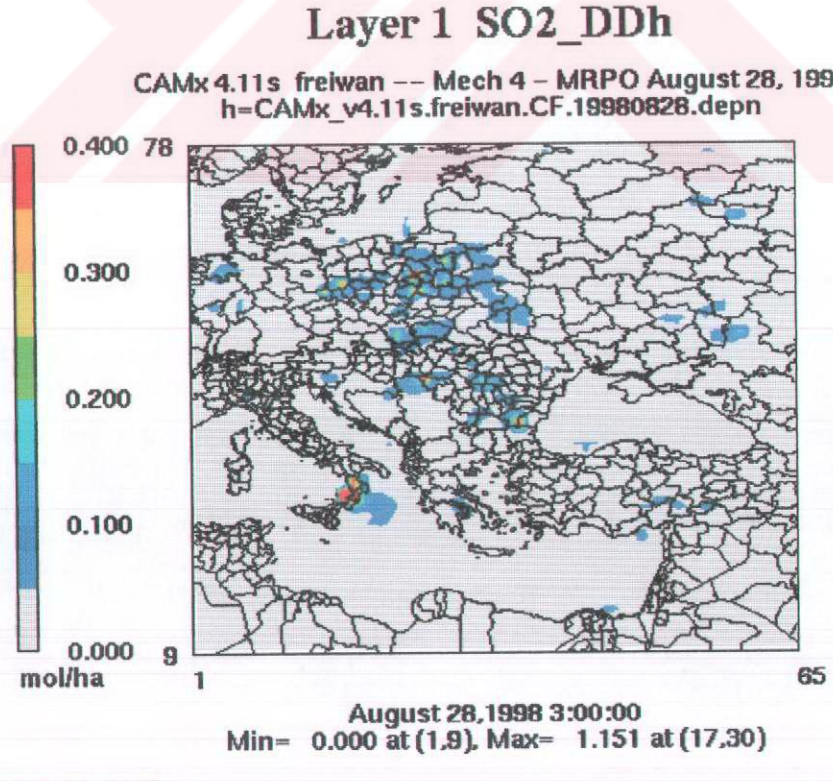

Figure E.7 b) 03:00 Z.

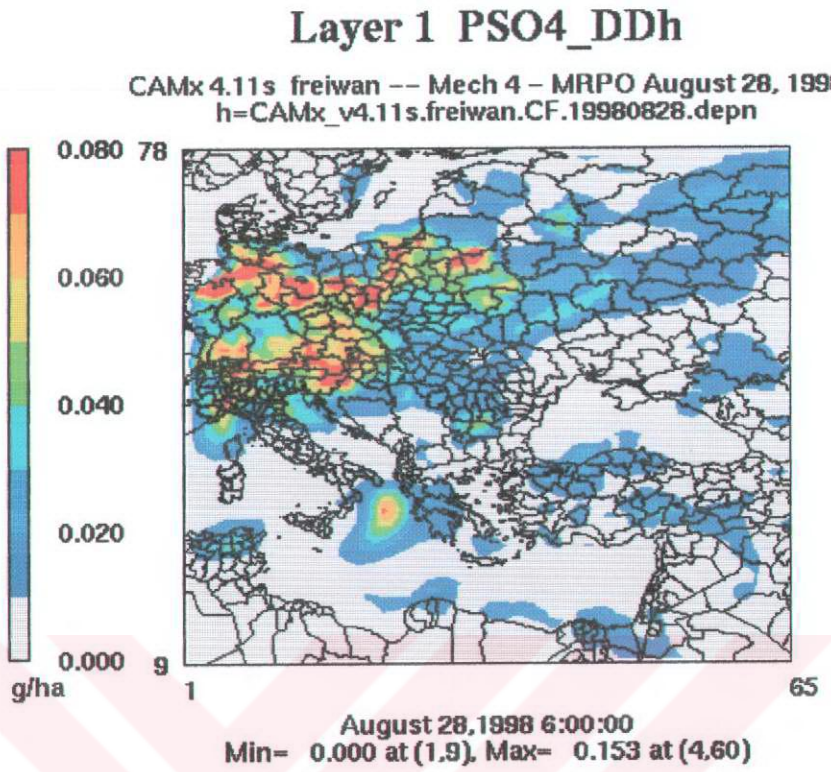

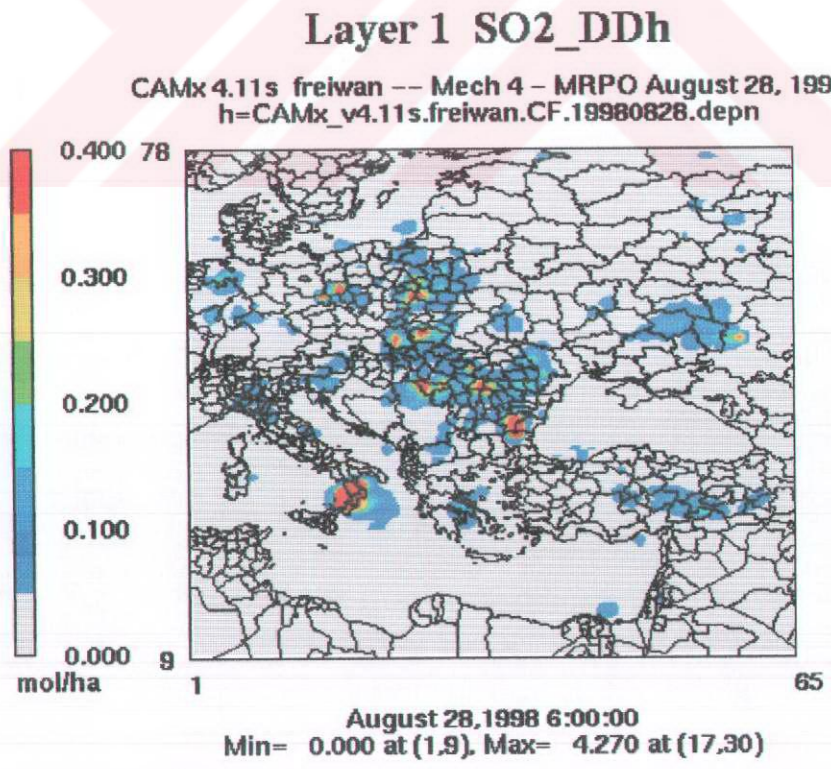

Figure E.7 c) 06:00 Z.

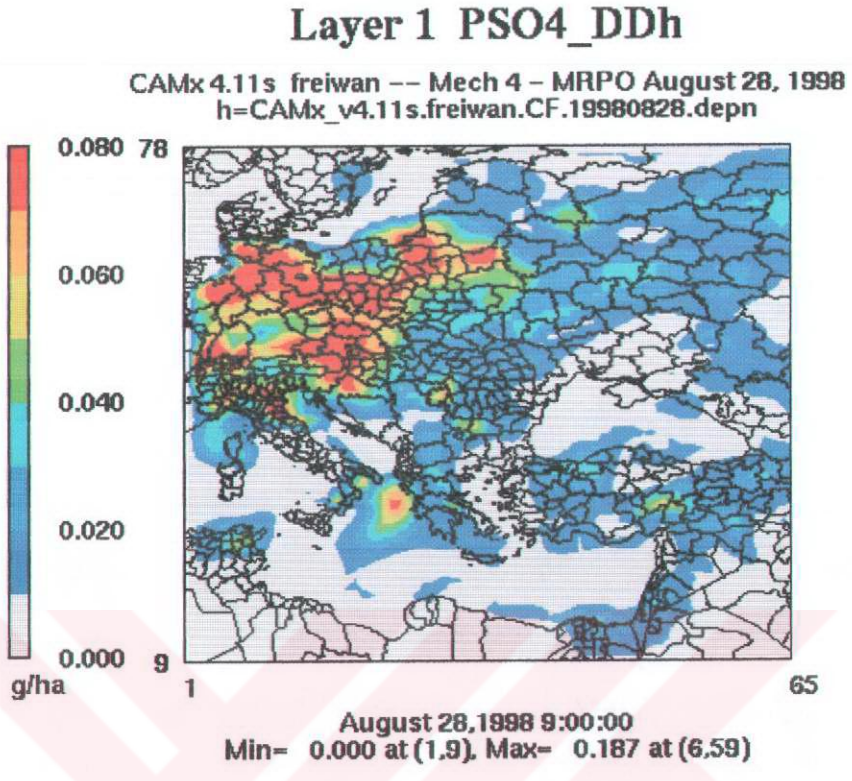

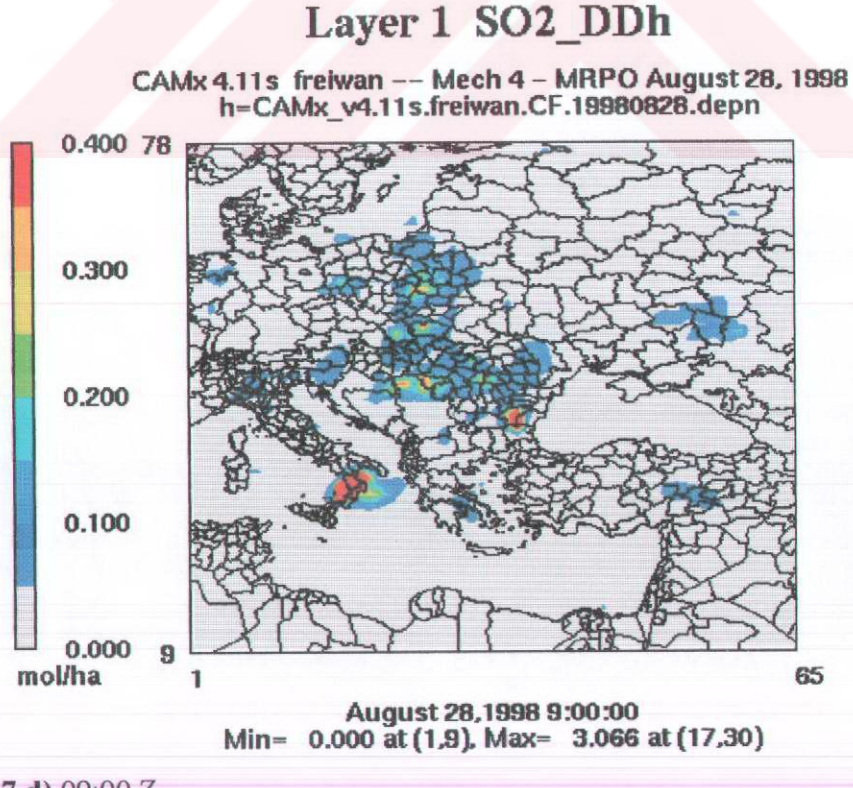

Figure E.7 d) 09:00 Z.

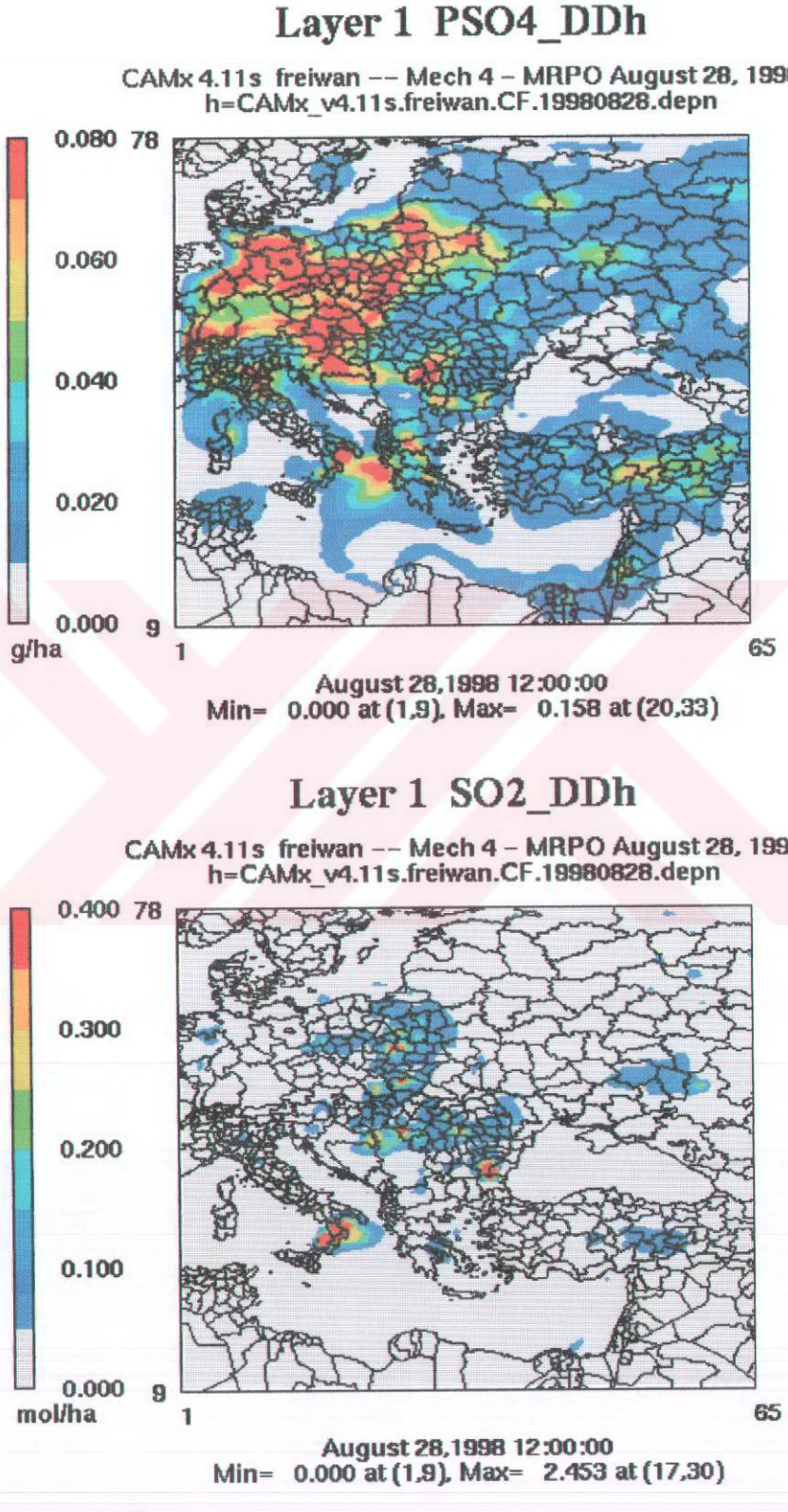

Figure E.7 e) 12:00 Z.

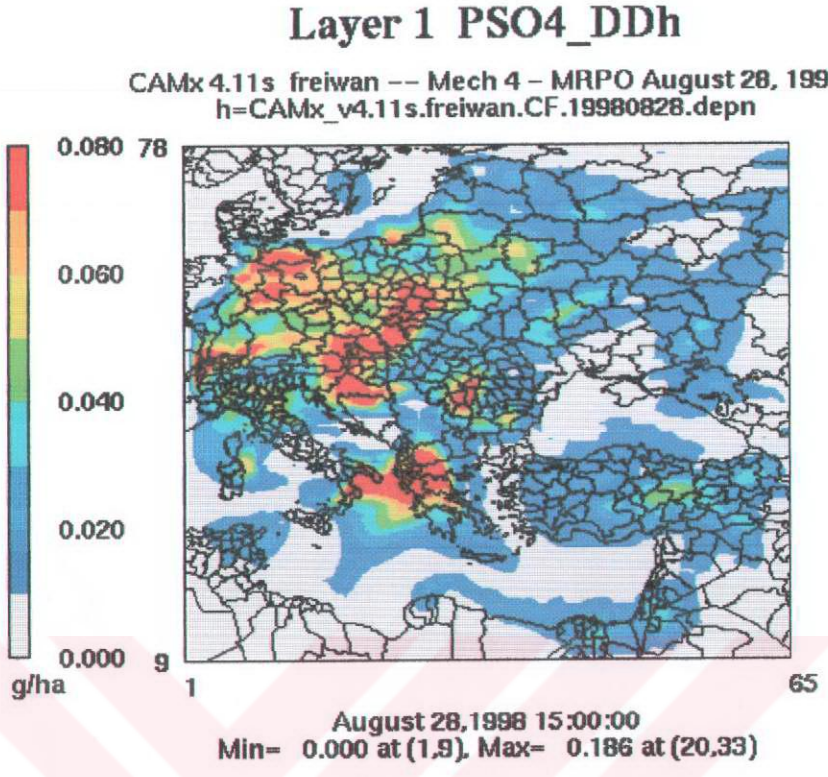

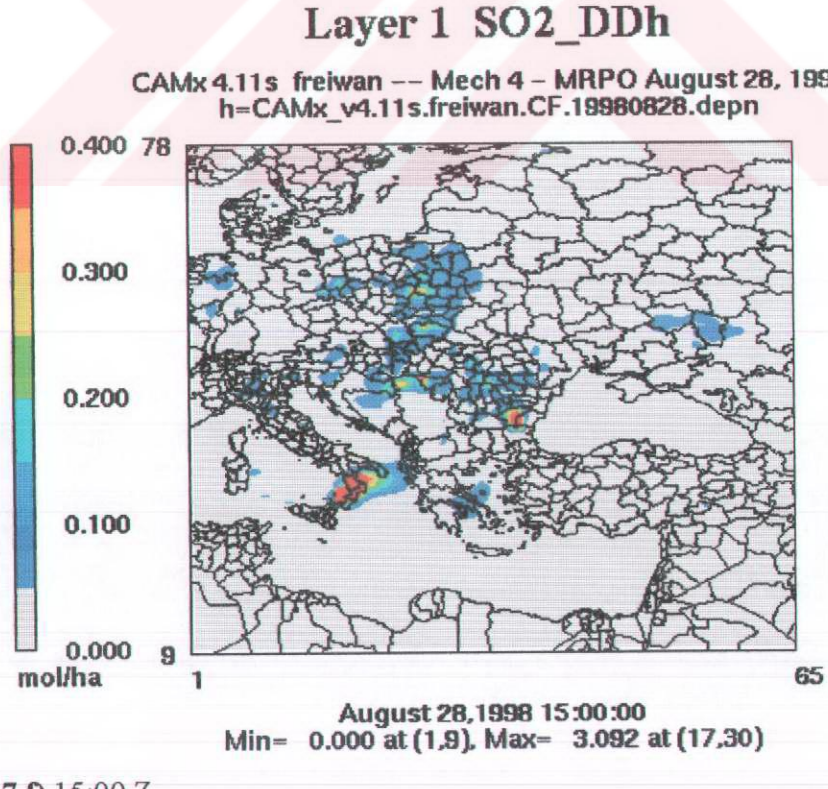

Figure E.7 f) 15:00 Z.

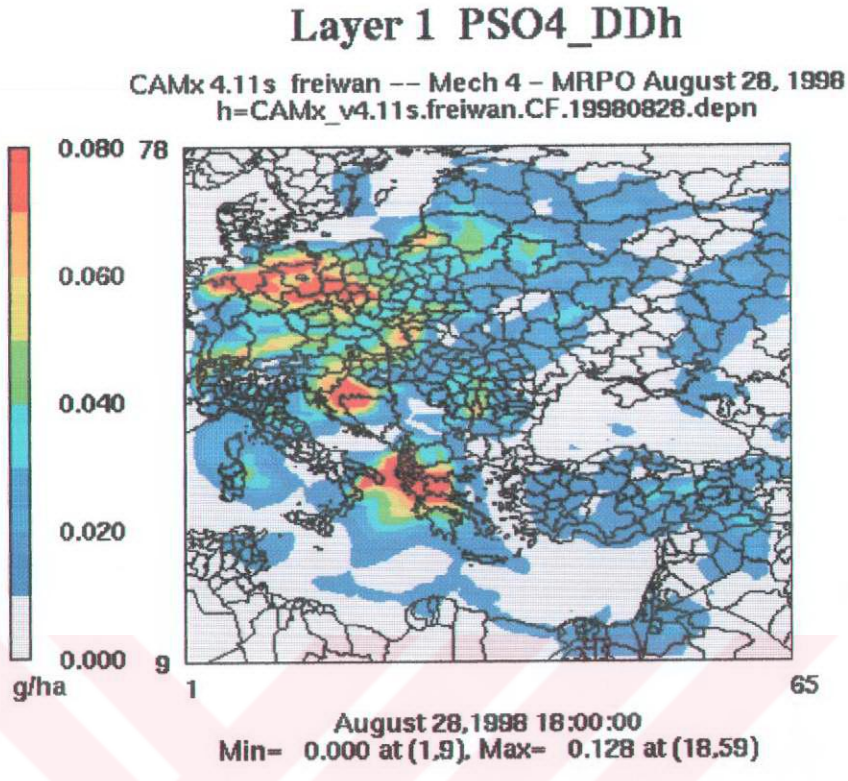

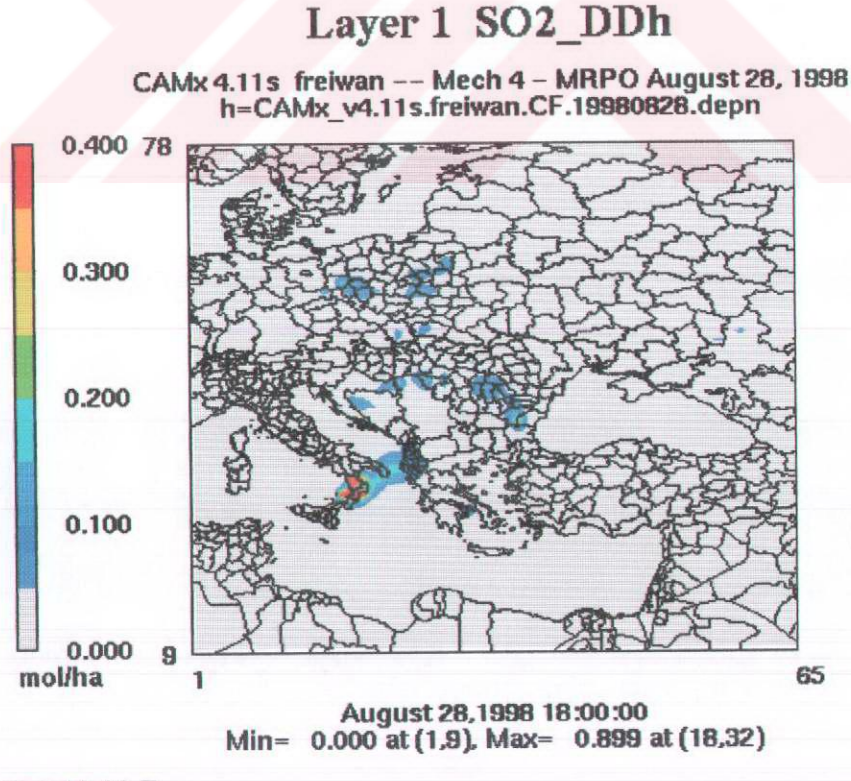

Figure E.7 g) 18:00 Z.

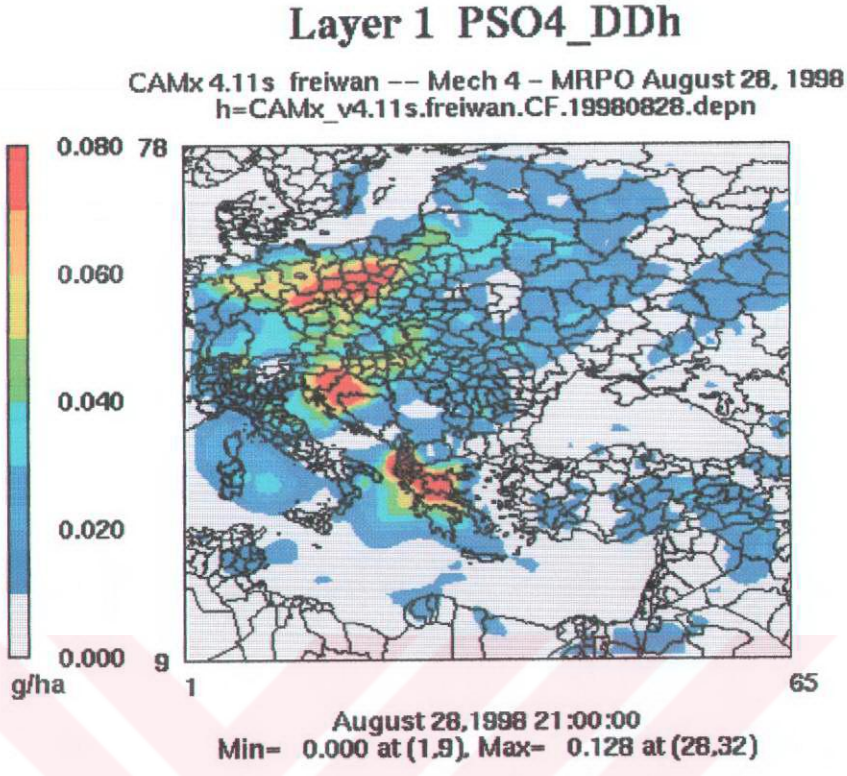

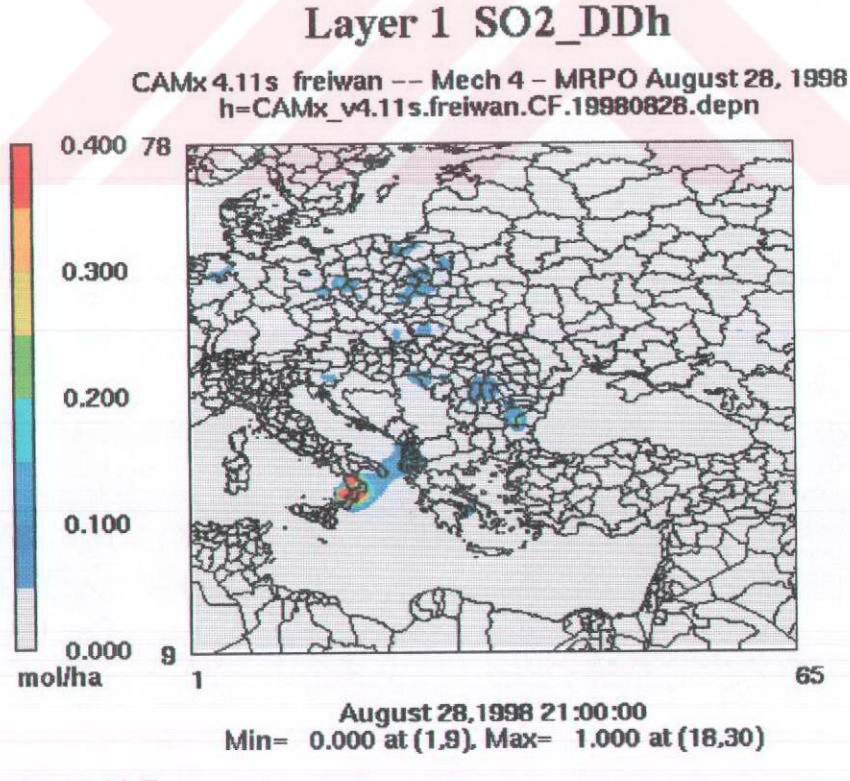

Figure E.7 h) 21:00 Z.

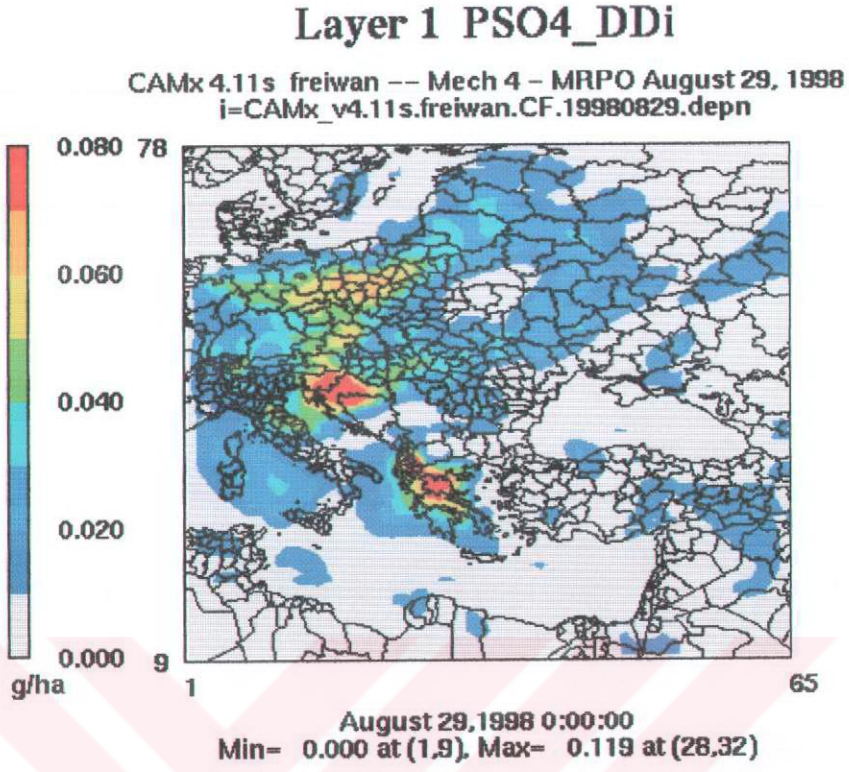

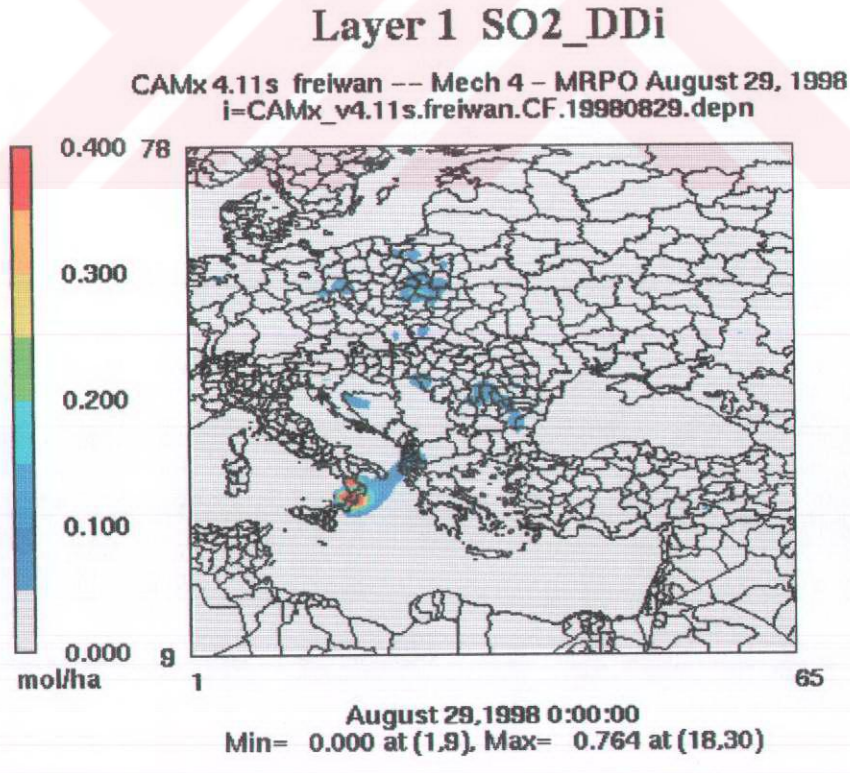

Figure E.8: The same as Fig. E.5 but for 29 Aug. 1998, a) 00:00 Z

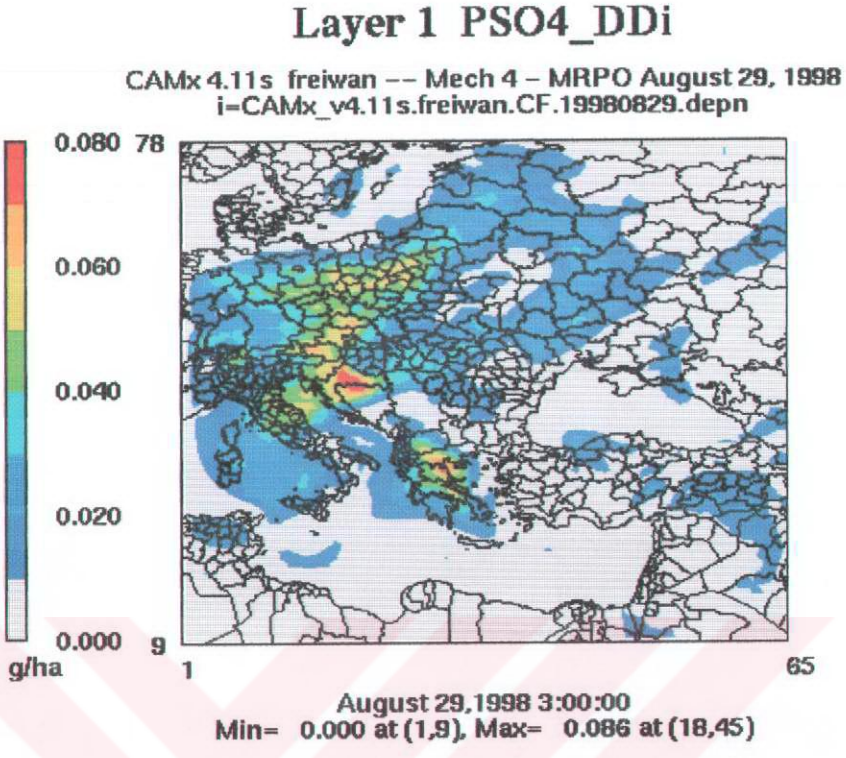

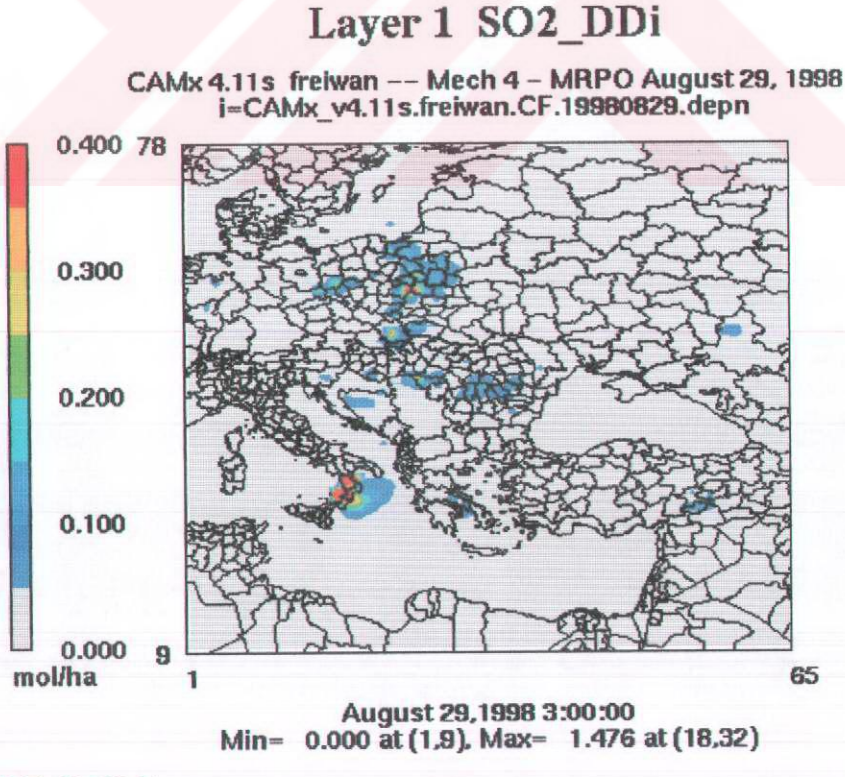

Figure E.8 b) 03:00 Z.

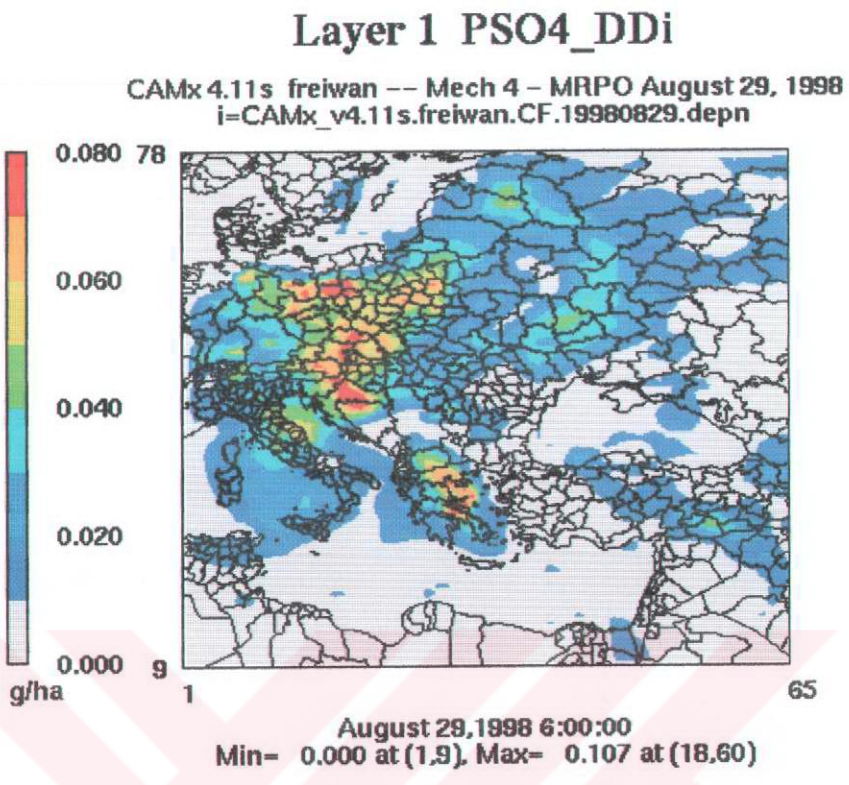

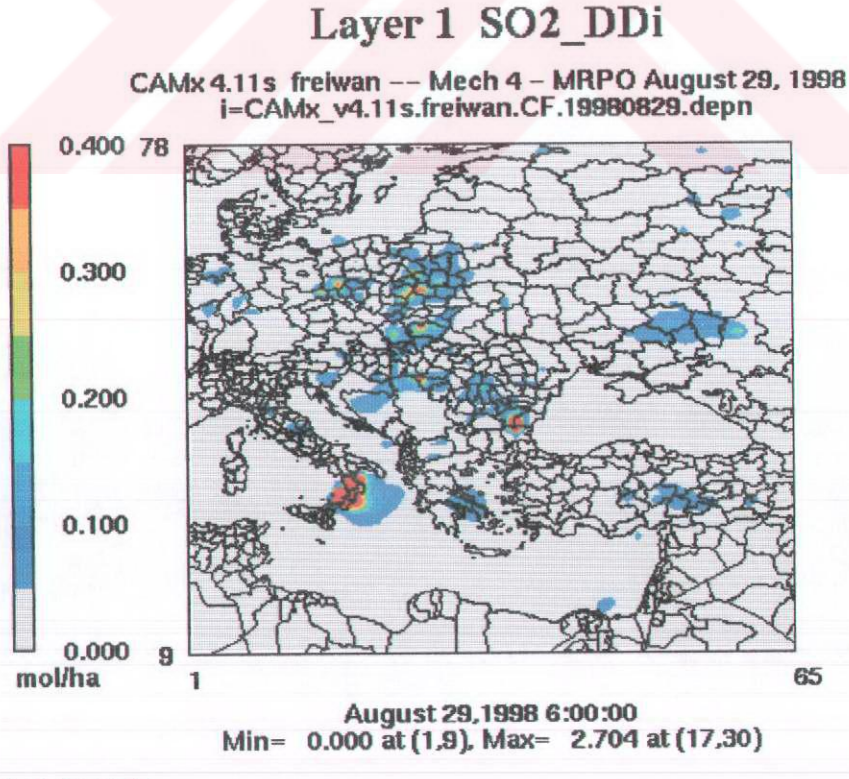

Figure E.8 c) 06:00 Z.

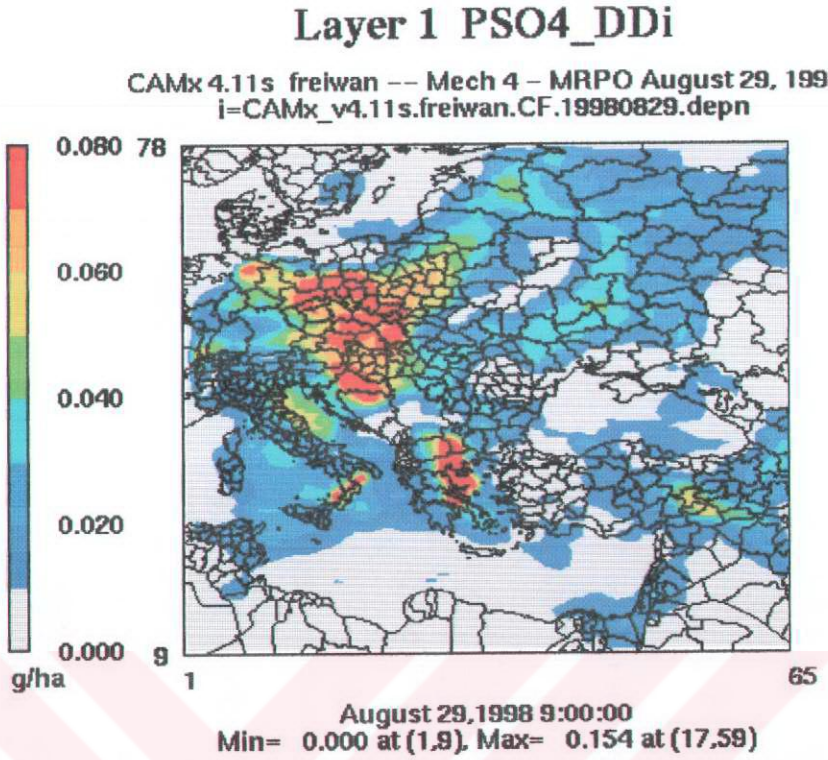

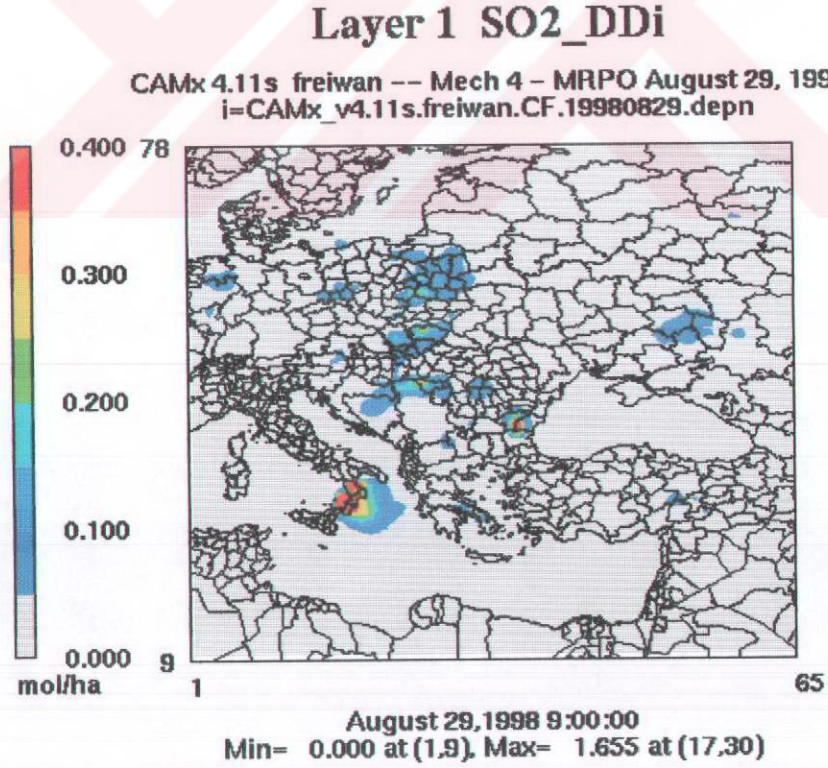

Figure E.8 d) 09:00 Z.

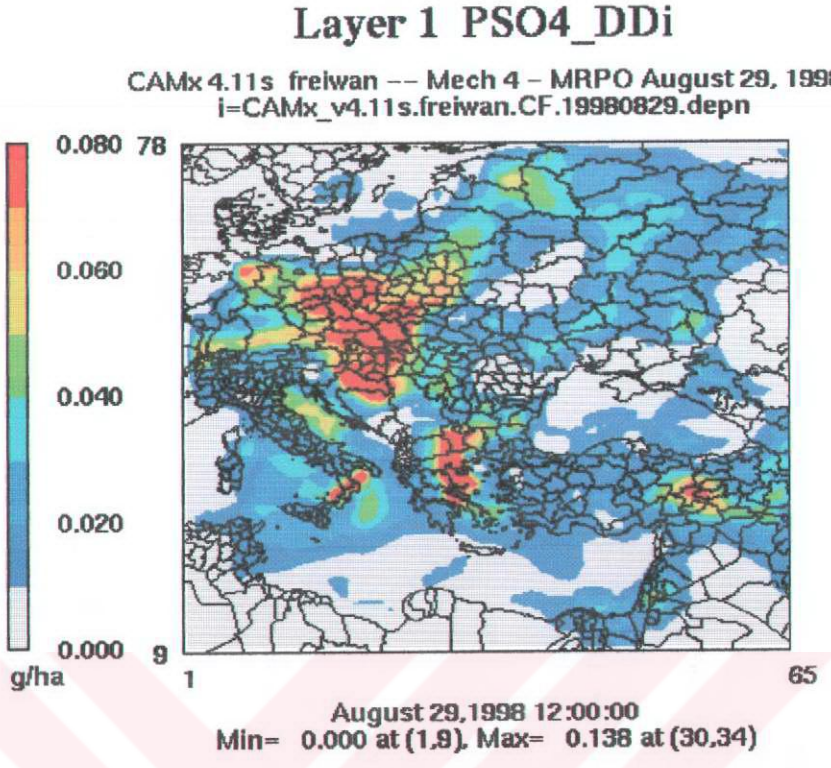

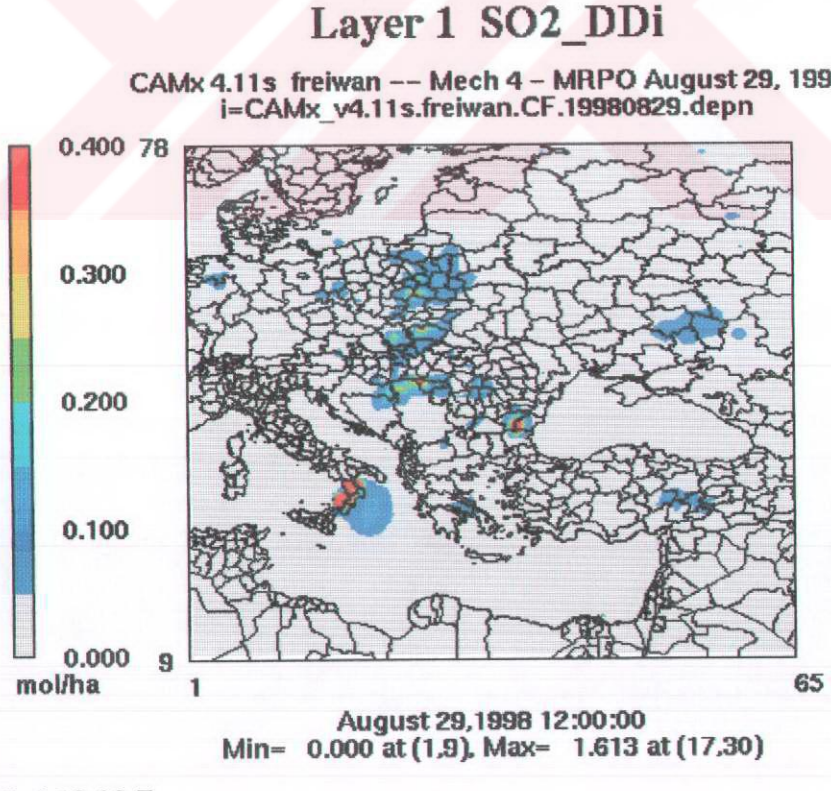

Figure E.8 e) 12:00 Z.

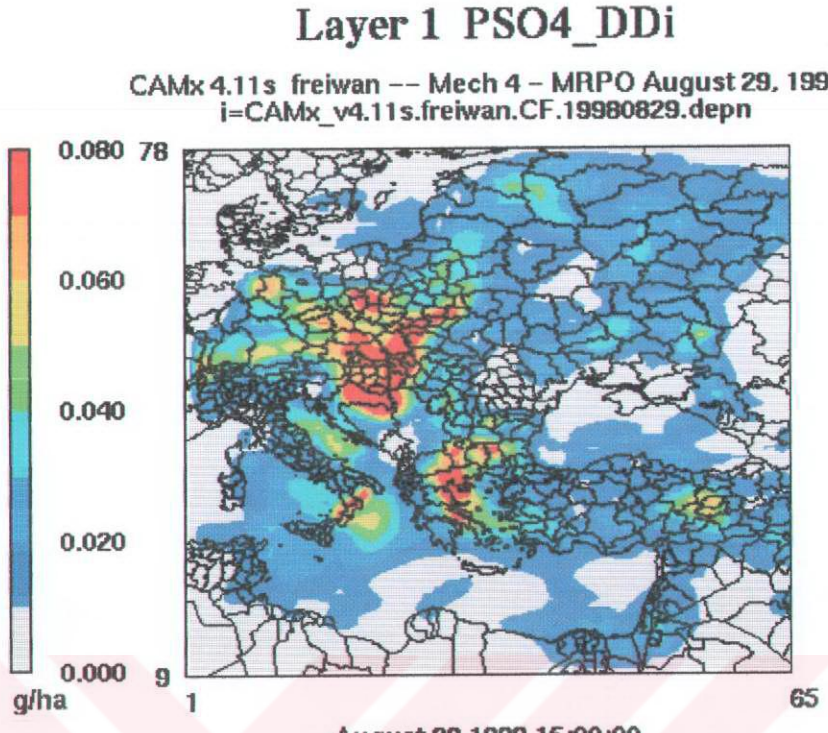

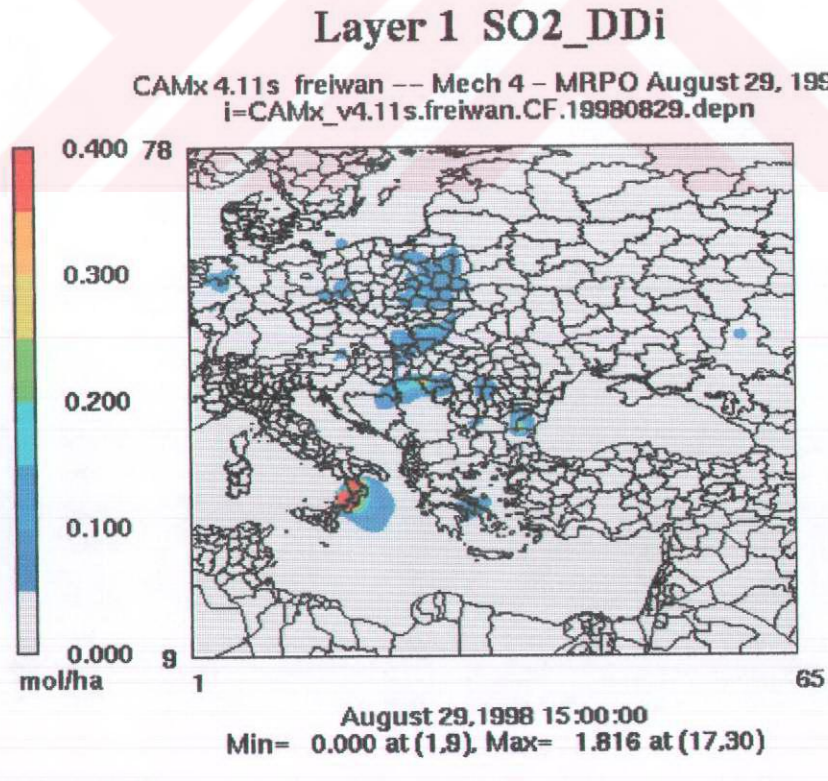

Figure E.8 f) 15:00 Z.

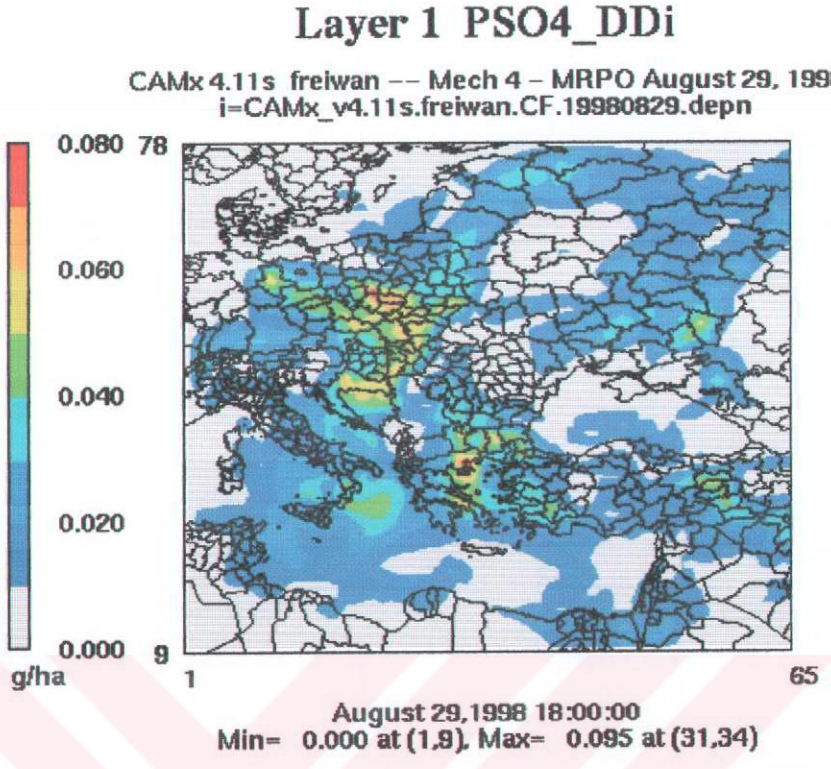

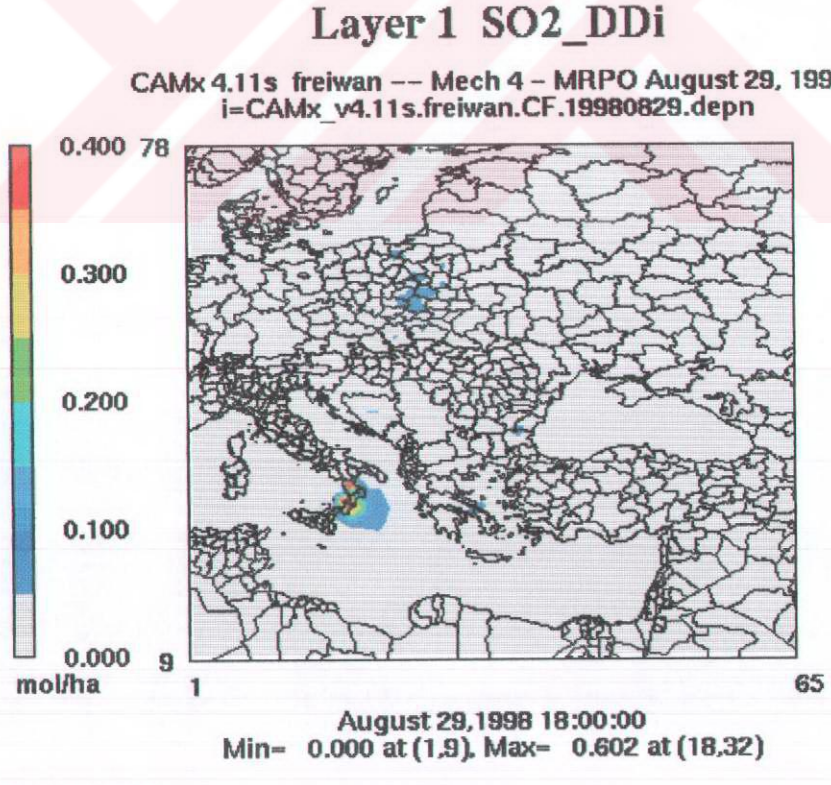

Figure E.8 g) 18:00 Z.

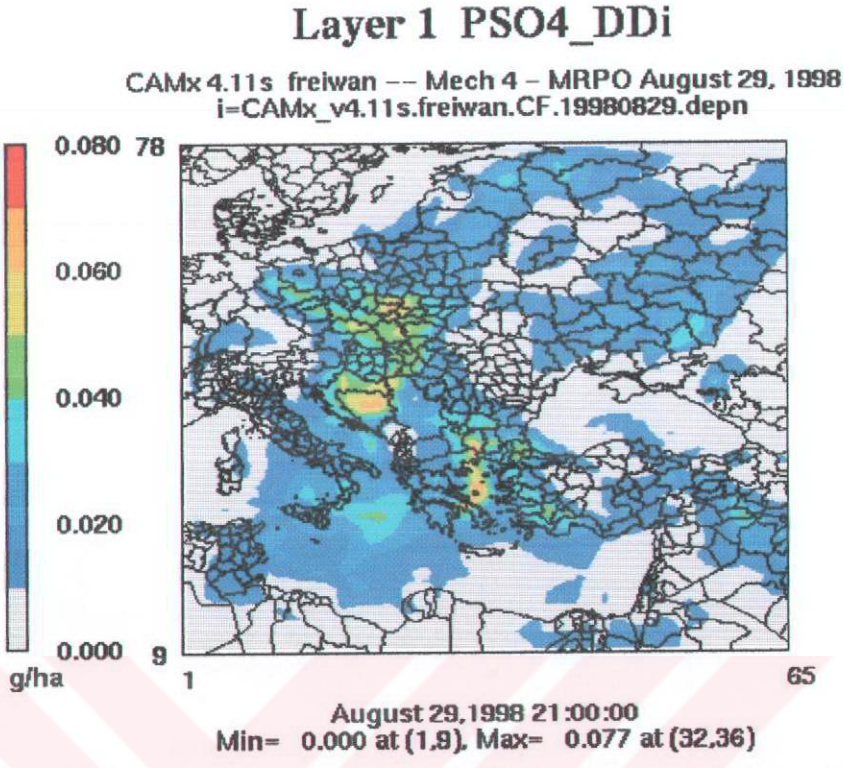

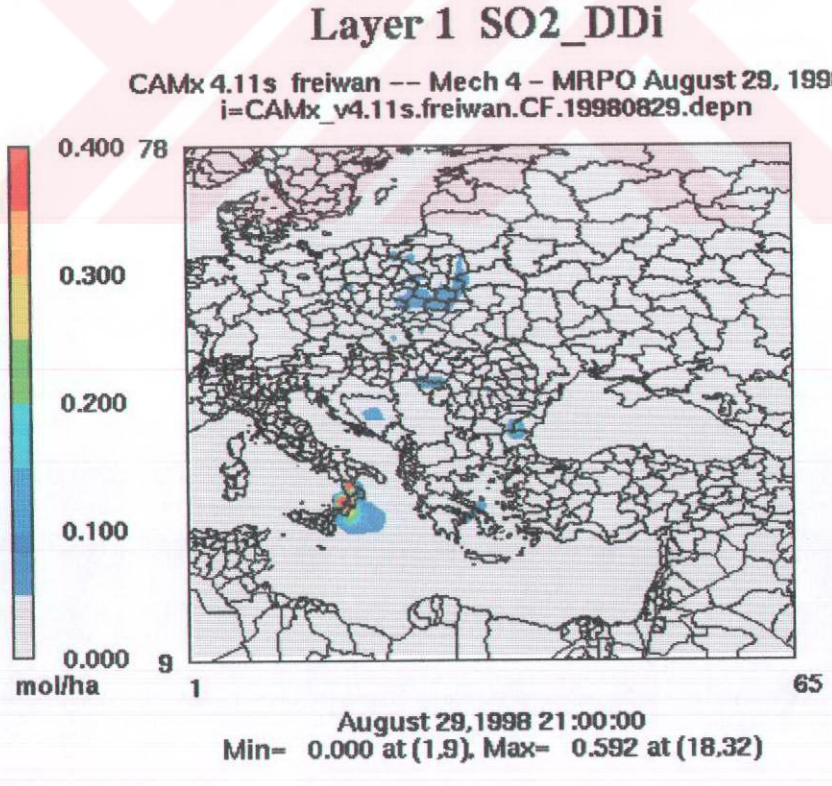

Figure E.8 g) 21:00 Z.

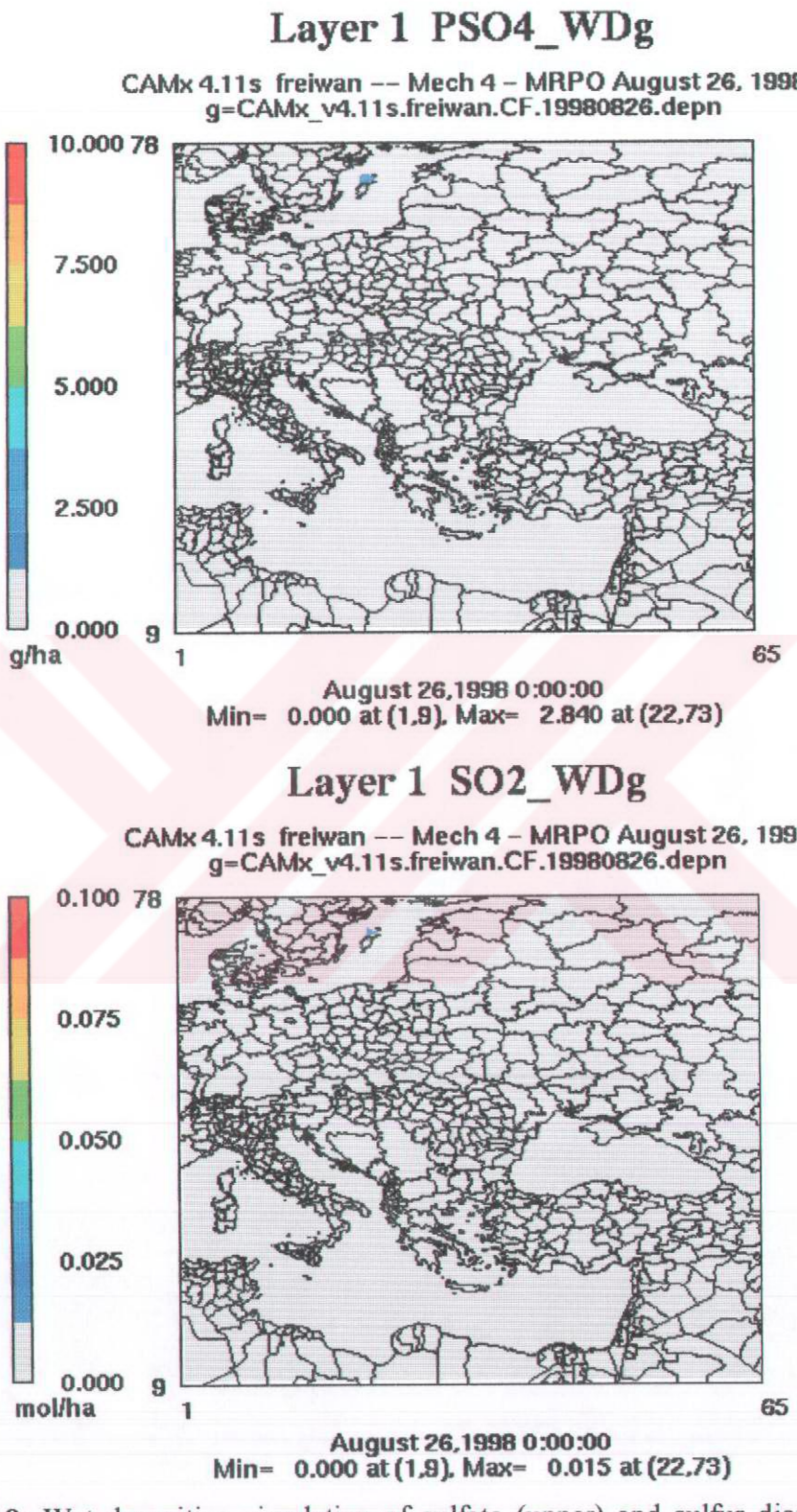

Figure E.9: Wet deposition simulation of sulfate (upper) and sulfur dioxide (lower) during the episodic period 26 – 29 August 1998; a) 26 August 1998 00:00 Z.

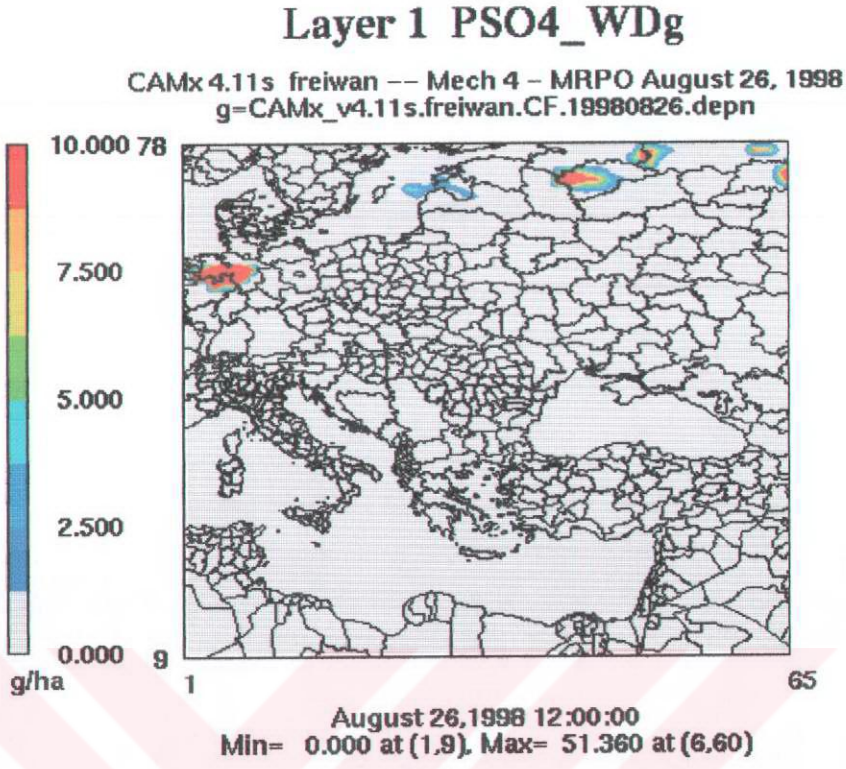

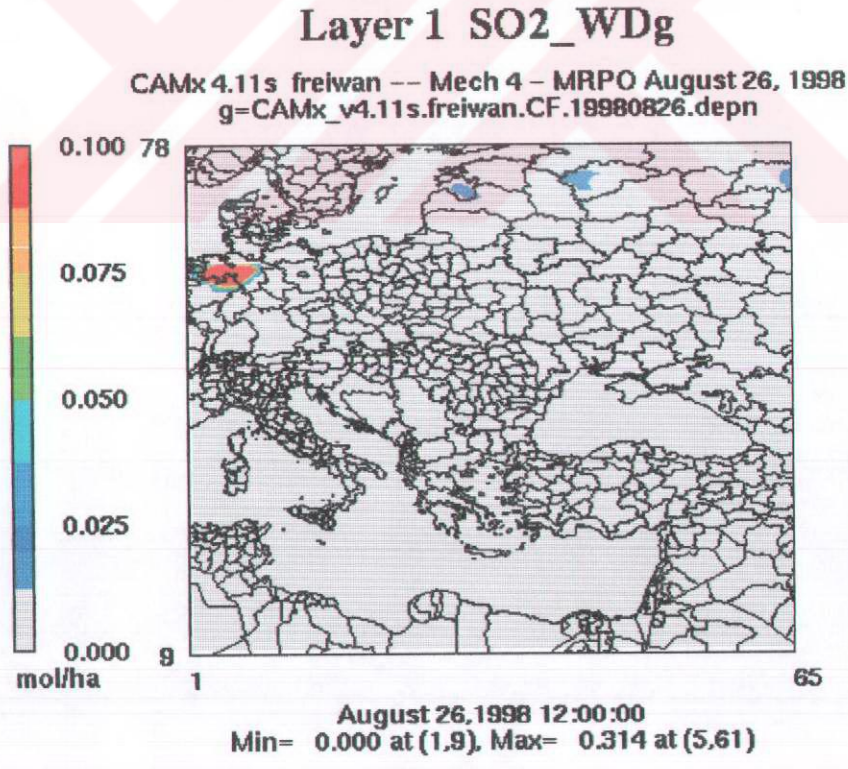

Figure E.9 b) 26 August 1998 12:00 Z.

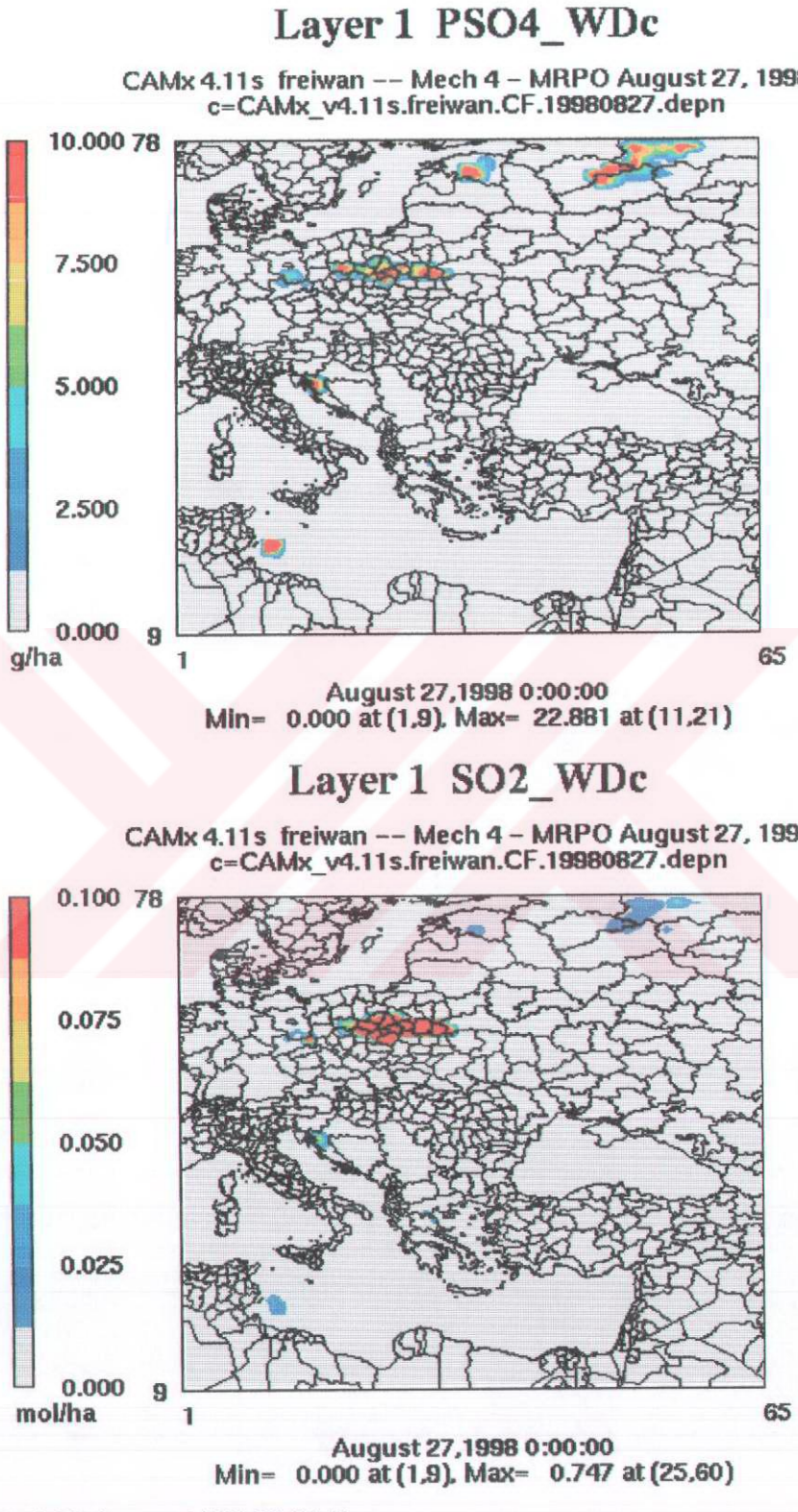

Figure E.9 c) 27 August 1998 00:00 Z.

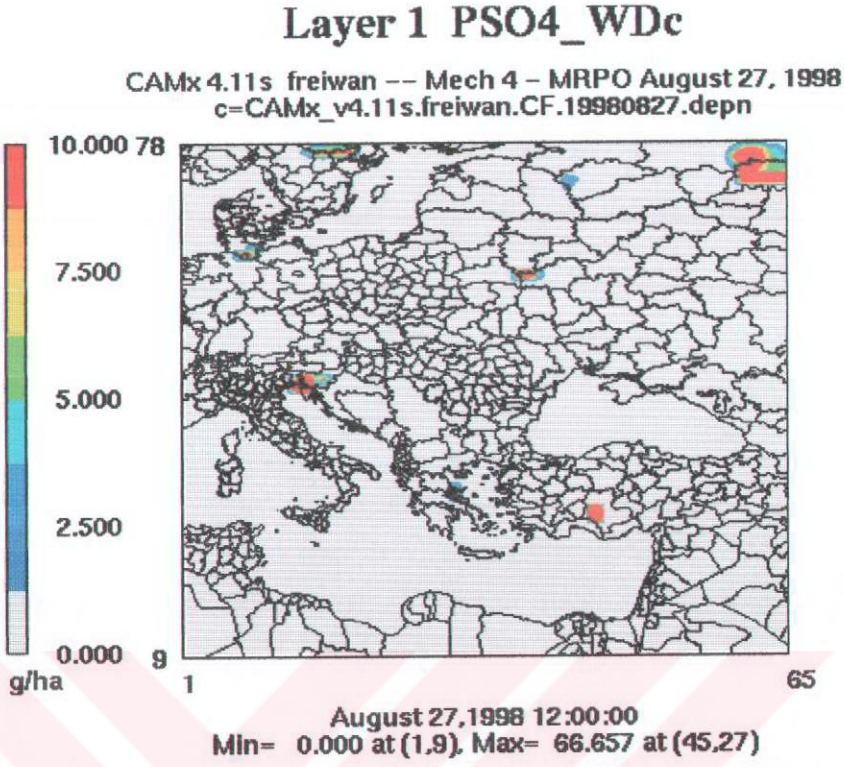

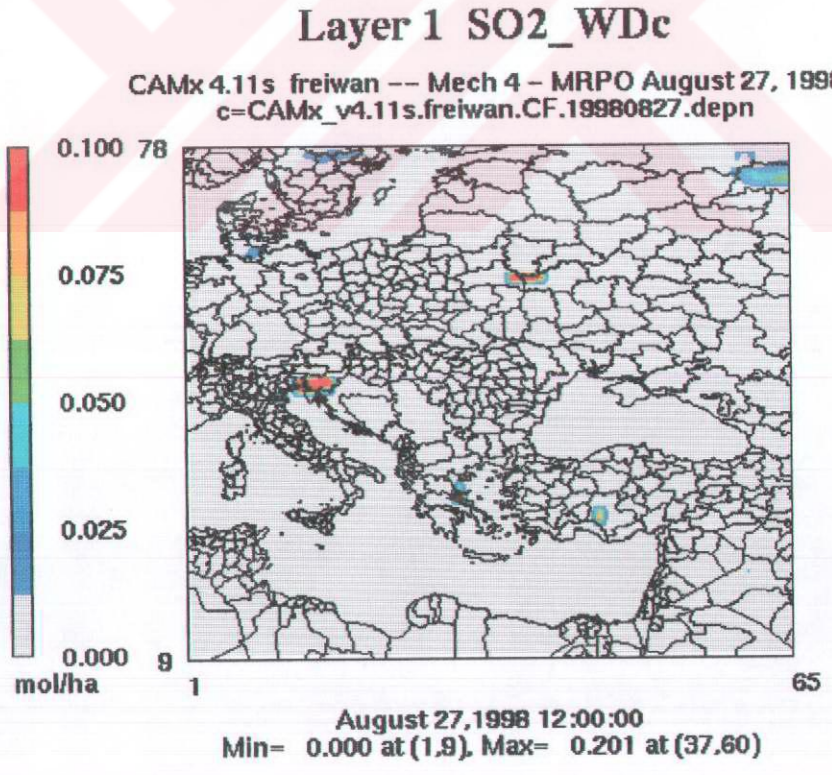

Figure E.9 d) 27 August 1998 12:00 Z.

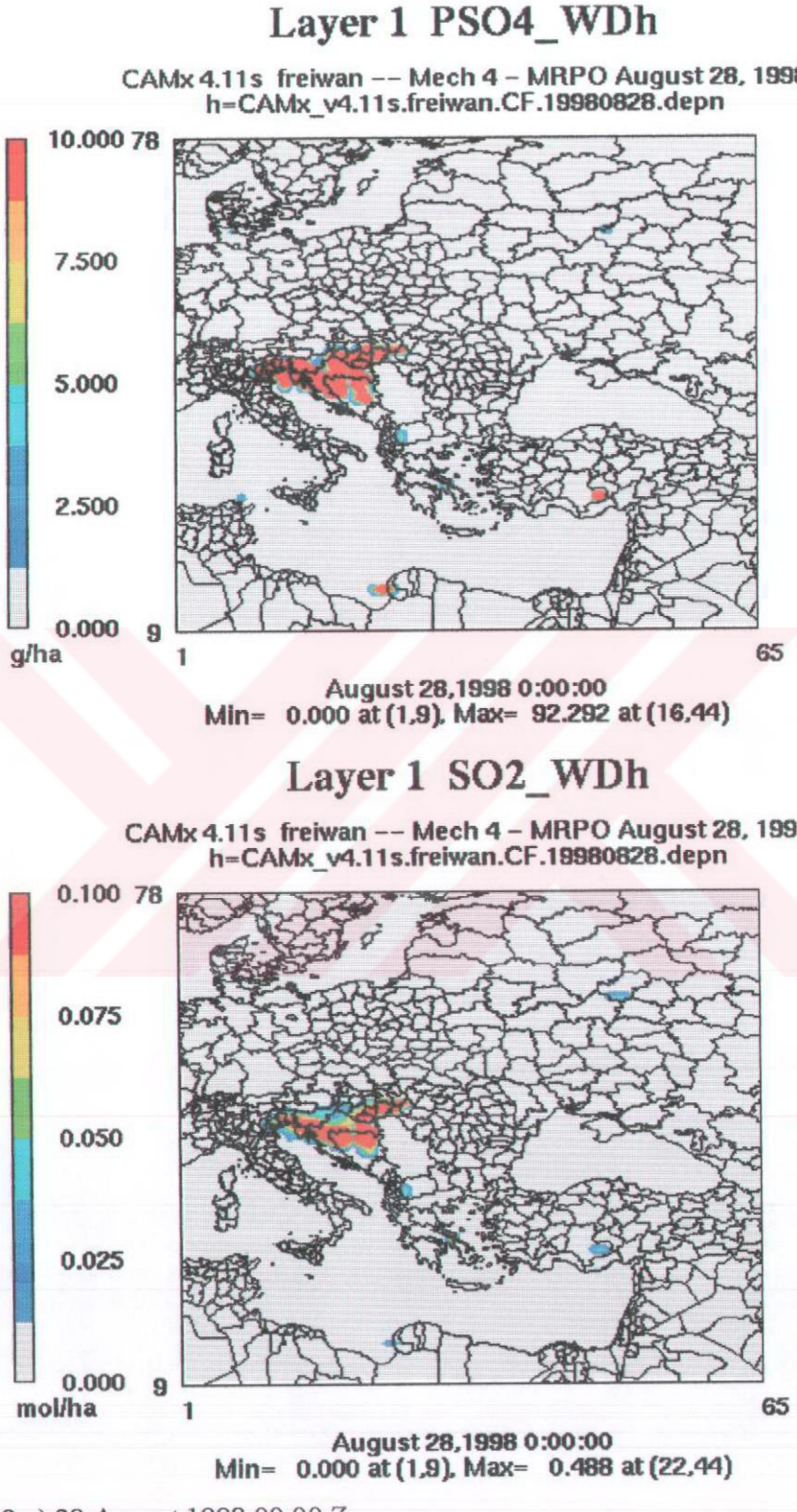

Figure E.9 e) 28 August 1998 00:00 Z.

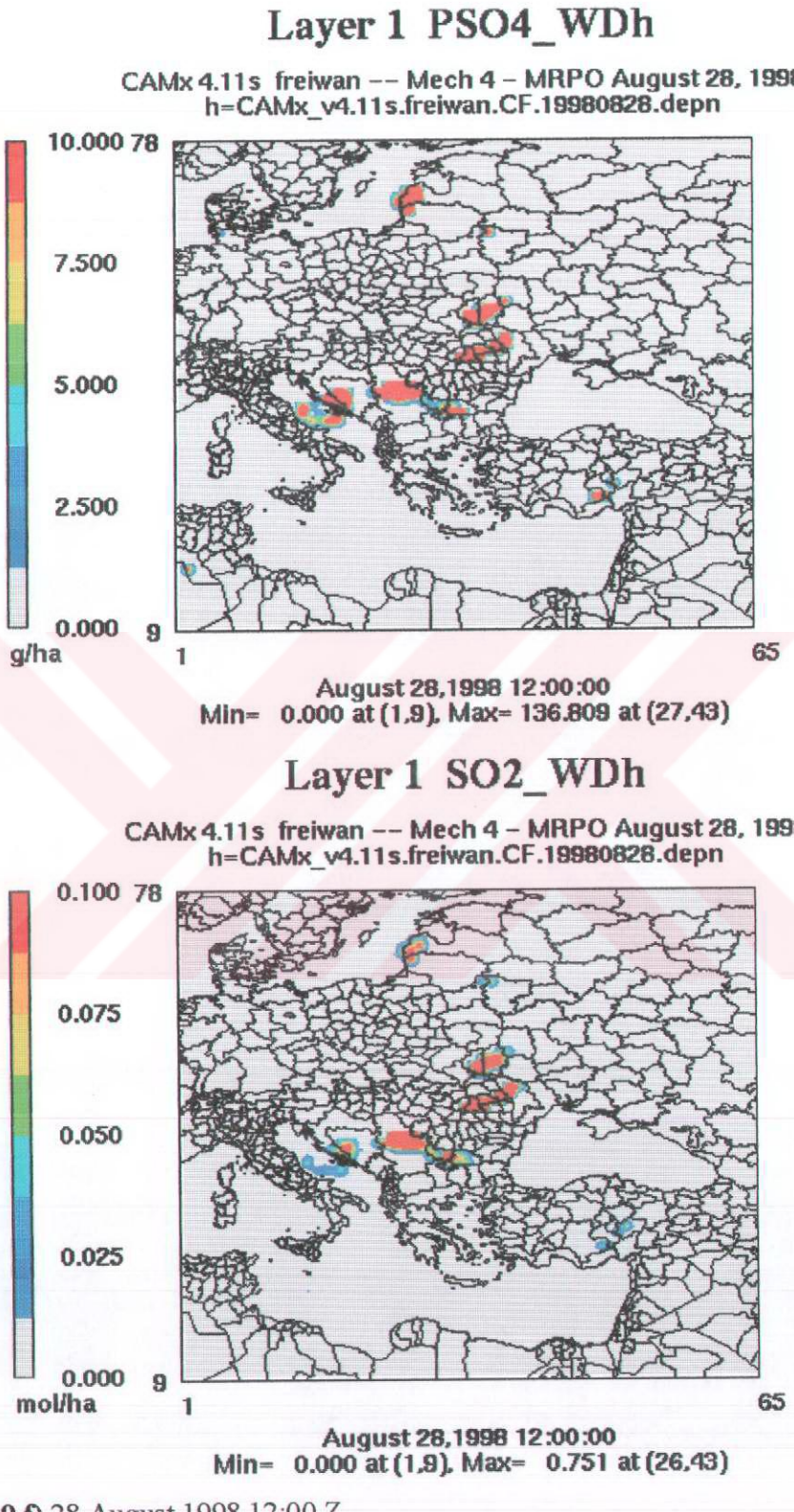

Figure E.9 f) 28 August 1998 12:00 Z.

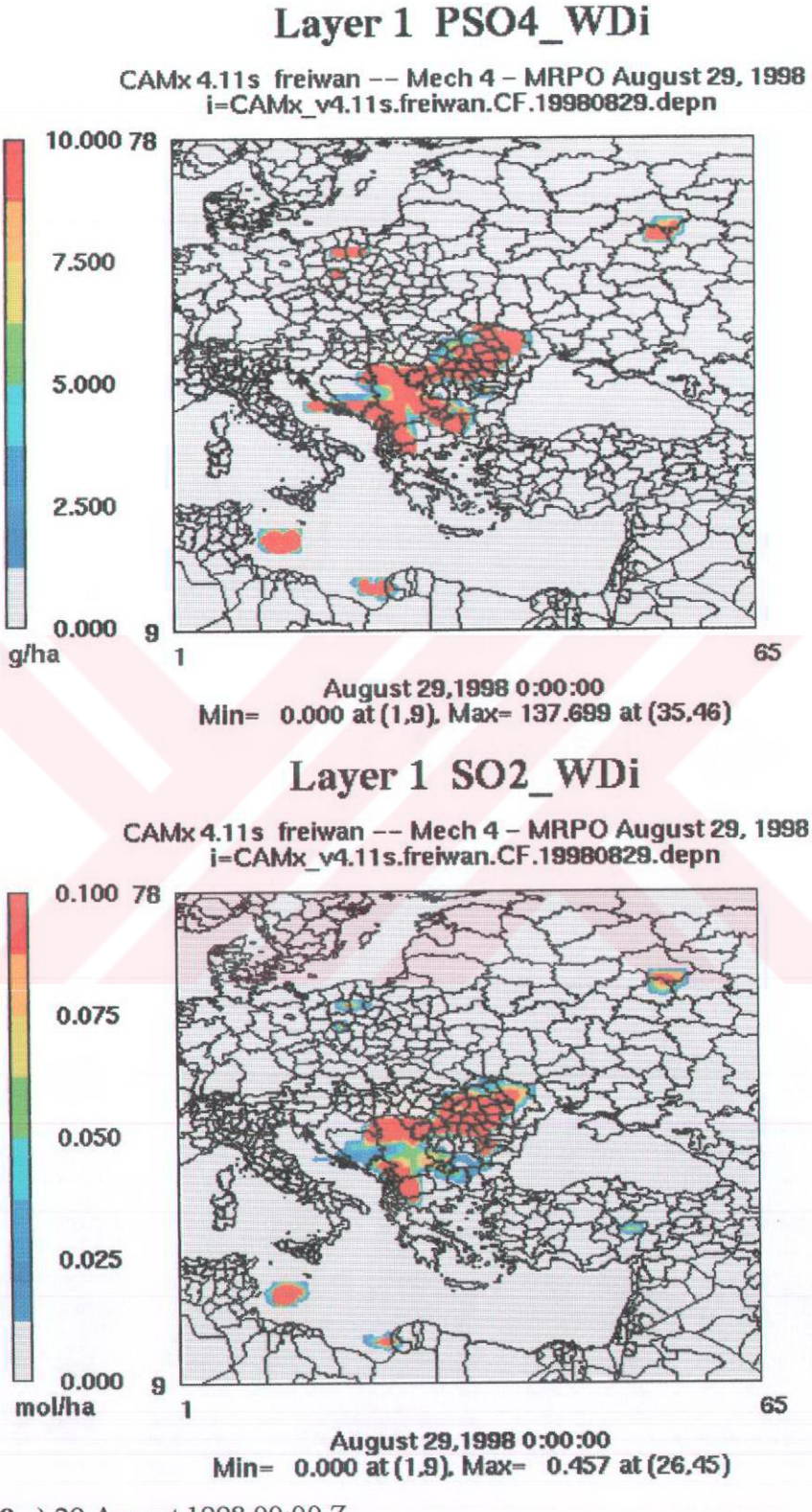

Figure E.9 g) 29 August 1998 00:00 Z.

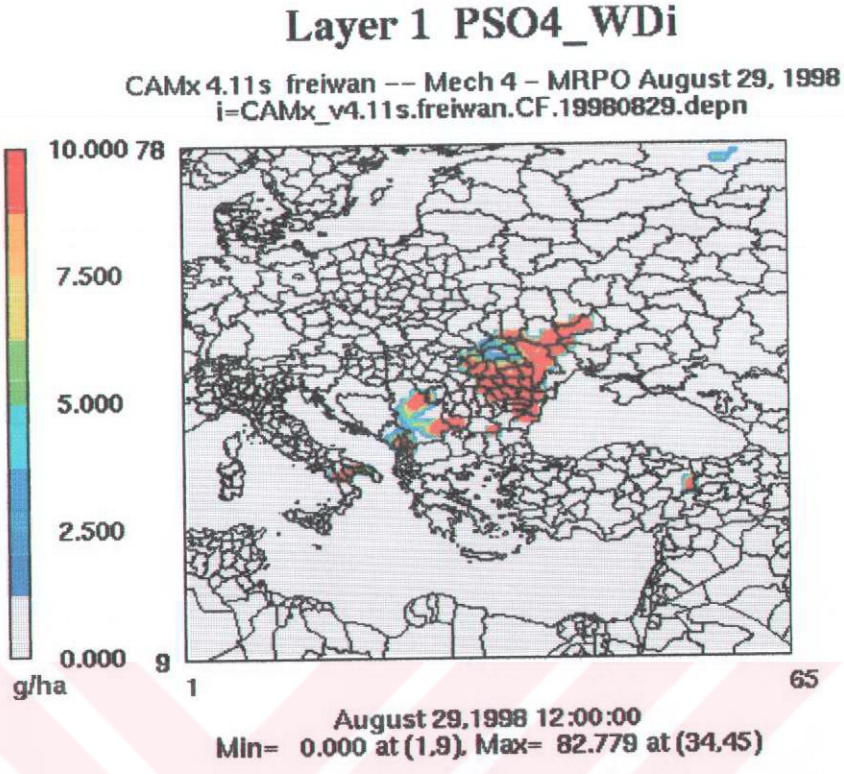

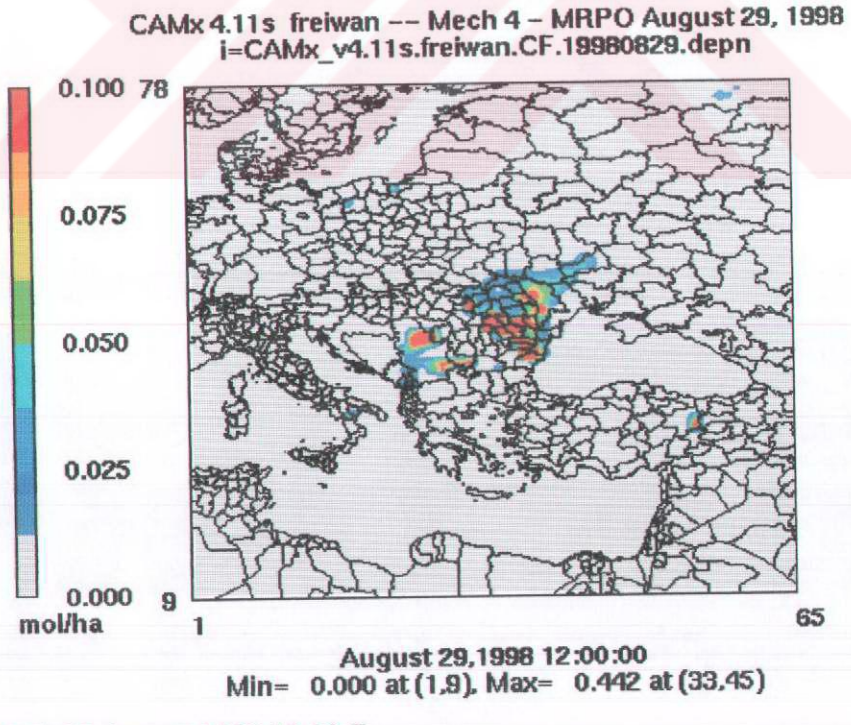

Figure E.9 h) 29 August 1998 12:00 Z.

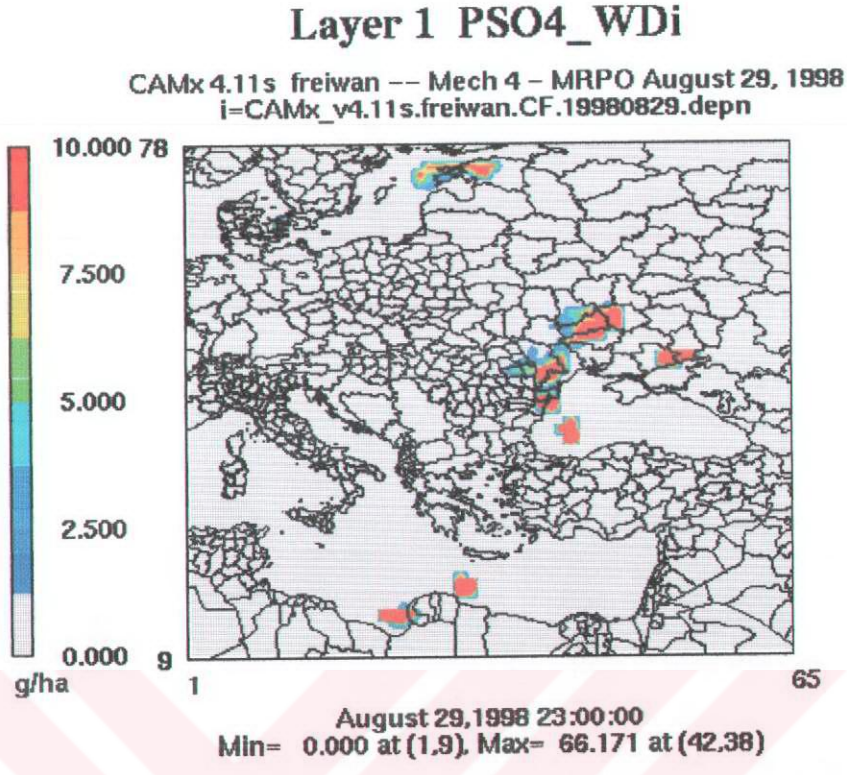

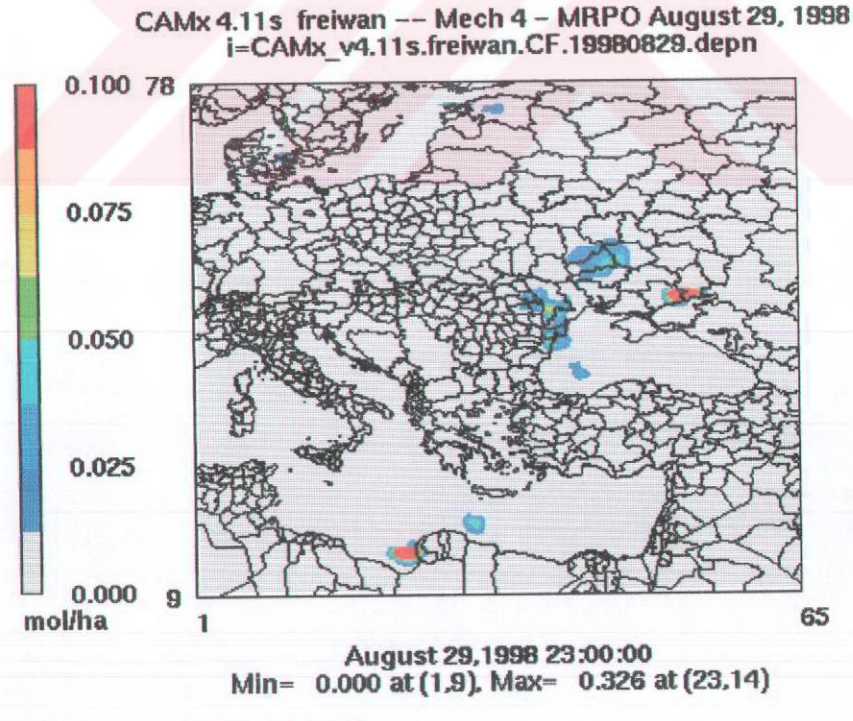

Figure E.9 i) 29 August 1998 23:00 Z.

CURRICULUM VITAE

Mr. Muwaffaq Freiwan was born in Amman on February 2, 1959. He completed his elementary and secondary education in Amman and graduated from Al Shaheed Faisal College in 1977.

He started his under graduate education in the Department of Meteorological Engineering in Istanbul Technical University in 1981 and awarded the degree of Meteorological Engineering in 1985.

After he had completed his Military Service between 1985 and 1987 he engaged the Jordan Meteorological Department in 1988 and still working to the department. He worked as a weather forecaster and then senior forecaster in National Forecasting Center. He worked as a weather report presenter in Jordan TV station for several years up to 1999. He transferred to the headquarter of Jordan Meteorological Department in August 2000 as a chief of the Climate Division in the Applied Meteorology Directorate. He started his graduate study in the Department of Meteorological Engineering in Istanbul Technical University in October 2001 and awarded his Master degree in Meteorological Engineering in January 2003. Immediately in the same month he started his Ph.D. education in the Meteorological Engineering Department.

He is married and he has four children.